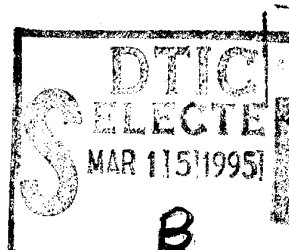


# AGARD

ADVISORY GROUP FOR AEROSPACE RESEARCH & DEVELOPMENT

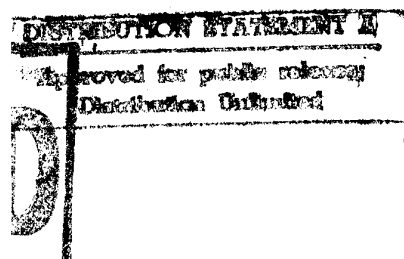
7 RUE ANCELLE 92200 NEUILLY SUR SEINE FRANCE



AGARDograph 323

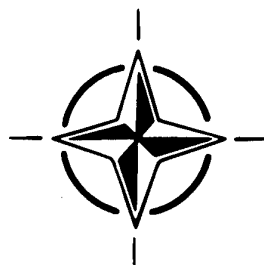
## Scale Effects on Aircraft and Weapon Aerodynamics

(Les Effets d'Echelle et l'Aérodynamique  
des Aéronefs et des Systèmes d'Armes)



*This AGARDograph has been produced at the request of the  
Fluid Dynamics Panel of AGARD.*

19950314 134



NORTH ATLANTIC TREATY ORGANIZATION

Published July 1994

*Distribution and Availability on Back Cover*

# AGARD

**ADVISORY GROUP FOR AEROSPACE RESEARCH & DEVELOPMENT**

7 RUE ANCELLE 92200 NEUILLY SUR SEINE FRANCE

**AGARDograph 323**

## **Scale Effects on Aircraft and Weapon Aerodynamics**

(Les Effets d'Echelle et l'Aérodynamique  
des Aéronefs et des Systèmes d'Armes)

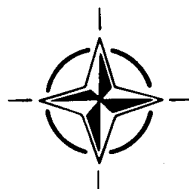
by

**A.B. Haines**  
3 Bromham Road  
Biddenham  
Bedford MK40 4AF  
United Kingdom

Edited by

**Professor A.D. Young**  
70 Gilbert Road  
Cambridge CB4 3PD  
United Kingdom

This AGARDograph has been produced at the request of the  
Fluid Dynamics Panel of AGARD.



North Atlantic Treaty Organization  
*Organisation du Traité de l'Atlantique Nord*

# The Mission of AGARD

According to its Charter, the mission of AGARD is to bring together the leading personalities of the NATO nations in the fields of science and technology relating to aerospace for the following purposes:

- Recommending effective ways for the member nations to use their research and development capabilities for the common benefit of the NATO community;
- Providing scientific and technical advice and assistance to the Military Committee in the field of aerospace research and development (with particular regard to its military application);
- Continuously stimulating advances in the aerospace sciences relevant to strengthening the common defence posture;
- Improving the co-operation among member nations in aerospace research and development;
- Exchange of scientific and technical information;
- Providing assistance to member nations for the purpose of increasing their scientific and technical potential;
- Rendering scientific and technical assistance, as requested, to other NATO bodies and to member nations in connection with research and development problems in the aerospace field.

The highest authority within AGARD is the National Delegates Board consisting of officially appointed senior representatives from each member nation. The mission of AGARD is carried out through the Panels which are composed of experts appointed by the National Delegates, the Consultant and Exchange Programme and the Aerospace Applications Studies Programme. The results of AGARD work are reported to the member nations and the NATO Authorities through the AGARD series of publications of which this is one.

Participation in AGARD activities is by invitation only and is normally limited to citizens of the NATO nations.

The content of this publication has been reproduced  
directly from material supplied by AGARD or the authors.

Published July 1994

Copyright © AGARD 1994

All Rights Reserved

ISBN 92-835-0754-1



*Printed by Specialised Printing Services Limited  
40 Chigwell Lane, Loughton, Essex IG10 3TZ*

# Recent Publications of the Fluid Dynamics Panel

## AGARDOGRAPHS (AG)

### Design and Testing of High-Performance Parachutes

AGARD AG-319, November 1991

### Experimental Techniques in the Field of Low Density Aerodynamics

AGARD AG-318 (E), April 1991

### Techniques Expérimentales Liées à l'Aérodynamique à Basse Densité

AGARD AG-318 (FR), April 1990

### A Survey of Measurements and Measuring Techniques in Rapidly Distorted Compressible Turbulent Boundary Layers

AGARD AG-315, May 1989

### Reynolds Number Effects in Transonic Flows

AGARD AG-303, December 1988

## REPORTS (R)

### Missile Aerodynamics

AGARD R-804, Special Course Notes, June 1994

### Progress in Transition Modelling

AGARD R-793, Special Course Notes, April 1994

### Shock-Wave/Boundary-Layer Interactions in Supersonic and Hypersonic Flows

AGARD R-792, Special Course Notes, August 1993

### Unstructured Grid Methods for Advection Dominated Flows

AGARD R-787, Special Course Notes, May 1992

### Skin Friction Drag Reduction

AGARD R-786, Special Course Notes, March 1992

## ADVISORY REPORTS (AR)

### Quality Assessment for Wind Tunnel Testing

AGARD AR-304, Report of WG15, July 1994

### Air Intakes for High Speed Vehicles

AGARD AR-270, Report of WG13, September 1991

### Appraisal of the Suitability of Turbulence Models in Flow Calculations

AGARD AR-291, Technical Status Reveiw, July 1991

### Rotary-Balance Testing for Aircraft Dynamics

AGARD AR-265, Report of WG11, December 1990

### Calculation of 3D Separated Turbulent Flows in Boundary Layer Limit

AGARD AR-255, Report of WG10, May 1990

## CONFERENCE PROCEEDINGS (CP)

### Computational and Experimental Assessment of Jets in Cross Flow

AGARD CP-534, November 1993

### High-Lift System Aerodynamics

AGARD CP-515, September 1993

### Theoretical and Experimental Methods in Hypersonic Flows

AGARD CP-514, April 1993

Accession For	
STIS GR&I	<input checked="" type="checkbox"/>
DTIC TAB	<input type="checkbox"/>
Unannounced	<input type="checkbox"/>
Justification	
By	
Distribution/Avail	
Availability Codes	
Dist	Avail and/or Special
A-1	



**Aerodynamic Engine/Airframe Integration for High Performance Aircraft and Missiles**  
AGARD CP-498, September 1992

**Effects of Adverse Weather on Aerodynamics**  
AGARD CP-496, December 1991

**Manoeuvring Aerodynamics**  
AGARD CP-497, November 1991

**Vortex Flow Aerodynamics**  
AGARD CP-494, July 1991

**Missile Aerodynamics**  
AGARD CP-493, October 1990

**Aerodynamics of Combat Aircraft Controls and of Ground Effects**  
AGARD CP-465, April 1990

**Computational Methods for Aerodynamic Design (Inverse) and Optimization**  
AGARD CP-463, March 1990

**Applications of Mesh Generation to Complex 3-D Configurations**  
AGARD CP-464, March 1990

**Fluid Dynamics of Three-Dimensional Turbulent Shear Flows and Transition**  
AGARD CP-438, April 1989

**Validation of Computational Fluid Dynamics**  
AGARD CP-437, December 1988

**Aerodynamic Data Accuracy and Quality: Requirements and Capabilities in Wind Tunnel Testing**  
AGARD CP-429, July 1988

**Aerodynamics of Hypersonic Lifting Vehicles**  
AGARD CP-428, November 1987

**Aerodynamic and Related Hydrodynamic Studies Using Water Facilities**  
AGARD CP-413, June 1987

**Applications of Computational Fluid Dynamics in Aeronautics**  
AGARD CP-412, November 1986

**Store Airframe Aerodynamics**  
AGARD CP-389, August 1986

**Unsteady Aerodynamics — Fundamentals and Applications to Aircraft Dynamics**  
AGARD CP-386, November 1985

**Aerodynamics and Acoustics of Propellers**  
AGARD CP-366, February 1985

**Improvement of Aerodynamic Performance through Boundary Layer Control and High Lift Systems**  
AGARD CP-365, August 1984

**Wind Tunnels and Testing Techniques**  
AGARD CP-348, February 1984

**Aerodynamics of Vortical Type Flows in Three Dimensions**  
AGARD CP-342, July 1983

**Missile Aerodynamics**  
AGARD CP-336, February 1983

**Prediction of Aerodynamic Loads on Rotorcraft**  
AGARD CP-334, September 1982

**Wall Interference in Wind Tunnels**  
AGARD CP-335, September 1982

**Fluid Dynamics of Jets with Applications to V/STOL**  
AGARD CP-308, January 1982

**Aerodynamics of Power Plant Installation**  
AGARD CP-301, September 1981

# Preface

The primary aims of this AGARDograph are:

- (i) to review the present state of knowledge on scale effects at high lift and low speeds,
- (ii) to update the reviews in AG-303 and AR-224 of scale effects in transonic flow and in particular, to comment on the achievements and limitations of the methodology proposed in AR-224 for testing in transonic tunnels and extrapolating results to full-scale,
- (iii) to review knowledge on scale effect on topics such as afterbody drag, flow over forebodies at high incidence, unsteady flow in open cavities, intakes, propellers and the effects of ice accretion,
- (iv) to draw attention to the large number of pseudo-Reynolds-number effects that can confuse the derivation of true genuine Reynolds-number effects.

Most space is given to objective (i). This is only to be expected: high lift at low speeds is fertile ground for genuine scale effects and yet, surprisingly, it has not been the subject of any previous AGARDograph. In the present document, the subject is considered logically, moving progressively from scale effect on single-element aerofoils to multiple aerofoils with deployed high-lift devices and then to three-dimensional wings including swept and slender wings and then, finally, to complete aircraft with all their practical complications.

Indeed, a deliberate feature of the AGARDograph is that in all areas, the emphasis is ultimately on the scale effect that has been observed in flight-tunnel comparisons for actual specific aircraft. It is clear that advances in aircraft design have led to the need for model tests to be undertaken at higher Reynolds numbers for the results to be extrapolated with confidence to full-scale. It is no longer true that a Reynolds number of say,  $Re = 6 \times 10^6$  is adequate either at low speeds or at transonic speeds. The data also demonstrate that scale effects at relatively high Reynolds numbers are not necessarily favourable; significant adverse effects have been observed and those are explained in principle in the AGARDograph.

Much has been learned about the reasons for scale effect but precise prediction can still be difficult and the report ends with a set of 20 recommendations for further research. The need for improved predictions of transition, for regular observations of transition in routine testing and for the application of CFD codes at both model and full-scale Reynolds numbers is emphasised.

This AGARDograph has been prepared at the invitation of the Fluid Dynamics Panel of AGARD.

# Préface

Les principaux objectifs de cette AGARDographie sont les suivants:

- (i) faire le point de l'état de l'art des effets d'échelle en hypersustentation à basse vitesse.
- (ii) mettre à jour les communications publiées dans AG-303 et AR-224, sur les effets d'échelle en écoulement transsonique, et, en particulier, de commenter les réalisations et les limitations de la méthodologie proposée dans AR-224 pour les essais en soufflerie transsonique et l'extrapolation des résultats en grandeur réelle.
- (iii) revoir l'état des connaissances en ce qui concerne les effets d'échelle sur la trainée d'arrière corps, l'écoulement à forte incidence autour des ogives, les écoulements instationnaires en cavité ouverte, les entrées d'air, et les effets de l'accumulation de glace.
- (iv) attirer l'attention sur les nombreux effets des pseudo-nombres de Reynolds qui peuvent créer la confusion quant à la dérivation des effets des vrais nombres de Reynolds.

La majeure partie de l'ouvrage est consacrée à l'objectif défini ci-dessus (i). Ceci n'est guère surprenant car le sujet de l'hypersustentation à basse vitesse représente un terrain fertile pour les effets d'échelle authentiques. Il est pourtant surprenant de constater qu'il n'a jamais fait l'objet d'une AGARDographie. Dans le présent document, le sujet est traité de façon logique, en commençant par l'effet d'échelle sur des profils à élément simple, pour examiner ensuite les profils multiples avec hypersustentateurs déployés, les voilures tridimensionnelles, y compris les ailes en flèche et les ailes minces, et enfin l'aéronef complet avec toutes les complications d'ordre pratique concomitantes.

A dire vrai, cette AGARDographie met délibérément l'accent sur les effets d'échelle observés lors des comparaisons faites entre différents appareils en soufflerie. Il est clair que suite aux progrès réalisés au niveau de la conception des aéronefs il est désormais nécessaire d'effectuer les essais sur maquette à des nombres de Reynolds plus élevés, pour que les résultats puissent être extrapolés en grandeur réelle en toute confiance. Dire qu'un nombre de Reynolds de  $Re = 6 \times 10^6$  par exemple, est adéquat à basse vitesse ou à vitesse transsonique, n'est plus possible. Les données recueillies indiquent également que les effets d'échelle aux nombres de Reynolds relativement élevés ne sont pas nécessairement favorables; des effets inverses appréciables ont été notés et le principe de ceux-ci est expliqué dans cette AGARDographie.

Beaucoup d'enseignements ont été tirés au sujet des causes des effets d'échelle mais les prédire avec certitude reste délicat. Ainsi, le rapport conclut par une série de 20 recommandations pour des futurs travaux de recherche. L'accent est mis sur la nécessité de améliorer la prévision de la transition, la réalisation d'observations régulières de la transition lors des essais courants et l'application des codes CFD aux nombres de Reynolds maquette et grandeur réelle.

Cette AGARDographie a été réalisée à la demande du Panel AGARD de la dynamique des fluides.

# Contents

	Page
<b>Recent Publications of the Fluid Dynamics Panel</b>	<b>iii</b>
<b>Preface</b>	<b>v</b>
<b>Préface</b>	<b>vi</b>
<b>1 Introduction</b>	<b>1</b>
<b>2 Scale, Reynolds Number and Pseudo-Reynolds Number Effects</b>	<b>1</b>
2.1 Scale Effects (not to be classed as Reynolds Number Effects)	2
2.1.1 Model geometric fidelity	2
2.1.2 Aeroelastic effects	3
2.2 Pseudo-Reynolds Number Effects	3
2.2.1 Type I effects	4
2.2.1.1 Tunnel calibration	4
2.2.1.2 Wall interference	4
2.2.2 Type II effects	6
2.2.2.1 Noise and stream turbulence	6
2.2.2.2 Transition position and length	7
2.2.2.3 Tunnel temperature	8
2.2.2.4 Rotational speed in propeller testing	9
2.2.3 Type III effects	9
2.2.3.1 Humidity	9
2.2.3.2 Thermal non-equilibrium	9
2.2.3.3 Model manufacturing accuracy	10
2.2.3.4 Model surface finish	10
2.2.3.5 Model support/mounting effects	10
2.2.3.6 Inclination of thrust vector	11
2.2.3.7 Final remarks	11
<b>3 Scale Effects at High Lift and Low Speeds</b>	<b>27</b>
3.1 Two-Dimensional Single Aerofoils	27
3.1.1 Sources of data	27
3.1.2 Types of stall	27
3.1.3 Sources of scale effect and their prediction	28
3.1.3.1 Bubble growth and bursting	28
3.1.3.2 Leading-edge stall by turbulent re-separation	30
3.1.3.3 Turbulent separation ahead of the trailing edge	31
3.1.4 Examples of scale effect	32
3.1.4.1 Early NACA tests	32
3.1.4.2 Other examples	33
3.1.4.3 Summary of conclusions	35
3.2 Two-Dimensional Multi-Element Aerofoils	35
3.2.1 Sources of scale effect	35
3.2.2 Examples of scale effect	37
3.2.2.1 Flap effectiveness	37
3.2.2.2 Slat effectiveness	40
3.2.2.3 Scale effect for complete configuration	40

	Page
3.2.3 Theoretical prediction of scale effects	42
3.2.4 Summary of conclusions	43
3.3 Three-Dimensional Wings	44
3.3.1 Sources of scale effect	44
3.3.2 Transition prediction for a sweptback wing	45
3.3.2.1 Transition due to cross-flow instability	45
3.3.2.2 Transition due to contamination along the attachment line	46
3.3.3 Examples of scale effect on wings of low sweepback	47
3.3.3.1 Conventional scale effect	47
3.3.3.2 Bubble-dominated scale effect	48
3.3.3.3 Slot-flow dominated scale effect	48
3.3.3.4 Transition-dominated scale effect	49
3.3.4 Examples of scale effect on wings of moderate sweepback	50
3.3.4.1 Early evidence: conventional and bubble-dominated scale effect	50
3.3.4.2 Recent evidence: transition-dominated scale effect	52
3.3.5 Examples of scale effect on slender wings	53
3.3.5.1 Sources of data	53
3.3.5.2 Slender wings with sharp leading edges	53
3.3.5.3 Slender wings with round leading edges	54
3.3.5.4 Updated interpretation of earlier results and conclusions	56
3.4 Complete Aircraft	57
3.4.1 Introduction	57
3.4.2 The overall picture	58
3.4.2.1 $C_{Lmax}$ : evidence from model tests	58
3.4.2.2 $C_{Lmax}$ : flight-tunnel comparisons	59
3.4.2.3 Post-stall pitching moments	60
3.4.3 Examples of scale effect for specific aircraft	60
3.4.3.1 UK aircraft 1945-1965	60
3.4.3.2 Boeing 747	61
3.4.3.3 The Fokker family	62
3.4.3.4 The Airbus family	63
3.4.4 3D problem areas	63
3.4.5 Summary of general conclusions	65
<b>4 Scale Effects at Transonic Speeds</b>	<b>139</b>
4.1 Introduction	139
4.2 Recapitulation of AGARD Methodology	139
4.3 Recent Research (including Experience with Methodology)	140
4.3.1 Effects of a rear separation	140
4.3.2 Conversion of aft transition to $Re_{EFF}$ with forward transition	141
4.3.3 Examples of scale effect	142
4.3.3.1 Wave drag	142
4.3.3.2 Shock-induced separation	143
4.3.3.3 Buffet-onset	144
4.4 Limitations on Ability to Apply Methodology	144
4.5 Research Not Directly Connected with Methodology	145
4.5.1 Unsteady flow in buffet	145
4.5.2 Combat aircraft wings	146
4.5.3 Slender wings	147
4.6 Conclusions and Possible Future Trends	147

	<b>Page</b>
<b>5 Scale Effects on Aircraft Drag</b>	<b>166</b>
5.1 Prediction of Wave Drag and Viscous Drag	166
5.2 Flight-Tunnel Comparisons	167
5.3 Afterbody Drag	168
5.3.1 Genuine or pseudo re-effect?	168
5.3.2 Evidence from research tests	169
5.3.3 Evidence from tests for specific aircraft	170
5.3.4 Conclusions	171
<b>6 Scale Effects in Flow over Bodies</b>	<b>180</b>
6.1 Transition and Types of Flow	180
6.2 Body Forces and Moments at High Incidence and Zero Yaw	182
6.3 Forebody Flow on the F/A 18	185
6.3.1 Surface flow patterns	185
<b>7 Scale Effects in other Important Areas</b>	<b>204</b>
7.1 Internal Store Carriage	204
7.2 Intakes	205
7.3 Propellers	206
7.4 Ice Accretion	208
<b>8 Conclusions and Recommendations</b>	<b>222</b>
<b>9 Acknowledgements</b>	<b>225</b>
<b>References</b>	<b>226</b>

## 1 INTRODUCTION

The prediction of scale effects is a vital element in the overall task of forecasting aircraft performance, stability and control on the basis of model tests in wind tunnels or other facilities. This fact has been recognised by the Fluid Dynamics Panel of AGARD in recent years. Two important documents were published in 1988: first, Agardograph 303<sup>1</sup>, which reviewed Reynolds number effects in transonic flow and second, the final report of Working Group 09 on "Boundary Layer Simulation and Control in Wind Tunnels". It was still felt, however, that a further Agardograph was needed: in particular, it was noted that there had never been an Agardograph on scale effect at high lift and low speeds, ie for aircraft in the take-off and landing conditions. This may appear surprising because it was known as long ago as 1933 that the low speed stalling characteristics of aerofoils and wings could vary considerably with Reynolds number. The first aim of the present Agardograph is to fill this gap while a second aim is to give examples of where scale effect has been observed in tests on actual aircraft configurations and to interpret this scale effect in terms of what has been learnt from research experiments and calculations. Despite the fact that the emphasis will be on scale effect at high lift and low speeds, there is no restriction to this speed range and the Agardograph also contains some further discussion of scale effects at transonic speeds and some reference to the more limited evidence available for supersonic speeds.

The determination of scale effects may, at first sight, appear to be a simple task. One can either test a model in a pressurised tunnel over a range of Reynolds number, or one can compare the results of tests on models of the same design but at different scales or, as the final arbiter, one can compare the results of model tests with the behaviour of the full-scale aircraft or weapon in flight. All these approaches are however beset with technical difficulties and uncertainties. Effects which initially may appear to be due to changes in Reynolds number are, on analysis, found to be due to some other variable and so, as in the case of AGARD 303<sup>1</sup>, it has been thought necessary to include in Chapter 2 at the start of this Agardograph a fairly lengthy description of these "pseudo-Reynolds number" effects which can confuse the story unless one can take great care in the reduction and interpretation of the test results. This chapter also stresses that the terms "scale effects" and "Reynolds number effects" are not necessarily synonymous.

Having dealt with the red herrings which serve to confuse the story, one still finds that there are substantial genuine Reynolds number and scale effects that are, in many cases, difficult to predict. This Agardograph discusses these effects under four broad headings:

- (i) scale effect at high lift and low speeds: this is discussed in depth, advancing logically from the evidence for two-dimensional single aerofoils to two-dimensional multiple aerofoils and then to three-dimensional wings, including the effects of sweepback, and finally to slender wings. Results for various specific aircraft are then described and interpreted in the light of the general research discussed in the preceding paragraphs,
- (ii) scale effect at transonic speeds: to avoid too much duplication with the earlier Agardograph, this is not handled in as much detail but the present document does contain some new material; in particular, it describes some experience in the use of the methodology proposed in the WG09 report<sup>2</sup> and some thoughts about its applicability in the future,

- (iii) scale effects on some of the main contributions to aircraft and weapon drag including viscous drag, wave drag, afterbody drag and spillage drag,
- (iv) scale effects in various important specific scale-sensitive areas such as forebody vortex flows, the flow in and near open cavities, the flow into an air intake, the flow over propellers and finally, the effects of ice accretion.

The Agardograph ends with some recommendations as to what is required to place the prediction and measurement of scale effects on a sounder basis. It is hoped that the present report will show that although much has already been learnt about the nature of likely scale effects, quantitative prediction for a new design is often still far from easy. It is often possible, in retrospect, to explain what happens but this may not necessarily help in predicting the scale effect for even the next configuration in the same family. This is particularly true at low speeds with the high-lift devices extended. It is hoped that the detailed review in this report will help to inculcate the right attitude of mind. The simple advice is that when faced with an apparently mysterious new result, one should stand back and consider what is the nature of the flow and whether and how this flow is likely to change with scale and/or Reynolds number. "Understand the flow" is a better maxim than "use the numbers from the last aircraft".

There are several respects in which the Agardograph is not fully comprehensive. Experiments in unsteady flow, apart from the specific case of the flow in and near cavities, are only mentioned in passing. For a general discussion of scale effects in unsteady flow, the reader is referred to Ref 4. Also, the Agardograph does not consider topics such as the scaling rules for the reingestion of flow into intakes near the ground.

## 2 SCALE, REYNOLDS NUMBER AND PSEUDO-REYNOLDS NUMBER EFFECTS

Most model tests in wind tunnels are undertaken at Reynolds numbers that are far below the values in flight. It is therefore a natural temptation to equate "scale effects" with "Reynolds number effects". Differences in Reynolds number are not however the only reason why there may be disagreement between model test and flight results. In many cases, the model may not represent the full-scale vehicle in all its detail, ie there may be a lack of geometric fidelity. Also, it is unlikely that the model and aircraft will have the same aeroelastic effects; in general, most wind tunnel models are classed as "rigid models" but aircraft, relatively speaking, are flexible. In addition, there are a multitude of reasons why pseudo-Reynolds number effects can be present. This is a term introduced by Aulehla<sup>3</sup> and Binion<sup>1</sup> to denote effects which, if unrecognised, will be wrongly interpreted as Reynolds number effects. Three broad types of pseudo-Reynolds number effect can be distinguished:

- I Those that arise through not allowing for the Reynolds-number dependence of parameters or corrections used in the reduction of the test data,
- II Those that arise because one has not appreciated that in the data being compared, Reynolds number is not the only independent variable that is changing as one varies Reynolds number, and
- III Those that are present because the test results are affected by some factor, not necessarily Re-dependent,

but which does not apply equally to all the data being compared.

Some examples of scale effect that are not Reynolds number effects, and of pseudo-Reynolds number effects are given below in §§2.1 and 2.2 respectively.

Turning to the genuine Reynolds-number effects, it is useful at the outset to distinguish between two types of effect as identified originally by Elsenaar<sup>6,2</sup>:

- (a) "Direct" Reynolds number effects which arise as a result of changes in the boundary layer (and wake) development for a fixed or "frozen" pressure distribution. A simple example of a direct effect is the change with Reynolds number in the skin friction on a flat plate,
- (b) "Indirect" effects associated with changes in the pressure distribution resulting from the changes with Reynolds number in the boundary layer and wake development. A good example of an indirect effect in transonic flow is the possible change with Reynolds number in the shock strength and hence, wave drag for a given lift coefficient.

Many other examples of direct and indirect effects will appear later in this Agardograph.

## **2.1 Scale Effects** (not to be classed as Reynolds number effects)

### **2.1.1 Model geometric fidelity**

Clearly, on small models, it is often not possible to reproduce many detailed features of the full-scale vehicle. The geometry is inevitably somewhat simplified on a small model and comparisons between test results on models at different scales may therefore become misleading as a guide to genuine Reynolds number effects. Testing of external store installations on combat aircraft provides many examples of this type of scale effect. For example, omission of details such as the crutch arms and other excrescences on an early standard multiple carrier was found to almost halve the measured drag increment of the store array when mounted externally on an aircraft model but this simplification often had to be accepted in tests on small models. In comparing the results of such tests with those on a fully representative larger model, the 2:1 factor would appear as a "scale effect" but it would clearly be quite wrong to conclude that it was a Reynolds-number effect. Arguably, this type of scale effect might have been predictable and allowed for in the interpretation of the results but it is not always as straightforward as this. Figs 2.1(a,b) are a good example of where model scale as distinct from Reynolds number has a marked influence on drag results even in tests that are strictly being made specifically to investigate Reynolds number effects. These results in Fig 2.1, taken from Ref 7, show how the measured drag of first, 1/4 scale and then full-scale stores vary with Reynolds number in tests in the DRA 5 metre tunnel and also, the ARA transonic tunnel in the case of the 1/4 scale stores. It will be seen that most of the 1/4 scale stores exhibit no significant variation of drag over a range of more than 3:1 in Reynolds number whereas with the full-scale stores, all the drag values decrease by up to 12% with increasing Reynolds number as would be expected by comparison with the predicted variation of skin friction drag. No attempt should be made to compare actual values in Figs 2.1(a,b); it is the different trends

that are significant. One can accept Fig 2.1(b) as being the correct trend with Reynolds number but the picture in Fig 2.1(a) is confused by other effects associated with the small model scale. Ref 7 suggests that one contributory factor in Fig 2.1(a) is that the excrescences on the store were scaled geometrically and that, as a result, they tend to be immersed in the relatively thick boundary layers at low Reynolds number but protrude out of the thinner boundary layer at higher Reynolds number. A similar remark could be made about the roughness bands used to fix transition which were not changed in sympathy with the test Reynolds number. Ref 7 further speculates that in the two cases in Fig 2.1(a) where there is some variation of drag - first, a decrease and then an increase with Reynolds number, - the explanation could be that a separation bubble on the nose of the bluff-nosed stores was changing in size; if so, this would be classed as a genuine Reynolds number effect. It should be noted that the graphs are plotted against R/metre; clearly, if, in cases where there are data for both 1/4 and full-scale models of the same store, an attempt had been made to plot all these data as a single curve against Reynolds number based on some representative store dimension, one would not have been successful: the "scale effects" would have disturbed the genuine trend with Reynolds number.

As another example having a link with the above, model geometry is also an important issue when comparing model and full-scale results for the effectiveness of conventional vortex generators. In the early work<sup>8</sup> on this subject, it was often found that the best results were obtained with a generator height equal to about the local boundary layer thickness. Expressed this way, one is tempted to conclude that in going from model to full-scale, one should scale the generators in sympathy with the local boundary layer thickness. However, this does not follow: the vortex generator effectiveness is determined by the paths of the vortices shed by the generators and in going from model to full-scale, one should maintain the same non-dimensional generator height above the wing surface. One then has to remember that the scale effect on the drag increment due to the generator contains a contribution from the fact that, full-scale, more of the generator is outside the boundary layer. One might consider this to be an indirect scale effect although it does not really satisfy the definition given earlier.

To move on to an example where simplification of the geometry leads to a "scale effect" that might not have been foreseen, it is common practice with a small model not to attempt to represent the true intake flow in tests where the aim, for example, is to measure the loads on the external stores. However, depending on the location of the stores, this can lead to results that are far removed from the full-scale values and where the differences might be wrongly interpreted as a Reynolds number effect. In illustration of this point, Fig 2.2<sup>9</sup> shows the effects of intake spillage on the carriage loads at zero incidence and sideslip for a range of store positions; it will be seen that the effects are very large for the store at station 3. The yawing moment, side force and pitching moment loads for the store in this position are 50 to 100% larger under maximum spillage conditions than with the cruise intake mass flow. It was also found in the same tests that the effects of fairing over a relatively small environmental control system inlet located on the inlet diverter, ie a relatively small change in model geometry, had a significant effects approaching 50% on the store pitching moments. Once again, comparison of results for the simplified small model and full-scale in flight would show significant scale effects but they would not be Reynolds number effects.



It may be argued that the above discussion has been unnecessary. Some readers may say that it is surely obvious that if one does not test the correct geometry on the model, one will not necessarily obtain the full-scale results. Nevertheless, to many experimenters, "scale effects" means the effects that arise because it is physically impossible to represent the correct geometry on a small model, or, as seen above, there are cases where it is not even clear what should be the correct representative model geometry to test. These ambiguities and uncertainties have to be identified before one can determine "Reynolds number effects" with any confidence.

### 2.1.2 Aeroelastic effects

There are two reasons why aeroelastic effects can lead to an apparent scale effect. First, with some aircraft, aeroelastic effects produce notable changes in the shape of the aircraft with operating condition and second, a nominally rigid model may change its shape significantly when tested at high pressure in a pressurised tunnel. The first reason is particularly important when testing models of combat aircraft with variable-sweep wings. Typically, for such aircraft, there can be a change in wing twist (increased washout) of as much as  $5^\circ$  in a manoeuvre condition relative to the shape in cruise. For this reason, the aerodynamic characteristics will be different from those measured with a rigid model in a wind tunnel. Attempts have been made to quantify these effects either by making flexible models with the same aeroelastics as the full-scale aircraft or, more simply, by making a family of rigid models simulating the full-scale twists in different operating conditions. Some comparative results from two such investigations are shown in Figs 2.3 and 2.4. These results, which were obtained in the ARA transonic tunnel in the 1970s, show that the differences, particularly in the tail-on pitching moments, can be quite significant.

In the first example in Fig 2.3, changing from the cruise wing to the manoeuvre  $6.8^\circ$  wing completely eliminates the pitch-up trend above about  $C_L = 0.6$  at  $35^\circ$  and  $0.8$  at  $50^\circ$  sweep and  $M = 0.8$ . Clearly, if only the results for the cruise wing had been obtained and if these had been compared with the full-scale aircraft behaviour in flight with no allowance for aeroelastic distortion, one would have been completely misled about the effects of Reynolds number.

A similar conclusion can be drawn from the second example in Fig 2.4 but it is a more complicated story. In this case, the wing of a variable-sweep design is at its maximum sweep ( $68^\circ$  on the leading edge) and, as shown in Fig 2.4(a), the tailplane is close to and below the outer wing trailing edge. The aerodynamics of this closely-coupled configuration is very complex, particularly at high incidence and at Mach numbers close to  $M = 1.0$ . Strong primary vortices are shed from the intake lip and from the nib/wing leading edge with the flow under the inner vortex containing a shock wave which can induce a secondary separation at transonic speeds. Serious non-linearities in the pitching moment characteristics were observed, as illustrated in Fig 2.4(c), and detailed analysis of the results showed that these occurred when the flow over the outer wing outboard of these vortex systems finally collapsed. It was also found that there was a close interaction between the tailplane and the flow development over the wing: for example, the precise Mach number for the serious pitching moment behaviour depended on the tailplane angular setting.

The aim in the selection of figures in Fig 2.4 is to illustrate how these characteristics are modified by the aeroelastics of the wing at high incidence. The aeroelastic effects result in the outer

wing trailing edge moving up and away from the tailplane, thus relieving the aerodynamic coupling between the surfaces. Figs 2.4(b,c) show that as a result, the serious pitch-up behaviour is alleviated considerably but not eliminated. In detail, with the high-incidence bent wing, there is a mild loss in stability near  $\alpha = 13^\circ$ ,  $C_L = 0.87$  which is mostly associated with a loss in lift-curve slope on the tailplane (Fig 2.4(d)). With the low-incidence wing, the change in tail lift-curve slope is in the opposite direction. These different trends on the tailplane were traced to differences in the flow development over the wing upper surface: on the high-incidence bent wing, the vortex system moves inboard and rearward more rapidly, thus increasing the effective downwash over the tailplane and hence giving the reduction in tail lift-slope. The effect of the wing aeroelastics on the flow development over the wing upper surface at incidences near and above  $\alpha = 19^\circ$  are more striking: with the basic low- $\alpha$  wing, Fig 2.4(e) shows that the suction peaks at  $0.9 \times$  semi-span have collapsed dramatically at  $\alpha = 19.1^\circ$  (and this collapse has in fact spread in to  $0.65 \times$  semi-span), whereas, with the high- $\alpha$  bent wing, this collapse is only just about to start at  $\alpha = 19.1^\circ$ . The effects of these changes in wing flow and tailplane aerodynamics on the overall pitching moment behaviour would be difficult to predict in the absence of the test on the bent wing. If one had only been able to compare results for the aeroelastic aircraft and a rigid model built with the cruise twist, the differences might easily have been considered to be a favourable "scale effect" or even, a Reynolds number effect. In passing, it may be noted that the description of the flow did contain at least one feature that could be the source of a genuine Reynolds-number effect in that the flow between the two vortices contains a shock-induced separation but there was no evidence as to the extent to which this determines the overall characteristics.

The above two examples show that it can be important to allow for the aeroelastic effects before drawing conclusions about Reynolds number effects from a flight-tunnel comparison but turning to the second reason why aeroelastic effects can be significant, a nominally "rigid" model wing can itself distort appreciably when tested in a pressurised tunnel. A sweep through a range of pressures to establish a trend with Reynolds number is therefore accompanied by changes in the aeroelastic distortion and thus, the aerodynamics of the model under test. This is a live topic at the present time; it is suspected that some unexpected results at high Reynolds number on some multiple-aerofoil configurations may be due to the aeroelastic distortion of the trailing-edge flap on the models (see §3.2). Strictly, aeroelastic effects in this sense should probably figure in the list of pseudo-Reynolds number effects.

### 2.2 Pseudo-Reynolds Number Effects

Pseudo-Reynolds number effects were discussed in both Refs 1,2 but they are such a vital issue that it was thought worthwhile, even at the expense of some repetition, to include a further discussion in this Agardograph. There is some extra material and the list of possible pseudo effects has become even longer.

Probably, the most important pseudo-Reynolds number effects are those relating to the tunnel facility itself. These are the leading examples of pseudo effects of type I, ie pseudo effects that arise because of a failure to recognise that parameters or corrections used in the reduction of the test data are themselves dependent on Reynolds number. This applies to all aspects of the empty tunnel flow calibration and also, the wall interference effects. The need to pay attention to these effects is highlighted by the inconsistencies in Figs 2.5 and 2.6.

Fig 2.5 was first presented<sup>10</sup> by McCroskey during the Round Table discussion at the end of the AGARD FDP Symposium on Wall Interference in 1983. While it is possible to argue that Fig 2.5 succeeds in indicating a clear trend with Reynolds number, the scatter in the data (drawn from many different sources) at a given Reynolds number is very large. One could have hoped for much less scatter bearing in mind that this is a very simple test case: the lift-curve slope at low incidence and low Mach number for the NACA 0012 aerofoil which could not possibly be described as an advanced aerofoil as regard its demands on the boundary layer. Errors in estimating tunnel wall interference were suspected as a major reason for the scatter.

In the present context, Fig 2.6 is even more disturbing. This picture is taken from a 1980 review<sup>11</sup> by Pozniak of the observed trends with Reynolds number in the variation of afterbody pressure drag. The results demonstrate a complete lack of consistency. However, from 1974 onwards, Aulehla has been able to show that the problem in this case was a failure to recognise that, in a pressurised tunnel, the basic tunnel flow calibration is likely to vary with stagnation pressure or unit Reynolds number.

These leading examples of pseudo-Reynolds number effects are discussed in more detail in §2.2.1 below and then, other pseudo effects of types II and III are introduced in §§2.2.2 and 2.2.3.

## 2.2.1 Type I effects

### 2.2.1.1 Tunnel calibration

As noted above, the implausible variation with Reynolds number of some test data for afterbody pressure drag prompted the thinking that the explanation might lie in a pseudo-Reynolds number effect associated with the empty tunnel flow calibration. Aulehla and Besigk<sup>12</sup> noted that the change with Reynolds number of the mean of the pressure coefficients on afterbodies under test in the DLR pressurised tunnel at Göttingen was virtually identical to the variation in the pressure coefficients for holes in the walls of the tunnel. This evidence suggested that the apparent increase in afterbody pressure drag with Reynolds number that had been observed in both the DLR and AEDC 16T tunnels might be due to a systematic error in the empty tunnel static pressure that had been used in the reduction of the results. Calibration of the tunnels over a range of Reynolds number confirmed this suspicion. Fig 2.7 shows<sup>13</sup> one example of the effect of allowing for the change with Reynolds number in the tunnel static pressure calibration; it will be seen that the apparent increase in afterbody pressure drag has virtually been eliminated by using the true calibration. It is noted in Ref 1 that the sensitivity of afterbody pressure drag near zero to errors in the tunnel calibration is given by the equation

$$\Delta C_D = \frac{2A}{A_w} \cdot \frac{\Delta M}{M(1+0.2M^2)} \quad (2.1)$$

where  $A$  is the body cross-sectional area,  $A_w$  the wing area, and  $M$  the tunnel Mach number.

Both the DLR and AEDC tunnels have perforated walls with 60° inclined holes and Aulehla<sup>14</sup> suggested that the reason for the change in static pressure calibration with unit Reynolds number was that the forward inclined perforations acted as flush inlets, whose recovery increased as the wall boundary layer became thinner with increase in Reynolds number. However, it would be wrong to conclude that one need only worry about this type

of effect in perforated-wall tunnels with inclined holes. In all tunnels, irrespective of whether they have ventilated walls with the calibration being in terms of the pressure in the surrounding plenum chamber or have solid walls with the calibration being in terms of a wall pressure far upstream of the model, the calibration can, in principle, be a function of the stagnation pressure because it is likely to vary with the thickness of the wall boundary layer.

Aulehla in a recent paper<sup>5</sup> has drawn attention to the fact that failure to allow for this variation in the tunnel calibration with pressure can be important in more than just partial-model testing. For example, it can also lead to a spurious trend with Reynolds number in shock position or in  $C_{L,max}$  in any case where these results are also varying significantly with Mach number. An example of this type of pseudo-effect, taken from Ref 5 is presented in Fig 2.8. These results are for the CAST 7/D0A1 aerofoil in the DLR Braunschweig 0.34 x 0.675 m tunnel. The upper picture suggests that an increase in Reynolds number from  $6 \times 10^6$  to  $11 \times 10^6$  gives an increase in  $C_{L,max}$  of 0.014 at  $M = 0.70$  and 0.027 at  $M = 0.76$  but before accepting these as a true Reynolds number effects, one has to eliminate the pseudo-effect due to a known error in Mach number associated with the error in tunnel static pressure that has been used in obtaining these results. The lower picture shows that in this Mach-number range,  $C_{L,max}$  decreases rapidly with Mach number. It is known that the mean wall pressure coefficients increased with Reynolds number in this tunnel, thus implying a decrease in the true Mach number relative to the nominal value. Aulehla shows in Ref 15 that this error in Mach number can account for about 70% of the observed apparent trends in  $C_{L,max}$  with Reynolds number. Similar pseudo-Reynolds number effects on shock position results from tests in the Göttingen tunnel before it was recalibrated in terms of unit Reynolds number were found to be sufficient to change even the direction of shock movement with Reynolds number and so, there is no doubt that these effects if ignored can be significant. There may also be changes with Reynolds number in the empty tunnel buoyancy and the flow angularity.

It should however be remembered that these pseudo-Reynolds number effects are only present when one ignores mistakenly, changes in the tunnel calibration with stagnation pressure. One should not deduce from Ref 14 that genuine Reynolds number effects on shock position (and  $C_{L,max}$ ) are always likely to be small; they can be substantial, as will be seen later in §4 on the basis of CFD calculations, where this issue of pseudo-Reynolds number effects does not arise. The issue about pseudo-effects should not be overplayed; in the author's opinion, the vast majority of 2D data are not affected in this way.

### 2.2.1.2 Wall interference

Both Refs 1,2 note that wall interference can be a source of pseudo-Reynolds number effects in tunnels with ventilated walls and particularly perforated walls. In future, one can hope that tunnels will be designed with self-adaptive walls to avoid these problems but this is outside the scope of the present Agardograph. The classic approach to the estimation of wall interference corrections in such tunnels was to calculate the corrections for a corresponding tunnel with closed walls and then to multiply by factors<sup>15</sup> which depended on porosity factors which were themselves functions of the slope,  $P$ , of the pressure drop versus outflow through the wall relationship. Goethert<sup>16</sup> in early work at AEDC presented results that showed that  $P$  for a wall of given geometry depended on the thickness of the wall boundary layer. Hence, in principle at least, it follows immediately that the wall interference corrections

depend on the tunnel unit Reynolds number. Despite these early indications, many establishments chose either to ignore wall interference or to determine their wall interference corrections by comparing the results of tests on a family of models of some standard test case at different scales. Reynolds number effects were avoided in pressurised tunnels by changing the pressure so that each model was tested at the same Reynolds number. While this approach may lead to a satisfactory first-order assessment of the wall interference, it cannot provide the accuracy required by present standards because it ignores the fact that as one changes the tunnel pressure, the boundary layer thickness on the walls and hence, the wall interference also changes. The present author believes that this could easily be a main contributory factor to the scatter in Fig 2.5.

Both Chan<sup>17</sup> and Jacocks<sup>18</sup> have confirmed that, with porous walls, the wall cross-flow characteristics are a function of the local wall boundary-layer thickness and Jacocks has correlated the classical wall porosity parameter,  $P = dC_p/d\theta$ , for a perforated wall with  $60^\circ$  inclined holes, with a non-dimensional wall parameter,  $(\tau/d)^2 Re_\delta^*$ , where  $\tau$  is the wall porosity,  $d$  the hole diameter and  $Re_\delta^*$  the Reynolds number based on the porous wall boundary-layer displacement thickness. This relationship is reproduced in Fig 2.9. The form of this relationship confirms the dependence on Reynolds number. With the aid of this result, it has become possible for AEDC to develop a pre-test procedure for predicting the wall interference in a tunnel with walls with  $60^\circ$  inclined holes. This has been applied successfully as demonstrated in Ref 19.

Reynolds number can enter into the wall interference corrections for a second reason. The boundary-layer growth on the walls is influenced by the pressures induced by the flow field around the model under test. This flow field is itself dependent on Reynolds number and a striking example of the effects of this on the wall interference at high subsonic speeds is provided by the results in Ref 18 and reproduced in Fig 2.10. A generic wing-body-tail model was tested in the AEDC 1T and 4T tunnels with two alternative wall open-area ratios, 3 and 7%. The test results in 4T can be accepted as essentially interference-free and it appears that an open-area ratio of 7% in 1T gives the same results without needing any corrections. Applying corrections estimated by an Euler code in an attempt to bring both the 3% and 7% 1T results into agreement fails in both the pre-test and post-test cases; indeed, it moves the results for the 3% open-area ratio in the wrong direction. Estimating the corrections by a Navier-Stokes code however almost achieves the desired aim. Primarily, this is because with the Navier-Stokes code, the shock position is predicted correctly; with the Euler code, the shock is too far aft because the viscous effects are being ignored. The viscous effects will vary with Reynolds number and so, it follows that the wall interference will also vary. This example illustrates the interlocking nature of Reynolds number and wall interference effects. Fig 2.11 provides<sup>20</sup> a more direct illustration of this point: it shows pressure distributions (note: upper and lower surfaces separated for clarity) measured near mid-semi-span on a 3D wing of a certain model mounted on the same sting in three different tunnels. The results are uncorrected for wall interference and the large change in model blockage from a trivial 0.16% in the AEDC 16T to a large 2.6% in the AEDC 4T is shown to affect the severity of the shock-induced separation (and consequently, shock position). Simple  $\Delta M$ ,  $\Delta \alpha$  interference corrections derived on the assumption that the walls of 4T would be expected to be too open at  $M = 0.91$  might reduce the differences but the point in the present context is that use of the large blockage data in a sequence over a range of Reynolds number would lead to the genuine Reynolds number effects being swamped by a substantial pseudo-Reynolds number

effect. The danger, well demonstrated in this example, is that if one did not look at the caption on Fig 2.11, one might imagine that the figure is a comparison between pressure distributions at three different Reynolds numbers.

One example where, at first sight, there are serious problems is the comparison in Figs 2.12(a,b) of two-dimensional data for CAST-10. These results were first presented in Ref 21; large variations in the drag-rise Mach number and maximum lift trends are apparent but when, as in Fig 2.12(c), the maximum lift at the drag-rise Mach number is plotted against Reynolds number, a much more consistent trend is obtained. This suggests that the problem in Figs 2.12(a,b) is that the Mach number is in error for some of the tests, probably because the wall interference corrections either have not been applied or need to be refined. Elsenaar in Ref 2 notes however that the distortion of Reynolds number trends by wall interference does not necessarily apply in all cases. The results for CAST-7 in Figs 2.12(d,e) taken from Ref 22, for example, show a reasonably consistent trend with Reynolds number when plotted directly, although at a given Reynolds number, there is again considerable scatter.

In two-dimensional testing, the results can also be affected by side-wall interference and again, this interference can depend on the unit Reynolds number. The standard method for correcting for side-wall interference was developed by Barnwell<sup>23</sup> and later extended by Sewell<sup>24</sup> to transonic flows. These methods yield a correction to Mach number which is a function of free stream Mach number, aerofoil chord/width ratio and side-wall boundary layer thickness and hence, varies with unit Reynolds number. This method has been criticised on the grounds that it assumes that the sidewall boundary layer is two-dimensional and that the sidewall boundary layer only influences the flow velocity in the streamwise direction. In the present context, however, the more pertinent comment is that it does not allow for a subtle form of interference that can be present when the flow over the aerofoil is supercritical and which again varies with Reynolds number. The favourable pressure gradient ahead of the peak suction reduces the thickness of the side-wall boundary layer, and when the flow is supercritical, this leads to an expansion field spreading across the aerofoil. Downstream of the peak suction, the side-wall boundary layer thickness starts increasing again and an oblique shock can originate from this point; this oblique shock lies across the aerofoil and can modify the supercritical development even at the central measuring station. For a "roof-top" type of pressure distribution, for example, this will happen when

$$b/c \leq 2(x_s/c)(M_\infty^2 - 1)^{-\frac{1}{2}} \quad (2.2)$$

where  $x_s$  is the chordwise position of the shock and  $M_\infty$  is the Mach number of the supersonic flow. This subtle form of interference was explored<sup>25</sup> in the 18 in x 8 in 2D tunnel at ARA in the late 1970s and a good example of its effect on the measured pressure distributions and drag is presented in Fig 2.13. In most cases, but not necessarily in all cases, the strength of the final shock will be reduced by the presence of the oblique shock. This type of interference would not be predicted by the method of Refs 23, 24; it is intimately related to the shape of the pressure distribution over the aerofoil under test, being greatest for cases where there is a high peak suction near the leading edge. The strength of the initial expansion due to the interference and the oblique shock will vary with the side-wall boundary layer thickness and hence, with the unit Reynolds number. In the tests reported in Refs 25 and 26, the

problem was alleviated by mounting fairly large fences over the aerofoil surface at about  $0.1c$  from the tunnel walls; the interference is then with the relatively thin boundary layer on the side of the fences rather than with the thicker boundary layer on the tunnel walls. The oblique shocks can be almost eliminated in this way and also, there is a great improvement in the two-dimensionality of the flow at the stall. Following these investigations, testing with fences became the standard practice in the ARA 2D tunnel. Ideally, however, removal of the side-wall boundary layer ahead of the model is needed to eliminate this subtle form of interference completely. If no attempt is made to alleviate the effect, the apparent trends with Reynolds number will be compromised by a pseudo-Reynolds number effect.

Side-wall interference can also be a problem in low speed testing at high lift. Side-wall boundary layer control systems have been developed<sup>27</sup> for use in the NASA Langley Low-Turbulence Pressure Tunnel where the model span/chord ratio is typically only 1.64. Figs 2.14(a,b) illustrate the large effects on  $C_{L,max}$  due to removal of the side-wall boundary layer by venting through an optimum pattern of slots in the endplate at the end of the aerofoil. In the present context, the important point to note is that quantitatively, the deficiency in  $C_{L,max}$  when operating with no suction is not the same in Fig 2.14(a) ( $R = 9 \times 10^6$ ) and Fig 2.14(b) ( $R = 16 \times 10^6$ ). Removal of the side-wall boundary layer is clearly needed to obtain the true 2D values of  $C_{L,max}$  but it is even needed to obtain the correct trends with Reynolds number.

### 2.2.2 Type II effects

Type II pseudo-Reynolds number effects arise when it is not appreciated that more than Reynolds number is varying in the model test or in the comparison. The most obvious example is afforded by the simple case of undertaking low speed tests in an atmospheric tunnel and not realising that Mach number as well as Reynolds number can be affecting the results. This example is however now so well-known that there is no need to list it amongst the pseudo-Reynolds number effects: in view of all the data now available from the large pressurised tunnels, there is little risk that the need to separate Re and M effects will not be appreciated; it is frequently mentioned in §3.

The next most obvious source of a type II effect is transition position but again, there is some doubt as to whether this should be in the list. While it is true that in some comparisons, the apparent effects of Reynolds number are really due to changes in transition position, one can argue that this change in transition position is itself the genuine Reynolds number effect that the comparison was designed to uncover. This uncertainty as to whether to regard transition position as a source of pseudo-Reynolds number effects arises because, unlike some of the other variables discussed later, transition position and Reynolds number are not independent variables. In passing, it is worth noting that transition position and its variation with Reynolds number should always, if possible, be recorded in the documentation about any tests to investigate Reynolds number effects but unfortunately, this is not always the case in the published literature, thus leading to considerable confusion, particularly when attempting to extrapolate data to higher Reynolds numbers.

The general recommendation in Ref 2 for model tests in transonic flow is to test with fixed transition thereby apparently avoiding any effects due to movements of transition but even then, one has to consider the possibility that at the higher test Reynolds numbers, transition may have moved ahead of the

artificial fix. At low Mach number and high lift, transition will generally occur close to the leading edge irrespective of whether transition is fixed artificially or not but the issue cannot be forgotten. The majority of tests at low Mach number are undertaken with natural transition and it is important to realise that small but significant movements of transition with Reynolds number may still occur.

Pseudo-Reynolds number effects can arise when the transition position varies with Reynolds number as a result of the noise spectrum and turbulence of the particular facility rather than the pressure gradients over the model under test. It is therefore logical, despite the major importance of transition position, to consider first in the sub-sections below, the effects of noise and stream turbulence, although strictly, these should perhaps figure in the list of sources of class III pseudo-Reynolds number effects rather than class II: in general, the noise and stream turbulence will not vary with Reynolds number during the test but there are examples where the stream turbulence of a facility increased at maximum stagnation pressure.

#### 2.2.2.1 Noise and stream turbulence

The effects of noise and stream turbulence are considered in some depth in §2.2 in Ref 1 and the discussion in the present report is mostly confined to an update in the light of new information.

Binion in Ref 1 comments that it is difficult to decouple the effects of noise and turbulence on the location of boundary layer transition. The original analysis<sup>28</sup> by Dougherty and Steinle of the results of tests with the AEDC  $10^\circ$  cone in a large number of major transonic tunnels suggested that noise was the primary variable; a broad correlation was established between transition position and the root-mean-square pressure fluctuation, as shown in Fig 2.15. Later, however, Murthy<sup>29</sup> re-analysed the data for some of the tunnels with the results shown in Fig 2.16. This figure suggests that the results for these tunnels correlate much better in terms of velocity fluctuations; when plotted against pressure fluctuations, no clear trend emerges. The final conclusion was that at transonic speeds as at low speeds, if the tunnel noise is less than about 1% rms  $C_p$ , turbulence rather than noise is the dominant mechanism. This conclusion has now been supported by the results<sup>30</sup> of further tests with the  $10^\circ$  cone in the AEDC Propulsion Wind tunnel (16T) undertaken to demonstrate the improvement in this tunnel which has resulted from the installation of a screen and honeycomb in the settling chamber. Figs 2.17(a,b) show that there have been improvements in transition Reynolds number at Mach numbers up to  $M = 1.3$ . Ref 30 notes that, at a given unit Reynolds number and Mach number, the results following the installation of the screen and honeycomb are now in reasonable agreement with the values obtained in flight tests with the cone (although there is still some disagreement between the trends with decreasing unit Reynolds number in the tunnel and increasing unit Reynolds number in flight). The important point in the present context, however, is that these improvements in the 16T have been achieved by reducing the stream turbulence rather than the noise. This is what one would have expected from a honeycomb and it is confirmed by the results in Figs 2.17(c,d) which show that the major change occurred in the total rather than the static pressure fluctuations.

In the present context, the significance of these values of  $Re_t$  is that they determine the values of Re (based on wing chord, model length, model diameter etc) beyond which the transition positions on the model will be brought forward by the influence

of stream turbulence or acoustic spectrum. If results from two different facilities with different values of  $Re_t$  are being compared, there will be a point in a Reynolds number sweep where this difference will distort the comparison and introduce a pseudo-Reynolds number effect.

Ref 1 notes that there is no known clear evidence that noise affects boundary-layer properties other than transition location but various investigations have shown that turbulence can have other effects. Green in Ref 31 concludes that a small increase in free stream turbulence can have the same effect on the shape of the boundary layer profile as a fractional increase in Reynolds number roughly 60 times as great when this is assessed on the basis of the value of the boundary layer shape factor in an adverse pressure gradient. One might therefore expect to find examples of where stream turbulence has affected separation-onset and the stalling characteristics in comparisons of data from different tunnels with different turbulence levels. Such evidence is however difficult to find but one example possibly illustrating this sort of effect is presented in Fig 2.18(a,b).

The data in Fig 2.18 are from model tests for the YF-16. Tests were made in the NASA Ames 11 ft tunnel on a 1/9 scale complete model and in the CALSPAN 8 ft tunnel on both this model and also a 1/15th scale model. Values of  $C_{Dmin}$  at  $M = 0.9$  from these tests are plotted in Figs 2.18(a) and extrapolated to full-scale for comparison with flight test data. There is a fair measure of agreement but in the present context, it is interesting to note that there is an increase in  $C_D$  (relative to the general decreasing trend) which occurs at about  $R = 9 \times 10^6$  in the CALSPAN tunnel and about  $R = 11 \times 10^6$  in the Ames tunnel. It is probable that the break in the curves is due to a forward movement of transition. The fact that it occurs at a lower Reynolds number in the CALSPAN tunnel implies that the transition Reynolds number is lower in this tunnel. Reference back to Fig 2.15 shows that this is consistent with the evidence from the tests with the  $10^\circ$  cone; it could indicate that the stream turbulence is greater in this tunnel. The comparison of the lift-incidence curves in Fig 2.18(b) is more intriguing: the pronounced break in the curve occurs at a higher  $C_L$  with the 1/15 scale model in the CALSPAN tunnel than with the 1/9 scale model in the Ames tunnel, despite the lower test Reynolds number. This is in the wrong direction to be explained readily as a Reynolds number effect (particularly in view of the genuine change with Reynolds number shown by the comparison of the two sets of results from the Ames tunnel) and it is tempting to suggest that higher stream turbulence has delayed the appearance of a separation. If so, this would be consistent with the results of the calculations by Green reported in Ref 31. In other words, a pseudo-Reynolds number effect associated with stream turbulence has reversed the sign of the genuine change with Reynolds number.

#### 2.2.2.2 Transition position and length

Fig 2.15 shows that even on the surface of a  $10^\circ$  cone, where there is no adverse pressure gradient, transition Reynolds numbers for most of the facilities in common use lie in the range,  $Re = 3 \times 10^6$  to  $5 \times 10^6$  and only in a few examples, does it approach  $10 \times 10^6$ . It follows that in any test programme with natural transition, covering a substantial range of Reynolds number, it is likely that an increase in Reynolds number will be associated with a forward movement of transition. Both contribute to the variation of the aerodynamic characteristics and, in general, extrapolation of the model test data to full scale will not be a simple extrapolation of the measured trends.

Figs 2.19-2.22 present some illustrations of the effects of

changes in transition position with Reynolds number. Fig 2.19 taken from an AGARD paper<sup>33</sup> written in 1973 and entitled "Effect of Reynolds Number" is a good example of where the results appear, at first sight, to be confusing but the explanation must lie in the effects of changes in transition position. On the left-hand side, after correcting for wall interference, the data consistently show an increase in lift-curve slope at  $M = 0.3$  with  $Re$  up to about  $Re = 4 \times 10^6$  whereas, on the right-hand side, the data show a decrease in lift-curve slope at  $M = 0.7$  with  $Re$  continuing up to  $Re = 40 \times 10^6$ . A reduction in boundary layer thickness should, at these Mach numbers, lead to an increase in lift-curve slope. It follows that the most obvious explanation for the apparent contradictory trends in Fig 2.19 is that on the left, the trend is genuinely related to the increase in  $Re$  whereas in the wider Reynolds-number range on the right, increase in Reynolds number leads to an associated forward movement of transition (and hence, to an increase in boundary-layer thickness despite the increase in  $Re$ ).

Fig 2.20 presents results from theoretical calculations<sup>34</sup> for a 3D wing with natural transition which illustrate the same point. It will be seen that the trends in lift and pressure drag with Reynolds number reverse at about  $Re = 3 \times 10^6$ . Below  $Re = 3 \times 10^6$ , the viscous effects (reduction in lift and increase in form drag) increase with  $Re$  as a result of a forward movement of transition but above  $Re = 3 \times 10^6$ , they decrease again because the increase in  $Re$  is not accompanied by any further forward movement of transition. The graph on the right shows that the changes in lift and drag are primarily due to changes in the effective rear camber of the wing allowing for the viscous effects. The value of this example relative to the earlier case is that the interpretation is based on the actual results of the calculations and is not simply speculative.

Fig 2.21 taken from Ref 35 is the standard picture that has been used<sup>2</sup> to introduce the AGARD methodology for testing at reduced Reynolds numbers at transonic speeds. Tests were made on a two-dimensional aerofoil over a range of transition positions and Reynolds numbers. The results with transition fixed at 0.07c or occurring naturally near the leading edge provide a genuine  $Re$ -sweep; the transition sweep at  $Re = 2.3 \times 10^6$  can be converted to a  $Re$ -sweep using an appropriate simulation criterion - see §5.1. If, however, only the tests with free transition had been performed, the data would have resembled those from the previous example discussed above.

The last comparison in Fig 2.22 is an even more striking example of the difficulties inherent in establishing Reynolds-number trends from tests with natural transition. The sequence of  $C_D$  -  $M$  curves from tests with transition fixed close to the leading edge clearly form a family giving a genuine Reynolds-number trend with transition in this position but allowing transition to occur naturally gives a completely different  $C_D$  -  $M$  variation at  $Re = 2.2 \times 10^6$ . The decrease in  $C_D$  between  $M = 0.70$  and  $0.76$  is due either directly or indirectly to a rapid aft movement in transition position on the upper surface as the supersonic region extends rearward. This low  $Re$ , transition-free curve is useless as a guide to the high  $Re$  behaviour: at  $Re = 20 \times 10^6$ , the  $C_D$  -  $M$  curve as plotted would apply both transition-fixed and transition-free because at high Reynolds number, it would not be possible to maintain any sizeable extent of laminar flow. Even if the transition positions in the transition-free tests at  $Re = 2.2 \times 10^6$  had been determined accurately, it would still be difficult to use it as a basis for predicting the high- $Re$  performance because, as seen from the earlier examples, transition position can affect not merely the skin friction drag but also the pressure (and wave) drag; theory could be used for a prediction but it would be laborious.

These examples should be sufficient to demonstrate the vital importance of transition position when interpreting apparent Re-effects. It is not simply an issue at transonic speeds; the same conclusion applies at low speeds (see §3).

One should not, of course, regard transition as a discontinuous change occurring at a certain point in the flow but rather as a process occurring over a certain transition length which is itself a function of Reynolds number. Failure to recognise this can introduce further pseudo-Reynolds number effects<sup>34</sup>.

The present state-of-the-art regarding models of the transition process in two-dimensional flow is well summarised by Narasimha and Dey in Ref 169. They show how it is possible to describe the transition region in such flows at low speed using the concept of turbulent intermittency first introduced by Emmons<sup>170</sup> with later developments by Schubauer and Klebanof<sup>171</sup> and by Narasimha<sup>172</sup>. Downstream of the onset of transition, ie downstream of the position at which the orderly motion of the instability waves first starts to break down into chaotic motion, the intermittency of the turbulent fluctuations increases and also, there is a rapid increase in the amplitude of turbulence which reaches a maximum where the flow is turbulent on average for 50% of the time. Thereafter, the turbulence intensity diminishes but the intermittency continues to increase until the flow can be classed as fully turbulent. In the transition model proposed by Narasimha and Dey, the velocity profile of the boundary layer in the transition region is given by a linear combination in the proportions  $(1-\gamma)$ :  $\gamma$ , of the mean flow in a laminar and turbulent boundary layers respectively. They proposed a correlation for a Reynolds number based on the length of the transition region, defined as

$$\lambda = x(\gamma=0.75) - x(\gamma=0.25)$$

in terms of the Reynolds number based on the streamwise distance from the origin of the flow. Gaudet et al<sup>173</sup> has modified this correlation to express it in terms of the boundary layer momentum thickness at transition-onset in the hope that it will now include some allowance for at least mild pressure gradients. This correlation is given by the equation

$$Re_{\gamma} = 9.63 Re_{\theta T}^{1.6}$$

For a given pressure distribution and level of free-stream disturbances,  $Re_{\theta T}$  would not be expected to vary with test Reynolds number and it therefore follows that an increase of test Re would lead to a decrease in  $\lambda$  in order to maintain constant  $Re_{\lambda}$ . This is what has been observed in practice<sup>173</sup>. It is an important result in the context of interpreting experimental results purporting to show the position of transition. For example, hot-film gauge measurements are generally used to indicate the position of the peak rms signal but, as noted above, this will be downstream of transition-onset: downstream by a distance that will reduce with increasing Reynolds number. This provides an explanation for the conclusion from several tests<sup>173,174</sup> that the value of  $N$  needed to predict transition by the  $e^N$  method apparently decreases with Reynolds number; this would not be true if the experiments were indicating transition-onset; in practice, however, this is not the case and so, deductions concerning the values of  $N$  are affected by the change in transition length with Re. A flight-tunnel comparison would not necessarily show the effects just discussed. The level of external disturbances is likely to be less in flight than in most tunnels - this would result in the transition position being further aft in flight and this would tend to offset the apparent effect of

Reynolds number on transition position when measured downstream of transition-onset.

Correct modelling of the transition length is particularly important for the accurate determination of skin friction both locally near transition and in obtaining overall drag estimates. Inaccurate modelling as in most existing theoretical methods which assume a discontinuous change can lead to a pseudo-scale effect but Gaudet<sup>173</sup> notes that the difference in transition length between tunnel and flight may be less than given by the above relationship for the effects of Re because the free-stream disturbances, as a proportion of dynamic pressure, are generally less in flight than in the tunnel.

### 2.2.2.3 Tunnel temperature

Possible pseudo-Reynolds number effects due to tunnel temperature have acquired extra significance following the introduction of cryogenic facilities. The most important issue is that data should be taken in conditions of thermal equilibrium between the model and stream but discussion of this point is deferred to §2.2.3.2 below. Here, stream temperature itself as a variable likely to change with Reynolds number is discussed.

Tests in the T2 cryogenic tunnel at ONERA-CERT, Toulouse, have shown that tunnel temperature can have an effect on the interpretation of the buffet data from tests on a half-model of a subsonic transport aircraft over a range of Reynolds number (and temperature). Results are presented in Figs 2.23(a-c). Tests were made at a given Mach number at three stagnation temperatures (300K, 180K and 120K corresponding respectively to  $Re = 3 \times 10^6$ ,  $6 \times 10^6$  and  $11 \times 10^6$  based on the wing mean chord). The buffet response as measured by an accelerometer near mid-semispan and a strain gauge (jauger) on the inner wing from tests with transition fixed at 0.07c is plotted against  $\alpha$  in Fig 2.23(a). The general impression is that there is no significant Reynolds number effect on the incidence for buffet-onset (in passing, it should be noted that this does not mean that there is no Re effect on  $C_L$  for buffet onset because  $C_L$  at a given incidence increases with Re). There is, however, some uncertainty in interpreting the results because, although the data at the two higher Reynolds numbers are almost identical, the results at  $Re = 3 \times 10^6$  show a different level prior to buffet-onset. This difference can be explained, at least in part, by the development of the unsteady pressure spectra with temperature. This is illustrated in Fig 2.23(b): the spectra for this pressure transducer at the three temperatures (three Reynolds numbers) are not the same when plotted against frequency but are almost identical when plotted against reduced frequency, ie frequency divided by the square root of the stagnation temperature. It follows that there is a shift with temperature in the relation between the response and excitation spectra and, as shown in Fig 2.23(c), the peaks in the spectra at the lowest Reynolds number tend to coincide with the structural frequencies, thus leading to the higher signal levels mentioned above. The responses can therefore be different even if the aerodynamic excitation is the same (assuming that the excitation spectra are not flat). The ONERA report on these tests concludes that the apparent advantage of cryogenic tunnels for aeroelasticity studies in permitting the determination of the effect of Reynolds number at constant static distortion of the model is therefore partly offset by a different development of structural and aerodynamic spectra with temperature. One must therefore take care when interpreting global measurements of the response of models.

### 2.2.2.4 Rotational speed in propeller testing

The accurate determination of Reynolds number effects on propeller performance is an extremely difficult task. Pseudo-Reynolds number effects are a major issue. Probably the best approach is to test model propellers in a pressurised tunnel and to compare the results at a given advance ratio and tip Mach number at different tunnel stagnation pressures but even in this case, one has to consider the possible effects of blade twist. If no pressurised tunnel is available, one is left with two possible approaches, viz

- (i) to test the model propeller at different forward speeds but maintaining the advance ratio by also changing the rotational speed, or
- (ii) to test two model propellers of the same design but at different scale.

Obviously, (i) is only admissible when Mach-number effects can be safely ignored but research tests have shown that with both these approaches, a second variable, propeller rotational speed, can apparently be as important as Reynolds number. The standard reference on this subject is currently Ref 37; Figs 2.24(a-d) are taken from this report.

Figs 2.24(a,b) demonstrate the existence of this effect due to propeller rotation. Fig 2.24(a) compares the measured and calculated variation of propeller efficiency with advance ratio,  $J$ , and  $\Omega^2 R^4 \text{ ft sec}^2$ . These measured results were obtained in tests on a model propeller with a diameter of 28.8 in. in the 8 ft x 6 ft tunnel at DRA Farnborough; the results plotted in Fig 2.24(a) are all taken from the range where it was found that genuine Reynolds number effects were small. It will be seen that at advance ratios above  $J = 1.2$ , the measured efficiencies at high rotational speeds fall well below the calculated values despite the fact that the effects of increasing tip Mach number are allowed for in the calculations. Fig 2.24(b) shows that similar effects of rotational speed are evident in tests on full-scale propellers at low forward speed in the 24 ft tunnel. When testing in a low speed tunnel, it is usual to simulate cruising values of  $J$  by running the tunnel as fast as possible and reducing propeller rotational speed. A complete line of power coefficient versus  $J$  at a fixed blade angle is thus made up of a number of segments, each associated with a different tunnel speed. Where they overlap, particularly at low  $J$ , where the rotational speed is greatest, there is almost always a discontinuity, as illustrated in Fig 2.24(b), where it will be seen that two values of power coefficient can be associated with the same  $J$ . In the past, these were dismissed as Reynolds number or Mach number effects but analysis has shown that the Reynolds number was too high and the Mach number too low for these to be the explanation. To quote from Ref 37, a plausible hypothesis for the apparent effect of rotational speed is that it arises from a centrifugally driven radial migration of the boundary layer, together with any separated flow at the spinner root junction; the consequently increased angular momentum of the mass of air being associated with the observed increase in power and reduction in efficiency. Precise experimental evidence in support of this hypothesis is however needed. In the present context, the important end-result of this analysis is that predictions of the performance of full-scale propellers from model test data has been successfully achieved in some cases by

- (a) avoiding testing at too low a Reynolds number ( $1 \times 10^6$  at 0.7 radius - see §7.3),

- (b) applying the correction plotted in Fig 2.24(c) for the genuine Reynolds number effect, and
- (c) applying the correction plotted in Fig 2.24(d) for the pseudo-Reynolds number effect due to propeller rotation.

Further experimental evidence is needed to extrapolate Fig 2.24(d) and to check that the corrections are satisfactory when applied to completely independent data. It is however now believed that with modern designs of propellers with better fairing of the blade roots, neither the  $Re$  nor the  $\Omega^2 R^4$  effect should be as large as predicted by Figs 2.24(c,d).

### 2.2.3 Type III effects

Pseudo-Reynolds number effects of Type III are caused by factors which, while not being in themselves  $Re$ -dependent, nevertheless affect the scale-effect comparison because they only affect some of the data being compared. Put more simply, any factor not allowed for correctly in the reduction of model test data from a tunnel test can potentially introduce a pseudo-Reynolds number effect of type III when the data are used in a flight-tunnel comparison.

The effects of tunnel turbulence and its acoustic spectrum should have been considered here but for convenience, they have already been discussed as a prelude to considering transition position in §2.2.2 above.

#### 2.2.3.1 Humidity

The effects of specific humidity are discussed in Ref 1 and no new evidence has been found while preparing this Agardograph. It is however worth repeating in Fig 2.25 the graph showing the results of calculations by Stanewsky<sup>38</sup> for the effect of humidity on the aerodynamic coefficients for the CAST-10 aerofoil at its design Mach number,  $M = 0.765$  at two pressures (ie two Reynolds numbers). The value of specific humidity at which the dewpoint temperature equals the free-stream static temperature is 0.07 and 0.018 for the 3- and 1-atm total pressure condition respectively and so, the effects of humidity are apparent at humidity values far below the saturation values. There is clearly a significant variation in each coefficient with specific humidity and a significant Reynolds number effect at a constant humidity. The higher the total pressure, the lower is the value of specific humidity at which the effects first appear and the greater the effects. Binion in Ref 1 warns against generalising from these results in Fig 2.25.

#### 2.2.3.2 Thermal non-equilibrium

Heat transfer into or out of the model under test can produce spurious effects on any data sensitive to the boundary-layer properties. The problem can be serious in short-duration intermittent facilities. A short study<sup>39</sup> in 1972 concluded that an increase of 1% in model-to-free stream temperature ratio would produce an effect roughly equivalent to a 3½% reduction in Reynolds number. The calculations in Ref 39 were only approximate but clearly indicated that the effects in a blowdown facility could be very significant.

Since 1988, some actual evidence from the ONERA-CERT T2 intermittent tunnel at Toulouse has been published<sup>40</sup>. A special test was made to analyse wall temperature effects with a model of the OALT25 aerofoil at  $M = 0.7$ ,  $\alpha = 0.25^\circ$ ,  $T_1 = 220K$ ,  $Re = 7.5 \times 10^6$ . There was no pre-cooling in this case ahead of the



run and so, the wall temperature decreased to equilibrium conditions during the run. The location of the beginning of transition varied appreciably during the run - from about 0.38c at 4 seconds after the start when  $T_w/T_{aw} = 1.25$ , to about 0.53c at 48 seconds when equilibrium conditions had been established. These experimental results were compared with calculations of wave amplification by linear stability theory and as shown in Fig 2.26(a), the experimentally determined positions of transition are consistent with the results of these calculations. In both cases, transition would be predicted accurately by using a value of  $N$  of about 7. Fig 2.26(b) shows that a change in Reynolds number from about  $8 \times 10^6$  to about  $11 \times 10^6$  would be needed to obtain the same change in transition position. Ref 40 concludes that a variation of 1% in  $T_w/T_{aw}$  is equivalent to a variation in  $Re$ ; this conclusion is consistent with evidence<sup>41</sup> from earlier tests by Dougherty and Fisher in flight and in the 4T tunnel at AEDC on the  $10^\circ$  cone. These results are reproduced in Fig 2.27; the results lead to the empirical relation

$$Re_t/Re_{\tau_{aw}} = (T_w/T_{aw})^7 \quad (2.3)$$

which was satisfied over at least a Mach number range from 0.55 to 2.0 and temperature ratios from 0.95 to 1.08.

It follows from the above discussion that cooling of the model surface is a possible way of simulating higher Reynolds numbers. This idea is explored in Ref 42.

### 2.2.3.3 Model manufacturing accuracy

The requirement that the models used in Reynolds number investigations should be manufactured to a high standard of accuracy may appear obvious but the testing of advanced sensitive aerofoil or wing design at high Reynolds numbers sets new target standards. Ref 43 is a good reference for indicating what is required in what is a highly sensitive test case. A 6 in chord model of a Lockheed supercritical shock-free aerofoil, CRYO 12X, was tested in the NASA Langley 0.3 m cryogenic tunnel. It was specified that the ordinates of the aerofoil should be maintained within  $\pm 0.001$  in of the true profile. The measured deviation from specification in the initial manufacture of model no 1 is shown in Fig 2.28(a). It will be seen that this only achieved a tolerance of  $\pm 0.004$  in. Fig 2.28(b) shows that viscous-inviscid calculations predict that this amount of deviation completely changes the character of the pressure distribution at the design condition at  $Re = 30 \times 10^6$ . The intended shock-free pressure distribution has been replaced by a distribution with a strong compression followed by a re-expansion. The calculations further show that the original specification of  $\pm 0.001$  in is needed to achieve the design aim. Further calculations for  $Re = 4 \times 10^6$  told a similar story suggesting that the stringent requirement in this case at least is related more to the aerofoil design than to the aim to test at high Reynolds number. Despite this last remark, it remains true that to obtain reliable trends with Reynolds number, high standards of manufacture are required. A second aerofoil was manufactured for the NASA Langley tests using a dimensionally stable, readily machineable material (VASCOMAX 200). Fig 2.28(c) shows that this model no 3 met the accuracy standard and Fig 2.28(d) indicates that as a result, there is a significant reduction in drag relative to model no 1.

### 2.2.3.4 Model surface finish

Surface roughness can introduce a pseudo-Reynolds number effect for two reasons:

- (i) it can lead to premature transition
- (ii) when the boundary layer is fully turbulent, it can increase the boundary layer thickness and hence, the drag.

Criteria for avoiding these effects are generally expressed in terms of a Reynolds number based on the roughness height and either the local velocity or the local skin-friction velocity<sup>44</sup>. To avoid the effect on transition, the allowable roughness height decreases with test  $Re$  in proportion to  $Re^{-3/4}$ . In other words, the requirement becomes more stringent at high  $Re$ . Another important consequence is that in a Re-sweep, the height of any roughness band used to fix transition should be progressively reduced; otherwise, there is a risk that either the band will fail to fix transition at low  $Re$  or that it will give excess drag at high  $Re$ . This advice is not always followed and, as a result, this is another reason why pseudo-Reynolds number effects can figure in the published literature.

The classic curve due to Nikuradse<sup>45</sup> showing the variation of admissible roughness height to avoid extra drag due to uniformly distributed roughness is reproduced in Fig 2.29 annotated<sup>46</sup> to indicate requirements in current tunnels including the NTF. The 2D test programme<sup>43</sup> discussed in the previous paragraph, §2.2.3.3, provides an example of where surface finish is thought to have led to extra drag at the highest test  $Re = 40 \times 10^6$ ; this is shown in Fig 2.30. It is not clear which of the two possible reasons for an increase in drag has applied in this case. Ref 46 notes that with a pressure-plotted model, the pressure holes themselves may be another source of roughness. They are known to cause transition<sup>47</sup> and are sometimes large enough relative to the local boundary layer thickness to lead to erroneous pressure readings<sup>48</sup>. Even the inspection of the surface finish can cause its problems: a contact profilometer can itself produce surface roughness<sup>49</sup>.

Recent evidence<sup>50</sup> indicates that roughness can be extremely important in cases where transition is induced by cross-flow. In tests with a large model, it was found that roughness height of merely  $0.5 \times 10^{-3}$  mm at the foot of a boundary layer 5 mm thick was sufficient to trigger cross-flow transition.

### 2.2.3.5 Model support/mounting effects

It is now generally recognised that flight-tunnel comparisons for particularly, drag and lateral and directional stability characteristics will only be a reliable guide to Reynolds number effects if appropriate corrections have been made for the support interference. Complete models for transonic testing are usually mounted on a sting either at the rear of the fuselage or from the top of the fin or as a blade sting from below. Testing at high Reynolds number accentuates the problem because the sting/fuselage diameter ratio becomes greater. A recent paper<sup>51</sup> from NASA Langley referred to experience which indicated that the sting corrections could amount to 9-10% of total aircraft drag and could vary with Mach number in a non-linear fashion. An early example of the importance of correcting for support interference concerned the drag of the VC10: a 4-engined aircraft with the engines mounted on the rear fuselage. Early predictions based on model test data underestimated the full-scale drag by as much as  $0.0010 C_D$  - not because of any  $Re$ -effect but because no corrections had been applied for the interference of the rear sting on the drag increment due to engine nacelles.

There were many examples in the early test report literature of where flight-tunnel comparisons indicated poor agreement in



directional stability characteristics which was ultimately traced to the need to distort the rear fuselage to admit the support sting: frequently, the presence of the sting prevented the true representation of any gully between the nozzles of a twin-engined combat aircraft. A good example of support interference effects on lateral characteristics is discussed in Ref 46. Fig 2.31 reproduced from Ref 46 presents results from comparative tests on a  $70^\circ$  arrow wing in several low speed tunnels. The results are for a fixed angle-of-attack of  $35^\circ$  where the upper surface flow and wake are dominated by leading edge vortices. It was expected that only the full scale test and model arrangement A would give the correct results but, in fact, only the full-scale gave the anticipated asymmetric behaviour. The spread in the other results indicates the difficulty in establishing whether Re-effects are present; clearly, support interference is the major problem. In contrast, the comparative effects on the lift characteristics are relatively slight.

Half-models are being increasingly used in both high and low speed tests for the sake of obtaining the highest possible test Reynolds number in a given facility. Experience in the testing of  $\frac{1}{2}$ -models in the 5 metre Pressurised Low Speed Tunnel at DRA Farnborough is described in Ref 53. In this tunnel, the  $\frac{1}{2}$ -models are supported with minimum clearance above an earthed plinth, as shown in Fig 2.32(a). The approaching tunnel floor boundary layer can be re-energised (BLRE) by high-pressure blowing through a nozzle extending across the greater proportion of the width of the test section at a point about a metre upstream of the model; the improvement in the boundary-layer profile is shown in Fig 2.32(b). Comparative tests were made with a  $1/13$  scale model of the A300B4 in a take-off configuration. Lift and pitching moment data through the stall at  $M = 0.2$  are shown in Figs 2.32(c-e) for the basic  $\frac{1}{2}$ -model with no plinth, the model with plinths having a height of alternatively 75 mm and 100 mm and a corresponding complete model at the same Reynolds number. For reference, the thickness of the floor boundary layer in the conditions for the results presented would be close to the 75 mm figure. Comparisons are presented for  $Re = 5.0 \times 10^6$  and  $6.45 \times 10^6$  without BLE and for  $Re = 5.0 \times 10^6$  with BLRE. These results are discussed in detail in Ref 53 but the comparisons are so interesting and relevant that it is worthwhile repeating the main points here:

- (i) at  $Re = 5.0 \times 10^6$ , without BLRE, all the  $\frac{1}{2}$ -model configurations stall dramatically nose-down whereas the complete model stalls less severely and nose-up,
- (ii) at  $Re = 6.45 \times 10^6$  (ie thinner floor boundary layer) without BLE, the change in pitching moments through the stall for the half-model with or without the favoured 75 mm plinth is now nose-up, ie in contrast to the results at  $Re = 5 \times 10^6$ , it is now consistent with the results for the complete model,
- (iii) at  $Re = 5.0 \times 10^6$ , with BLRE, this consistency is maintained and also, the stall occurs slightly later with the  $\frac{1}{2}$ -model than for the complete model (without BLRE, the reverse has applied). The detailed discussion in Ref 53 suggests that in this case the  $\frac{1}{2}$ -model results may be more reliable than the complete model because of the need to make further corrections for support interference on the complete model results.

Clearly, these stalling characteristics are a highly sensitive test case. The pitching moments indicate that the overall result is a fine balance between whether an inner or outer wing stall comes first. A plinth increases the effective width of the fuselage and

local angle-of-attack on the inner wing and so, a plinth that is too high provokes an inner wing stall. A plinth with a height similar to the floor boundary layer thickness coupled with BLRE gives the best results but, in the context of the present Agardograph, the important point is that the  $\frac{1}{2}$ -model technique, if not applied with care and understanding, is capable of introducing effects which themselves vary with Re and hence, have to be classed as pseudo-Reynolds number effects because they relate to the tunnel floor boundary layer rather than any genuine Re-effect on the flow over the wing. To interpret the results of a Re-sweep successfully is a difficult task.

### **2.2.3.6 Inclination of thrust vector**

An important recent discovery is that part of the apparent jet-interference drag for a transport aircraft with underwing nacelles can be explained by a deviation of the thrust vector from the engine centre-line. This phenomenon was first discovered in tests in the Deutsche Airbus Low Speed Tunnel at Bremen and then confirmed in the DNW tunnel<sup>54</sup>. It has also been deduced from laser velocimetry tests by DLR-SM/ES in the jet of a full-scale A320 engine. It has implications for the analysis of flight test drag data where it has usually been assumed that the thrust vector is aligned with the engine axis. Also, there is no intrinsic reason why the magnitude of the effect should be the same in model and full-scale tests; if it is different, this would produce another pseudo-Reynolds number effect.

### **2.2.3.7 Final remarks**

There is a danger that one can become too obsessed with pseudo-Reynolds number effects and think that there are no genuine Re-effects. This temptation should be resisted: one should always remember that if the existence of the various possible pseudo-Reynolds number effects is recognised from the outset and allowed for in the reduction and interpretation of the results, they can then be forgotten; what is left can be accepted as the genuine Re effects. For example, taking the first pseudo effect discussed, ie the effects of errors in the empty tunnel flow calibration, if it had been recognised from the outset that the calibration was likely to depend on the tunnel stagnation pressure, the pseudo effect would never have appeared. Similar remarks could be made about most of the items discussed in the paragraphs above. So now, belatedly, let us turn to the genuine effects. Many of these are large and significant.

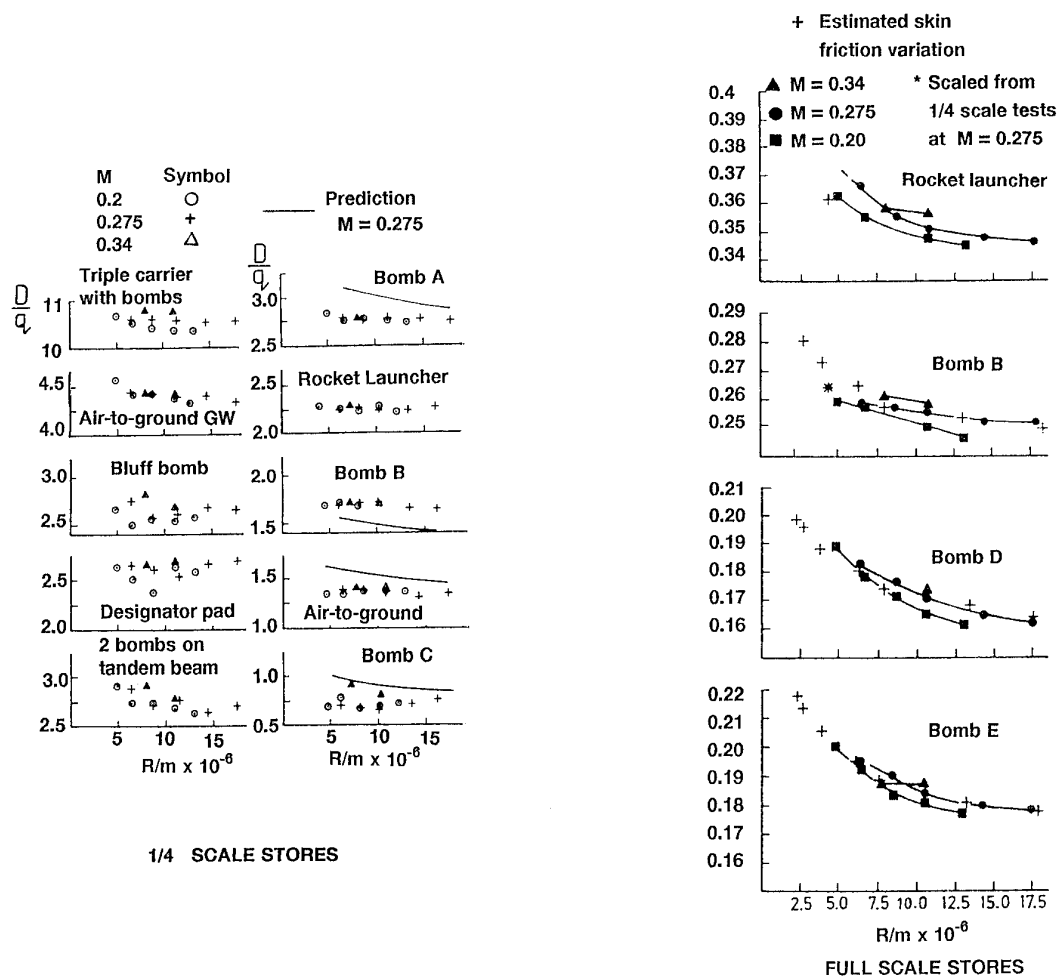


FIG 2.1 Effect of Re on Store Drag  
(from ref 7)

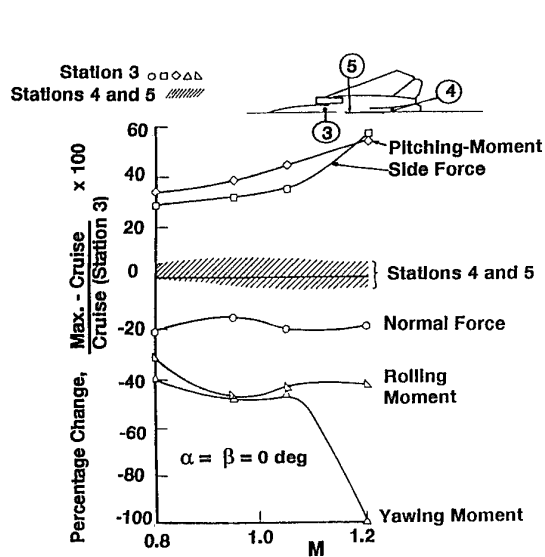


FIG 2.2 Effect Of Intake Spillage On Store Loads  
(from ref 9)

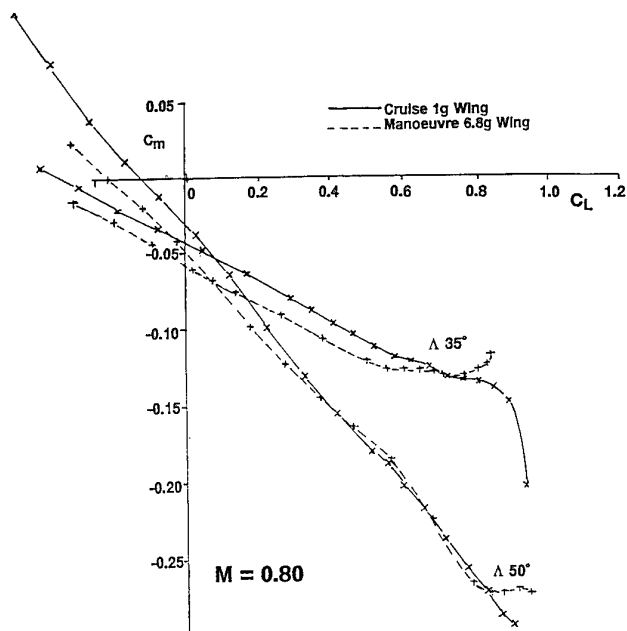
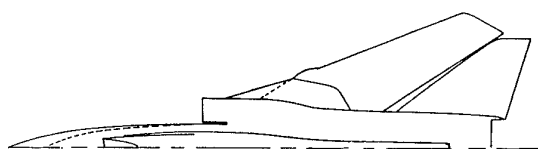
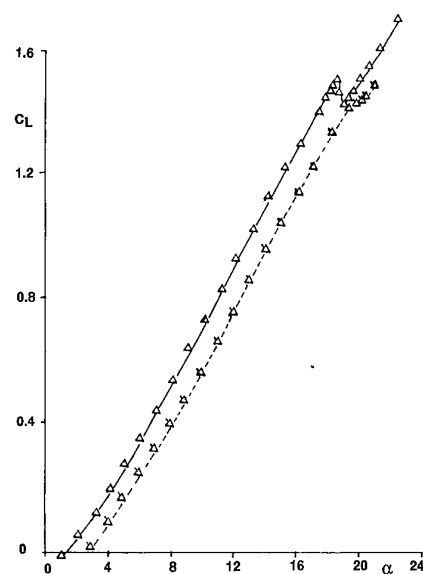


FIG 2.3 Effect of Aeroelastic Distortion  
example 1

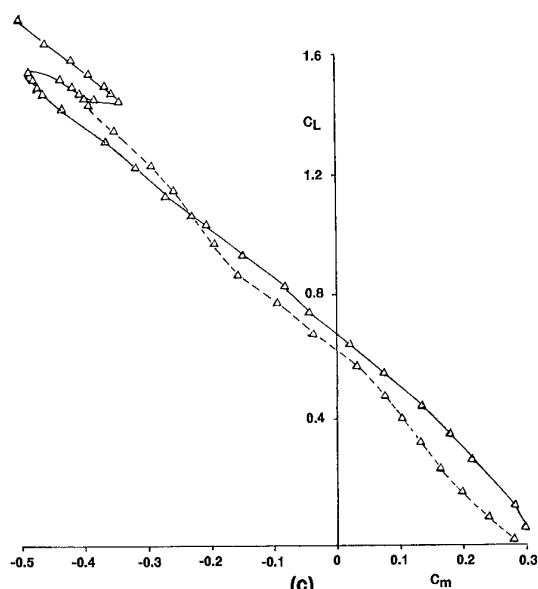


(a)

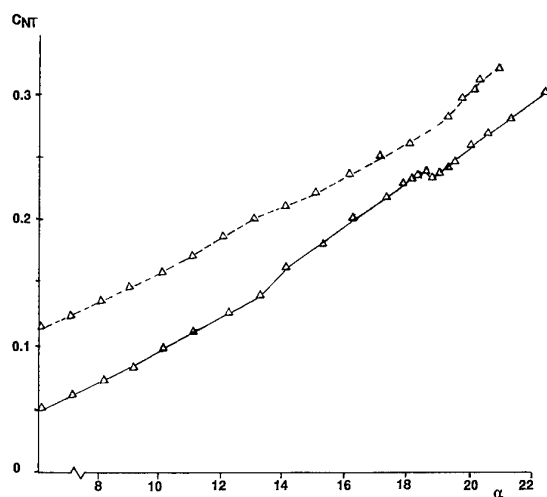
— Low Incidence wing  
 - - - High Incidence wing



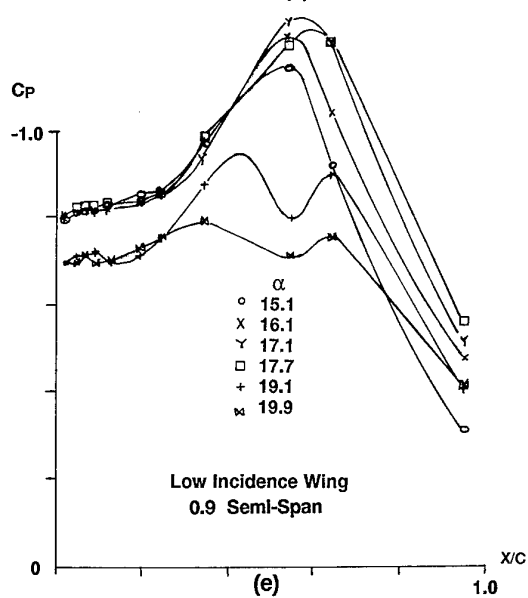
(b)



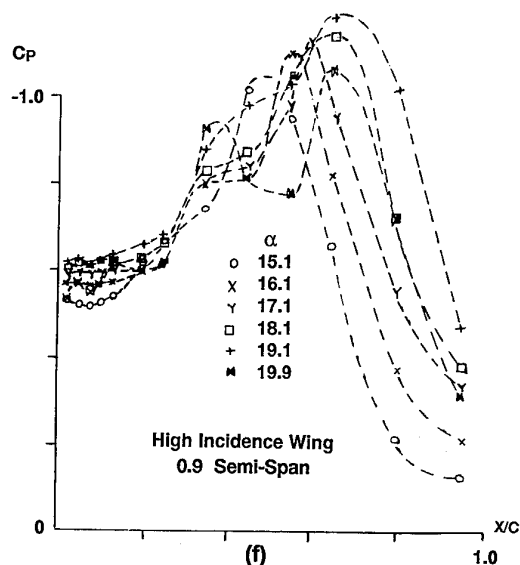
(c)



(d)



(e)



(f)

FIG 2.4 Effect of Aeroelastic Distortion  
 example 2

# REYNOLDS NO. EFFECTS — MODEL OR FACILITY? (McCROSKEY)

LIFT CURVE SLOPE — NACA 0012

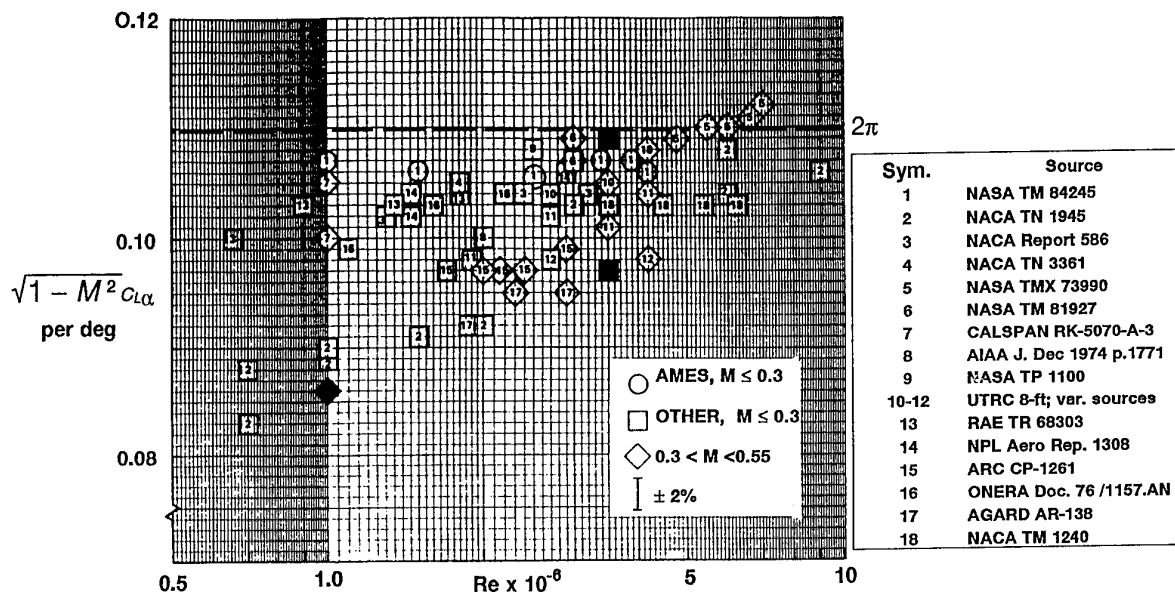


FIG 2.5 Effects of Re on Lift-Curve Slope of NACA 0012:  
Model or Facility?  
(from ref 10)

SYM	SPONSOR	Re VARIED BY	EFFECT ON
A	LEWIS	SCALE	NOZZLE
B		DENSITY	
C	AFFDL	DENSITY	AIRFRAME
D			NOZZLE
E	LANGLEY	DENSITY TEMP SCALE	NOZZLE

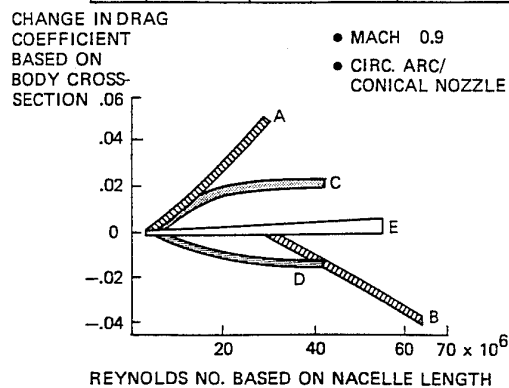


FIG 2.6 Effect of Re on Afterbody Pressure Drag  
(from ref 11)

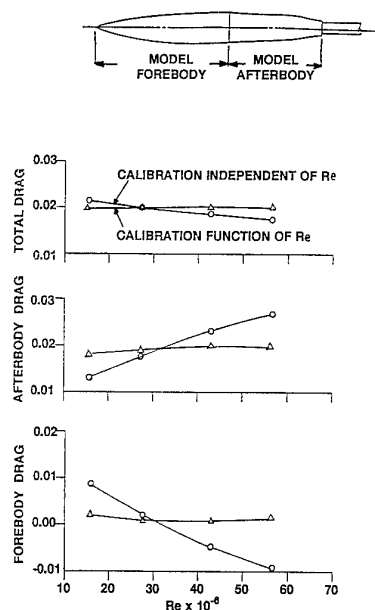


FIG 2.7 Effect of  $Re$  and Tunnel Calibration on Afterbody Pressure Drag  
(from ref 13)

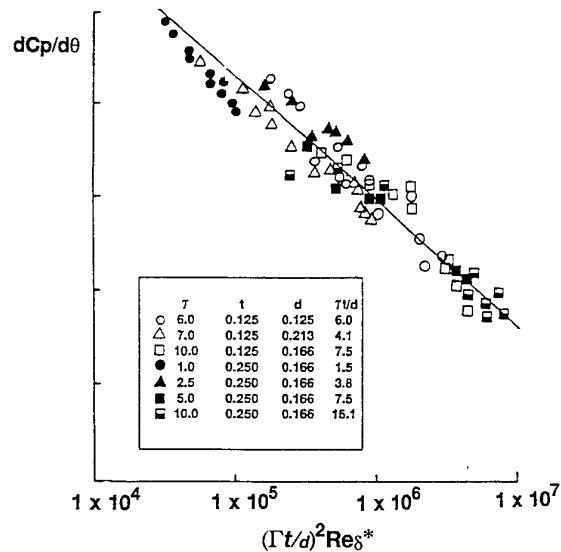


FIG 2.9 Perforated Wall Porosity Characteristic:  
60° Inclined Holes  
(from ref 18)

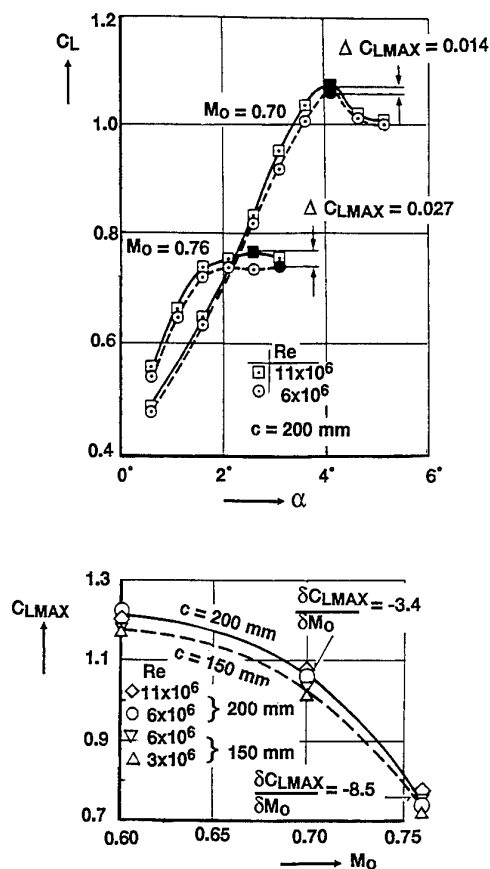


FIG 2.8 Effect of  $Re$  and Tunnel Calibration on  $CL_{MAX}$  (see § 2.2.1.1)  
(from ref 5)

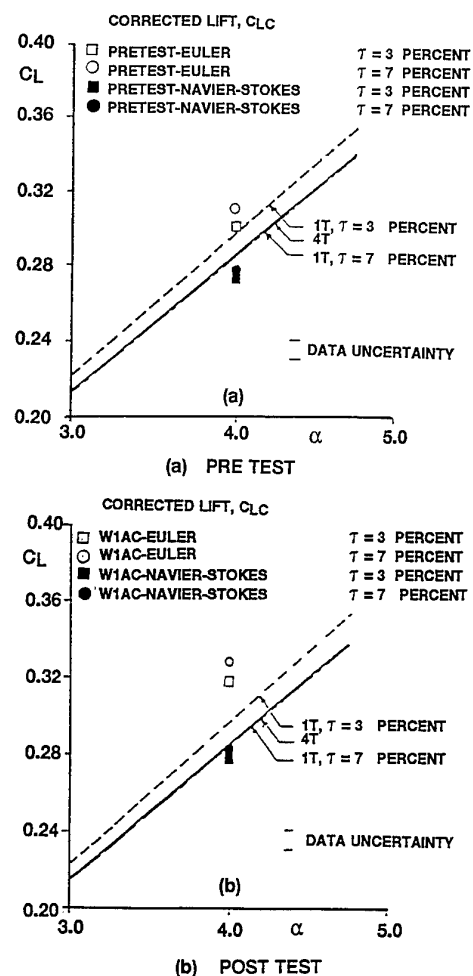


FIG 2.10 Tunnel Interference Predictions  
(from ref 19)

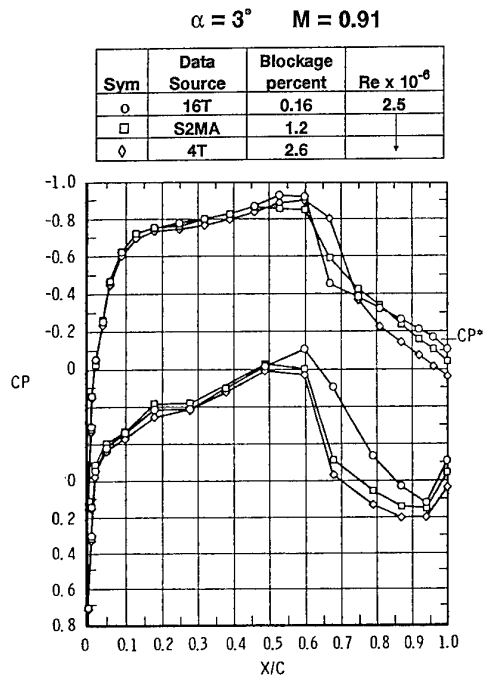
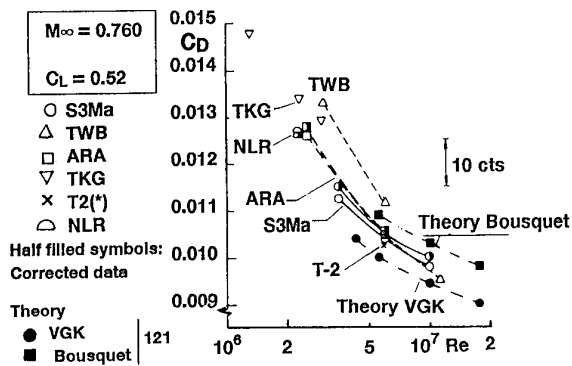
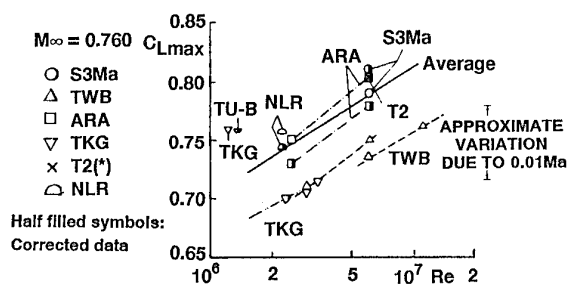


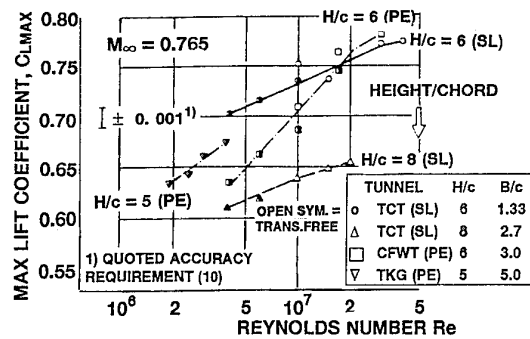
FIG 2.11 Effect of Model Blockage on Pressures near Mid-Semi-Span of 3D Wing  
(from ref 20)



(d) Variation of Drag with Re

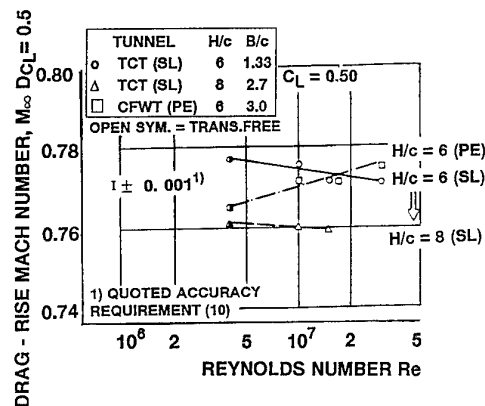


(e) Variation of Maximum Lift with Re  
CAST-7



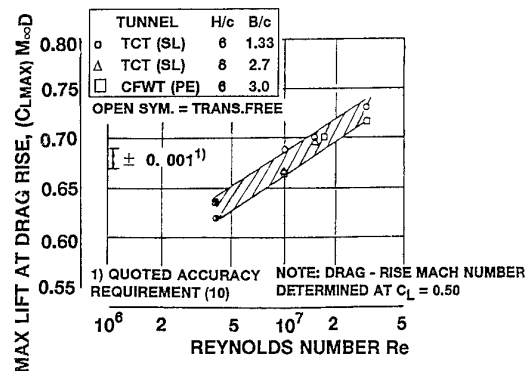
(a) Variation of Maximum Lift with Re

CAST - 10



(b) Variation of Drag - Rise Boundary

CAST - 10



(c) Variation of Maximum Lift at Drag - Rise  
CAST-10

FIG 2.12 Effect of Re and Facility on 2D Data  
(from ref 2)

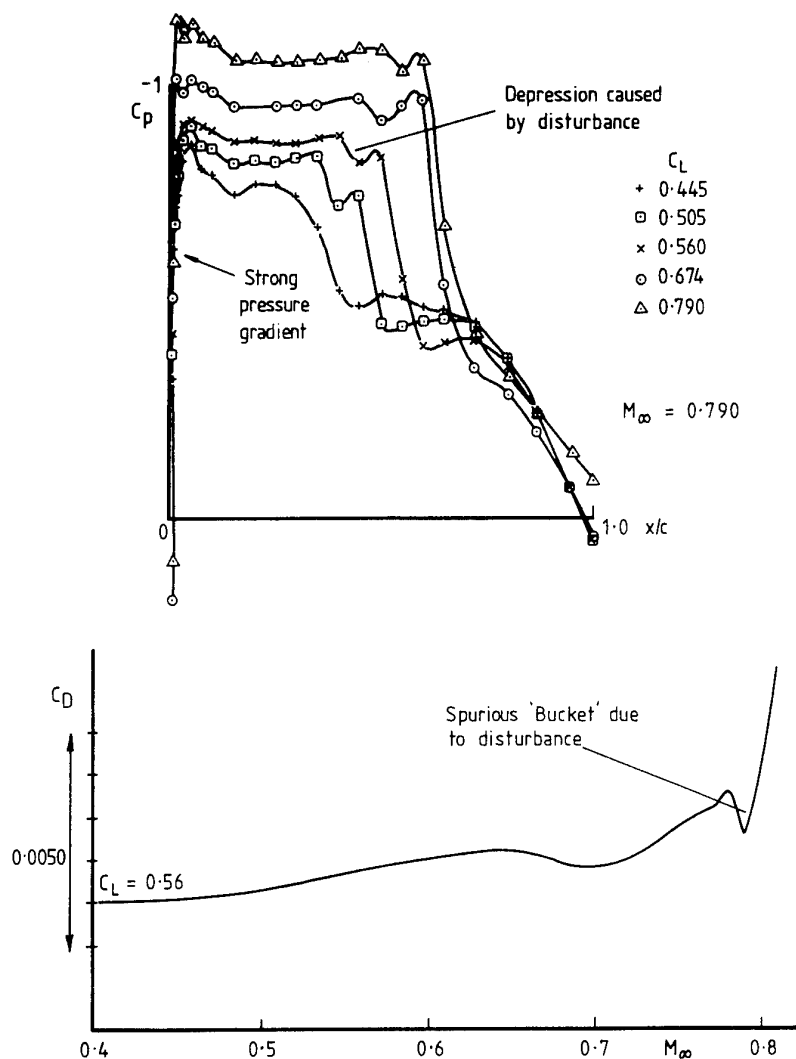


FIG 2.13 Effect of Side Wall Interference at Transonic Speeds  
(from ref 25)

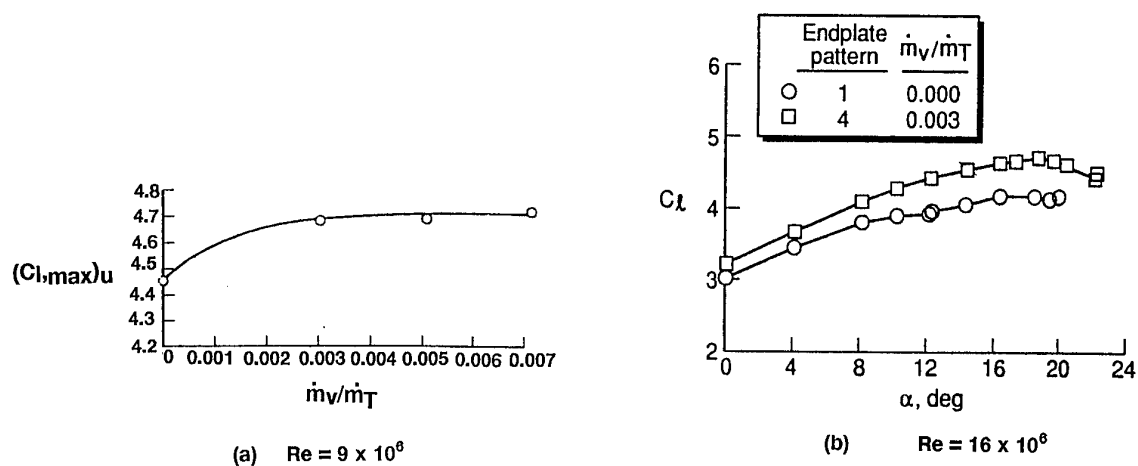


FIG 2.14 Effect of Venting  $M = 0.2$   
NASA Langley LTPT  
(from ref 27)

Sym	Tunnel	Sym	Tunnel
○	AEDC Tunnel 16T	◻	NASA/Ames 12 PT
●	AEDC Tunnel 16T (Walls Taped)	▽	RAE Bedford 8 x 8 SWT
△	AEDC Tunnel 4T	■	NASA/Langley 16 TT
▲	AEDC Tunnel 4T (Walls with Tape or Screen)	▲	NASA/Langley 16 TDT
◊	ONERA 6 x 6 S - 2 Modane	◆	NASA/Langley 8 TPT
◊	NASA/Ames 11 TWT	●	NSR & DC 7 x 10 T
◊	NASA/Ames 11 TWT (Walls Taped)	◻	NASA/Langley 4 SPT
◊	NASA/Ames 14 TWT	◊	RAE Bedford 3 x 4 HSST
◊	NASA/Ames 14 TWT (Walls Taped)	◻	NASA/Ames 9 x 7 SWT
◊	Calspan 8 TWT	◻	NASA/Langley 4 SUPWT (TS No. 1)
◊	ARA Ltd. Bedford 9 x 8	◻	Flight Data Fig.17

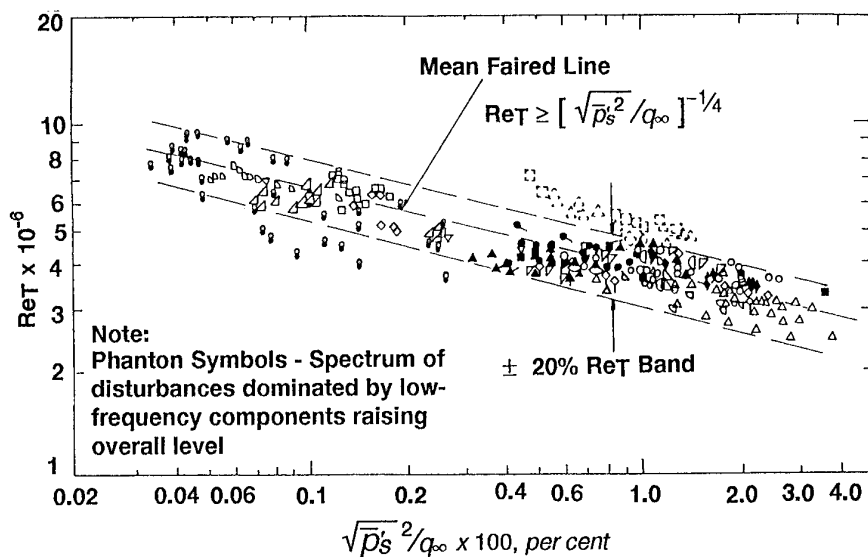


FIG 2.15 Original Correlation between  $Re_T$  and  $10^6$  Cone Surface Pressure Fluctuations (from ref 28)

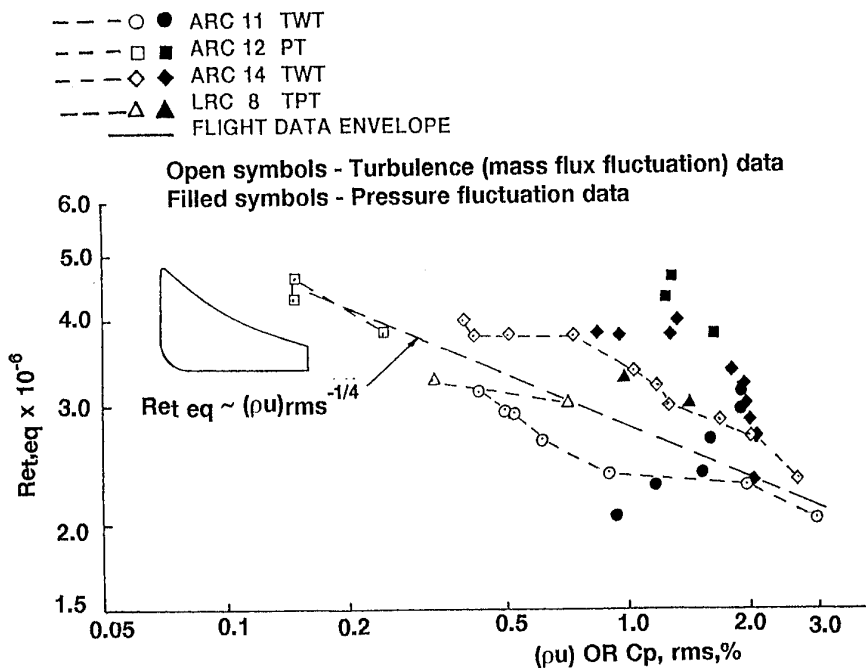
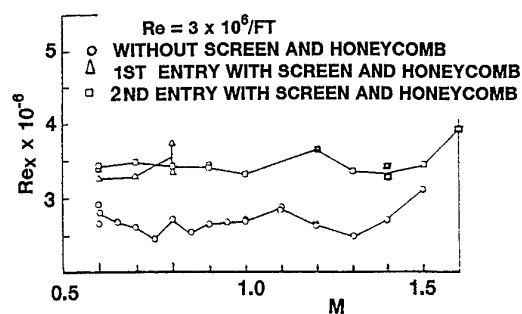
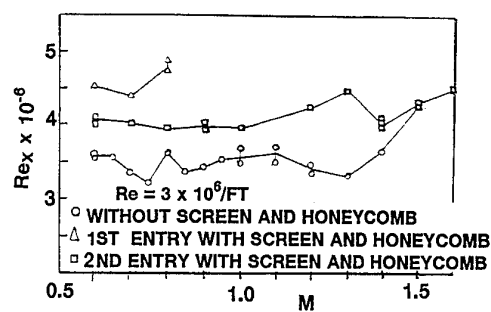


FIG 2.16 Revised Correlation with either Velocity or Pressure Fluctuations (from ref 29)

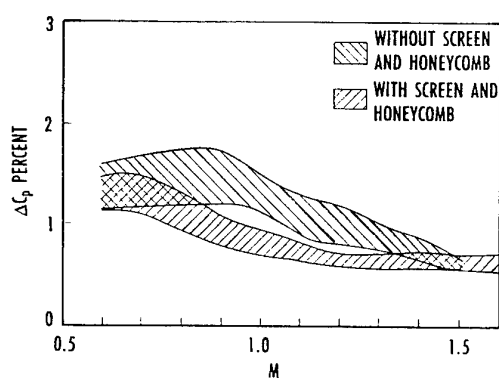




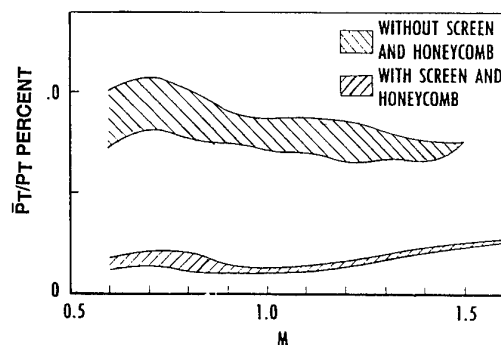
(a) Onset of Transition



(b) End of Transition

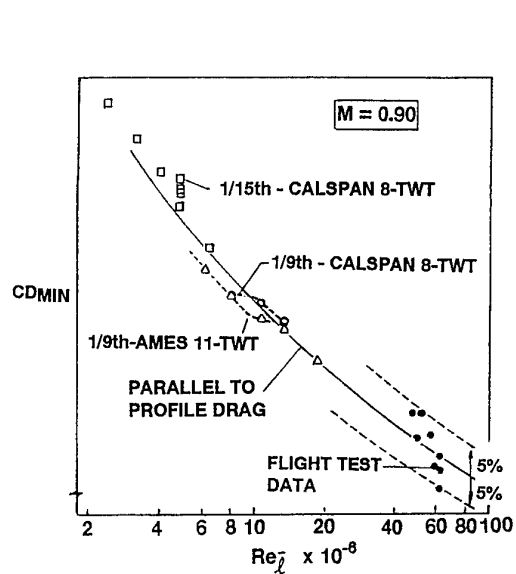


(c) Static Pressure Fluctuations

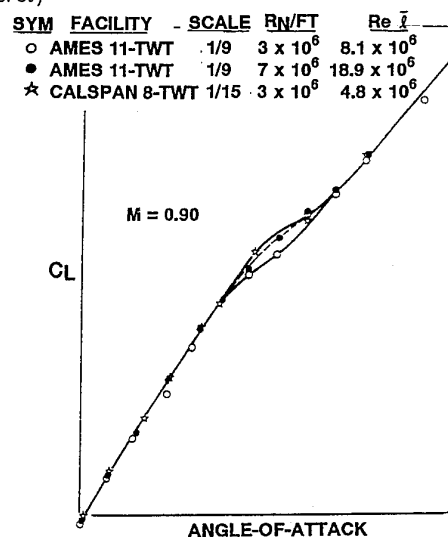


(d) Total Pressure Fluctuations

FIG 2.17 Effect of Addition of Screen & Honeycomb in Tunnel 16T  
 (from ref 30)



(a)



(b)

FIG 2.18 Comparison of Model Test Data for YF - 16  
 (from ref 32)

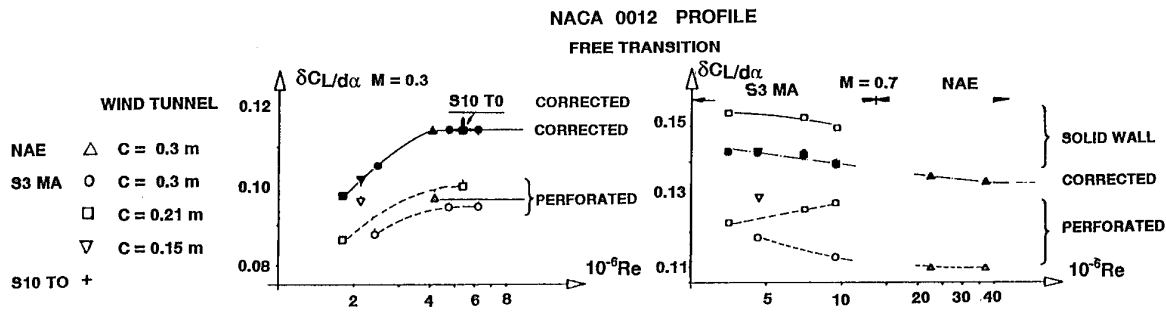


**FIG 2.19** Effect of  $Re$  - or Transition Position?  
(from ref 30)

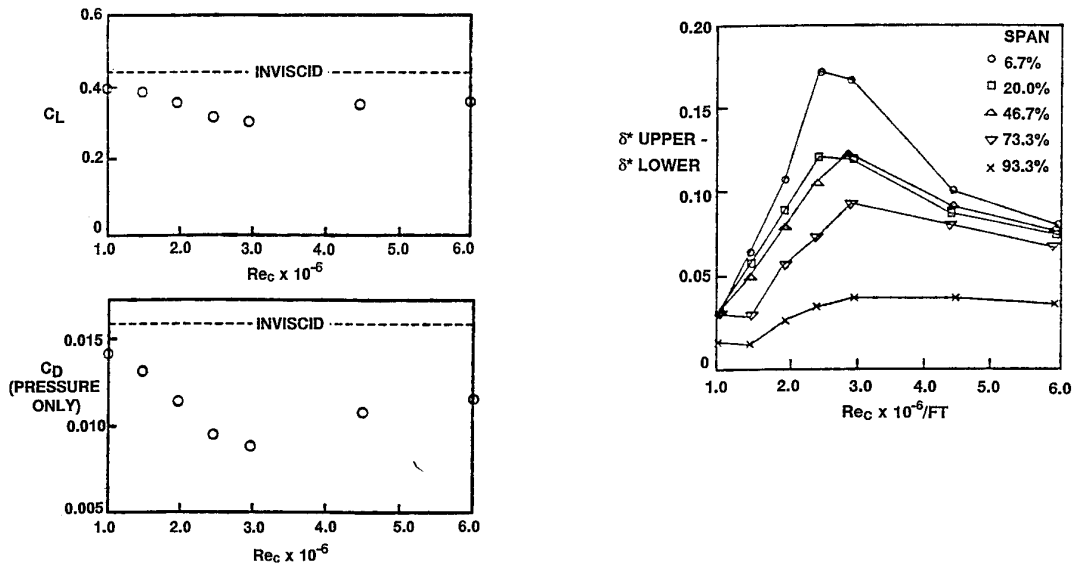


**FIG 2.20** Calculated Viscous Effects on 3D Wing at  $M = 0.75$ ,  $\alpha = 0^\circ$   
(from ref 34)

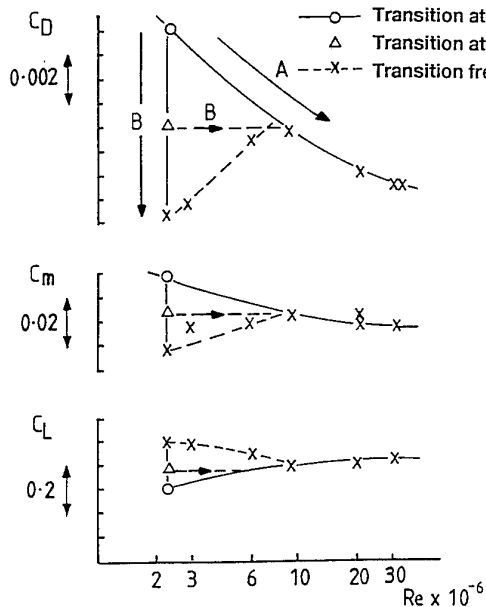


**FIG 2.21** Effect of  $Re$  and Transition  
2D Tests at Design Condition  
(from ref 35)

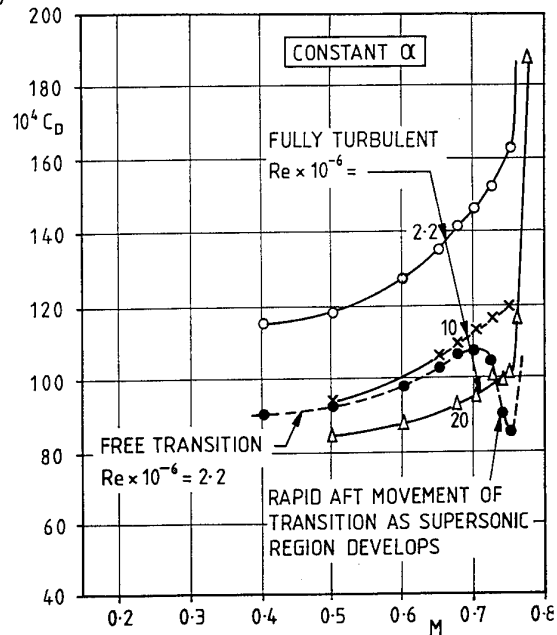
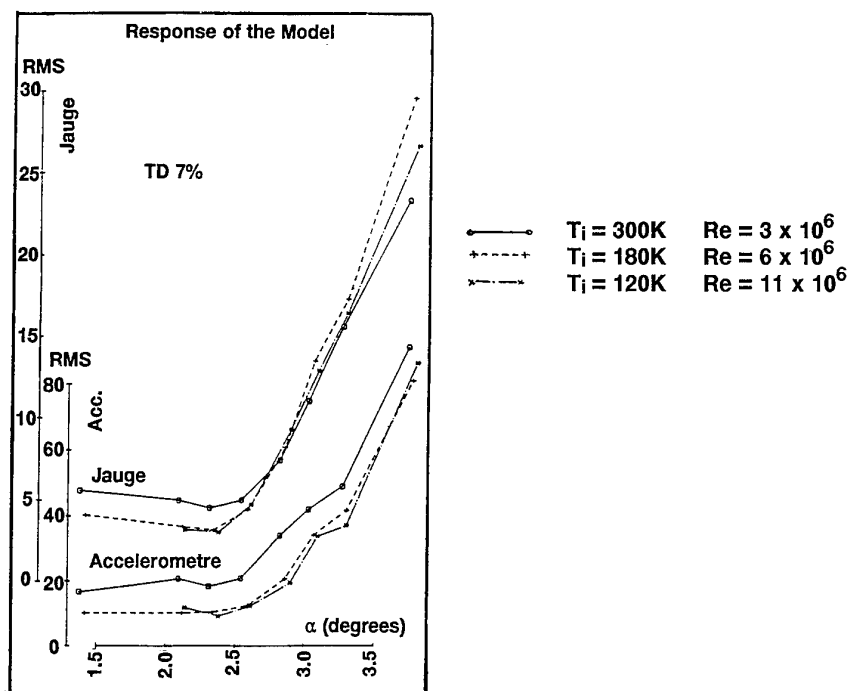
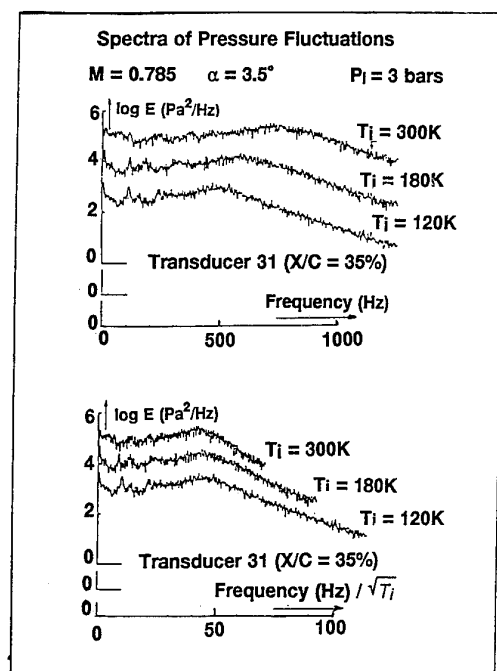


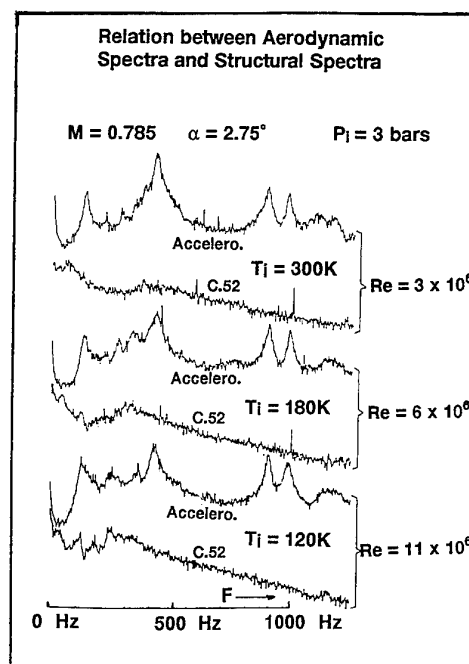
**FIG 2.22** Comparison of Transition Free and  
Transition Fixed 2D Data



(a)

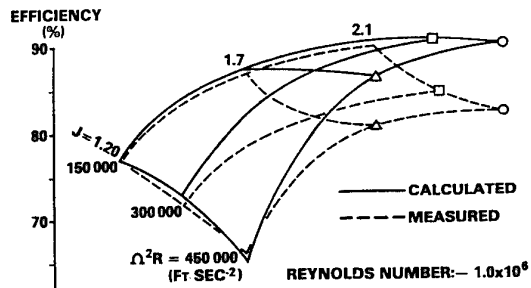


(b)

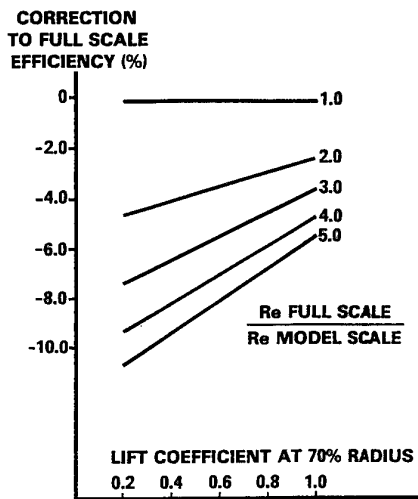


(c)

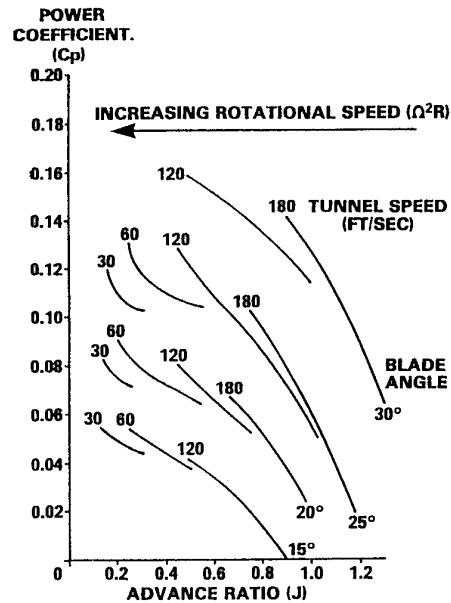
**FIG 2.23 Buffet Results from 1/2 Model Tests**  
**T2 Cryogenic Tunnel at ONERA/CERT**  
 (from ref 36)



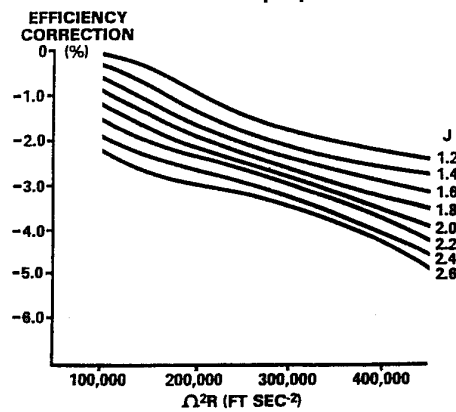
(a) Variation of efficiency with J and  $\Omega^2 R$  at constant Reynolds Number



(c) Correction for Reynolds Number



(b) Wind tunnel measurements of an 8.5' diameter propeller



(d) Correction for  $\Omega^2 R$

FIG 2.24 Effect of Rotational Speed on Propeller Test Data  
(from ref 37)

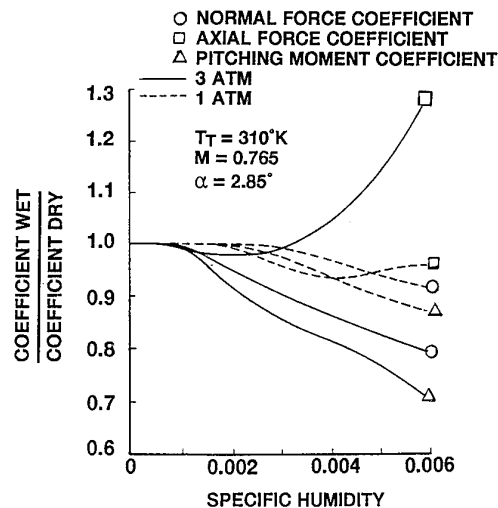


FIG 2.25 Effect of Humidity on Aerodynamic Coefficients for  
2D CAST - 10 Aerofoil  
(from ref 1)

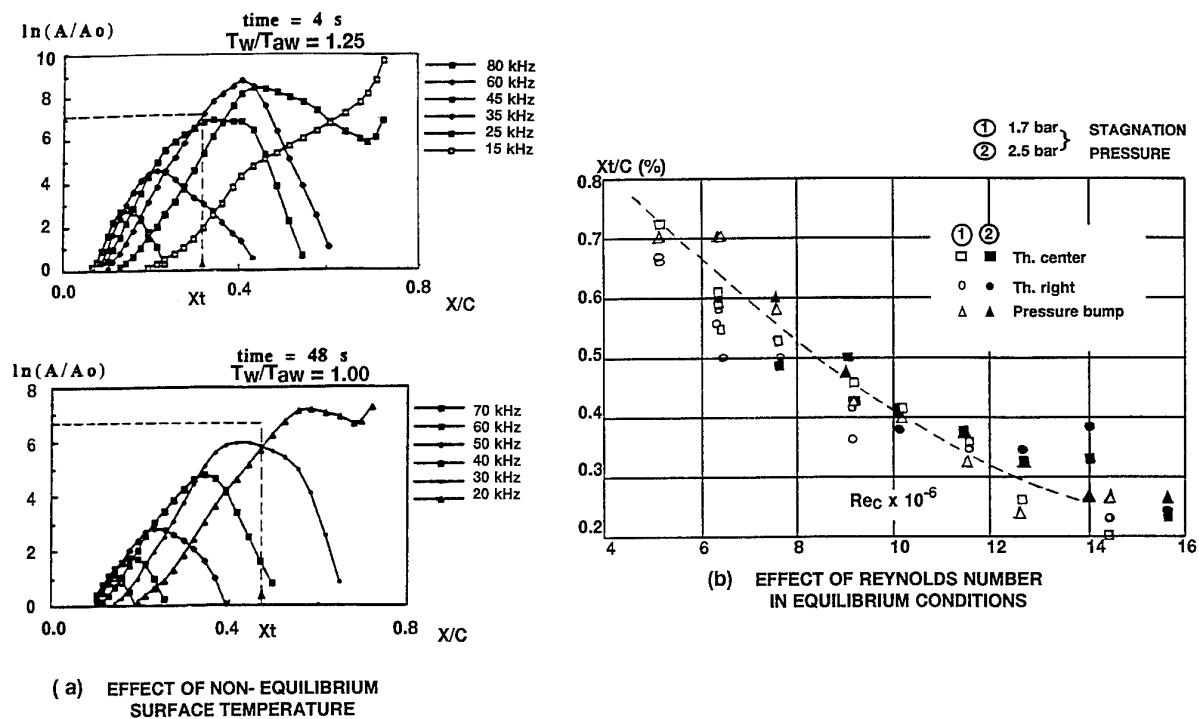


FIG 2.26 Results from T2 Cryogenic Tunnel  
(from ref 40)

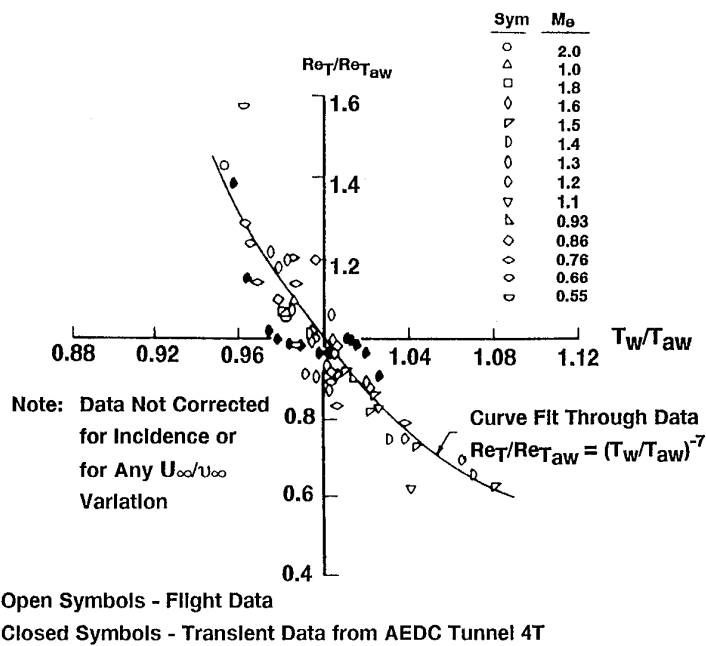


FIG 2.27 Effect Of Non-equilibrium Surface Temperature:  
10° Cone Test  
(from ref 41)

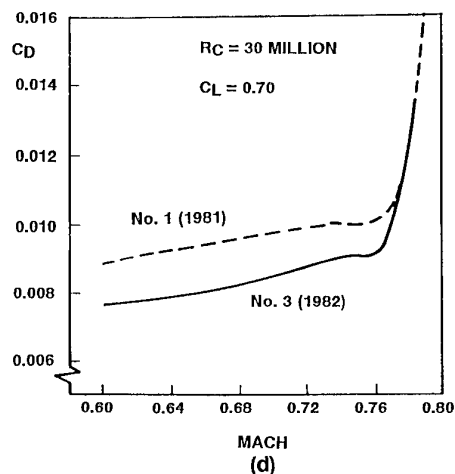
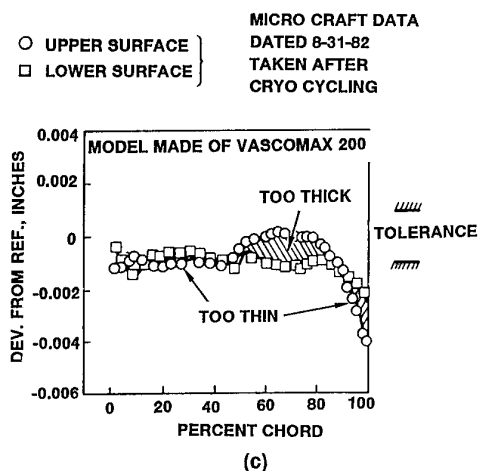
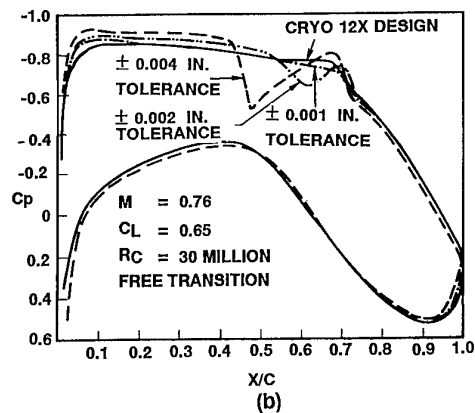
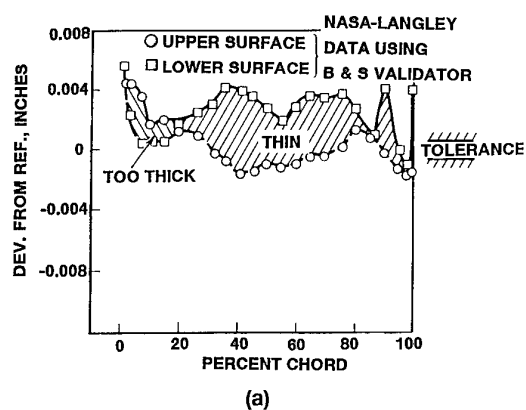


FIG 2.28 Effects of Model Dimensional Accuracy  
(from ref 43)

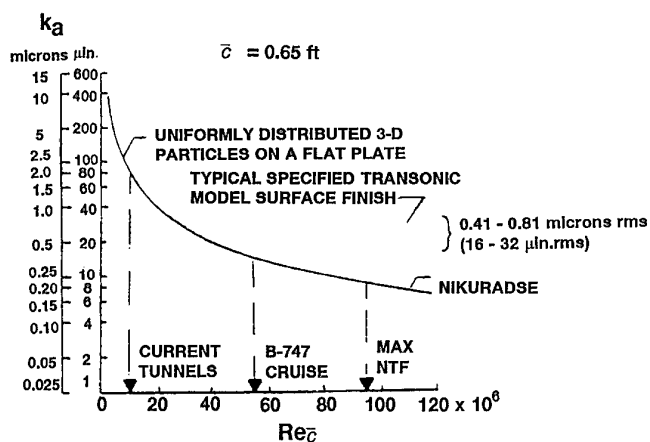


FIG 2.29 Admissible Roughness ( $k_a$ ) for typical NFT-sized models  
(from ref 46)

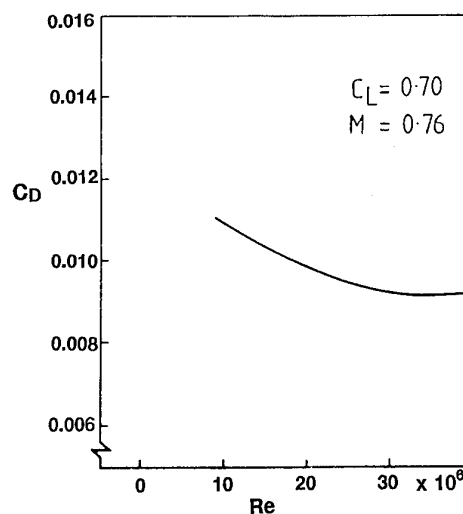


FIG 2.30 Effect of  $Re$  on Drag at Drag Divergence  
(from ref 43)

Effect of Model Surface Finish

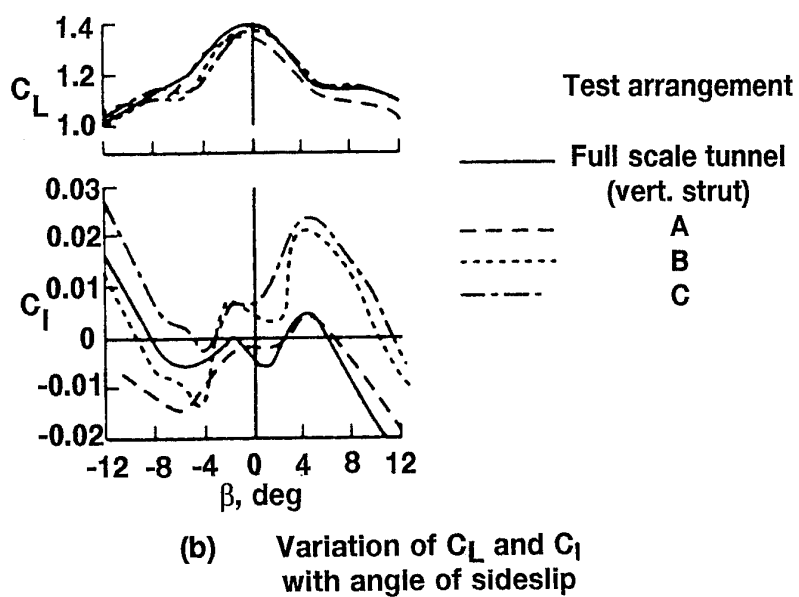
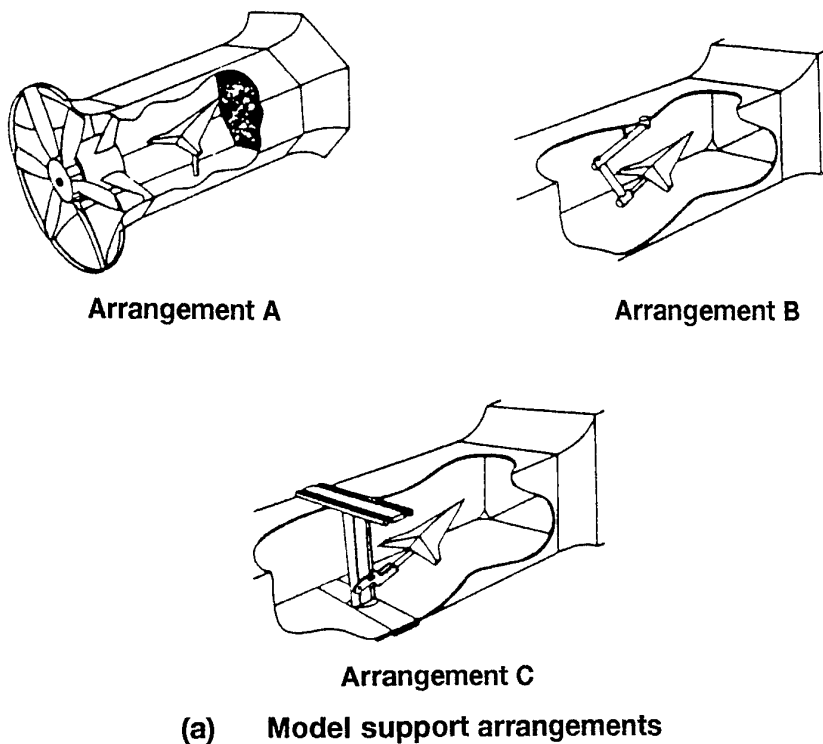
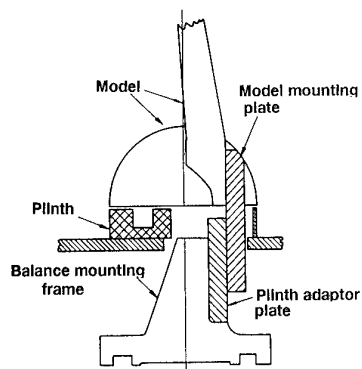
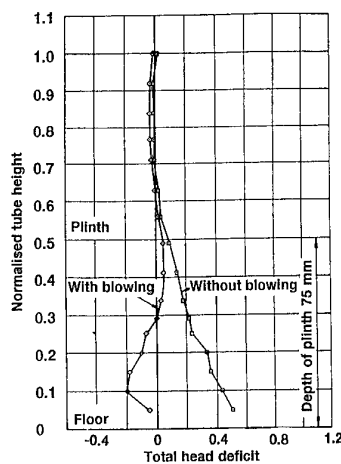


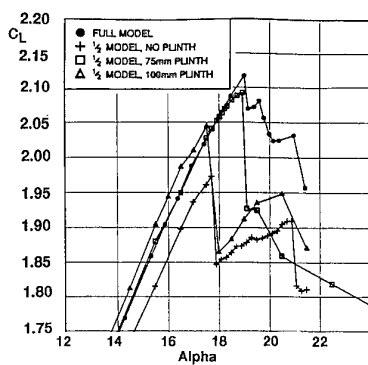
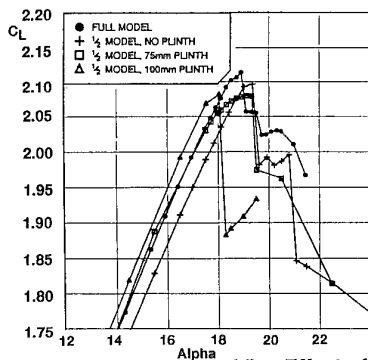
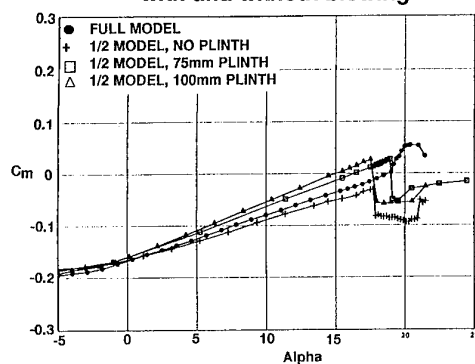
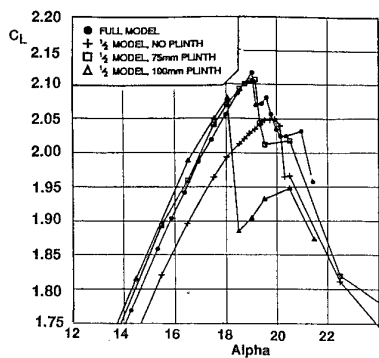
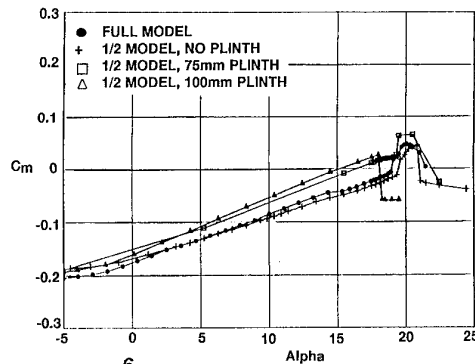
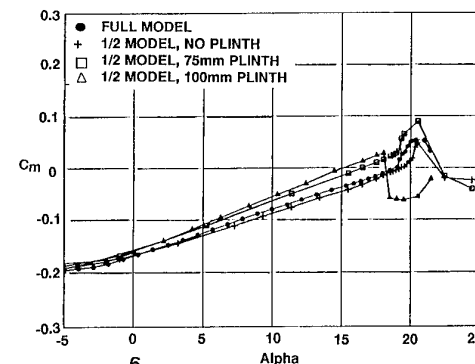
FIG 2.31 Low Speed Directional Stability Characteristics  
at  $\alpha = 35^\circ$   
(from refs 46, 52,)



(a) Half-model mounting geometry



(b) Comparison of velocity profiles with and without blowing

(c) Effect of Plinth, no BLRE,  $Re = 5.0 \times 10^6$   
 $M = 0.20$ (d) Effect of Plinth, no BLRE,  $Re = 6.45 \times 10^6$   
 $M = 0.20$ (e) Effect of Plinth, with BLRE,  $Re = 5.0 \times 10^6$   
 $M = 0.20$ FIG 2.32 Effect of Half-model Mounting Technique  
(from ref 53)



### 3 SCALE EFFECTS AT HIGH LIFT AND LOW SPEEDS

#### 3.1 Two-Dimensional Single Aerofoils

##### 3.1.1 Sources of data

Until fairly recently, most of the two-dimensional data that have been used to illustrate the variation of maximum lift at low speeds with Reynolds number for simple aerofoils with high-lift devices retracted were obtained in the period between 1935 and 1950 in NASA tunnels, particularly the NASA Langley two-dimensional Low-Turbulence Pressure Tunnel. Results for a large number of aerofoils in the NACA families, eg the NACA 6-series, at Reynolds numbers from  $Re = 3.0 \times 10^6$  to  $9.0 \times 10^6$  were published in Ref 55. The tests on some of these sections were later extended up to  $Re = 25 \times 10^6$  and the results reported in Ref 56. Over the years, many authors have attempted to collate and interpret these data. Notable amongst these analyses are those by Jacobs and Sherman<sup>57</sup> in 1934, Loftin and Bursnall<sup>58</sup> in 1950, McCullough and Gault<sup>58</sup> in 1951, Gault<sup>59</sup> in 1957, Evans and Mort<sup>60</sup> in 1959, van den Berg<sup>61</sup> in 1969, van den Berg<sup>62</sup> again in 1981 and finally, Woodward<sup>63</sup> in 1988. These reports make fascinating reading as one proceeds from speculation to qualitative understanding and ultimately, in some respects at least, to quantitative interpretation.

Subsequently, the emphasis shifted to three-dimensional sweptback wings and, as a result, high-lift tests on single-element plain two-dimensional sections are more difficult to find in the open literature. However, tests on a 17% thick supercritical aerofoil are reported in Ref 64 (1972) and also, there is some evidence<sup>65</sup> from tests in the HST at NLR in Holland. Recently, the Langley Low-Turbulence Pressure Tunnel has been heavily used again but aerofoils with the high-lift devices retracted have only occasionally figured in the published results usually as the datum case in test programmes<sup>66</sup> in which the main emphasis has been on the stalling characteristics of transport aircraft multi-element wing sections with high-lift devices extended.

##### 3.1.2 Types of stall

It has been known for many years that the stalling characteristics of single-element wing sections and the variation of these characteristics with Reynolds number can depend greatly on the section thickness-chord ratio and shape. Melvill Jones<sup>3</sup> in 1934 noted that the stall can be sudden or gradual depending on Reynolds number, stream turbulence, aerofoil shape and surface condition (roughness). It had already been realised that with a thin section at low  $Re$ , it was usual for the flow to separate near the leading edge and that with an increase in thickness and/or  $Re$ , this tendency would disappear and be replaced by a separation ahead of the trailing edge.

It follows that the appropriate starting point for any discussion of scale effects on aerofoil stalling characteristics is to describe the different types of stall that can occur. For the past 40 years, it has been standard practice to adopt the classification put forward by McCullough and Gault<sup>58</sup>. Initially, they listed three types of aerofoil stall but later<sup>59</sup>, Gault added a fourth type and in this Agardograph, the list has been further extended to include a fifth type that has been discussed by van den Berg<sup>62</sup> and others. The list of 4 types as defined by Gault in Ref 59 and as described by Woodward et al in Ref 63 is set out below and illustrated schematically in Figs 3.1, 3.2(a-d) which have been taken directly from Ref 63. The four types of stall are

- (a) thin-aerofoil stall
- (b) leading-edge stall
- (c) combined leading- and trailing-edge stall
- (d) trailing-edge stall.

In this Agardograph, category (b) has been further sub-divided into two types of stall (b,e) according to whether the flow breakdown is due to (b) a failure of the flow to reattach behind the bubble, ie bubble bursting, or alternatively (e), a separation of the turbulent boundary layer a short distance downstream of the reattachment point.

Typical  $C_L$ - $\alpha$  curves for each of these are shown schematically in Fig 3.1. The flow patterns and boundary layer states are sketched in Figs 3.2(a-e). At points A on the  $C_L$ - $\alpha$  curves, the flow patterns and boundary layer states for the four cases are similar: the boundary layer from the stagnation point to just beyond the peak suction position is attached and laminar; it then separates but this is quickly followed by transition and reattachment. In other words, there is a short laminar separation bubble followed by an attached turbulent boundary layer back to the trailing edge. Moving up the curves from points A, the subsequent development in the four cases is seen to be radically different. The main features are as follows:

- (a) For the thin-aerofoil stall, at the point B, the short bubble breaks down into a long bubble with a re-attachment point further aft. With further increase of incidence, the re-attachment point moves steadily back towards the trailing edge. This implies a progressive increase in boundary layer momentum thickness,  $\theta_{RT}$ , at the re-attachment point and hence, in the boundary layer thickness at the trailing edge. Ultimately, the lift begins to decrease at point C as a result of the rapidly growing boundary layer thickness at the trailing edge, and this usually happens when re-attachment is occurring aft of about 50% chord. This long-bubble development therefore produces a "gradual stall". It will be noted that the words "the short bubble bursts at point B to form a long bubble ...." have not been used in the above description because the present author is not convinced that a discontinuous change of this nature always occurs in the development of a long bubble. Gaster<sup>67</sup>, for example, noted that, in one of his tests, the expansion process of a long bubble was gradual and there was no sharp clear-cut "burst".
- (b) For the leading-edge stall, the general approach in most of the early literature was to interpret this type of stall as being due to the bursting of a short laminar separation bubble. However, in a little known reference written in 1959, Evans and Mort<sup>60</sup> suggested that there could be two possible mechanisms: either the bursting of a short bubble or a re-separation of a turbulent boundary layer almost immediately behind the point at which the short bubble re-attaches. Much later in 1981, van den Berg<sup>62</sup> showed that, in many cases, the second interpretation, far from being the exception to a general rule, was in fact the most likely explanation. Sketches for the two types of leading-edge stall are included as Figures (a) and (e) in Fig 3.2.

Both van den Berg and Woodward<sup>63</sup> suggest that conceptually, there is little difference between a long-bubble stall and a short-bubble bursting type of stall: the differences merely lie in when a long bubble forms and whether, on formation, it can re-attach well ahead of the trailing edge. Woodward notes that "as thickness

and/or Reynolds number is increased from an initial, well-defined thin-aerofoil stall, the point B moves to a higher value of incidence and the resulting long bubble becomes progressively longer until the point of re-attachment is either close to the trailing-edge or in the wake". This attempt to rationalise the long-bubble (a) and short bubble bursting (b) types of stall into the same family does not alter the fact that the physical nature of the two types of stall and the development of the pressure distributions with incidence are radically different. As we have seen, the thin-aerofoil stall is progressive and gradual with re-attachment still generally occurring ahead of the trailing edge at  $C_{L,max}$ , whereas with the short-bubble bursting leading-edge stall, the presence of the bubble has a trivial effect on the pressure distributions until the bubble bursts and the flow over the complete upper surface collapses,  $C_{L,max}$ , occurs when this happens and it is an abrupt stall.

The semantics of whether a short-bubble burst is really a long bubble with no re-attachment ahead of the trailing edge may be less important than the distinction between stalls (b) and (e). These stalls are superficially similar and, in practice, difficult to distinguish: both are abrupt and occur with little warning. It is however still important to try and differentiate between them as the section modifications required to improve the stall in the two cases could be different. This is an important issue in the design of helicopter rotor blade sections. These two types of leading-edge stall are discussed further in §§3.1.3.1 and 3.1.3.2.

- (c) In the third type of stall, classified by Gault as 'combined leading- and trailing-edge stall', the short bubble continues to contract with incidence until beyond the incidence at which the turbulent boundary layer begins to separate near the trailing edge. Bursting of the short bubble quickly follows and may indeed be provoked by an interaction with the rear separation. In other cases, the two developments may occur in the opposite order but in every case, the stall is characterised by a complex interaction between what is happening near the leading- and trailing-edges. This type of stall can be either abrupt or gradual depending on which element is the dominant partner. Woodward<sup>63</sup> in his description continues "in some cases a local region of incipient separation has been reported<sup>68</sup> just downstream of the short bubble re-attachment and this too promotes separation near the trailing-edge." It may be argued that the extra fifth type of stall discussed above is covered by these words and that, therefore, the fifth type as described is just a special case of this third interactive type. However, the present author prefers to continue to think of it as a separate category on the grounds that the turbulent separation does not occur near the trailing edge.
- (d) Finally, 'trailing-edge stall' as illustrated in Fig 2.3(d). In this case,  $C_{L,max}$  is determined by a rear separation spreading forward from the trailing edge. The short laminar separation bubble has degenerated to being merely the mechanism by which the boundary layer becomes turbulent. The stall is now generally a gradual stall but there are exceptions, eg see Ref 325.

Gault in Ref 59 used the test data for no fewer than 130 different aerofoil sections to derive Fig 3.3 which classifies the type of stall in terms of Re and profile

geometry as expressed by the upper-surface ordinate at 0.0125c. Only three aerofoils of the large total studied were judged to be definitely inconsistent with this correlation; with one exception, all aerofoils with  $y_{0.0125c}$  greater than the range covered in the figure exhibited a trailing-edge stall. Gault admitted that, in some cases, the decisions as to which type of stall applied were somewhat arbitrary and uncertain but he considered that the boundaries between the three fundamental types of stall, ie (a), (b) and (d), were reasonably distinct; as might have been expected, the region for the combined stall type (d) straddled the upper boundary for (b) and the lower boundary for (d). Much more is known today than in 1959 about how to predict transition and separation-onset but it is fair comment that all features in this correlation chart are still perfectly plausible in the light of present knowledge. Various important conclusions can be drawn from this chart:

- (i) increases in thickness/chord, camber and Re all tend to change the type of stall in the direction (a)→(b)→(c)→(d),
- (ii) it is possible for a single aerofoil to exhibit all the types of stall depending on the Reynolds number. Fig 3.4 shows an example\* where this is true. This is a good illustration of the difficulties in predicting the scale effect on  $C_{L,max}$  and behaviour at the stall, particularly for cases where a leading-edge or thin-aerofoil stall is observed in the tunnel tests at low Reynolds number. Clearly, the change in  $C_{L,max}$  with Re is not necessarily continuous and possibly, not even monotonic and also, a single graph expressing this variation is only part of the story as regards scale effect on the stalling characteristics,
- (iii) even at  $Re = 10^7$ , not all aerofoils will have a trailing-edge stall. It follows that discontinuous changes in the trends with Re may still occur at higher Re. It will be seen later that this is even more likely with a multiple-element aerofoil and hence, the current high level of activity in the subject.

### 3.1.3 Sources of scale effect and their prediction

The aim here is to indicate which aspects of the flow development in the five types of stall are sensitive to changes in Re and thereby, to facilitate interpretation of the test data being discussed.

#### 3.1.3.1 Bubble growth and bursting

In general, the lift coefficient and chordwise position at which the laminar boundary layer over a given aerofoil separates is not strongly dependent on Reynolds number. Indeed, for a given pressure distribution, there would be no changes with Re but one may find that, in some cases, the pressure distribution near the leading edge for a given lift will vary with Re. Obviously, this could happen in the case of a combined stall of type (iii) where a rear separation may be reducing the circulation around the section at the lower Reynolds numbers. Nevertheless, it is fair comment to say that, in most cases, the

\*It should be noted that in this figure and all subsequent figures giving the results of tests in two-dimensional flow, for convenience,  $C_L$  is the section lift coefficient; in most of the original references,  $C_l$  is chosen as the notation.

scale effects evident in stalls dominated by a laminar separation are related to what happens in the separation-bubble itself and particularly in and just downstream of re-attachment.

Figs 3.5(a,b) present expanded views<sup>58</sup> of the surface pressure distribution and boundary-layer profiles in typical short bubbles. Many investigations have shown that one can distinguish between two parts of the bubble; a forward part where the separated flow is laminar and the pressure remains approximately constant and a rear part between transition and re-attachment where there is a near-linear pressure-rise back on to virtually the pressure distribution predicted for inviscid flow. This is illustrated in the sketch in Fig 3.6 taken from Ref 69 by Horton. In passing, it should be noted that the transition process in a separation bubble has been shown to be markedly different from that on, for example, a flat plate at zero incidence. On the flat plate, transition occurs through the appearance of turbulent spots but in the case of a separation followed by transition in an adverse pressure gradient, the turbulent flow starts to remember its Tollmien-Schlichting history<sup>70</sup>.

For the past 25 years, it has been generally accepted that bursting occurs when there is a sudden failure of the turbulent shear layer to re-attach to the surface. Refs 69 and 71 by respectively Horton and van Ingen contain descriptions as to how to predict this failure to re-attach. Figs 3.7-3.10 have been reproduced from Ref 69 to illustrate various features of the short bubble development and bursting process and how it depends on Reynolds number. To comment briefly on these figures,

- (a) Fig 3.7 shows that a correlation can be established between the length of the laminar part of the bubble,  $l_1/\theta_s$  and  $Re_{\theta_s}$ , the Reynolds number based on the boundary layer momentum thickness at the point at which the laminar layer separates. A reasonable collapse of the experimental data is obtained with the relation

$$l_1/\theta_s = 4 \times 10^4 / Re_{\theta_s} \quad (3.1)$$

- (b) a relationship is then established, as shown in Fig 3.8, between the length of the turbulent part of a bubble,  $l_2/\theta_s$ , and the pressure-rise coefficient,  $\sigma$ , where  $\sigma$  is the parameter introduced by Crabtree<sup>72</sup> and defined by

$$\sigma = (p_R - p_s)/\frac{1}{2}\rho U_s^2 = 1 - (u_R/u_s)^2 \quad (3.2)$$

The favoured theoretical prediction is the curve with a dissipation coefficient,  $C_d$ , of 0.0182,

- (c) The bubble growth and busting can then be predicted graphically as shown schematically in Fig 3.9, the points T being a function of  $Re_{\theta_s}$  as given by (3.1) and re-attachment being predicted to occur when

$$(\theta/u_s \times du/dx) = -0.0082 \quad (3.3)$$

Remembering that at re-attachment, experiment has shown that the local velocity is approximately equal to that predicted for inviscid flow, it follows that, for this particular example, re-attachment is not possible, ie bursting will occur, if  $Re_{\theta_s} < 175$ ,

- (d) expanding the analysis to cover a range of inviscid pressure distributions, produces the results shown in Figs 3.10(a,b,c). The parameter, P, which appears in Fig 3.10(a) was introduced by Gaster<sup>67</sup>. It is a non-

dimensional parameter describing the pressure distribution in the vicinity of the bubble:

$$P = (\theta_s^2 \rho / \nu) \Delta u / \Delta x \quad (3.4)$$

where  $\Delta u$  is the rise in velocity over the length of the bubble,  $\Delta x$ .

Various conclusions can be drawn from these figures:

- (i) for a given pressure gradient over the bubble, increase of  $Re$  will decrease the length of the bubble,
- (ii) for a given  $Re$ , an increase in incidence on an aerofoil will generally lead to a decrease in  $Re_{\theta_s}$  and an increase in  $(-P)$  and thus, there is one factor tending to increase and another factor tending to reduce the length of the bubble. In practice, a decrease is often observed,
- (iii) the value of the pressure-rise parameter above which bursting will occur is only weakly dependent on  $Re_{\theta_s}$ , the values ranging between 0.27 and 0.36. These compare with the value of 0.35 originally suggested by Crabtree in Ref 72,
- (iv) a reasonable statement of the total length of the bubble at bursting is given by the relation

$$l/\theta_s = 6 \times 10^4 / Re_{\theta_s} \quad (3.5)$$

It follows from this equation that the Reynolds number  $U_s \times l/\nu$  is constant and so,  $l$  does not depend on  $\theta_s$  but on  $U_s$ .

The Horton method discussed above is based on the simple criterion that  $(\theta/U \times dU/dx)_R = \text{constant} = -0.0082$  for all re-attaching turbulent shear layers. Experience has shown that it tends to give slightly pessimistic results, ie it may forecast bursting when, in fact, it does not happen. van Ingen in Ref 71, on the other hand, shows good agreement between experiment and predictions based on Stratford's zero skin friction pressure distribution<sup>73</sup>. This is the limiting adverse pressure distribution which a turbulent boundary layer can just negotiate without separating. Examples of this agreement are shown in Figs 3.11(a,b) for the highest and lowest test Reynolds numbers at which a closed bubble was observed in a test on a Wortmann aerofoil<sup>71</sup>. The test Reynolds numbers in this case are very low by normal standards and so, the bubbles are long and cannot really be described as 'short bubbles'.

Perhaps the most important graph is that reproduced as Fig 3.12 and taken from Ref 67 by Gaster. On the basis of all available data, Fig 3.12 shows that, at bubble burst,  $Re_{\theta_s}$  is a function of P and hence, at bubble burst, the length of the bubble can be treated as a function of either  $Re_{\theta_s}$  or of  $(\theta_s/U_s \times \Delta U/\Delta x)$ . Young and Horton in Ref 67A show that, by making certain simplifying assumptions, one then obtains that at bubble burst,  $\Delta U/U_s = \text{constant}$  where  $\Delta U$  is the change of velocity from separation to re-attachment of the bubble and so, to the first order, we are back to the Crabtree criterion.

To place the above in the context of scale effect on leading-edge stall on aerofoils, one can say that increase of Reynolds number will

- (i) increase of chord Reynolds number by factor F reduces non-dimensional momentum thickness by  $F^{1/2}$ ,

- (ii) hence  $Re_{0s}$  increased by  $F^{1/2}$ ,
- (iii) hence  $1/\theta_s$  decreased by  $F^{1/2}$ ,
- (iv) hence, reduction in  $|\Delta U|$  and hence, (-P) at given condition but (-P) for bubble burst increased, Fig 3.12,
- (v) hence, two reasons for favourable scale effect on incidence for bubble burst: increase in  $Re_{0s}$  and increase needed to attain (-P) for bubble burst.

Quantitatively, the most important factor is the contraction of the laminar part of the bubble with increase in Reynolds number.

To turn to the question as to how to predict whether there is a short or long bubble. The original criterion put forward to Owen and Klanfer<sup>74</sup> stated that the bubble would be long or short according to whether  $Re_{0s}$  was less than or greater than about 450. Converting to  $Re_{0s}$ , this becomes  $Re_{0s} \approx 125$ . This criterion fell out of favour because it was associated with the hypothesis that a fundamental change in the stability of the separated laminar shear layer occurred below this critical Reynolds number leading to delayed transition and a longer bubble. It is now known that this hypothesis is not the correct explanation of a long bubble but the appearance of Fig 3.12 suggests that the Owen-Klanfer criterion can still be used as a first guide. For  $Re_{0s} < 125$ , a long bubble should undoubtedly form but experimental evidence such as that in Ref 67 suggests that long bubbles can also form with  $Re_{0s}$  as high as 240. Explorations<sup>67</sup> of the flow within different bubbles showed that the flow in the forward part of the bubble including the transition position<sup>325</sup> was essentially the same, irrespective of whether it was a short or long bubble. The differences lay in the rear part of the bubble where, in a long bubble, the pressure distribution showed a smoother and slower return to the corresponding unseparated curve. This can be deduced from Figs 3.13<sup>67</sup> which presents correlations against  $Re_{0s}$  - of both the total bubble length and the length of the dead-air region in the front part of the bubble: it will be seen that the long bubble points show much less scatter from the mean curve when one considers the dead-air region rather than the total length.

Another relatively unknown paper<sup>75</sup> by Kao includes a method for predicting the pressure-rise in the rear part of the bubble once the point of re-attachment is known. Kao analysed a number of pressure distributions on thin aerofoils exhibiting long-bubble, thin-aerofoil stall and found that all these distributions almost collapsed on to a single curve when plotted in the form of  $\sigma$  (as defined earlier) against  $x/x_R$  where  $x$  is measured from the leading edge (ie approximately the separation location) and  $x_R$  is the point of re-attachment. This curve is presented in Fig 3.14; it is interesting and significant that the maximum value of  $\sigma$  is near 0.35, ie the Crabtree value for bubble bursting. Also included on this figure are the results of an analysis by Roshko and Lau of pressure measurements in the separated regions of various forebodies with re-attachment surfaces; the analogy is clearly confirmed. On an aerofoil with a thin-aerofoil stall, as the incidence is increased, the long bubble progressively extends aft and the peak suction decreases in order to maintain this pressure-recovery curve.

### 3.1.3.2 Leading-edge stall by turbulent re-separation

As noted in §3.1.2, bursting of a short separation bubble is not the only possible mechanism for provoking an abrupt leading-edge stall. The other possibility is a re-separation of the

turbulent boundary layer soon after re-attachment. This possibility was first pointed out by Wallis<sup>77</sup> who considered that this was the more likely mechanism except at low Reynolds numbers. The two mechanisms, still described in 1959 as hypotheses, were considered in some detail by Evans and Mort in Ref 60. They pointed out that leading-edge stalls had been observed at values of  $Re_{0s}$  higher than the values thought to correspond to bubble bursting. They suggested tentatively that the second mechanism should apply to all leading-edge stalls when  $Re_{0s} > 350$ . They succeeded in correlating these cases in terms of two parameters, the peak velocity on the upper surface and the average velocity gradient between the positions where the velocity had decreased by respectively 1% and 6% from this peak value, the values being extracted from calculations of the velocity distributions. It was found that for these cases,  $C_{L,max}$  corresponded with when

$$u_{e,max} \times (du_e/ds)^{-1/6} = 2.0 \quad (3.6)$$

$Re_{0s}$  for all these cases was greater than 370; cases with lower values of  $Re_{0s}$  did not satisfy this relation and were thus presumed to be examples of bubble bursting. Further independent evidence in support of this relation is reported by Kao in Ref 75 and Moore in Ref 78.

The most convincing analysis indicating that not all leading-edge stalls are associated with the bursting of a short bubble is however that contained in Ref 62. van den Berg based his analysis on theoretical calculations of the flow around the nose of symmetrical Joukowski sections. Laminar separation was assumed to take place when the pressure gradient parameter

$$\lambda_s = (\theta_s^2 v)(dU/ds) = -0.09 \quad (3.7)$$

If one makes the crude assumption that the average pressure gradient over the bubble equals the pressure gradient at separation, it follows that  $P$  is also -0.09 and then from Fig 3.12, bubble burst will occur when  $Re_{0s} < 125$ . The theoretical calculations showed that for the Joukowski aerofoils assumed to be typical, the average pressure gradient was somewhat greater than at separation and it was more accurate to use  $P = -0.10$  and hence,  $Re_{0s} = 140$ . Lines corresponding to  $Re_{0s} = 125$  and 140 were calculated and plotted on the chart in Fig 3.3 with the result shown in Fig 3.15. On this analysis, bubble bursting cannot occur above the line corresponding to  $Re_{0s} = 140$  and this implies that bubble bursting is confined to the lower values of  $Re$  cannot occur in most of the area assigned to 'leading-edge stall'. In the majority of cases, therefore, another mechanism must be responsible and van den Berg continues to show that a re-separation of the turbulent boundary layer probably occurs close behind the point of re-attachment. Fig 3.16(a) presents some experimental results for the NLR airfoil 7703 at  $\alpha = 18.1^\circ$ ,  $Re = 3 \times 10^6$ . This aerofoil exhibits an abrupt stall at  $\alpha = 19.1^\circ$ . The figure gives the pressure distribution in the leading-edge region, the position and extent of the laminar separation bubble as indicated by an oil-flow test and the wall shear-stress development downstream of the bubble. At first sight, these results do not suggest that a turbulent re-separation is imminent but van den Berg argues in favour of looking at a separation parameter,  $a^+$ , representing the ratio of the pressure forces to the shear forces in wall quantities. Dimensional analysis suggested

$$\frac{\rho^{1/2} \gamma}{\tau_w^{3/2}} \frac{dp}{ds} \quad (3.8)$$

This parameter has been used in extensions of the law of the wall for flows with large pressure gradients, including nearly

separated flows<sup>79</sup>. A large value of  $a^+$  means that the boundary layer is near to separation. The data in Fig 3.16(a) was replotted in terms of this parameter with the results shown in Fig 3.16(b). It will be seen that  $a^+$  first decreases, then increases to reach a maximum at about  $s/c = 0.14-0.15$  before decreasing again. The shape of these curves suggests that separation is likely to occur near the position for  $a^+_{max}$ . The present author suspects that one could have drawn the same conclusion from calculating and plotting the distribution of the boundary layer shape factor,  $H$ . These remarks have implicitly assumed that the turbulent boundary layer being considered is a normal turbulent layer. van Ingen, notes<sup>2</sup> however that the boundary layer momentum thickness downstream of a bubble can be much greater than for a normal turbulent boundary layer starting at the laminar separation point and this could further accentuate the tendency for a turbulent separation to occur. Turbulence intensity in this region has also been observed to be higher than normal.

To sum up, there appears to be clear evidence for the existence of the two types (b,e) of leading-edge stall and except at low  $Re$ , it seems likely that (e) will be met more often. It is, of course, possible that the onset of the turbulent re-separation may quickly interact with the bubble and cause it to burst.

### 3.1.3.3 Turbulent separation ahead of the trailing edge

As we have seen, an increase in  $Re$ , eg from model to full-scale, makes it more likely that the stall will be initiated by a separation of the turbulent boundary layer ahead of the trailing edge. The primary reason for this change lies in the strong favourable scale effect often observed in leading-edge stall. As a result, the flow near the leading edge remains attached up to a higher angle-of-attack and this increases the likelihood that the flow will separate first near the trailing edge. As will be seen later, however, there is also the possibility that there will be some adverse scale effect on the incidence at which a rear separation first appears, particularly at high Reynolds numbers.

Scale effects on trailing-edge stall are to be expected because of the large changes with  $Re$  in the thickness of the turbulent boundary layer towards the trailing-edge. These can arise for several reasons. It will be recalled that at the start of §2, the distinction between direct and indirect scale effects was explained. Both types of effect are involved here but Woodward in Ref 63 found it useful to introduce a further subdivision of the direct scale effects:

- (a) changes with  $Re$  in the direct effects for a fixed transition position. In the present context, the most important of these is the fact that with increase in  $Re$ , a turbulent layer can withstand a larger pressure-rise without separating,
- (b) changes in the direct effects due to a change in transition position with Reynolds number. These can be very significant in low speed, high lift conditions because most model tests are undertaken with free transition.

In addition to the above, there are the indirect effects associated with the changes in pressure distribution as a result of the decrease in boundary layer thickness with Reynolds number. Any prediction method and any interpretation of scale-effect comparisons has to allow for the three types of effect set out above and, as far as possible, this advice has been followed in the writing of this Agardograph. It is wise to state at the outset that the direct effects of type (b) and the indirect effects are not

necessarily favourable and hence, despite the overriding importance in many cases of the direct effects of type (a), one should not be surprised to find adverse overall scale effects. This applies particularly when we move on to multiple-element wings and three-dimensional wings but examples can be found even when interpreting data for simple single aerofoils.

Woodward in Ref 63 quoted some simple relations to indicate the likely magnitude of the variation of turbulent boundary layer thickness at the trailing edge with Reynolds number. With a fixed transition position and considering only the development of the turbulent layer, the momentum thickness varies as

$$\theta_{turb} \text{ is proportional to } (Re)^{-1/5}$$

It follows that for a threefold increase in  $Re$ , for example, there is a 20% reduction in boundary layer thickness. This does not appear to be too significant but it has ignored the effect of the initial length of laminar boundary layer where momentum thickness

$$\theta_{lam} \text{ is proportional to } (Re)^{-1/2}$$

As a result, the starting thickness of the turbulent boundary layer decreases by 43% for the same threefold increase in  $Re$ . If a short laminar separation bubble is present, there is an even larger effect. McGregor<sup>80</sup> found that the boundary layer thickness at re-attachment

$$\theta_{RT} \text{ was proportional to } (Re)^{-1}$$

This implies a 67% reduction in starting thickness, some of which could actually be ascribed to a forward movement of transition in the bubble. The growth of turbulent boundary layer thickness in the two cases, with and without a laminar separation bubble are compared in Fig 3.17. These simple relations ignore the conclusion of van Ingen<sup>2</sup> that the separation bubble may also have a large effect on the turbulence structure of the downstream turbulent layer.

It follows from the above discussion that favourable scale effect on a rear stall is more likely to be observed in the  $Re$ -range in which a laminar separation is still present but progressively being eliminated by an increase in Reynolds number. Ultimately, however, with increase in  $Re$ , transition may move ahead of the bubble and this could produce an adverse scale effect because of the greater length of turbulent boundary layer (direct effect of type (b)).

One can therefore create a reasonable qualitative picture of the scale effects that may affect a rear stall of type (d). It is more difficult to suggest a simple method for quantitative prediction. It is generally accepted that the correct approach to the prediction of turbulent separation is to use the best possible method, eg a lag-entrainment method<sup>81</sup>, to calculate the boundary layer development;  $C_r = 0$  is generally used to indicate separation (despite what was written above in discussing re-separation after re-attachment). The difficulty with using the shape factor,  $H$ , is that, as shown by Cross in Ref 2, the critical value of  $H$  for separation varies significantly with the pressure gradient. Reference should be made to van Ingen in Ref 2 for a review of the state-of-the-art in turbulent separation prediction capabilities in 1988. He notes that A M O Smith showed<sup>82</sup> in 1970 that the methods of Stratford<sup>73</sup>, Head<sup>83</sup> and Cebeci and Smith<sup>84</sup> had all produced methods that gave prediction accuracies that justified their further use in general engineering analysis. Later reviews of the subject are

contained in Refs 85, 86. A clearer idea of the actual scale effect on type (d) stalls will come from the interpretation of examples from existing test data in §3.1.4 below.

### 3.1.4 Examples of scale effect

#### 3.1.4.1 Early NACA tests

The aim in the present section of the Agardograph is to discuss some selected examples of the effects of Reynolds number on  $C_{L,max}$  for two-dimensional single aerofoils and to interpret these results in terms of the types of stall that have been described in the previous paragraphs. It was seen at the outset of §3.1 that the scale effects can be large: Fig 3.4, for example, shows that  $C_{L,max}$  for NACA 64<sub>1</sub>-012 almost doubles between  $Re = 0.7 \times 10^6$  and  $Re = 9.0 \times 10^6$ . This one example shows the possible magnitude of the effects but by looking at the results for a collection of different aerofoils, one gains a better idea of where the large scale effects are to be expected and why. It is hoped that by offering an interpretation of some of the limited data in the public domain, it will help others to interpret their own particular data.

As noted earlier, the natural starting point is to consider the large stockpile of data from the NASA Langley Low-Turbulence Pressure Tunnel. Ref 61 by van den Berg contains a very clear presentation of the results from these tests and Figs 3.18(a-e) are mostly taken from this report. Figs 3.18(a-d) show the variation with Reynolds number of  $C_{L,max}$  for respectively 6%, 9%, 12% and 18% thick NACA 6-series sections and Fig 3.18(e) presents data for various other well-known NACA sections. By taking these figures from van den Berg's report, one has the advantage of his assessment of whether the stalls are gradual or abrupt; this is very helpful in arriving at an intelligent interpretation of the data.

The main conclusions to be drawn from Figs 3.18(a-e) are

- (i) when the stall is of type (a), ie thin-aerofoil stall, and one is well below the boundary for leading-edge stall, there is little variation in  $C_{L,max}$  with  $Re$ . This is shown by the results for the 6% thick sections in Fig 3.18(a) at  $Re \leq 10^7$  and for the biconvex sections in the same figure,
- (ii) as one approaches the boundary with leading-edge stall,  $C_{L,max}$  begins to increase rapidly. This is shown by the results for the 6% thick sections above  $Re = 10 \times 10^6$  and for the 9% thick symmetrical sections above  $Re = 6 \times 10^6$  and cambered section, NACA 64-409 above  $Re = 10^6$  in Fig 3.18(b). The increase in  $C_{L,max}$  for the 6% thick sections above  $Re = 10 \times 10^6$  is somewhat difficult to interpret. Loftin and Bursnall in Ref 56 associate the increase with a forward movement of transition towards the laminar separation point thus limiting the size of the long bubble and suggest that the increase in  $C_{L,max}$  with  $Re$  is ultimately arrested at  $Re = 25 \times 10^6$  by the appearance of a rear separation as part of the stalling process, ie the stall is then of type (c). van den Berg, however, in Ref 61 noting that the stall throughout the Reynolds-number range where the increase is occurring is always a gradual stall, speculates that the stall may have changed to type (d), ie a trailing-edge stall. The results for the 9% thick sections are more understandable as with increasing  $Re$ , there is clearly a transition from thin-aerofoil stall to leading-edge stall and finally, to trailing-edge stall. If the results for the 6% thick

sections at  $Re = 15$  and  $20 \times 10^6$  had been classed as abrupt stalls, one would have postulated the same interpretation as for the 9% thick sections. The present author believes that these results for the 6% thick sections can be thought of as a smooth transition from thin-aerofoil stall to a mixed leading- and trailing-edge stall of type (c),

- (iii) a large favourable scale effect on  $C_{L,max}$  occurs in the range where the stall is of the leading-edge type (b). For the NACA 6-series sections, this is observed between  $Re$  values of

$6 \times 10^6$  and  $12 \times 10^6$  for 9% thick, symmetrical sections,  
 $10^6$  and  $4 \times 10^6$  for the 9% thick, 64-409, cambered section,  
 $0.8 \times 10^6$  and  $3 \times 10^6$  for the 12% thick, symmetrical NACA 64<sub>1</sub>A212.

It will be noted that the  $Re$ -range in which there is substantial scale effect moves to lower Reynolds numbers with increase in thickness or camber. This is to be expected in the light of the changes in upper surface pressure distribution with aerofoil geometry: increases in thickness and/or camber will move the peak suction and laminar separation location further aft, thus increasing  $Re_{0s}$  for a given  $Re$  based on chord. The results for the 9% thick sections in Fig 3.18(b) at a Reynolds number such as  $Re = 6 \times 10^6$  are a first indication of how data at subscale Reynolds numbers can be highly misleading. At first sight, a test at  $Re = 6 \times 10^6$  would suggest that adding modest camber (corresponding to a design of  $C_l$  of 0.2) to the symmetrical section gives an increase in  $C_{L,max}$  of about 0.3 but this is only because of the change with camber in the  $Re$ -range for large scale effect; the true high  $Re$  gain in  $C_{L,max}$  is only about 0.2.

Reasons why there should be a significant favourable scale effect in the range where there is a leading-edge stall were explained earlier in §§3.1.3.1 and 3.1.3.2. The stall on NACA-009 at  $Re = 5.8 \times 10^6$  at the foot of the increase of  $C_{L,max}$  with  $Re$  was used by Oskam<sup>87</sup> as an example of the use of his viscous-inviscid interaction method of calculating the velocity distributions and boundary layer development. Some results from these calculations are shown in Fig 3.19; the velocity distribution on the upper surface near the nose in Fig 3.19(a) and the skin friction distributions downstream of the bubble in Fig 3.19(b). The calculations reveal the presence of a small bubble, do not predict that this bubble will burst and finally indicate that the critical point for possible turbulent re-separation lies about 2% downstream of re-attachment. These calculations do not give complete agreement with experiment in that they would not predict a stall even at  $\alpha = 12^\circ$ ,  $C_L = 1.26$  whereas in the experiment,  $C_{L,max} = 1.10$ . However, there are two reasons why the calculations could be optimistic: first, the model of the re-attachment process does not include any representation of the overshoot below the inviscid curve shown in Fig 3.19(c) and second, they do not allow for the extra turbulence induced by the bubble and re-attachment process. These may seem small points but the results are very sensitive to small points: for example, decreasing the Reynolds number from  $5.8 \times 10^6$  to  $5.0 \times 10^6$  would be sufficient to predict turbulent re-separation. It follows

from these calculations that the observed scale effect above  $Re = 5.8 \times 10^6$  is likely to be a favourable scale effect on a turbulent separation in the presence of a short bubble.

- (iv) finally, significant scale effect can also be observed when the stall is of types (c) or (d), ie turbulent separation at the rear with or without a leading-edge stall. The scale effect can be either favourable or adverse; in many cases, if one does not have sufficient points on the curve of  $C_{L,max}$  against  $Re$ , the scale effect may appear to be negligible at high  $Re$  but, as we will see below, this can be misleading, particularly if one then has to extrapolate the curve. Strongly favourable trends are evident in the results for the highly cambered 12% thick sections in Fig 3.18(c), the 18% thick sections in Fig 3.18(d) and the 12% thick sections in Fig 3.18(e). These trends can be ascribed to two effects: first, the favourable direct scale effect on the pressure-rise that can be negotiated by the turbulent boundary layer on the rear upper surface without separating and second, the likely disappearance with increasing  $Re$  of the laminar separation bubble near the leading edge. Ref 58 notes that the presence of a laminar separation bubble was found to accentuate the tendency for a rear separation to occur on NACA 63<sub>3</sub>-018. On the other hand, at higher Reynolds numbers, the scale effect can become adverse due to the effects of transition moving forward with increasing Reynolds number, particularly, it is suggested in some references, if this means that transition has moved ahead of the point where the laminar boundary layer would separate. The most glaring example of this trend is afforded by the results in Fig 3.18(d) for NACA 8318 (and, to a lesser extent in the results for NACA 65<sub>(112)</sub>A111 in Fig 3.18(e)). These particular curves are not taken from Ref 61 but from Refs 57 and 58 respectively. It was noted in Ref 57 that NACA 8318 was deliberately included in the test series to demonstrate this effect. Ref 57 states that, at the higher Reynolds numbers where  $C_{L,max}$  is falling with  $Re$ , transition is definitely occurring ahead of where a laminar boundary layer would separate and so, the stall must be of the trailing edge type; the decrease of 0.2 in  $C_{L,max}$  between  $Re = 10^6$  and  $Re = 10^7$  can only be explained by a forward movement of transition with  $Re$ .

This trend for  $C_{L,max}$  first to increase and then to decrease with  $Re$  when it is a trailing-edge stall, so obvious for NACA 8318, can also be seen in other results. If the reader ignores the curves in Figs 3.18(b,c) and looks merely at the points read off the measured data, it is in fact present in all cases in these figures for Reynolds numbers above  $Re = 8 \times 10^6$ . The decrease with  $Re$  in these cases does not amount to more than 0.1 but this can still be significant for a civil transport. It should be remembered that all these tests were made with natural transition; the results emphasise the need to be able to predict transition position accurately even when considering a two-dimensional simple aerofoil; it is not enough to say it is near the leading edge.

The above description of scale effects being based merely on the values of  $C_{L,max}$  may create the wrong impression in suggesting that scale effects on thin-aerofoil stall are minimal. At low Reynolds number, the long bubble will form at an incidence well below that for  $C_{L,max}$  and then the re-attachment point moves aft with increase in incidence. The presence of the long bubble will lead to increases in drag and nose-down pitching

moment prior to  $C_{L,max}$ . At higher Reynolds number, the first appearance of the long bubble and these resulting effects will be delayed to higher  $C_L$  and so, in this sense, the stalling characteristics in a thin-aerofoil stall can be very  $Re$ -dependent. For example, considering NACA 63-006 for which there is no significant scale effect on  $C_{L,max}$  ( $= 0.83$ ) below  $Re = 10^7$ , there are sizeable differences in drag above  $C_L = 0.2$  and the  $C_L$  for the rapid rise in drag increases from 0.55 at  $Re = 3 \times 10^6$  to 0.76 at  $Re = 6 \times 10^6$ . Hence, in this sense, the scale effects on the stalling characteristics are greatest in the  $Re$ -range when it is a thin-aerofoil stall.

### 3.1.4.2 Other examples

As noted earlier, the emphasis in the last 40 years has been on two-dimensional tests with high-lift devices deployed and on three-dimensional tests. There are therefore only a few examples to draw on to illustrate scale effect on two-dimensional aerofoil sections with the high-lift devices stowed. However, there are 6 useful references that should be discussed.

First, Ref 64 contains the results of tests in the NASA Langley Low-Turbulence Pressure Tunnel on the 17% thick supercritical aerofoil used on the T-2C aircraft. This aerofoil design is shown in Fig 3.20(a); it has a relatively flat upper and lower surface and a large leading-edge radius. Tests were made up to  $Re = 25 \times 10^6$  and results are included for three Mach numbers,  $M = 0.15, 0.22$  (and 0.30, not included here). As an added bonus, there are a few comparisons of pressure distributions measured on a three-dimensional model and on the aircraft in flight. The variation of 2D  $C_{L,max}$  with  $Re$  is shown in Fig 3.20(b) where it is compared with results for NACA 4412 and NACA 63<sub>3</sub>-018 to provide a link with Figs 3.18(d,e). It will be seen that very high values of  $C_{L,max}$  are achieved at high Reynolds number with this section: more than 2.0 at  $M = 0.15$  and 0.22; even at  $M = 0.30$  (not shown in Fig 3.20), when the upper surface flow is supercritical, the value is still 1.8.

As would be expected for a 17% thick, well cambered section, the stall is of type (d), ie a turbulent separation close to the trailing edge. A laminar separation bubble was observed at the lowest test Reynolds number,  $Re = 2.0 \times 10^6$ , with turbulent re-attachment but by  $Re = 5.8 \times 10^6$ , this has degenerated into merely the transition mechanism. Increasing the Reynolds number from  $2.0 \times 10^6$  to  $Re = 17 \times 10^6$  improves the pressure recovery at the rear of the upper surface but the extent of the rear separation having shown little change up to  $Re = 9.0 \times 10^6$ , spreads forward by about 0.05c at a given incidence between  $Re = 9.0 \times 10^6$  and  $Re = 17 \times 10^6$ . This increase in trailing-edge separation results in a decrease of about 0.11 in  $C_{L,max}$  at  $M = 0.15$  (Fig 3.20(b)). At  $M = 0.22$ , the forward extension of the separation is not as marked and it does not lead to any reduction in  $C_{L,max}$ . The authors of Ref 64 repeat the same explanation for the scale effect on  $C_{L,max}$  at high Reynolds number, viz a forward movement of transition leads to a thicker boundary layer on the rear upper surface, this effect outweighing the direct effect of  $Re$  on boundary layer thickness which, at lower  $Re$ , has produced the improvement in  $C_{L,max}$  with  $Re$ .

The second example is taken from Ref 89 which describes the aerodynamic development of the wing of the A300B. Fig 3.21 shows the variation of  $C_{L,max}$  with Reynolds number for various modifications of the leading-edge design of the basic section; the curves on this figure which are not identified are for nose shapes tested but apparently rejected on the grounds that they were not the best compromise between all requirements. Strictly, these are not 2D test data because they were obtained

from tests in the BAe Hatfield 7 ft x 9 ft atmospheric tunnel on a constant-chord untapered sweptback wing half-model with a minor fillet to ensure that the stall does not start near the root or tip. They can therefore be described as being obtained under quasi-two-dimensional conditions. The results are included here as another example of where testing at too low a Reynolds number can give a very misleading idea of the relative merits of different nose shapes. The favoured design on the basis of both low and high speed tests was Droop 2A which at  $Re = 2.5 \times 10^6$  gave an improvement of 0.33 relative to the basic section whereas at  $Re = 1.5 \times 10^6$ , the figure would have been 0.47 and at  $Re = 0.5 \times 10^6$ , it was only 0.05. All these Reynolds numbers are, of course, ridiculously low by modern standards but the example illustrates the difficulties of obtaining reliable comparisons in a standard-size atmospheric tunnel. From the earlier discussion on the NACA tests, it is no surprise to find that droop, ie extra camber, moves the main scale effect to lower Reynolds numbers. Data obtained at  $Re = 1.5 \times 10^6$  would have been misleading and it is far from certain that  $Re = 2.5 \times 10^6$  is adequate.

The third example comes<sup>65</sup> from tests in the LST and HST at NLR, Amsterdam. Results for two wing sections are shown in Fig 3.22(a); in both cases, there is a significant increase in  $C_{L,max}$  with increasing  $Re$  in the test range. For the modified 7703 section, shown in Fig 3.22(b), it amounts to 0.26 between  $Re = 10^6$  and  $Re = 3.3 \times 10^6$  and the increase does not appear to be complete; a large increase might have been forecast since it is a highly cambered, 13.8% thick section clearly designed to give considerable rear loading. On the basis of earlier examples, however, it would be unwise to assume that the increase in  $C_{L,max}$  with  $Re$  would continue indefinitely; it is likely that eventually,  $C_{L,max}$  would decrease again slightly. The second wing section, F-29-16, whose shape can be deduced from Fig 3.31(a), gives an increase of about 0.16 in  $C_{L,max}$  between  $Re = 1.8 \times 10^6$  and  $Re = 6.9 \times 10^6$ ; appreciable differences are present in the  $C_L - \alpha$  curves over a wide range of incidence prior to  $C_{L,max}$ , as can be seen from Fig 3.22(c) and Fig 3.22(d) shows that this favourable scale effect is due to the delayed appearance of a turbulent separation on the rear upper surface. These two examples are therefore consistent with earlier data and are further evidence that a sizeable favourable scale effect can exist when it is a trailing-edge stall and this can persist up to at least  $Re = 6$  or  $7 \times 10^6$ .

The next example is the only modern example in the list. It again comes<sup>66,90</sup> from the NASA Langley LTPT; the aerofoil is 14.48% thick and forms part of a joint NASA/ Douglas research programme. A new side-wall boundary layer control system was installed ahead of these tests to eliminate or at least alleviate the side wall interference discussed earlier in §2.2.1.2. Fig 3.23 taken from Ref 90 shows the variation of  $C_{L,max}$  with Reynolds number at various Mach numbers from  $M = 0.15$  to  $M = 0.32$ . The curve that has been quoted in many other papers is the curve for  $M = 0.20$  which shows a marked increase in  $C_{L,max}$  between  $Re = 3 \times 10^6$  and  $6 \times 10^6$  followed by apparently little change up to  $Re = 18 \times 10^6$ . This is however a case where it could have been advisable to have more points on the curve. However, the new significant point in Fig 3.23 is that the precise shape of the curve of  $C_{L,max}$  versus  $Re$  is dependent on Mach number: at  $M = 0.15$ ,  $C_{L,max}$  decreases with  $Re$  above  $Re = 5.5 \times 10^6$  while at  $M = 0.26$ ,  $C_{L,max}$  increases up to  $Re = 9.0 \times 10^6$ , and indeed as drawn, up to  $Re = 18 \times 10^6$ . There was a suggestion of this Mach-number effect in the results for the 17% thick supercritical section discussed above as the first example. Any interpretation by the present author must be speculative but one could suggest that contributory causes of the Mach-number effect could be

- (i) with increase in Mach number, transition could be induced whatever the Reynolds number by a shock wave in a position that does not vary significantly with  $Re$ . Hence, the factor that gives a reduction of  $C_{L,max}$  tends to vanish,
- (ii) at low  $Re$ , the boundary layer thickness on the rear of the upper surface increases with Mach number because the starting thickness has been increased by the pressure-rise through the shock at the higher stream Mach numbers.

Some calculations of the pressure distributions and boundary layer development are needed to confirm or disprove these suggestions but whatever the explanation, the results are a warning that the scale effect on a conventional trailing-edge stall can be sensitive to small changes in Mach number.

The next example<sup>91</sup> in this group does not include any striking evidence of Reynolds-number effects but is helpful because it offers further clear evidence that there are two mechanisms for leading-edge stall. This report discusses the results of dynamic stall experiments in the US Army AMRDL 7 ft x 10 ft tunnel at NASA Ames on NACA 0012, various modifications of NACA 0012 and ONERA's "0012a Extension Cambre" aerofoil<sup>92</sup>. The dynamic stall mechanism was studied in great detail with the aid of oil smoke flow visualisation, conventional hot-wire anemometers, skin friction gauges, reverse-flow hot-wire probes and miniature pitot-static pressure tubes facing both upstream and downstream. The tests on the basic NACA 0012 and with the section modified to give a leading-edge radius of 0.010c rather than 0.0158c - aerofoils which according to the McCullough and Gault classification should exhibit leading-edge stall and on which, in these tests, a short bubble formed as one approached the stall, gave no indication of bubble bursting. Instead, the abrupt flow breakdown occurred when a turbulent separation already present downstream of 0.3c suddenly came forward to just behind the bubble; at this moment, re-attachment behind the bubble was still observed. Further support to the conclusion that the stall was not associated with bubble bursting was provided by additional tests in which transition was tripped artificially ahead of laminar separation: it was found that there was no change in the stalling characteristics, thus proving that the laminar separation in the basic tests played no significant part in determining the stall characteristics. The ONERA Cambre aerofoil displayed a relatively gradual trailing-edge type of stall and so, the only two aerofoils in the test series that did exhibit bubble bursting were a sharp leading-edge modification to NACA 0012 with a leading-edge radius of 0.005c and the ONERA Cambre aerofoil inverted on which the stall was more abrupt than on any other configuration. The value of these tests in the present context is that the two types of leading-edge stall were clearly distinguishable with the specialised instrumentation. Fig 3.24 compares the normal force variations in a typical dynamic stall cycle for a reduced frequency,  $k = \omega c/2U$ , of 0.15 for the three types of stall observed in these tests. This comparison shows that the distinction between the two types of leading-edge stall is far from academic in its implications for helicopter rotor blade design. Ref 91 should be consulted for further details.

No significant Reynolds number effects were observed between  $Re = 2 \times 10^6$  and  $3.5 \times 10^6$  in this last example but at the lowest test Reynolds number of  $Re = 1.5 \times 10^6$ , the stall occurred at a slightly lower incidence. One can conclude that the results offer further support to the thesis that, except at very low Reynolds numbers, leading-edge stall is generally associated with turbulent re-separation rather than bubble



bursting. Ridder<sup>93</sup> in tests on a special model with an elliptical leading edge did, in fact, observe the change between the two mechanisms as he increased Reynolds number.

Finally, one should mention Ref 108. This will be discussed at some length in §3.2.2.1 when considering the results with high-lift devices extended but it does also include results for two single-element, 11% thick aerofoils with very different nose shapes. The variations of  $C_{L,max}$  with Reynolds number for these sections illustrate different trends:

- (i) for the section with the larger nose radius,  $C_{L,max}$  increases by about 0.16 between  $Re = 3 \times 10^6$  and  $Re = 5 \times 10^6$  and then increases slightly by about 0.02 with Reynolds number up to  $Re = 18 \times 10^6$ , and
- (ii) for the section with the smaller nose radius,  $C_{L,max}$  increases by 0.05 between  $Re = 3 \times 10^6$  and  $Re = 7 \times 10^6$  but then decreases by about 0.03 with further increase in  $Re$  up to  $Re = 12 \times 10^6$ .

Morgan et al, the authors of Ref 108, note that these contrasting trends, ie a rapid increase followed by a gentle increase or alternatively an increase followed by a decrease, are typical of what one expects for respectively, a trailing-edge and a leading-edge stall. This is consistent with forecasts based on the pressure distributions for these two particular sections but, at first sight, is inconsistent with the earlier discussion in this Agardograph where the possibility of  $C_{L,max}$  decreasing with Reynolds number at high  $Re$  was not mentioned until trailing-edge stalls were being discussed. However, the present author believes that there may be no inconsistency here if what is implied by the statement in Ref 108 is that decreases in  $C_{L,max}$  at high  $Re$  are to be expected with sections where the stall at the lower Reynolds numbers but only at the lower  $Re$  is a leading-edge stall; the decrease at high  $Re$  then occurs when the transition moves ahead of the point at which the laminar boundary layer was separating. Quite possibly, if this hypothesis is correct, the actual curve of  $C_{L,max}$  against  $Re$  for (ii) would have shown a slight discontinuity if there had been more experimental points on the curve (there were only 3 points in these tests) rather than a smooth decrease.

### 3.1.4.3 Summary of conclusions

To summarise,

- (i) increases in drag and nose-down pitching moment prior to  $C_{L,max}$  in a thin-aerofoil stall are postponed to higher  $C_L$  as  $Re$  is increased,
- (ii) large favourable scale effect on  $C_{L,max}$  can be observed in the  $Re$ -ranges in which the stall changes from thin-aerofoil to the leading-edge type and in which there is a leading-edge stall. This can continue up to  $Re = 25 \times 10^6$  for a very thin or sharp-nosed section,  $12 \times 10^6$  for a 9% thick symmetrical section or  $4 \times 10^6$  for a cambered, 9% thick section,
- (iii) very large favourable scale effects can be observed up to Reynolds numbers as high as  $6 \times 10^6$  when the stall is a trailing-edge stall but at higher Reynolds numbers, reductions in  $C_{L,max}$  with  $Re$  of 0.1-0.2 can occur if the effects of a forward movement of transition outweighs the normal beneficial effect of increasing  $Re$  on the ability of a turbulent boundary layer to withstand an adverse pressure gradient without separating,

- (iv) the scale effect on trailing-edge stall can depend on the Mach number,
- (v) except at low  $Re$ , leading-edge stall is more likely to be due to a turbulent re-separation than to the bursting of a laminar separation bubble. This could make it easier to predict the scale effect from CFD calculations,
- (vi) in many cases of practical interest, testing at  $Re = 6$  or  $7 \times 10^6$  will be sufficient to avoid the largest scale effect but it is not sufficient to eliminate all scale effect and unfavourable scale effect at higher  $Re$  should not be treated as experimental scatter.

## 3.2 Two-Dimensional Multiple-Element Aerofoils

### 3.2.1 Sources of scale effect

In this section of the Agardograph, the discussion moves on to consider the likely scale effects on the flow over a multiple-element aerofoil, eg slat-main wing-flap combination, still in two-dimensional flow. Every report on the subject starts with a picture such as Fig 3.25 which is an annotated version of a figure first published in Ref 94 and repeated in Ref 63. The first point to stress at the outset is that, despite what is written in some textbooks, the function of the slots is not to provide high-energy air to boost a tired boundary layer. Anyone in any doubt on this point should consult the classic Wright Brothers lecture<sup>95</sup> by A M O Smith and the more recent survey paper<sup>96</sup> by Woodward and Lean. Smith identifies five favourable effects inherent in a slotted configuration:

- 1 the presence of the downstream elements, eg wing relative to slat or flap relative to main wing, induces considerably greater circulation on the upstream elements,
- 2 the trailing edges of the forward elements are in a region where the local velocity is appreciably higher than free-stream and this, therefore, reduces the pressure-rise to be negotiated by the boundary layer on the upper surface of the upstream elements,
- 3 the presence of the upstream element reduces the peak suction on the downstream element,
- 4 the development of the wakes of the forward elements - mostly in an accelerating flow as a result of the inviscid flow field around the slotted multiple aerofoil layout - occurs off-the-surface of the rear elements and hence in a more efficient manner than if it was occurring on the surface,
- 5 each new element starts out with a fresh boundary layer at its leading edge which, being relatively thin, is better able to withstand a given adverse pressure gradient.

These effects are illustrated in Fig 3.25; the high-lift device works essentially because it manipulates the inviscid flow; the viscous effects can act as a restraint on what can be achieved.

There are many possibilities for scale effect in the flow illustrated in Fig 3.25; the discussion below is largely based on Woodward's presentation in Ref 63. Many of the effects are interrelated and often, it is not immediately obvious what is the trigger for the sequence of events in the stall. However, to list the main possibilities:

- (i) on the slat, at low Reynolds number, it is likely that there will be a bubble separation which, for a highly loaded slat, could be shock-induced. With increasing Reynolds number, experience has shown that this can suddenly change to a separation ahead of the slat trailing-edge. This implies an almost discontinuous change from bubble-dominated to conventional scale effect, to use Woodward's terminology. Woodward notes that for many take-off configurations, the slat is very highly loaded and the initial separation occurs on this element. This may not be immediately apparent even in oil flow experiments because the thick slat wake frequently engulfs the main wing and triggers separation also on this element,
- (ii) there are separations in the coves on the back of both the slat and main wing and, in principle at least, these could be sensitive to changes in Reynolds number,
- (iii) the stall may originate from a separation ahead of the trailing-edge of the flap shroud in a similar manner to a trailing-edge stall on a thick single-element wing. This tendency may be accentuated by the presence of a separation bubble near the nose of the main wing. The separation on the flap shroud may be caused directly by the pressure rise between the peak suction and the shroud trailing-edge or may be influenced by the indirect effects of a separation on the flap or the direct effects arising from the interaction between the slat wake and main wing boundary layer (the words 'direct' and 'indirect' are here being used in the sense defined at the beginning of §2). A separation on the flap becoming more pronounced with increase in incidence has the effect of reducing the circulation around the flap and hence of reducing the peak suction on the flap and this will increase the required pressure-rise on the upper surface of the main wing, thus aggravating the tendency for the flow to separate on this surface,
- (iv) the viscous effects on the flap are likely to be highly sensitive to Reynolds number. Woodward describes this scale effect as a slot-flow dominated scale effect. This is apt because it would not exist in the same way if there were no slot but the phrase does not entirely convey to the newcomer to the subject the possible nature of these complex effects. This is going to be a leading feature of many of the examples of scale effect to be discussed later in §3.2.2 and so, one must pause at this point to discuss in detail how the stalling characteristics can vary as the position of the flap is changed relative to the main wing.

The most comprehensive set of data on the effect of flap position is that discussed in Refs 63, 96 and extracted from Ref 97. These data were obtained from tests on a quasi-two-dimensional end plate model; the results are presented in Fig 3.26(a) where  $\Delta C_{l,max}$  is the change in  $C_{l,max}$  relative to the best value achieved in area B. It is known that at small flap gaps and moderate incidence, there is a significant interaction between the main wing plus its wake, and the flap, which leads to a reduction in the loading and peak suction on the flap. As a result, the flow over the flap remains attached; as the incidence is increased, the thickness of the wing wake increases and this is amplified in the flow over the flap by the adverse pressure gradient and wake/boundary layer interaction. The displacement effect of this thick viscous layer leads to a large lift loss relative to the inviscid level, which increases with increasing incidence, and hence to the rounded top to the lift

curve as shown. At intermediate gaps, the interference between the wing plus wake and the flap, at low incidence is not large enough to depress the peak suction on the flap sufficiently to allow an attached flow. However, as incidence increases, the thickness of the wing wake increases and, at some point, the resulting interference does become sufficient to permit an attached flow (Fig 3.26(b)). The resulting viscous layer is now thinner than at the smaller gaps and hence, the lift at a given incidence is greater as shown in Fig 3.26(a). At the largest gaps, the interference never becomes sufficient to cause the flap flow to attach and hence, the lift at all incidences is less than at the smaller gaps and  $C_{l,max}$  is also substantially lower, Fig 3.26(a) shows that the boundary in the (x-z) plane between the good intermediate gaps and the unattractive large gaps marks a very sudden and dramatic fall in  $C_{l,max}$ . Clearly, without the understanding of the complex flow, the  $C_l - \alpha$  curves for different flap locations would have been difficult to interpret. It is important to note that the wing wake and flap boundary layer do not have to merge for there to be significant interaction between them; the displacement effects of the wake flow and the imposed pressure gradients in the interaction are vitally important.

The end-plate model tests just discussed were all made at the same Reynolds number but the implications for scale effect are obvious. With increase in Re, the wing wake and flap boundary layer become thinner and so, a configuration that has been in area B in a model test at low Re can be in area C at higher Re, thus producing the 'negative Reynolds-number effect' noted in many recent references, i.e. a decrease in  $C_l$  at a given incidence with increasing Reynolds number. The effect of an increase in Re is equivalent to the effect of an increase in the size of the gap. In other words, the best slotted flap position at full-scale might well be a position that may have been rejected at first sight of the model test results because, at these Reynolds numbers, it lay in area A.

It may be helpful at this point to include one example<sup>98</sup> from the published literature in support of the above description of the flow over a wing-flap combination. The tests in this case were made in the LST at NLR Amsterdam at  $Re = 2.51 \times 10^6$  in a special research experiment designed to serve as a test case for CFD developments. The configuration was not a practical design in the sense that it would have been impossible to stow the particular flap shroud as tested in the flaps retracted configuration. The geometry is such that

- (i) there is no separation on the flap shroud, and
- (ii) the wing wake and flap boundary layer do not merge ahead of the flap trailing-edge.

The geometry is shown in Fig 3.27(a), the measured  $C_l - \alpha$  curve in Fig 3.27(b) and the measured pressure distributions over the wing and flap at two incidences in Fig 3.27(c). Measured velocity profiles above the wing upper surface at the lower test incidence ( $6^\circ$ ) are shown in Fig 3.27(d) and similarly, above the flap in Fig 3.27(e). Calculations were made in 1980 by NLR by an inviscid/viscous method where the potential flow problem is solved by a revised version of the 2D NLR panel method and the presence of the viscous shear layers is modelled in the inviscid flow by an outflow boundary condition on the aerofoil surface and the wake centre-line as discussed in Ref 87. Fig 3.27(f) compares the calculated and measured velocity and momentum thickness distributions on the flap upper surface at  $\alpha = 6^\circ$  and finally, Fig 3.27(g) presents a comparison of the measured pressure distribution over the flap at  $\alpha = 6^\circ$  with the distributions calculated with and

without allowance for the viscous effects. It was not possible to present a similar comparison for  $\alpha = 13.1^\circ$  since the calculations forecast reversed flow in the wake but this was not observed in the experiments. However, in 1988, the same experimental results were used as a test case for the latest UK theoretical method, FELMA, and Fig 3.28 presents a successful comparison<sup>99</sup> for  $\alpha = 13.1^\circ$ . FELMA is a compressible Finite Element Method developed by King at BAe (Hatfield) for calculating the inviscid flow around multiple-element aerofoils coupled by Williams of DRA to an integral method for calculating the viscous flow close to the aerofoil and its wake. The coupling can be performed by either a semi-inverse (SI) scheme or by a quasi-simultaneous (QS) approach; the two procedures gave the same results within engineering accuracy. The main points to note from this example are:

- (i) a laminar separation bubble is present on the main wing upper surface at both incidences,
- (ii) the static pressure and the potential flow velocity vary across the wake above the flap and the velocity defect in this wake is very large,
- (iii) the wing wake and the flap boundary layer do not merge ahead of the flap trailing edge,
- (iv) there is reasonable agreement between the calculated and measured velocities and momentum thicknesses on the flap but the calculations predict a laminar separation ahead of where transition is observed in the tests. A similar difference was observed on the wing lower surface but the significant point in the present context is that transition is occurring well aft on the flap, thus allowing plenty of scope for a forward movement of transition with Reynolds number if the tests had been extended to higher Reynolds numbers,
- (v) despite (iii), the effects of the wing wake on the pressures on the upper surface of the flap are dramatic and, as a result, the loading on the flap is substantially below the predicted loading for inviscid flow and indeed, the loading decreases with increasing incidence,
- (vi) generally, the agreement between experiment and the results from the FELMA method for viscous flow is very good with the marked change in the pressure distribution over the flap due to viscous effects being well predicted. Bearing in mind, however, that this is a relatively easy test case, King and Williams conclude that further improvements to the method are still desirable, particularly as regards the development of viscous layers over the flap where the wing wake is in a region where there is a strong adverse pressure gradient,
- (vii) the comparisons confirm that, except possibly near the extreme trailing-edge, the flow over the flap is attached and so, the configuration is in area A. This is confirmed by the shape of the lift-incidence curve (see Fig 3.26(a)). This leaves open the possibility that, at higher Reynolds numbers, the configuration could be in area B or even C. It would clearly be helpful if some suitable configuration were chosen and calculations made by FELMA for a range of Reynolds numbers to demonstrate this type of scale effect.

### 3.2.2 Examples of Scale Effect

#### 3.2.2.1 Flap effectiveness

The early tests in the NASA Langley LTPT included a number of examples where a split flap was added to one of the NACA 6-series sections. The scale effects on  $C_{l,max}$  are to be found in Ref 61. van den Berg concluded that with these split flaps, it was unlikely that there would be any appreciable Reynolds number effect on the flow over the flap and so any scale effects would come from the flow over the basic section. It appeared that the increment in  $C_{l,max}$  from the flap decreased with increasing Reynolds number for a thin section and increased with Re for a thick section; there was little variation above  $Re = 4-6 \times 10^6$ . A surprising result was that with a split flap, one could obtain an abrupt stall even with a thick section.

However, the emphasis in an Agardograph being written in 1993 should be on slotted flaps. Perhaps the most striking feature discussed in §3.2.1 above was the possibility of 'negative scale effect' for a wing with a slotted flap. The first example below shows that this phenomenon should not have been hailed as a new discovery in recent reports. It is present in the results described in Ref 88 written in 1947. Tests were made in the NACA Langley 2-D Low Turbulence Pressure Tunnel on a model of NACA 65<sub>(112)</sub>A111(approx) airfoil with a 0.35c slotted flap at Reynolds numbers from  $Re = 2.4 \times 10^6$  up to  $Re = 25.0 \times 10^6$ . Initially, the setting of the flap was optimised at  $Re = 2.4 \times 10^6$ ;  $C_{l, \alpha}$  curves for these settings at deflections from  $35^\circ$  to  $45^\circ$  are shown in Fig 3.29(a). It will be noted that the curve for the  $40^\circ$  configuration described as ideal has the characteristic shape discussed earlier where there is an increase of lift-curve slope at incidences approaching the stall. Racisz notes that tuft studies showed that the flow over the flap upper surface was separated over most of the incidence range but that it became attached in the range where there was an increase in the slope. This is consistent with the conclusions from the analysis of later data in the UK National High Lift Programme discussed in §3.2.1 and shown in Fig 3.26(a). Fig 3.29(a) shows that this characteristic is still present but to a much smaller extent when the flap at  $40^\circ$  is moved to a slightly different position or when the deflection is increased to  $45^\circ$ . An increase in Reynolds number to  $9 \times 10^6$  has a dramatic effect on the results as shown in Fig 3.29(b). The  $40^\circ$  configuration judged as ideal on the basis of the  $Re = 2.4 \times 10^6$  results shows a marked adverse Re-effect in that  $C_{l, \alpha}$  at a given incidence at low  $\alpha$  drops by almost 0.3 at  $Re = 9.0 \times 10^6$  relative to  $Re = 2.4 \times 10^6$  and while it is true that  $C_{l,max}$  shows an increase with Re of about 0.2, the value at  $Re = 9.0 \times 10^6$  is not as good as the best that can be obtained with a smaller deflection of  $35^\circ$ . So, the final conclusion is that, as a result of the tests at  $Re = 9.0 \times 10^6$ , one should choose  $35^\circ$  rather than  $45^\circ$  and move the flap about 1% further up relative to the ideal position for  $35^\circ$  at  $Re = 2.5 \times 10^6$  (x and y are the chordwise and normal to chord dimensions of the centre of the leading-edge radius of the flap relative to the flap shroud trailing-edge (x positive forward and y positive down). The  $35^\circ$  setting with (-1.98, 3.21) was chosen as the best position and tested up to  $Re = 25 \times 10^6$  and the variation of  $C_{l,max}$  with Re is plotted in Fig 3.29(c). It will be seen that above  $Re = 13 \times 10^6$ , there is a small reduction of about 0.09 in  $C_{l,max}$  by  $Re = 25 \times 10^6$ . There is no particular change in the shape of the  $C_{l, \alpha}$  curve in this range: as at  $Re = 9.0 \times 10^6$ , it has well-rounded top suggesting that this flap position at these Reynolds numbers is in area A in Fig 3.25. The reduction in  $C_{l,max}$  with Re probably implies that the flap position should have been re-optimised again at  $Re = 25 \times 10^6$ .

or possibly that there is a forward movement of transition with  $Re$ .

The results in Ref 88 should therefore have sounded a warning that the effects of the wing wake on the flow over a slotted flap could be very sensitive to changes in Reynolds number. It certainly became generally accepted that, in many cases, the optimum flap gap was likely to be a function of Reynolds number. It was argued, eg in Ref 94 in 1970 that, in the optimum position, the boundary layers on the flap shroud lower surface and flap upper surface would just meet and that this conclusion provided a means of estimating how the optimum gap would reduce with increasing Reynolds number. However, in the light of present knowledge, this remark and other conclusions in the reports from this period should be treated with caution. For example, Ref 94 written in 1972 concludes that, for the wing-flap configuration considered, the effect of the wake from the main wing was small compared with that of the flap boundary layer itself. This is however misleading and it should not be treated as a general conclusion. In arriving at the conclusion, the development of the boundary layer over the flap upper surface was taken from experimental measurements and, therefore, already contained the influence from the proximity of the main wing wake which, at that time, could not be calculated. Also, one should note that the conclusion was based on a study for merely zero incidence; also, there was a separation at the flap trailing edge and the velocity defect in the wing wake was relatively mild compared with values observed in configurations of current practical interest. Hence, there are several reasons why the conclusion may not read across to present design exercises.

Tests in the NLR HST at Amsterdam in the early 1980s demonstrated the adverse scale effect that could be present in the flow over a slotted flap configuration. It was, in fact, clearly shown in the proving tests on the 2-D test setup in this tunnel<sup>100</sup>. The results of these tests are shown in Fig 3.30. Tests were made at  $M = 0.19$  and at Reynolds numbers from  $1.8 \times 10^6$  to  $6.9 \times 10^6$ . The results for the basic section with high-lift devices retracted present a familiar picture: increase of  $Re$  produces a more linear  $C_L - \alpha$  curve and an increase in  $C_{L,max}$  of about 0.22, suggesting a reduction with  $Re$  in the boundary layer thickness: an example of conventional scale effect associated with the reduction of boundary layer thickness with Reynolds number. Deployment of a single slotted flap and even more, deployment of the slat and double slotted flap introduces an adverse scale effect. At moderate incidences, there is a reduction of  $C_L$  with  $Re$  at a given incidence of 0.04 and 0.24 respectively for these two cases and even although these adverse effects tend to clear up as the stall is approached, the favourable scale effect on  $C_{L,max}$  decreases from 0.22 for the basic section to respectively 0.12 and 0.07. The results for  $Re = 1.8 \times 10^6$  therefore convey a very optimistic idea as to the high  $Re$  performance of these multi-element configurations.

Obert in Ref 101 presents results from several extensive series of two-dimensional tests in the LST and HST at NLR in support of the development of the Fokker F-29. The work had begun in the mid-1970s with tests on high-lift devices on the advanced NLR aerofoil, NLR 7301. Consideration of primarily the high-speed data then led to the development of modified sections with smaller leading-edge radii; two of these sections, 'NLR 7703 modified' and F-29-12 are shown in Fig 3.31(a). Both these sections were tested with a range of high-lift devices, 'NLR 7703 modified' at Reynolds numbers up to  $Re = 3.2 \times 10^6$ , and F-29-12 at high  $Re$  up to  $Re = 6.9 \times 10^6$  in the HST. A selection of results is presented in Figs 3.31(c,d,e). The results for 'NLR 7703 modified' with devices extended appear encouraging: a large increase in  $C_{L,max}$  with  $Re$  up to  $Re = 3.2 \times$

$10^6$ , particularly for the slat  $10^\circ$ , double slotted flap  $35^\circ/20^\circ$  configuration. However, the later tests on F-29-12 at higher Reynolds numbers show how unwise it would have been to extrapolate the results on 'NLR 7703 modified' to higher  $Re$ . With F-29-12, the same slat/flap combination gives a value of  $C_{L,max}$  that hardly changes with  $Re$  between  $Re = 2.0 \times 10^6$  and  $Re = 6.9 \times 10^6$  but even this statement is open to misinterpretation. It does not mean there is no scale effect in this range; it means that the favourable scale effect on the basic wing has been offset by an adverse scale effect associated with a separation on the flap which becomes more pronounced with increase in Reynolds number. Fig 3.31(b) confirms that this is the correct interpretation since the pressure distributions indicate that with the flap at merely  $20^\circ$ , there is a separation ahead of the flap trailing edge with the separation position moving forward with increase in Reynolds number. Fig 3.31(e) highlights the decrease in the flap contribution to  $C_{L,max}$  with increase in  $Re$ , the adverse scale effect becoming more pronounced with increasing flap deflection. Fig 3.31(d) shows the reduction with  $Re$  in the  $C_L$  at a given incidence. It would have been of interest to have seen how much of the adverse scale effect could have been recovered by a change in flap position or flap shape.

Turning now to the more recent work in the NASA Langley LTPT, there are many references to consult, eg Refs 66, 90, 102, 105-108 and 112. The results discussed in Ref 102 provide a particularly clear example of adverse scale effect due to viscous interactions. Fig 3.32(a) compares the  $C_L - \alpha$  curves for a 4-element airfoil/slat/vane/main flap configuration at  $Re = 2.8 \times 10^6$  and  $Re = 12 \times 10^6$ . There is an appreciable reduction of  $C_L$  at a given incidence at moderate incidences and the results of CFD calculations shown in Fig 3.32(b) show convincingly that the explanation lies in the contrasting development of the wing wake at the two Reynolds numbers. At  $Re = 2.8 \times 10^6$ , the thickness of the wake grows dramatically over the flap but at the higher Reynolds number, the wake is relatively thin and, as a consequence, the separation on the main flap is far more pronounced and the circulation over the flap has collapsed. These theoretical calculations were made by a 2D analysis code by Kusenose et al<sup>103</sup> which employs a full potential solver coupled with a viscous model based on that used in the Euler code of Drela<sup>104</sup>. Fig 3.32 shows that these calculations correctly indicate the reduction in  $C_L$  at a given incidence; their help in showing the reason for the negative scale effect demonstrates the value of performing such calculations for more than one  $Re$ : a practice that could with advantage be followed more often. At high incidences approaching the stall, the thickness of the wing wake will increase even at the higher Reynolds number and, as a result, the interaction will tend to reduce the loading on the flap. This has the effect of alleviating the separation on the flap and so, the actual loading on the flap is greater than at lower incidences and positive scale effect is restored at the stall. Possibly, despite this improvement, a different flap position nearer to the wing wake would have given a better  $C_{L,max}$  at high Reynolds number.

Major test programmes have been undertaken in the NASA Langley LTPT in association with the Douglas Aircraft Company. In the present context, the studies<sup>90,66</sup> on two landing configurations are of particular interest because they exhibit different sensitivity to Reynolds number. In both cases, the first move was to optimise the position of the leading-edge slat at a gap of 2.95%, an overhang of -2.5% and a deflection of  $30^\circ$  (the same position for both flap configurations). Flap I was a single-segment flap and II had an additional auxiliary flap, ie II was in total, a 4-element aerofoil - for the

nomenclature of the geometry, see Fig 3.33(a). Both were optimised at a Reynolds number of  $9.0 \times 10^6$  and the variation of  $C_{L,max}$  with Reynolds number is shown in Fig 3.33(b); much larger effects are shown for the single segment flap. This is ascribed in Ref 66 to the different geometries of the flap arrangements and, in particular, to the fact that, as might have been expected, the gap is much smaller with the single-segment flap. The single-segment flap was optimised with a gap of 1.32%, an overhang of +1.0% and a deflection of  $30^\circ$  and the two-segment flap with the main flap having a gap of 2.9%, an overhang of -1% and a setting of  $35^\circ$ . The  $35^\circ$  setting had to be abandoned for the single-segment flap because, as shown in Fig 3.33(c), the flow was separated on the flap upper surface (but see later as to how this could have been avoided). With the two-segment arrangement, the presence of the auxiliary flap (set with an additional  $15^\circ$  deflection and a gap of 0.68% and an overhang of 0.75%) increases the velocity at the trailing-edge of the main flap and hence, higher peak suctions can be accepted on the main flap without the risk of flow separation. With the single-segment flap, to arrive at an optimum position, the flap has to be positioned nearer to the main wing to take advantage of its downwash and the proximity of the wake. Plausibly, therefore, one might have expected the greater sensitivity to Reynolds number in the results for the single-segment flap.

Fig 3.33(d) shows that the changes in  $C_{L,max}$  with Reynolds number with the single-segment configuration I are due to changes in the lift contribution from the main wing. Compared with the results at the design Reynolds number,  $Re$ , of  $9.0 \times 10^6$ ,

- (i) at  $Re = 5 \times 10^6$ , there is a reduction of the slope of the  $C_L - \alpha$  curve for the main wing contribution - this implies a thicker boundary layer,
- (ii) at  $Re = 16 \times 10^6$ , the curve breaks at a lower incidence.

The nature of the changes that lead to the lower values of  $C_{L,max}$  at the two non-design Reynolds numbers is therefore different but - and this is the important conclusion added by the present author - the trends are completely consistent with what would have been expected from Fig 3.26(a) discussed in §3.2.1. One is tempted to say that the configuration is in area A at  $Re = 5 \times 10^6$ , area B at  $Re = 9 \times 10^6$  and area C at  $Re = 16 \times 10^6$  but this is not completely fair because the changes on the flap are trivial. However, there is certainly a similarity in that the changes on the main element are flap-induced.

With the two-segment flap II with a much larger wing/flap gap, the story is somewhat different. Comparison of Figs 3.33(d,e) shows that the flap is more highly loaded with II; also, figures in Ref 90 not reproduced here show that the adverse pressure gradients over the rear of the main element upper surface are less severe with II. For these two reasons, it is possibly not surprising that the reasons for the small reduction in  $C_{L,max}$  with  $Re$  between  $Re = 9 \times 10^6$  and  $Re = 16 \times 10^6$  are to be found on the flap and auxiliary flap rather than on the main wing.

Valarezo in Ref 105 note that these tests in the NASA Langley LTPT are now being extended to include surveys of the flowfield above the flap. At the time of writing Ref 105, some early data for the maximum lift condition on one particular configuration showed that the wakes from the slat and main wing had completely merged over the flap and that the air in this combined wake was very slow-moving and indeed, reverse flow was observed in a condition where the flap surface pressures gave no sign of flow separation - see the pressure distribution in Fig 3.33(f). These observations could be relevant to the fact that, in discussions when collecting material for this

Agardograph, the author has heard of various cases where the scale effects on drag at high lift have apparently not been consistent with the scale effects on lift: the regions of reverse flow will contribute to the loss of total head in the final wake and hence, to the drag.

Another area where testing at low Reynolds number can be misleading is in the effects<sup>106</sup> of adding a split flap at the trailing edge as a means, for example, of altering the spanwise lift distribution on a three-dimensional wing. In the 2D tests in the NASA Langley LTPT, the action of the split flap was simulated by adding a wedge to the lower surface at the trailing edge (Fig 3.34(a)). Tests of this nature were undertaken with the  $30^\circ$  single-segment flap configuration discussed above with the results shown in Fig 3.34(b). It will be seen that the increment in  $C_{L,max}$  generally increases with the angle of the wedge but at the higher Reynolds number ( $9 \times 10^6$ ), the increment for a  $60^\circ$  wedge is only about 0.06 compared with almost 0.20 at  $Re = 5 \times 10^6$ . The increment in lift from the wedge is obtained on the main wing rather than on the flap and with the wedge fitted, the results show that an earlier flow breakdown is provoked on the main wing at the higher Reynolds number. This again demonstrates that the sensitivity of the flow to small changes in the configuration geometry is greater at the higher Reynolds number and clearly, there is a need to test at the highest possible  $Re$ .

The emphasis in the discussion of the above examples on the scale effect depending on the interaction of the slat/wing wake on the flow over the flap might lead the reader to conclude that little could be achieved in reducing adverse scale effect by modifications to the flap surface geometry or by attempting to control the flow over the flap surface. One is tempted to conclude - wrongly - that it is all a question of the relative positions of the component surfaces. Obviously, as seen, relative position and angular setting of the flap can have a first-order effect but local changes in shape etc can also notably change the scale effect. The aim should be to suppress or at least, to control the separations that develop on the flap at Reynolds numbers above that at which the configuration was optimised. Two examples of where this approach has been rewarding will now be discussed.

First, Douglas Aircraft redesigned<sup>106</sup> the shape of the single-segment flap discussed above and this gave notable improvements and incidentally reduced the sensitivity of the design to changes in Reynolds number. The revised shape of this advanced flap is compared with the original shape in Fig 3.35(a) and the performance improvements are shown in Fig 3.35(b):  $C_{L,max}$  at the design  $Re$  of  $9.0 \times 10^6$  is increased by 0.07, the lift at a given incidence at moderate to high incidences is increased and the drag is reduced considerably, particularly around the approach condition ( $C_L = 3.1$ ) where the reduction amounts to as much as 29%. The measured pressure distributions plotted in Figs 3.35(c,d) provide the explanation: at  $\alpha = 8^\circ$ , the flow separation evident on the upper surface of the original flap is suppressed by the modification and it is then possible to develop more lift on the flap by reoptimising the position to increase the peak suction still without a separation. At  $\alpha = 21^\circ$ , where there was no separation to suppress, one retains the advantage of the higher peak suction. Incidentally, these pressure distributions for the original shape confirm that, as was hinted earlier, the original flap I was operating in area B of Fig 3.26(a). The original flap was optimised at a position with positive overhang (overlapping) and a gap of between 1.5 and 2.0% but the advanced flap could with advantage, be brought nearer with negative or zero overhang and a gap of between 1 and 1.5%. However, for this Agardograph, Fig

3.35(e) is the important picture since it shows that having eliminated the tendency to separation on the flap upper surface, one has also eliminated the reduction in  $C_{L,max}$  with Re above the design Reynolds number. In other words, one should not assume that optimising a flap configuration for a Reynolds number such as  $Re = 9 \times 10^6$  necessarily produces a design highly tuned to this Reynolds number. The moral is that one should not merely look at the values of  $C_{L,max}$  but one should study the pressure distributions at and below the stall and then consider whether it is easy to modify the shape to avoid any tendency to separation. If it is, one may devise a shape that reduces the sensitivity to Reynolds number. One hesitates to put this forward as dogmatic advice bearing in mind that in the earlier example in Fig 3.26 discussed in §3.2.1, the best  $C_{L,max}$  was obtained in area B where there was a separation on the flap at incidences below the stall. However, the overall improvements from the Douglas advanced flap in the present case are very striking; to strengthen the argument, one should remember that in practice, one is not merely looking for a good  $C_{L,max}$ ; also important are a lower  $\alpha$  for a given lift, and even though it is a landing configuration, a reduction in drag may be attractive because it could imply a reduction in the noise on the approach. If, at the same time, one can reduce the sensitivity to Re at high Re, so much the better.

The second example continues the same theme but instead of changing the flap shape to suppress a separation, the tests<sup>107</sup> investigated what could be achieved through the use of small vortex generators. Once again, the tests are on the 2D model of the Douglas section with the vortex generators mounted on the upper surface of the single-segment flap at a setting of  $35^\circ$ . It will be remembered that this configuration without any vortex generators was rejected on account of the separation over the flap evident in the pressure distribution in Fig 3.33(c). Tests were made with two types of vortex generator - a delta-wing type with a height-to-chord ratio of 0.45% and a low-profile trapezoid micro-vortex generator with a height-to-chord ratio of only 0.18% ( $h = 0.04''$ ) mounted at various positions on the flap. Results at  $Re = 5 \times 10^6$  and  $9 \times 10^6$  with the micro-generators mounted at 25% flap chord in a contra-rotating array are presented in Fig 3.36(a-d). The results show that at moderate incidences, the vortex generators almost eliminate the separation and greatly increase the lift at a given incidence and reduce the drag at both Reynolds numbers. Also, there are no adverse effects near  $C_{L,max}$  where the separation was not present at  $Re = 9 \times 10^6$  even without the generators. In this case, there was no improvement in  $C_{L,max}$  but it should be noted that there was no attempt to re-optimize the flap. Fig 3.36(e) illustrates the concept of applying these vortex generators (note - stowed in cruising flight) and Fig 3.36(f) shows their effect on the wake profile at the two Reynolds numbers. The general message is the same as from the previous example - by suppressing the separation on the flap, one can reduce the dependence on Reynolds number and by implication, reoptimize the configuration and obtain a better  $C_{L,max}$ .

### 3.2.2.2 Slat effectiveness

In general, it is difficult to discuss the scale effect on slat performance in isolation since the effects of the slat may depend on whether the flow on the flap system is sensitive to the interaction with the slat wake. However, let us discuss cases where either there is no flap or at least, to the first, order, we can ignore the flow over the flap. At the start of §3.2.1 where it was noted that the scale effect on the flow could be discontinuous when and if the flow breakdown at high incidence changed from a bubble separation at low Reynolds number to a trailing-edge separation at high Reynolds number. An example

of this change will be included in §3.3.2: it has to be deferred until then because the relevant experiment was made on a three-dimensional wing of relatively low sweep rather than a two-dimensional aerofoil. However, one example can be quoted here where deflection of a slat on its own changed the scale effect from one typical of leading-edge stall to one typical of trailing-edge stall. This is shown in Fig 3.37; these results are taken from Ref 108: the decrease in  $C_{L,max}$  with Re above  $Re = 9 \times 10^6$  evident on the clean wing is not present when the slat is extended. The same change in type of stall is evident in the results in Fig 3.38 drawn from Ref 109: without the slat, there is appreciable scale effect between  $Re = 2 \times 10^6$  and  $Re = 6 \times 10^6$  whereas, with the slat deflected, there is little change with Reynolds number. One can speculate that with the clean wing in this case, the increase in Re has delayed the appearance of a leading-edge separation but with the slat extended, there is only a slight effect on a trailing-edge stall.

Returning to the Douglas/NASA tests in the NASA Langley LTPT, the tests discussed earlier were on typical landing configurations. Tests were also made<sup>90</sup> on a take-off configuration where the slat was deflected to  $20^\circ$  and the single-segment flap was at  $10^\circ$ . It is appropriate to discuss this case here because the slat was highly loaded and flap deflection was not sufficient to cause any flow separation on the upper surface of the flap. Fig 3.39(a) shows that there is a loss of about 0.15 in  $C_{L,max}$  between  $Re = 9 \times 10^6$  and  $Re = 16 \times 10^6$  at  $M = 0.15$ . The main wing enters the stall first and it is soon followed by the slat and then, by an increase in the lift contribution from the flap. This is a further example of the flap response to the downwash and wake interaction from the forward components coupled with the fact that at  $10^\circ$  deflection, the flap can carry the extra loading without stalling. The adverse scale effect is observed on both the main wing and the slat but it is very sensitive to the test Mach number: with increasing Mach number, it fades out until at  $M = 0.30$ , there is a slight increase in  $C_{L,max}$  with Reynolds number. In other words, the reduction in  $C_{L,max}$  with Mach number is less pronounced at the higher Reynolds numbers as shown in Fig 3.39(b). This can be explained as follows:  $C_{L,max}$  is determined primarily by flow separation on the main element and hence, is a function of the pressure-rise over this element; at low Mach number, the peak suction at the start of this pressure-rise is reduced by the proximity of the slat but with increase in Re, this effect becomes less pronounced because of the increased effective gap between the slat and main wing - hence, the adverse scale effect - but as the Mach number is increased, the peak suction tends to become limited by the "compressibility effect" which becomes a little less pronounced at high Reynolds number because of the thinner boundary layer - and hence, the slightly favourable scale effect. These thoughts are speculative on the part of the present author but are supported by general experience. At  $M = 0.20$  there is, coincidentally, no scale effect on lift but on measured drag in the climb, it amounts to a reduction of 10% between  $Re = 5 \times 10^6$  and  $20 \times 10^6$ ; mysteriously, this effect vanishes at higher Mach numbers.

Scale effects above  $Re = 5 \times 10^6$  in these cases with a slat deflected but only limited interaction with the viscous effects in the flow over the flap are therefore not dramatic. The picture is very different in §3.2.2.3 below when there is a major interaction.

### 3.2.2.3 Scale effect for complete configuration

In the final examples to be discussed here, the results are dominated by the complete viscous interaction. Results which

at first sight are concerned with the optimisation of slat deflection and position are, in fact, strongly influenced by details of the flow over the slotted flaps. In other words, in these examples, various strands in the discussion are brought together. The examples are selected to demonstrate the difficulties of predicting the scale effect without a full understanding of the flow. For all the NASA/Douglas examples discussed in §3.2.2.1 above, the slat was in the same position and at the same angle. Now, let us consider what happens to the scale effect on the flap as we move the slat. Figs 3.40(a-c) taken from Ref 108, present the effect of Reynolds number on the  $C_{L_{\max}} - \alpha$  curve,  $C_{L_{\max}}$ ,  $C_{L_i}$  at  $\alpha = 0$  and the  $C_m - C_{L_i}$  curve all for  $M = 0.2$  for 3 different configurations. The different trends in Figs 3.40(a,b) are particularly striking in that the double-slotted flap is in the same position and setting for these two cases and the only difference is that the slat is deflected  $35^\circ$  in Fig 3.40(a) and  $30^\circ$  in Fig 3.40(b). One should note that

- (i)  $C_{L_{\max}}$  increases with Re, particularly between  $Re = 5 \times 10^6$  and  $9 \times 10^6$  before falling slightly with the slat at  $35^\circ$  whereas, with the slat at  $30^\circ$ , it decreases with Re particularly between  $Re = 3 \times 10^6$  and  $9 \times 10^6$ ,
- (ii)  $C_{L_i}$  at  $\alpha = 0$  does not change with Re in the first case whereas it decreases dramatically between  $Re = 3 \times 10^6$  and  $9 \times 10^6$  in the second case,

The pitching moment data are enlightening. They indicate that

- (iii) with the slat at  $35^\circ$ , the flap loading increases with Re more than the slat loading as would be expected if the only effect of Re was the direct effect of a reduction of boundary layer thickness with Reynolds number,
- (iv) with the slat at  $30^\circ$ , only the slat loading increases with Re and this implies in view of what we have already seen that, at the lowest Reynolds number (but not at higher Re), the flap loading was boosted by the flow being attached as a result of the interaction with a particularly thick slat/wing wake (thicker than with the slat at  $35^\circ$ ).

As might be expected, the  $35^\circ$  setting was preferred.

Ref 108 gives results for two different double-slotted flap arrangements: the flap + auxiliary flap discussed in the Douglas papers<sup>90</sup>, Fig 3.33(a), and the small-vane + flap configuration shown in Fig 3.32(a). A favoured configuration with this second arrangement produces the results shown in Fig 3.40(c). It will be seen that these results are completely different from those for the favoured case with the other double-slotted flap, showing a very substantial reduction in lift at a given incidence below  $\alpha = 12^\circ$ . Again, looking at the pitching moment data, it appears that below  $\alpha = 12^\circ$ , an increase in Re produces an increase in slat loading with no corresponding increase in flap loading (indeed, the flap loading must decrease with Re) while, above  $\alpha = 12^\circ$ , there is an increase on both surfaces. The explanation lies in the fact that, for this configuration, the slat is only deflected to  $24^\circ$  and hence is more highly loaded; hence, a thick wake at low Re and better flow over the flap.

It follows that although at first sight, Fig 3.40 is concerned with the effects of slat setting, the basic reason for the different scale effects lies in what happens on the flap as a result of the interaction with the slat/wing wake. One would not be able to predict the scale effect even qualitatively unless one knew whether the flow over the flap at low Reynolds number was attached or separated. Quantitative prediction remains difficult

even when one does understand the flow. Clearly, it is not possible to devise simple rules that will work in all cases; the hope for the future lies in the development of accurate CFD methods - see §3.2.3.

Having discussed the effect of slat setting, let us turn to the effects of slat position. Figs 3.41(a,b) present the results of slat optimisation exercises at  $Re = 5 \times 10^6$  and  $Re = 9 \times 10^6$ ; these results are again taken from the NASA Langley programme in the LTPT; the slat is at  $30^\circ$  and the two-segment flap is at  $35^\circ/15^\circ$ . As might have been expected, the optimum slat position moves nearer to the wing with increasing Reynolds number. Less immediately predictable is the fact that the optimum position is much more highly tuned at the higher Reynolds number ( $9 \times 10^6$ ). However, this feature of the results is consistent with other data discussed earlier. One can note that at  $Re = 5 \times 10^6$ , the shape of the  $C_{L_i} - \alpha$  curve suggests that with the slat in the optimum position, the flow over the configuration is in region A of Fig 3.26 and, if so, the variation of performance with slat position would be expected to be relatively gradual. At  $Re = 9 \times 10^6$ , the shape of the  $C_{L_i} - \alpha$  curve is beginning to change, ie less reduction in slope at incidences before the stall and a somewhat more abrupt stall and this suggests that the flow over the configuration is moving into area B and hence, by reference to Fig 3.26, the more rapid reduction in  $C_{L_{\max}}$  as one moves the slat away from the optimum position is perhaps to be expected. The important point to note is that if one had only been able to test at  $Re = 5 \times 10^6$ , and had not realised that the slat gap for optimum performance would change by as much as 0.7%, one would have lost 0.12 in  $C_{L_{\max}}$  at  $Re = 9 \times 10^6$ . Ref 66 highlights the importance of this conclusion:  $Re = 5 \times 10^6$  could be a typical Reynolds number for a stall-critical section on a 3D half-model in a pressurised tunnel such as the 5 metre tunnel or F1 at le Fauga and  $Re = 9 \times 10^6$  could be the corresponding Reynolds number for the same section in flight. For a larger aircraft,  $Re = 16 \times 10^6$  could be the flight value and so, the intriguing thought about Fig 3.41 is how could it be used to predict the performance and optimum position at  $Re = 16 \times 10^6$ ?

The separations that occur in the slat and flap shroud coves are another possible source of scale effect. These separations were studied in a programme at NLR reported in Ref 110. Tests were made with the basic slat, the slat with the hook rounded off and with a fairing in the cove - see Fig 3.42(a). These changes in configuration had no significant effect on the lift data but, as shown in Fig 3.42(b), the two modifications gave large reductions in drag in the incidence range  $9^\circ < \alpha < 13^\circ$ . At higher incidences, the fairing in the cove gave an appreciable increase in drag. Flow visualisation tests showed that the main reason for the reductions in drag was a smaller cove separation and the increase in drag came from high velocities in the slot with the fairing present. Perhaps of more interest in the context of scale effect is the fact that with the basic slat, there were two separations which could change with Reynolds number; the cove separation itself and a laminar separation on the main wing upper surface. However, in the one case where a serious attempt was made to look for scale effect on these separations, the programme described in Ref 111 and about to be discussed below, it has to be admitted that no evidence was found of any change with Reynolds number in the size of these cove separations.

It is appropriate to end this list of examples by presenting some of the results from an extensive European wind tunnel research programme on high lift systems<sup>111</sup>. This programme included 2D tests by both ONERA F1 at le Fauga and in the NLR LST and HST at Amsterdam on 2D models representative of the

59% span section of the A310 wing. Taken together, these tests covered a Reynolds number range from  $Re = 1.9 \times 10^6$  to  $Re = 16.4 \times 10^6$ . In addition to measurement of surface pressures and wake surveys, boundary layer surveys were made at 8 stations on the take-off configuration and 9 stations on the landing configuration at selected conditions of Reynolds number and Mach number. There are also skin friction measurements at the trailing edge of both the slat and main wing and on the flap while, in the F1 tunnel, thermography was used to detect the transition position. Results from these tests are presented in Figs 3.43(a-d).

Two configurations were tested representing respectively a take-off and landing setting of the high-lift devices. For both configurations, favourable scale effect on  $C_{l,max}$  was observed up to  $Re = 6.7 \times 10^6$ . This can be at least partly explained by the fact that at low Reynolds numbers, laminar separation bubbles were present on all three surfaces. Above  $Re = 6.7 \times 10^6$ , however, there is little further change in  $C_{l,max}$  with  $Re$  for the landing configuration and  $C_{l,max}$  actually decreases with  $Re$  for the take-off configuration - by about 0.11 by  $Re = 16.4 \times 10^6$ . This decrease in  $C_{l,max}$  with  $Re$  was linked to a forward movement of transition on both the flap and the slat with  $Re$ . A loss of overall circulation with increasing  $Re$  is confirmed by the variation of maximum local Mach number on the slat plotted in Fig 3.43(b), and the boundary layer displacement thickness values for 2 positions above the main wing as plotted in Fig 3.43(d) show that the effect of the forward movement of transition is outweighing the normal direct effect of  $Re$  on boundary layer thickness. For the landing configuration, transition is less sensitive to Reynolds number because a velocity peak exists at the leading edge on the flap and hence, the pressure gradients behind this peak control the transition position. It will be noted that a sizeable Re-effect on boundary layer thickness is present at station 4 on the rear of the main wing upper surface at Reynolds numbers below  $6 \times 10^6$ ; the profiles in Fig 3.43(c) show that the wing boundary layer and slat wake merge between stations 3 and 4. It should be mentioned that these effects of Reynolds number were obtained at a Mach number of  $M = 0.22$ . The effects of Mach number become large above this Mach number, eg a reduction of about 0.4 in  $C_{l,max}$  by  $M = 0.30$ . This reflects a limitation on the slat maximum Mach number with increasing stream Mach number and it is probable that Reynolds number effects would become less important or at least different with increase in Mach number.

This final example has therefore emphasised the importance of knowing where transition occurs in 2D tests at high Reynolds number and, by implication, knowing also where it occurs on the aircraft in flight. It also confirms that it is wrong to assume that Reynolds number effects do not exist beyond  $Re = 5\text{--}6 \times 10^6$ .

### 3.2.3 Theoretical prediction of scale effects

On several occasions in the discussion in §§3.1 and 3.2, it has been stressed that, in the absence of tunnels capable of producing full-scale results, there is a need to be able to use CFD to forecast the scale effect. There are two possible approaches: either a coupled viscous-inviscid method or a Navier-Stokes code. Four examples of what is possible at the present time are presented in Figs 3.44, 3.45 and 3.46.

First, Fig 3.44(a) shows an example of what can be achieved through the use of FELMA, the BAe/DRA 2D viscous/inviscid interaction method described in Ref 99 applied with the aid of 2D/3D geometric conversions. This is a more demanding case

than that discussed earlier and shown in Fig 3.28. In Fig 3.44(a), a very good agreement between theory and experiment is shown despite the fact that almost throughout the incidence range covered by the comparison, some flow separation is present. Below  $\alpha = 18.5^\circ$ , the flow over the slat lower surface separates in the cove region; between  $\alpha = 18.5^\circ$  and  $22.0^\circ$ , flow separation occurs over the last 10% of the flap upper surface; for a small range of incidence between  $\alpha = 22^\circ$  and  $23^\circ$ , contrary to what was said above, the flow is attached over the entire aerofoil, but at  $C_{l,max}$ , the flow is starting to separate on the main wing but has remained attached over the flap because of the interaction with the thick wing wake. Beyond  $\alpha = 23^\circ$ , the separation on the main wing spreads rapidly forward to about 80% chord and the theory cannot cope any further. The success of the theory in predicting that  $C_{l,max}$  will be 4.11 at  $\alpha = 22.5^\circ$  is impressive.

The second example taken from Ref 112 is an even more severe test case for any theoretical prediction method. It is a case where there is a significant progressive reduction in lift-curve slope before the stall. As illustrated in Fig 3.44(b), the loading has collapsed on the two-segment flap. This is not because of a flow separation on the flap surface but because the attached flow over the flap has been influenced by the thick wake from the forward surfaces. The success of any theoretical method is then critically dependent on whether the method is capable of calculating the growth of the wake in a region of adverse pressure gradient. The method<sup>103</sup> used by Boeing couples a multi-element full potential solver with an integral wake model with several empirically-based parameters, one of which governs the wake growth in an adverse pressure gradient. Fig 3.44(c) shows the sensitivity of the calculated pressure distributions over the double-slotted flap to this parameter; in this case, the author believes that  $F_w = 0.20$  would appear to be the better value but Ref 112 stresses that more evidence is needed before one can be sure that this value can be used in general. Rogers et al in Ref 113 comment that this coupled viscous/inviscid method has proved to be useful as an effective engineering design tool but that it is limited by its inability to compute beyond maximum lift conditions and also, it may have problems with certain features such as flap wells, thick trailing edges or unsteady effects.

Navier-Stokes methods have been investigated by a number of different authors<sup>114-116</sup> but, at present, further progress in turbulence modelling is required before one can obtain acceptable results in conditions where the flow is partly separated. Nevertheless, some impressive comparisons have been obtained for cases where there is certainly interaction between viscous layers in a multi-element configuration. The third example<sup>117</sup>, plotted in Fig 3.45, shows a comparison between the pressures over the 4-element NASA/Douglas slat/wing/double-slotted flap discussed earlier and predictions by the method of Mavriplis<sup>116</sup>. This method uses an unstructured grid approach but Rogers et al in Ref 113 argue that this type of approach will tend to be of limited accuracy because of the very large aspect ratio of the triangular cells required to resolve high Reynolds number boundary layer flows. Also, such methods make large demands on computer memory and so, Rogers et al prefer a structured-grid approach.

Ref 113 includes results computed by the NASA Ames structured grid code for two-, three- and four-element aerofoils and some of these results are reproduced in Figs 3.46(a-d). Rogers concludes that they have produced a Navier-Stokes code that is robust and which can produce numerical simulations in a matter of minutes. The Baldwin-Barth<sup>118</sup> turbulence model gave significantly better results than the Baldwin-Lomax



model<sup>119</sup> when the code was applied to a single element NACA 4412 aerofoil although the accuracy was far from perfect near the trailing edge. The Baldwin-Barth model is much easier to use for a multi-aerofoil because it does not require a length scale and so, all the results presented here use this model. Also, all the results except for the patched grid results in Fig 3.46(a) have been obtained using the Chimera overlaid grid technique. Considering first the results for the 2-element configuration in Figs 3.46(a-c), these show fairly good agreement with the experimental data from Ref 120. As regards the pressure distributions in Fig 3.46(a), the most noticeable difference is in the value of the peak suction on the flap nose but Ref 113 notes that this may be due to an uncertainty in how the flap geometry is defined. The velocity profiles in Fig 3.46(b) again show good agreement with experiment in general. As with the pressure distributions, the largest discrepancy is at the leading edge of the flap but it is encouraging to see that the calculations are very successful in capturing the wake from the main element in the profile at the flap trailing edge and also, both theory and experiment show that there is a separation ahead of the flap trailing edge (but they differ slightly in the size of this separation). Fig 3.46(c) shows that the calculations are very good in predicting  $C_{L,max}$  and the decrease in  $C_L$  beyond the stall. Results for a 4-element configuration are presented in Fig 3.46(d); here, the comparison is with the experimental data of Omar et al in Ref 121 for a NASA 9.3% thick blunt-based aerofoil with a slat deployed at  $47.2^\circ$  and two trailing-edge flaps at  $30^\circ$  and  $49.7^\circ$ . Again, in general, there is good agreement except that, once again, the theory underpredicts the separation on the flap evident at the lower incidences.

Despite this progress with Navier-Stokes methods, it is clear that simpler methods have not outlived their usefulness. One noteworthy example of the simpler methods is the method by Henderson described in Ref 175. This method uses an iterative application of a panel method to solve for the separated wake displacement surface using entirely inviscid boundary conditions and achieves remarkable success in predicting  $C_{L,max}$  provided the separation point is known or can be predicted by a normal viscous-inviscid approach and provided the wakes of successive surfaces in a multi-element aerofoil are non-confluent. Application of the method to a 4-element aerofoil predicted too high a value for  $C_{L,max}$  but by a mere 2%. The results in Ref 175 appear to be critically dependent on knowing the separation point accurately: separation over the last 2-5% of a surface can have a significant effect on the lift. This relatively simple approach should be valuable in predicting the performance of optimum configurations.

Further details of the latest CFD developments are to be found in Ref 113 but this is an Agardograph on scale effects rather than on CFD developments. It is unfortunate that, except for the single case plotted in Fig 3.32, none of the reports dealing with CFD calculations include results for more than one Reynolds number. The present author would make a plea that there should be a serious attempt to apply the CFD methods over a range of Reynolds numbers. This would not only increase our knowledge about scale effect but also, would show whether it is practicable to construct a methodology in which CFD methods are used to convert tunnel data on  $C_{L,max}$  at low speeds to full scale.

### 3.2.4 Summary of conclusions

There are five principal sources of scale effect on the results for 2D multi-aerofoils:

- (i) conventional scale effect related to the decrease of boundary layer thickness with Reynolds number,
- (ii) bubble scale effect related to the favourable effects of increasing Re on bubble development,
- (iii) a sudden change from (ii) to (i) on a slat and possibly, main wing,
- (iv) movements of transition with Re, and
- (v) a change in the interaction between the wake of forward surfaces on the flow over a rear surface such as a slotted flap.

The scale effect due to (i, ii and iii) is generally favourable and tends to dominate up to  $Re = 5 \times 10^6$ . (iv, v) can however lead to unfavourable effects at Reynolds numbers above that at which the high-lift devices have been optimised in a tunnel test. Typically, reductions in  $C_{L,max}$  of about 0.1 due to (iv) have been observed but those due to (v) are the most difficult to predict varying from being non-existent to as much as 0.4 in  $C_L$  at a given incidence or in  $C_{L,max}$ .

To interpret and predict scale effects due to source (v), it is important to know whether, in the tunnel tests, the high lift system has been operating in areas A, B or C where

in A, the flow over the flap(s) is attached both at moderate incidences and at the stall, as a result of the loading being depressed by the interaction from the downwash/wake from the forward surfaces,

in B, the flow over the flap(s) is separated at moderate incidences but is attached at the stall for the reason quoted for A,

in C, the flow over the flap(s) is separated at both moderate incidences and at the stall.

If A applies in the tunnel test, it is possible that an increase in Reynolds number will initially bring a gradual increase in  $C_{L,max}$  and then, little further change provided that the configuration remains in area A. Otherwise, if it transfers into area B, increasing Reynolds number will bring a reduction in  $C_L$  at a given incidence and possibly an increase in  $C_{L,max}$  prior to a reduction in  $C_{L,max}$ .

If B applies in the tunnel test, there is a strong likelihood that there will be some adverse scale effect on  $C_{L,max}$  which could be substantial and appear abruptly with increase in Re. If C applies in the tunnel test, it is unlikely that the high lift device configuration will have been chosen.

Adverse scale effects on  $C_{L,max}$  can be avoided or at least, alleviated if it is possible to modify the flap shape or control the boundary layer by vortex generators to suppress a separation on the flap at incidences approaching or near the stall.

There is an interaction between the scale effects and the stream Mach number; generally the scale effects will become smaller with increase in Mach number; an adverse effect may even turn into a favourable effect with increase in Mach number.

The positioning and setting of the high-lift devices should be optimised at the highest possible Reynolds number. Looking to the future, one can hope that it will be possible to use CFD

to allow for any deficiency in the Reynolds number of the tunnel test. Some of the conclusions about how to change a given configuration to improve the performance or to eliminate an adverse scale effect may appear to run counter to intuition. Understanding the flow in detail is absolutely vital; it is hoped that the interpretation of the various examples discussed in this Agardograph has made its contribution to this understanding.

Finally, one must refer to Ref 122 which describes a semi-empirical method for predicting the attainable  $C_{L,max}$  that could be achieved with a multi-element wing. Compared with much of the previous discussion, this may at first sight appear to be delightfully simple. It is based on a "Pressure Difference Rule" which in concept is derived from ideas originally put forward by A M O Smith<sup>84</sup>. Analysis of experimental data showed that, at a given Reynolds/Mach number combination, maximum lift would correspond with a certain pressure difference between peak suction and trailing edge and that this rule applied irrespective of whether it was a single-element aerofoil or was fitted with a leading-edge device such as a slat. The variation of this pressure difference with Reynolds number and Mach number is shown in Fig 3.47(a). It is of course true that there are widely different pressure peak levels even on a single-element aerofoil depending on the free-stream condition but if the pressure distributions are scaled by the peak suction pressure coefficient (this follows A M O Smith's idea of a canonical pressure form), Valarezo and Chin show that the shape of the pressure distributions collapse on to the same curve beyond  $Re = 5 \times 10^6$  for a single-element aerofoil as shown in Fig 3.47(b) and again to the same curve when one considers the leading-edge region on an aerofoil with slat as can be seen from Fig 3.47(c,d) (with admittedly, some appreciable variation with Reynolds number). Hence, it is argued that it is not unreasonable to expect that a single criterion such as the Pressure Difference Rule will apply to both a clean and a slatted leading edge.

As noted above, the suggestion that one can predict scale effect on  $C_{L,max}$  on the basis of the simple curves in Fig 3.48(a) may appear strange after all the previous discussion but it must be stressed that what one is aiming to do with this prediction method is to determine the highest possible maximum lift that might be attainable if one was able to discover the appropriate geometry. It is not a method to find the value of maximum lift or to predict the scale effect for a particular geometry. It rests crucially on statements in Ref 122 that "a multielement airfoil properly configured will always stall when either the leading-edge device or the main element has started to stall. The trailing-edge device does not appear to be directly involved in the stall." In other words, in the language of the present Agardograph, Valarezo and Chin are saying that, for a multielement aerofoil "properly configured", it will be in area A and will remain in A whatever the Reynolds number. Scale effect in such a case will be mostly due to sources (i, ii and iii) above and it is therefore not surprising that the scale effect on the attainable  $C_{L,max}$  reduces to curves such as those shown in Fig 3.47(a). One should note that as suggested, for example, by Fig 3.26(a) in practical design one cannot forget the flow over the flap so readily and, for reasons already discussed, "optimum designs" in their attempt to achieve the maximum lift values predicted by this method, may well have scale effect extending to much higher Reynolds numbers than suggested by the curves in Fig 3.47(a).

### 3.3 Three-Dimensional Wings

#### 3.3.1 Sources of scale effect

Four categories of scale effect have been introduced during the discussion of scale effect on two-dimensional wings with and without high-lift devices. These are:

- (i) conventional scale effect associated with the reduction of boundary layer thickness with Reynolds number,
- (ii) bubble-dominated scale effect associated with the changes with Reynolds number in the characteristics of a laminar separation bubble,
- (iii) slot-flow dominated scale effect associated with the changes with Reynolds number in the flow separations and viscous interactions between boundary layers and wakes in the flow around a slotted multi-element wing, and
- (iv) transition-dominated scale effect.

This last item (iv) was not specifically identified in any list of sources of scale effect but, as will be appreciated from the detailed discussion, changes in transition position with Reynolds number have frequently been invoked in explanation of the observed scale effects, particularly at the higher Reynolds numbers. In general, however, in 2D flow, with a smooth surface and low stream turbulence, there is no natural mechanism whereby the transition position can move ahead of the peak suction position. This is not true on a three-dimensional wing with a swept leading edge where there are two such mechanisms: crossflow instability and second, contamination along the leading-edge attachment line. Both of these and particularly the second can have a fundamental effect on the scale effect encountered on a 3D swept wing at high lift and it is therefore appropriate to start the discussion for 3D wings with a summary as to how to predict the effects of Reynolds number on transition position on a swept wing. This is the subject of §3.3.2 and then, in §§3.3.3, 3.3.4 and 3.3.5, a selection of examples of scale effect are presented for respectively wings of low sweepback, wings of moderate sweepback and finally, slender wings. In §3.3.3, the examples are arranged under the headings of the four different types of scale effect in order to demonstrate that, in practice, one can encounter all these types. Most of the examples are taken from research experiments or calculations designed to improve the understanding and interpretation of the scale effects that can be encountered. It is only on one or two cases that these cases relate to a real aircraft; evidence for actual aircraft is, in general, presented in §3.4.

One general point should be mentioned at the outset. For a high aspect ratio wing of low sweep, it is often possible to view the onset of the stall in a quasi-two-dimensional manner and to link the data back to results obtained in two-dimensional flow but the development of the stall and  $C_{L,max}$  itself can be influenced radically by the fact that on a tapered wing, the local Reynolds number varies along the span. This means, for example, that in a case where the scale effect changes with increasing  $Re$  from bubble-dominated to conventional, there will be a range of  $Re$  where the change has already occurred near the root but it is still to come at higher Reynolds numbers near the tip. As a result, the flow breakdown in this  $Re$ -range may be completely different from that observed at both lower and higher Reynolds numbers and the scale effect in such a case on, for example, the pitching moment characteristics can

be large and difficult to predict. Examples of this sort of behaviour are included in §§3.3.3, 3.3.4 and 3.3.6.

### 3.3.2 Transition prediction for a sweptback wing

On a two-dimensional wing, leaving aside the possible effects of roughness, external turbulence or noise, transition is induced by either the existence of a laminar separation bubble or more often, by a boundary layer instability of the Tollmien-Schlichting type. On a three-dimensional wing with a swept leading edge, both these two mechanisms continue to exist but two other possibilities have to be considered: crossflow instability and contamination along the leading-edge attachment line. These two phenomena are now well-known and are discussed in many references, eg Michel in Ref 2, Arnal et al in Ref 125, Poll in Ref 132; they will be considered in some detail below in §§3.3.2.1 and 3.3.2.2. It will be seen later that when considering scale effect at high lift on a swept 3D wing, crossflow is, in general, less important than contamination along the attachment line (ALT).

In 1972, Hall and Treadgold<sup>123</sup> surveyed the difficulties in predicting transition - as they saw them at that time. They simplified the problem by not including the bubble mechanism but, even so, the task was clearly complex. It is best summarised in the one picture taken from Ref 123 and reproduced here as Fig 3.48. Calculations described in Ref 123 showed that the relative positions of the various boundaries in Fig 3.48 are highly sensitive to both wing sweep and pressure distribution. It will be noted that in addition to the three transition-inducing mechanisms, there is a further boundary indicating where a turbulent attachment-line boundary layer that has re-laminarised subsequently fails to do so. Re-laminarisation as a phenomenon likely to affect aircraft wings in practice was viewed in 1972 with some scepticism, but it has now been observed in flight and certainly, it is a real possibility in many model tests at high lift. Fig 3.48 indicates schematically what is likely to happen at four different Reynolds numbers. Sudden forward movements of transition are always liable to lead to adverse scale effect and Fig 3.48 indicates that three such movements are possible. With increase in Re, one can cross three boundaries corresponding respectively to the onset of crossflow instability, the onset of turbulent contamination along the attachment line but followed by re-laminarisation and finally, the boundary corresponding to a failure to re-laminarise. Losses in  $C_{L,max}$  due to the second and third of these changes have been observed in recent research by Boeing and these examples will be included in §3.3.3. Fig 3.48 already suggests that cross-flow instability may only have to be considered in practice when re-laminarisation has occurred after ALT.

Fig 3.48 also indicates what are the relevant parameters to use in the prediction of transition through the different mechanisms:

- (i) Tollmien-Schlichting instability: estimate the point where the laminar boundary layer becomes unstable by the  $e^N$  method and then use the Granville<sup>124</sup> criterion to predict the distance from instability to transition,
- (ii) crossflow instability: prediction related to a parameter,  $\chi$ , where

$$\chi = \frac{V_{max} \delta_c}{\nu}$$

where  $V_{max}$  = maximum value of the crossflow velocity within the boundary layer  
and  $\delta_c$  = crossflow boundary layer displacement thickness.

The value of  $\chi$  leading to transition lies in the range  $100 < \chi < 140$ .

The parameter,  $\chi$ , is generally described as a cross-flow Reynolds number but clearly, the choice of a suitable velocity and length to include in the definition is somewhat arbitrary. This point is discussed further in §3.3.2.1 which introduces two refined criteria developed by ONERA.

- (iii) contamination along the attachment line: prediction related to a Reynolds number, Re, based on the velocity parallel to the leading edge and a characteristic length proportional to the boundary layer thickness (constant on an infinite swept wing) in the flow along the attachment line. The value of Re leading to transition depends on the size of the disturbance triggering the contamination but it lies in the range  $240 < Re < 700$  (see later),
- (iv) relaminarisation: prediction related to a parameter, K, introduced by Launder and Jones<sup>126</sup>: relaminarisation is possible for  $K > 3 \times 10^{-6}$  and highly probable for  $K > 5 \times 10^{-6}$ .

Items (ii, iii and iv) will now be discussed in more detail.

#### 3.3.2.1 Transition due to crossflow instability

To quote from Ref 63, "for the flow over a swept wing, the streamlines just above the boundary layer are curved in plan view by an amount depending on the wing sweep and pressure distribution. At each position along the streamline, the net pressure force is exactly balanced by the centrifugal force due to the velocity and curvature. Within the boundary layer, the velocity is reduced and the streamline curvature has to change to restore the balance, with the result that a crossflow develops. Numerous experiments<sup>127,128</sup> have established that this crossflow can become unstable and lead to transition, this instability being characterised by the 'crossflow Reynolds number,  $\chi$ ', defined as above." This parameter,  $\chi$ , was first introduced by Beasley in Ref 168.

Michel, Arnal and Coustols of ONERA/CERT<sup>129</sup> surveyed a large amount of experimental transition data and showed however that cross-flow transition did not take place for a unique value of  $\chi$ . Attempts to modify  $\chi$  in terms of other quantities related to the cross-flow profile were unsuccessful but it was found that a better collapse of the data could be obtained by using two parameters in combination, viz,  $\chi$  and the shape factor,  $H_{12}$ , of the streamwise boundary layer. This refined C1 criterion<sup>125</sup> is shown plotted in Fig 3.49(a). ONERA/CERT then proceeded to develop a second criterion, C2, taking account of stability calculations which showed that the most unstable direction for wave amplification was not the cross-flow direction but was at a small angle,  $\epsilon$ , to this direction where  $\epsilon$  generally lies between  $1^\circ$  and  $5^\circ$ . A Reynolds number was then defined on the basis of the displacement thickness,  $\delta_{1\epsilon}$ , of the boundary layer in this direction. To be precise,

$$Re_{\delta_{1\epsilon}} = 1/\nu \int (U_{\infty} \sin \epsilon - U_e) dy$$

where  $U_e(y) = U(y) \sin\epsilon + W(y) \cos\epsilon$  and  $U_e$  is the resultant potential velocity.

A correlation was then established based on three parameters, this new Reynolds number, the shape factor of the streamwise boundary layer and the stream turbulence. This provided the C2 criterion which is shown in Fig 3.49(b). Arnal et al consider that this C2 criterion is the more realistic criterion and there have certainly been examples of where C2 has been successful and C1 has failed dramatically. Further details of the studies at ONERA/CERT can be found in Refs 125, 129, 130 and 131.

### 3.3.2.2. Transition due to contamination along the attachment line

It has been known for more than 25 years that, when the sweepback and/or Reynolds number are high enough, the flow along the leading-edge attachment line of a sweptback wing will become unstable and induce transition at this attachment line and, as a result, the boundary layer over the entire wing becomes turbulent. Poll, when at Cranfield in the late 1970s, instituted a research programme<sup>132,133,134</sup> to study this topic in detail and one of the aims of this programme was to produce reliable transition prediction criteria. Fig 3.50 is a sketch<sup>132</sup> illustrating the flow near the leading edge. Poll confirmed the deductions of earlier workers that the definition of a relevant Reynolds number for this phenomenon should be based on the velocity parallel to the leading edge and a length related to the thickness of the boundary layer in the attachment-line flow. Different authors have defined this length and hence the Reynolds number in different ways but it now appears to be generally agreed that the most appropriate definition is that introduced by Poll in Ref 132, viz

$$\bar{Re} = \frac{U \sin\phi}{v} \left[ \frac{v}{a} \right]^{1/2} \quad (3.1)$$

where  $U$  = free stream velocity

$\phi$  = sweep of the leading-edge or attachment line

and  $a$  = velocity gradient normal to, and away from, the attachment line and hence, a function of nose curvature.

Note: the form of this equation is due to Poll but the notation follows that introduced by Woodward et al in Ref 63.

Other authors have used the laminar momentum thickness,  $\theta_{le}$ , as a characteristic length and it can be shown that

$$Re_{\theta_{le}} = 0.404 \bar{Re} \quad (3.2)$$

where  $Re$  = Reynolds number based on a streamwise reference length and velocity.

$\bar{Re}$  is preferred to  $Re_{\theta_{le}}$  which loses its physical significance when the boundary layer is turbulent. Woodward et al note in Ref 63 that  $\eta = [v \times 1/a]^{1/2}$  which is the characteristic length in  $Re$  has been shown to be proportional to the boundary layer thickness in the flow in the region of a stagnation point and Poll justifies the choice on the grounds of dimensional analysis. For an infinite swept wing,

$$\bar{Re} = \sin\phi \left[ \frac{R_e}{a} \right]^{1/2} \quad (3.3)$$

Hence,  $\bar{Re}$  increases and turbulent contamination becomes more likely with increase in sweep and Reynolds number and reduction in curvature. A well rounded leading edge is needed to delay contamination.

Poll in his programme at Cranfield initially used a long, constant chord model with a circular leading edge that could be set at various angles of sweep. Tests were made both with the smooth model and also, in the presence of disturbances generated by circular trip wires of different diameter wrapped around the leading edge of the model at its upstream end. Two graphs abstracted from Ref 132 are presented as Figs 3.51(a,b) to give an idea of the results. In Fig 3.41(a),  $s/\eta$  is the distance from the upstream end of the attachment line measured along the attachment line non-dimensionalised by the characteristic length,  $\eta$ , referred to above and in Fig 3.51(b),  $d$  is the diameter of the trip inducing a disturbance. Various conclusions can be drawn from these figures and other supporting evidence in Refs 132, 133:

- (i) for a smooth wing in a stream of low turbulence (note: turbulence is only important if it exceeds 0.8%), the first bursts of turbulence can be correlated by a single function of  $s/\eta$ ; at a long distance from the upstream tip, they appear at about  $Re = 600$ . Complete turbulence was established at a value of  $Re$  about 100 higher than that for the first bursts,
- (ii) when a trip is added, these values of  $\bar{Re}$  decrease with  $d/\eta$  between 0.8 and 2.0 until for  $d/\eta > 2.0$ ,  $Re$  for first turbulence bursts is about 245 and for complete turbulence, about 300. The discontinuity at  $d/\eta = 1.55$  corresponds with when the transition front reaches the trip,
- (iii) the values of  $\bar{Re}$  do not vary with  $d/\eta$  when  $d/\eta \leq 0.8$  and Poll concluded that transition was then determined by disturbances originating in the free-stream. He recommended that point B, ie  $d/\eta = 0.82$ , should be taken as a guide to the maximum allowable roughness for the surface to be described as 'smooth'.

On the basis of these results, the criteria which have been in general use are:

- 1 for gross contamination, transition due to contamination along the leading-edge attachment line will occur when

$$\bar{Re} \geq 245 - 300 \quad (3.4)$$

- 2 in the absence of contamination, eg when it has been suppressed by the use of a 'Gaster bump' or similar device, transition will occur when

$$\bar{Re} \geq 600 \quad (3.5)$$

(Gaster had shown<sup>135</sup> much earlier that the spanwise spread of turbulence could be delayed by creating a local stagnation point on a specially shaped protuberance which became known as a 'Gaster bump').

Note: there is now some uncertainty as to whether (3.4) necessarily applies near the side of a fuselage as suggested in Ref 132. For many wing-fuselage combinations, the local  $C_L$  is very low at the side of the fuselage and this may inhibit the development of ALT; in one of the examples discussed in §3.3.4.2, contamination was not observed until  $Re = 450$  at a station on the inboard wing. Further research is needed to

clarify the present situation where it appears that  $\bar{Re}$  lies in the range  $245 < Re < 700$ .

The final figure in this group taken from Ref 132 shows the variation of the critical sweep angle for attachment line transition with leading-edge radius for a typical cruise flight condition ( $M = 0.8$ , 10,000 ft altitude). It will be seen that most of the full-scale aircraft selected for inclusion on this picture will have transition at the leading edge (but all except the largest might escape this problem if fitted with a Gaster bump or similar device). On the other hand, attachment line transition (ALT) will, in general, not be encountered in model tests; it is, therefore, a source of scale effect between model and full scale unless the boundary layer is manipulated in the model test. In the present context, the important point to note is that this picture refers to the cruise condition. At high-lift with devices deployed, the values of  $Re$  for a given wing are likely to be very different because the attachment line has moved around the leading-edge on to the lower surface of the wing or leading-edge high-lift device. As a result, the local curvature at the attachment line on either a slat or main wing is likely to be much lower than on the wing in the cruise condition. Hence, 'a' for a given wing will be lower and  $\bar{Re}$  higher, opening up the possibility that attachment line contamination (ALT) will be encountered in the tunnel tests as well as on the full-scale aircraft. Hardy, in Ref 136, for example, found that on one particular sweptback wing he was investigating,  $a = 5$  on the main wing and  $a = 20$  on the slat at high lift compared with  $a = 100$  in the cruise. It follows that ALT is a phenomenon likely to affect the scale effect within the range of tunnel tests in a pressurised tunnel such as the 5 Metre Tunnel or the F1 tunnel at le Fauga. This, if recognised, is a fact that can be exploited since it means that one can obtain experimental evidence on the consequences of the forward movement of transition to the attachment line.

The critical values of  $\bar{Re}$  quoted above were based on the results of experiments on an untapered model for which the attachment-line boundary layer thickness and hence,  $\bar{Re}$  was essentially constant along the span. In practice, however, aircraft wings are tapered and also, the local value of  $C_l$  and hence, the position of the attachment point will vary along the span. There are therefore two reasons for  $Re$  to vary likewise and in further work at Cranfield<sup>134</sup>, Paisley suggested that the spanwise rate of growth of the boundary layer might be an additional relevant factor. Further tests were made on a non-lifting tapered cylinder and these produced results similar in form to those on the infinite untapered model but the size of trip wire needed to initiate transition at a given value of  $Re$  was reduced by about  $\Delta(d/\eta) = 0.6$  where

$$\eta = [\nu \times l/a]^{1/2} = \text{characteristic length}$$

This is a substantial change and suggests that the attachment-line on a tapered wing is considerably more sensitive to disturbance than would be predicted by Fig 3.51(c). On the other hand, Paisley concludes from the results for the tapered cylinder that, in flight, it is possible that laminar flow might be found over a small region near the tip on all but the largest aircraft. The implications of  $Re$  varying along the span will be further considered when discussing examples in §§3.3.3, 3.3.4 and 3.3.6.

Finally, we come to the question as to whether it is possible for the turbulent boundary along the attachment line to re-laminarise. Launder and Jones<sup>126</sup> showed that laminarisation could occur in a strongly favourable pressure gradient in a 2D flow and that the relevant parameter was

$$K = \frac{\nu}{U^2} \frac{du}{dx} \quad (3.6)$$

Launder and Jones found that re-laminarisation was possible if

$$K \geq 3 \times 10^{-6} \quad (3.7)$$

and was highly probable if

$$K \geq 5 \times 10^{-6}$$

It is general practice in a prediction for a 3D wing to apply  $K$  along a streamline.

### 3.3.2.3 Summary of implications for scale effect

On the basis of calculations reported in Ref 63, it appears that, for transport wings, ie wings of low sweep at high lift, low speed with devices deployed,

- (i) ALT was most likely to occur for Reynolds numbers above about 1/4-full scale,
- (ii) transition due to cross-flow instability was unlikely to occur until a Reynolds number about twice that for the onset of ALT,
- (iii) re-laminarisation was a possibility only over small ranges of Reynolds number near the onset of ALT.

These conclusions were based initially on calculations for a wing with a particular flexible Krueger leading-edge device but Ref 63 notes that they were subsequently confirmed by further calculations for wings with other more relevant devices. The present author feels however that, at the present time, more experience is needed before they can be generally accepted. This reservation applies particularly to conclusions (i,iii) bearing in mind that some laminar flow has been observed in flight (see later in §3.3.4) in research tests on both the A310<sup>111</sup> and the Boeing 737-100<sup>138</sup>. Also, looking to the future, a more determined effort may be made to avoid ALT and its adverse consequences, eg by the use of a Gaster bump or similar device.

It is natural to expect that with increase of sweep, it is even more likely that, on the full-scale aircraft, ALT will dictate that transition occurs at the attachment line. However, this does not necessarily follow: the aircraft are smaller and calculations reported in Ref 152 for a slender wing with a round leading edge have shown that re-laminarisation at the model scale may persist up to very high Reynolds numbers such as  $Re = 40 \times 10^6$  based on wing mean chord. Results for swept and slender wings will be discussed in §§3.3.4 and 3.3.5 but first, in §3.3.3, we return to the high aspect ratio wing of relatively low sweep. Evidence for actual complete aircraft is discussed in §3.3.6.

### 3.3.3 Examples of scale effect on wings of low sweepback

#### 3.3.3.1 Conventional scale effect

Woodward et al in Ref 63 used tests in the DRA 5 m Tunnel on a 1/13 scale model of the A300B with its slat and double-element flap deflected to settings appropriate for a landing configuration as an example of simple conventional scale effect. Results are presented here in Fig 3.52; the top of the  $C_l - \alpha$  curve is well rounded and  $C_{l_{max}}$  increases with Reynolds

number throughout the test range from  $Re = 2.5 \times 10^6$  to  $Re = 6.7 \times 10^6$ . The increase amounts to about 0.06 between  $Re = 2.5 \times 10^6$  and  $Re = 4.0 \times 10^6$  but only another 0.04 thereafter. Measured pressure distributions confirmed that the nature of the stall did not change with  $Re$  and that most of the increase in  $C_{L,max}$  came from the outer wing sections. This is the type of result that was anticipated in the discussions that led to the building of the 5 m Tunnel: significant scale effect up to  $Re = 5 \times 10^6$  and then at a reduced rate and no obvious problems in extrapolation up to the full-scale result. It is a particularly simple example: although scale effect was locally more apparent on the outer wing, the differences across the span were not enough to produce a change with Reynolds number in the manner in which the wing flow stalled. However, this would not necessarily be true in all cases and this is why many high-lift tests at Reynolds numbers of  $2.5 \times 10^6$  or less have been found to be completely misleading. One such example is to be found in Chapter 10 of Ref 137.

This second example concerns a transport aircraft for which four large-diameter high-bypass-ratio nacelles were being retrofitted at underwing locations in place of smaller baseline nacelles, as illustrated in Fig 3.53(a). Tunnel tests at low Reynolds number indicated that this retrofit could be undertaken with no penalty in low speed  $C_{L,max}$  but in flight, there was a 10% loss in  $C_{L,max}$ . The explanation of this glaring scale effect was found from flow visualisation tests: flow separation was observed on the sides of the large-diameter nacelles at high angles of attack and high flap deflections leading to the formation of large vortices which trailed back over the inner wing. The paths and strength of these vortices were found to be almost independent of Reynolds number but, on the other hand, the separations on the outer wing were very sensitive to Reynolds number as for the A300B example discussed above. As a result, the stall at the low tunnel Reynolds number was dictated by the outer wing flow and so, the change of inner nacelle design had no effect on  $C_{L,max}$  whereas at high Reynolds numbers in flight, the stall was dictated by the flow over the inner wing near the nacelles. CFD was used to devise a modification of the outer wing which would give a flow at the tunnel Reynolds numbers resembling that observed at full-scale with the real wing. Thus equipped, some vortex generating vanes were attached to the inboard side of the engine nacelle with the results shown in Fig 3.53(b): an effective 'fix' had been obtained at both model and full-scale. The use of CFD to modify the geometry of the model to obtain a representative full-scale flow is a refinement to an idea which had been used many times in the past in a more ad hoc manner but, even with CFD, it needs a good understanding of the flow developments near the stall. Quantitatively, it must remain a poor substitute to being able to test at Reynolds numbers beyond the range where there is significant scale effect. This example which concerned a test on an actual aircraft model was introduced into the discussion at this point to highlight the fact that conventional scale effect might not be as innocuous as one might think from the previous example in Fig 3.52.

### 3.3.3.2 Bubble-dominated scale effect

Two examples are included in Ref 63. The first come from tests on a 0.315 scale model of the BAe Hawk in the DRA 5 m tunnel at Reynolds numbers up to full scale; the top of the  $C_L - \alpha$  curves are shown in Fig 3.54 for the wing configuration in which the stall breaker strips had been removed. It will be seen that the stall at all test Reynolds numbers is very abrupt and there is a large increase of  $C_{L,max}$  of about 0.18 between  $Re = 4.1 \times 10^6$  and  $Re = 7.3 \times 10^6$ . Both features suggest that it is a leading-edge stall, ie type (b) or (e) of Fig 3.2 and in-flight oil flow visualisation confirmed the presence of a laminar

separation bubble near the leading edge. The stall in flight was very sudden, generally involving a wing drop - consistent with the belief that it is a leading-edge stall exhibiting gross scale effect in the manner shown for the 9 and 12% thick two-dimensional aerofoils in Fig 3.18(b,c).

The second example is more intriguing. It is taken from tests on a half-model (DRA Model 477) with a simple, tapered, untwisted wing, and fitted with a 12½% chord slat and a single-slotted flap set at 20°. In the first tests on this model, results were obtained at merely three Reynolds numbers and Ref 7 offered a plot showing a smooth increase in  $C_{L,max}$  with  $Re$  between  $Re = 2.1 \times 10^6$  and  $Re = 5.8 \times 10^6$  with most of the increase being complete by  $Re = 4.2 \times 10^6$ , as shown in Fig 3.55(a). However, later tests with far more test Reynolds numbers showed that there was, in fact, a very rapid increase in  $C_{L,max}$  with  $Re$  near  $Re = 3.2 \times 10^6$ . Flow visualisation tests at low Reynolds number showed that the initial stall occurred on the outboard 20% of the slat span and it was found that by adding roughness to this part of the slat, this could be prevented. However, as can be seen from Fig 3.55(b), the results were very sensitive to the spanwise extent of the roughness. Fig 3.55(c) shows plots of the normal force on both slat and main wing obtained from integration of pressure measurements at 84% semi-span. It will be seen that, with no roughness, loss of lift at the stall occurs simultaneously on both slat and main wing whereas with roughness, the slat lift continues to increase for a further small increase in incidence after the main wing has stalled. Woodward et al deduced from these results that the sudden increase in  $C_{L,max}$  at  $Re = 3.2 \times 10^6$  corresponded to a change from a bubble separation on the slat to a trailing-edge separation on the main wing. The scale effect above  $Re = 3.2 \times 10^6$  can therefore probably be classed as conventional scale effect.

It should perhaps be added that a change from a bubble-dominated to a conventional scale effect would not necessarily always give as large an increase in  $C_{L,max}$  as that evident in Fig 3.55(a) and indeed, it is possible, certainly on wings of higher sweep, to be in the opposite direction. This result in Fig 3.55(c) could be a particularly dramatic example because the relatively low  $C_{L,max}$  at the lower Reynolds numbers is due to the combined effect of a bubble separation on the slat coupled with a separation on the main wing at least partly caused by the influence of the thick wake from the slat. The disappearance of the bubble on the slat therefore also leads to a major reduction in the unfavourable slat wake/wing interference and so, there are two reasons for the improvement in  $C_{L,max}$ . The important point about this example is that it shows that there can be a near-discontinuity in the variation of  $C_{L,max}$  with  $Re$  of as much as 0.25. Simple extrapolation of results from an atmospheric tunnel would not have allowed for this effect. On wings of low sweepback, it is thus vital to be able to test at Reynolds beyond those at which the stall is bubble-dominated.  $Re = 2-3 \times 10^6$  is not adequate. The F1 and 5 m Tunnels were built in the hope that  $Re = 6-7 \times 10^6$  would be sufficient; we will return to this point later after reviewing all the evidence.

### 3.3.3.3 Slot-flow dominated scale effect

This topic has already been treated extensively in §§3.2.1 and 3.2.2.1 and one would expect that many of the characteristics noted in two-dimensional flow would continue to apply on a three-dimensional wing of low sweepback and high aspect ratio. One example confirming this point is presented in Fig 3.56. These results are again taken from Ref 63 and were obtained in tests on a high aspect ratio, low-sweep, transport

wing in the DRA 5 m Tunnel. It should by now be a familiar picture: at low Reynolds number, the flow on the highly-deflected slotted flap is attached over the whole incidence range up to the stall and the lift-incidence curve has a well-rounded top; at the intermediate Reynolds number, the flow over the flap is separated at low incidence but then attaches as incidence is increased giving a sharp increase in lift-curve slope and a higher  $C_{L,max}$  and a less well-rounded top to the lift curve and then finally, at high Reynolds number, the flap flow is separated over the complete incidence range and  $C_{L,max}$  is significantly lower - by about 0.12 - than at the intermediate Reynolds number. This is just a repeat of the story told earlier in the basis of Fig 3.26, and of Fig 3.29 where the results were obtained in 1947. It shows what can happen if the positioning of the high-lift devices is not adjusted to suit the Reynolds number. As noted earlier, the devices should be re-optimised at high Reynolds number in positions where the surfaces are nearer to each other.

Some of the results discussed earlier showed that scale effect dominated by the viscous-inviscid interactions in the flow around slotted devices can persist up to relatively high Reynolds numbers. A further example of this is provided by evidence from the 3D tests in the recent cooperative European research programme<sup>111</sup>. Wake surveys indicated that an increase in Reynolds number from  $Re = 7.4 \times 10^6$  to  $Re = 10.5 \times 10^6$  - a relatively small change on a log  $Re$  basis - reduced the mixing between the wing and flap wakes as shown in Fig 3.57. As we have seen when discussing the two-dimensional data, increased separation of the effective surfaces and their wakes is not necessarily a favourable development and it is interesting that  $C_{L,max}$  is actually decreasing with  $Re$  in this range.

### 3.3.3.4 Transition-dominated scale effect

It was noted above in §3.3.2 that attachment-line contamination (ALT) was the most likely reason for this form of scale effect. Calculations reported in Ref 63 were made by DRA to illustrate the possible loss in  $C_{L,max}$  when transition moved forward to the attachment line. The results of these calculations are shown in Fig 3.58. For all 4 aircraft mentioned on this figure, this forward movement predicted on the basis of  $Re = 300$  occurs at Reynolds numbers below the flight value (but above the test value in existing tunnels). Typically, the loss in  $C_{L,max}$  when it occurs is about 10% and thus is highly significant.

Turning to experimental data, possibly the clearest evidence in the published literature are the results from recent tests in the DRA 5 m Tunnel by Boeing/JADC presented in Refs 102, 112. The first tests on a simple swept wing showed that with increasing  $Re$ ,  $C_{L,max}$  initially rose but then reached a maximum before decreasing by as much as 7% by the highest test Reynolds number - see Fig 3.59(a). Without further investigation, this might have been accepted as evidence of ALT but supporting studies did not support this explanation. Flow visualisation revealed that a laminar separation bubble was present outboard but not inboard; a wire trip placed on the inboard lower surface across the attachment line had no effect even at the lowest Reynolds number and finally, calculations predicted that  $Re$  was above 240 even at the lowest test Reynolds number. For all these reasons, it had to be accepted that the correct interpretation of the results was that, at Reynolds numbers below that for the peak  $C_{L,max}$  but not at higher  $Re$ , re-laminarisation was occurring over at least part of the span. This hypothesis was supported by calculations of the parameter,  $K$ , introduced earlier; Fig 3.58(b) shows that  $K = 3 \times 10^6$  was reached on the inner but not the outer wing between  $Re = 10 \times 10^6$  and  $13 \times 10^6$ . In other words, failure to re-laminarise can lead to a reduction in overall  $C_{L,max}$  of 7%.

A new leading edge was then designed for the wing as shown in Fig 3.59(c). The aim here was to reduce the curvature around the leading edge and hence, the favourable pressure gradients seeking to promote re-laminarisation. This may appear to be a curious aim but the hope was that without re-laminarisation at any Reynolds number, the scale effect would be monotonic and gently favourable - and therefore more predictable. On the basis of the calculated values of  $K$  shown in Fig 3.59(d), re-laminarisation would not now be expected above about  $Re = 7 \times 10^6$  over most of the span. The hope then was that there would be a smooth variation of  $C_{L,max}$  with  $Re$  but, in fact, as shown in Fig 3.59(e), a much larger decrease in  $C_{L,max}$  of about 15% with  $Re$  was now observed within the test range. This time, the 15% decrease appeared to correlate with when  $Re$  exceeded 240 (Fig 3.59(f)) and so, the decrease in  $C_{L,max}$  can now be ascribed to contamination along the attachment line (ALT).

To express the conclusion from these two examples in general terms: ALT can lead to reductions in  $C_{L,max}$  of the order of 10% or more; this occurs immediately if there is a failure to relaminarise but if relaminarisation occurs, it will be delayed to a higher Reynolds number. In other words, the possibility that relaminarisation will be present over a range of Reynolds number affects the Reynolds number at which the decrease in  $C_{L,max}$  occurs. As a personal opinion, it is possible that further research will show that this conclusion is oversimplified: there may be examples where two reductions in  $C_{L,max}$  occur - one near the Reynolds number for ALT and relaminarisation and the second (and more significant) to when relaminarisation fails. Research on slender wings to be described later suggests that it may be wrong to assume that the boundary layer development downstream of ALT + relaminarisation is the same as if ALT had not occurred - hence, the possibility of two breaks in the curve.

It will have been noted that the values of  $\bar{Re}$  and  $K$  in the last examples varied along the span. This characteristic is analysed in more detail in Refs 63 and 136. Two wings were studied; one of these is the simple tapered, untwisted model 477 which provided one of the examples for slot-flow dominated scale effect but here, it is being tested as a plain wing with the high-lift devices retracted. With the aid of hot-film gauges, it was possible to study the first appearance of turbulence spots and their growth to complete turbulence. Although spots were first seen near the root, complete turbulence was achieved first near the tip. Fig 3.60 shows the variation of the intermittency factor with Reynolds number for various stations across the span. Qualitatively, this variation across the span can be explained in terms of the spanwise variation of  $Re$  due to two conflicting factors:

- (i) the variation of chord length on the tapered planform: hence larger local Reynolds numbers and higher  $Re$  inboard,
- (ii) the spanwise loading giving higher local incidences and a lower value of 'a' at the attachment line: hence higher  $Re$  outboard.

For the fixed incidence condition of Fig 3.60, it can be assumed that the variation of 'a' with Reynolds number at a given spanwise position is small and, if so,  $Re$  is proportional to  $[Re]^{1/2}$  at each spanwise position. The attachment line transition front would then be predicted to move along the leading edge giving lines that were roughly parallel rather than diverging as in Fig 3.60. Evidently, therefore, this simplified analysis is not allowing for all the relevant factors; we will

come back to this topic when discussing the results for DRA model 495 in §3.3.4 below.

Finally, there are two examples in the recent literature where research testing has shown that some laminar flow can be present in flight at relatively high Reynolds numbers. First, in the GARTEur flight tests on an A310 in a take-off configuration<sup>111</sup>, hot film gauges indicated that the boundary layer along the slat attachment line was still laminar at Reynolds numbers higher than  $Re = 7.3 \times 10^6$  whereas, in the 3D model in the DRA 5 m Tunnel, ALT had already occurred at this Reynolds number (note: it is true that a laminar separation bubble was observed in the tunnel test but this merely indicates that re-laminarisation was taking place). Thibert<sup>111</sup> ascribes the differences between flight and tunnel largely to the fact that the belt for the flight test instrumentation gave a very smooth surface while the roughness was greater on the wind tunnel model; also, the relative size of the slat brackets was greater on the tunnel model. Whatever the explanation, the result suggests that one should not necessarily accept the oft-stated conclusion that ALT always dictates what happens on a transport aircraft in flight.

The second example comes from the NASA Langley Research subsonic transport high-lift research programme. Flight tests are being made on a B737-100 aircraft (Fig 3.61(a)); some preliminary results from this programme are given in Ref 138 and some of these will now be described in detail. The outboard wing sections on this aircraft at high lift are made up of 5 elements: a slat, a main wing and a fore, mid and aft flap. The geometry with the flaps at alternatively 15°, 30° and 40° are shown in Fig 3.61(b); it will be noted that when the flap deflection is increased, the slat deflection also changes. Fig 3.61(c) shows that at the higher incidences, the scale effect between tunnel and flight is very large but this is hardly surprising since the tunnel data were obtained at a Reynolds number of only  $1.4 \times 10^6$  based on wing mean chord compared with a flight value of  $Re = 11 \times 10^6$ . One of the most interesting parts of Ref 138 is however the assessment of the flow over the slat and in particular, the flow along and near the attachment line. Figs 3.61(d,e) present the results of Preston-tube measurements on the slat. Figs 3.61(e,g) with the flap at 40° provide a coherent story: the mystery at first sight lies in the high values of  $C_p$  at incidences between  $\alpha = 2.5^\circ$  and  $\alpha = 9^\circ$  but these are explained by Yip et al in the following way. The increase in  $C_p$  was due to a sudden increase in the Preston-tube total-pressure reading. This suggested that the tube was protruding out of a thin laminar boundary layer. Although the value of  $Re$  was less than 245 over part of the test incidence range, comparison with Gaster's results<sup>135</sup> at Cranfield indicated that there was little chance for the attachment line boundary layer to remain laminar at this particular station which was just outboard of where disturbances would be shed by the flight instrumentation belt. In any case, there appears to be no correlation between the behaviour of  $C_p$  and the  $Re - \alpha$  curve. On the other hand, there was very clear correlation with the  $K - \alpha$  curve. On this basis, one can say that re-laminarisation occurs at about  $\alpha = 2.5^\circ$  when  $K > 3 \times 10^{-6}$  but then fails at about  $\alpha = 9^\circ$  as a result of the development of a suction peak followed by an adverse pressure gradient on the slat upper surface (as shown by pressure distributions not reproduced here). Unfortunately, the explanation of the results with the flap at 15° is not so clear-cut: the disappearance of any effect at about  $\alpha = 8^\circ$  can again be linked to the pressure distribution but there is no apparent reason why the effect does not appear in the flight at 10,000 ft or why at 20,000 ft, re-laminarisation apparently needs  $K$  to be greater than  $6 \times$

$10^{-6}$ . Despite these uncertainties, the important point for this Agardograph is that these results have provided evidence that re-laminarisation can occur in flight at a Reynolds number based on wing mean chord of  $11 \times 10^6$ .

### **3.3.4 Examples of scale effect on wings of moderate sweepback**

#### **3.3.4.1 Early evidence: conventional and bubble-dominated scale effect**

In the 1950s, tests were made in the RAE (Farnborough) 10 ft x 7 ft tunnel on a number of simple sweptback wings of moderate aspect ratio; these included studies of the flow behaviour at high lift and low speeds at Reynolds numbers from about  $2 \times 10^6$  to  $6 \times 10^6$ . The scale effect evident in these results was reviewed in detail in Ref 139 written in 1964 and although the wings were tested without high-lift devices and their geometry is not necessarily typical of current practice, it is still of interest to refer to some of the conclusions in Ref 139.

Most of the scale effect observed in these tests relates to the progressive disappearance with increasing  $Re$  of the swept-wing equivalent of the 2D long-bubble stall, ie stall type (a) in §3.1.1. The geometry of the wings was simple: no twist and the same section at all stations from root to tip. At the lower Reynolds numbers, separation-onset occurred at a value of  $C_l$  well below the wing  $C_{l,max}$  and, in general, at a value of  $C_l$  that could be forecast from 2D data interpreted by applying simple sweep concepts. The development of the separation however was quite different: on a wing with a leading-edge sweep of more than about 35°, the leading edge separation bubble rolls up into a part-span vortex which generally moves inboard with increase of  $C_l$  and which trails across the wing at an angle of about 20° outward relative to the free-stream direction. The flow over the top of this vortex re-attaches to the wing upper surface until ultimately, with increase in incidence, the vortex either lifts off the surface or bursts. The rate of inward movement of the part-span vortex is a function of the wing spanwise loading, the 2D section characteristics and the variation of the local Reynolds number, ie the wing planform. The presence of the vortex while it is lying across the wing and moving inboard with increasing incidence can generally be recognised from the overall force and moment characteristics: a nose-down change in the pitching moments followed by a nose-up change at the final flow breakdown. An increase of Reynolds number in the range where these wings have a leading-edge long-bubble type of separation generally leads to an increase in the  $C_l$  for separation-onset and so, the changes in the force and moment characteristics occur at higher incidence and are more abrupt at high Reynolds number. This type of scale effect was usually observed in the  $Re$ -range up to about  $Re = 6 \times 10^6$ .

To illustrate this scale effect, the evidence from oil flow visualisation tests was analysed to establish the correlation between the condition at which a bubble separation first appeared at a given spanwise station and the local Reynolds number at this station. This analysis was undertaken for three swept wings with the results shown in Figs 3.62(a,b). The relevant geometry for these wings is

Wing A: 43° leading-edge sweep,  $A = 3.5$ , 6% thick RAE 101 section streamwise, 8.2% thick normal to the leading edge,



Wing B: 53° leading-edge sweep,  $A = 3.1$ , 7.5% thick, RAE 101 section streamwise, 12.5% thick normal to the leading edge,

Wing C: 51.5° leading-edge sweep,  $A = 3.1$ , 7.5% thick section with a smaller leading-edge radius than RAE 101, 12.1% thick normal to the leading edge.

It will be seen that for all three wings, the derived values of local  $C_L$  at which the part-span vortex first originated at any particular station increased rapidly with  $Re$  but in the two cases where data could be obtained up to Reynolds numbers above  $Re = 4 \times 10^6$ , this rapid variation tended to die out at about  $Re = 5.5 \times 10^6$ . It was concluded<sup>139</sup> that at higher Reynolds numbers, the stall would be associated with the bursting of a short bubble or with a turbulent separation ahead of the trailing edge.

Several examples of scale effect on the force and moment results for various sweptback wings tested at this time are to be found in Ref 139. Results for one of the most interesting cases is reproduced in Fig 3.63. These results were obtained<sup>140</sup> in the 19 ft pressure tunnel at NASA Langley; the wing had a leading-edge sweep of 47.7° and a slightly cambered section, 10% thick normal to the leading edge. At  $Re = 1.1 \times 10^6$ , the stall is initiated by a leading-edge separation: a part-span vortex sheet appears and lies over the outer wing giving the nose-down change in pitching moment above  $C_L = 0.3$ ; it then moves inboard with increase in  $C_L$  and a pitch-up follows at about  $C_L = 0.6$ . The leading-edge separation is still observed up to about  $Re = 5 \times 10^6$  but above  $Re = 3 \times 10^6$ , a trailing-edge separation occurs first. At  $Re = 6 \times 10^6$ , when the leading-edge separation is no longer present, the pitching moment curve is completely linear up to about  $C_L = 0.8$  but there is then an abrupt pitch-up which, to judge from the left-hand graph, corresponds with when trailing-edge separation becomes significant. These results are for a model without tailplane and do not necessarily imply that the stability characteristics for a complete aircraft would be unacceptable but the reaction of the aircraft designer to these pitching moments could well be to investigate whether he could find a palliative to reduce the pitch-up trend. Ideas that were tried included a fence around the leading edge at some suitable spanwise position or a forward extension of the leading edge on the outer wing. The important point for this Agardograph is that these tests showed that any evidence on the effectiveness of such devices obtained at  $Re = 2.5 \times 10^6$  could be completely misleading. For example, Fig 3.64 shows the effects of adding a LE chord extension: at  $Re = 2.5 \times 10^6$ , they look very encouraging in that there is then a linear pitching moment curve up to  $C_L = 0.9$  whereas on the basic wing, there is a pitch up above  $C_L = 0.7$ . At  $Re = 6.1 \times 10^6$ , however, the comparison is almost exactly reversed. These results were explained in Ref 141. To be effective, the chord extension has to balance out the effects of a part-span vortex sheet originating near the inboard end of the chord extension: direct effects due to the vortex itself and indirect effects due to its ability to restrain the inward movement of the outer wing leading-edge vortex. At  $Re = 2.5 \times 10^6$ , this additional vortex sheet forms at a very low incidence when its strength is weak and the pitching moment changes that accompany its inward movement to the inner end of the chord extension are relatively small but at  $Re = 6.1 \times 10^6$ , it forms at a higher  $C_L$  and so the nose-down followed by a nose-up trend are clearly evident. These changes are present at a lower  $C_L$  than on the basic wing because the leading edge of the chord extension is sharper. This suggests that the scale effect may not be complete at  $Re = 6.1 \times 10^6$ ; indeed, ultimately, the chord extension may lose its ability to influence the results in either direction because its effectiveness depends on its being able to provoke a separation near the leading edge.

The results with the chord extension are by no means unique in demonstrating that adverse scale effect can be encountered. Fig 3.65 compares results for four 50° swept wings, all with the same planform and thickness/chord ratio but different section shapes. The wing with the RAE 101 section is the basic wing for the comparison for the chord extension just discussed; the "NACA 3" wing has a NACA 3-007.5 section with a leading-edge radius of 0.0119c compared with 0.0043c for the RAE section; "Droop B" has a similar nose radius together with 0.015c camber on an "m = 0.8" camber-line and "Droop C" has a leading-edge droop of 0.0315c, a leading-edge extension of 0.025c and a nose radius of 0.025c. Viewed as two-dimensional sections, it is clear that this progression is in the direction of increasing the abscissa of the correlation graph in Fig 3.3 and so, it is no surprise to find that in terms of the flow over the swept wings at high incidence, the progression takes us from the premature appearance of a leading-edge vortex (long bubble) on RAE 101 at low Reynolds number to a trailing-edge stall on wings B and C at high Reynolds number. All the 3 extra wings improve the pitching moment characteristics at low Reynolds number but the scale effect is adverse with Droops B and C, trivial with NACA 3 and strongly favourable with RAE 101. The adverse scale effect with Droops B and C reflects two features of the flow patterns: the disappearance of the leading-edge part-span vortex and its associated lift and second, the fact that without this vortex, it is easier for a trailing-edge separation to spread forward.

Unfortunately, RAE were unable to test these wings at Reynolds numbers higher than  $Re = 6.1 \times 10^6$  but van den Berg in Ref 61 correlated some results on swept wings tested by NACA where the tests extended to  $Re = 11 \times 10^6$ . His conclusion was that the maximum usable  $C_L$  defined by the  $C_L$  at which pitch up occurred tended to increase rapidly with  $Re$  up to  $Re = 6 \times 10^6$  but there was little further change for the wings tested between  $Re = 6 \times 10^6$  and  $Re = 11 \times 10^6$ . This is obviously a conclusion that may depend on the wing section geometry. As regards the actual  $C_{L,max}$ , van den Berg comments that for thin, highly swept (note: 'highly swept' here means 45° - 50°) wings,  $C_{L,max}$  varies little with  $Re$  whereas with thick wings at moderate sweep (35° or less), large increases could occur and extend up to  $Re = 10 \times 10^6$ . This is as would be expected by analogy with the 2D data.

To conclude this paragraph of the Agardograph, it is worth noting that some experience in the development of the BAe Harrier is relevant to the above discussion. Small fences wrapped around the wing leading edge were introduced to improve the usable lift at Mach numbers such as  $M = 0.6$ . Tests<sup>142</sup> were made in the ARA 9 ft x 8 ft transonic tunnel to investigate how such fences derive their effectiveness. Fig 3.66(a) shows the geometry of the wing and a typical fence and Figs 3.66(b-e) present some results. Fig 3.66(b) shows that there is a substantial improvement in the lift at incidences above about 13° incidence and Figs 3.66(c-d) illustrate how this improvement is achieved in the flow over the wing outboard of the fence. On the basic wing, without a fence, two flow separations were observed at high incidence: a leading edge separation starting near the tip and spreading in to about 75% semispan at  $\alpha = 10^\circ$  and a rear separation appearing first at  $\alpha = 4^\circ$  at about 75% semispan and then spreading inboard and forward, the two separations merging at about  $\alpha = 10^\circ$ . The leading-edge fence was then positioned at 81.5% semispan, the results of earlier tests on a smaller complete model having shown that the effectiveness of the fence was critically dependent on its precise spanwise position. The addition of the fence interrupts the flow along the leading-edge attachment line and therefore causes this flow to separate. Two primary stand-

off vortices form, one rotating in an anticlockwise sense looked at from upstream and streaming over the lower surface and the other rotating in a clockwise sense and streaming over the upper surface. At moderate incidences when the flow close to the leading edge immediately outboard of these vortices is attached, the upper primary vortex streams back as shown in sketch (i) in Fig 3.66(c). At higher incidences, however, when the leading-edge separation initiated near the tip has spread into this neighbourhood, the air in this three-dimensional separation is drawn into a secondary anti-clockwise vortex lying forward and outboard of the primary vortex as illustrated in sketch (ii). As soon as this interaction is established, the secondary vortex strength appears to increase rapidly, and the extra wing lift is produced by the suction on the wing upper surface below this vortex - see Figs 3.66(d). This description has been given in some detail to indicate that the effectiveness of the fence and its sensitivity to its spanwise position comes from the fact that the flow system induced by the fence has to interact with the wing leading-edge separation. This is therefore the explanation why, to obtain the good results, the fence had to be sited at 78% semispan on the 1/10 scale complete model, 81% semispan on the 1/7.5 scale half model and 84% on the full-scale aircraft in flight. This demonstrates the scale effect on the leading-edge separation and the change with increasing Reynolds number from a leading-edge to a trailing-edge separation on the wing near 75-80% semispan. In this case, however, the leading-edge separation still occurs in flight on the outermost sections; otherwise the fences would not have continued to be effective in flight. The story is an interesting example of how scale effect can manifest itself in practice.

### 3.3.4.2 Recent evidence: transition-dominated scale effect

The results to be discussed in this part of the report were all obtained from tests<sup>136,143,144</sup> in the DRA 5 m Tunnel on the DRA model 495 which can be considered to be a 1/3 scale model representative of a low-level strike fighter. The general layout of the model is shown in Fig 3.67(a). The wing is mounted in a high position; it has an 8% thick supercritical section and can be fitted with an 18% chord leading-edge slat and a 33% chord single-slotted trailing-edge flap. A special feature of the geometry is that the slat brackets are profiled as shown in Fig 3.67(b) to minimise their wakes and hence, hopefully avoid premature separation in their vicinity. For the tests<sup>144</sup> exploring the transition-dominated scale effect, the slat was set at 35° deflection and the flap at 20°. The slat was positioned close to the location giving maximum  $C_{l,max}$  - see later.

The investigation into the occurrence of attachment line transition (ALT) on this wing is important for at least three reasons: first, ALT occurs within the test Reynolds range in the 5 m Tunnel; second, there is a significant spanwise variation in the value of  $Re$  and third, it is found that there is also a significant spanwise variation in the value of  $Re$  needed to provoke ALT. The values of  $Re$  derived from the measured pressure distributions are presented in two ways in Figs 3.67(c,d): Fig 3.67(c) shows the variation with incidence in the unit Reynolds number required to give  $Re = 300$  and Fig 3.67(d) shows the variation of  $Re$  for a given unit Reynolds number,  $Re/m$ , of  $14.5 \times 10^6$ . It has already been explained that two opposing factors control the spanwise variation of  $Re$ : the wing taper leading to a decrease in  $Re$  from root to tip and second, the spanwise distribution of the local incidence which, through its effect on the position of the attachment line and hence on the velocity gradient away from the attachment line, tends to give an increase in  $R$  from root to tip. The results demonstrate that, at moderate incidences, the second factor outweighs the first but at high incidences near to  $C_{l,max}$  the first is the only significant

factor: hence, there is a change with incidence in the sign of  $dRe/ds$  along the attachment line.

Data from hot-films on the slat surface were analysed to determine the state of the attachment-line boundary layer with the results shown in Figs 3.67(e-g). Laminar and turbulent boundary layer states are also identified on Fig 3.67(d). Ref 144 notes that calculations of the relevant parameters showed that neither re-laminarisation nor cross-flow instability should occur in these tests and so, the results in Figs 3.67(e-g) indicate when ALT is occurring. The results are surprising for several reasons:

- (i) at the inboard station, there is little sign of turbulence until  $Re > 450$  whereas, from Poll's research on an infinite swept wing, one would have forecast that ALT would have been provoked by disturbances from the side of the fuselage at  $Re > 300$ . Hardy, in Ref 144, suggests that a possible explanation is that the reduced slat lift near the wing root results in an attachment line position close to the nose leading to very low values of  $Re$ , ie lower than those shown for the "inboard station". Ref 145 showed that a very rapid decay of turbulence is possible at low values of  $Re$ ,
- (ii) at the outboard station, on the other hand, ALT appears to correlate with  $Re = 300$ . Here, one might have hoped for ALT to be delayed beyond  $Re = 700$  and Hardy suggests that the most likely explanation for the earlier contamination is that it is induced by surface irregularities and possible disturbances from the slat support brackets which intrude slightly into the slat heel. The spanwise variation in  $Re$  may be significant. Paisley and Poll found<sup>134</sup> that wing taper (and hence a spanwise variation in  $Re$ ) reduced the size of permissible roughness. It was not possible to confirm by any quantitative analysis that this was the correct explanation but the results are a warning that on a practical design,  $Re = 300$  may be a good figure to associate with ALT even when turbulence is not caused by disturbances from the side of the fuselage.

So, contrary to what might have been a reasonable expectation, transition occurs first outboard and then spreads inboard - in the case plotted in Fig 3.67(d), it occurs at  $\alpha = 17.5^\circ$  at the outboard station,  $23^\circ$  at the mid station and beyond  $28^\circ$  at the inboard station. This gradual spread of turbulent flow leads to a reduction in  $C_{l,max}$  with Reynolds number as shown in Fig 3.67(h). The decrease of about 1% in  $C_{l,max}$  between  $Re = 10 \times 10^6$  and  $Re = 13.5 \times 10^6$  may not appear to be very much but it is significant relative to the increase that might have been forecast on the basis of conventional scale effect. ALT is clearly an effect that has to be allowed for in the extrapolation of the tunnel data to full-scale. Tripping the attachment-line boundary layer might make it easier to extrapolate but one would then have to check on the likelihood of re-laminarisation on the inner wing. The present author considers that Refs 136 and 144 are important references. Their importance lies not so much in the precise conclusions as to where ALT occurs first on this particular wing but on the guidance the reports offer to other aerodynamicists analysing the scale effect on their wings. The gradual nature of the changes with  $Re$  in the stalling characteristics in contrast to the sudden changes noted earlier with less swept wings results from the substantial variation across the span when ALT occurs.

The test data for DRA model 495 can also be used as evidence as to how the optimum slat position varies with Reynolds number and whether, as with the less swept wings, it is important to re-optimize the position chosen from low Re tests to suit conditions at higher Reynolds number. These questions are addressed in Ref 143; relevant results are reproduced in Figs 3.67(j,k,l). The actual variation in the best  $C_{L,max}$  with Re is shown in Fig 3.67(j) to be broadly similar to that observed on the corresponding transport research wing model 477 (it is only the variation with Re that is significant; the difference in the values of  $C_{L,max}$  at a given Re is of no consequence because of the differences in geometry). However, the scale effect on the optimum slat position as illustrated in Figs 3.67(k,l) is less apparent than the data for less swept wings or 2D sections that were discussed earlier. This is a reflection of the fact that the changes in  $C_{L,max}$  with slat position around the optimum position at a given Reynolds number are not very great on model 495. Mach number is far more important than Reynolds number; this is due to the flow on the outer wing being locally supersonic on the slat near  $C_{L,max}$  at  $M = 0.22$  and being supersonic on both wing and slat by  $M = 0.28$ . The limitations imposed by the flow being supersonic are discussed in detail in Ref 143.

### 3.3.5 Examples of scale effect on slender wings

#### 3.3.5.1 Sources of data

Vortical flows over slender wings at high lift have been the subject of many FDP Symposia but, leaving aside a paper<sup>146</sup> by Poll at the 1983 meeting, there is little reference to Reynolds number or scale effects at these meetings until one reaches 1988 and 1990. Clearly, there was a feeling in many quarters that Reynolds number effects were of secondary importance. In some respects, this is of course true: notably as regards the formation of the primary vortex in the flow over a sharp-edged wing for which, at all Reynolds numbers, the vortex originates at the wing apex. However, in other detailed respects, particularly with a round-nosed slender wing, research in the past 10 years has confirmed that subtle Reynolds-number effects are present and can be very important. The three most useful sources of information are

- (i) the International Vortex Flow Experiment<sup>147,148,149,150</sup> and later associated work<sup>151</sup> principally at NLR in Holland. This was a joint theoretical and experimental programme started in 1983 and involving FFA, NLR, AFWAL, DLR, MBB, Dornier and the Technical Universities of Delft and Braunschweig. The emphasis was on the results at transonic speeds such as  $M = 0.85$  but experimental data were in fact obtained at Mach numbers from 0.2 up to  $M = 4.0$ . A major aim of the programme was to provide data for the validation of computational methods, in particular Euler methods. Most of the data were obtained on cropped delta wings with  $65^\circ$  leading-edge sweep with alternatively sharp or round leading edges. The transonic data will be reviewed later in §4.3 but low speed, high lift results for sharp-edged wings are described below in §3.3.5.2,
- (ii) the extensive research at DRA Bedford on 4% thick slender wings with round,  $60^\circ$  swept leading edges. These results were described briefly in Ref 63 and then more extensively<sup>152</sup> at the ICAS meeting in Stockholm in 1990. Tests were made at both low speeds and supersonic speeds and the low speed data are discussed in §3.3.5.3 below. A very recent reference, Ref 153, presents the results of a further DRA low speed test on a  $60^\circ$  swept panel model,

- (iii) a major programme of flow visualisation tests in both flight and tunnel of the vortical flows over the  $60^\circ$  delta wing of the F-106B at NASA Langley and described by Lamar in Refs 154, 155.

These three programmes have greatly improved our understanding of the possible scale effects in the flow over slender wings at high lift and low speeds and so, it is sensible to base the discussion in this Agardograph primarily on what has been learnt from these programmes, noting in the final section §3.3.5.4, how this information helps in the interpretation of some earlier data.

#### 3.3.5.2 Slender wings with sharp leading edges

Elsenaar and Hojmakers in Ref 151 list the features in the flow over a slender wing at high lift which could in principle be subject to scale effect. Considering just the flow at low speeds over a wing with sharp leading edges, there are three such features: first, the development of the boundary layer starting at the primary attachment line on the wing upper and lower surfaces; second, the secondary separation and finally, the breakdown of the vortex. This list does not include the formation of the primary vortex since, with a sharp leading edge, this depends merely on the wing geometry. Also, at low speeds, one would not expect to find significant Reynolds number effects on the flow over the rear upper surface between the primary vortices (this is not true at transonic speeds as will be seen later in §4.3).

The results discussed in Ref 151 were obtained in tests in the HST at NLR on a pressure-plotted model with a sharp  $60^\circ$  swept leading edge. The model geometry is shown in Fig 3.68(a); the model has nominally the same scale and geometry as the sharp-edged configuration used in the "International Vortex Flow Experiment" but there are small differences - in particular, the fuselage does not protrude above the wing upper surface. The pressure plotting facilities were very extensive: 230 holes on the upper surface and 30 on the lower surface. Spanwise pressure distributions at three chordwise stations are presented in Fig 3.68(b) for a range of incidences at  $M = 0.2$  at two Reynolds numbers,  $Re = 2.7 \times 10^6$  and  $9 \times 10^6$  based on wing root chord. The tests were made transition free but calculations described in Ref 148 suggested that the boundary layer at the primary attachment line would be completely turbulent at the higher test Reynolds number and mostly turbulent except near the wing apex even at the lower Reynolds number; this was confirmed by acenaphthene tests.

The boundary layer state at the primary attachment line and the test Reynolds number would not be expected to have much influence on the boundary layer development over the inner wing but this cannot be said about their possible effect on the secondary separation under the primary vortex. Looking at the spanwise pressure distributions in Fig 3.68(b), it will be realised that the flow outboard and forward of the primary attachment line, first accelerates up to the position of the peak ( $-C_p$ ) under the primary vortex core but then the boundary layer encounters an adverse pressure gradient under which a secondary separation will occur. The free shear layer thus formed will roll up into a secondary vortex - see Fig 3.69(a). Immediately downstream of the secondary separation line, the flow is directed along this line and this will be recognised as a familiar feature of many oil flow pictures of the flow over slender wings. If this separation lies in a direction approximately coincident with a ray from the wing apex, it is reasonable to assume that there is no change in boundary layer state along the secondary separation line; a kink in the line

would imply such a change: a laminar separation would be located further inboard than a turbulent separation. As noted by Elsenaar and Hoeijmakers in Ref 151, the secondary and primary separations are intrinsically coupled and the calculations reported in Ref 148 indicated that the position of the secondary separation can have a major effect on the strength (and position) of the primary vortex. Calculations were made by the NLR VORSBA panel method for computing incompressible flow with free vortex sheets and by the NLR VORSEP panel method for computing fully three-dimensional incompressible flow around thin pointed delta-like wings of arbitrary shape with leading-edge and trailing-edge vortex sheets with the results shown in Fig 3.69(b). Results are presented for various assumed positions of the secondary separation and for a case with no secondary separation. It will be seen that an earlier secondary separation leads to an inboard movement and weakening of the peak suction under the primary vortex. In the model tests, secondary separation was observed to occur at about 75% semispan at this incidence and Fig 3.69(c) shows that the calculated results with this secondary separation position agree reasonably with the experimental data as regards the primary vortex; outboard of the secondary separation line, one cannot rely on the theoretical results; the strength of the secondary suction peak is weaker in the experiment.

Figs 3.69(c,d) again taken from Ref 148 compare the calculated streamline patterns over the wing with respectively a laminar and a turbulent separation. Changes in Reynolds number, if they lead to a change in the state of the boundary layer downstream of primary re-attachment, could lead to a significant effect. In the NLR tests, however, as noted earlier, the boundary layer is mostly turbulent even at the lower Reynolds number but there are still some effects worthy of discussion in the comparison presented in Fig 3.68(b). The results at the lower incidences are qualitatively as one might have forecast: the increase in Reynolds number leads to a slight outboard shift in the location of the secondary separation and, as a result, to a strengthening of the primary vortex. Also, the peak suction associated with the secondary vortex becomes more visible. Ref 148 suggests that this is due to the free shear layers becoming thinner with increase in Reynolds number and the secondary vortex becoming more compact and tending to stand clear of the viscous layer on the wing. The results at high incidence, eg  $15^\circ$  and  $20^\circ$ , are more puzzling: at  $x/c_R = 0.6$  and  $0.8$ , the secondary separation and primary vortex core both move inboard with Reynolds number, ie move in the opposite direction to what one might have predicted. Elsenaar and Hoeijmakers in Ref 148 suggest that this is another consequence of the increase with Reynolds number in the strength of the secondary vortex. To forecast this scale effect accurately, one needs a theoretical method capable of predicting the full flow field including the secondary vortex. The reader may react that these effects are academically interesting but too small to be important for the design of a practical aircraft. This could however be a wrong conclusion - the spanwise shifts in the vortex cores may appear to be small in themselves but could still be significant in determining whether there is any adverse interaction between the vortices and any tail surfaces at the rear of the aircraft.

Similar remarks can be made about vortex bursting. The general belief, as expressed in the literature, eg Ref 157, is that Reynolds number has only a trivial effect on vortex breakdown and certainly, it was small, ie less than  $1^\circ$  in incidence, in the NLR tests being discussed. However, the present author remains unconvinced that it is safe to conclude that the effects of Re on vortex bursting can always be ignored. This point will be discussed again in §4.5.3.

### 3.3.5.3 Slender wings with round leading edges

Turning now to the case of a slender wing with a cambered, round leading edge - probably, the important case for practical applications - the most appropriate starting point is to consider the results<sup>152</sup> from the DRA programme at RAE Bedford. Tests were made in the 8 ft x 8 ft tunnel on three pressure-plotted half models of slender wing-body combinations. The wings all had the same delta wing planform with a leading-edge sweep of  $60^\circ$ , a thickness-chord ratio of 4% and a leading-edge radius virtually constant across the span of 0.13% x centre-line chord. Two of the wings were cambered, the third was symmetrical. Tests were made over a wide range of Reynolds number from  $Re = 6.4 \times 10^6$  to  $28.5 \times 10^6$  based on wing mean chord. Tests were not made at free-stream Mach numbers below  $M = 0.5$  but the data for  $\alpha = 11.7^\circ$ ,  $M = 0.6$  for the cambered wing A presented in Figs 3.70(a,b) can, for the purpose of this Agardograph, be treated as a low speed, high lift condition with a reasonable development of vortical flow.

With the change to a round leading edge, one would expect to find that the primary vortex would form first near the tip and then move towards the apex with increase in incidence. However, the results in Figs 3.70(a,b) from a test with free transition, show that on the round-nosed slender wing A, this is far from the end of the story. The Reynolds number effects are clearly substantial, particularly between  $Re = 6.4 \times 10^6$  and  $Re = 19 \times 10^6$  and they are still present to some extent up to the highest test Reynolds number,  $Re = 29 \times 10^6$ , based on the wing mean chord. They appear to influence even the nature of the development of the flow at high incidence. At the lowest test Reynolds number,  $Re = 6.4 \times 10^6$ , the isobars suggest that there is a part-span primary vortex originating from point P. The oil flow visualisation shows the characteristic outflow beneath this vortex and the secondary separation in this outflow. One can therefore say that the flow pattern is similar in character to that on the sharp-edged wings discussed above except for the fact that it is a part-span vortex rather than a vortex originating at the wing apex. At the high test Reynolds number, on the other hand, the isobars are closely packed near the leading edge suggesting a flow with cylindrical rather than conical symmetry. Upstream of point P, at this higher Reynolds number, the oil runs along and from the leading edge and Ashill et al in Ref 152 note that this, coupled with the pressure distributions in this region, suggest a 'short bubble' separation whereas the the part-span vortex flow at the low Re can be thought of as analogous to a long bubble. Poll in a Round Table discussion at an earlier AGARD FDP meeting<sup>158</sup> had suggested that the flow breakdown near the leading edge of a slender wing was likely to change its character with Reynolds number in a manner similar to that observed on an inclined circular cylinder and that this change would occur at a Reynolds number based on leading-edge radius of between  $Re = 0.5 \times 10^5$  and  $Re = 1.0 \times 10^5$ . It is therefore noteworthy that, in the tests being discussed here, the highest test Re based on leading-edge radius is  $Re_p = 0.7 \times 10^5$ .

For the above interpretation to be correct, one has to accept that the boundary layer at the leading edge is evidently not fully turbulent even at the highest test Reynolds number. Ashill et al in Ref 152 used the transition and re-laminarisation criteria introduced earlier to check whether this was likely. The results of these calculations are reproduced in Fig 3.71(a). They indicate that at this incidence ( $\alpha = 11.7^\circ$ ), contamination along the leading-edge attachment line, ALT, should occur at all the test Reynolds numbers but that complete re-laminarisation should follow for Reynolds numbers up to about  $Re = 13 \times 10^6$  and that the leading-edge flow will not be fully completely

turbulent even at  $Re = 38 \times 10^6$ . These calculations therefore support the interpretation put forward for the observed flow pictures. As noted above, the Reynolds number based on the wing mean chord is not a meaningful parameter on which to generalise the results. It is preferable to quote the values based on leading-edge radius; on this basis, re-laminarisation is complete up to  $Re_p = 0.3 \times 10^5$  and may still be present at  $Re_p = 0.9 \times 10^5$ .

The reader meeting the above results for the same time may be surprised to find such scale effects existing in results for slender wings and also that the interpretation depends on the ability of the flow near the leading edge to re-laminarise after ALT has occurred. Acceptance that the interpretation is on the right lines has however been strengthened by the results of a later test on a  $60^\circ$  swept, constant chord panel model in the  $3.96 \text{ m} \times 2.74 \text{ m}$  Low Speed Wind Tunnel at DRA Bedford. This model had a NACA 4412 section with a chord length normal to the leading edge of  $1 \text{ m}$  and a leading-edge radius,  $\rho$ , of  $0.0158 \text{ m}$ . The relatively large size of this model enabled it to be pressure plotted extensively and also, miniature hot film gauges were mounted at six spanwise stations to establish the boundary-layer state. A comprehensive picture of the leading-edge flow characteristics is plotted in Fig 3.72. This picture will be described in detail because other workers should find that the creation of such a picture for their particular wing should help greatly in the interpretation and prediction of scale effect for their own wing. It is recognised that, in general, the precise experimental evidence of boundary layer state will not be available but, even so, use of predicted values of  $Re$  and  $K$  as for the previous example, should enable the diagram to be constructed. In passing, it should be noted that Ref 153 is also an excellent paper to consult to learn how the upper-surface flow at the higher Reynolds numbers can be influenced by disturbances shed from the attachment line.

The boundaries in Fig 3.72 were based on evidence from the experimental data for sections near mid-semi-span; it should be noted that the values of  $Re_p$  were based on the leading-edge radius and the component of the free-stream velocity in the direction normal to the leading edge. The fact that the maximum value of  $Re_p$  for the onset of ALT occurs at a positive incidence is a consequence of the wing camber. It will be seen that ALT is complete at values of  $Re$  varying from  $735 \pm 50$  at low  $Re$  to  $575 \pm 50$  at high  $Re$  which are much higher than the value of 300 quoted earlier as a general criterion for cases where ALT is induced by a gross disturbance from the root. However, it is not unique in this respect: higher values were obtained by Poll<sup>132</sup> in his Cranfield experiments and also by Hardy<sup>144</sup> in his tests on a less swept wing. As suggested by Hardy<sup>144</sup>, the explanation could lie in the relatively low values of  $Re$  near the wing root. The fact that the critical value of  $Re$  for onset of transition decreases with increase in  $Re_p$  supports the conclusion that ALT is induced by small disturbances on the leading edge. As with the slender wing being discussed above, although ALT has occurred at the higher incidences, re-laminarisation is either 'probable' or 'possible' over the whole test  $Re$ -range.

The shaded area in Fig 3.72 indicates where the presence of a short bubble has been identified from the measured pressure distributions. Oil flow visualisation suggested that a short bubble continued to exist in all the areas where re-laminarisation is judged to be 'probable' but not where re-laminarisation is judged to be 'possible'. Ashill and Betts in Ref 153 identify three types of leading-edge separation on the locus for flow breakdown shown in Fig 3.72:

- (i) at  $Re_p < 12000$ , it is due to the bursting of the short laminar separation bubble - thus creating a 'long bubble' type of vortex flow,
- (ii) at  $12000 < Re_p < 20000$ , oil flow visualisation suggested that turbulent re-separation was occurring immediately after reattachment of the short bubble,
- (iii) at  $Re_p > 20000$ , it is due to turbulent separation with no preceding laminar separation.

As would be expected by analogy with the 2D data discussed earlier, there is appreciable favourable scale effect on flow breakdown in the low  $Re$ -range where the stall is of the 'long bubble' type but perhaps, the more interesting result is that at higher Reynolds numbers, there is a slow decrease with Reynolds number in the incidence for flow breakdown. A trend of this nature has been noted in many earlier examples for 2D aerofoils or less swept wings and has generally been ascribed without real proof to a forward movement of transition with Reynolds number. This cannot however be the explanation in the present case and, at the present time, it would not be possible to predict this unfavourable scale effect. Various possible explanations are mentioned in Ref 153; the present author is attracted by the idea that the turbulent boundary layers at mid-semi-span are of the low Reynolds number type for which the normal similarity rules do not apply. Green<sup>159</sup>, following on from earlier work of Coles, suggested that the normal trend for the onset of separation of a turbulent boundary layer to be delayed with increase in Reynolds number would reverse at low Reynolds numbers because, at these low Reynolds numbers, the outer part of the boundary layer profile becomes increasingly full as the Reynolds number decreases. This reversal is now well established in the analysis<sup>160</sup> of the scale effect on shock-induced separation at transonic speeds (see §4.3.3 for a fuller discussion). The maximum values of boundary layer momentum thickness Reynolds number achieved at the peak suction position in these slender wing tests is less than 1000 and hence, the value is well within this 'low Reynolds number range' which Coles had forecast would extend up to some value in the range 2000 to 5000.

All the data so far discussed in this section of the Agardograph were obtained with free transition. It is natural to enquire, in view of the significant scale effects, whether it would be possible to obtain the high  $Re$ -result at low Reynolds numbers by fixing transition in some appropriate (but possibly non-standard) fashion. This was investigated in the DRA slender-wing tests and some of the results are reproduced in Figs 3.71(b-d). The starting point for this study lay in comparisons such as those shown in Fig 3.71(b) of the pressure distributions around the leading edge at different Reynolds numbers. These show that the position of the primary separation line does not vary significantly with Reynolds number but the pressures in this region decrease notably between low and high Reynolds number. This is what one would expect from a tendency for the secondary separation to disappear with increasing Reynolds number and one would forecast qualitatively from the pictures in Fig 3.69(a) for the flows with and without a secondary separation. The adverse pressure gradient inducing the secondary separation is, in fact, less severe at the lower Reynolds numbers, thus suggesting that this is a laminar separation that could be postponed by fixing transition ahead of the secondary separation line. An 'upper surface' trip was therefore applied, as shown in Fig 3.70(c) inboard of the leading-edge suction peak and this produced a flow at  $Re_{c \text{ bar}} = 12.7 \times 10^6$  similar to that obtained at  $Re = 28.5 \times 10^6$  with free transition. Clearly, to attain its objective, this type of trip might have to be repositioned according to the test Reynolds number - further inboard at lower  $Re$ . An alternative

approach was to use a trip at the leading edge with the results plotted in Figs 3.71(c,d). The data with this leading-edge trip show virtually no scale effect but the shape of the pressure distributions around the leading edge are not the same as those obtained with free transition at the highest test Reynolds number.

So, the message from these tests is that an upper surface trip suitably located to create a turbulent boundary layer ahead of the secondary separation may be a useful method of avoiding large difficult-to-predict scale effects but a leading-edge trip should not be used. This last remark would apply even more strongly to the coarse roughness bands around the leading edge that tended to be used 40 years ago (see the remarks later about the flight-tunnel comparison<sup>161</sup> for the Fairey Delta).

There is still one feature of the slender-wing flow patterns in Fig 3.70 that calls for some comment in the context of scale effect. Downstream of point P at the higher Reynolds number, the oil flow tests revealed a series of disturbances being shed from near the leading edge. Inspection showed that these originated at the pressure-plotting stations and this is just one illustration of many examples that could be quoted<sup>153,162,163,164,165,166</sup> of where, despite high standards of surface finish, it is difficult to avoid such disturbances at high Reynolds number near the leading edge where the boundary layer is very thin. The presence of these disturbances may have affected the pressure readings and hence, the plotted isobar patterns. Just possibly, they may have contributed to the scale effect although it is noteworthy that, in the tests on the panel model, similar disturbances did not prevent the formation of a laminar separation bubble.

These disturbances from the leading edge at high Reynolds number could have a direct bearing on one of the main results from the NASA Langley flight programme on the F-106B aircraft. This programme<sup>154,155</sup> represents an impressive use of the vapor-screen technique to study the vortex flow over the upper surface of the 60° delta wing. The photographs were taken from the rear or side. Fig 3.73(a) is reproduced from Ref 154 to help the reader understand the pictures from the front-mounted, aft-looking video camera used in the flight test. The left-hand portion of the picture shows the arrangement of the light sheet, video camera and seeding probe on a plan-view sketch of the aircraft. The camera field of view is highlighted on the right-hand side in terms of the monitor image. Towards the top is the wing trailing edge, intersecting the right side is the wing leading edge, and across the lower left corner is a portion of the fuselage. In the middle of the image, parallel to the trailing edge, is a line depicting the light-sheet footprint; this does not extend to the leading edge because of the wing camber. The expectation ahead of the tests was that the vapor-screen pictures would show the position of a single vortex per wing panel with the position of the vortex depending on lift coefficient, Mach number and possibly Reynolds number. This expectation was based on what had been observed in tests on a large model in the NASA Langley 30 ft x 60 ft tunnel, see Fig 3.73(c). In the event, however, when the vortex flow first appeared with increasing angle-of-attack, eg at  $\alpha = 17^\circ$  at  $M = 0.4$ ,  $Re = 30 \times 10^6$  based on wing mean chord in Fig 3.73(b), three vortex-core regions were visible; at  $\alpha = 20^\circ$ , there were two cores and ultimately, at  $\alpha = 23^\circ$ , just a single core. The angle-of-attack required to obtain a single vortex was found to depend on Reynolds number, the single vortex being formed at a lower angle at the higher flight altitudes, ie lower Reynolds numbers. Lamar comments in Ref 154 that it is possible to reconcile the flight and tunnel results on this basis since the Reynolds number in the tunnel tests was only  $12 \times 10^6$ , ie about half the lowest value in the flight tests.

The present author believes that it is possible to offer some further speculative comments at this point. It seems reasonable to link the existence of the multiple vortices in the flight tests on the F-106B with the disturbances shed from the leading edge inboard of point P on the DRA cambered slender wing at high Reynolds number - see Fig 3.70(b). Various observations then fall into place. For example, the disappearance of the multiple vortices with increasing angle-of-attack could be explained by the expected inward movement of point P with angle-of-attack. Also, the fact that the angle-of-attack for the change to a single vortex increased with Reynolds number could imply that P at a given angle-of-attack moves out with increase of  $Re$ . Clearly, all the evidence shows that, even with the highest standard of model or aircraft manufacture, it is difficult at high Reynolds number to avoid disturbances being shed from the leading-edge region; whether these have any substantial effect on the final flow breakdown is still not clear.

As noted earlier, the DRA programme also included a test on the corresponding symmetrical slender wing and results from this test are presented in Fig 3.74. These results are for a lower incidence than for the selected cases for the cambered wing. The link between the two lies in the fact that the Euler calculations predict similar values for the peak suction near the leading edge. The scale effects evident in the results for the symmetrical wing with free transition are not the same as for the cambered wing but Ashill et al show that one can explain the differences in a consistent manner. The differences in question are in the pressure distributions very close to the leading edge. For both wings, the peak suction increases with Reynolds number but the significant difference lies in the effect of Reynolds number on the gradient aft of this peak suction: for the cambered wing, this gradient did not vary much with  $Re$  whereas, with the symmetrical wing, the boundary layer can apparently stand a much steeper gradient at high Reynolds number. This suggests a change in the state of the boundary layer and this is just what one would predict using the normal criteria. ALT is present in both cases but, for the symmetrical wing, the value of  $K_{max}$  at the highest test Reynolds number is only just greater than  $2.0 \times 10^{-6}$  as compared with  $2.8 \times 10^{-6}$  for the cambered wing. These values suggest that, for the symmetrical wing, re-laminarisation is unlikely to occur at the highest test Reynolds number and hence, the primary separation is a separation of a turbulent boundary layer - a situation not met in the tests on the cambered wing. Another difference between the results for the two wings is that the addition of a leading-edge trip on the symmetrical wing, while again producing results that do not vary with  $Re$ , increases rather than decreases the area of wing affected by separated flow. This may come as no surprise to those familiar to testing practices in tests on two-dimensional aerofoils where use of a transition trip in the region of a strong adverse pressure gradient frequently leads to a premature flow separation. It merely reinforces the conclusion that, on a slender wing, leading-edge trips should not be used.

#### **3.3.5.4 Updated interpretation of earlier results and conclusions**

Before summarising the main conclusions from this discussion on scale effects on slender wings at low speeds, it is interesting to revisit two of the most-often quoted comparisons in this area. First, the flight-tunnel comparison on the Fairey Delta 2 in Fig 3.75(a); this was originally presented in Ref 161 as a comparison where the test Reynolds numbers in flight and tunnel were very similar and where, hopefully, one might have expected good agreement between the two sets of data in features such as the reattachment of the flow from over the top

of the primary vortex. In fact, however, the area of separated flow is shown to be somewhat greater in the tunnel tests. With hindsight, however, two comments can be made about this comparison: first, the values of  $Re_p$  lie in the range where changes in the nature of the leading-edge separation might be expected and second, the comparison may be invalid because transition was fixed in the tunnel test in a very crude manner with a coarse band of carborundum wrapped all around the leading edge. If the comparison is accepted as genuine, it might indicate a change similar in nature but not in degree to that shown in Fig 3.70(b); in other words on this interpretation, the difference in Reynolds number is sufficient to be significant.

The second comparison<sup>167</sup> shown in Fig 3.76(b) has been quoted in many reviews. The data comes from flight tests on the F-111 TACT aircraft; they appear to show that at  $Re_c = 20 \times 10^6$ , the leading-edge flow has separated and a vortex is present whereas at  $Re_c = 40 \times 10^6$ , the flow is attached. With hindsight, one possibly wonders if the data are conclusive in proving that the flow is attached at the higher Reynolds number or whether a short cylindrical laminar separation bubble is still present near the leading edge as at high Reynolds number in the recent DRA slender-wing tests. In the Round Table discussion at the 1983 FDP meeting<sup>158</sup>, Poll noted that the Reynolds numbers of this comparison, when based on the wing leading-edge radius, were in the range  $0.5 - 1.0 \times 10^5$  where one might have expected a change in the leading-edge flow. One should therefore not be surprised to find scale effects of this type are present at Reynolds numbers that are very high when based on wing mean chord.

The main conclusions regarding scale effect on the flow over slender wings at high lift and low speeds are as follows:

- (i) if the wing has a sharp leading edge, the only feature of the flow that is likely to be directly subject to scale effect is the position of the secondary separation; changes in this position can however affect the strength of the primary vortex. These effects may only be significant when the change in Reynolds number leads to a change in the state of the boundary layer approaching the secondary separation. If an increase in  $Re$  leads to a change from a laminar to a turbulent boundary layer, the secondary separation point will shift outboard and the primary vortex will strengthen,
- (ii) if the wing has a round leading edge, the scale effects can be more substantial and can persist up to relatively high Reynolds numbers when these are based on a dimension such as the wing mean chord,
- (iii) the appropriate parameter for identifying these scale effects is the Reynolds based on the wing leading-edge radius. When  $Re_p < 12000$ , the primary vortex separation is analogous to a long bubble and scale effects are favourable. In the range  $12000 < Re_p < 20000$ , the flow will be transitional and both a short laminar separation bubble and a turbulent separation may exist. At higher  $Re_p$ , a turbulent separation is more likely and the flow breakdown can change its character. The scale effect on flow breakdown in this last range can be adverse but this may only apply if the Reynolds number at separation when based on boundary layer momentum thickness is less than about  $2 \times 10^3$ ,
- (iv) trips around the leading edge should not be used. They may eliminate scale effect but give the wrong pressure distribution and a premature flow breakdown. Trips on the upper surface appropriately located to produce a turbulent boundary layer ahead of the secondary separation may however be helpful in producing a higher effective test Reynolds number in model tests at low  $Re$ ,
- (v) at high Reynolds numbers, high standards of surface finish are required in both flight and tunnel. Even then, it may be difficult to prevent the appearance of disturbances from near the leading edge or multiple vortices. It is not clear whether and to what extent their presence affects the overall scale effect.

The pleasing feature of the detailed analysis of the recent information for slender wings is the way in which a continuous link can be established back in so many respects to the analysis of the results for wings of lower sweepback or even the results for two-dimensional aerofoils.

### 3.4 Complete Aircraft

#### 3.4.1 Introduction

All the preceding paragraphs in §3 have effectively been a prelude to a study of the evidence on scale effect at high lift and low speeds for specific complete aircraft. Arguably, the present chapter including the evidence from several flight-tunnel comparisons is the most important chapter in the Agardograph but the previous chapters were needed to provide the groundwork for the interpretation of the flow over the complete aircraft with high-lift devices extended. With two exceptions, all the evidence to be presented relates to civil transport aircraft and to set the scene, Fig 3.76(a) shows typical Reynolds numbers, based on wing mean chord, on the approach for transport aircraft and Fig 3.76(b) gives the operating envelopes for the three major low speed tunnels which have been used for testing large models of transport aircraft. These two pictures demonstrate that although all these tunnels allow one to investigate scale effect over a sizeable Reynolds-number range, considerable extrapolation to flight has often still been required.

It may sound easy to compare the flight and model test values of say,  $C_{L,max}$  but, in reality, it is far from easy. One wants to compare like with like but one does not measure the same quantities under the same conditions. These issues are addressed in various papers such as Refs 176 and 177. To quote from Ref 176, "the principal item to be estimated from the flight tests is the FAR stall speed. This speed is defined as the minimum speed obtained during a full stall that is approached at the rate of 1 knot per second. This minimum speed occurs during a dynamic manoeuvre and the airplane usually will be somewhere between 0.80 and 0.90 g at the time this minimum speed is reached. This FAR stall speed is used by the FAA as one consideration in determining take-off and landing speeds for aircraft certified within the US. The corresponding FAR  $C_{L,max}$  is defined without considering the reduced load factor existing at the time  $V_{stall}$  occurs. Another stall speed is the 1 g stall speed, which is defined as that speed which occurs just as the normal acceleration breaks to a reduced value. This speed also is measured during a dynamic manoeuvre and may not occur at exactly 1 g normal acceleration. This 1 g stall speed is used as the basis for setting the take-off and landing speeds by the US Air Force. The corresponding  $C_L$  historically has been used as  $C_{N,max}$  in the structural analysis of the aircraft. Also to be estimated is the true  $C_{L,max}$  achieved during the stall manoeuvre, where  $C_L$  is defined as  $nW/qS$ . This maximum lift coefficient usually



occurs at a speed below the 1 g stall speed and is the flight  $C_{L,max}$  most nearly corresponding to the one measured in the wind tunnel." Typically, for civil transport aircraft, the FAR stall speed is about 0.94 x the speed corresponding to the true  $C_{L,max}$  and hence, the FAR certified  $C_{L,max}$  can be about 13% higher than the value that should be compared with the result from the model tests.

Having selected the correct  $C_{L,max}$  to be derived from the flight tests to compare with the tunnel data, one must be sure that the test Mach numbers are the same. It has already been mentioned several times that both  $C_{L,max}$  and the scale effect on  $C_{L,max}$  can depend on Mach number and one cannot allow for this by any simple rules. Some typical examples of the effects of Mach number are shown in Figs 3.77(a-c). The results<sup>89</sup> in Fig 3.77(a) were obtained in tests in the 8 ft x 8 ft pressurised tunnel at DRA Bedford on a swept, constant-chord panel model as part of the development programme for the A300B. Qualitatively, these results are as one might have forecast: there is appreciable scale effect at low Mach number as noted earlier for wings with a leading-edge type of stall at the lower Reynolds numbers and also, an appreciable decrease in  $C_{L,max}$  with Mach number at constant Re as a result of the flow becoming supersonic over the slat or wing upper surface. As a result, the favourable scale effect becomes somewhat less pronounced with increase in Mach number. This should not however be accepted as a general conclusion that will apply in all cases. For example, it is not true of the results in Figs 3.77(b,c) where there is a tendency for the favourable scale effect actually to increase with Mach number. These are the 2D results<sup>108</sup> from the LTPT at NASA Langley which were discussed earlier in §3.2.3 but here, they have been cross-plotted to demonstrate the Mach-number effects. Fig 3.77(c) also illustrates that these M-effects can be sensitive to small changes in geometry - in this case, a change of the size of the gap from 0.030c to 0.025c.

Differences in geometry between the model and the full-scale aircraft affect nearly every flight-tunnel comparison. Generally, the model wing is manufactured with the 1 g twist, and some companies then apply corrections to the test results to allow for the estimated change in twist at high incidence. Corrections also have to be made for the bending of the high-lift devices and particularly when the model is being tested in a pressurised tunnel, the slat brackets on the model have, for strength reasons, to be oversized relative to the brackets on the aircraft. This is illustrated in Fig 3.78 which compares the model and full-scale brackets at three stations across the span on one typical model. The figure also lists some guidelines for good model design practice. The model should have the same number of tracks at the same spanwise positions as on the aircraft and the width of the full-scale brackets should be retained. When volume has to be added, it should be added underneath rather than on top and all holes should be sealed as in flight. The geometry at the ends of the slats both at the wing root and at any cut-outs in the leading edge, eg to admit a pylon for the engine nacelle, should be modelled faithfully as these are vital areas that can affect the value of  $C_{L,max}$  by more than any genuine Reynolds number effect. A poorly designed set of slat tracks can completely alter the development of the flow breakdown at the stall.

It will be seen later that the underwing nacelle installations typical of many subsonic transports can have a major influence on the low speed stall. Accurate representation or allowance for the intake and jet effects is therefore necessary for the flight-tunnel comparisons to be meaningful. Evidence will be discussed in §3.4.4 showing that the values of  $C_{L,max}$  and of  $C_L$  at high incidence can be sensitive to the precise intake mass flow; Fig 3.88(e), for example, shows that a blocked nacelle can

reduce the slope of the lift-incidence curve by about 10% at an incidence  $10^\circ$  below  $C_{L,max}$  and reduce  $C_{L,max}$  by as much as 0.17. To obtain an idea of the drag in the second segment climb from take-off, it is necessary to undertake tests with turbine powered simulators to establish the jet effects which, typically, can amount to up to 80 drag counts.

Much of the subsequent discussion concerns the values of  $C_{L,max}$  and how they vary with Reynolds number but for the aircraft designer and operator, there are other important issues: the scale effect on the attitude in the approach, the drag in the second segment climb and whether the pitching moment characteristics show an adequate degree of pitch-down at the stall.

As a guide to the amount of scale effect that should be treated as "significant", it is worth noting at this point the trade factors quoted by Garner, Meredith and Stoner in Ref 112

- (i) a 1.5% increase in maximum lift coefficient is equivalent to a 6600 lb increase in payload at a fixed approach speed,
- (ii) a 0.10% increase in lift coefficient at constant angle of attack is equivalent to reducing the approach attitude by one degree. For a given aft body-to-ground clearance angle, the landing gear may be shortened for a saving in airplane empty weight of 1400 lb,
- (iii) a 1% increase in take-off L/D is equivalent to a 2800 lb increase in payload or a 150 nm increase in range."

These figures, which relate to a heavy transport aircraft, provide the justification for treating a 1% increase in  $C_L$  at a given incidence or in  $C_{L,max}$ , ie typically 0.02 in  $C_L$ , as significant.

$C_{L,max}$  data for 15 different aircraft have been assembled to provide an overall picture of the scale effect that has been observed in practice. This is discussed in §§3.4.2.1 and 3.4.2.2 below and then in §3.4.2.3 some examples are given to illustrate the difficulties met in predicting the scale effect on the pitching moments. Having thus presented the overall picture, individual examples are then discussed in detail in §3.4.3 and some important 3D design features that influence the scale effect are described in §3.4.4. The general conclusions are summarised in §3.4.5.

### 3.4.2 The overall picture

#### 3.4.2.1 $C_{L,max}$ : evidence from model tests

$C_{L,max}$  versus Re curves from model tests for 12 different aircraft are presented in Figs 3.79(a,b). In Fig 3.79(a), the datum for  $\Delta C_{L,max}$  is the value at  $Re = 1.5 \times 10^6$  while in Fig 3.79(b), it is the value at  $Re = 2.5 \times 10^6$ . The results for aircraft A-D are for the clean aircraft with high-lift devices retracted and those for E-J are with high-lift devices extended - in most cases, to produce a landing configuration. For M, N and P, several curves are presented corresponding to different settings of the high-lift devices. In view of this sensitivity of  $\Delta C_{L,max}$  to the setting of the devices, Fig 3.79(c) presents some examples of  $\Delta C_{L,max}$  plotted against  $\delta_F$  where  $\delta_F$  is the setting of the trailing-edge flaps.

The results on the first sheet, Fig 3.79(a), are for early aircraft designed in the 1940-1965 period; Fig 3.79(b) extends the story up to the present time. Some of these results will be discussed in detail in §3.4.3 but first some leading conclusions:



- (i) in Fig 3.79(a), the favourable scale effect is substantial between  $Re = 1 \times 10^6$  and about  $Re = 3.5 \times 10^6$ ; this is a familiar picture for wings exhibiting a leading-edge stall at these Reynolds numbers,
- (ii) clearly, therefore, results at Reynolds numbers below about  $Re = 3.5 \times 10^6$  can be very misleading. A good example of this is afforded by the results for the first aircraft A. Addition of the nacelles - two nacelles per wing panel in this case, one mounted above and one below the wing at the same station - has no effect on  $C_{L,max}$  at  $Re = 1 \times 10^6$  but at higher Reynolds numbers when the leading-edge separation on most of the wing is delayed to higher  $C_L$ , there is a clear adverse effect from the nacelles; oil flow tests revealed the presence of localised separations in the wing leading-edge/nacelle junctions,
- (iii) it is therefore more sensible to consider the scale effect above say,  $Re = 2.5 \times 10^6$  as in Figs 3.79(b,c). Considering all the data (including that in Fig 3.79(a)) on this basis, one then finds that the scale effect on  $C_{L,max}$  between  $Re = 2.5 \times 10^6$  and  $Re = 6.5 \times 10^6$  is still favourable in all cases and amounts to 0.10 in  $C_L$  or more in many cases,
- (iv) for aircraft E-J, this favourable scale effect does not appear to be complete by  $Re = 6.5 \times 10^6$ . This appears to conflict with earlier evidence on 2D aerofoils but one should remember that these Reynolds numbers are based on the wing mean chord and that typically, the wing tip chord can be less than half the mean chord,
- (v) for aircraft M,N,P, however, a new trend appears: the favourable scale effect only persists up to about  $Re = 5 \times 10^6$  and there is then a tendency for  $C_{L,max}$  to decrease with further increase in Reynolds number. There is a strong hint in the results for aircraft P that, in some cases at least, the nacelle installation is responsible: adding strakes on the top and side of the nacelles gives an improvement at the higher Reynolds numbers and, therefore, succeeds in maintaining the favourable trend to at least near  $Re = 6.5 \times 10^6$ ,
- (vi) Fig 3.79(c) shows that, as would have been expected from the discussion in §3.2, the scale effect on  $C_{L,max}$  varies with the setting of the high-lift devices. It is only a limited set of data but it suggests, again as might have been expected, that it would be difficult to devise any general rules. A simplistic approach would have predicted that the favourable scale effect should increase at large flap angles on the grounds that acceptable flap angles would be limited at low Reynolds number by the effects of a flow separation on the flap but this is only observed in one case (aircraft J). In the other cases,  $\Delta C_{L,max}$  first increases and then decreases with  $\delta_F$ ,
- (vii) it is only for aircraft J that one would have the courage to say that the scale effect beyond the range of the model tests is likely to be trivial. In all other cases, the scale effect does not appear to be complete and for three of the later aircraft, M, N and P, extrapolation would appear to be particularly difficult: it is necessary to have a detailed knowledge of the flow breakdown at  $C_{L,max}$  before one can even answer the question "will the scale effect beyond  $Re = 6.5 \times 10^6$  be favourable, adverse or non-existent?"

#### 3.4.2.2 $C_{L,max}$ : flight-tunnel comparisons

We now come to what might be described as the "crunch figure": Fig 3.80(a) which presents the comparison for 9 different aircraft of the  $C_{L,max}$  values as derived from flight tests and as measured in model tests at the highest possible test Reynolds number of about  $Re = 6.5 \times 10^6$ . To present the data, the decision was taken to plot the results against  $\delta_F$  not expecting necessarily to find a correlation against  $\delta_F$  but merely for the sake of clarifying the presentation. In the event, however, a message did emerge from the figure: there is a tendency for the scale effect to become less favourable with increase in  $\delta_F$ .

Perhaps the first point to note about Fig 3.80(a) is the relatively wide spread of the values of  $\Delta C_{L,max}$  on the graph, ranging from +0.23 to -0.13. Although there may be a family resemblance about some of the curves, the differences from one aircraft to another are sufficient to cast doubt on whether it is safe to assume that, having determined the value of the scale effect,  $\Delta C_{L,max}$  for one aircraft design that has already flown, the same value will apply to the next aircraft in the same family that is still to fly for the first time. It may be argued that there is no alternative to this practice but, at the very least, one should study the details of the flow breakdown on the models of the two aircraft in the tunnel. The assumption that  $\Delta C_{L,max}$  will be the same on the second aircraft design should not be made if there is a clear difference in how the two aircraft stall in the tunnel tests. Negative values of  $\Delta C_{L,max}$  ie lower values of  $C_{L,max}$  lower in flight than in the tunnel, tend to cause consternation when they appear and there are three such cases in Fig 3.80(a). It is noteworthy that there is no example of a negative  $\Delta C_{L,max}$  at  $\delta_F = 0$ , ie with flaps retracted. This may suggest that the negative values are examples of the negative scale effect discussed when considering multi-element aerofoils and a detailed study of some of the cases suggests that this is indeed part of the story. There are examples where, in the model tests, the flow over the flaps is separated at moderate incidences but the becomes attached as one approaches the stall. In other words, to use the language of §3.2, in the model tests, the flaps are operating in area B and to recall what was said on pages 56, 76, there is then a strong likelihood that at higher Reynolds numbers, there will be some adverse scale effect which could be substantial.

It will be seen later however that local flow separations triggered by detailed features in the 3D aircraft geometry can also be very important. Stall-onset does not necessarily occur near the station on the span where the section lift coefficient reaches its maximum but in one of three problem areas - near the body-side, near the position of the nacelle installation or possibly near the wing-tip. The overall scale effect can depend on the relative scale effect in these three problem areas. It is found that the scale effect on the flow in these areas is often different and, as a result, changes in Reynolds number may lead to a change in the position along the span at which the stall is initiated and hence, a change in the subsequent development of the stall. With hindsight, one can often offer an explanation for the scale effect in any particular case but this does not necessarily enable one to predict the scale effect in the next case even if it is an aircraft in the same family. Experience has shown that the scale effect can depend on small details of the geometry in the problem areas: details that without this experience might have been judged to be unimportant.

An obvious question that the reader might ask is whether there is any link between Figs 3.79 and 3.80, eg does a rapid

increase in  $C_{l,max}$  with  $Re$  in Fig 3.79 infer that there will be a further increase at higher Reynolds numbers in Fig 3.80? Similarly, is a break in the curve nearer  $Re = 5 \times 10^6$  in Fig 3.79(b) just the beginning of a trend that gathers momentum to produce a negative  $\Delta C_{l,max}$  between tunnel and flight in Fig 3.80? These questions cannot be answered from the results as plotted in Figs 3.79 and 3.80(a) but Fig 3.80(b) is a tentative attempt to produce a complete picture of the scale effect for one of the aircraft that provided the information for Figs 3.79 and 3.80(a). It may or may not be typical but the available data suggests that there is a "hiccup" in the upper range of the model tests (ie  $Re$  between  $5 \times 10^6$  to  $6.5 \times 10^6$ ) in the generally favourable scale effect. The "hiccup" cannot be plotted with any precision: it could be more abrupt than shown and either greater or smaller in actual magnitude but certainly, in this case, one can say that this reduction in  $C_{l,max}$  is not the start of an unfavourable trend that continues up to flight Reynolds numbers. A similar result is shown in Fig 3.80(c) which is taken<sup>178,179</sup> from the open literature. This figure contains results for the Boeing 737-300 as obtained from model tests in the University of Washington 8 ft x 12 ft and NASA Ames 12 ft tunnels and the NASA Langley Transonic Dynamic Tunnel (TDT) operating with either air or Freon 12 compared with the flight value of  $C_{l,max}$ . To quote from Ref 178, "a simple straight line extrapolation on a semi-logarithm graph from UWAL Reynolds number test conditions to flight simply is not possible". It will be seen that the sparse data in this case suggest that the favourable scale effect is interrupted by a decrease between  $Re = 3 \times 10^6$  and  $5 \times 10^6$  which, to judge from the data discussed in §3.3.4.2, could imply a forward movement of transition due to spanwise contamination of the attachment-line boundary layer. The graph is a further reminder of the need to include a fair number of test Reynolds numbers in order to define the curve of  $C_{l,max}$  versus  $Re$  with some precision. This is needed to help in the interpretation particularly of cases exhibiting adverse scale effect. The "hiccups" in the two examples in Figs 3.80(b,c) could possibly be explained in terms of a forward movement of transition due to transition at Reynolds numbers above the "hiccup" being induced by ALT in the manner described earlier in §3.3.3.4. The picture would obviously be clearer if data could have been obtained immediately beyond the  $Re$ -range of the model tests but a more practical suggestion is to appeal for detailed flow visualisation tests always to be made to establish the reasons for the scale effect: flow visualisation in the tunnel where  $C_{l,max}$  is decreasing with  $Re$  - to aid intelligent prediction - and in flight to understand the reasons for the further scale effect - to gain experience to aid prediction. These are not unrealistic suggestions: recently, much has been learnt from detailed tuft studies in flight attached by Crowder's cones on the wing and flap surfaces of an aircraft in the Airbus family.

Mack and McMasters in Ref 178 sum up Boeing's experience in the past 40 years as shown in Fig 3.80(d). The results from many different sources that have been collected to produce Figs 3.79 and 3.80(a) would lead to very similar conclusions. Some possible reasons for the present uncertainty will be listed in §3.4.5 after the detailed discussion of some of the results.

### 3.4.2.3 Post-stall pitching moments

As noted earlier, scale effect on  $C_{l,max}$  is not the only matter that can cause concern<sup>180</sup>. In practice, scale effect on the post-stall pitching moments can be equally important - in one case in the 1960s, ignorance on this point caused a fatal accident of a new civil transport. Scale effect on the pitching moments is likely to be particularly noticeable in the Reynolds-number range in which a bubble-type separation is progressively changing to a trailing-edge separation, ie between  $Re_c = 1 \times 10^6$  and  $Re_c =$

$6 \times 10^6$  for the civil transport aircraft types under consideration. The spanwise variation in  $Re_c$  at which this change takes place (due to the wing taper) is a major reason for this scale effect: at a Reynolds number in the middle of the range in which this change is occurring, the flow breakdown at the stall could be very different to what is observed at either lower or higher Reynolds numbers.

Some striking examples of the scale effect on the post-stall pitching moments are presented in Figs 3.81(a,b,c). In the first figure, Fig 3.81(a), curves showing the variation of pitching moment coefficient,  $C_{PM}$ , about the aft CG with  $\alpha$  through and beyond the stall are shown for a range of Reynolds numbers from  $Re = 1.8 \times 10^6$  to  $Re = 8.0 \times 10^6$  for three different configurations. Stalling angles of attack are marked on each curve. At low flap angle with sealed slats, the shape of the pitching moment curve is relatively unchanged except for the change caused by the increase in stalling angle with Reynolds number. For large flap angles, however, the change can be rather dramatic in the sense of the post-stall pitch up reducing with increasing Reynolds number. Therefore, to select a high lift configuration that has acceptable post-stall pitch characteristics in flight, high Reynolds number testing and a clear understanding of the physics of the stall are required.

Figs 3.81(b,c) are two further cases included to illustrate the unpredictable nature of the changes in pitching moment with Reynolds number. Fig 3.81(b) shows the effect of a change made to the leading-edge flap to improve the pitching moment characteristics at low Reynolds number but when tests were made at higher Reynolds number, these showed that the change was unnecessary. On the other hand, Fig 3.81(c) shows that two configurations which gave similar characteristics at low Reynolds number, produced very different results at high Reynolds number. Clearly, without an understanding of the flow physics at the stall, the risk of encountering unacceptable stall characteristics in the flight tests can be substantial. The aim<sup>180</sup> must be to obtain an unambiguous pitch-down; to rely on a favourable scale effect to produce this as in Fig 3.81(a) would be highly risky as shown by Fig 3.81(c).

## 3.4.3 Examples of scale effect for specific aircraft

### 3.4.3.1 UK aircraft 1945-1965

The first set of results<sup>139</sup> in Fig 3.82(a) were obtained in 1948 in the RAE 10 ft x 7 ft tunnel at Farnborough on a model of the Short 14/46 bomber.  $C_l - \alpha$  curves are presented for the wing-fuselage, flaps retracted, with and without nacelles. There may be some surprise that it was thought appropriate to include in this Agardograph, data from so long ago for a configuration that may now be somewhat forgotten; however, the results do provide some evidence on issues that are still relevant today.

The aircraft had a symmetrical wing with an aspect ratio of 6.12, a taper ratio of 0.28 and  $17^\circ$  leading-edge sweep. The nacelles each contained two engines mounted symmetrically around the wing, one above the other, at about 0.37 semi-span. There were fillets in the wing leading-edge-nacelle junctions. The main conclusions from Fig 3.82(a) supported by flow visualisation by tufts are

- (i) at  $Re_c = 1.1 \times 10^6$ , the stall is of the long-bubble type,
- (ii) an increase in Reynolds number to  $Re_c = 2.5 \times 10^6$  is sufficient to change the type of stall over most of the wing to either the bursting of a short bubble or a turbulent separation. On the outer wing, however, the long-bubble persists up to at least  $Re_c = 3 \times 10^6$ ,

- (iii) the nacelles have no effect on  $C_{L,max}$  at  $Re_c = 1.1 \times 10^6$  because irrespective of whether they are present or not the stall is initiated near the leading edge but at higher Reynolds numbers they have a major adverse effect because they lead to a localised separation in the wing leading-edge-nacelle junctions in a region where the flow would be attached in the absence of the nacelles. This was still present in flight and the fillets had to be redesigned.

This is therefore the first example of where results at  $Re < 2.5 \times 10^6$  are completely misleading and where, because of the wing taper,  $Re_c = 3.8 \times 10^6$  is not sufficient and  $Re = 5.6 \times 10^6$  would be preferable (note - no high lift devices extended in this case).

The next example is the Comet 1. Results<sup>139</sup> are shown in Fig 3.82(b); they were again obtained in the RAE 10 ft x 7 ft tunnel at Farnborough and are included here to illustrate that Reynolds numbers of at least  $Re_c = 3.5 \times 10^6$  are needed to give a realistic comparison between the two outer wing sections. The sections differed in leading-edge radius: very sharp ( $\rho = 0.0060c$ ) for the original section and greatly increased ( $\rho = 0.0141c$ ) for the modified section. Even at  $Re_c = 3.55 \times 10^6$  there must be some doubt as to whether the scale effect with the original section is complete or whether, at some higher Reynolds number, the change in type of stall that has already occurred with the modified section between  $Re_c = 1 \times 10^6$  and  $Re_c = 2 \times 10^6$  would be observed with the original section. However, the modified section at  $Re_c = 4 \times 10^6$  gave results in good agreement with flight.

Next, the Trident; with hindsight, one can say that the development of the Trident marks the moment in the UK when it began to be realised that Reynolds numbers of at least  $4 \times 10^6$  and preferably  $Re = 6 \times 10^6$  were needed not merely for research but for actual development tests for all new transport aircraft. Work on the Trident began quite logically with trying to build on past experience. The aim in the initial tests in the atmospheric low speed tunnel at Hatfield was to produce a stall development on the model that was at least similar to or if possible better than that achieved on a model of the Comet at comparable Reynolds numbers and to achieve a value of  $C_{L,max}$  that would extrapolate on the best possible estimates to give the required full-scale value. From previous experience on the Comet, it was expected that the main difficulty would lie in the fact that in the atmospheric tunnel, one would either have to accept an outer wing stall that would not be there in flight or would have to modify the model outer wing geometry to prevent this stall. In the event, however, this problem was not met in this case and the only doubts before the first flight tests were stirred by the fact that a model tested in the CAT at NPL at Reynolds numbers up to  $7 \times 10^6$  had suggested that  $C_{L,max}$  would decrease markedly between  $Re = 4 \times 10^6$  and  $Re = 7 \times 10^6$ . There was uncertainty as to whether to accept this evidence because of the relatively high turbulence level in the CAT at maximum pressure but the first flight tests confirmed that the hopes raised by the early low Reynolds number tunnel tests were not being realised: the aircraft had a progressive tip stall and also, the value of  $C_{L,max}$  was significantly lower than expected. This led to an extensive flight development programme with a great deal of complementary testing in the atmospheric low speed tunnel. Many modifications were investigated such as changing the angle of the drooped leading edge, adding vortex generators on the droop knuckle plate, fairing the discontinuity at the inner end of the droop with a Kruger flap and incorporating two spoilers and a fence at appropriate positions on the span.

All this activity was aimed not merely at obtaining the required value of usable  $C_{L,max}$  but also of obtaining a stall reasonably free of buffet, an adequate nose-down pitch and the right degree of lift break at  $C_{L,max}$ ; the same objectives would apply today. All the tunnel tests had to be made with the wrong wing geometry which was regularly modified to give the same flow development as on the full-scale aircraft in the flight tests. In retrospect, these tunnel tests at a completely inadequate Reynolds number were judged to have been useful in suggesting which modifications to try on the aircraft but only because they were proceeding in parallel with the flight tests. Even then, the conclusions from flight and tunnel did not always agree, eg vortex generators on the droop knuckle plate were beneficial in flight but not in the tunnel at  $Re_c = 1 \times 10^6$ .

Eventually, tests were made with a highly representative model in the RAE 8 ft x 8 ft tunnel at Bedford at Reynolds numbers from  $Re_c = 1.1 \times 10^6$  to  $Re_c = 4.3 \times 10^6$  at  $M = 0.2$ . These confirmed the above conclusion about the effect of the vortex generators: no effect on  $C_{L,max}$  at  $Re = 1.1 \times 10^6$  but an improvement of about 0.10 at  $Re = 4.3 \times 10^6$  thus implying a change in the nature of the stall in this Reynolds-number range. Results from the tunnel tests on the model with vortex generators present are shown plotted in Figs 3.83(a,b). As with the two previous examples, the increase in Reynolds number leads to the stall becoming more abrupt to judge from the  $C_L - \alpha$  curves but the more significant changes are in the pitching moment characteristics. The nose-up trend evident at the stall at  $Re_c = 1.1 \times 10^6$  is replaced by an appreciable nose-down break at  $Re_c = 3.3 \times 10^6$  and above in agreement with what had been deduced from the flight tests.

To show that this experience with the Trident was not an isolated example, Fig 3.83(c) presents the pitching moment data from tests in the RAE 8 ft x 8 ft tunnel on a model of another civil transport design. A decisive pitch-down is evident at  $Re_c = 3.6 \times 10^6$  but not at  $Re_c = 1.4 \times 10^6$  and  $2.7 \times 10^6$ . One should not be misled by this figure into thinking that testing at  $Re_c = 0.9 \times 10^6$  would have been acceptable: while the results at the lowest test Reynolds number coincidentally gave a pitch-down trend similar to that at the highest Reynolds number, the nature of the stall is completely different: this leads, for example, to a premature pitch-up trend at about  $\alpha = 8^\circ$  (compared with  $\alpha = 16^\circ$  for the pitch-down at the higher  $Re$ ).

To sum up these early examples, they have all shown a changeover from bubble-dominated scale effect to conventional scale effect in the range  $1 \times 10^6$  to  $4 \times 10^6$  and they have all shown the dangers of testing in the middle of this range and the desirability of being able to test at say,  $Re = 6 \times 10^6$  to be safe. It was this reasoning that led to the building of the 5 metre tunnel at Farnborough (and the F1 tunnel at Le Fauga).

### 3.4.3.2 Boeing 747

The Boeing 747 is one of the best documented examples of a flight-tunnel comparison on the low speed stall thanks to a paper<sup>176</sup> given by McIntosh and Wimpres presented at an AGARD Symposium in 1974. It is also the most innocuous example as regards scale effect in all the aircraft assembled in Figs 3.77 and 3.78 being aircraft J in Fig 3.77 and aircraft 8 in Fig 3.78. The scale effect on  $C_{L,max}$  is small and favourable in the entire Reynolds-number range: it only amounts to 0.10 or less between  $Re = 1 \times 10^6$  (based on wing mean aerodynamic chord) and flight. Ref 176 offers an explanation for this non-typical behaviour. To quote from Ref 176, "... it was recognised that the 747 had a leading-edge device that might render past wind-tunnel-to-flight-test correlations inaccurate.

Past Boeing airplanes had a leading-edge device, either a Krueger flap or slat, that was relatively sharp, creating high suction peaks and rapid pressure recoveries which would make the flow sensitive to Reynolds number effects. The 747, on the other hand, had a leading-edge device that was carefully designed using aerodynamic theory to produce a smooth pressure distribution having no severe gradients at high angles of attack. With the gradient selected to give no separations at low Reynolds number, no appreciable increase in lift should be expected as Reynolds number is increased."

Results for the 747, abstracted from Ref 176 are plotted in Figs 3.84(a,b). The tunnel data were obtained in model tests in the NASA Ames 12 ft pressure tunnel where the Reynolds number could be varied from about  $Re = 1.2 \times 10^6$  to  $7.5 \times 10^6$ . Ref 176 comments that the  $C_{L,max}$  data in Fig 3.84(a) shows enough linearity when plotted on a semi-logarithmic basis to allow extrapolation to the full scale Reynolds number of  $30$  to  $40 \times 10^6$  and the agreement of the extrapolated value with the flight test data is within 2%.

The pitching moment data in Fig 3.84(b) were also considered to show satisfactory agreement. Again to quote from Ref 176, "a small pitch-up in the stall is permissible and tends to hold the airplane to a slightly lower speed before it pitches down out of the stall. This permissible pitch-up must cause only a limited excursion in angle-of-attack, say 4 to 6 degrees, involve essentially no increase in  $C_L$  once the pitch-up begins, and must be followed by strong pitch-down to ensure a good clean break away from the stall ... There is practically no change in wind tunnel pitching moment data with Reynolds number probably as a result of the cambered leading-edge flap. The flight data show slightly superior stability at stall entry than the wind tunnel data indicate. They also show that the wind tunnel predicted quite accurately the flight values for the incipient pitch-up and the angle of recovery."

To reiterate: this example which appears to be so straightforward is not typical of the present scene: one should remember Fig 3.80(c)!

### 3.4.3.3 The Fokker family

Reynolds-number effects figure prominently in Obert's account<sup>101</sup> of 40 years' experience in High Lift R&D at the Fokker Company. Much of the data comes from the 2D tests at NLR that were discussed in §3.2.2 but development tests for different marks of the F-28 and for the F-29 also provide some useful evidence.

The F-28 Mk 1000, the original version of the F-28, was not fitted with any leading-edge high-lift device; reliance was placed on the wing section design which had a large leading-edge radius and the use of a double-slotted flap with movable vane. The model tests showed that at low Reynolds number, there was a premature tip stall while at  $Re = 5 \times 10^6$ , a sudden flow separation occurred over the whole wing at the stall. Some stall control device was therefore needed to initiate the stall on the inner wing and the development tests in tunnel and flight were aimed at finding such a device and one that would not degrade the  $C_{L,max}$  too severely. Ultimately, the configuration was frozen with a single short leading-edge stall fence combined with a stall strip just inboard of the fence. Fig 3.84(a) shows that, like the results for the Boeing 747, the variation of  $C_{L,max}$  from the model tests when plotted against  $Re_c$  on a semi-logarithmic basis can be extrapolated reasonably to agree with the flight results for both flaps retracted and extended cases. This is somewhat coincidental because, as also shown by Fig 3.84(c),

the effect of the stall fence is also dependent on  $Re$ . Also, there is the normal uncertainty about the actual shape of the curve between model and flight Reynolds numbers.

Later, higher values of  $C_{L,max}$  were required on the F-28 Mk 6000 and the decision was taken to introduce a leading-edge slat. Ref 101 gives a detailed account of the extensive model test programme that preceded the selection of slat geometry for the aircraft. During this model test programme, large favourable Reynolds number effects on drag were observed particularly between  $Re = 2.8 \times 10^6$  and  $5.0 \times 10^6$ . When the prototype aircraft first flew, the designers were surprised by the performance: the values of  $C_{L,max}$  were much higher than predicted and were in fact higher than thought to be useful. The scale effect on  $C_{L,max}$  is shown in Fig 3.84(d). This picture can be regarded as being at the opposite extreme from the Boeing 747: far from being trivial, the scale effect is very large, varying from 0.52 in  $C_L$  with flaps retracted to 0.27 with flaps deflected  $42^\circ$ . (The fact that the slat angle is slightly lower in flight than in the tunnel can be ignored). Obert drew the following conclusions from the development of the F-38 Mk 6000:

- (i) small details on the high-lift devices have to be reproduced accurately in model tests,
- (ii) significant three-dimensional effects can occur in the flow around slats on swept wings, particularly as concerns drag,
- (iii) tailoring stalling characteristics of an aircraft equipped with slats in combination with a T-tail requires great care. Again, wind tunnel tests at high Reynolds numbers are seen to be mandatory,
- (iv) significant Reynolds-number effects may still occur above  $Re_c = 5 \times 10^6$ .

The present author would support all these conclusions; they could have also been drawn from experience on other aircraft. In (iii), there is no need to include the reference to T-tails. Perhaps one comment should be added:  $Re_c$  of  $5 \times 10^6$  is equivalent to only  $Re = 2.5 \times 10^6$  on the tip chord and so, the presence of significant scale effects to higher Reynolds numbers may not be too surprising and it is quite possible that if model tests had been made at  $Re_c = 6.5 \times 10^6$ , the flight-tunnel comparison for this aircraft would not have looked out of place on Fig 3.80.

In the later development of the Fokker family, there was a shift to advanced transonic wing sections and ultimately, less blunt leading edges. It was found that Reynolds number affected not only the overall characteristics but the optimisation of the detailed geometry. Fig 3.84(e) shows two examples of Reynolds-number effects taken from a much larger amount of data in Ref 101 from the further studies in aid of the F-29. Without the slat, the scale effect above  $Re_c = 1.6 \times 10^6$  is again large and favourable but, as can be seen in the right-hand figure, this is not true with the slat deflected when typically, the improvement in  $C_{L,max}$  is only 0.05 or less. This is an example of where the positioning of the high-lift device, ie the slat, had been optimised at a very low Reynolds number ( $1 \times 10^6$ ) but where a smaller gap was needed to maintain good performance at higher Reynolds numbers. Obert comments however that the results suggest that for sections with relatively thick leading-edges and on wings with a moderate sweep angle, these high-lift devices are not very effective - a comment that would probably not have been made if the only data available had been those obtained at  $Re = 1 \times 10^6$ .

### 3.4.3.4 The Airbus family

The results<sup>63</sup> of model tests on the A300B have already been used as an example of conventional scale effect: they were discussed in §3.3.3.1 and shown in Fig 3.52. They indicated significant favourable scale effect between  $Re_c = 2.5 \times 10^6$  and  $5 \times 10^6$  and this continued but at a reduced rate up to  $Re = 7 \times 10^6$ . No change in the nature of the stall was detected in this range and pressure plotting data indicated that the scale effect came mostly from the outer wing.

Moving on to the A310, Ref 177 presents the results of a flight-tunnel comparison of the high-lift performance of the A310. The lift curves are compared in Fig 3.85(a). The model test data were obtained in the F1 tunnel at  $Re_c = 8 \times 10^6$  and they are compared with flight test data obtained in the second segment climb up to  $1.2 V_{S_{min}}$ , one engine having failed and the other at full power and in stall tests down to  $V_{S_{min}}$  with 2 engines. The model test data are plotted as obtained with a rigid model and then corrected for the different twist under these conditions of the flexible aircraft. The agreement is remarkable except that  $C_{L_{max}}$  for the landing configuration is about 0.05 higher in flight than derived from the tunnel tests. Fig 3.85(b) presents the complementary picture for the drag polar. Corrections have been applied for

- (i) the estimated drag of any items on the aircraft but not represented on the model,
- (ii) the predicted change in skin friction drag between tunnel and flight,
- (iii) the effect on drag of the need to trim out the effect of flying with a single engine,
- (iv) the excess spillage drag with the failed engine.

Again, good agreement is shown.

Further evidence on Reynolds-number effects on the A310 was obtained in the GARTEur exercise as described by Thibert in Ref 111. The variation of the overall  $C_{L_{max}}$  with  $Re$  from model tests at  $M = 0.25$  in the 5 m and F1 tunnels for both take-off and landing configurations with and without nacelles is shown plotted in Fig 3.86(a). Section data for the station at 59% semi-span are plotted in Fig 3.86(b). The overall  $C_{L_{max}}$  increases with  $Re$  up to almost  $Re_c \approx 7 \times 10^6$ . Thibert comments that the trends in the section data are in broad agreement with what was found in 2D tests (and shown in Fig 3.43(a-d)). The general impression is for an increase in  $C_l$  at a given incidence up to  $Re = 7 \times 10^6$  followed by a slight decrease at higher Reynolds numbers. Figs 3.86(c,d) compare the model test results at the highest Reynolds number with those obtained from flight tests. Contrary to what was shown in the earlier flight-tunnel comparisons for the A310, this comparison shows that  $C_l$  for the aircraft in flight is slightly less than in the tunnel test. A similar difference near maximum lift can be seen in the sectional data for the 0.59 station in Fig 3.86(d) in the case of the landing configuration and Thibert notes that this is due to the flap that carries more lift in the wind tunnel than in flight; he suggests that it could be due to small differences in slot geometry. Further analysis is needed; it may be relevant that the Mach number for these GARTEur comparisons was 0.25 whereas it was 0.2 for most of the other comparisons for Airbus aircraft. However, the differences are relatively small.

There are two papers in the open literature describing the development of the high lift systems for later aircraft in the Airbus family. Flaig and Hilbig in Ref 181 give a broad review of how the design of the high-lift devices for these aircraft has been tackled and Fig 3.87(a) abstracted from Ref 181 shows the

arrangement of the high-lift devices on various aircraft in the family. It will be noted that all the aircraft are fitted with slats and either single- or double-slotted flaps but there are a lot of detailed differences both at the body-side and in the vicinity of the nacelle installations. Ref 181 lays particular stress on the need to optimise the design to minimise the three-dimensional interference effects in these areas and near the wing tip - the regions highlighted in Fig 3.87(b). A close examination of the data for these aircraft has indeed shown that not only the absolute results but also the magnitude and even the sign of the scale effects can depend significantly on detailed three-dimensional features in these areas. As noted in Ref 181, to avoid serious detrimental effects, one has to introduce vortex-generating devices such as strakes on the engine nacelles. It is found that the effects of these palliatives also vary with Reynolds number. The influence of the nacelle installation has been found to be particularly important. This is not surprising: merely to look at the geometry in Fig 3.87(a) highlights why this should be so: the nacelles are becoming larger relative to the wing and in position, they are becoming more close-coupled. The slat which on the A310 could be continuous across the span has had to be broken to admit the nacelle pylon on later aircraft. It has been found that even quite minor changes to the nacelle shape and orientation can influence the scale effect on the high-lift performance.

This emphasis on the three-dimensional problems does not mean that one can forget all the preceding discussion on slot-flow and transition-dominated scale effect. Wedderspoon in Ref 182 includes some evidence reproduced here in Fig 3.87(c,d) showing that the optimisation of the slat positions for the A320 varies significantly with Reynolds number between  $Re = 1.4 \times 10^6$  and  $Re = 3.5 \times 10^6$ . The  $C_{L_{max}}$  contours are similar in character but suggest a higher position for the slat to suit the higher Reynolds number. The drag contours for the two Reynolds numbers are very different, the contours for the higher Reynolds number suggesting that there is a true optimum position (different from what is required for the best  $C_{L_{max}}$ ).

To sum up, the evidence from the later aircraft in the Airbus family is more complex than that described for the original A300 and for the A310. The scale effect can be larger and not necessarily favourable. Even the high Reynolds-number performance depends more than in the past on detailed features of the 3D geometry.

### 3.4.4 3D problem areas

The main problem areas were identified on Fig 3.87(b). As noted earlier, the stall can start in these areas rather than near the station for the maximum local  $C_l$ . On a transport aircraft with a single pair of underwing nacelles, the inner wing panel between the fuselage-side and the nacelle is often the critical area; on a 4-engined aircraft, it can be the central panel between the two nacelles. With the high-lift devices extended, flow separation may occur first either at the body-side trailing edge then spreading forward with increase in angle-of-attack or alternatively near the pylon-wing leading-edge junction then spreading rearward and inboard. These two areas of separated flow can interact with each other and the stall development can depend in a subtle manner on which separation occurs first and which is the dominant partner. Prediction of the overall scale effect is not a straightforward task because the scale effect in the two regions is not necessarily the same and hence, the nature of the stall development can change with Reynolds number. For a 4-engined aircraft, one also has to consider what happens in the region of the outer nacelle. The discussion

below concentrates on the effects of the nacelle installations and on the fact that on many aircraft, the leading-edge device has to have a cut-out to admit the nacelle pylon and also does not extend to the side of the fuselage. There is no discussion of problems near the wing tip.

Figs 3.88 and 3.89 contain some illustrations of the 3D interference effects on the inner wing and of how they can be alleviated. It should be noted that although Fig 3.87(b) was a picture of the A320, these examples in Figs 3.88 and 3.89 do not necessarily refer to the A320. They are taken from the results for several different aircraft and the general aims are to give an idea of the likely magnitude of the various effects that can be observed and to indicate whether they are likely to be subject to scale effect and, if so, in which direction. It is a complex story; the source of the problems may often be detailed features of the geometry near the wing leading-edge but the consequences may depend on the setting and design of the high-lift devices both at the leading-edge and at the trailing-edge.

First, let us consider the basic effects of an underwing nacelle installation necessitating a cut-out in a leading-edge slat. Figs 3.88(a,b) present two examples of what happens relative to the ideal situation with no cut-out. Fig 3.88(a) is taken from Obert's account<sup>101</sup> of the development of the F-29; it shows the effect of the slat cut-out on the stall development and maximum lift as observed in model tests at  $Re_z = 5 \times 10^6$ . Obert comments that provided great attention is paid to details of the pylon-slat-leading edge intersection, the loss in lift can be made negligible. Actually, the reduction in  $C_{L,max}$  in this particular case is about 0.15 and, arguably, this should not be classed as "negligible". However, the next example for a different aircraft is perhaps more encouraging in supporting Obert's contention. These results are shown in Fig 3.88(b).  $C_L - \alpha$  curves are compared: these relate to the ideal wing-alone situation with no slat cut-out and no nacelle, the real situation with a cut-out but still with no nacelle and finally, the real situation with cut-out and two alternative nacelles. The effects on  $C_L$  at high incidence and on  $C_{L,max}$  are surprisingly large. The introduction of the cut-out without mounting the nacelle reduces  $C_{L,max}$  by 0.38 but most of this loss is regained when the pylon and nacelle are fitted. The ultimate difference relative to the ideal situation is a loss of merely 0.04 or 0.06 in  $C_{L,max}$  for the two nacelle installations being considered.

These results are explained qualitatively by the sketches in Figs 3.88(c,d). These indicate that the lift-induced vortex shed at the inboard side of the nacelle affects the flow at the pylon-wing junction by adding downwash and upwash components to the flow. In many cases, the downwash component applied to the cut-out region depresses the stall in that area while the upwash component is added in an unstressed area and therefore causes no stall problems. To further strengthen the favourable downwash flow component, Douglas introduced the idea of mounting a pair of strakes on the forward top of the nacelle as an additional means of relieving the local angle of attack in the cut-out region and thus improving the boundary layer behaviour in this region. The strake effects are discussed later. It should be noted that the nacelle effects would not be obtained from a solid body mounted in place of the nacelle. This is shown by the comparative results in Fig 3.88(e). In this case, blocking off the intake completely has an adverse effect on the lift-curve slope from about  $10^\circ$  below the incidence for  $C_{L,max}$  and also, it reduces  $C_{L,max}$  by 0.17. Even just blocking the core duct and thus giving an intake mass-flow ratio of 0.41 compared with basic value of 0.7 leads to a reduction of 0.05 in  $C_{L,max}$ .

Experience has shown that when there is a cut-out in the slat or leading-edge to admit the pylon, the detailed geometry near this cut-out becomes most important not only in determining the  $C_{L,max}$  and the scale effect but also in obtaining results that are reasonably repeatable. Results of tests on different models in different tunnels sometimes do not agree at the same Reynolds number and the explanation is often thought to lie in the model representation of the detailed geometry.

If the results in, for example, Fig 3.88(b) were representative of all the available evidence, the reader might not be too excited but an example such as that presented in Figs 3.88(f,g) should be sufficient to ring some alarm bells. In this case, model tests were made with two alternative nacelle designs mounted at the same spanwise position on a civil transport wing and, with the high-lift devices set for landing,  $C_{L,max}$  was 0.17 lower with nacelle II than with nacelle I; clearly, this is a very large difference; it corresponds to a change of  $3^\circ$  in the incidence for  $C_{L,max}$ . It cannot be dismissed as an isolated freak result. A very similar result was obtained in the F1 tunnel at the higher Reynolds number of  $6.0 \times 10^6$  but then in flight, the comparison was completely different: nacelle II gave a slightly higher  $C_{L,max}$  than nacelle I. It cannot be said that these surprising results are fully understood. At first sight, the geometrical differences between the two nacelles would not have been expected to produce such a radical difference in the scale effect. Nacelle I is a double-body nacelle with a short duct cowl ending in the fore-and-aft vicinity of the slat leading edge while nacelle II is a single-body nacelle with a long duct cowl. There are other less obvious differences, eg with I, the pylon leading edge at its intersection with the nacelle is sharper and further forward and thus, closer to the plane of the intake which is itself further aft relative to the wing leading edge. One must also remember that the explanation is not necessarily related to the local flow near the nacelle station. For example, the reason why the change of nacelle has apparently less effect with the high-lift devices in the take-off position (see Fig 3.88(g)) is that, in this case, flow separation occurred first near the side of the fuselage rather than near the nacelle: hence, less sensitivity to the nacelle design might be expected. It is possible that, with the high-lift devices at the setting for landing, the increase of  $Re$  from  $6 \times 10^6$  to full-scale might be sufficient to move the start of the stall from the nacelle to the fuselage side. This suggestion is not entirely speculative: a study of other evidence from the tests with tufts indicates that the local scale effect is more likely to be favourable near the nacelle than at the side of the fuselage. Another possibility is that the relevant factor for the scale effect with the landing configuration is that, in the tunnel tests, the flow over the flaps at the stall is largely attached having been separated at lower incidences; this raises the possibility of a negative scale effect in the light of the earlier discussion in §3.2. All these points are included to give an idea of the complex nature of the flow and of the wide range of interacting factors that have to be considered in order to arrive at a realistic interpretation.

Fig 3.88(d) indicates that the critical region on the wing near the nacelles is on the inboard side of the nacelle. Douglas introduced the idea of mounting a strake on the forward, inboard top of the nacelle as a means of relieving the local angle of attack inboard of the nacelle and thus, improving the boundary layer behaviour on the wing upper surface in this region. The vortex flow induced by a strake is shown diagrammatically in Fig 3.89(a). It will be noted that the path of the strake-induced vortex at high incidence diverges laterally away from the nacelle towards the wing root and this leads to the need to introduce a second strake on the outboard side of the nacelle to control the flow immediately inboard of the

nacelle. This is illustrated in Fig 3.89(b): in this example, a single strake mounted on the inner side of a nacelle on the outer wing of a transport aircraft has succeeded in reducing the area of wing inboard of the nacelle where the flow has separated but has not eliminated the separation close to the nacelle; to achieve more in this region, a second strake on the outer side of the nacelle is needed. Fig 3.89(c) presents a set of tuft flow patterns with and without 2 strakes at two Reynolds numbers,  $Re = 1.5 \times 10^6$  and  $6 \times 10^6$ . It will be seen that:

- (i) the addition of the strakes in this case is effective in suppressing the separation inboard of the nacelle at the incidence corresponding to  $C_{Lmax}$ ,
- (ii) as a consequence, (these words are inserted deliberately), the separation near the body side develops earlier. This is just one example of a commonly observed interplay between these two separations,
- (iii) the local scale effect on the separation at the body-side is certainly not favourable and appears to be adverse. This again is an example of a result observed fairly generally - some favourable scale effect on separations near the nacelle but a tendency to adverse scale effect in the three-dimensional situation at the body side.

Fig 3.89(d) shows a set of results indicating that the gain in  $C_{Lmax}$  due to the addition of the strakes increases with Reynolds number from 0.02 at  $Re = 1.5 \times 10^6$  to about 0.10 at  $Re = 6.5 \times 10^6$  for the landing configuration. This should not be regarded as a general result; gains of 0.2 or more have been observed while in other cases, the strakes may be ineffective. One should emphasise that the ability of a strake to induce a vortex flow as in Fig 3.89(a) is likely to be sensibly independent of Reynolds number. The reason for the wide spread in values of  $\Delta C_{Lmax}$  due to the strakes and in its variation with  $Re$  lies in the nature of the wing flow that is influenced by the vortex and in whether  $C_{Lmax}$  is being determined by the flow in this region or not.

Another sensitive region is at the inner end of the slat leading edge and in the gap between here and the side of the fuselage. Various ideas for preventing a premature separation in this region have been investigated including a horn at the end of the slat as shown in Fig 3.90(a). This produces a vortex system as sketched in Fig 3.90(b). Results for one case where two sizes of horn were compared are presented in Fig 3.90(c). The tests with nacelle II (see Fig 3.88(f)) showed that changing from the small to the large horn improved  $C_{Lmax}$  by about 0.32 in the take-off configuration, 0.1 in the approach case and virtually no change with the landing configuration. This sequence is however somewhat misleading as an indication of what can be achieved with a large slat horn. The reason why the gain fades away with the landing configuration is that then, at this Reynolds number ( $2.6 \times 10^6$ ), with nacelle II, the region near the nacelle dictates the stall. As can be seen, the large horn still gives a gain in  $C_{Lmax}$  of 0.1 relative to the small horn with the landing configuration if one uses the results with the better (at model test  $Re$ ) nacelle I. To judge from the results being discussed earlier, it is quite possible that at flight Reynolds numbers, the improvements from using a large horn would be greater than those shown in Fig 3.90(c).

By the end of this discussion, the reader may begin to wonder whether the values of aircraft  $C_{Lmax}$  and the scale effect in  $C_{Lmax}$  have any relation to predictions based on multiple aerofoil or simple 3D wing research as described in §§3.2 and 3.3! This would clearly be going too far: all the lessons learnt from the research still apply but, on the other hand, precise values of  $C_{Lmax}$  and even the sign of the scale effect from tunnel to flight can be influenced appreciably by practical details of the full-

scale aircraft; in one case known to the author, "appreciably" implies 0.35 in  $C_{Lmax}$ . It is not possible to suggest simple rules for predicting the scale effect. As noted earlier,  $Re = 2.5 \times 10^6$  is not high enough and the examples quoted above suggest that  $Re = 6.5 \times 10^6$  with modern designs leaves room for appreciable uncertainty. Since at present, it is not possible to carry out complete model tests for aircraft development at Reynolds numbers higher than about  $Re = 6.5 \times 10^6$ , the best advice is to amass as much experience as possible in the interpretation of scale effect on existing aircraft and always to include flow visualisation in any tunnel or flight test programme. "Know your flow" has long been a maxim in tests at transonic speeds; the same maxim applies at high incidence and low speeds.

### 3.4.5 Summary of general conclusions

The general conclusions of this discussion on the scale effect on the low speed stalling characteristics with the main emphasis on transport aircraft with underwing nacelles are as follows:

- 1 up to  $Re = 2.5 \times 10^6$ , the scale effect on  $C_{Lmax}$  is generally strongly favourable and, as a result in most cases results obtained in atmospheric low speed tunnels at say,  $Re = 1.5 \times 10^6$  can be very misleading,
- 2 in the range of model tests between  $Re = 2.5 \times 10^6$  and  $Re = 6.5 \times 10^6$ , the scale effect on  $C_{Lmax}$  generally continues to be favourable although on several recent aircraft, there is a tendency for this not to persist above  $Re = 5 \times 10^6$ ,
- 3 the magnitude of the favourable scale effect on  $C_{Lmax}$  between  $Re = 2.5 \times 10^6$  and  $Re = 6.5 \times 10^6$  depends on the design of the wing and high-lift devices and for the aircraft considered, it varied from 0.04 to 0.17,
- 4 in 1965, it would have been correct to expect that the further scale effect on  $C_{Lmax}$  between model data at  $Re = 6.5 \times 10^6$  and full-scale in flight to be small and probably still favourable. Today, however, the position is very different and for the aircraft considered here, the changes in  $C_{Lmax}$  in this range vary between +0.23 and -0.13,
- 5 the risk of encountering adverse scale effect between model test and flight is greater when the high-lift devices are fully deflected for a landing configuration,
- 6 prediction of the  $C_{Lmax}$  in flight from the model test data in existing tunnels has therefore become more difficult. The scale effect is likely to be significant; it may be either favourable or adverse. Allowing for what has been seen in earlier paragraphs in the Agardograph, there are five possible reasons for a negative scale effect on  $C_{Lmax}$ :
  - (i) contamination along the attachment line (ALT),
  - (ii) a failure to relaminarise after ALT,
  - (iii) increased suction and adverse pressure gradients and hence greater possibility of separation on the trailing-edge flaps,
  - (iv) adverse scale effect (or at least the absence of any favourable scale effect in regions where the separation is due to complex 3D interference effects,

- 7 underwing nacelle installations especially when they imply a cut-out in the leading-edge high-lift device can create problems which modify the scale effect; they can be relieved by the addition of vortex-generating strakes on the nacelles but the effects of the strakes also depend on Reynolds number (because of changes in the flow to be influenced by the vortex flow). Similar remarks could be made about devices introduced to energise the flow near the side of the fuselage,
- 8 equally important and perhaps even less predictable are the scale effects on the post-stall pitching moments. One should be particularly wary about accepting the evidence of results in the range at the lower Reynolds numbers where  $C_{L,max}$  is increasing rapidly with  $Re$ . Because of the wing taper, the Reynolds number for these changes is higher for sections near the tip than further inboard and, as a result, the pitching moment behaviour in this range may be completely unrepresentative of what happens at either lower or higher Reynolds numbers,
- 9 successful interpretation in retrospect of the scale effect in any particular does not necessarily mean that one is well placed to predict quantitatively the scale effect for the next aircraft design that has not yet flown. One must undertake model tests at the highest possible test Reynolds number and study in detail the flow breakdown at the stall. Flow visualisation tests should be included whenever possible in both tunnel and flight. Even when one has obtained an apparently satisfactory design, one should study its sensitivity to small changes in geometry and operating condition. In this way, one can obtain a better understanding of the physics of the flow and only then will one begin to have confidence in predictions of scale effect.



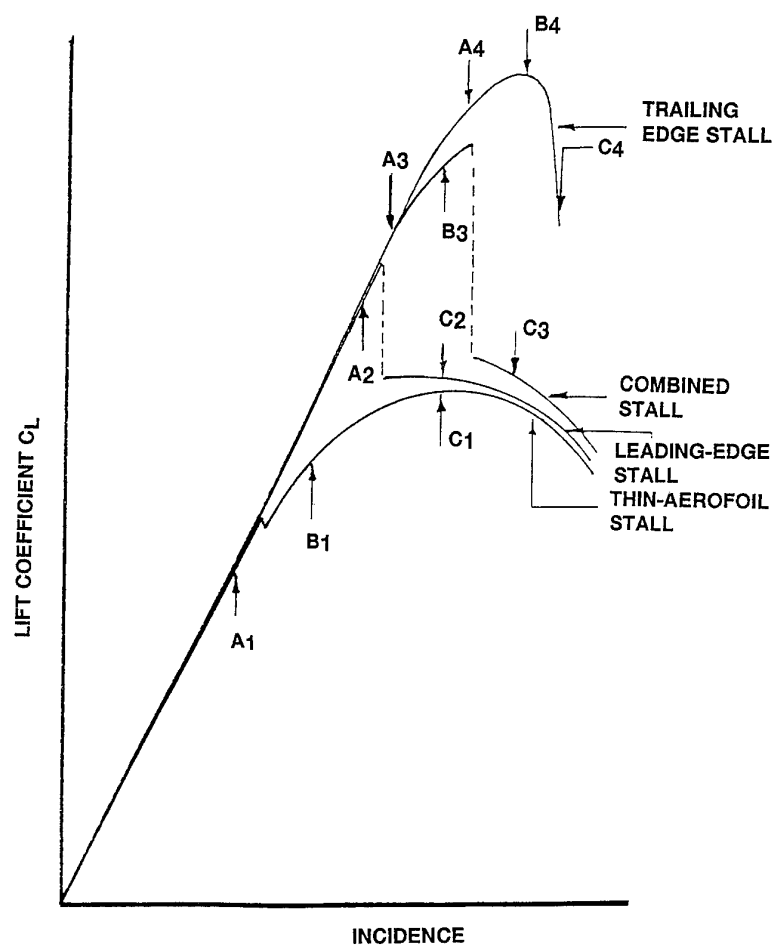


**FIG 3.1** Typical  $C_L \sim \alpha$  Plots for Four Different Aerofoil Stall Patterns  
(from ref 63)

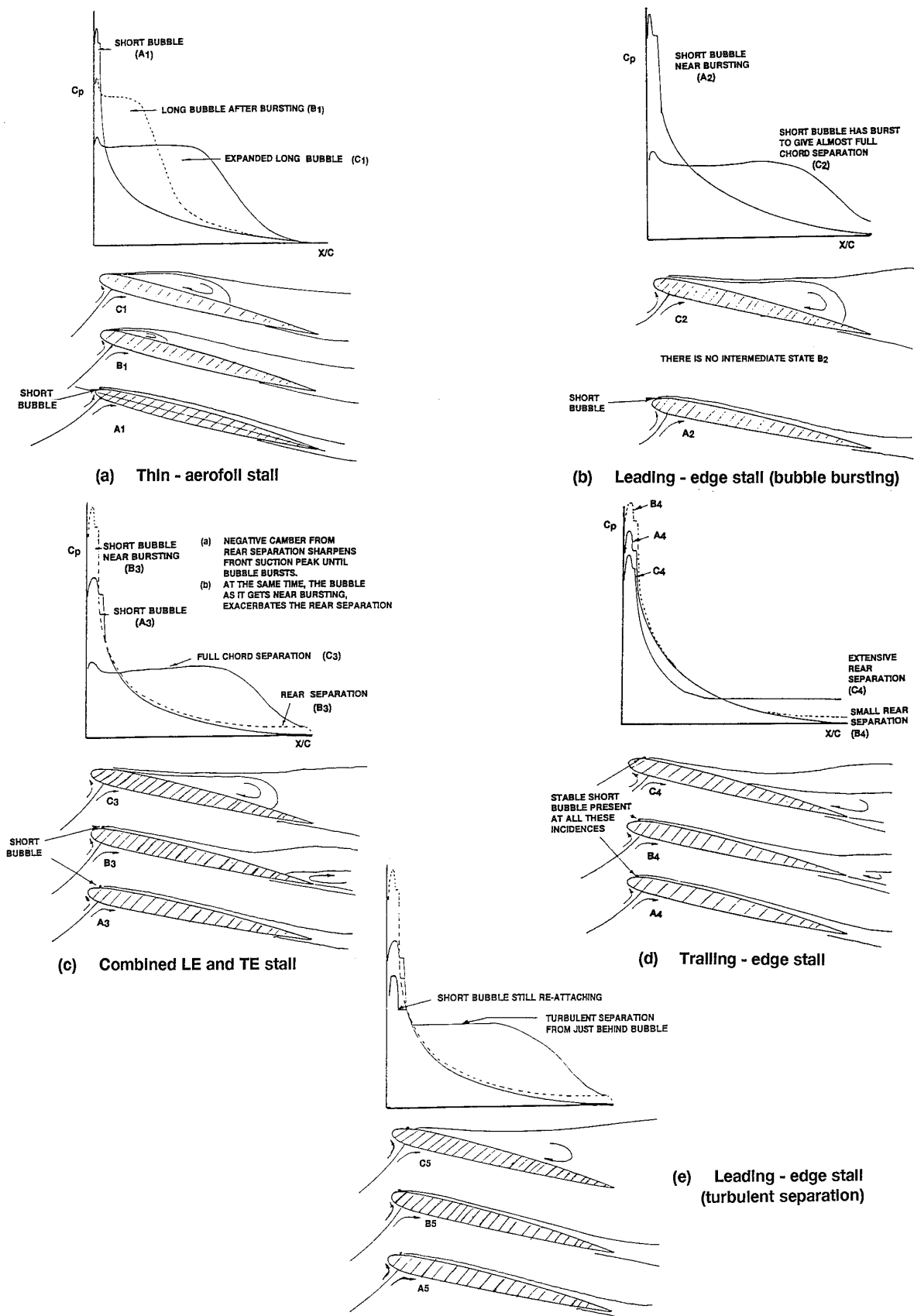


**FIG 3.2 Pressure Distribution and Boundary Layer States for Different Types of Stall**  
(from ref 63)

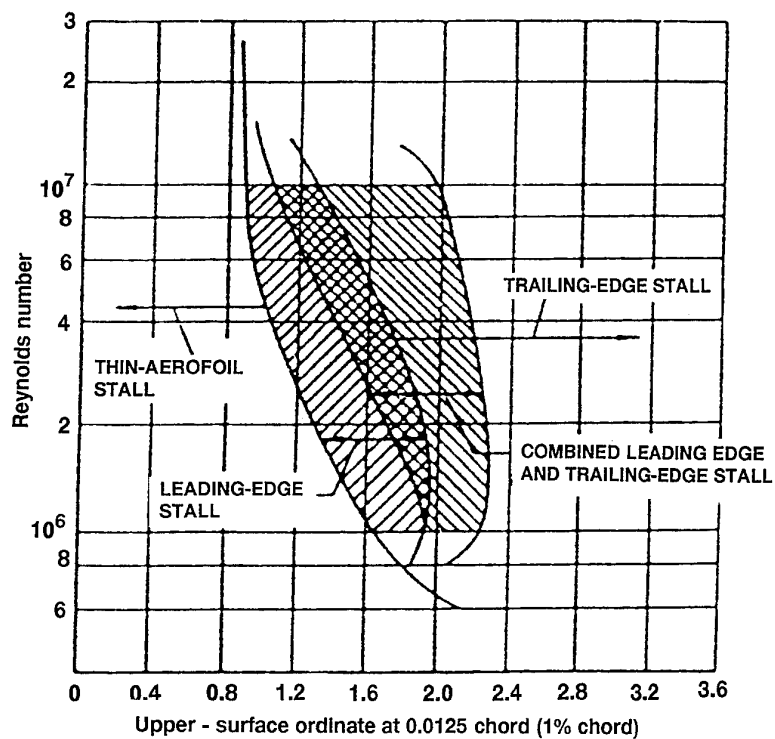


FIG 3.3 Correlation of aerofoil stall patterns  $10^6 < R < 10^7$  (from ref 59)

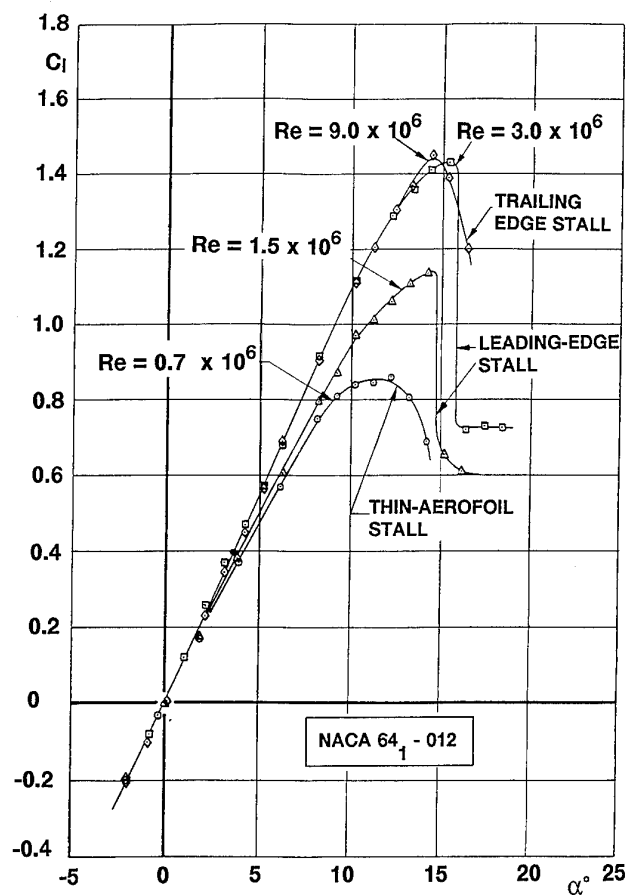
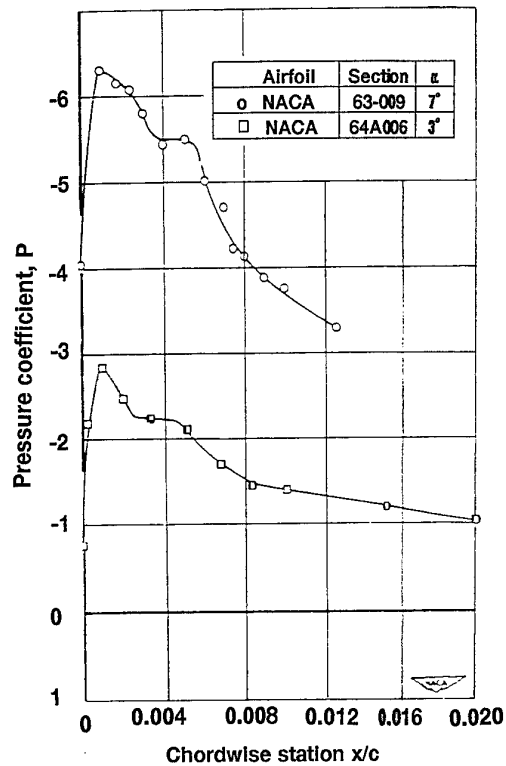
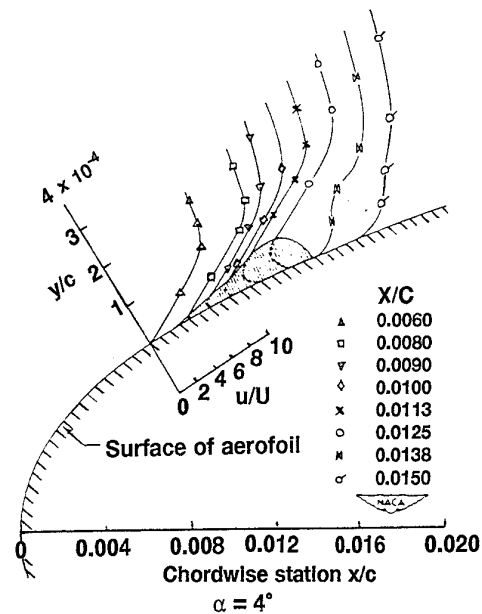


FIG 3.4 Illustration of Change in Type of Stall with Re (from ref 61)



(a) Surface Pressures



(b) Boundary-Layer Velocity Profiles

FIG 3.5 Features of Short Laminar Separation Bubble  
(from ref 58)

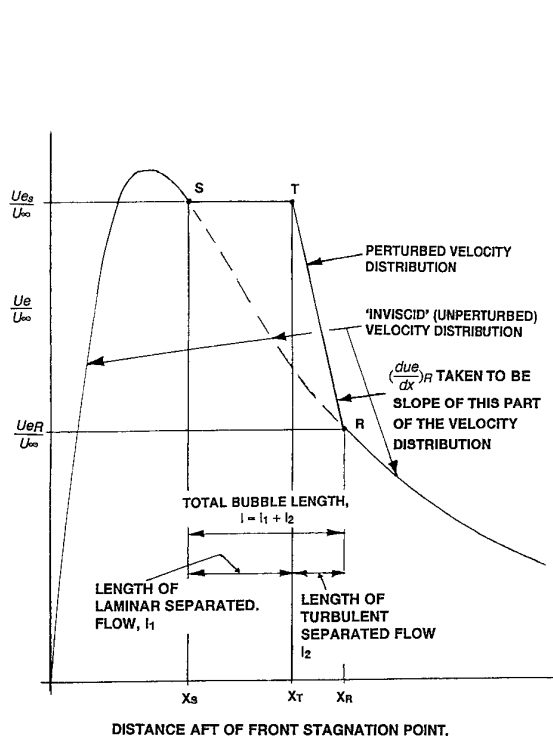


Fig 3.6 Simplified Model of Laminar Separation Bubble  
(from ref 69)

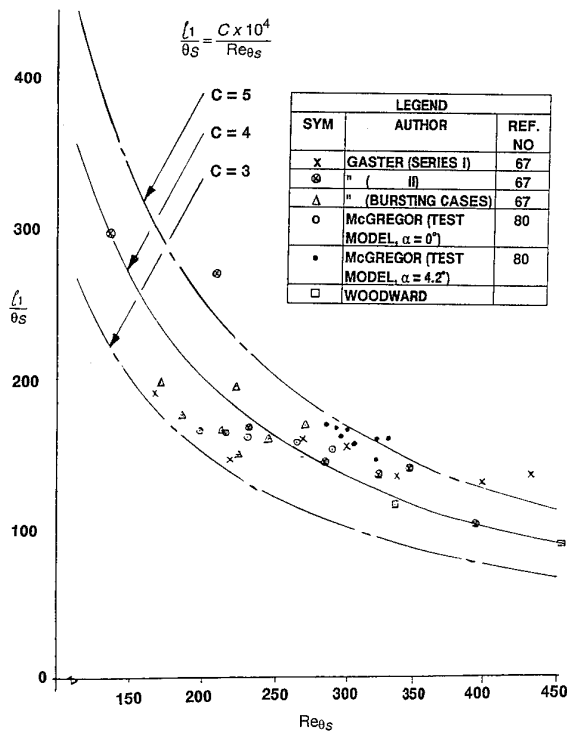


FIG 3.7 Variation of Non-dimensional Length of Separated Laminar Flow with  $Re_{\theta S}$   
(from ref 69)

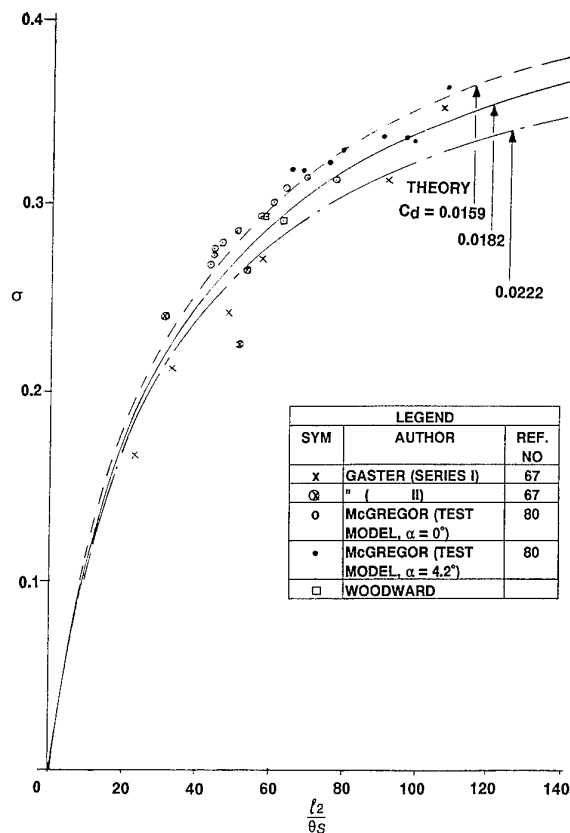


FIG 3.8 Comparison of Calculated and Measured Variation of Pressure Recovery Parameter with Length of Turbulent Part of the Bubble  
(from ref 69)

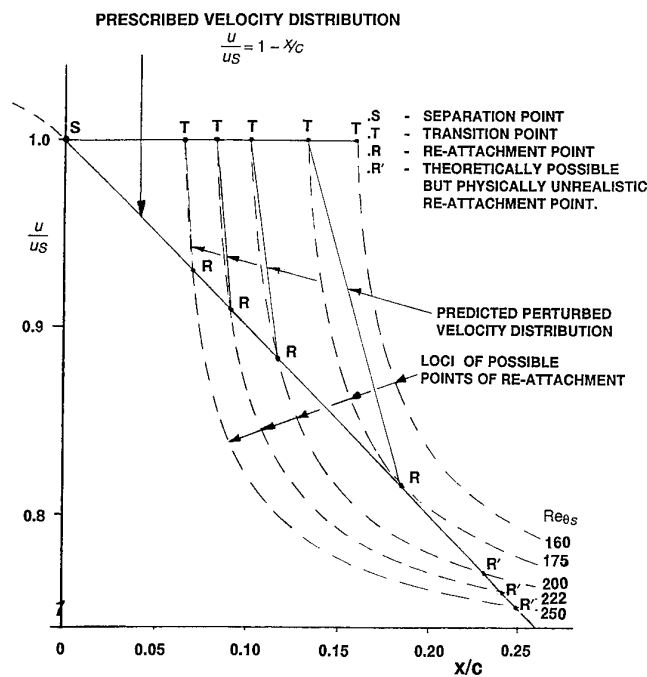


FIG 3.9 Example of Graphical Prediction of Bubble Growth and Bursting  
(from ref 69)

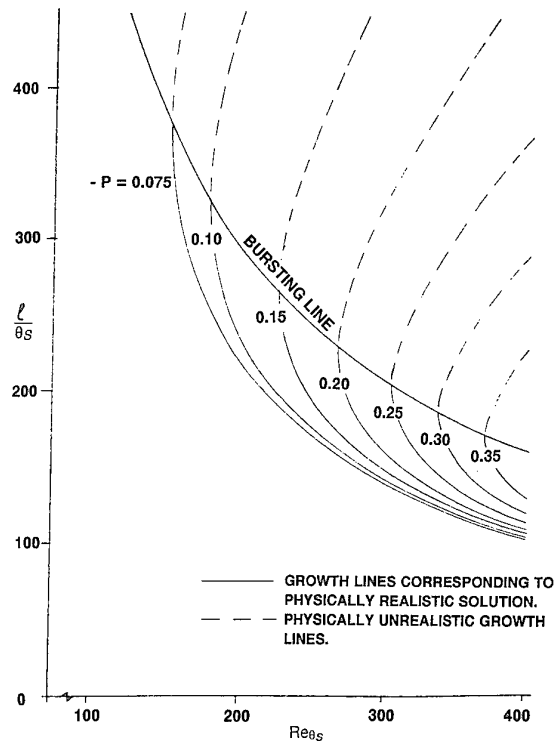


FIG 3.10(a) Bubble Growth Lines at Constant P  
 (Gaster Parameter)  
 (from ref 69)

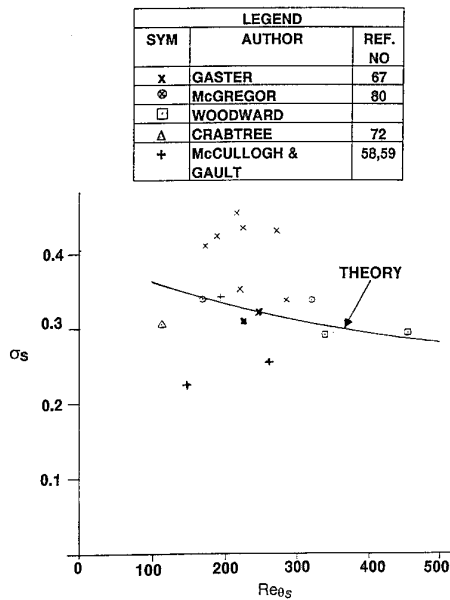


FIG 3.10(b) Comparison Between Theoretical and Experimental Pressure Recovery Parameters at Bursting  
 (from ref 69)

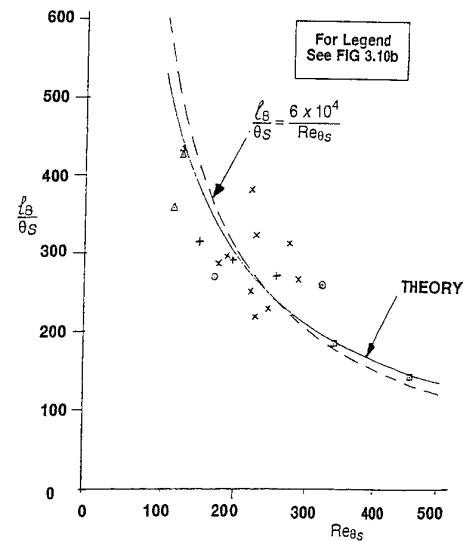


FIG 3.10(c) Comparison Between Theoretical and Experimental Bubble Lengths at Bursting  
 (from ref 69)

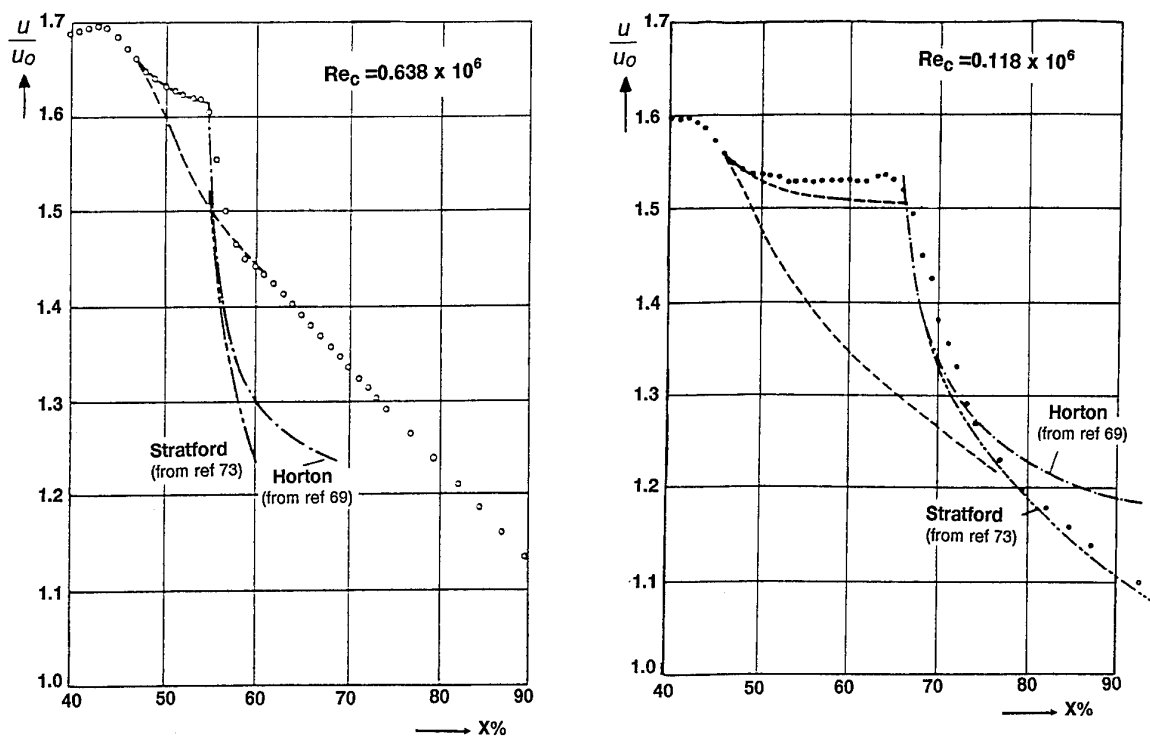


FIG 3.11 Measured vs Predicted Comparisons for Bubbles on Wortmann Airfoil (from ref 71)

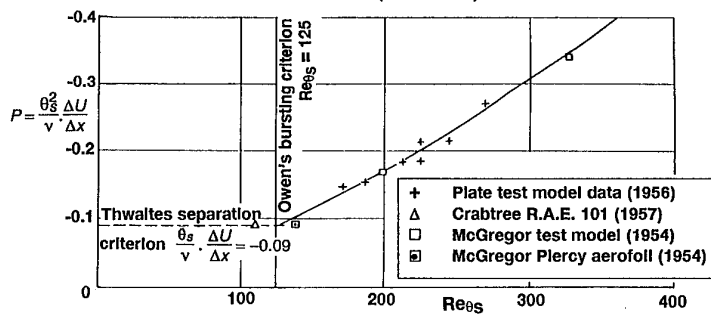


FIG 3.12 Relationship between  $Re_{\theta_s}$  and  $P$  at Bursting (from ref 67)

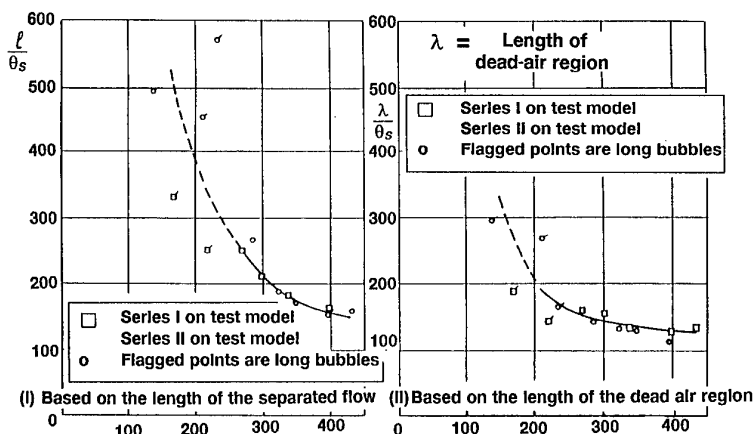


FIG 3.13 Bubble Length versus Reynolds number for Series I and II tests (from ref 67)

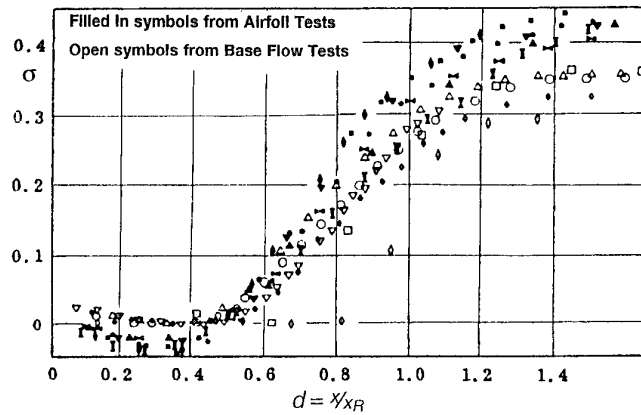
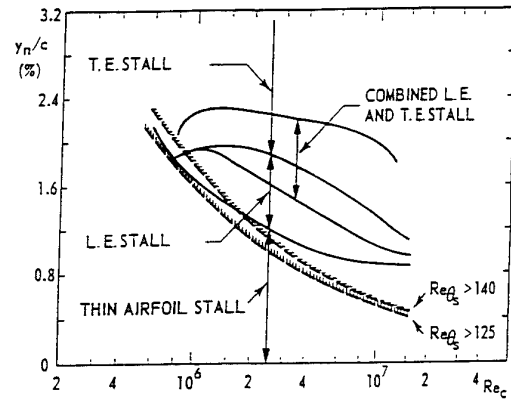
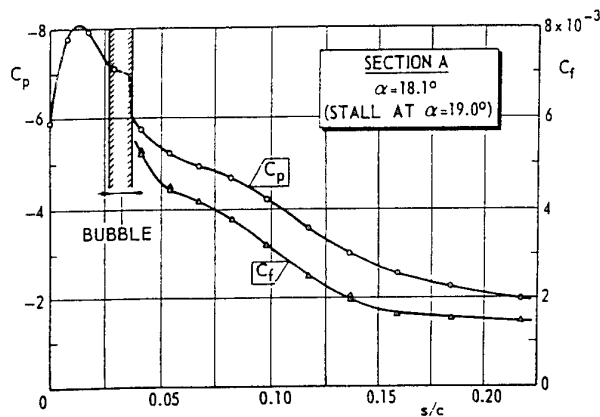


FIG 3.14 Pressure Distribution in Reduced Coordinates for Long-Bubble Stall  
(from ref 75)

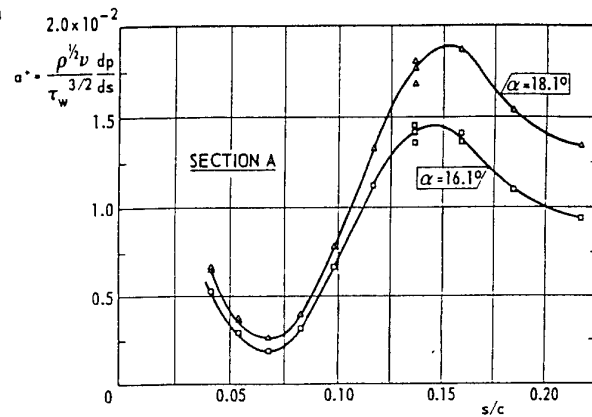


Gault's graph for types of airfoil stall and calculated lower-bounds for the laminar boundary-layer Reynolds number at separation

FIG 3.15 Types of Airfoil Stall and Predicted Upper Boundaries for Bubble Bursting  
(from ref 62)

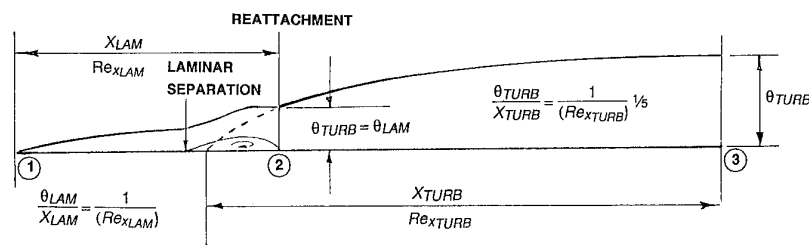
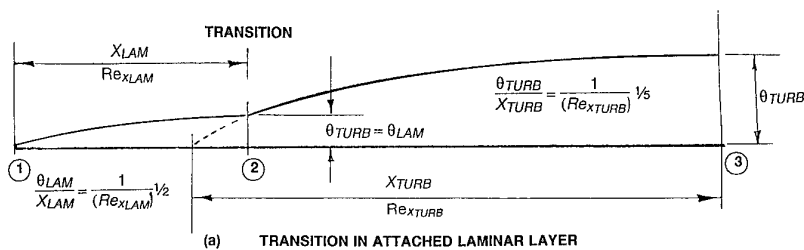


(a) Surface shear stress and pressures in L.E. region



(b) Separation parameter  $a^+$

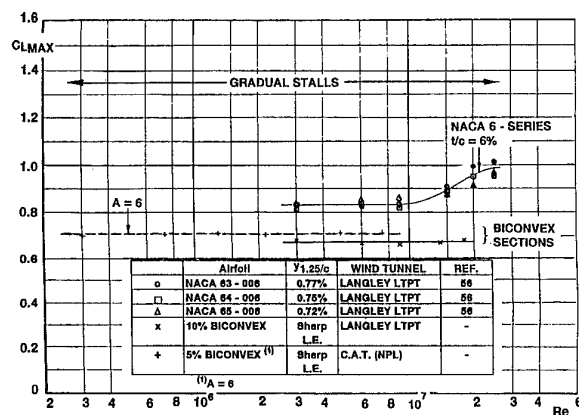
FIG 3.16 Interpretation of Stall for NLR7703  
(from ref 62 van den Berg)



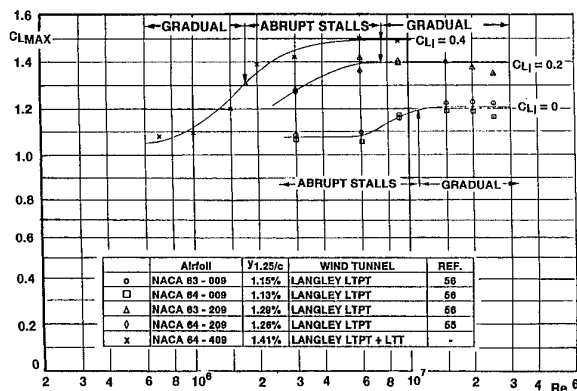
(b) TRANSITION IN SEPARATED LAMINAR LAYER (SHORT BUBBLE)

FIG 3.17 Origin of Scale Effect due to Reynolds Number Scaling of Viscous Layer Thickness  
(from ref 63)

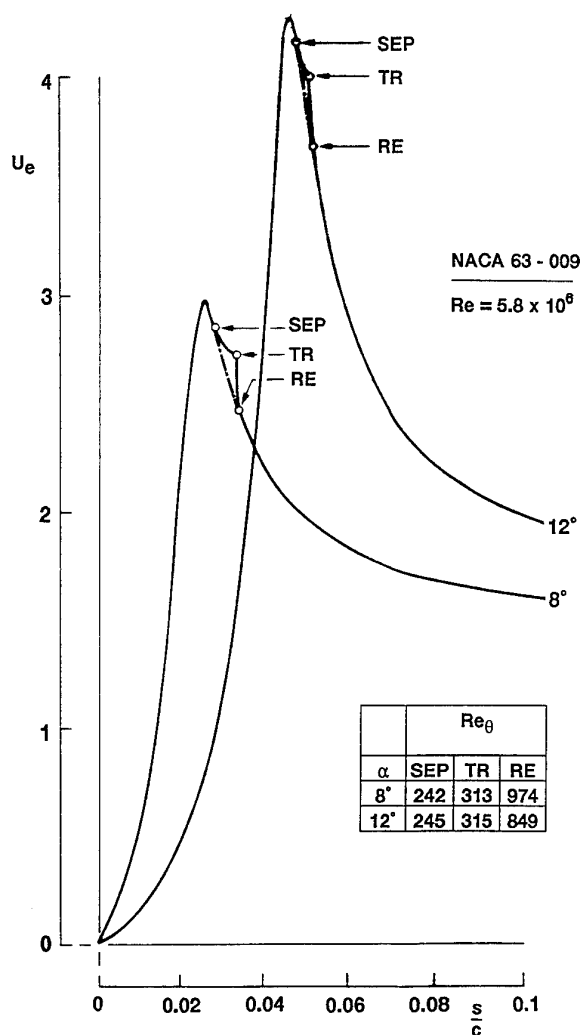




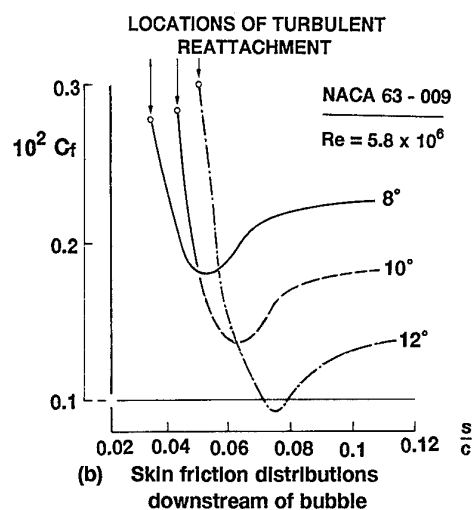
(a) 6% Thick or sharp-nose



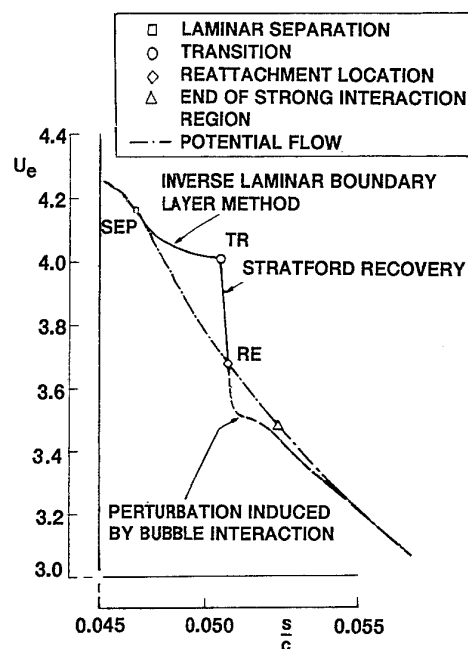
(b) 9% Thick sections

FIG 3.18 Variation of  $CL_{MAX}$  with  $Re$   
(mostly from ref 61)

(a) Velocity distributions on forward U.S.



(b) Skin friction distributions downstream of bubble



(c) Velocity distribution in vicinity of bubble

FIG 3.19 Theoretical Predictions for NACA 63 - 009  
(from ref 87)

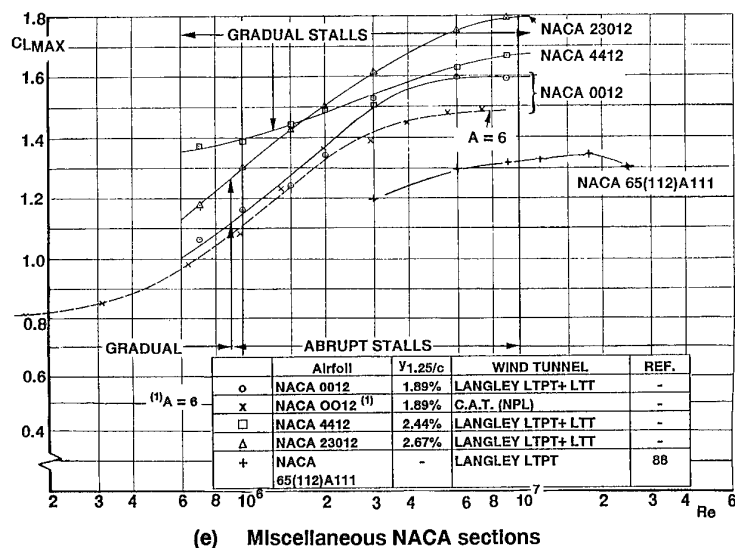
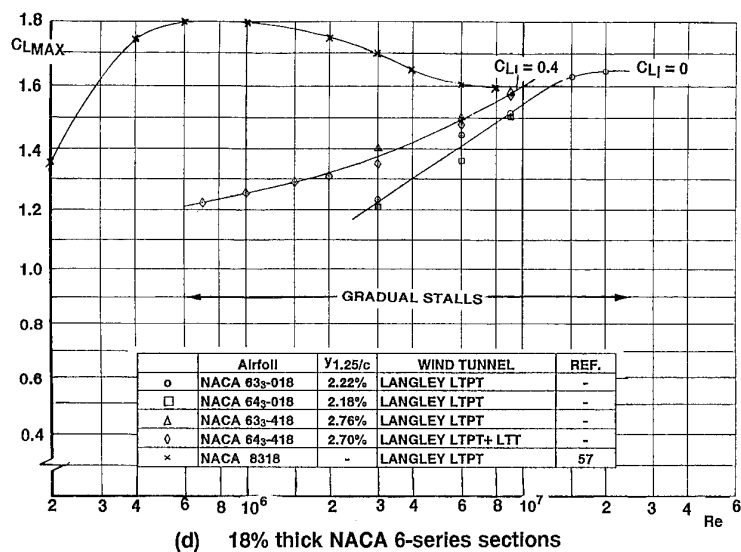
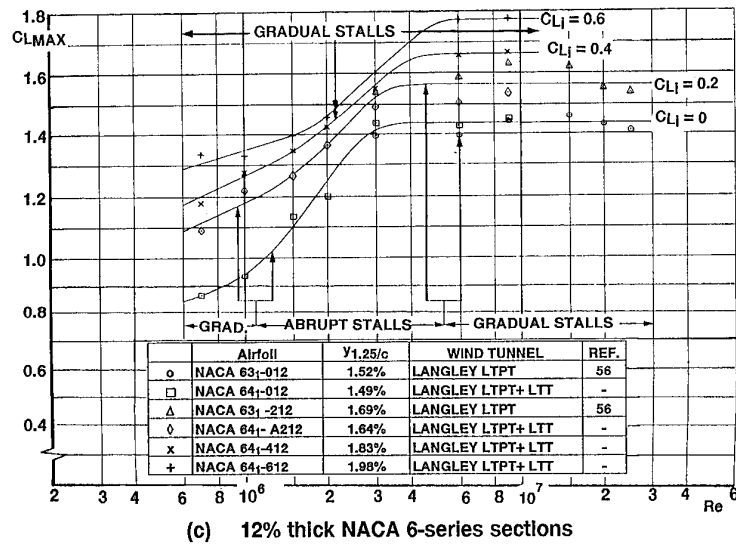
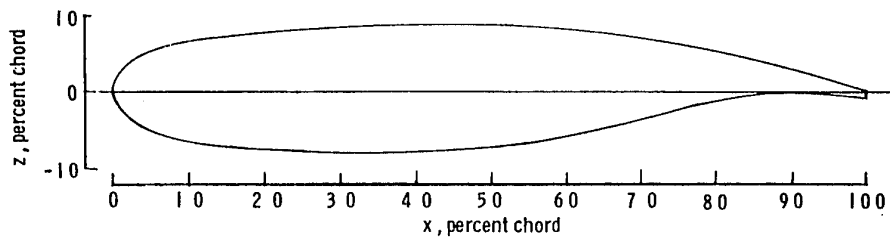


FIG 3.18(cont'd) Variation of  $CL_{MAX}$  with  $Re$   
(mostly from ref 61)



(a) Airfoil Shape

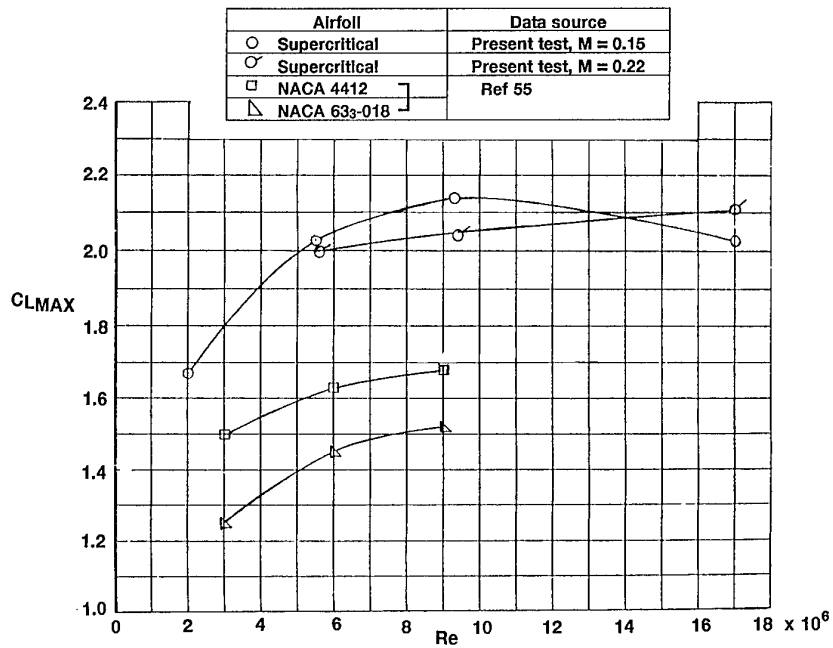
(b) Variation of  $C_{LMAX}$  with  $Re$ 

FIG 3.20 Results for NASA Supercritical Aerofoil  
for the T2C  
(from ref 64)

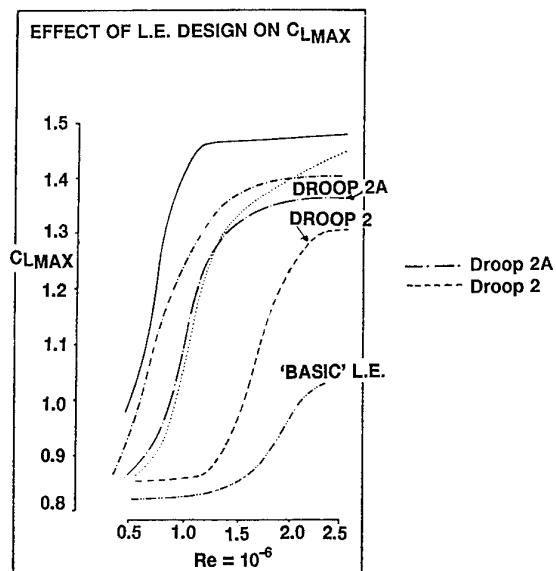
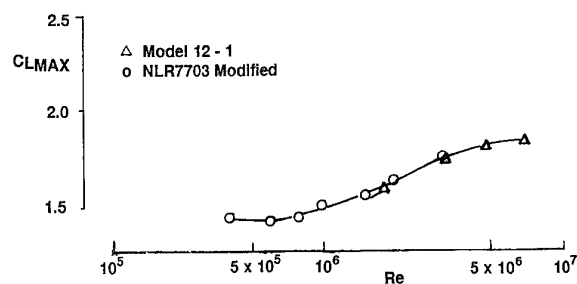
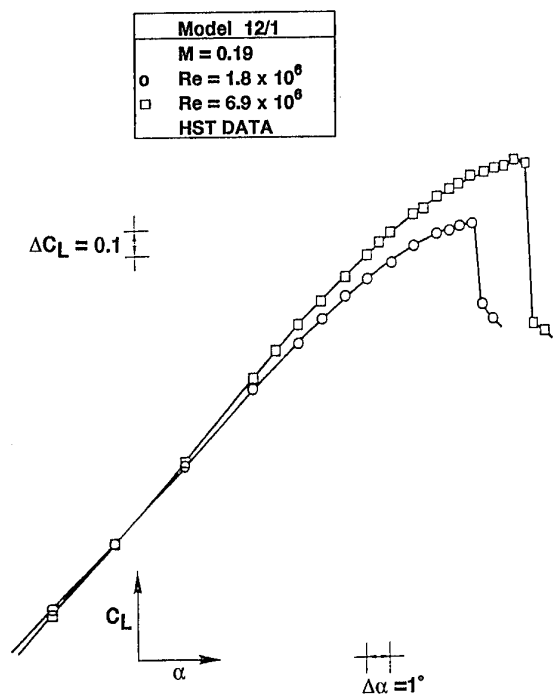
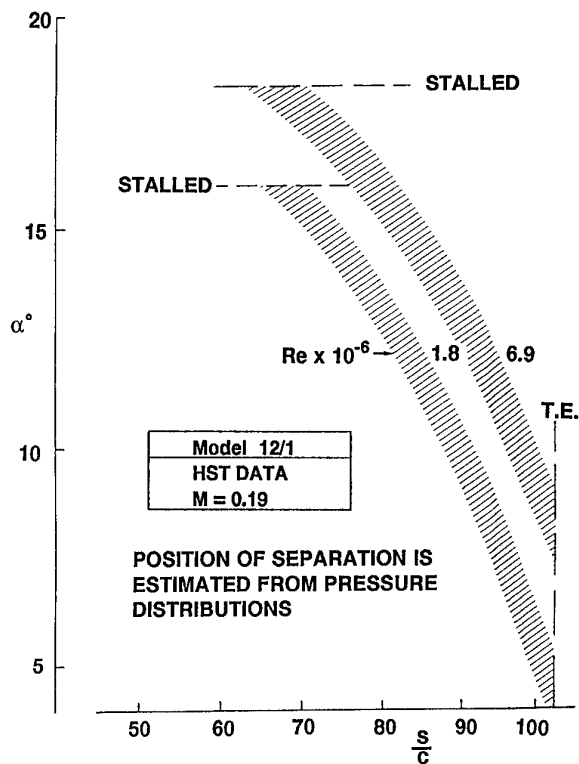


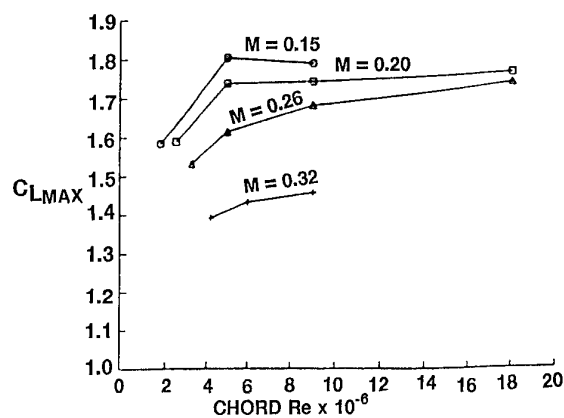
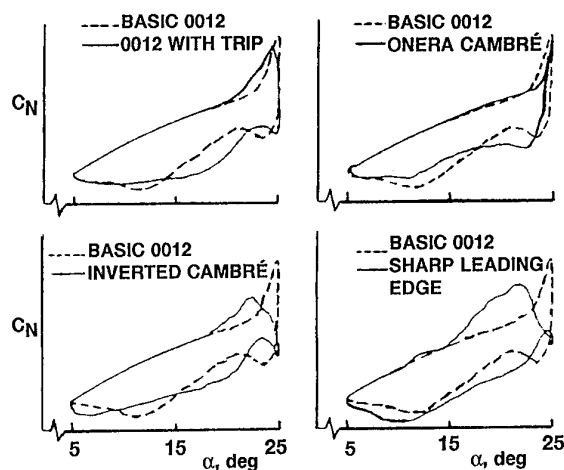
FIG 3.21 Effect of Leading-Shape: A300B Development  
(from ref 89)

(a) Variation of  $C_{LMAX}$  with Re

(b) Shape of 7703 modified

(c) Effect of Re on  $C_L - \alpha$ 

(d) Effect of Re on rear separation

FIG 3.22 Results from NLR Tests  
(from ref 65)FIG 3.23 Results from Recent NASA Langley Tests  
(from ref 66)FIG 3.24 Comparison of normal force on airfoils with different stall characteristics  
( $\alpha = 15^\circ + 10^\circ \sin \omega t$ ,  $k = 0.15$ ,  $Re = 2.5 \times 10^6$ ).  
(from ref 91)

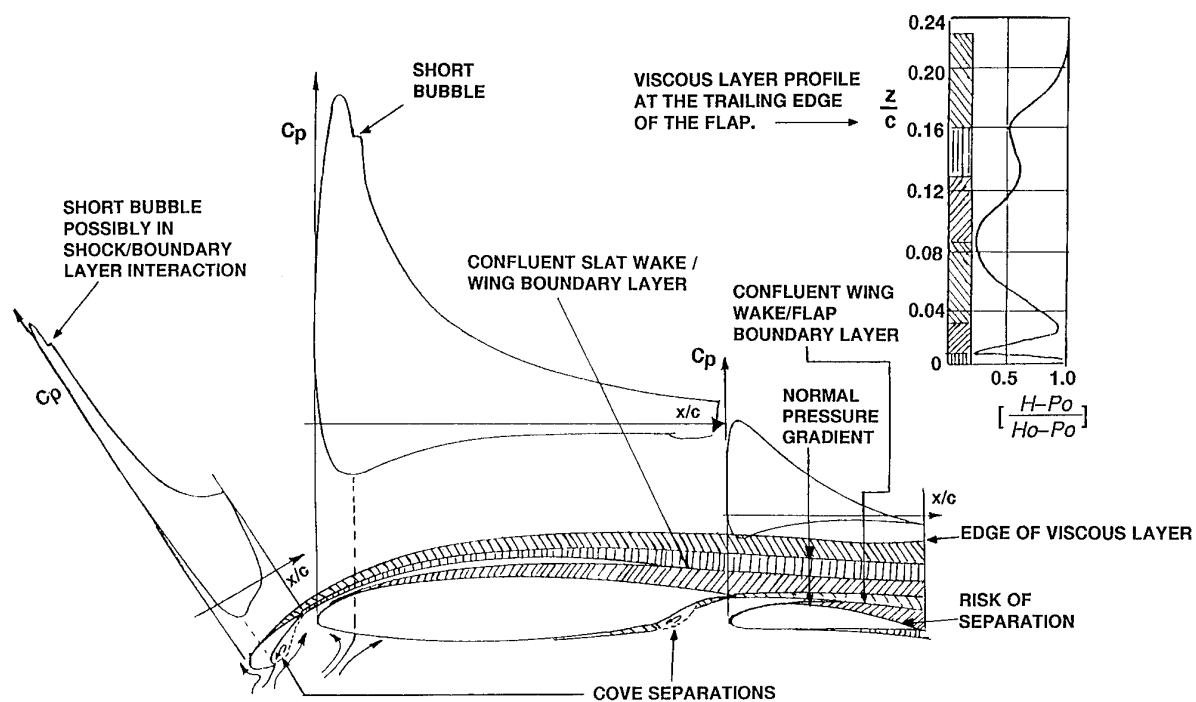


**Fig 3.25 Pressure Distributions and Viscous Layer on Slat/Wing/Flap combination**  
(from refs 94,63)

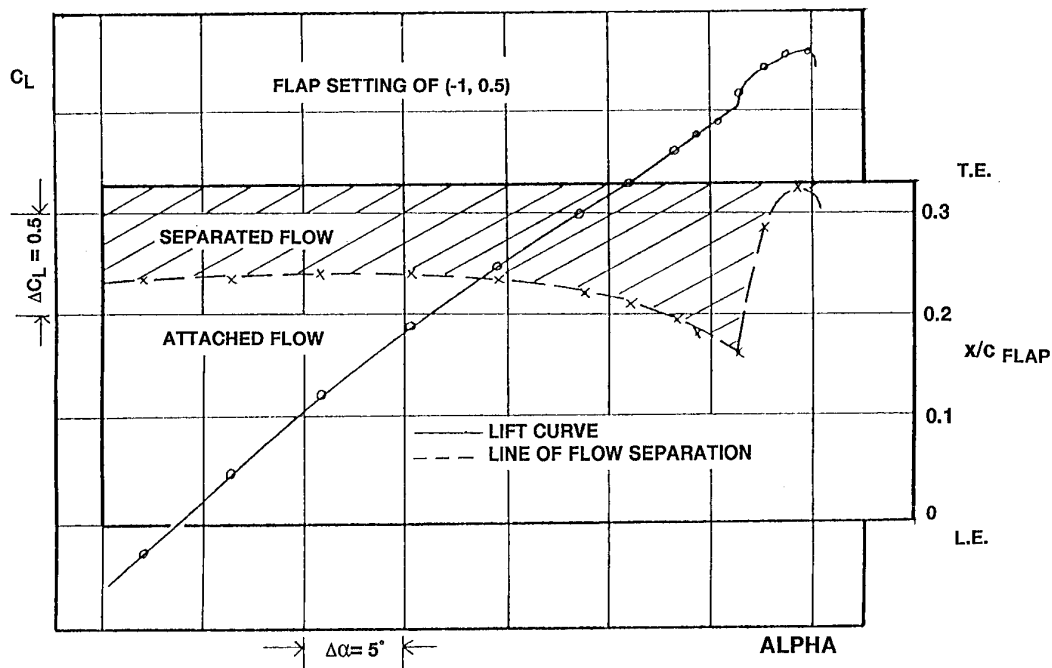
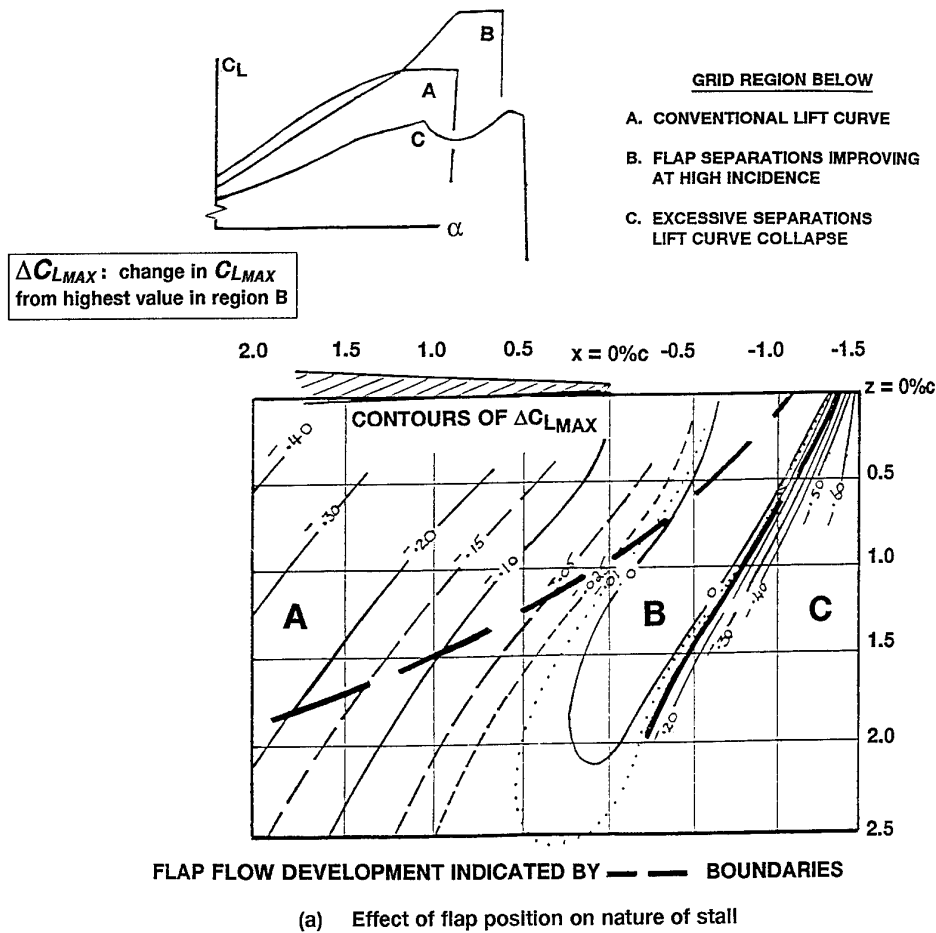


FIG 3.26 Results from Tests on a  $40^\circ$  Single-Slotted Flap on a Quasi-2D End-Plate Model  
(from refs 63,97)

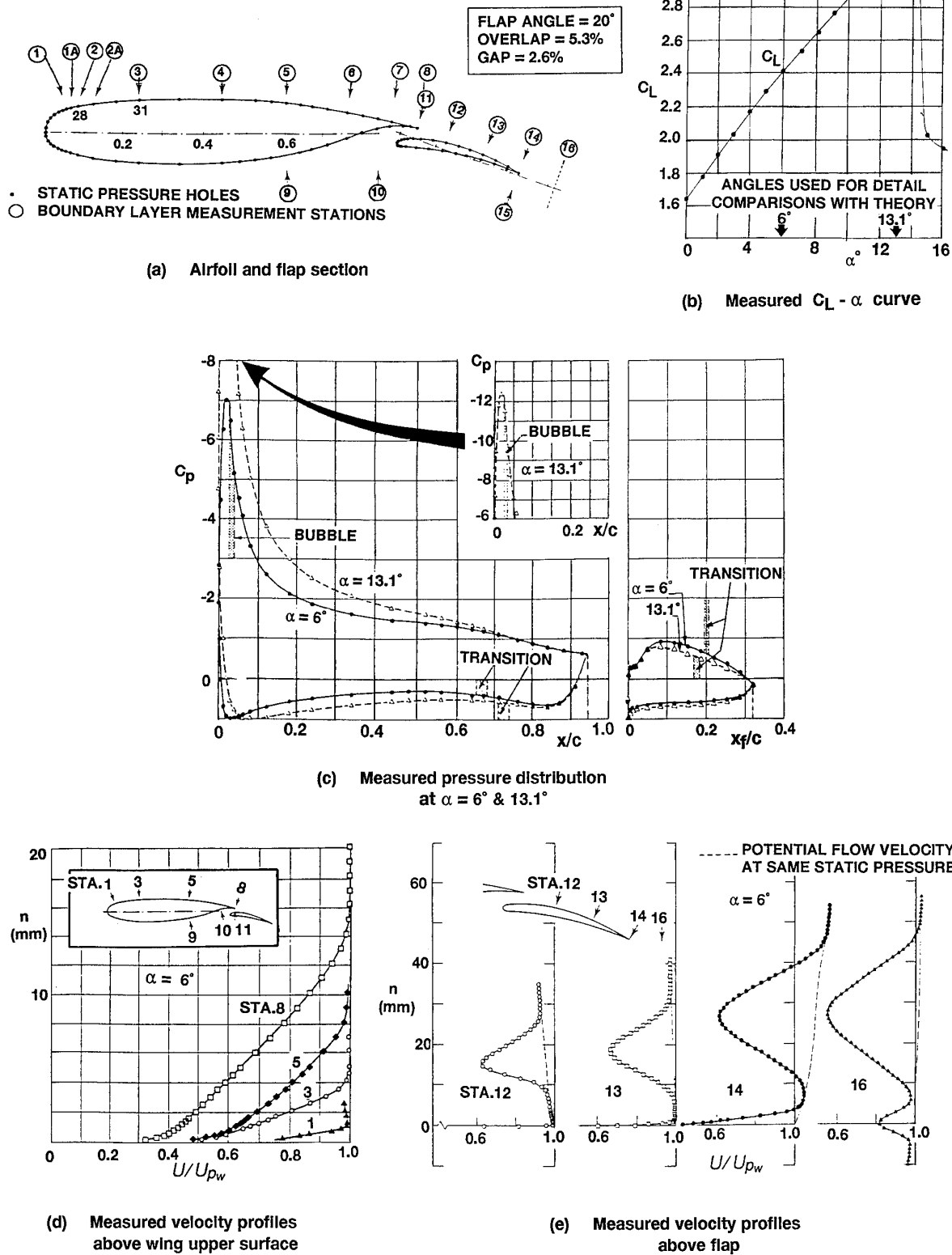
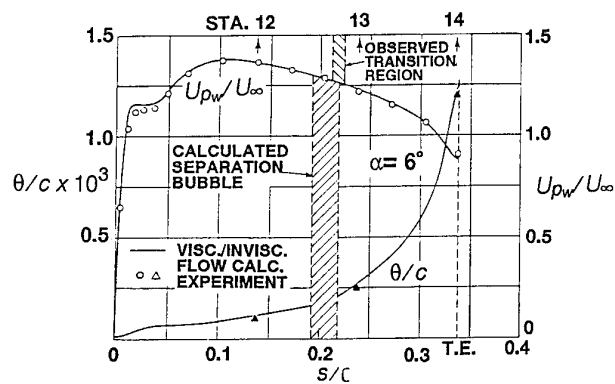
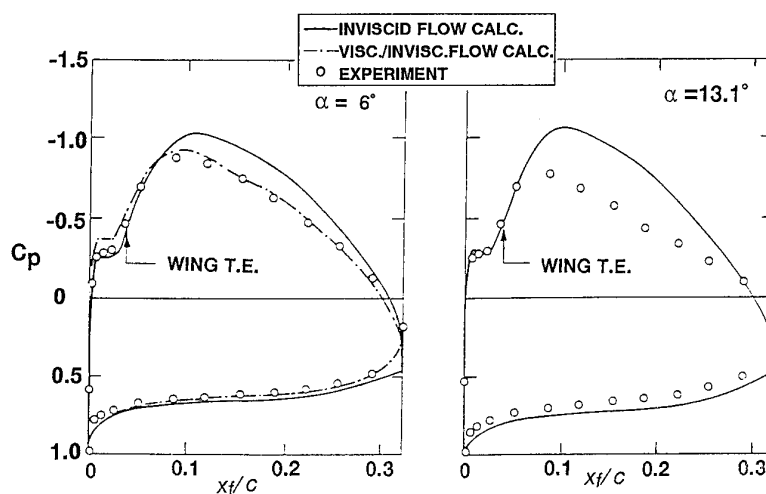


FIG 3.27 NLR 2D Wing-Flap: Large Gap Test Case  
(from ref 98)



(f) Comparison between calculated and measured velocity and momentum thickness development:  
Flap upper surface,  $\alpha = 6^\circ$



(g) Comparison between calculated and measured pressure distribution on Flap

FIG 3.27(cont'd) NLR 2D Wing-Flap: Large Gap Test Case  
(from ref 98)

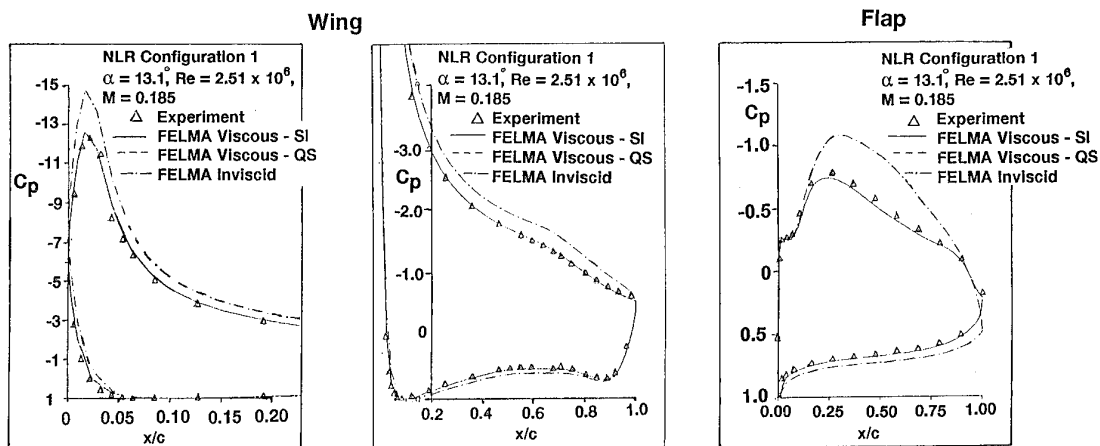
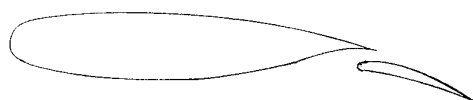


FIG 3.28

Comparison of NLR Measured Data with  
UK Felma calculation  
(from ref 99)



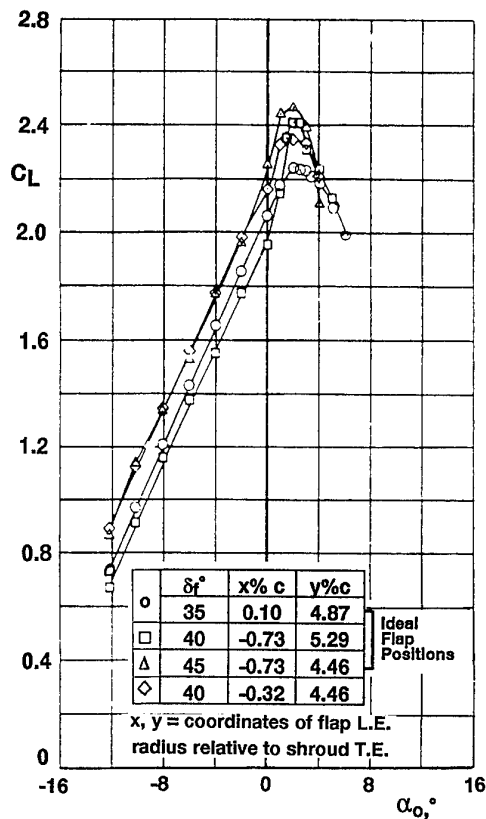
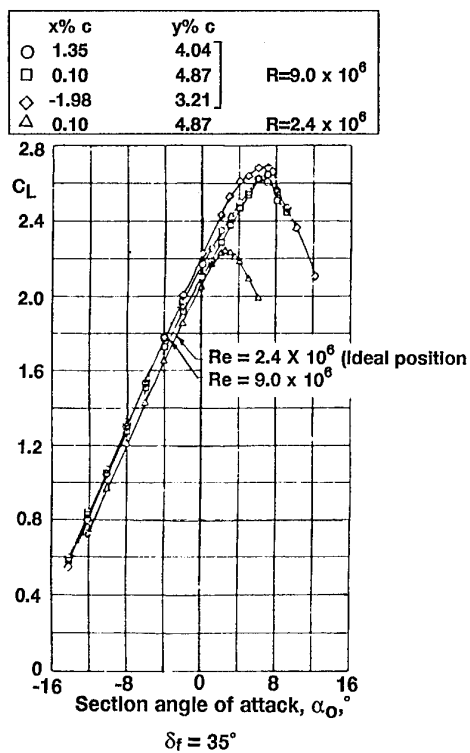
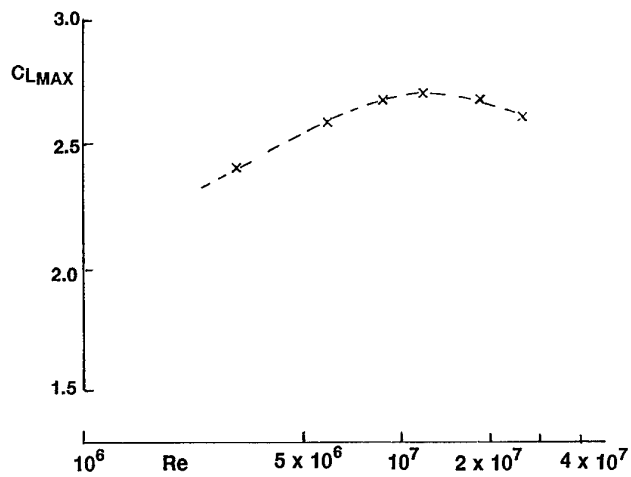
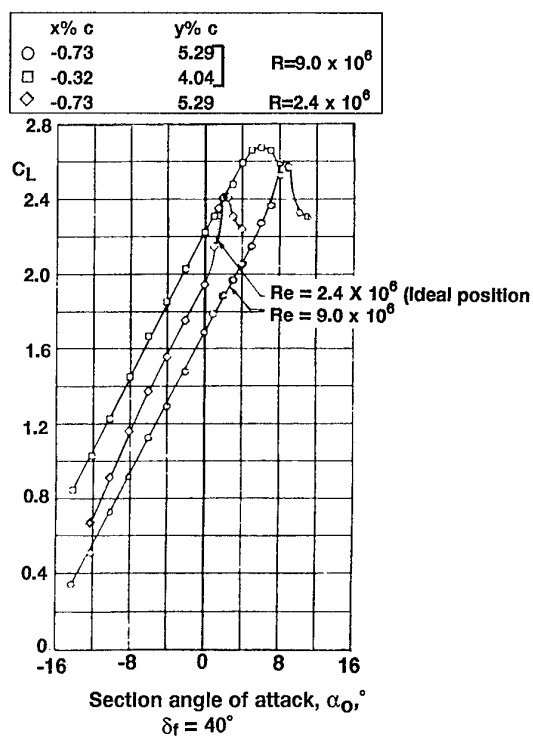
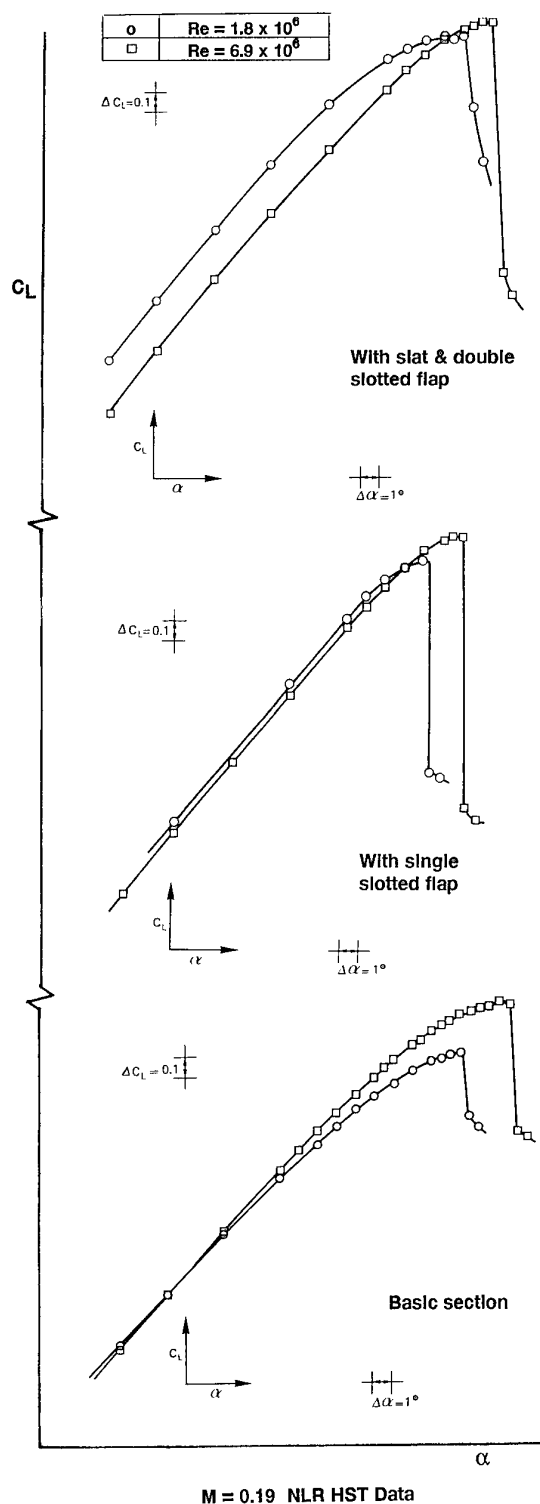
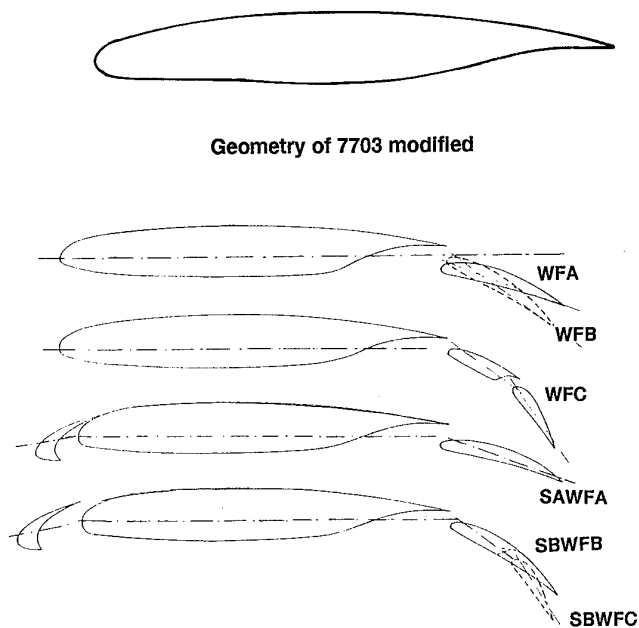
(a)  $C_L - \alpha$  curves for  $Re = 2.4 \times 10^6$ (b) Comparison of results for  $Re = 2.4 \times 10^6$  and  $9.0 \times 10^6$ (c)  $C_{LMAX}$  variation with  $Re$  for configuration optimised at  $Re = 9.0 \times 10^6$ 

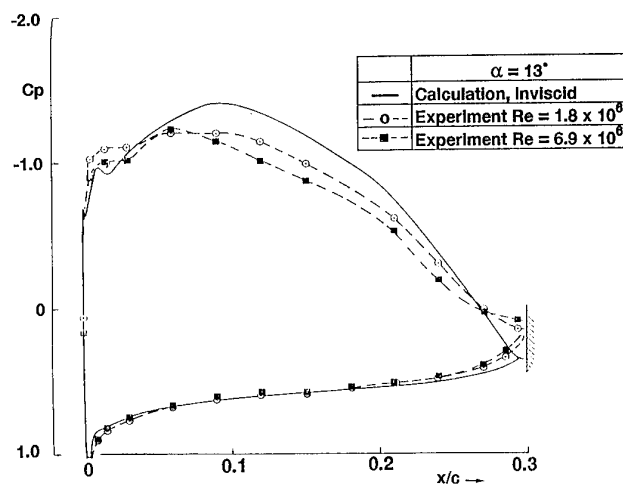
FIG 3.29 Results for NACA Multi Airfoil  
NACA 65(112)A111: 1947 Tests.  
(from ref 88)



**FIG 3.30** NLR Multi Airfoil Scale Effect Comparison  
(from ref 100)



**(a)** Geometry of high lift devices tested on F-29-12



**(b)** Scale effect on separation on F-29-12 WFA flap at  $\delta_f = 20^\circ$

**FIG 3.31** NLR Multi-Airfoil 2D Test Data  
(from refs 65,101)

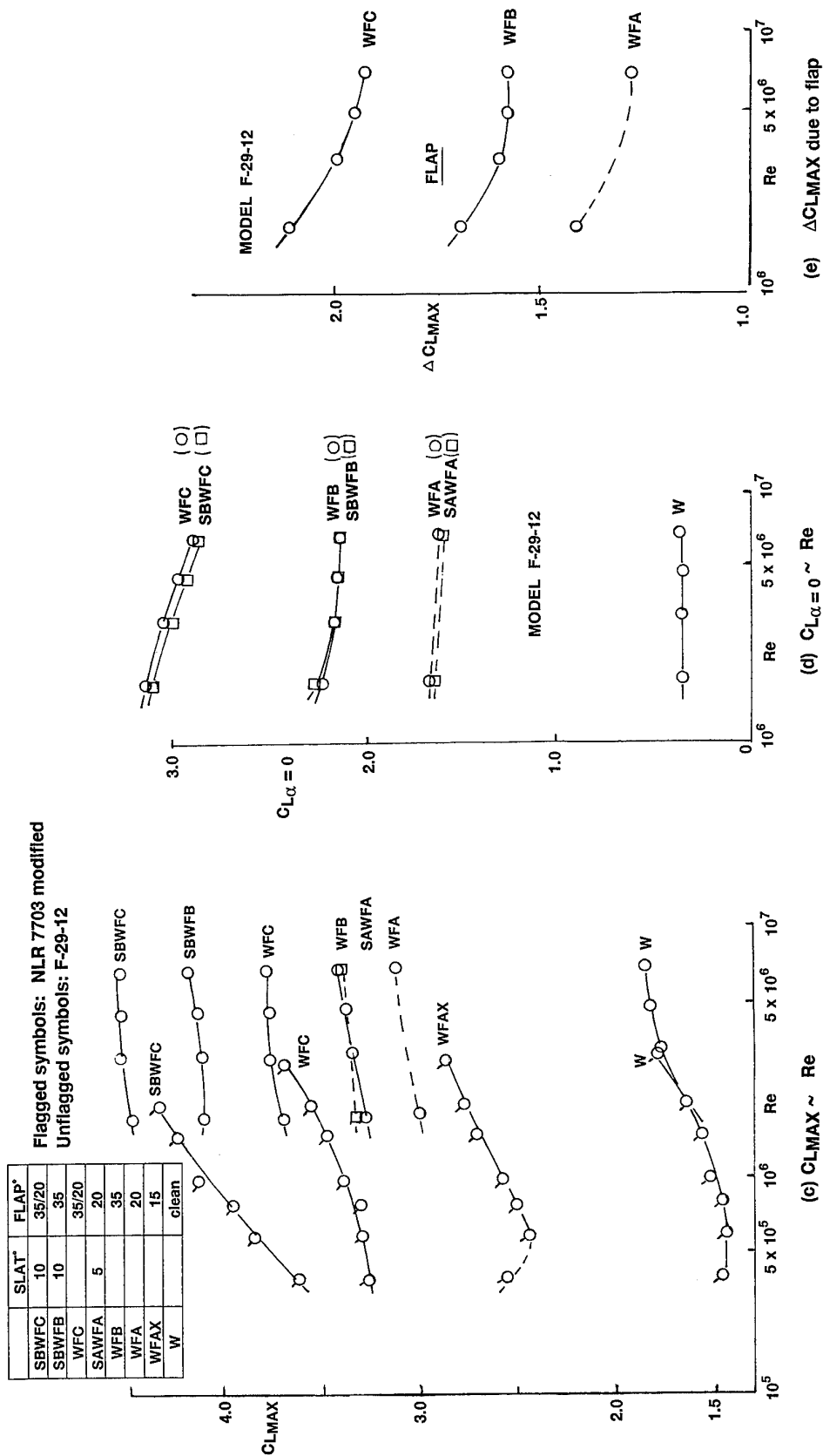
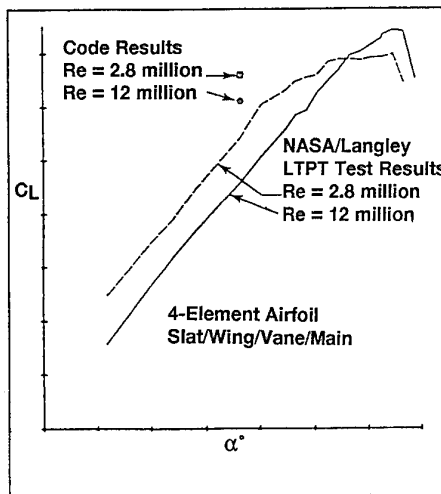
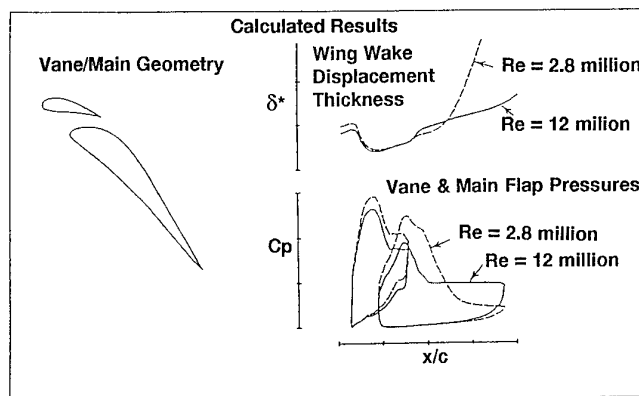


FIG 3.31(cont'd)  
NLR Multi-Airfoil 2D Test Data  
(from refs 65,101)

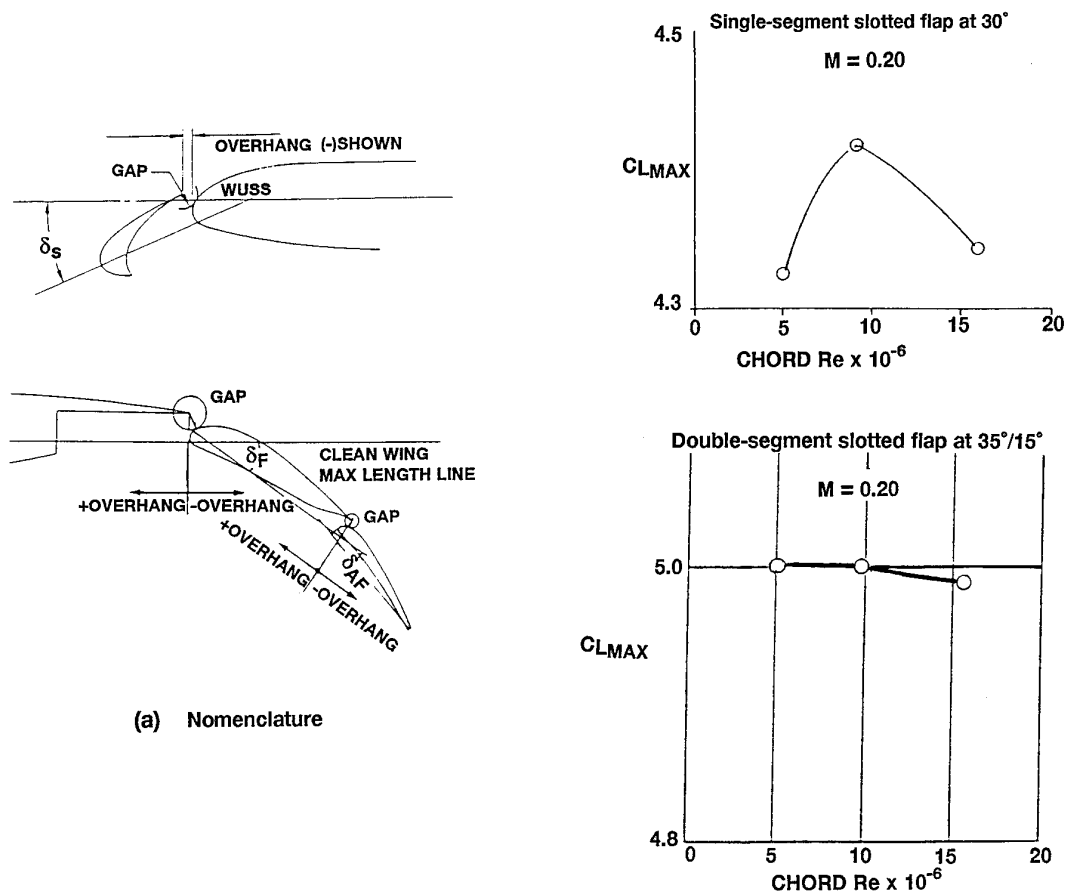


(a) Adverse Reynolds number of effect on lift



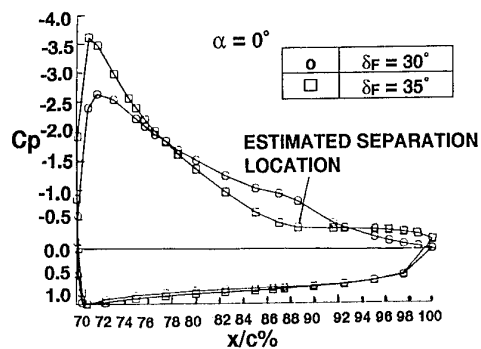
(b) Wing wake/flap interaction at low and high Reynolds number

FIG 3.32 Results from NASA Langley/Boeing 2D Tests  
(from ref 102)

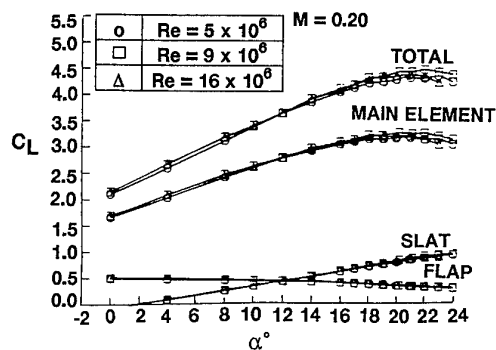


(b) Variation of  $CL_{MAX}$  with Re  
(Slat at 30°, configurations optimised at  $Re = 9 \times 10^6$ )

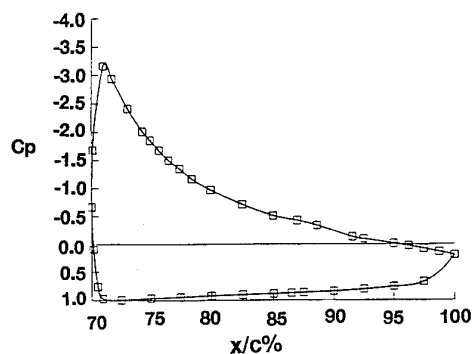
FIG 3.33 NASA Langley/Douglas 2D Tests  
(from refs 66, 90)



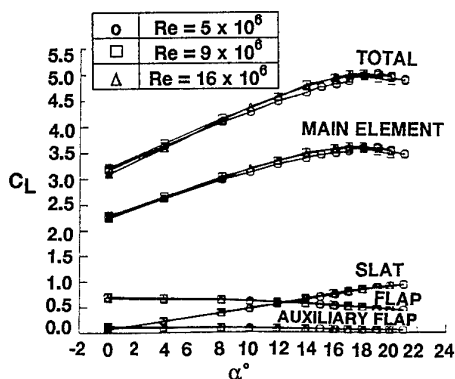
(c) Surface Pressures on single-segment flap at an Approach-like Condition



(d) Reynolds no. effect on lift: Single-segment flap at  $30^\circ$

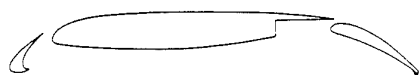


(f) Flap surface pressures: No separation but reverse flow present in confluent wake

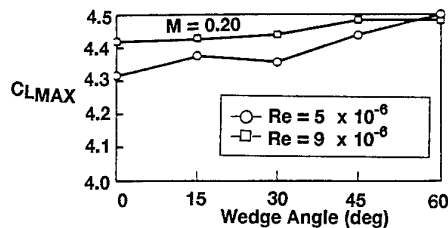


(e) Reynolds no. effect on lift: Double-segment flap at  $35^\circ/15^\circ$

FIG 3.33 (cont'd) NASA Langley/Douglas 2D Tests  
(from refs 66, 90, 105)



(a) Geometry: Single-segment slotted flap at  $30^\circ$



(b) Effect of  $Re$  on  $CL_{MAX}$

FIG 3.34 Effect of Wedge Simulating a Split Flap  
(from ref 106)

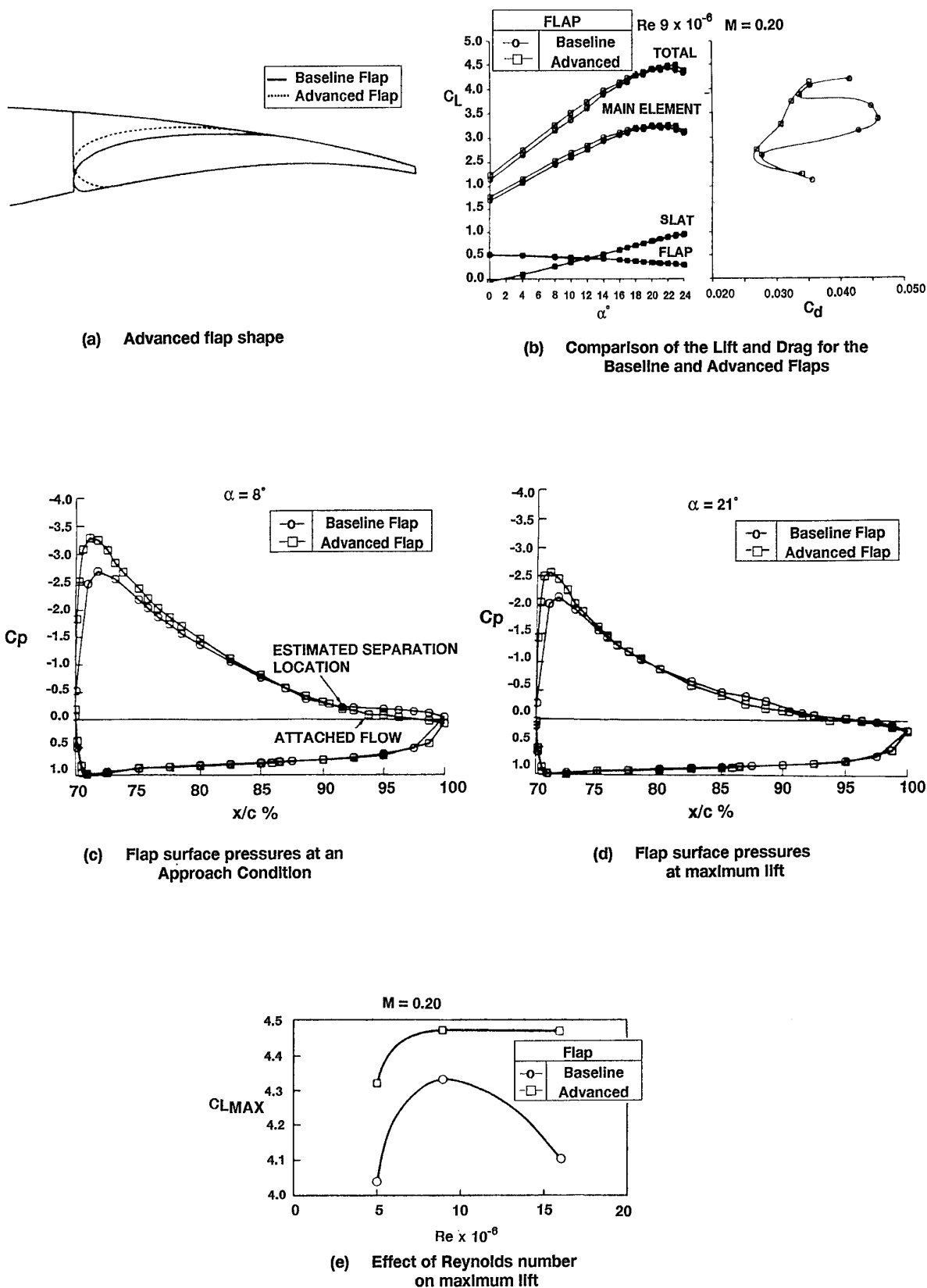
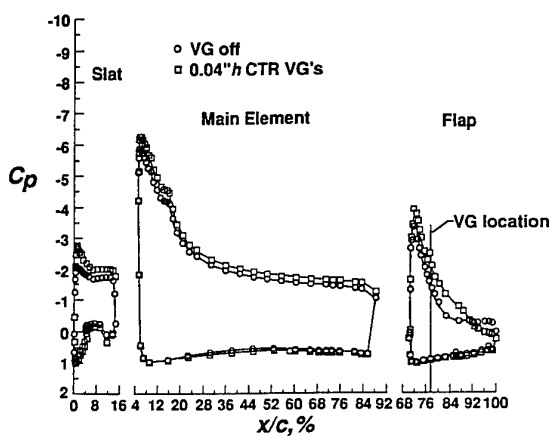
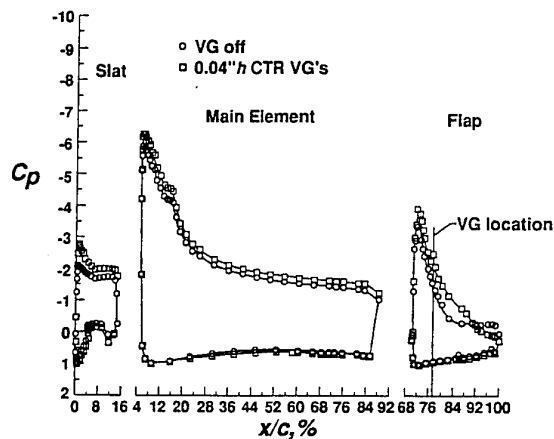
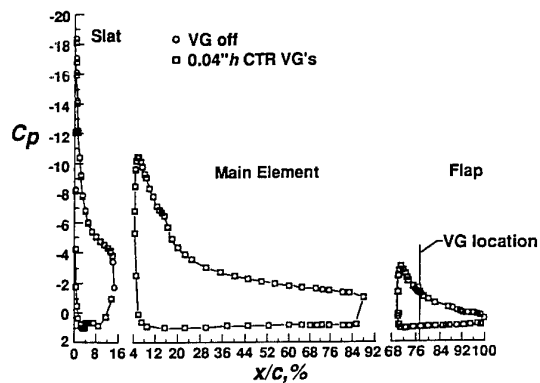
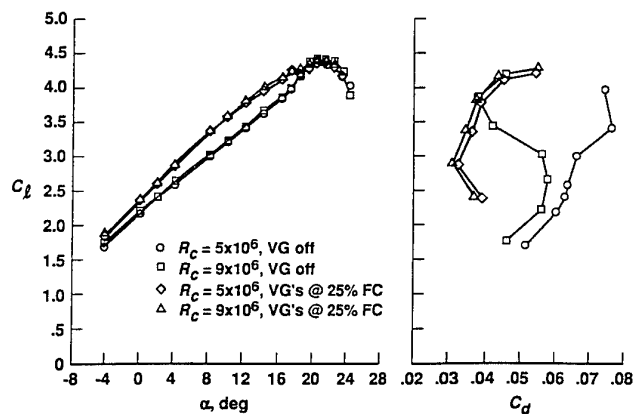
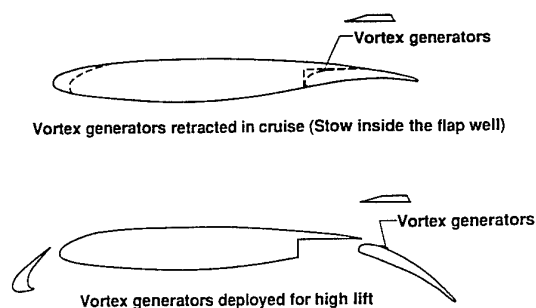


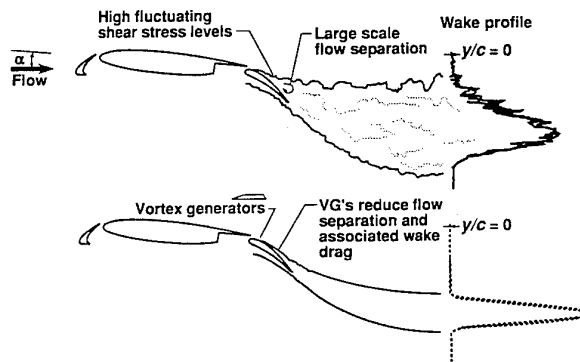
FIG 3.35 Effect of Douglas Advanced Single-Segment Slotted Flap  
 $\delta_S = 30^\circ$ ,  $\delta_F = 30^\circ$   
 (from ref 106)

(a) Pressure Distributions:  $\alpha = 8^\circ$ ,  $Re = 5 \times 10^6$ (b) Pressure Distributions:  $\alpha = 8^\circ$ ,  $Re = 9 \times 10^6$ (c) Pressure Distributions:  $\alpha = 20^\circ$ ,  $Re = 9 \times 10^6$ 

(d) Lift and Drag

FIG 3.36(a-d) Effect of Vortex Generators on Results at  $M = 0.2$  with Single-Segment Flap at  $35^\circ$  (Slat at  $30^\circ$ )

(e) Vortex generator concept



(f) Flow physics concept

FIG 3.36 (a-f) NASA Langley/Douglas Investigation of Vortex Generators on Single-Segment Slotted Flap (from ref 107)

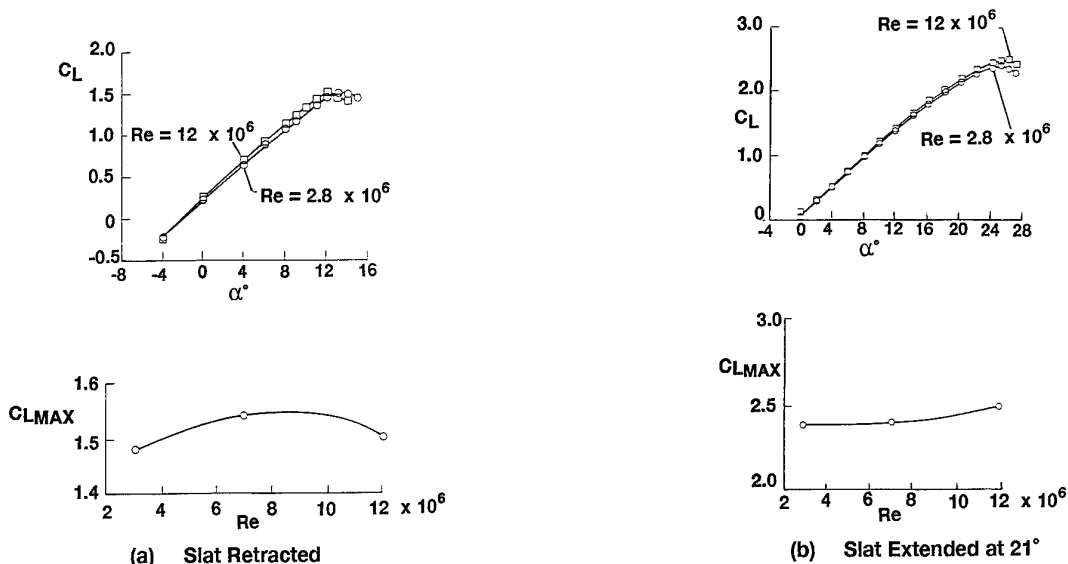


FIG 3.37 Effect of Slat on Scale Effect at  $M = 0.2$  of Section with Relatively Sharp L.E. (Slotted Flap Stowed)

(from ref 106)

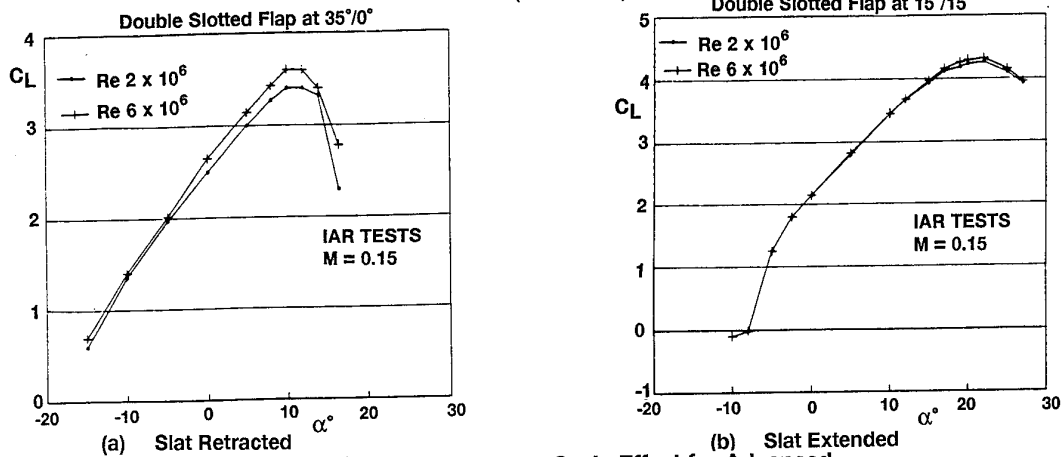


FIG 3.38 Effect of Slat on Scale Effect for Advanced Airfoils for Commuter Aircraft

(from ref 107)

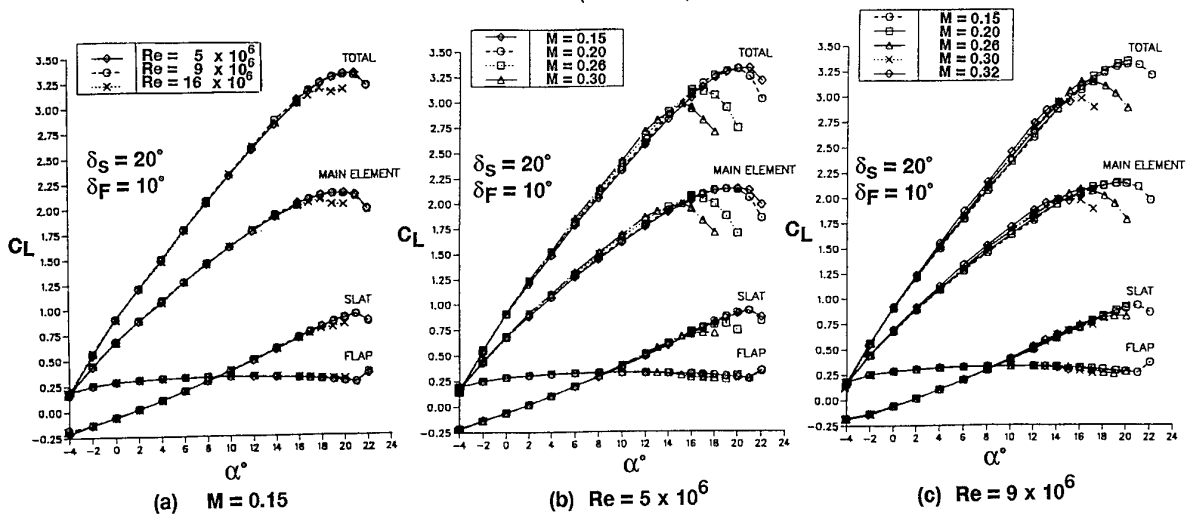
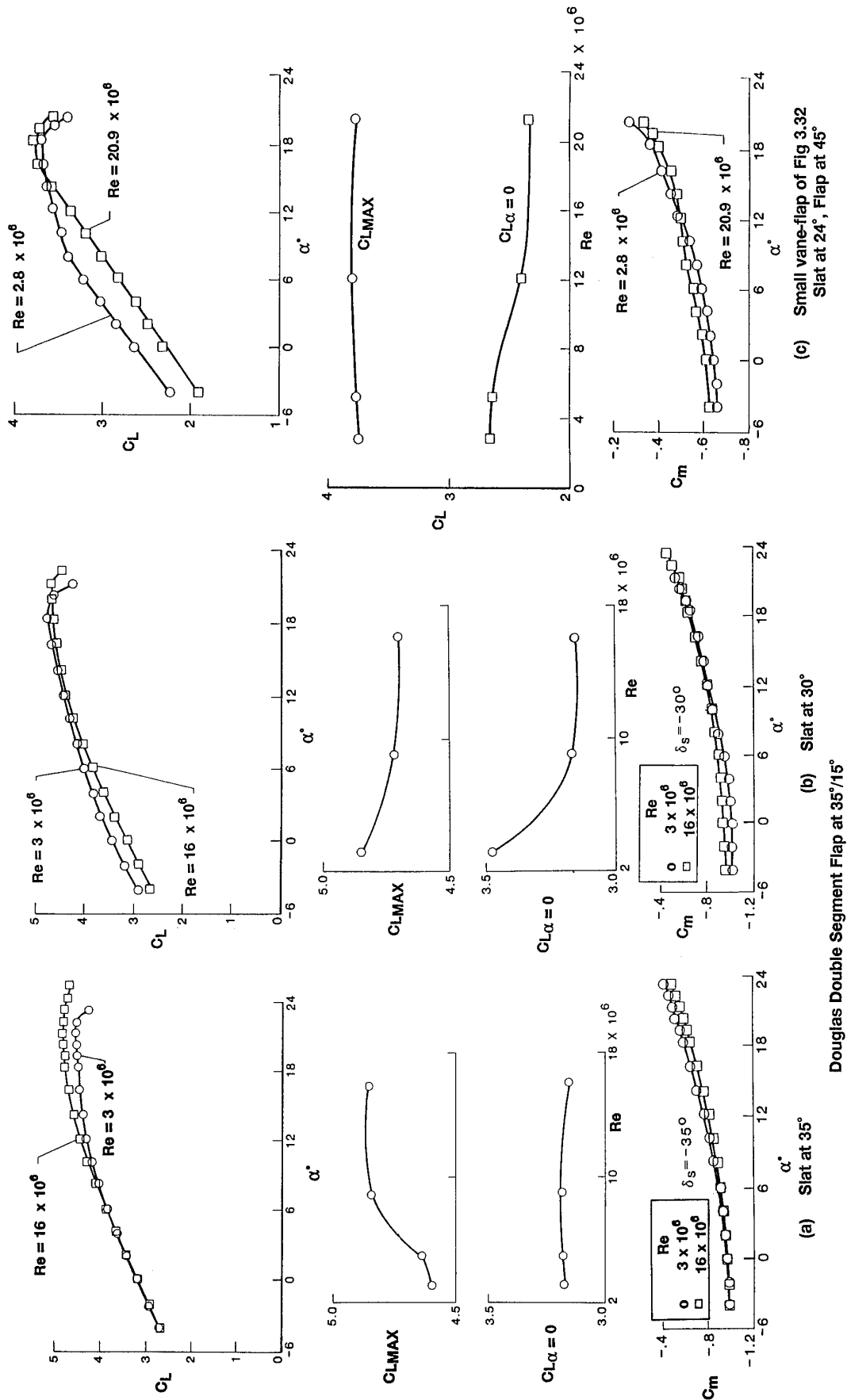


FIG 3.39 Effects of  $Re$  and  $M$  on Performance of Take-Off Configuration ( $\delta_S = 20^\circ$ ,  $\delta_F = 10^\circ$ )

(from ref 90)





**FIG 3.40 Effect of Slat Setting on Flap Performance**  
(from ref 108)

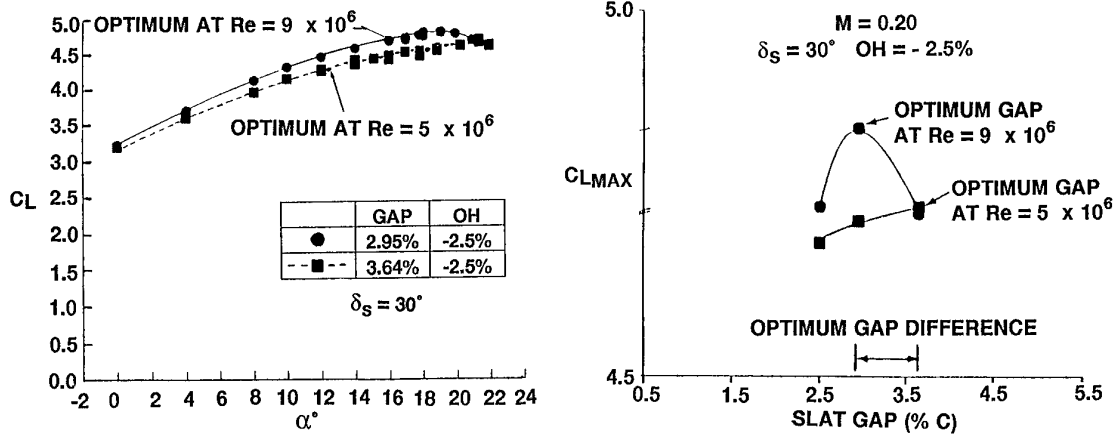


FIG 3.41 Effect of Reynolds Number on Slat Gap Optimization  
(from ref 66)

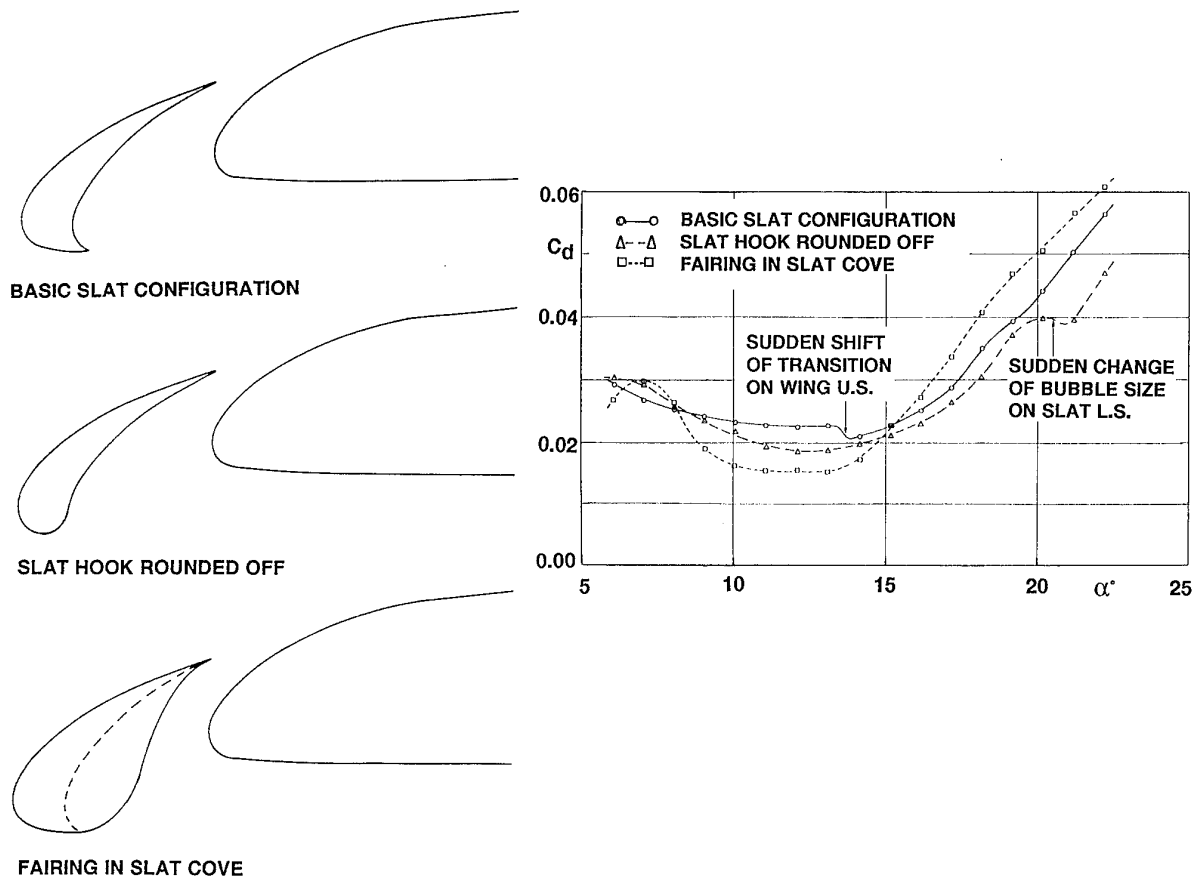


FIG 3.42 Effect of Slat Cove Modifications on Drag:  
NLR 2D Tests  
(from ref 110)

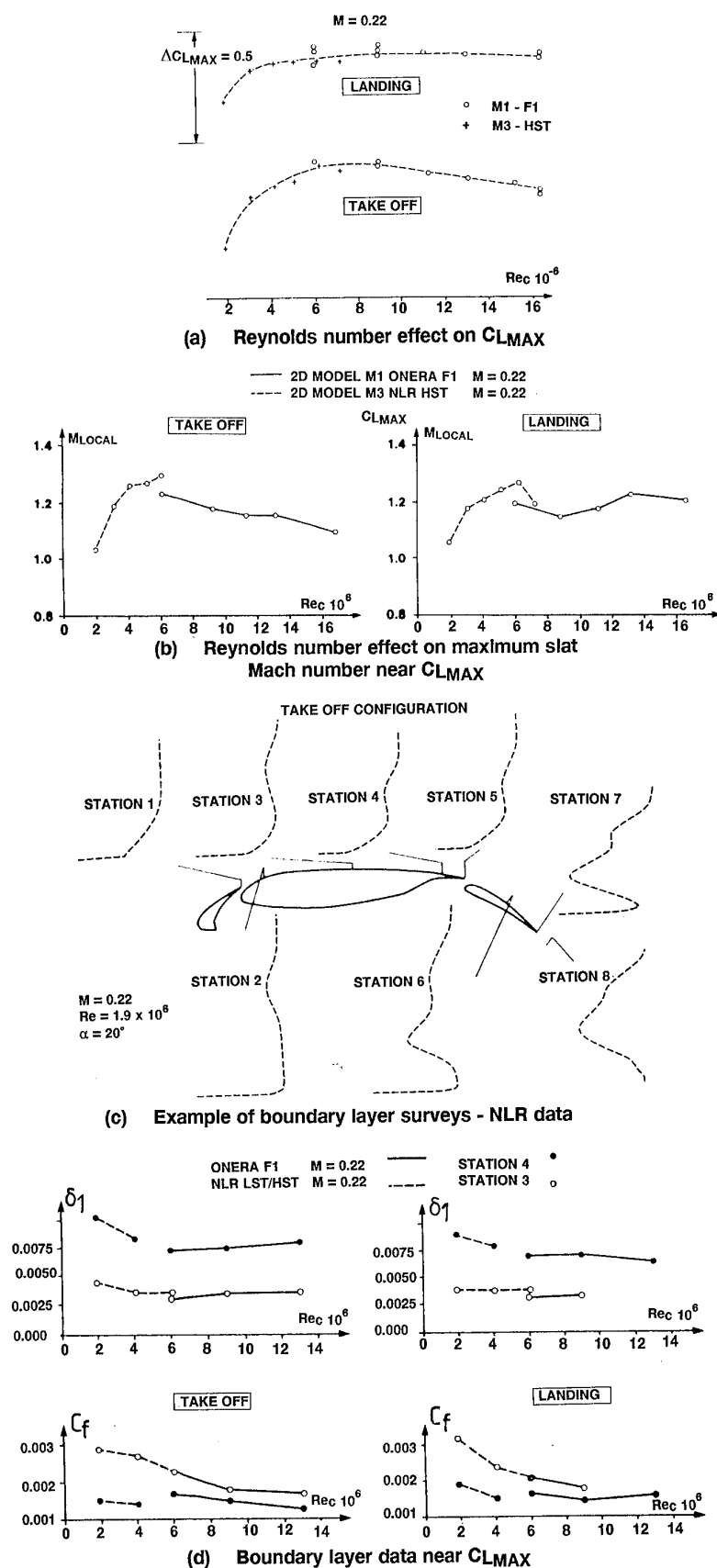
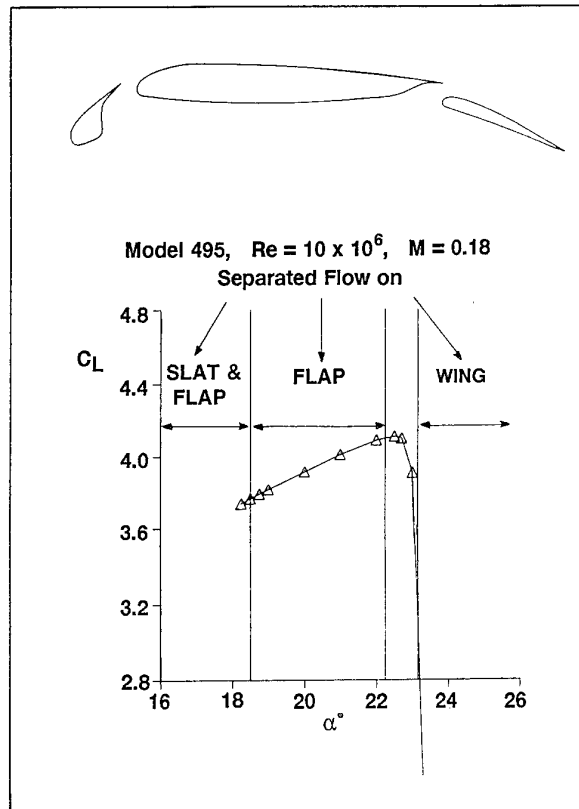


FIG 3.43 2D Results from Garteur High Lift Research Programme  
(from ref 111)



(a) Use of FELMA to predict  $C_L$  near  $C_{LMAX}$  for 3-Element 3D Wing

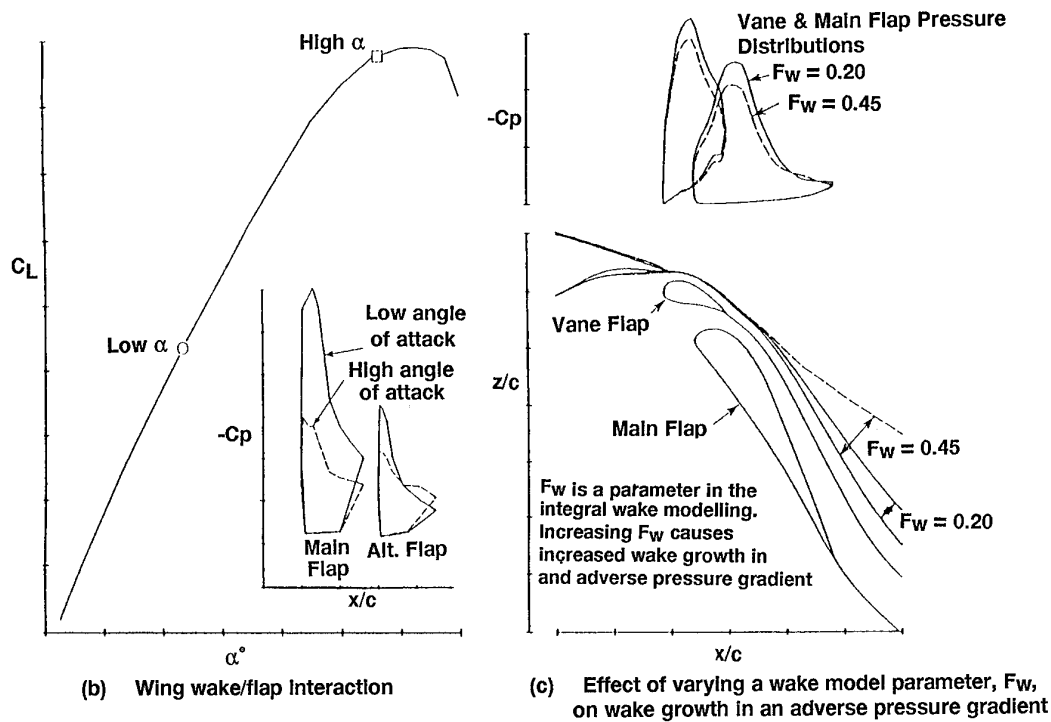


FIG 3.44 Boeing Theoretical Predictions for Wing Wake/Flap Interaction  
(from refs 99, 112)

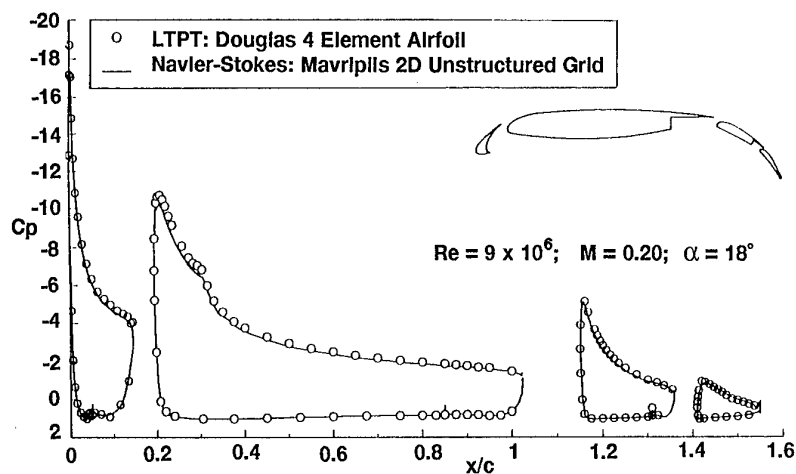
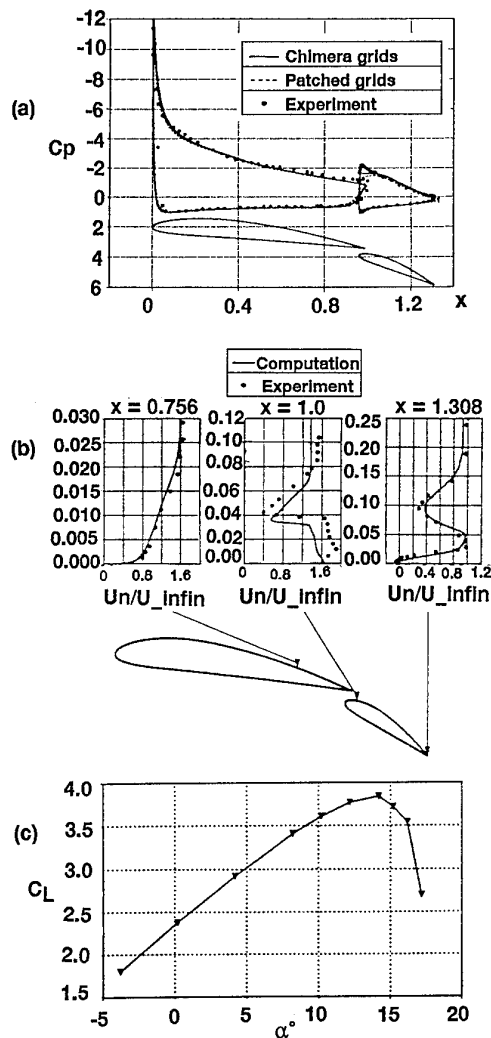
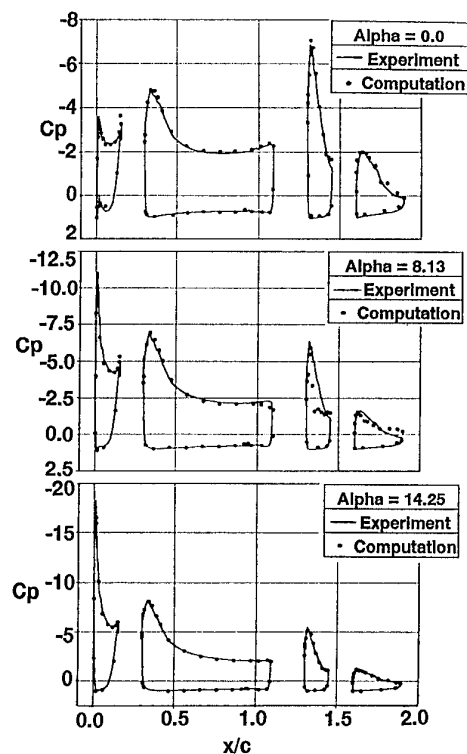


FIG 3.45 Navier-Stokes calculation (unstructured grid)  
for 4-Element Multi-Airfoil  
(from ref 117)



(a),(b),(c) Navier-Stokes calculation (structured grid)  
for 2-Element Airfoil



(d) Navier-Stokes calculation (structured grid)  
for 4-Element Airfoil tested by Omar et al (ref121)

FIG 3. 46 NASA Ames N-S Calculations  
(from ref 113)

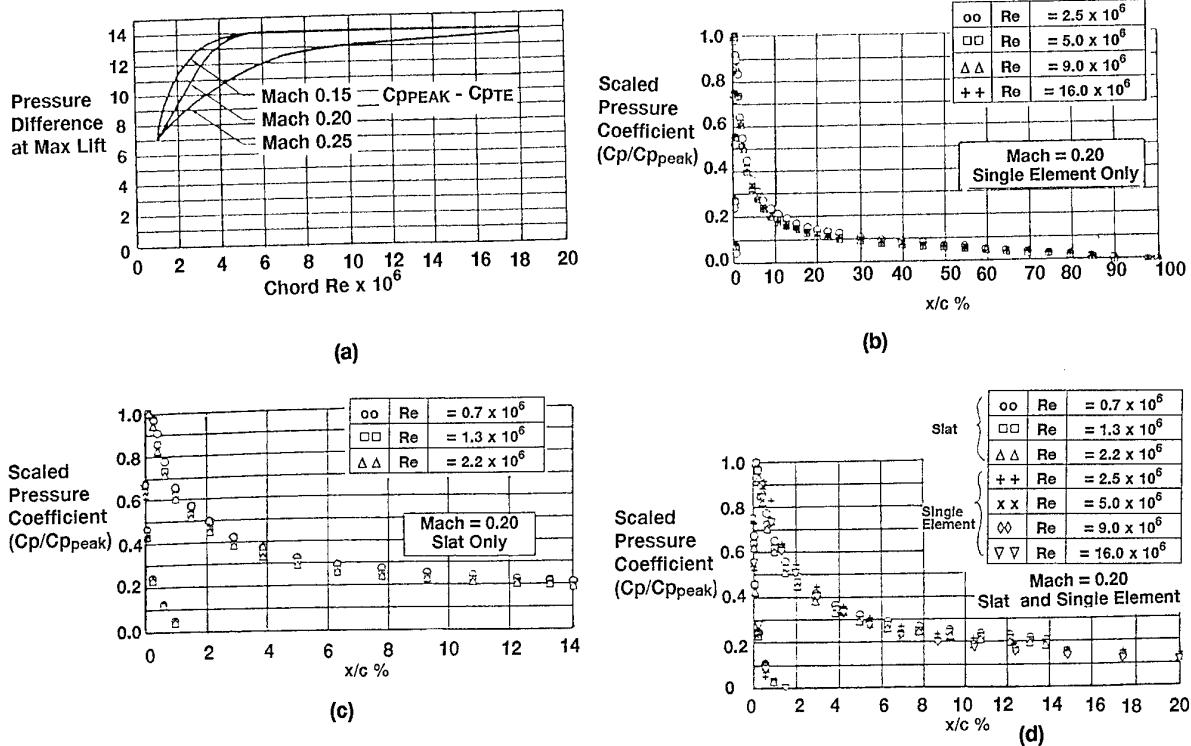


**FIG 3.47 Evidence in Support of Douglas Maximum Lift Prediction Method for Multi-Element Wings**  
(from ref 122)

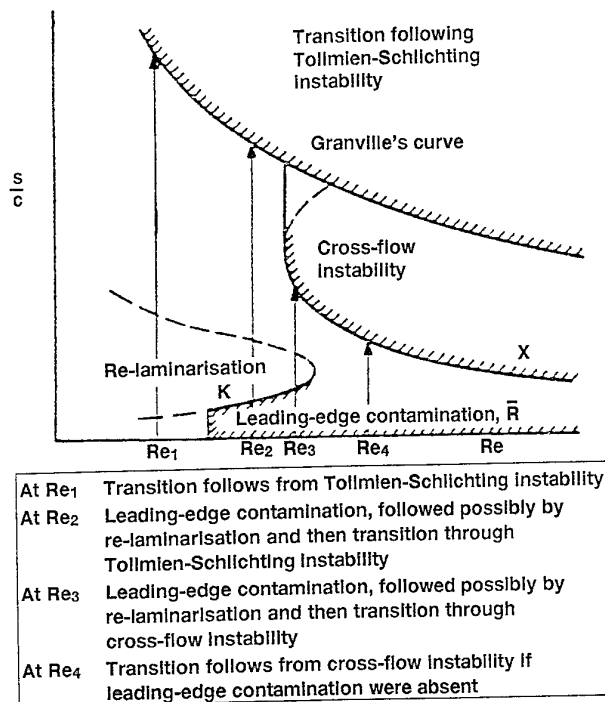


**FIG 3.48 Schematic Sketch of Re Effects on Transition or Boundary Layer Instability on 3D Swept Back Wing**  
(from Hall and Treadgold, 1972 ref 123)

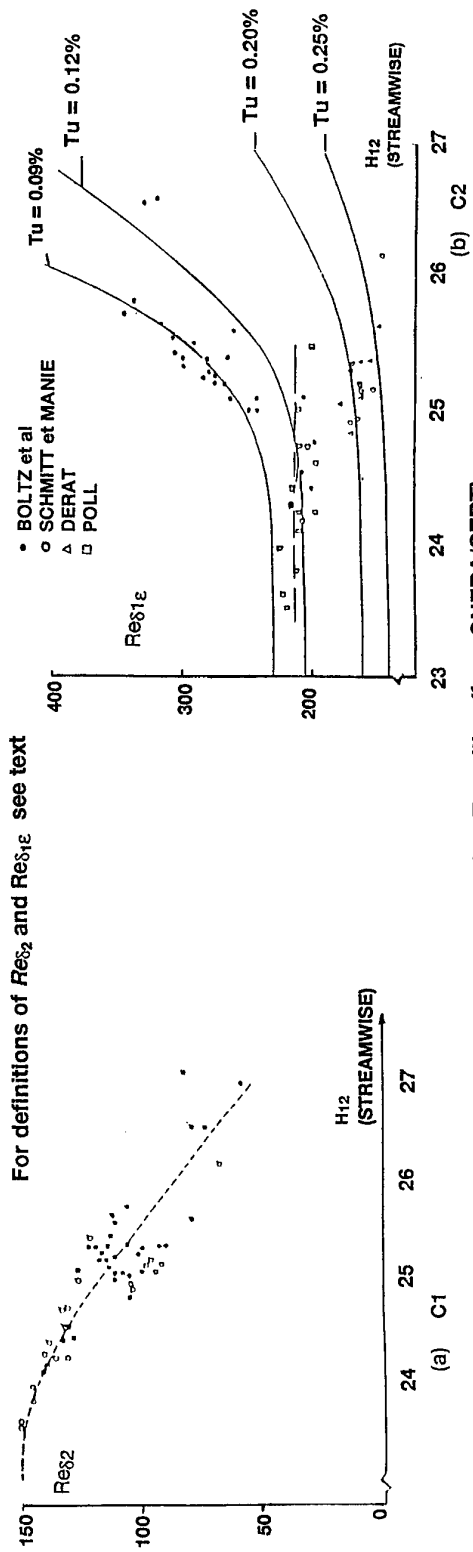


FIG 3.49 Criteria for Cross Flow Transition (from ONERA/CERT)  
(from ref 129)

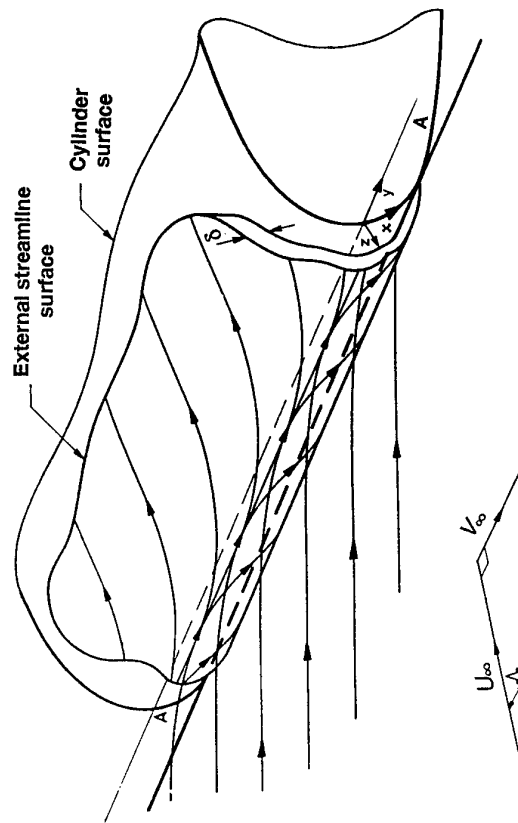


FIG 3.50 Flow Near the Leading Edge of a Swept Cylinder  
(from ref 132)

(a) Transition characteristics in the absence of a trip wire

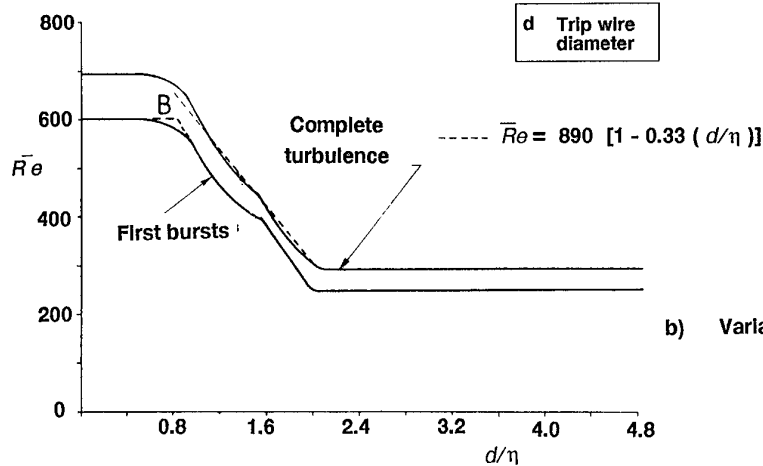
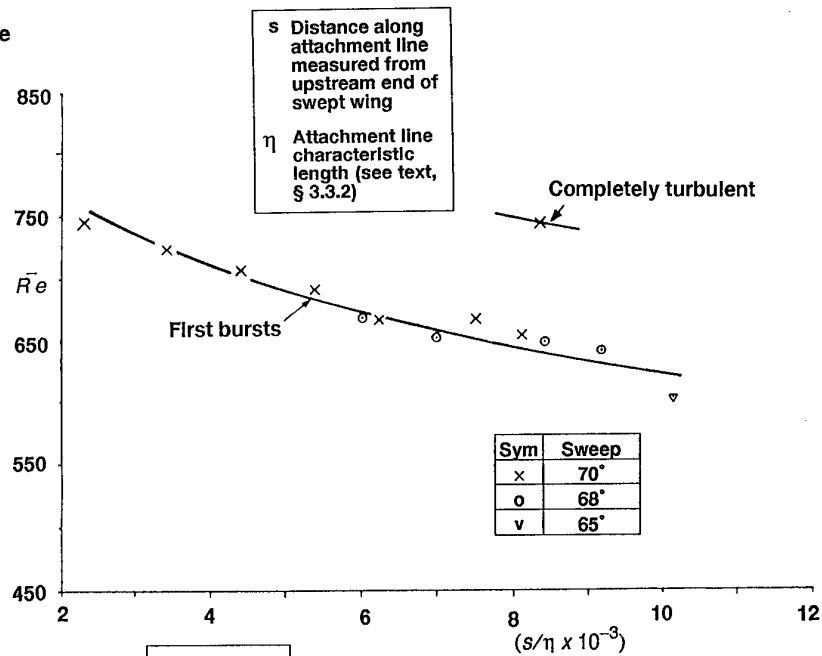
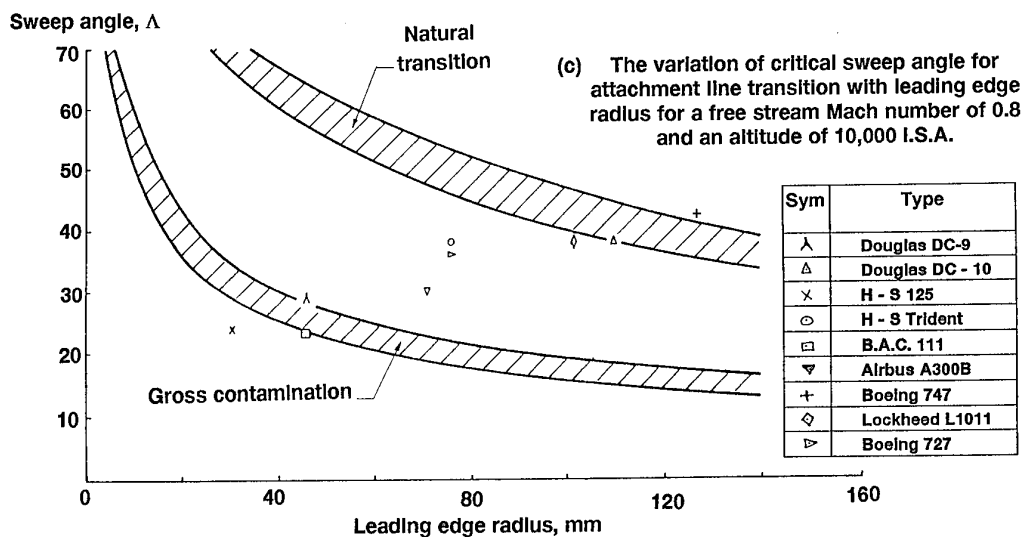
b) Variation of  $\bar{Re}$  crit. with  $d/\eta$  in the limit as  $s/\eta$  tends to infinity

Fig 3.51 Attachment Line Transition: Results from Cranfield: Cruising Flight Research by Poll  
(from ref 132)



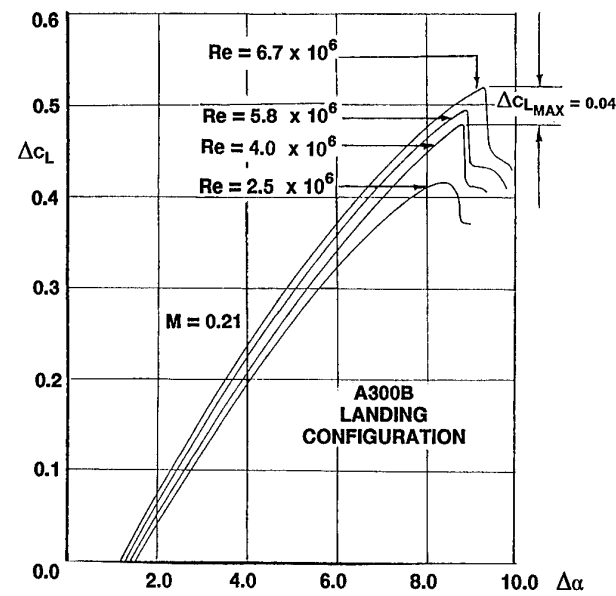


FIG 3.52 Example of Conventional Scale Effect  
(from ref 63)

(a) Effect of nacelles on  $CL_{MAX}$ :  
Flight-Tunnel comparison

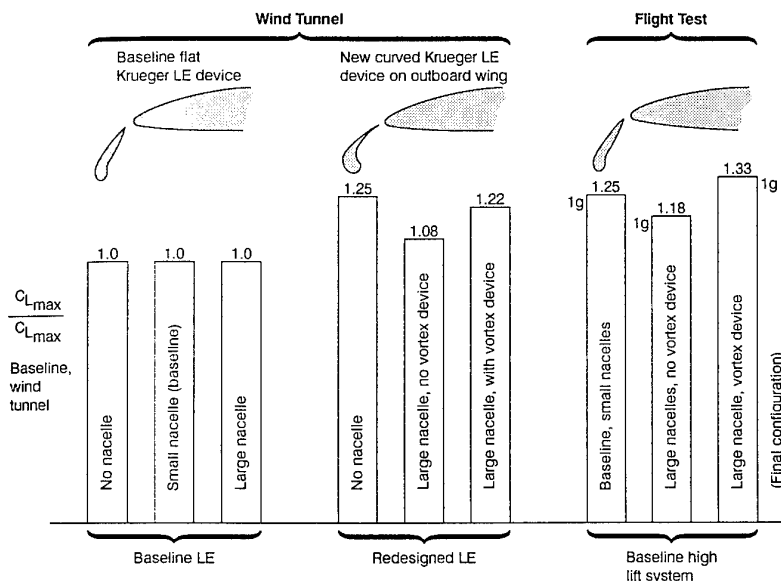
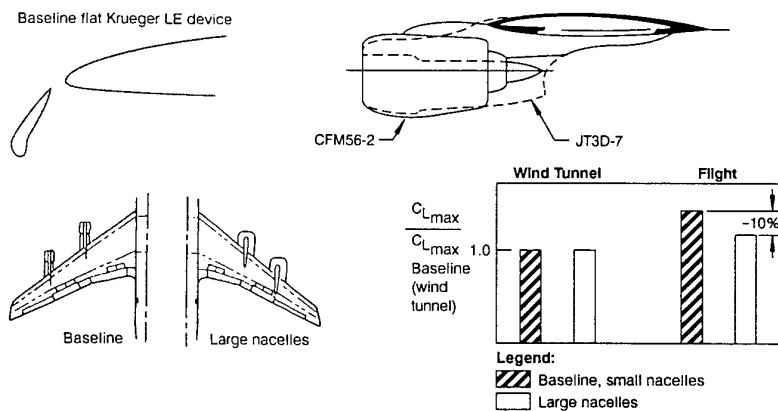
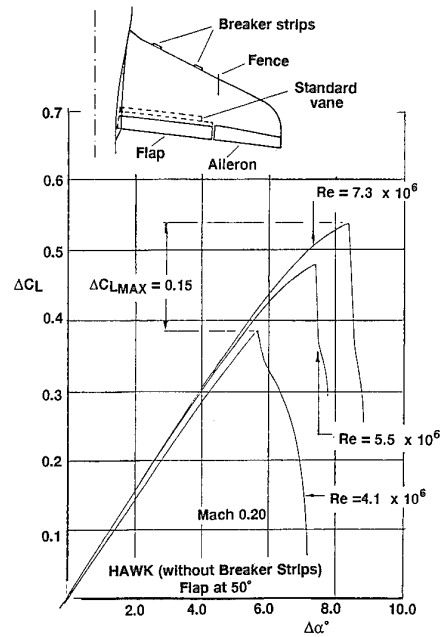
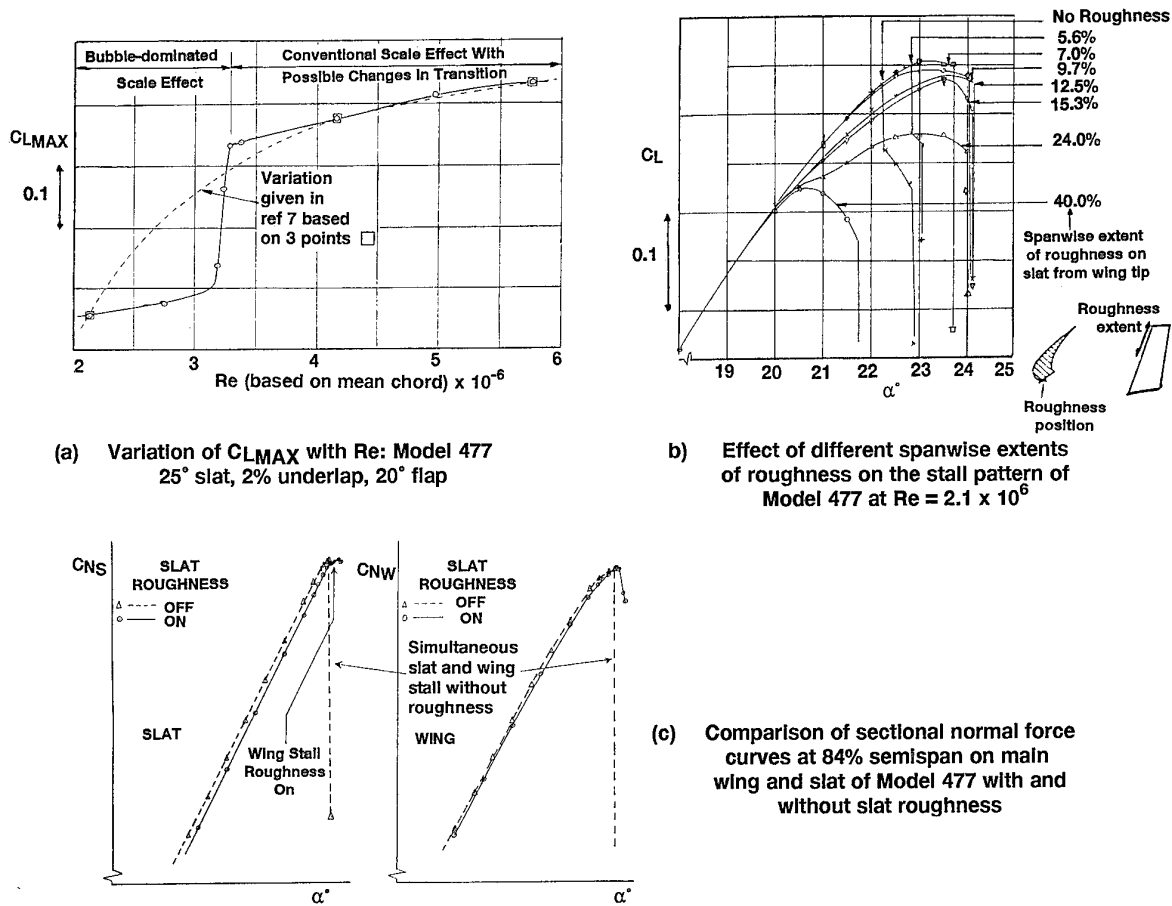


FIG 3.53 Example of Consequences of Spanwise Variation  
in Conventional Scale Effect  
(from ref 137)

b) Use of modified geometry on  
Tunnel Model to solve nacelle problem



**FIG 3.54 Example of Bubble-Dominated Scale Effect**  
(from ref 63)



**FIG 3.55 Example of Bubble-Dominated Scale Effect Changing to Conventional Scale Effect (at  $Re \sim 3.4 \times 10^6$ )**  
(from ref 63)

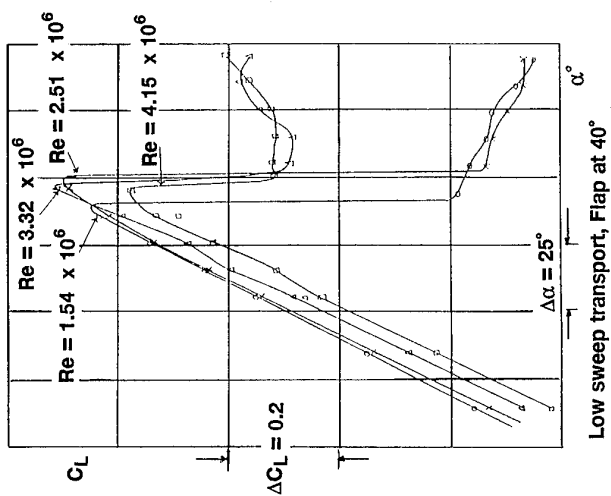


FIG 3.56 Example of Slot-Flow  
Dominated Scale Effect  
(from ref 63)

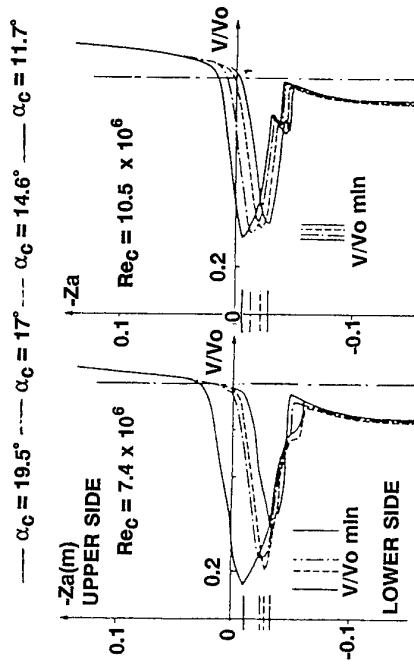


FIG 3.57 Scale Effect on Merging of Flap and Wing Wakes  
(from ref 111)

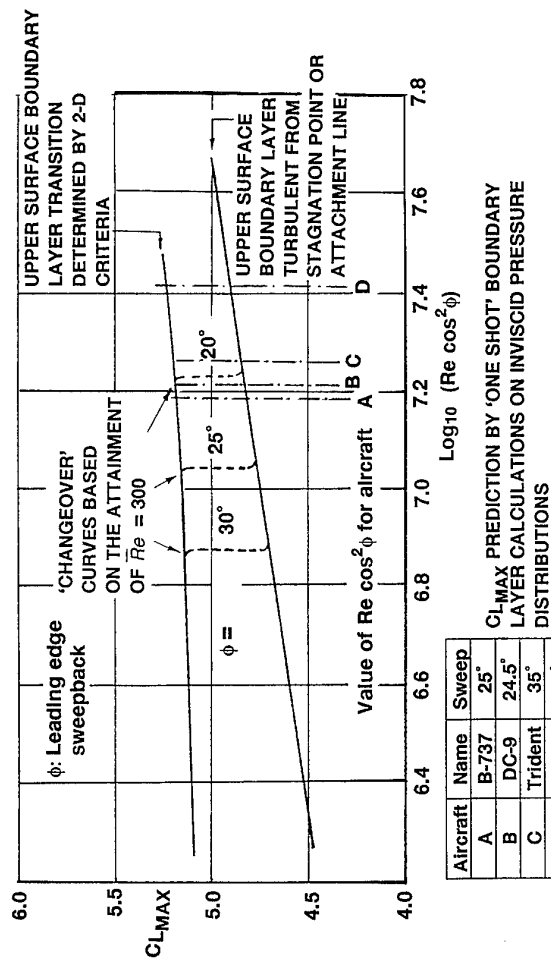
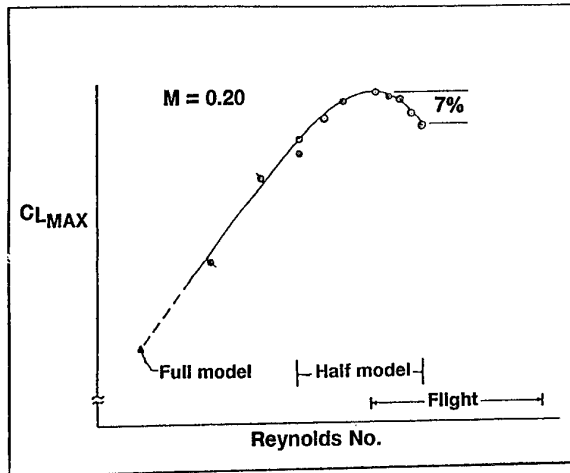
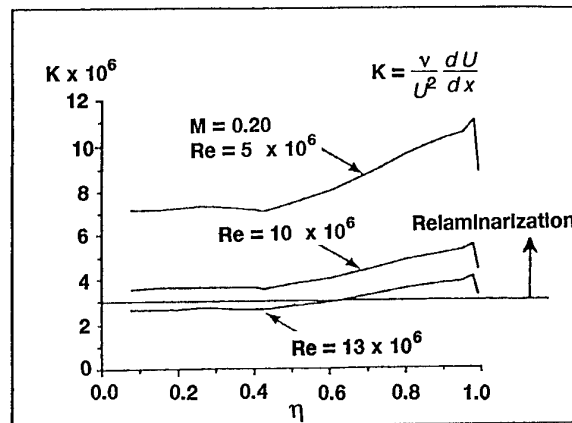


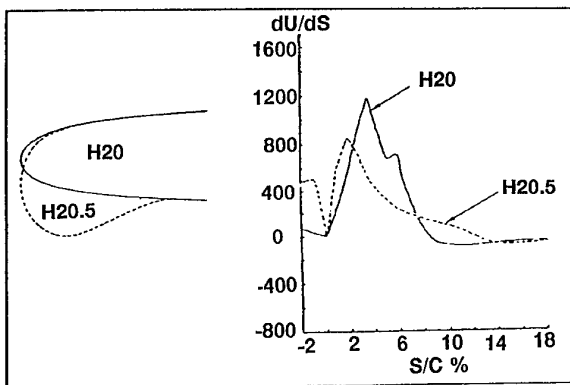
FIG 3.58 Predicted  $C_{LMAX}$  Variation with Reynolds Number: Effect of ALT  
(calculated originally for flexible Krueger leading-edge device  
but thought to apply more generally)  
(from ref 63)



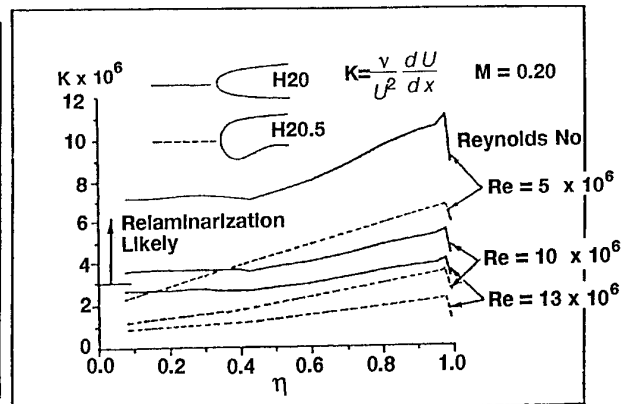
(a) Variation of  $CL_{MAX}$  with Reynolds number for a simple swept wing



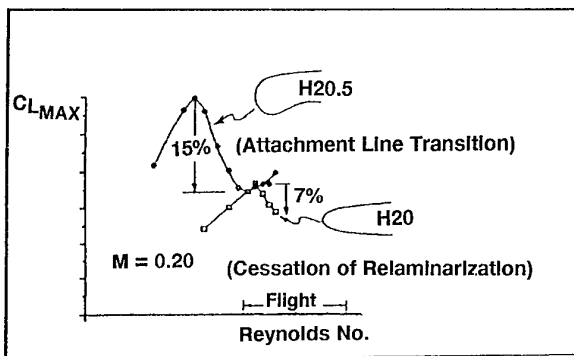
(b) Spanwise variation of the relaminarization parameter  $K$  for a simple swept wing



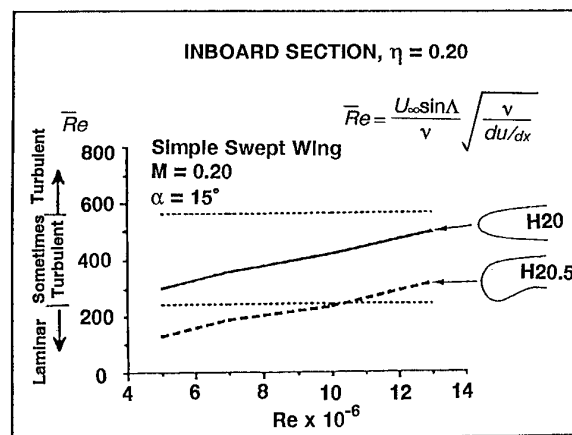
(c) Leading edge shape modification to reduce velocity gradients



(d) Effect of leading edge shape modification on the relaminarization parameter  $K$



(e) Effect of leading edge shape modification on  $CL_{MAX}$  variation with Reynolds number



(f) Effect of leading edge shape modification on the attachment line Reynolds number  $\bar{Re}$

FIG 3.59 Examples of Transition - Dominated Scale Effect  
(from ref 102)

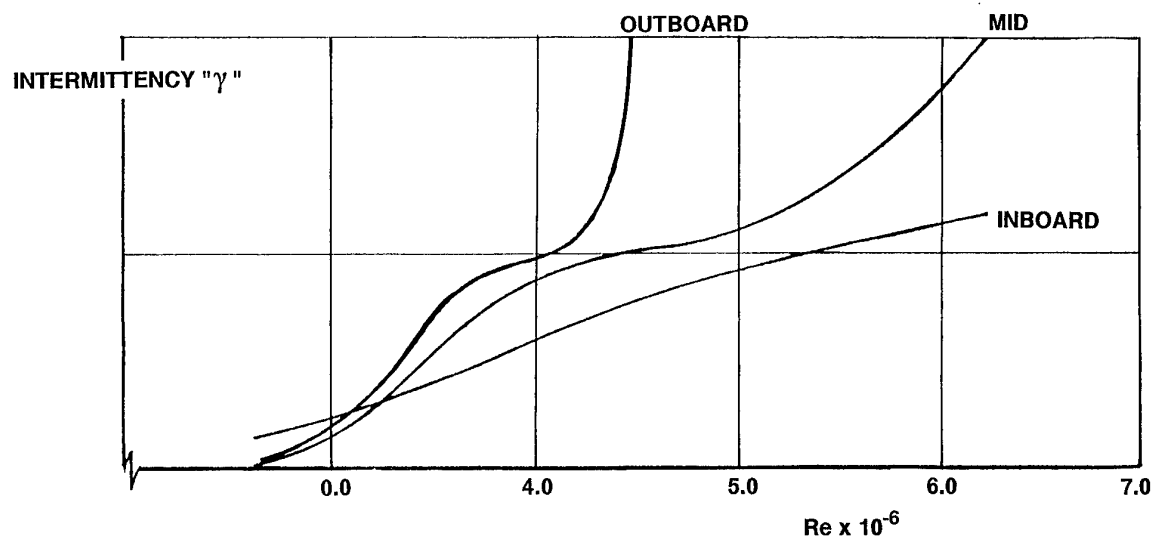
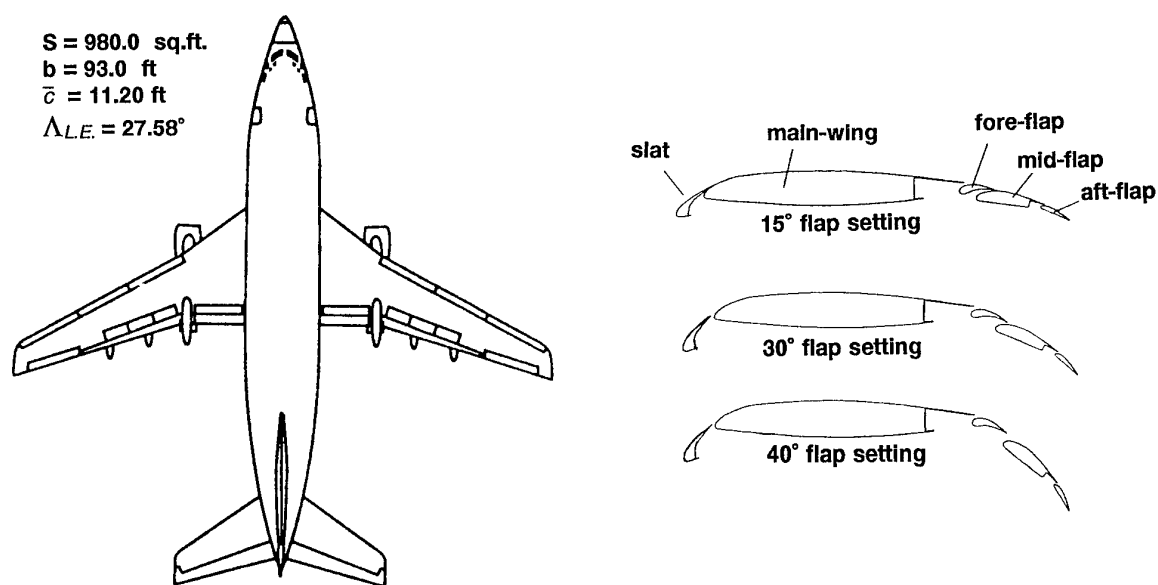


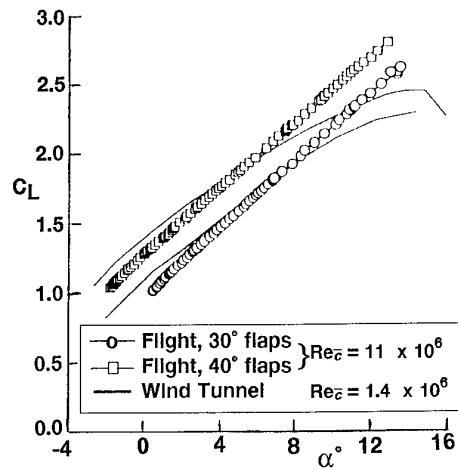
FIG 3.60 Spanwise Variation of Attachment Line Turbulence  
with Reynolds Number - Model 477 with Plain Leading-Edge  
(from ref 63)



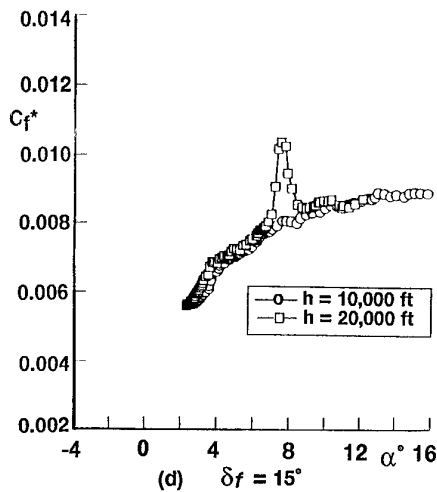
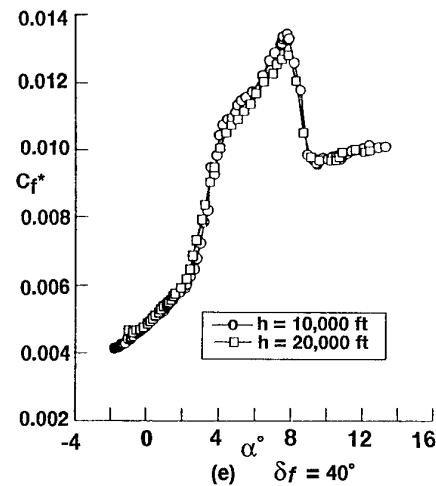
(a) Planform view of the B737 - 100 aircraft

(b) Wing sections at various flap settings

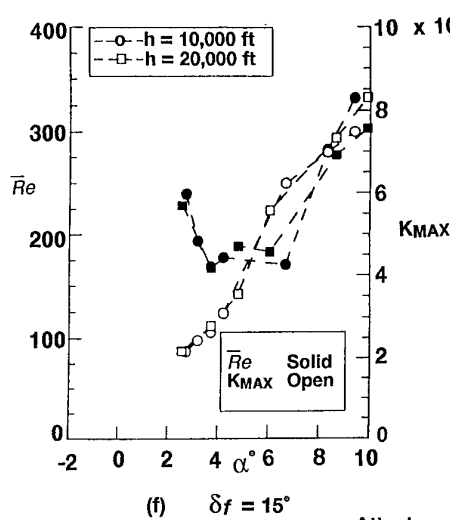
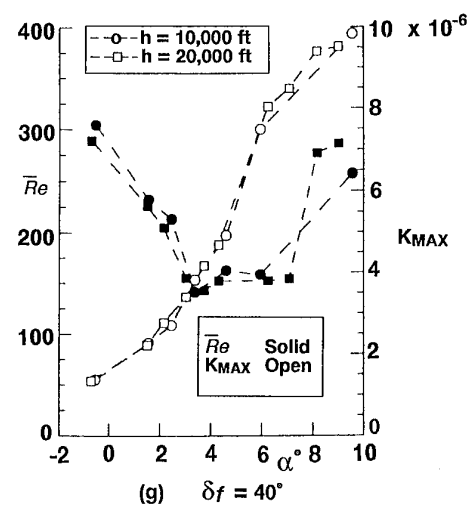
FIG 3.61 NASA Langley Subsonic Transport High-Lift Research Program  
(from ref 138)



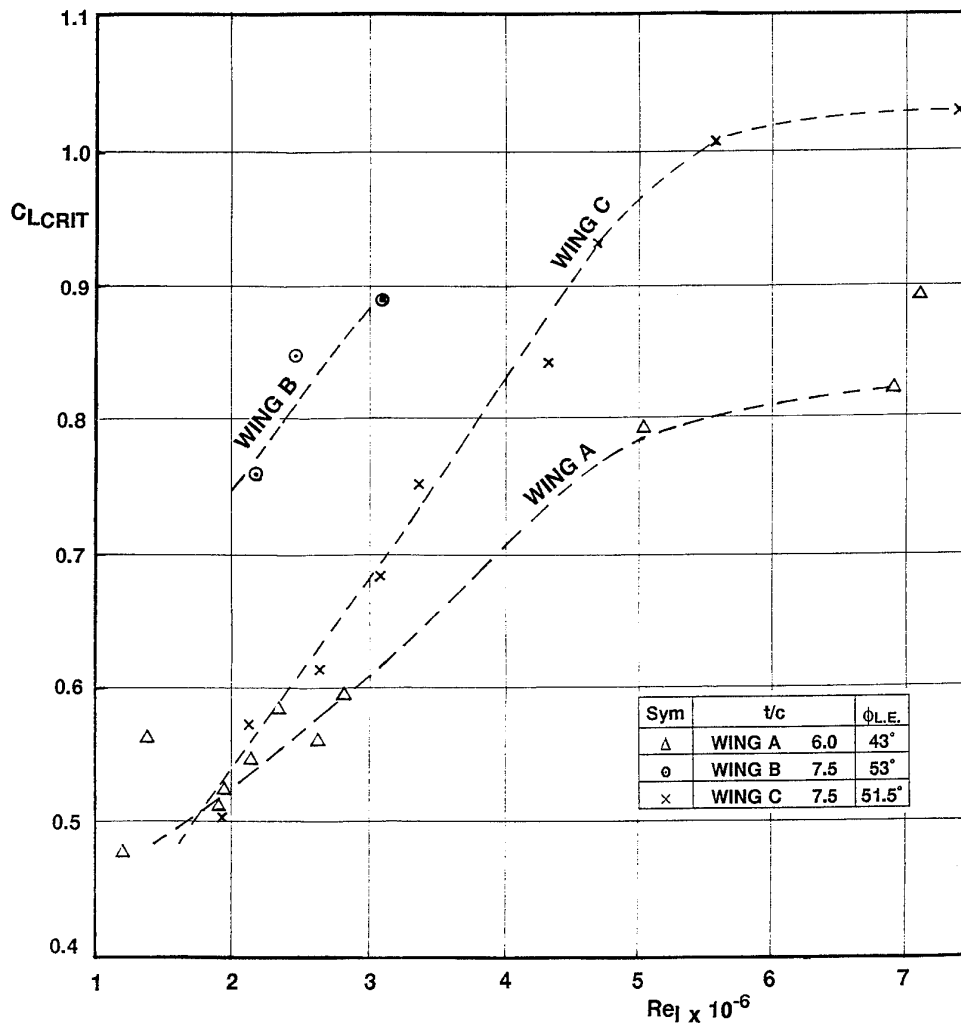
(c) Comparison of flight and wind-tunnel lift data

(d)  $\delta_f = 15^\circ$ (e)  $\delta_f = 40^\circ$ 

Preston-tube measurements on slat  
(humps believed to indicate where tube  
protrudes out of thin laminar b.l.)

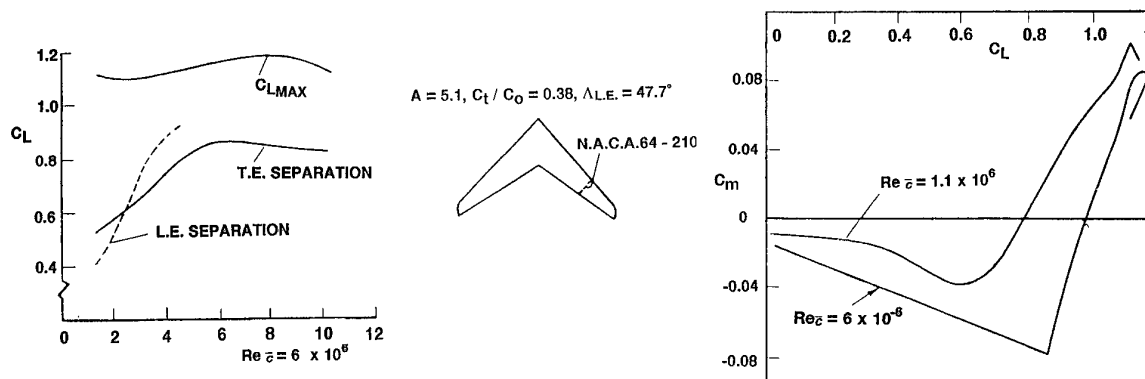
(f)  $\delta_f = 15^\circ$ (g)  $\delta_f = 40^\circ$ 

Attachment-line Reynolds number and  
relaminarization characteristics for the  
slat upper surface.

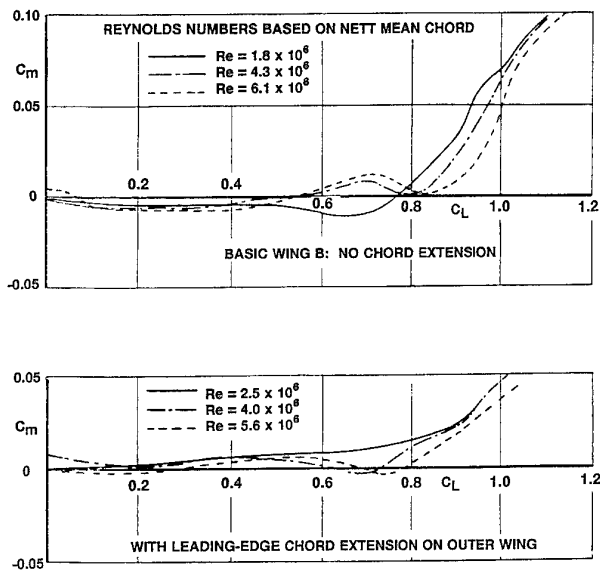


$C_{LCRIT}$  = APPROXIMATE VALUE OF  $C_L$  FOR FORMATION OF  
LONG BUBBLE SEPARATION NEAR LEADING EDGE  
 $Re_l$  = LOCAL REYNOLDS NUMBER

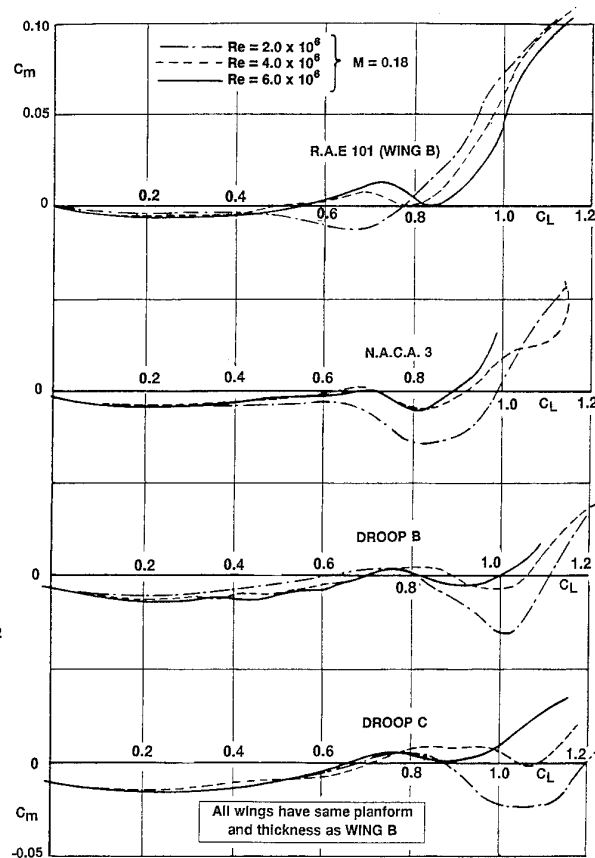
FIG 3.62 Effect of Reynolds Number on Formation of Long Bubble  
(Origin of Part-Span Vortex Sheet)  
(from ref 139)



**FIG 3.63 Scale Effect on Results for N.A.C.A. Swept Back Wing:**  
**N.A.C.A. Langley 19 ft Pressure Tunnel**  
 (from ref 140)

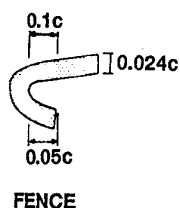
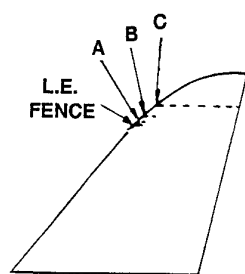


**FIG 3.64 Scale Effect on Effects of Chord Extension**  
 (from ref 139)

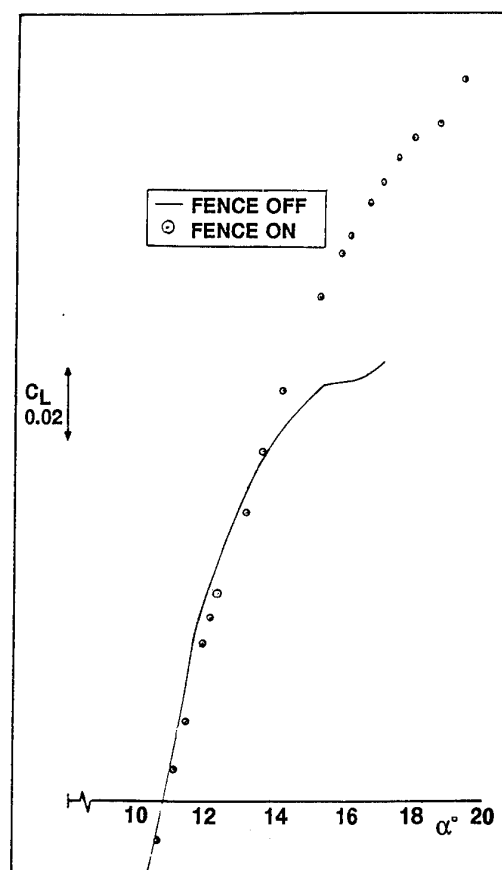
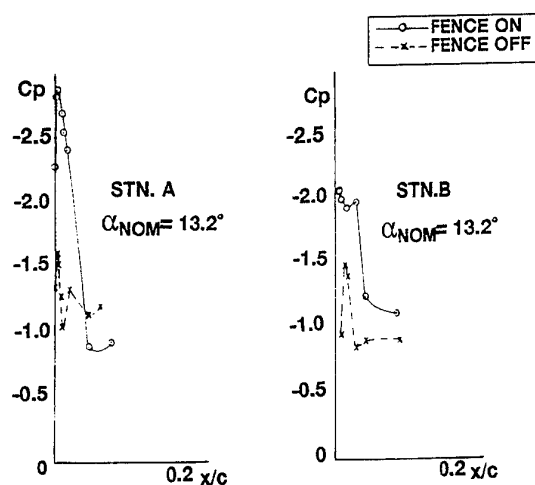
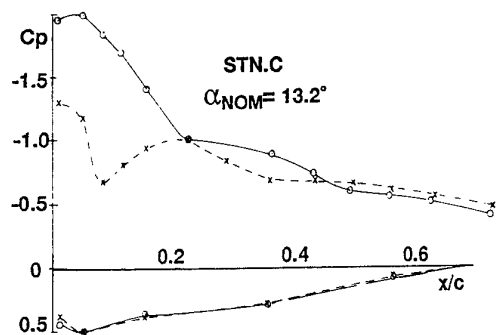


**Fig 3.65 Effect of Section Shape on Scale Effect on**  
**50° Swept Wings**  
 (from ref 139)

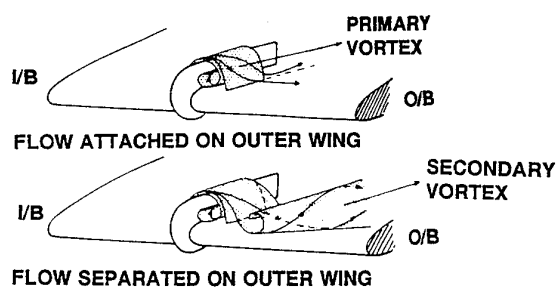




(a) Harrier model geometry

(b) Effect of fence on overall  $C_L \sim \alpha$ 

(d) Effect of fence on outer wing pressures



(c) Fence effect on wing upper surface flow

FIG 3.66 Effect of Leading Edge Fence on Usable Lift on Harrier  $M = 0.6$   
(Scale effect on optimum span-wise position of fence  
due to scale effect on outer-wing separation - see text)  
(from ref 142)

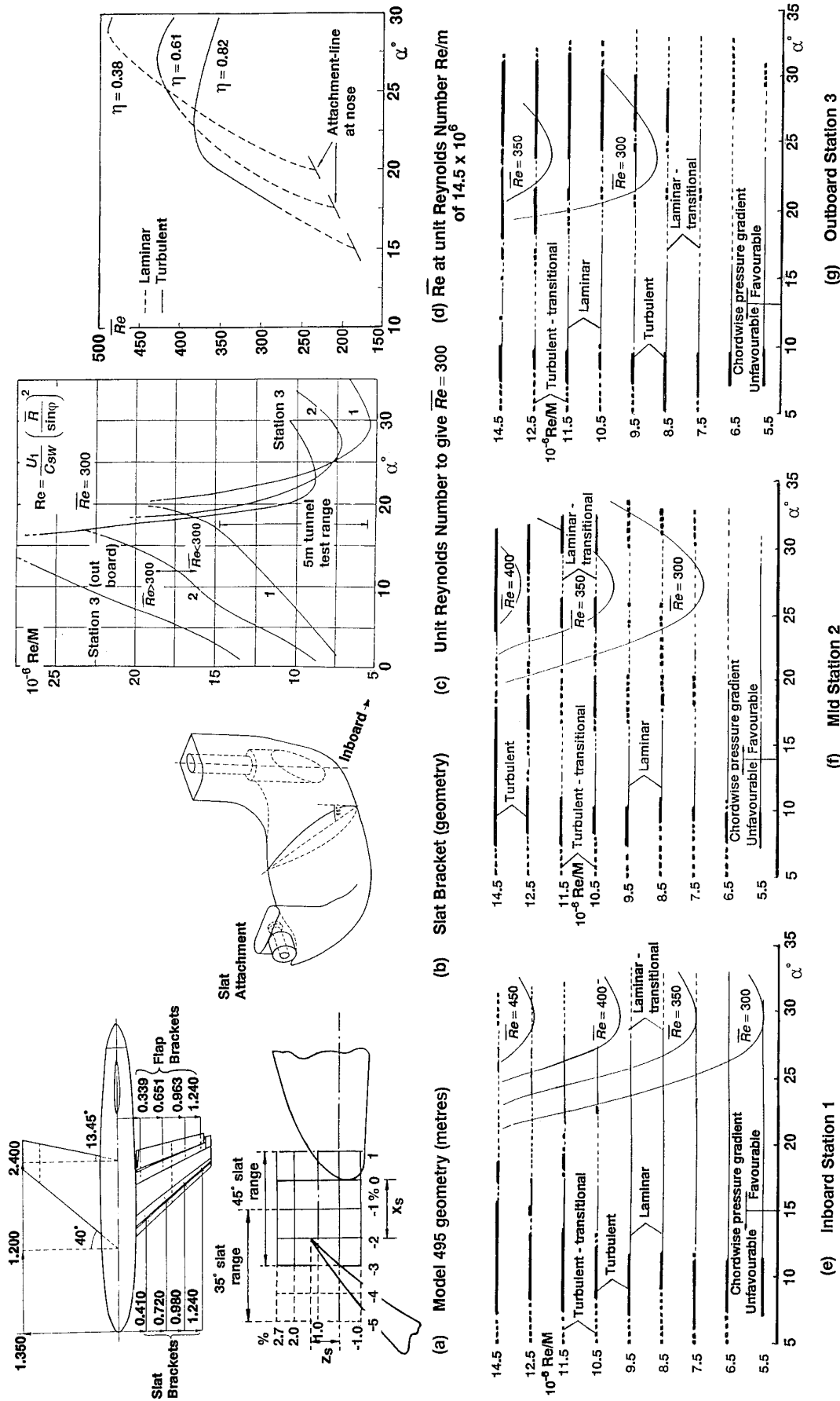
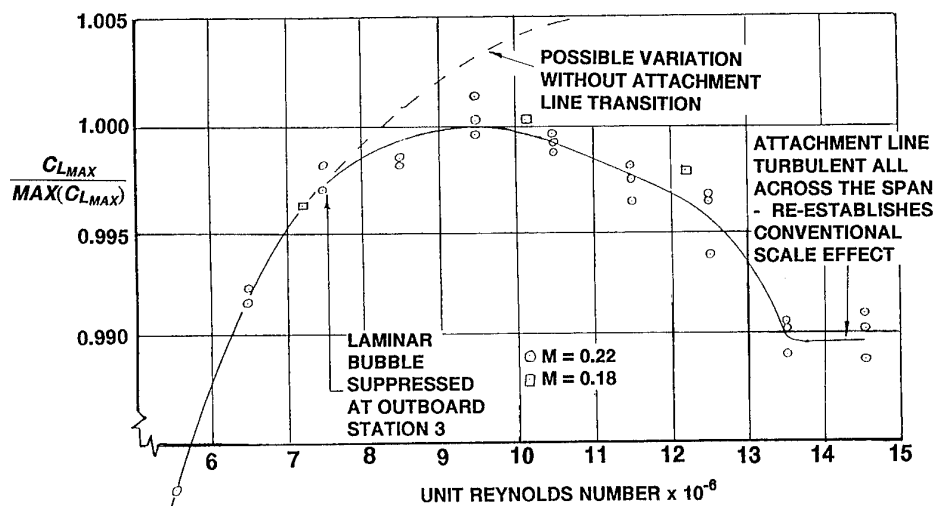
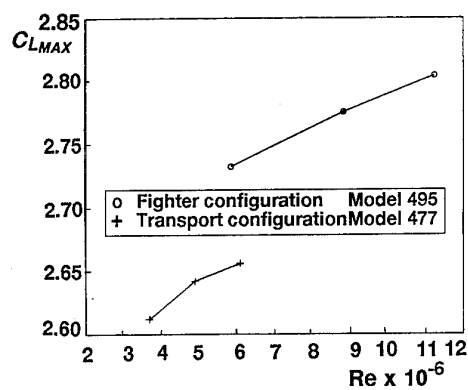
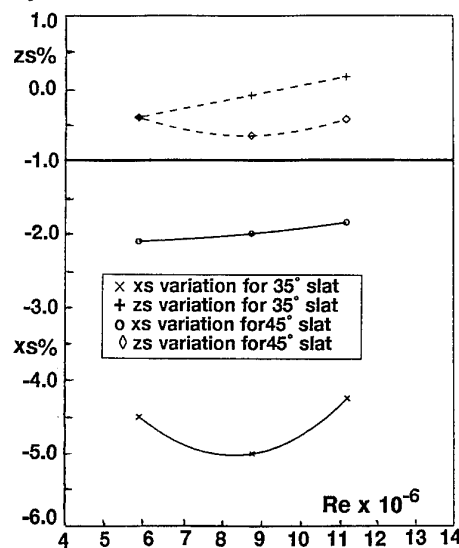


FIG 3.67 Results from DRA Strike-Fighter Research Model Tests in 5m Tunnel

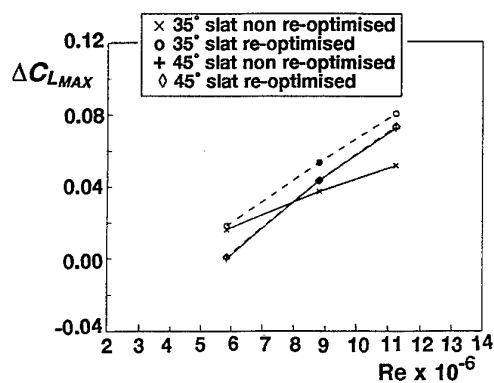
(from refs 136, 142, 143)

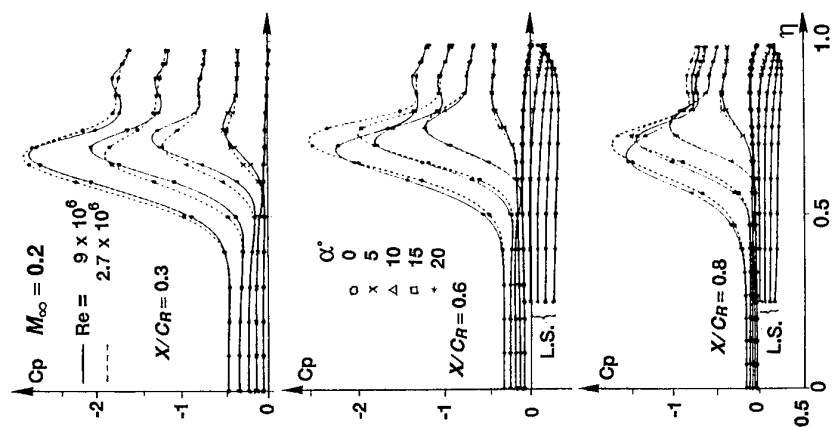


(h) Variation of maximum lift with Reynolds Number

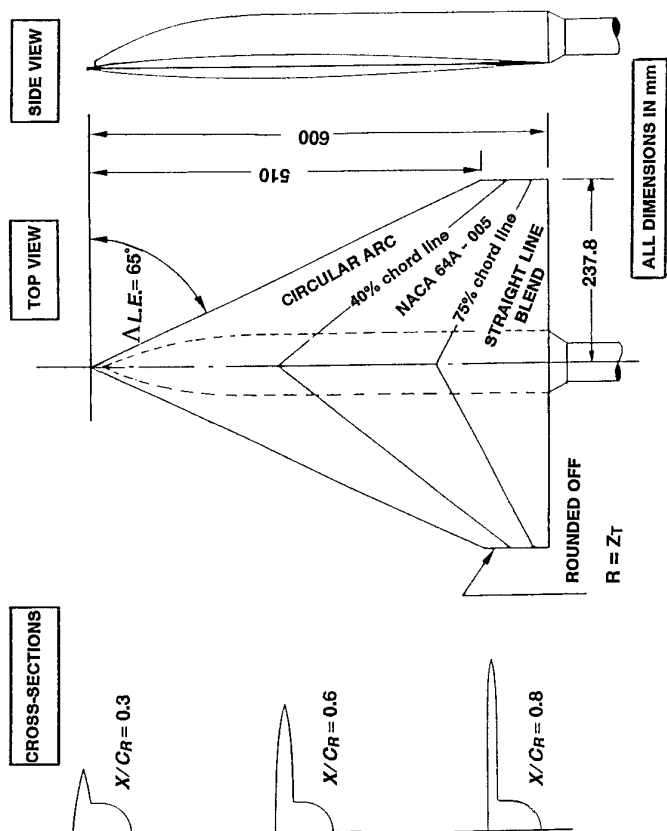
(j) Comparison of variation of  $C_{LMAX}$  with Reynolds Number for combat aircraft and transport aircraft

(k) Variation of optimum slat position with Reynolds Number

(l) Gain in  $C_{LMAX}$  obtained by re-optimising slat position at each Reynolds NumberFIG 3.67 (cont'd) Results from DRA Strike-Fighter Research Model Tests in 5m Tunnel  
(from refs 136, 142, 143)



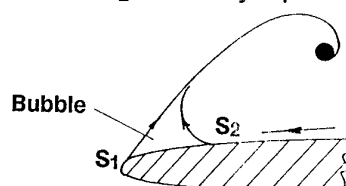
(b) Effect of  $Re$  on spanwise pressure distributions at  $M = 0.2$



(a) Slender Wing Model Geometry

FIG 3.68 Results for Sharp-Edged Delta Wing Tested at NLR  
(from ref 150)

S<sub>1</sub> Primary separation line  
S<sub>2</sub> Secondary separation line

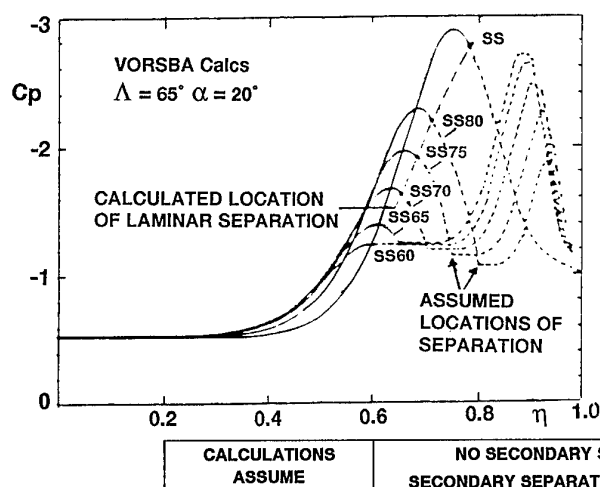


Flow with secondary separation

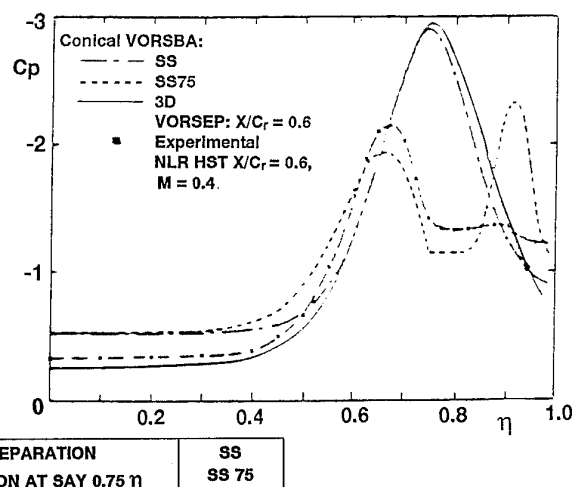


Smith's conception of separation from a smooth surface

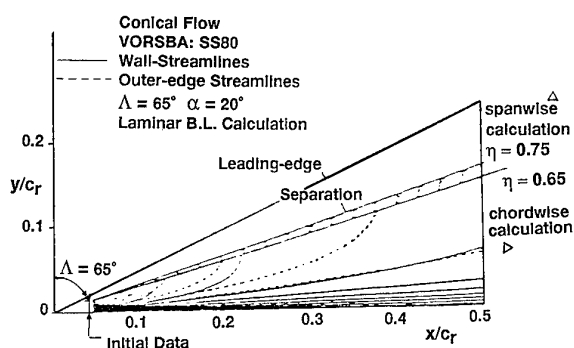
(a) Illustrative pictures reproduced from ref 151



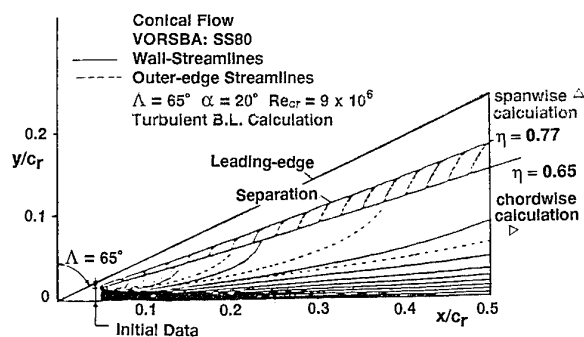
(b) Spanwise pressure distribution for various assumed locations of secondary separation



(c) Comparison of theoretical and experimental  $C_p$  distributions



(d) Calculated streamline patterns (laminar boundary layer)



(e) Calculated streamline patterns (turbulent boundary layer)

FIG 3.69 Influence of Secondary Separation on Upper Surface Flow on Sharp-Edged Slender Wing (from ref 148)

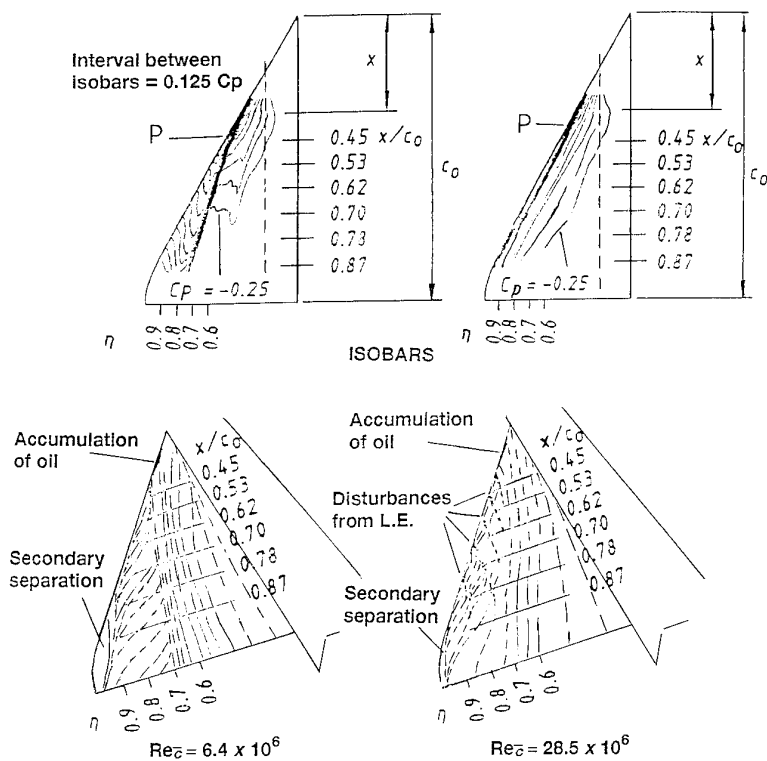
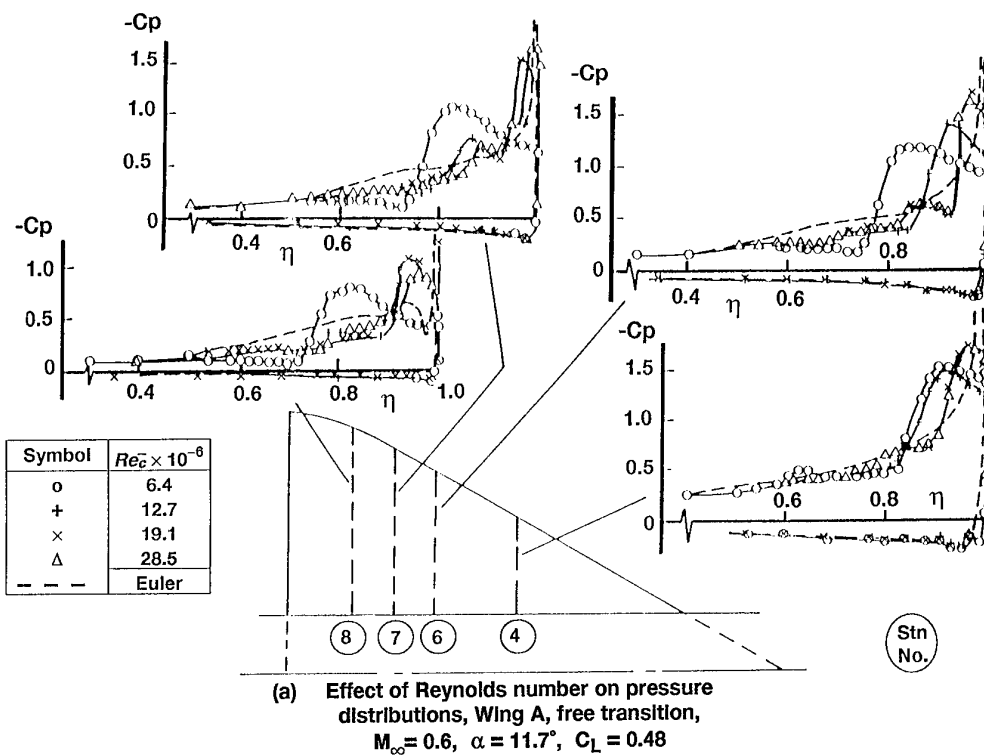
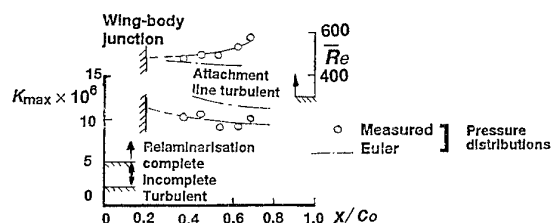
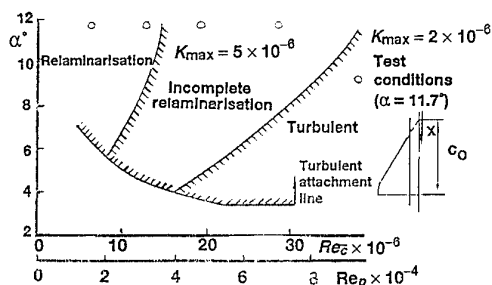


**FIG 3.70** Effect of  $Re$  on Flow over DRA Cambered Slender Wing Free Transition  
(from ref 151)

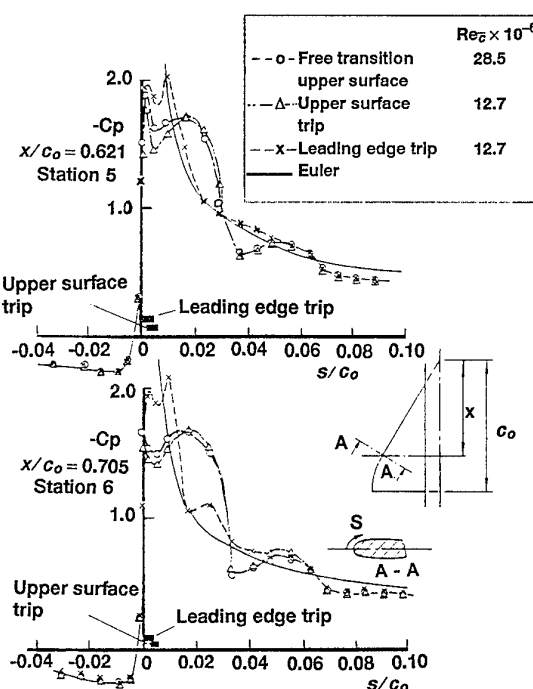


Axial variations of attachment-line contamination and relaminarisation parameters,  $\alpha = 11.7^\circ$ ,  $Re_{\bar{c}} = 6.4 \times 10^6$

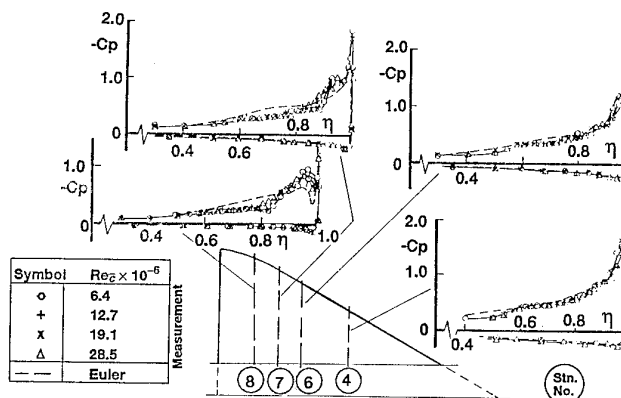
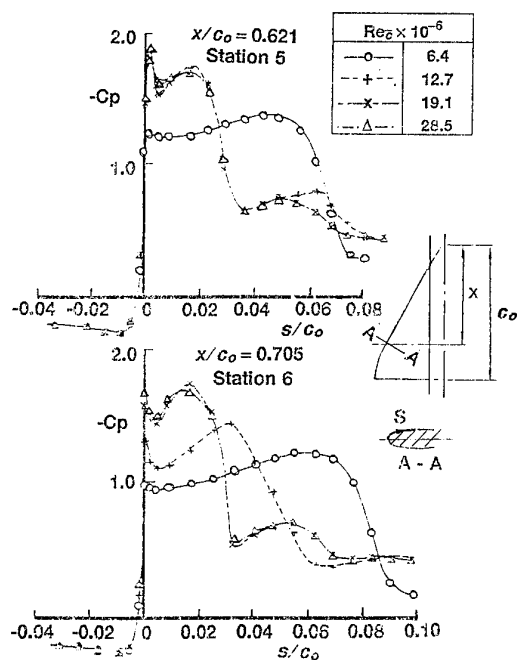


Attachment-line contamination and relaminarisation boundaries,  $x/c_o = 0.705$

(a) Calculated attachment-line and leading-edge relaminarisation conditions, Wing A,  $M_\infty = 0.6$



(c) Comparisons of pressure distributions around leading-edge, Wing A,  $M_\infty = 0.6$ ,  $\alpha = 11.7^\circ$



(d) Effect of Reynolds number on pressure distributions, Wing A, leading-edge trip,  $M_\infty = 0.6$ ,  $\alpha = 11.7^\circ$ ,  $C_L = 0.48$

(b) Pressure distributions around leading-edge Wing A, free transition,  $M_\infty = 0.6$ ,  $\alpha = 11.7^\circ$

FIG 3.71 Effect of Re and Transition Fixing on Results for DRA Cambered Slender Wing (from ref 151)

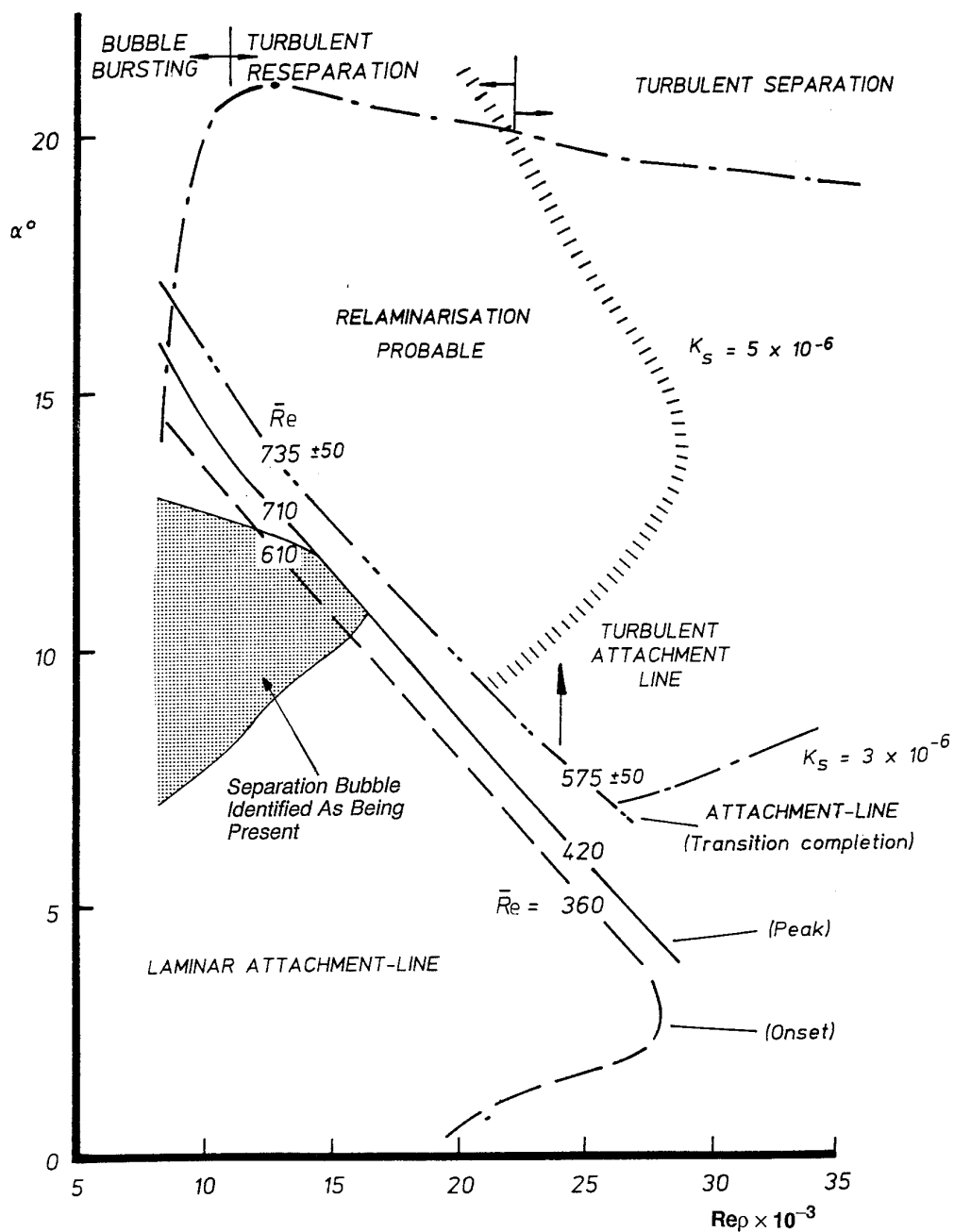
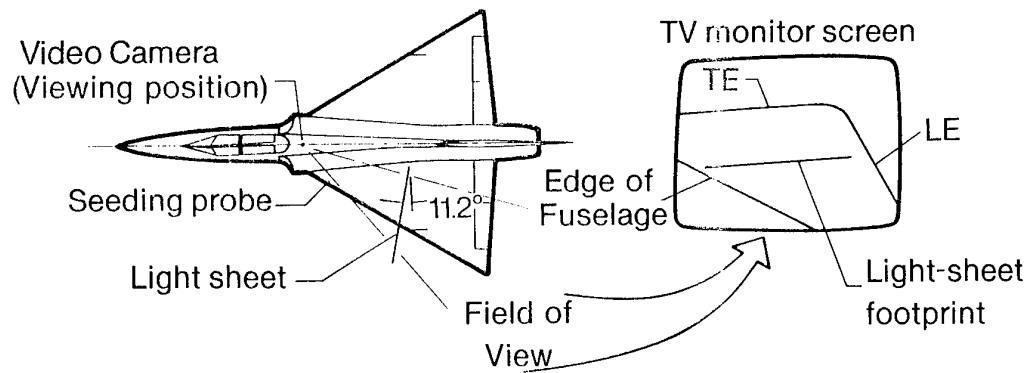
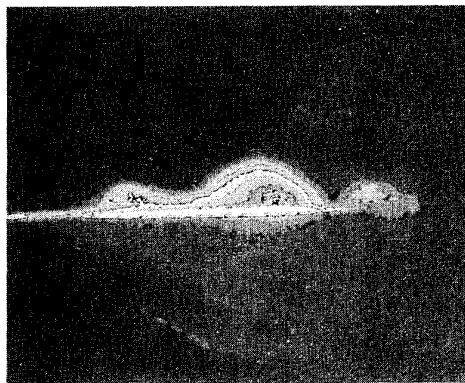


FIG 3.72 Boundaries and Regions of Leading-edge Flow Characteristics in Angle of Incidence ( $\alpha$ ) - Reynolds number ( $Re_p$ ) - plane DRA 60° Swept Panel Model  
(from ref 153)

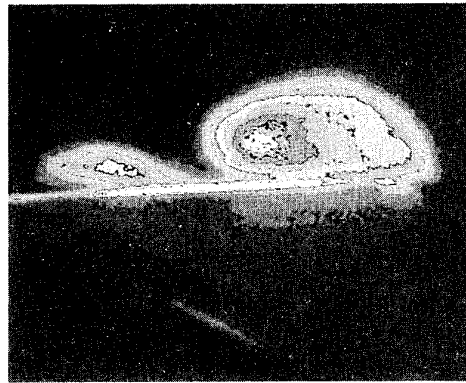




(a) In-flight leading-edge-vortex flow visualization of F-106B

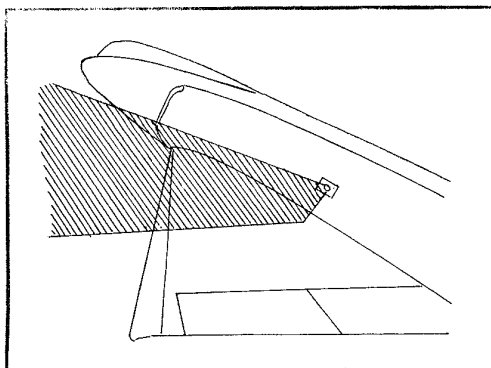


$\alpha = 17^\circ$

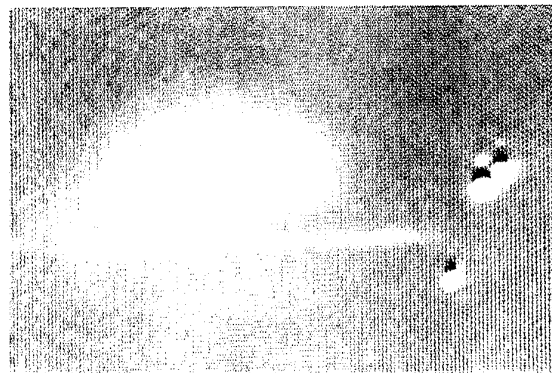


$\alpha = 20^\circ$

(b) In-flight vapour screen images.  $M = 0.4$ ,  
 $Re_n = 30 \times 10^6$ , altitude 25000ft, 1g maneuver



3/4 rear view



$\alpha = 20^\circ$

(c) Wind tunnel vapour screen image:  
Langley 30ft x 60ft tunnel,  $M = 0.1$ ,  
 $Re_n = 12 \times 10^6$ ,  $\alpha = 20^\circ$ , elevons  $5^\circ$  trailing edge up

FIG 3.73 Flow Visualisation Results from NASA-Langley Tests on F-106B  
(from ref 152 )

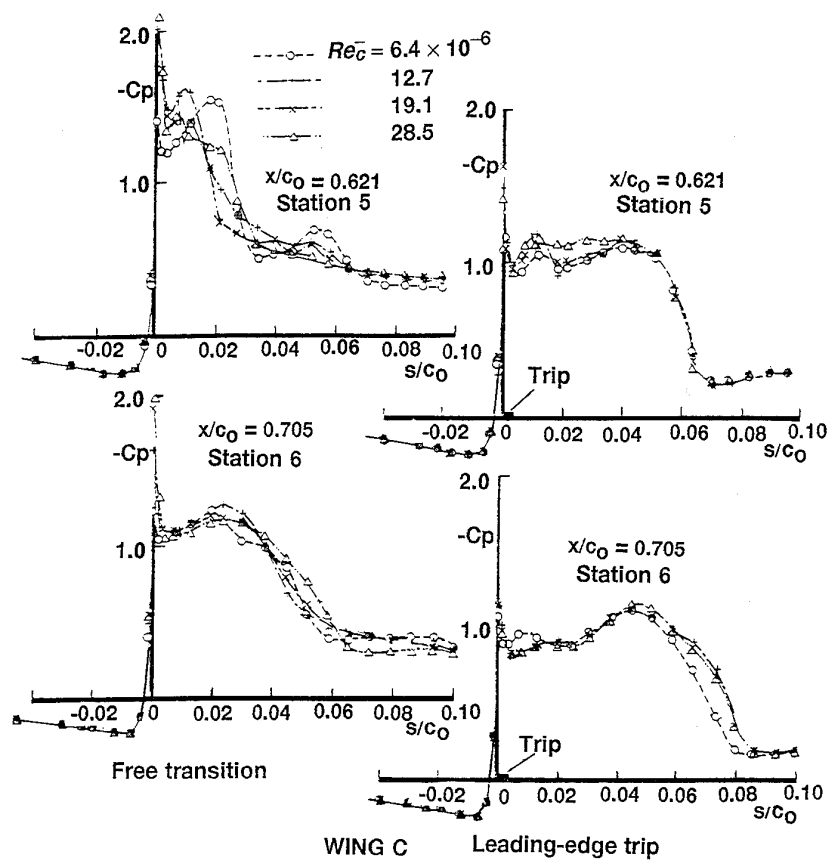
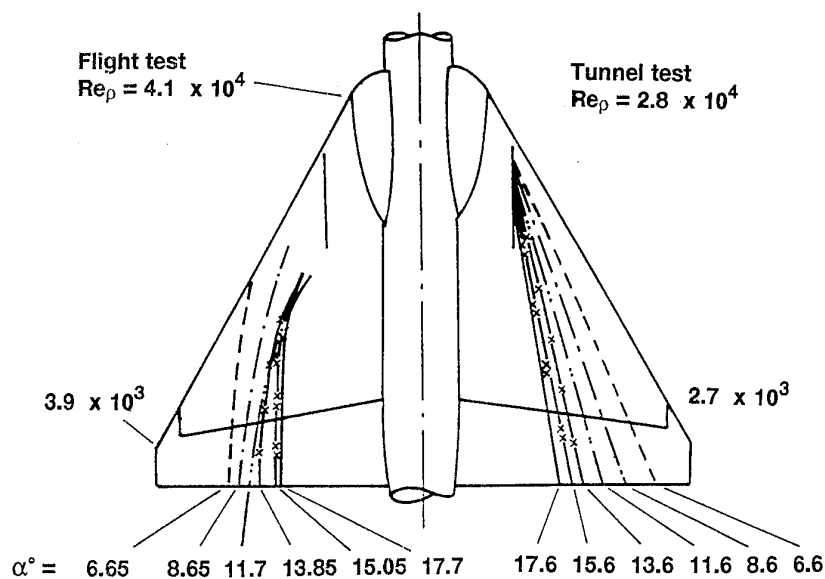
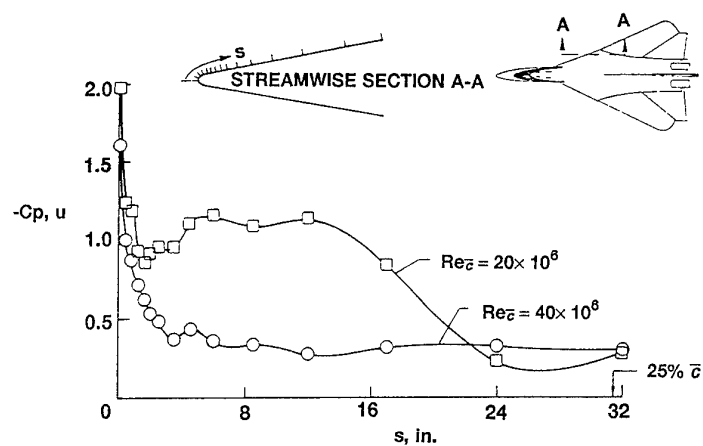


FIG 3.74 Effect of  $Re$  and transition fixing on flow over  
DRA symmetrical wing  
(from ref 151)



(a) Variation of reattachment-line position with incidence, Fairley Delta 2 flight and tunnel tests  $M_\infty = 0.5$

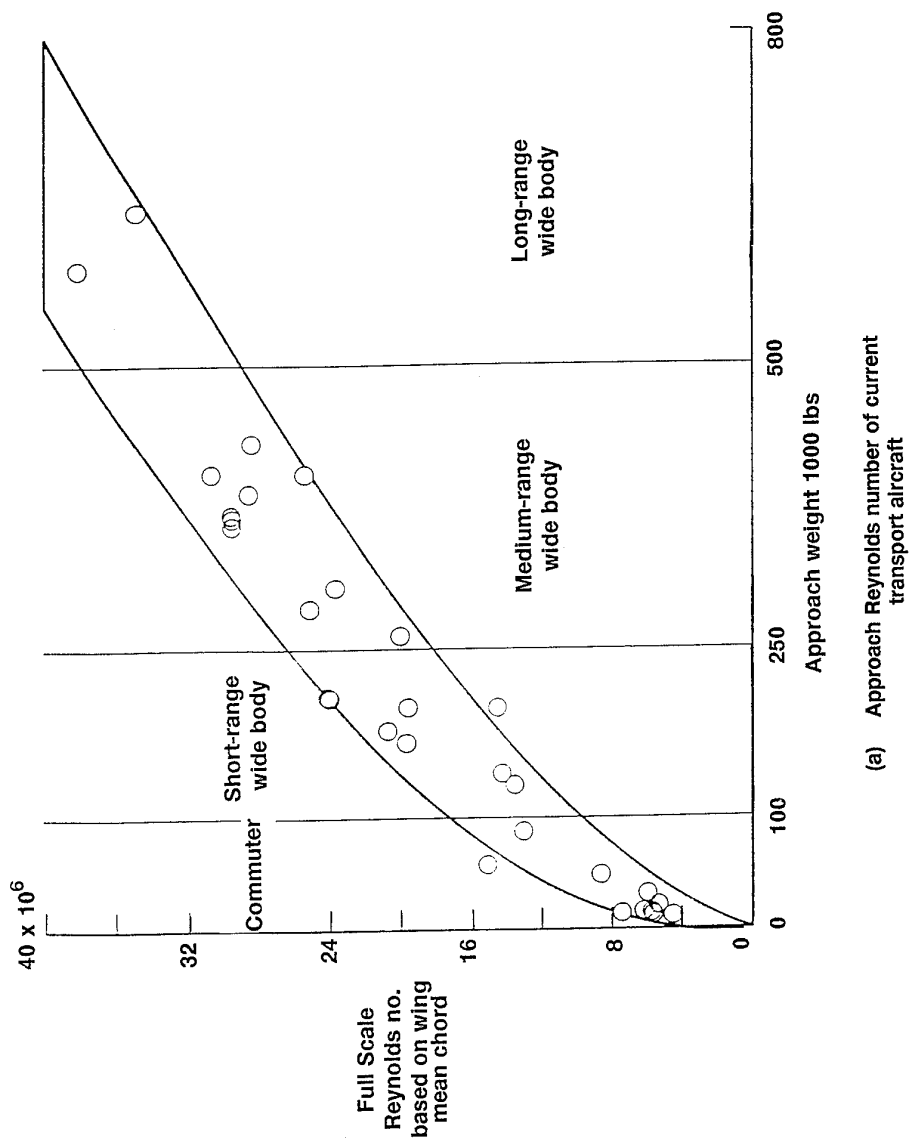
(from ref 161)



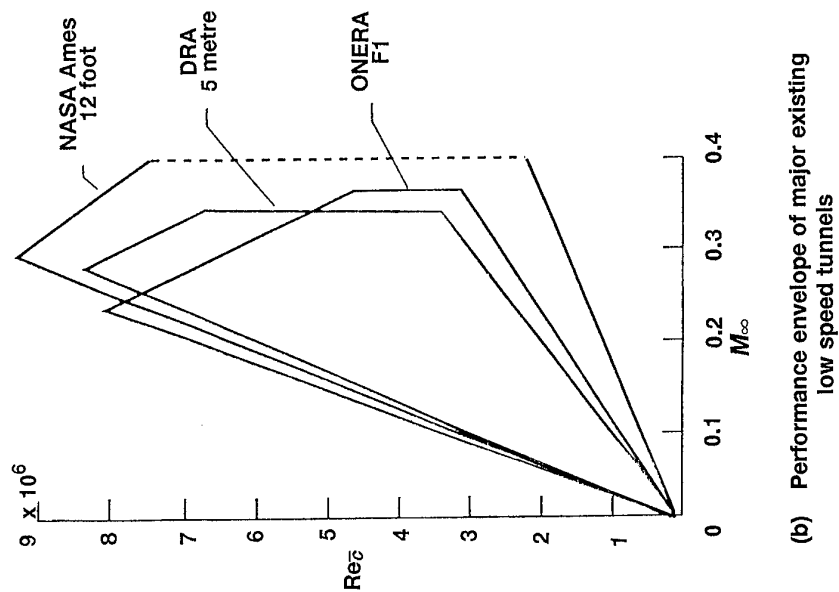
(b) Effect of Reynolds number on vortex flow development F-111 TACT flight experiment:  $\alpha = 6^\circ$ ,  $M_\infty = 0.6$

(from ref 167)

FIG 3.75 Further Examples of DRA Research on Slender Wings

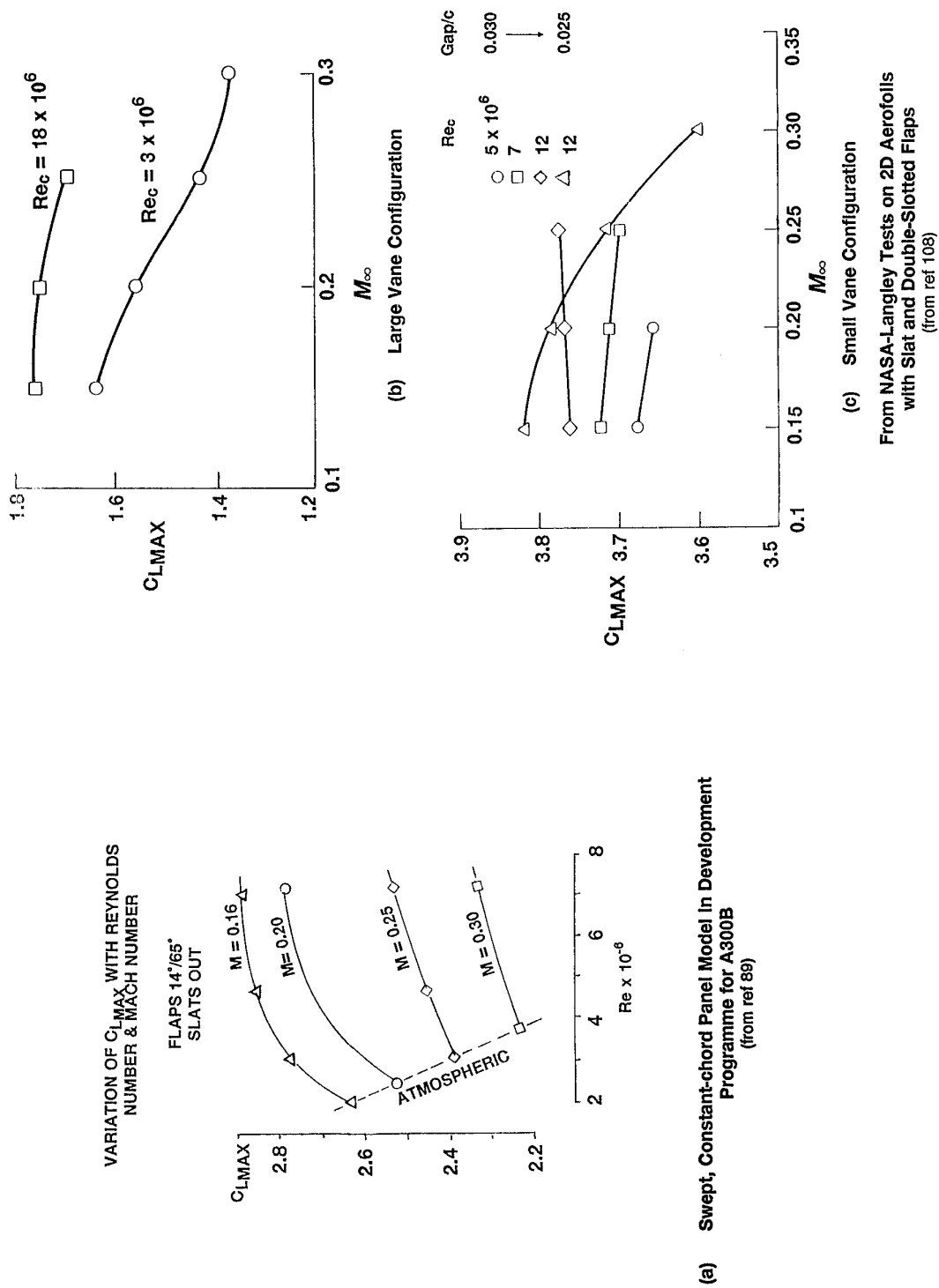


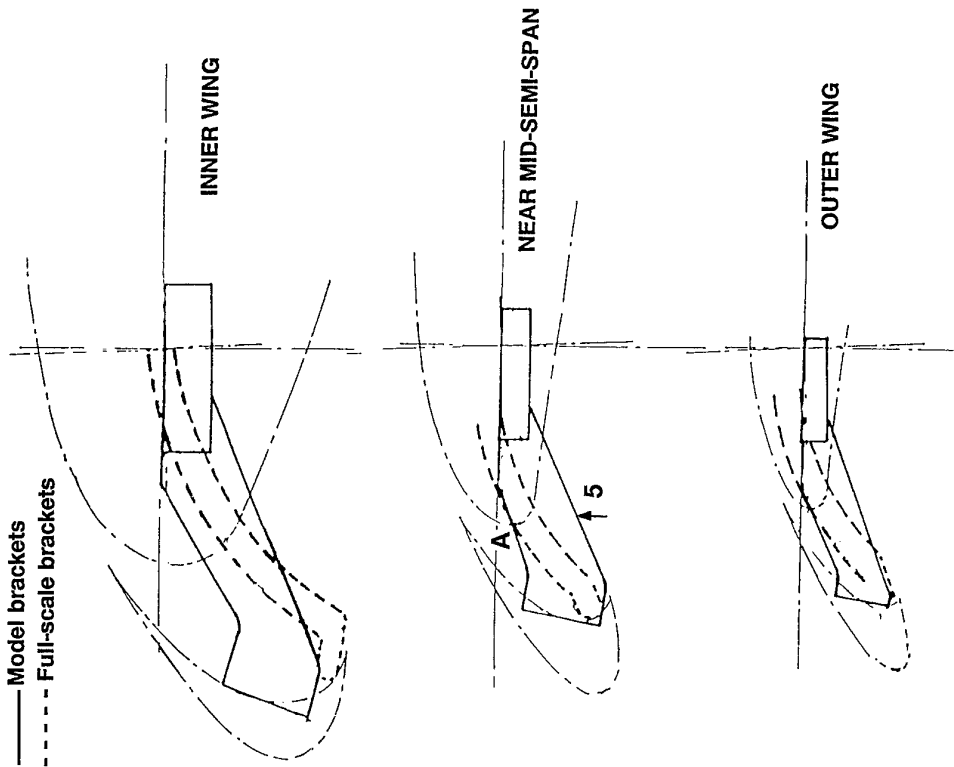
(a) Approach Reynolds number of current transport aircraft



(b) Performance envelope of major existing low speed tunnels

FIG 3.76 Tunnel-Flight Reynolds Number Mismatch of 3 Low Speed Tunnels Used in Support of the Development of Recent Civil Transports

FIG 3.77 Effect of Mach Number on Low Speed  $C_{LMAX}$



#### GUIDE-LINES FOR MODEL DESIGN

1. Retain full-scale number of brackets
2. Retain full-scale spanwise positions
3. Retain full-scale track width
4. Whenever possible, same point A as full-scale
5. If necessary to add bracket volume, add on the bottom rather than on top
6. Whenever possible, use circular cross-section at back of slat
7. Seal carefully around brackets
8. Prevent any inward and upward flow through gap on wing lower surface

FIG 3.78 Design of Slat Brackets for Model Tests in Pressurised Tunnel

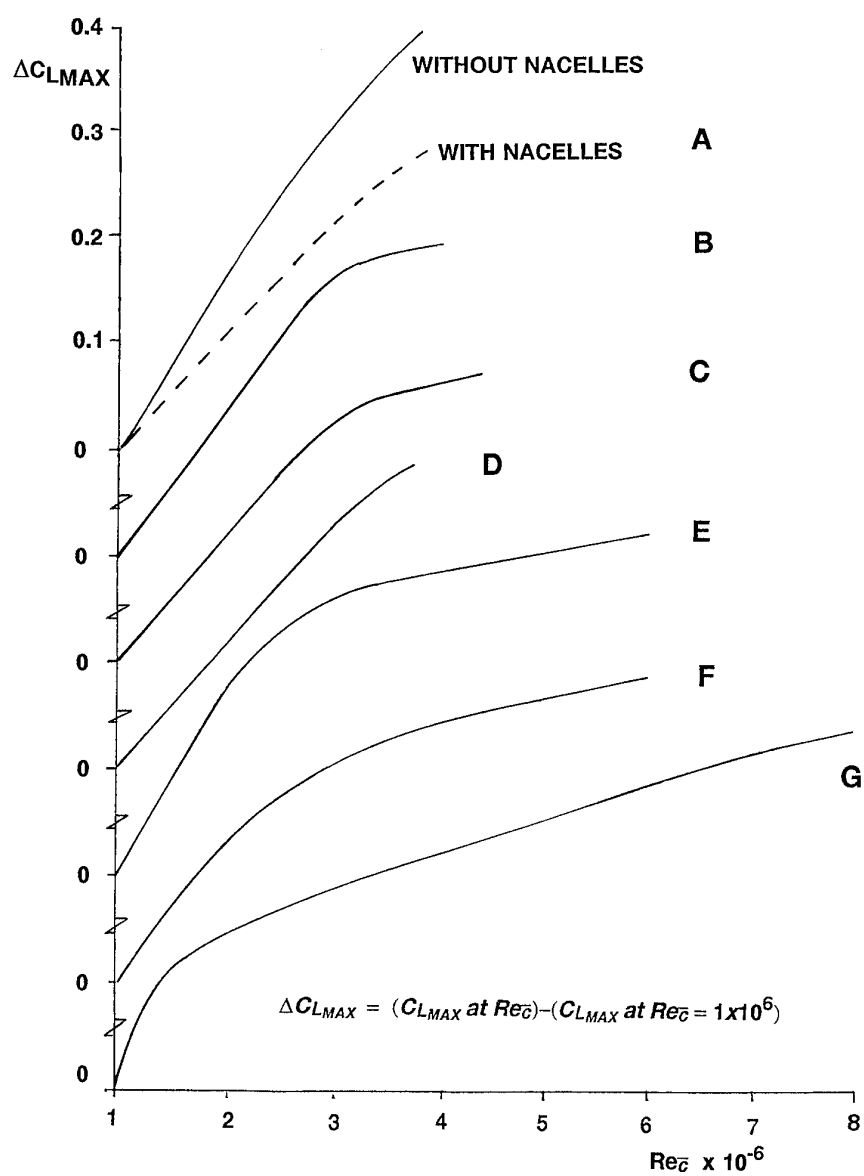


FIG 3.79(a) Scale Effect On  $C_{LMAX}$   
Model Tests for Various Aircraft

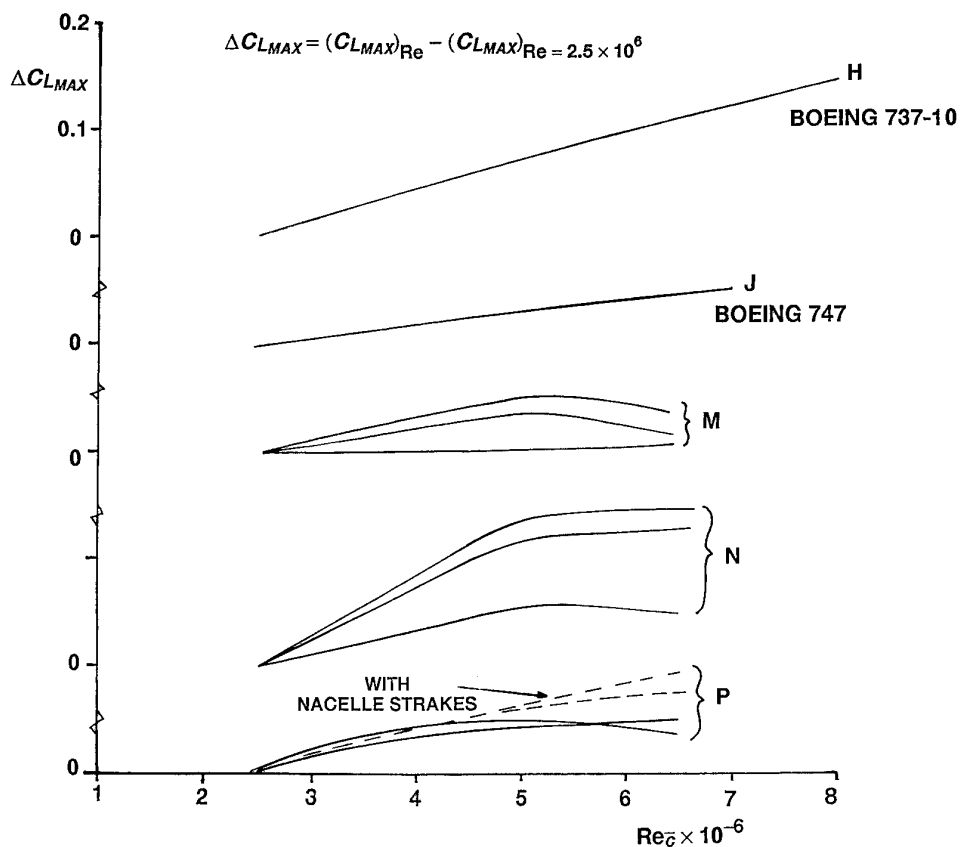


FIG 3.79 (b) Scale Effect On  $C_{LMAX}$   
Model Tests for Various Aircraft (cont'd)

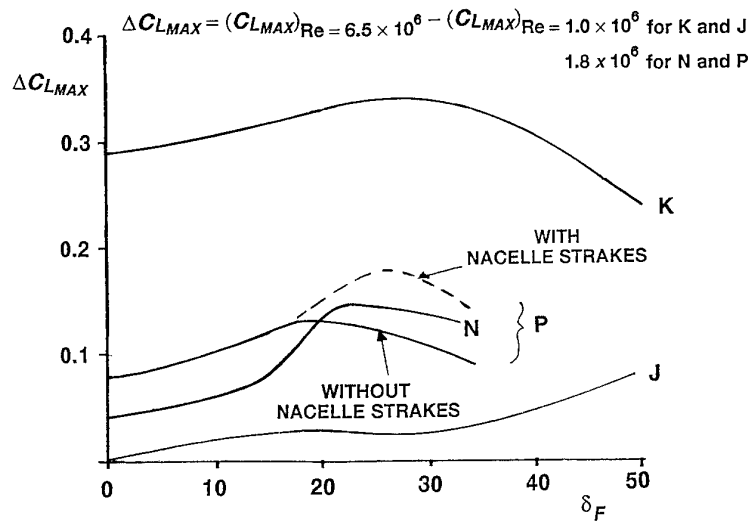


FIG 3.79(c) Effect of Flap Setting on Scale Effect on  $C_{LMAX}$   
Model Tests for Various Aircraft



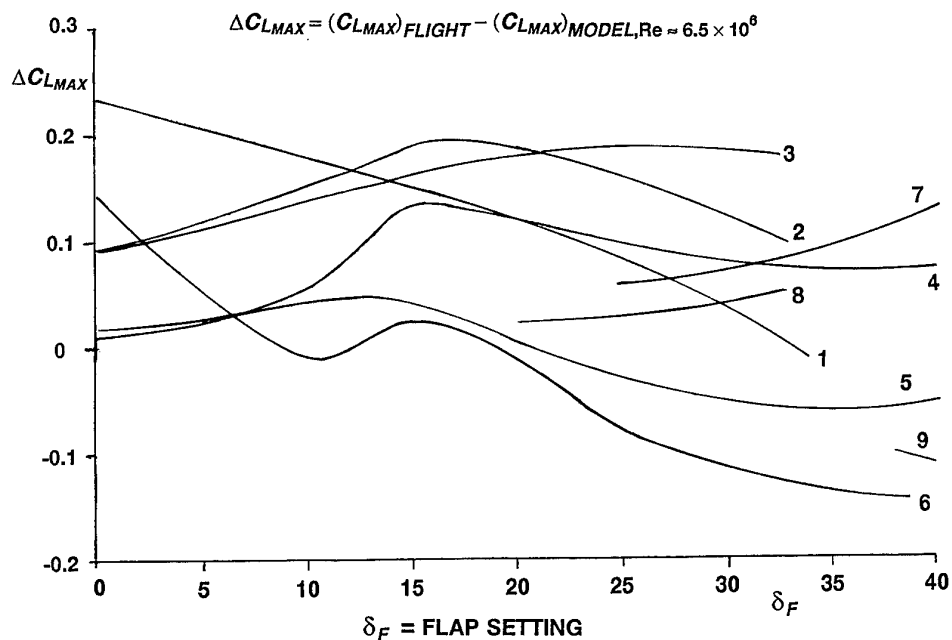
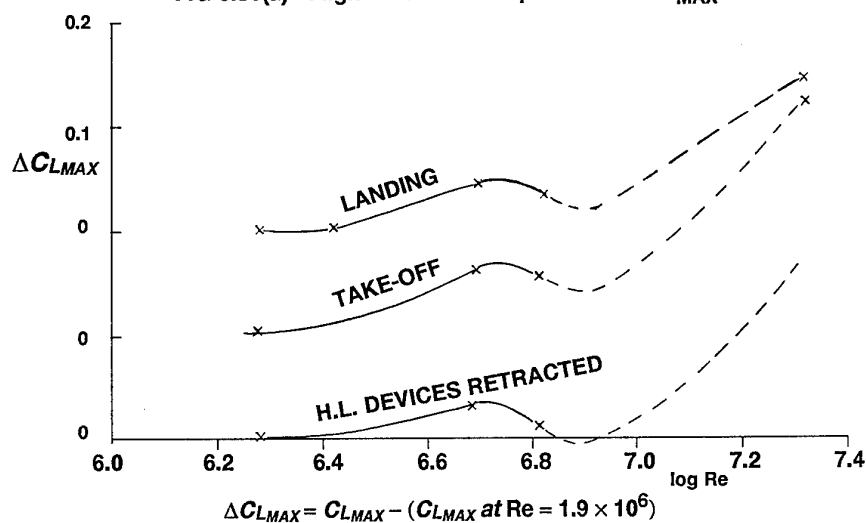
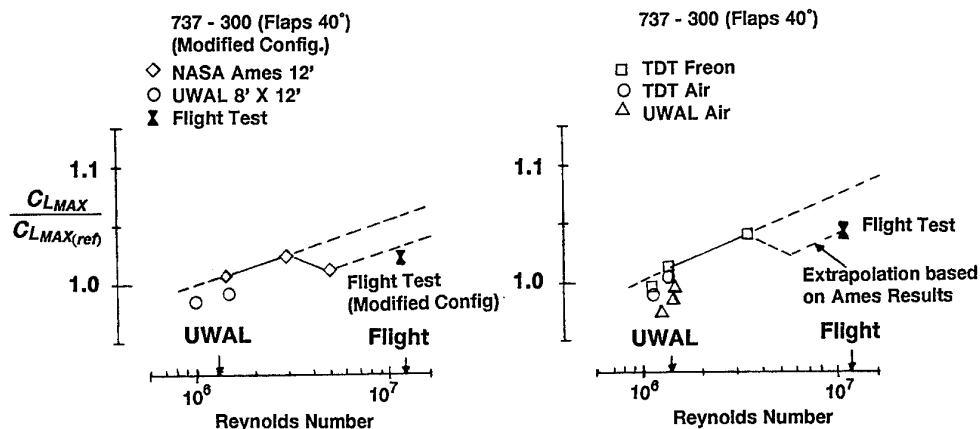
FIG 3.80(a) Flight - Tunnel Comparisons of  $C_{LMAX}$ 

FIG 3.80(b) Composite Picture for one of the Aircraft included in Figs. 3.79 and 3.80(a)

FIG 3.80(c) Wind Tunnel-to-Flight Scaling of Maximum Lift Coefficient for a Boeing 737-300  
(from ref 178)

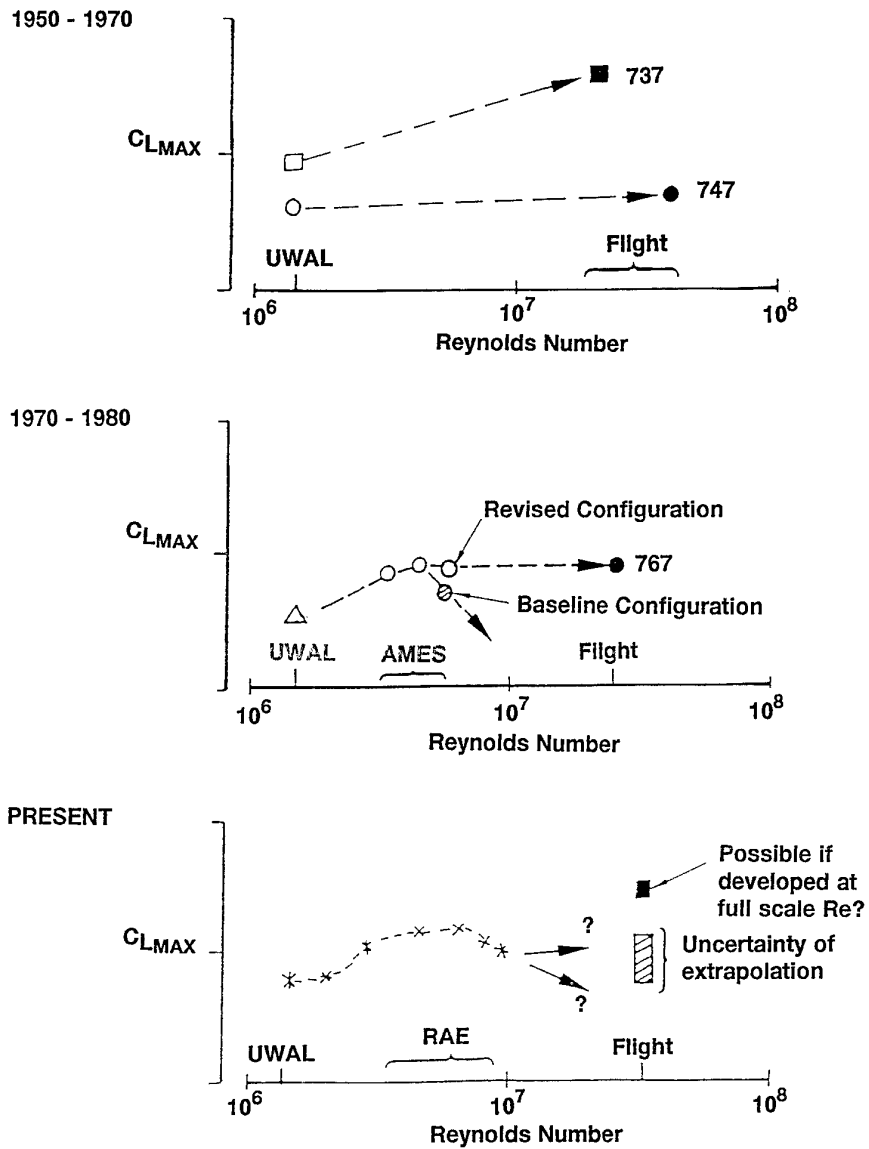
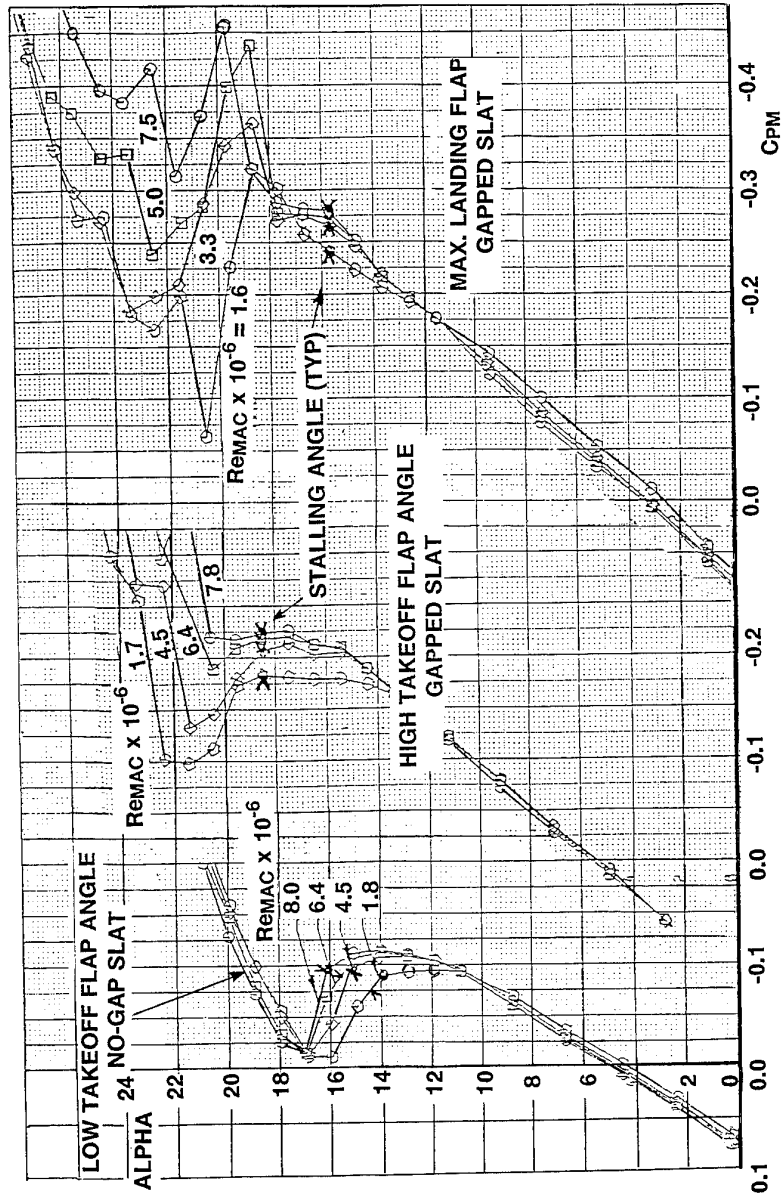


FIG 3.80(d)

An Outline History of High-Lift Wind Tunnel-To-Flight:  
 Assessment by Mack and McMasters (Boeing)  
 (from ref 178)



CPM: Pitching moment coefficient about aft C.G.

FIG 3.81(a) Effect Of Reynolds Number On Post-stall Pitching Moments

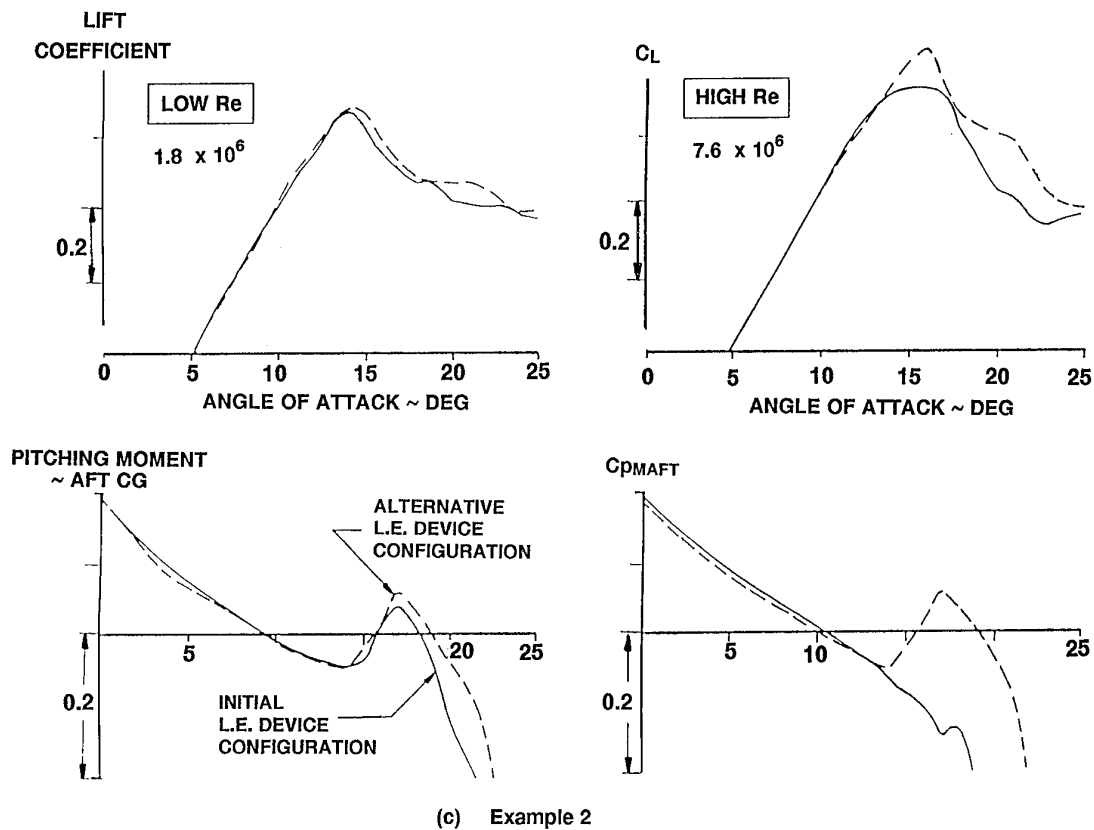
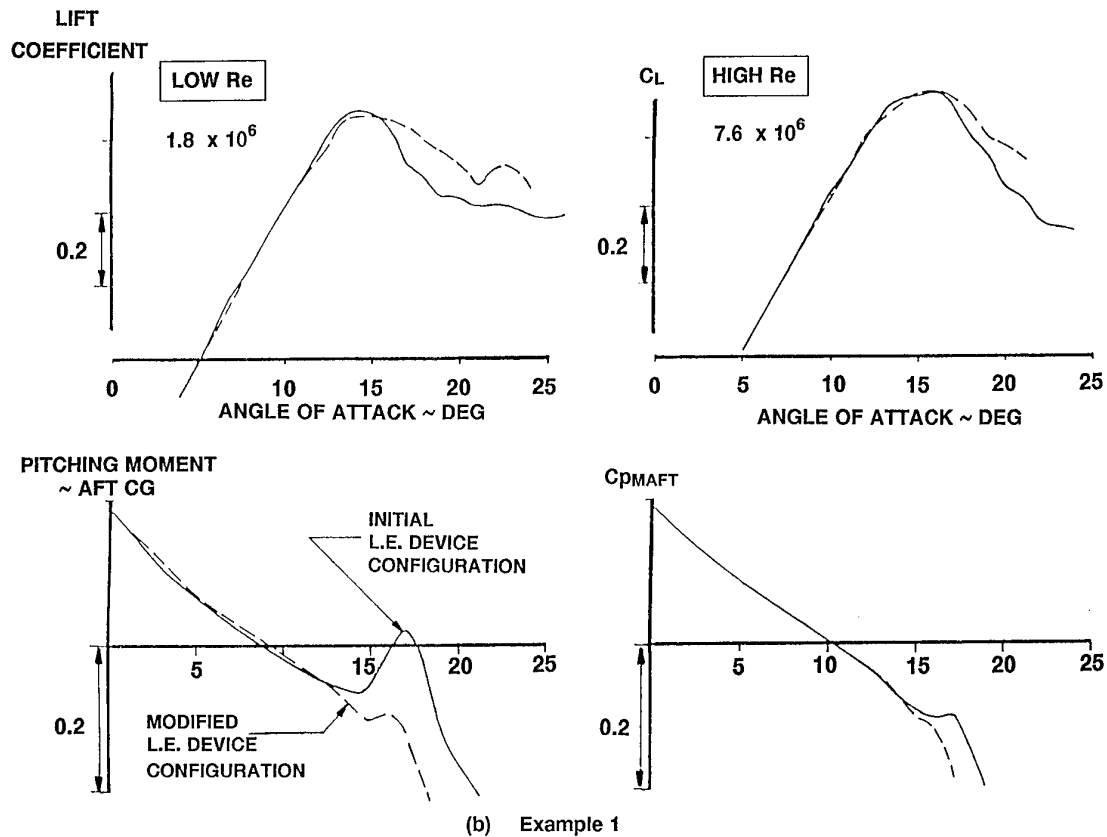
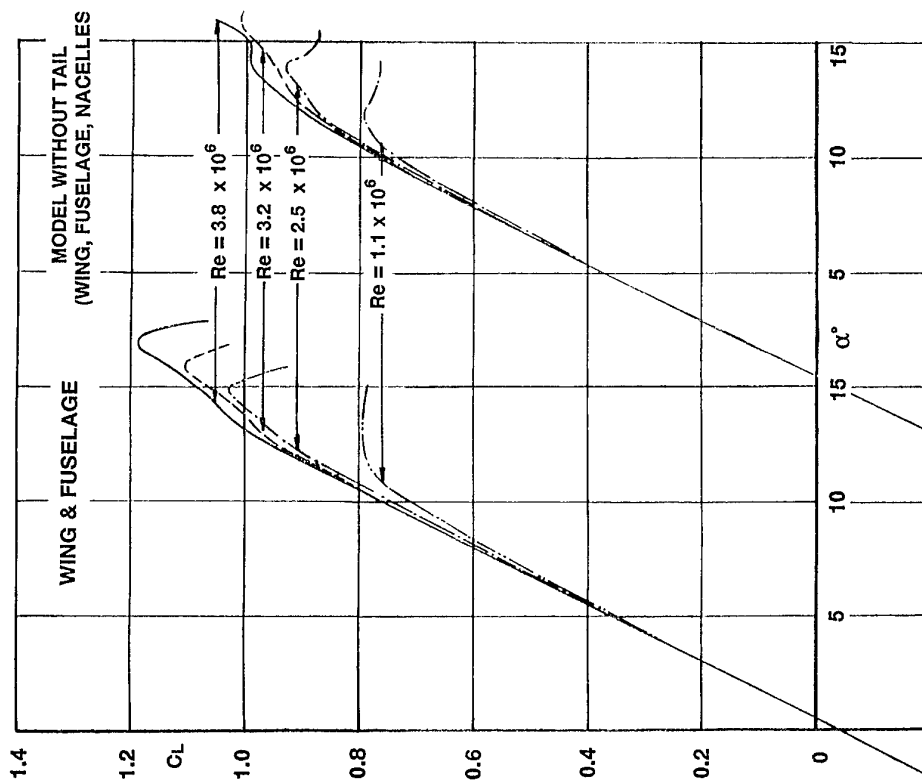
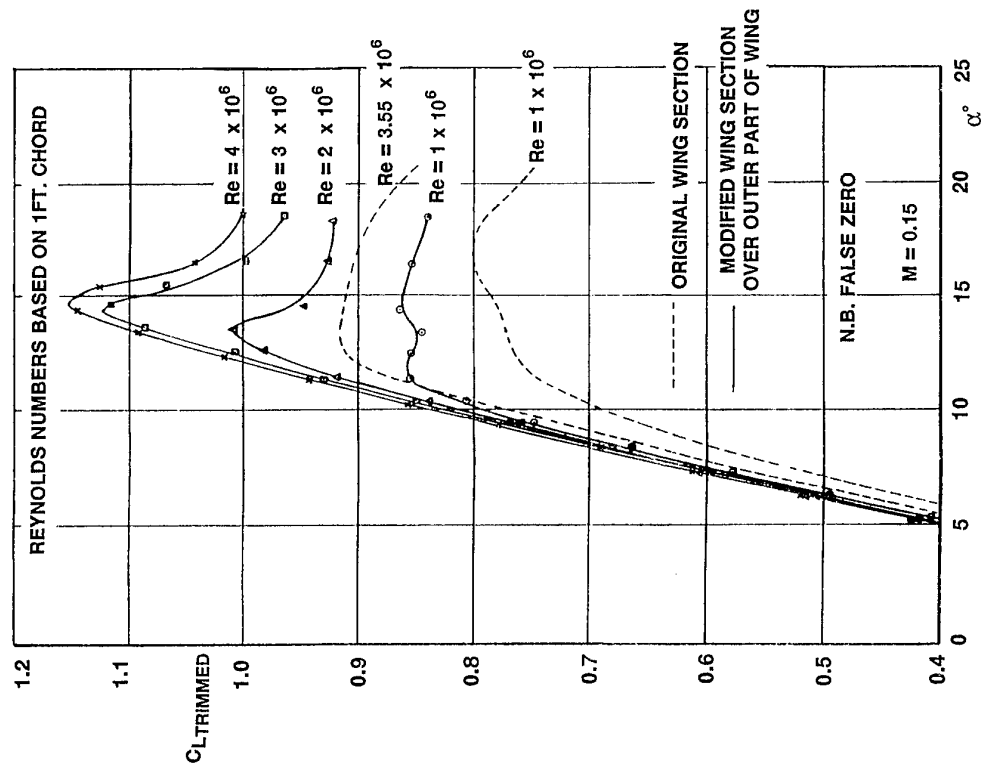
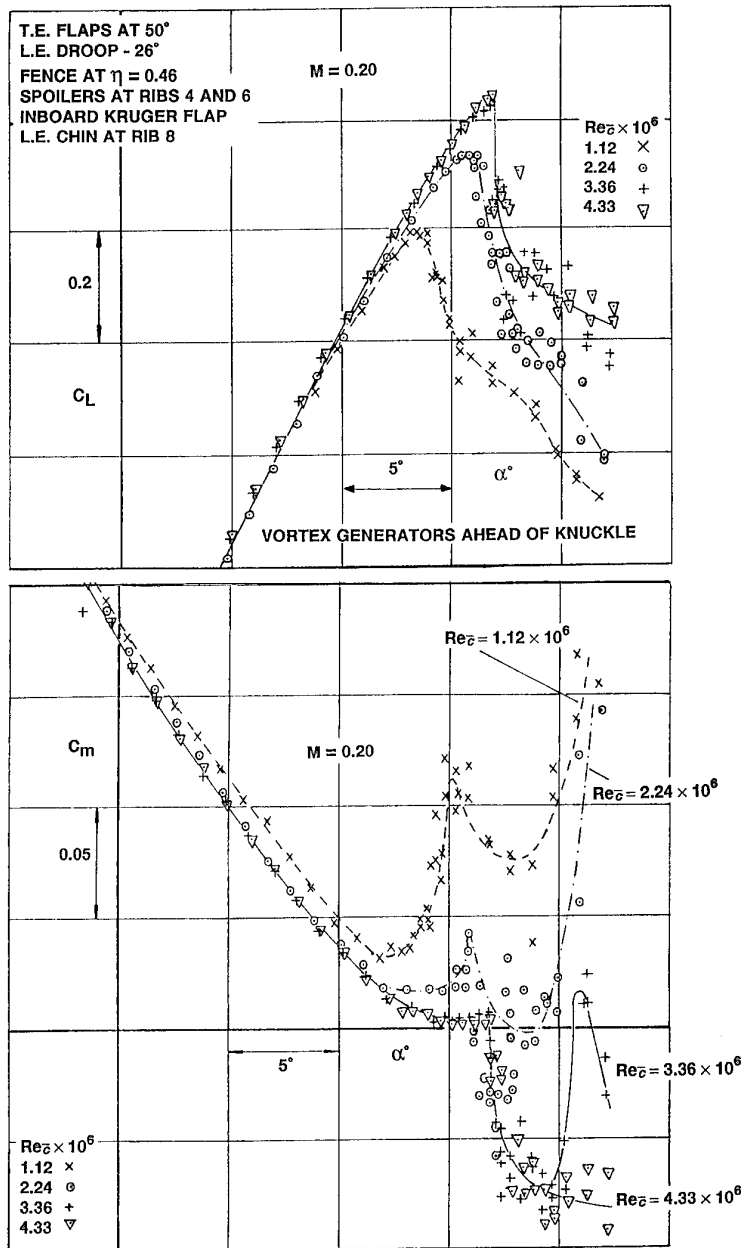


FIG 3.81(b,c) Effect of Test Re on Takeoff Slat Tailoring

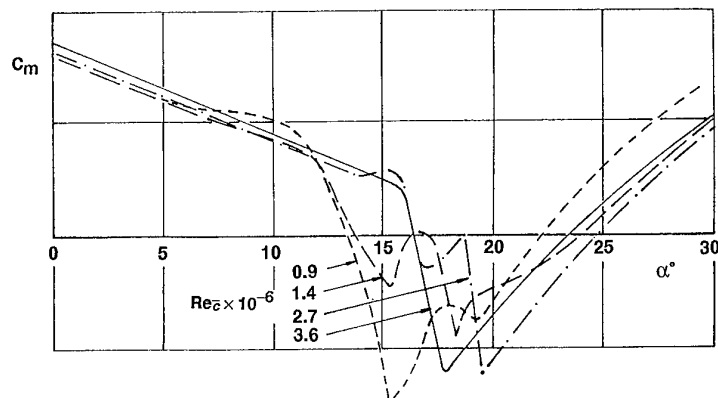


(a) B14/46

(b) COMET 1  
WING, FUSELAGE, NACELLES (NO TAIL)FIG 3.82 Scale Effect for Early UK Aircraft  
(from ref 139)

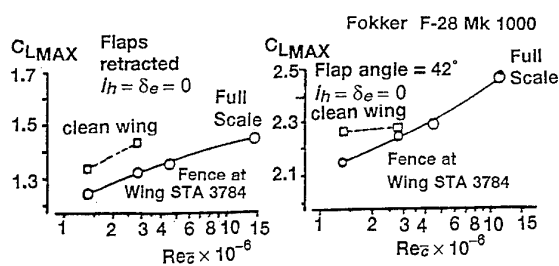
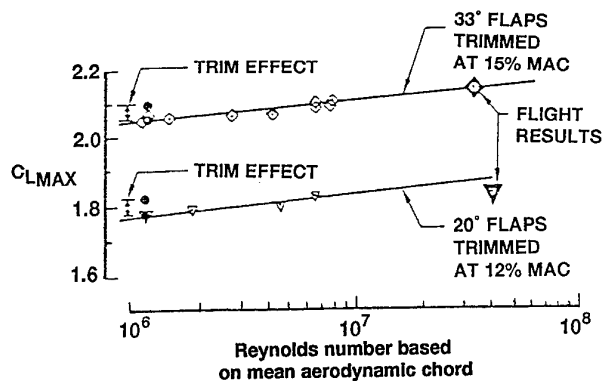


(a,b) TRIDENT

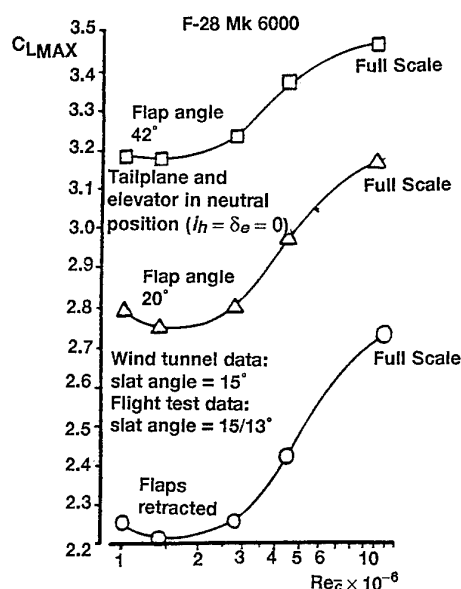
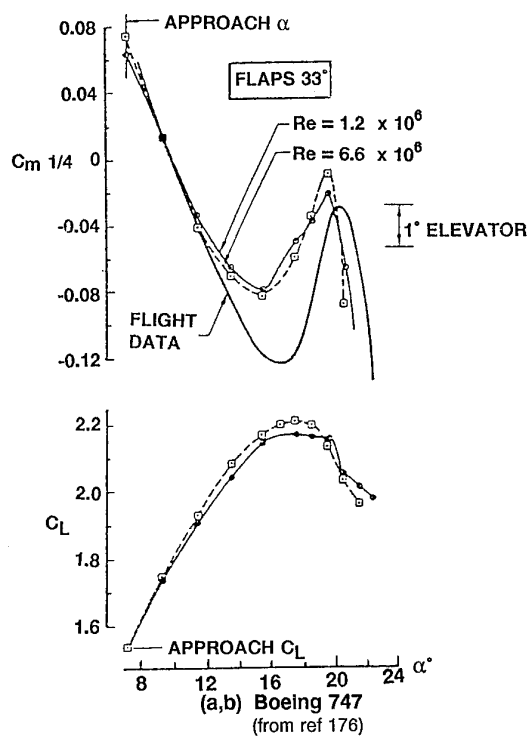


(c) Early UK Subsonic Transport

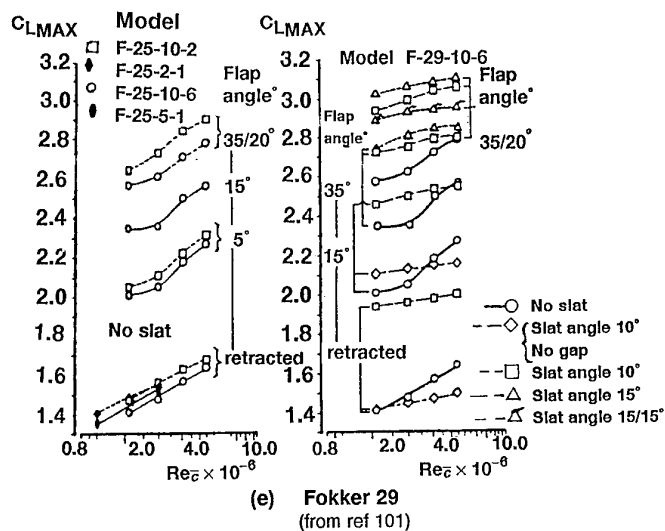
FIG 3.83 Scale Effect for Early UK Aircraft (cont'd)  
 (from ref 139)



(c) Effect of Reynolds number on maximum lift for F-28 MK1000 (from ref 101)

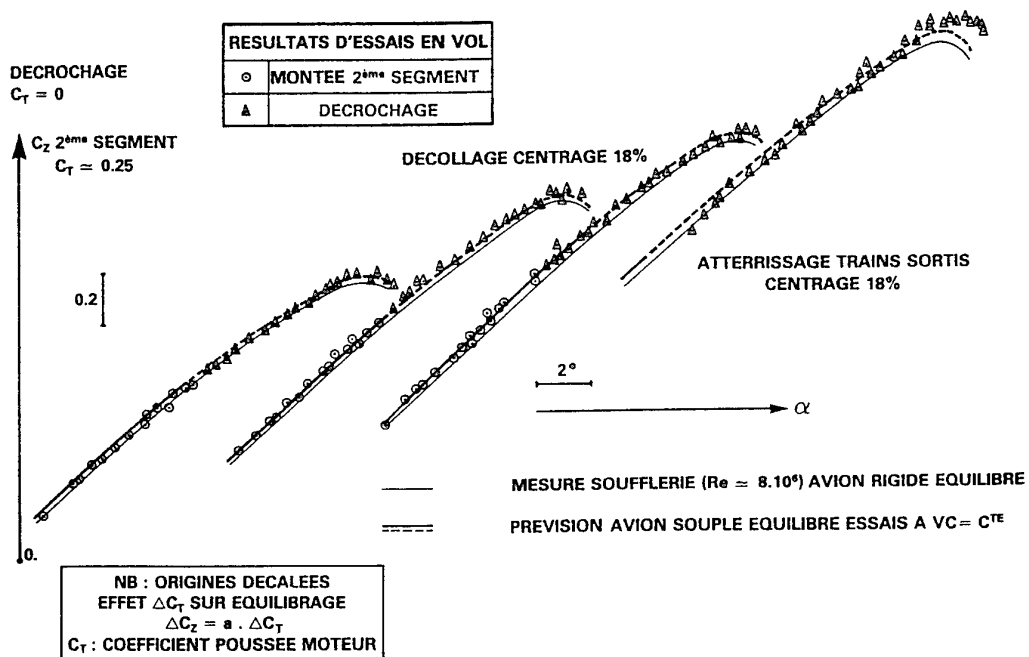


(d) Fokker 28 (from ref 101)

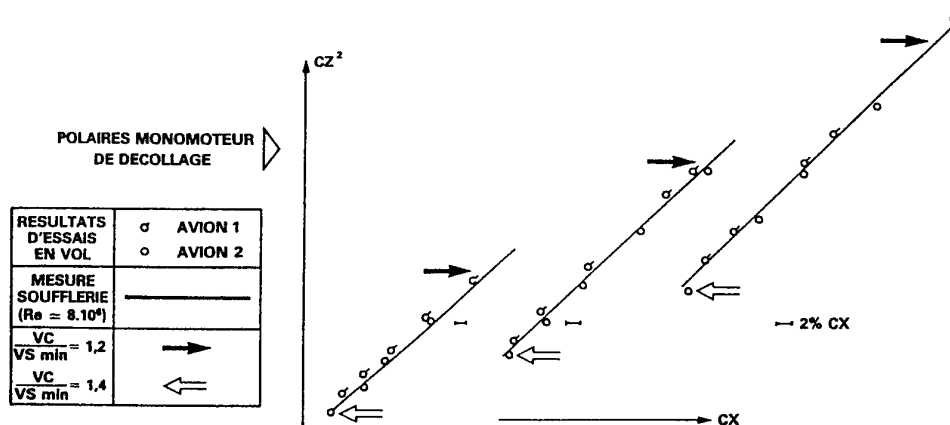


(e) Fokker 29 (from ref 101)

FIG 3.84 Scale Effect on Low Speed Stalling Characteristics



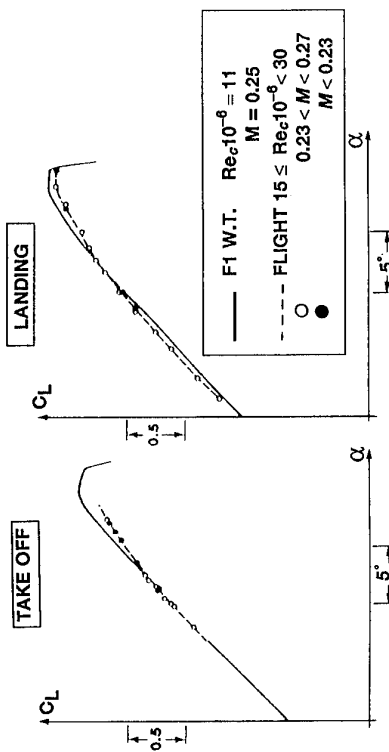
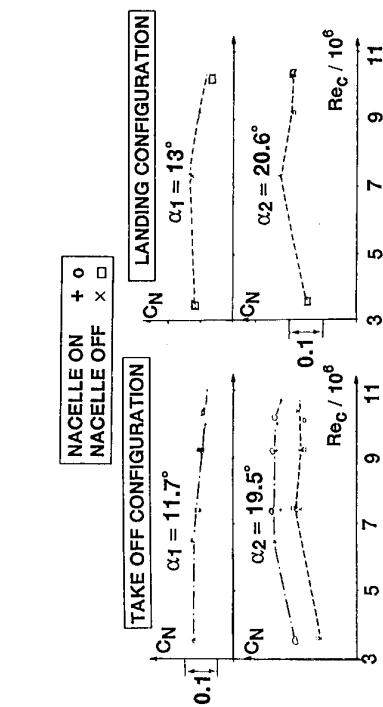
(a) Lift



(b) Drag

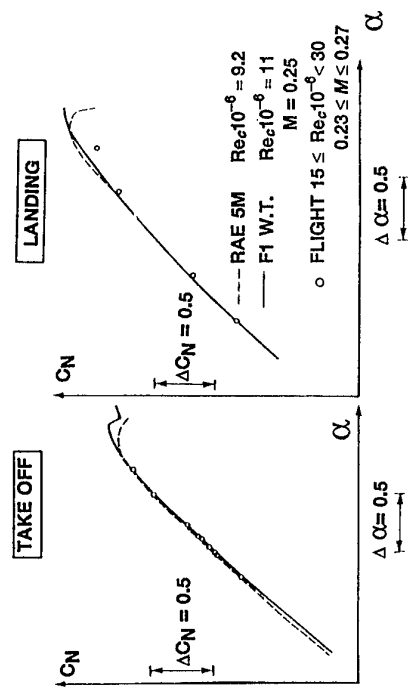
FIG 3.85 Flight-Tunnel Comparison for the A310  
(from ref 177)



(a) Scale effect on  $CL_{MAX}$  from model tests

(b) Scale effect on section normal force at 0.59 x semi-span from model tests

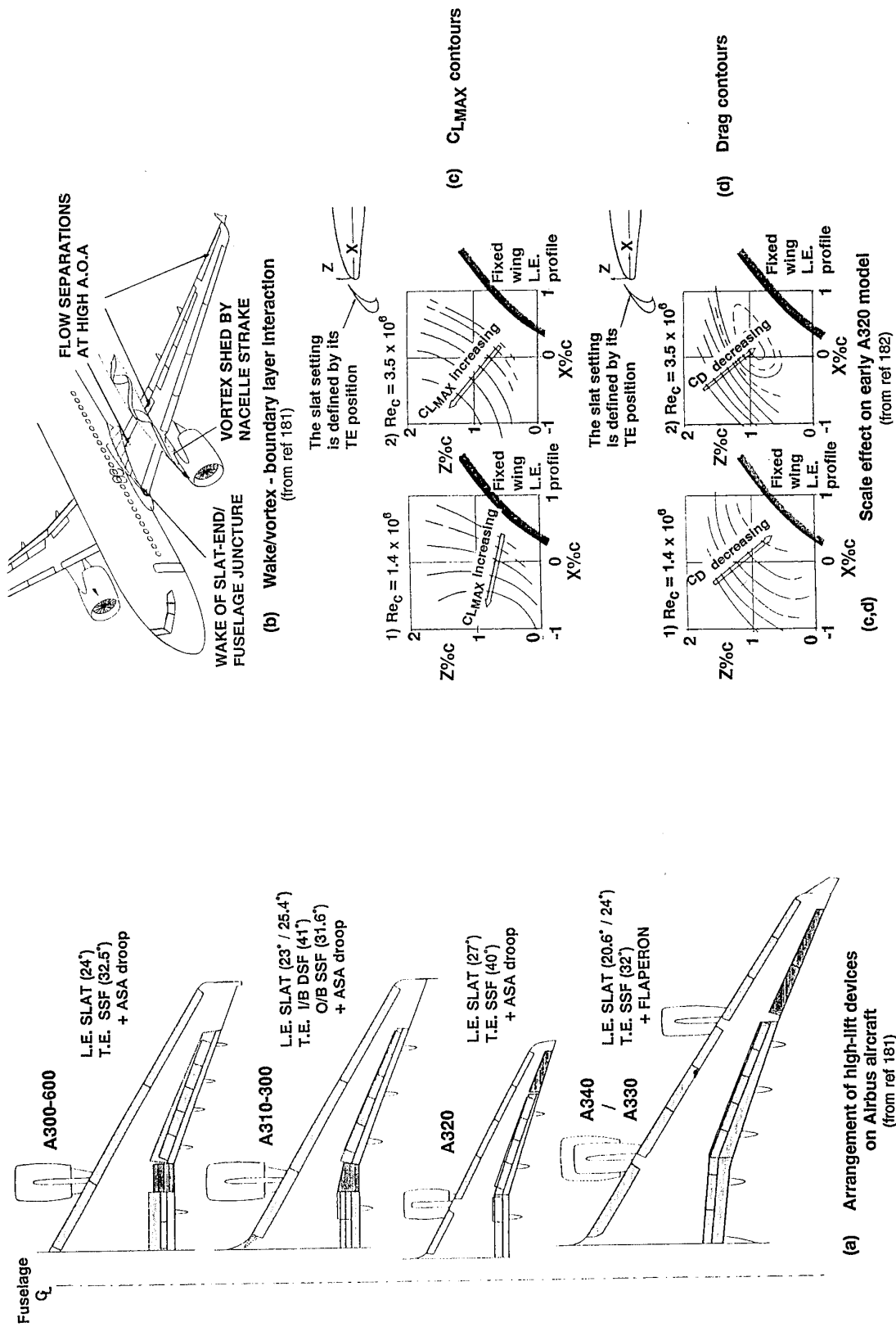
(c) Flight-Tunnel comparison for total lift



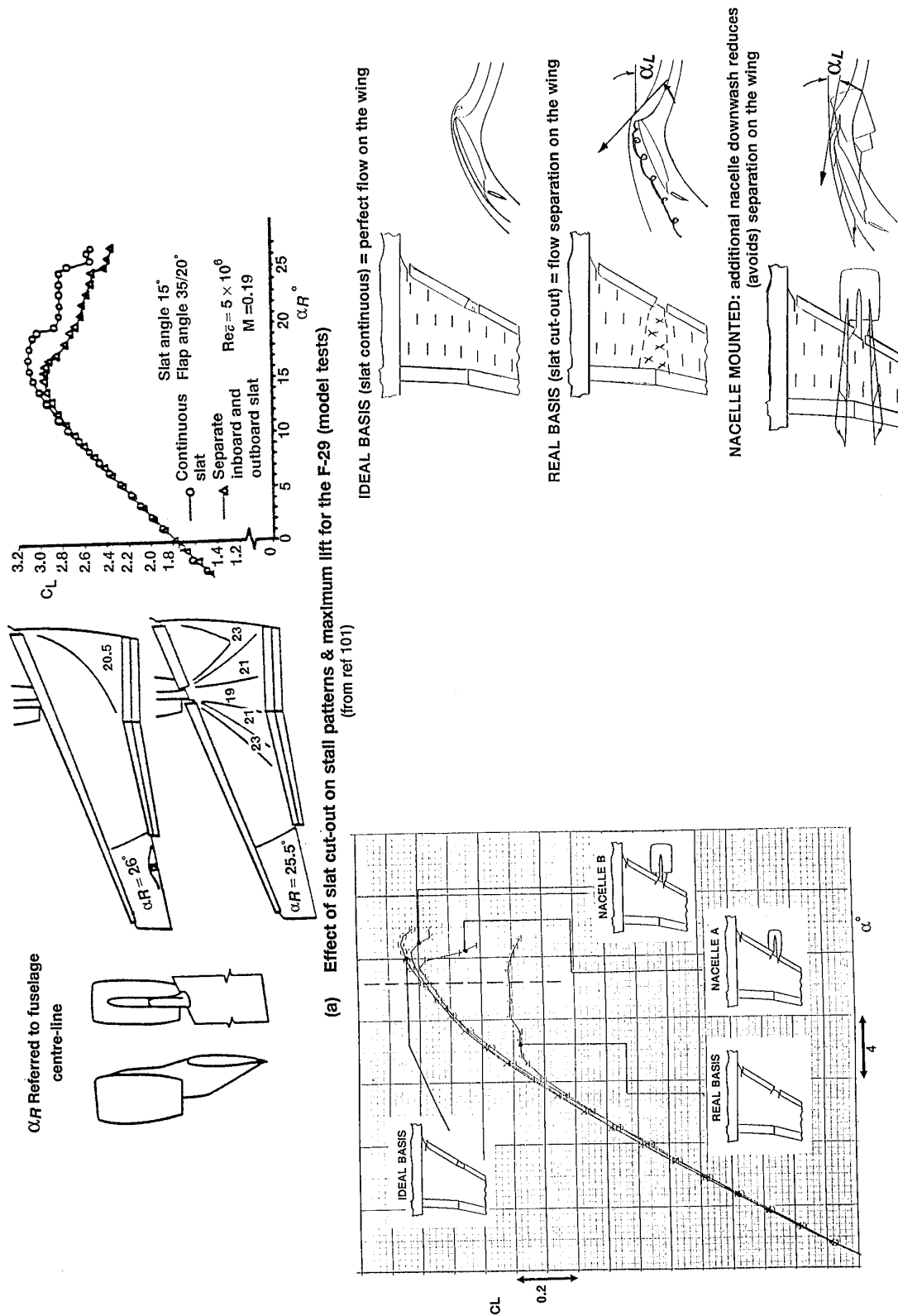
(d) Flight-Tunnel comparison for section normal force at 0.59 x semi-span

FIG 3.86 Results from GARTEur Exercise on A310

(from ref 111)



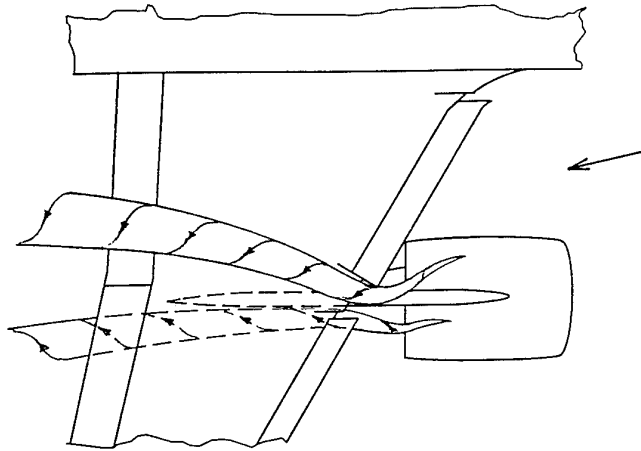
**FIG 3.87** Figures in Support of Discussion for Airbus Aircraft  
(from ref 111)



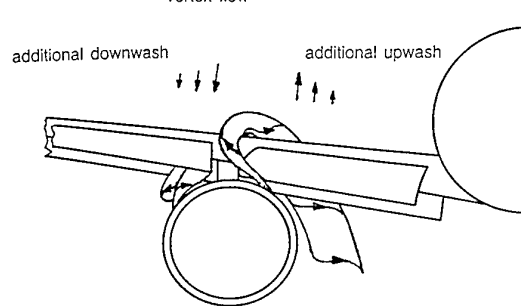
(b,c) Effect of slat cut-out and nacelle installation on lift characteristics

FIG 3.88 Effect of Nacelle Installation

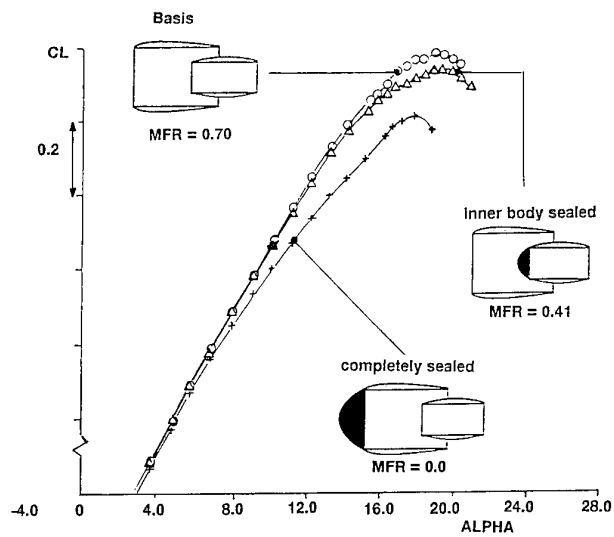
Incidence: appr. 1 deg below  $\alpha_{max}$



due to nacelle lift and  
vortex flow

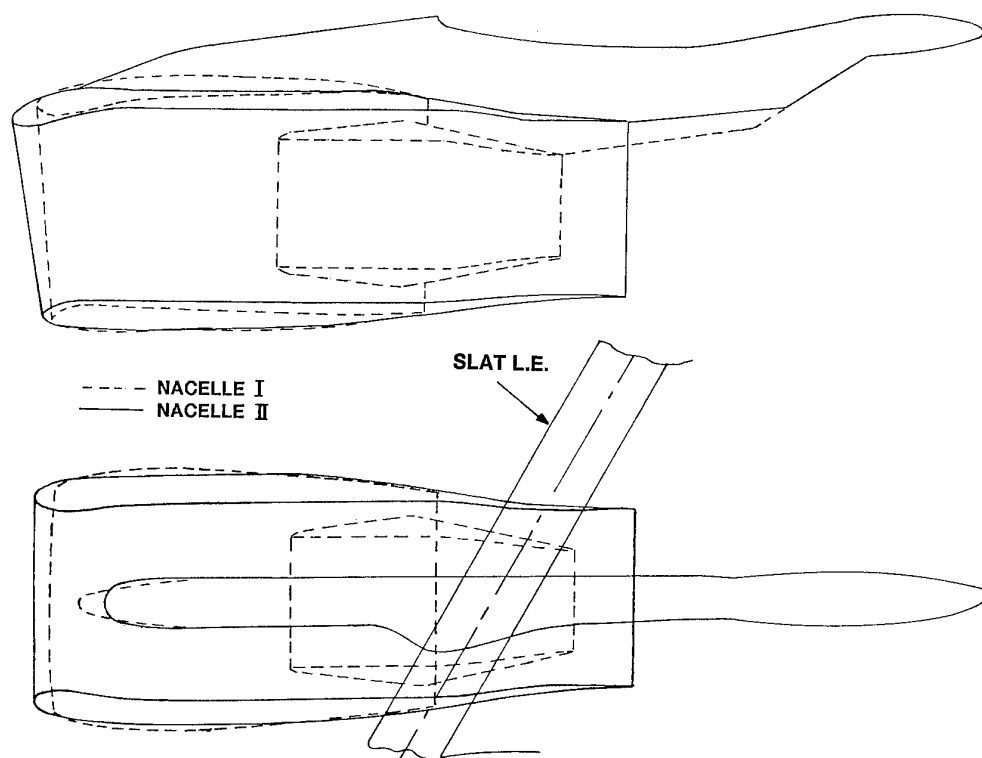


(d) Nacelle-induced lift vortex effects at high incidence

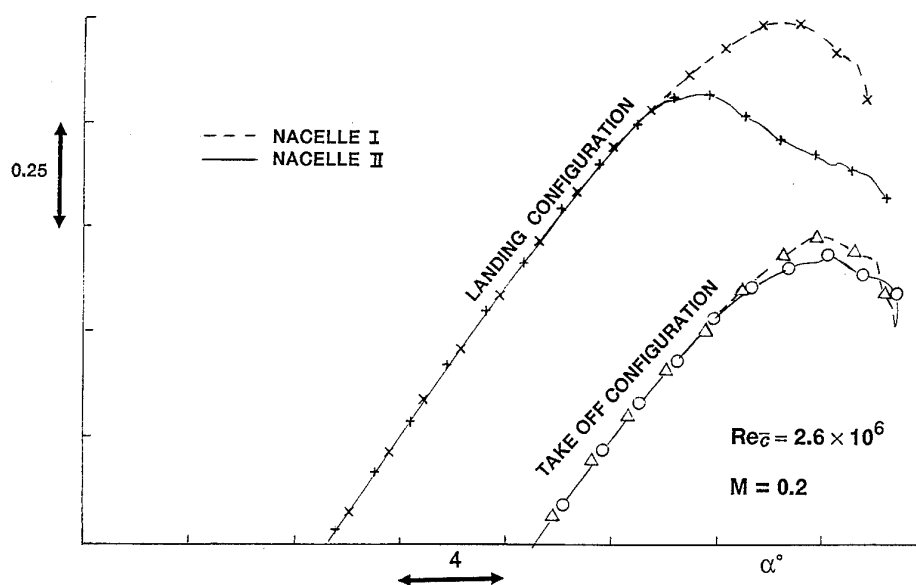


(e) Effect of intake mass flow: underwing nacelle on typical civil transport

FIG 3.88 Effect of Nacelle Installation



(f) Comparative nacelle geometry



(g) Effect of nacelle installation on lift at high incidence

FIG 3.88 Effect of Nacelle Installation

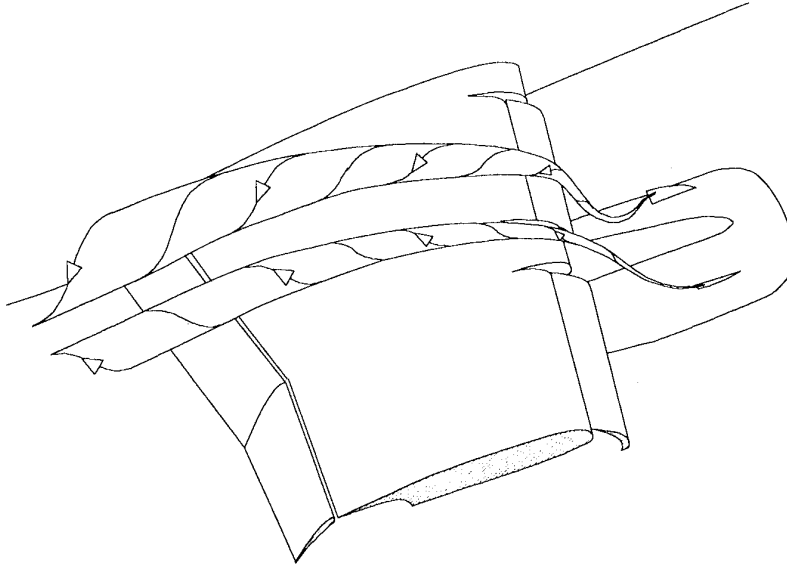
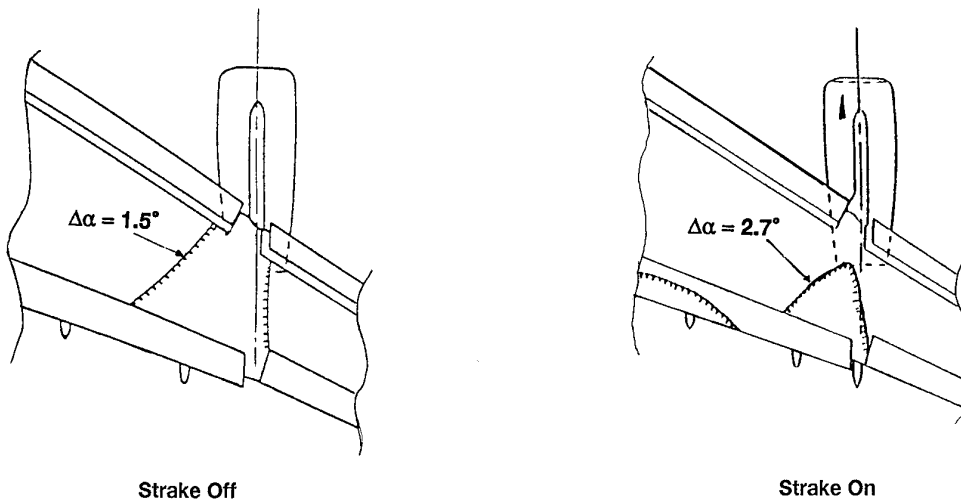
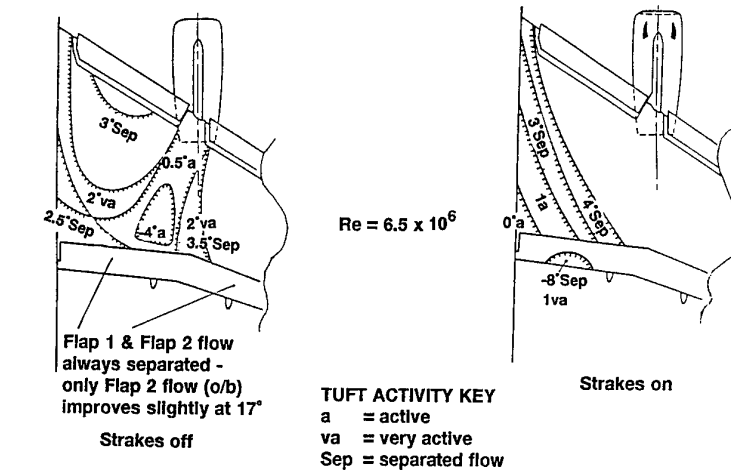


FIG 3.89 (a) Nacelle Strake Vortex System at High Incidence



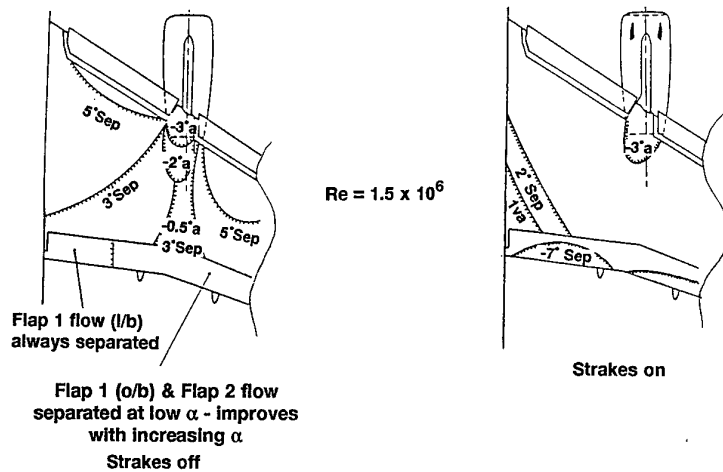
Boundaries for separated flow at  $\Delta\alpha$   
 $\Delta\alpha = \alpha - (\alpha \text{ for } C_{L_{MAX}} \text{ at } Re = 6.5 \times 10^6)$   
 $M = 0.2$

FIG 3.89 (b) Effect of Single Strake on Flow Separation Inboard of a Nacelle on an Outer Wing

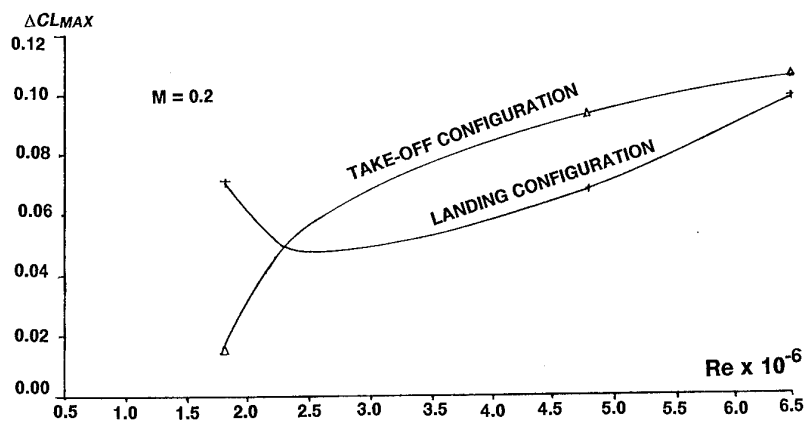


$$\text{Boundaries for } \Delta\alpha = \alpha - (\alpha \text{ for } C_{L_{MAX}} \text{ at } Re = 1.5 \times 10^6) \\ = \alpha - 17^\circ$$

$$M = 0.2$$

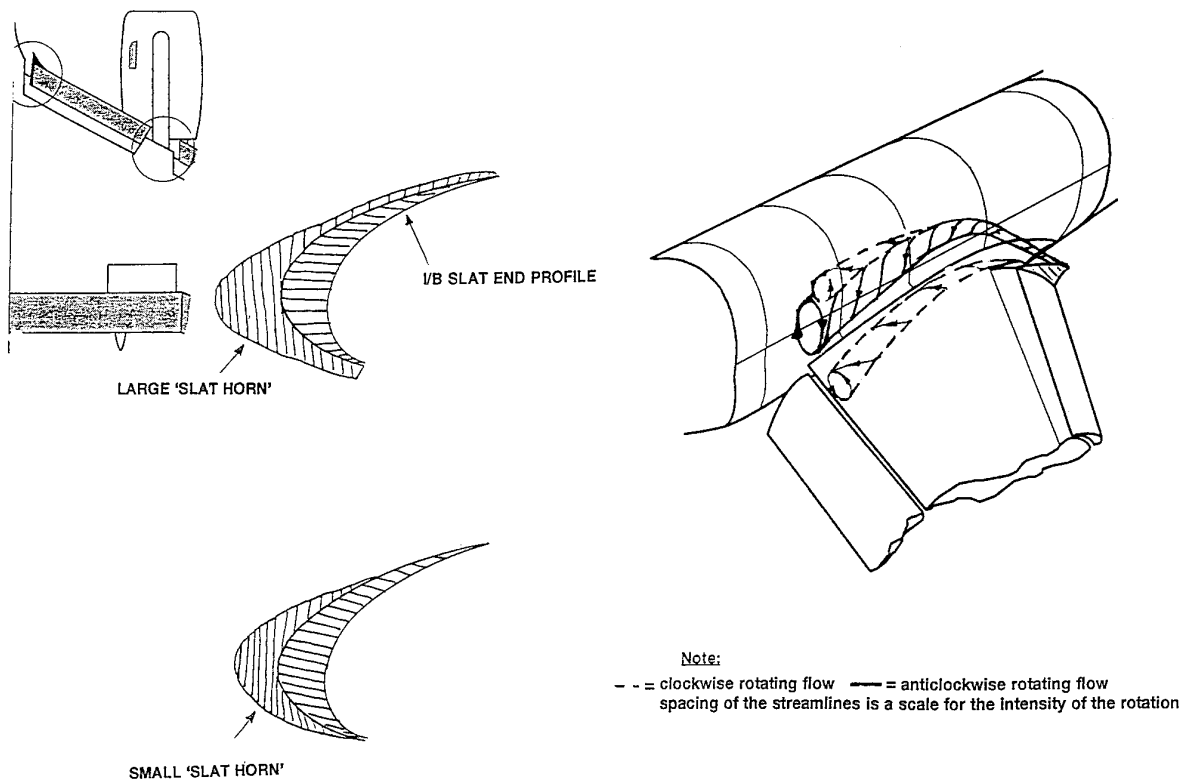


(c) Effect of strakes on inner wing flow at high incidence



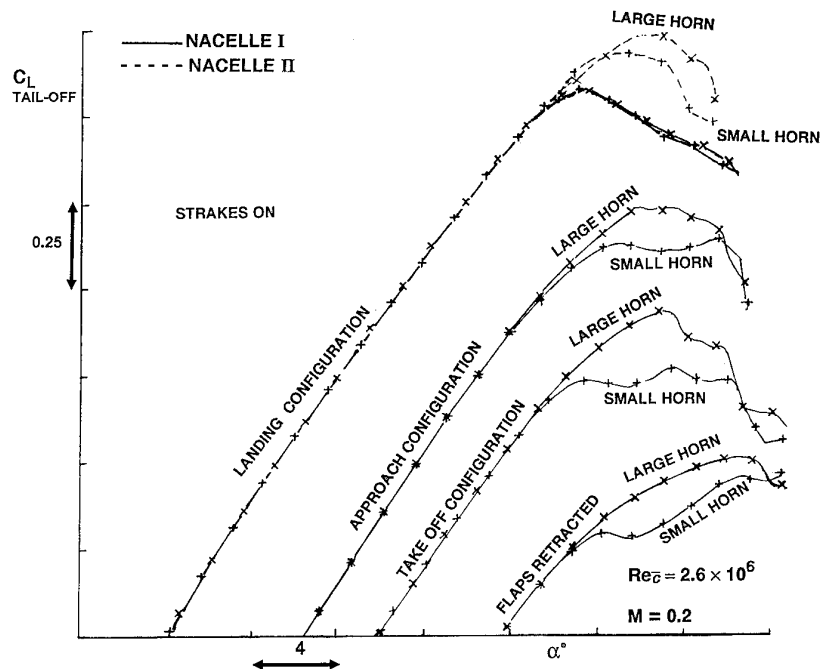
(d) Scale effect on  $\Delta C_{L_{MAX}}$  due to strakes

FIG 3.89 Effect of Nacelle Strakes



(a) Geometry

(b) Vortex action



(c) Lift results

Effect of Slat Horns

FIG 3.90 Slat-end/Fuselage Side Problem Area



## 4 SCALE EFFECTS AT TRANSONIC SPEEDS

### 4.1 Introduction

An Agardograph<sup>1</sup> on Reynolds Number Effects at Transonic Speeds was published in 1988 and also in 1988, AGARD FDP Working Group 09 reported<sup>2</sup> on "Boundary Layer Simulation and Control" in tests in transonic tunnels at typical test Reynolds numbers in the range  $2\text{--}6 \times 10^6$ . There is therefore little need to include here a further comprehensive review of the evidence at transonic speeds. However, useful extensions of the 1988 publications are still possible in three areas:

- (i) AGARD WG 09 proposed a methodology for testing in existing transonic tunnels (excluding the NTF and the ETW) and extrapolating the results to full scale. Parts of this methodology had been used for many years but some aspects and notably the introduction of CFD into the extrapolation procedure were new. In detail, some features of the methodology were left ill-defined in the hope that experience in the use of the methodology would clarify these points. Since 1988, some experience has been gained and this is reviewed in §4.3 below. This work has been useful not merely in the interests of the methodology but in contributing to a better understanding of the sources of scale effect at transonic speeds,
- (ii) some new evidence on scale effects on the unsteady flow in buffet and also, scale effect on the flow over highly swept and slender wings. This evidence is reviewed in §4.4,
- (iii) some thoughts are tabled in §4.5 about how wing design developments in the future are likely to modify conclusions about scale effect at transonic speeds.

As a prelude to this new material, §4.2 repeats in summary form, the main features of the AGARD methodology.

### 4.2 Recapitulation of AGARD Methodology

The methodology introduced in Ref 2 and summarised in Ref 183 assumes that at least one of two possible approaches can be followed in a model test on a wing design at transonic speeds. Tests should either be made

- (i) over a range of Reynolds number with transition fixed at a position close to where it would be forecast to occur in flight, or
- (ii) with the boundary layer manipulated in the tunnel test to produce a viscous flow behaviour closer to that forecast for the flight Reynolds number. At the present time, this implies testing with a series of alternative transition positions but in the future, this could imply the use of suction. The issue of how best to match the viscous flow behaviour in flight raises various questions that will be addressed in detail in §4.3.

So, we either have a Reynolds-number or a transition-sweep. In the second case, a simulation criterion then has to be chosen to convert the transition position at the model test Reynolds number into an effective Reynolds number that would give the same viscous flow behaviour with transition at the position forecast for the full-scale aircraft in flight. Whenever possible, both approaches should be practised but obviously, for the first

approach, one needs a tunnel with either variable pressure or variable temperature capability.

Results<sup>184</sup> from a simple example in which both approaches were practised are presented in Fig 4.1. A two-dimensional aerofoil was tested over a range of Reynolds numbers and transition positions. The results with transition either fixed at  $0.07c$  or occurring naturally near the leading edge provide a Reynolds-number sweep from  $Re = 2.3 \times 10^6$  to  $Re = 30 \times 10^6$  but if it had only been possible to test at  $Re = 2.3 \times 10^6$ , moving transition aft to  $0.30c$  would have given a reasonable simulation of data at  $Re = 8 \times 10^6$  and then, one would have had to extrapolate to  $Re = 30 \times 10^6$  with the aid of CFD calculations.

Fig 4.2 is a diagrammatic picture taken from Ref 2. It was drawn to convey the essence of the AGARD methodology. The AGARD Working Group recommended that, ahead of the tests, CFD calculations should be made by the most advanced theoretical method conveniently available which allowed for weak but not strong viscous-inviscid interactions such as a laminar separation, a shock-induced or a rear separation ahead of the trailing edge. In Fig 4.2, the results of these calculations are compared with the measured test data, both being plotted against Reynolds number or, for the second approach, effective Reynolds number. The variable on the ordinate scale had not yet been defined; clearly, it should be some aerodynamic characteristic that can be expected to vary with Reynolds number. Obvious candidates include  $C_D$  or  $C_{D_{wave}}$  at a given  $C_L$ ,  $C_L$  at a given  $\alpha$ ,  $C_{pTE}$ ,  $M_{sh}$  etc where  $C_{pTE}$  is the pressure coefficient at the trailing edge and  $M_{sh}$  is the local Mach number-component normal to the shock immediately ahead of the shock.

Since 1988, theoretical methods have become available that are capable of allowing for limited regions of flow separation, eg near the trailing edge and indeed, many of the results to be quoted in §4.3 below were obtained by such methods. Even so, the AGARD recommendation that one should use a method that can only allow for effectively the displacement effects of the boundary layer carries an incidental advantage in that any divergence between the computed and measured trends with Reynolds number can be taken as a useful indication of where the measured results are being influenced by a strong viscous interaction not allowed for in the calculations. In looking at transonic results for a transport aircraft in a design cruise condition, the most likely type of a strong viscous-inviscid interaction would be a rear separation ahead of the trailing edge and, in such a case, the divergence between the measured and computed trends present in Fig 4.2 below  $Re_{crit}$  indicates the Re-range in which this separation is present. In off-design conditions for a transport aircraft or even design conditions for a military aircraft  $Re_{crit}$  could indicate the Reynolds number below which a major flow separation is present - either near the leading edge or at the shock or at the rear. The definition of  $Re_{crit}$  is therefore that it is the Reynolds number below which the measured and computed trends diverge but one should always attempt to identify the flow phenomenon not allowed for in the calculations that causes this divergence; if no explanation can be obtained by an independent approach, one should question whether the divergence is due to some error in either the measured or computed results and, if this were so, it would be wrong to treat the break as indicating a genuine  $Re_{crit}$ .

The basic rules in the AGARD methodology for extrapolating the measured data to full scale Reynolds number are

- (i) from  $Re_{test}$  to  $Re_{crit}$ , follow the measured trend (extrapolated if necessary),
- (ii) from  $Re_{crit}$ , move parallel to the computed trend.

Ref 2 distinguished between 5 scenarios according to the relative values of  $Re_{model\ test}$ ,  $Re_{crit}$  and  $Re_{flight}$ . The two most important scenarios are illustrated in Figs 4.3 and 4.4. In scenario 3 in Fig 4.3,  $Re_{crit}$  lies in the Re- or effective Re-range covered in the tunnel tests and extrapolation should be fairly straightforward: once one has established that the model test with the furthest aft transition position has produced an effective Reynolds number above  $Re_{crit}$ , the conversion from a transition position to an effective Re plays no further direct part in the extrapolation to full-scale. In scenario 4 in Fig 4.4, however, the extrapolation is much more uncertain. One has to extrapolate the measured trend to  $Re_{crit}$ ; the slope of this extrapolation depends on what simulation criterion has been chosen for the conversion from transition position to effective Re and secondly, a method is needed for estimating  $Re_{crit}$  with some precision. It would be wrong to assume that the extrapolation of the measured trends should extend to where the curves intersect the computed trends; this would be tantamount to accepting the CFD results as correct in an absolute sense but the methodology is only trying to use CFD as a guide to the variations with Re. In practice, estimating  $Re_{crit}$  may not be too much of a problem as in detail, the measured and computed results may contain plenty of clues. Perhaps the most reliable approach is to say that  $Re_{crit}$  is the Reynolds number above which  $C_f$  never falls to zero in the CFD calculation. It will be realised that the reason why aft-fixing has been adopted as a suitable technique is that one is trying to move the testing from scenario 4 to scenario 3.

It will be realised that pictures such as Figs 4.2, 4.3, 4.4 are idealised diagrams; in reality, the trends against Re may not be linear and the discontinuities may be smeared. Perhaps this was the first reason why experience was needed: to discover whether real results are like the simplified pictures. The second and more difficult point was that AGARD WG 09 left the final choice of a simulation criterion for the conversion into effective Re to the user of the methodology. Ref 2 made some suggestions for the user to consider: one could either use

- (a) a zero-level criterion such as the boundary layer momentum thickness at the trailing edge of the equivalent flat plate, or
- (b) a "first-order" criterion such as shock position, shock strength or the boundary layer momentum or displacement thickness at the trailing edge of the real wing, or
- (c) a "second-order" or local criterion such as the boundary layer shape factor near the trailing edge or the non-dimensional length of a shock-induced separation bubble.

The choice of a suitable simulation criterion will be discussed in depth in §4.3.2 below.

Further questions where experience was needed included

- (i) for a model test with aft transition, does the effective Re vary substantially with the operating condition, ie  $C_L$ , Mach number etc?
- (ii) can one retain, whatever one's interest in the test results, the same simulation criterion for the conversion to effective Re or does one have to change according to

whether one is primarily interested in scale effect on drag or alternatively, scale effect on buffet-onset or some other feature of the results?

- (iii) does the methodology including the CFD extrapolation to full-scale offer a satisfactory correlation with flight results?
- (iv) what are the present limitations to the use of the methodology?

Research since 1988 has helped to provide answers to some of these questions and, in doing so, has cast some further light on the sources of scale effect at transonic speeds; the results of this research are described in §4.3 below.

### 4.3 Recent Research (including experience with methodology)

Most of the results to be discussed in this section were obtained from an analysis by the present author of a comprehensive set of calculations for two modern two-dimensional aerofoil designs. Results for one of these sections (A) were reported in Ref 183; the other example (B) is not available in the open literature.

#### 4.3.1 Effects of a rear separation

The results in Ref 183 for the first aerofoil A provide some clear support for the basic approach of the methodology as expressed in Fig 4.2. Aerofoil A is RAE 5229<sup>185</sup>. The section has a thickness/chord ratio of 14% and significant rear camber; it is one of a family of aerofoils of 'convex' sections with a sharp trailing edge, the term 'convex' implying that the adverse pressure gradients over the rear 40-50% of the upper surface increase monotonically downstream except very close to the trailing edge. Model tests on aerofoil A were made in the 8 ft x 8 ft tunnel at DRA Bedford at Reynolds numbers of  $Re = 6 \times 10^6$ ,  $10 \times 10^6$  and  $20 \times 10^6$  with transition fixed at 0.05c. The range of the study was then extended greatly by making CFD calculations for Reynolds numbers up to  $Re = 65 \times 10^6$  with transition at 0.05c and for transition positions varying from 0.05c to 0.40c at  $Re = 6.05 \times 10^6$ . Two codes were used for these calculations: VGK, the original RAE version<sup>186</sup> of the Garabedian-Korn method and BVGK, an improved version<sup>187</sup> of the VGK method where, in particular, the equations for the turbulent boundary layer development are integrated by an inverse method which is computationally more efficient for flows approaching separation. Results for the aerofoil design condition,  $M = 0.735$ ,  $C_L = 0.65$ , are presented in Figs 4.5(a,b).

Calculations by VGK yield the "computing trends" as defined in the AGARD WG methodology. BVGK, on the other hand, is capable of allowing for a limited rear separation near the trailing edge and as shown in Fig 4.5(a), gives very good agreement with the "measured trends" between  $Re = 6 \times 10^6$  and  $Re = 20 \times 10^6$ .  $Re_{crit}$  in this particular case is near  $Re = 20 \times 10^6$ . Below  $Re_{crit}$  the shock strength and hence the wave drag and the total drag increase more rapidly as Re is reduced and these trends are due to a loss in rear loading associated with a rear separation very close to the trailing edge as shown in Fig 4.5(b). This is not an isolated example; Fig 4.5(c) presents results for the second aerofoil B; as with aerofoil A, the variation of  $C_{Dwave}$  with Re increases as Re is reduced below the value at which the rear separation extends forward of 0.97c towards 0.95c. These calculations for aerofoil B were made by an Euler code with a similar treatment to BVGK and hence,

capable of allowing for the rear separation;  $C_f = 0$  is used to define where rear separation is occurring.

A study of the pressure distributions in the cases just discussed was sufficient to show that the extra scale effect at the lower Reynolds numbers was due to the presence of a rear separation. Increasing the Mach number (or  $C_L$ ) into conditions where the shock strength is greater introduces the possibility that the extra drag variation with  $Re$  below  $Re_{crit}$  is also related to the presence of a shock-induced separation. Under these conditions,  $Re_{crit}$  varies with  $M$  and  $C_L$  as shown for aerofoil B in Fig 4.5(d). The increase in  $Re_{crit}$  is clearly correlated with a shock-induced separation since it occurs when  $M_{shock}$  exceeds about 1.25. Ultimately, with increase of  $C_L$  and hence  $M_s$ , extra wave drag is present whatever the Reynolds number and hence, is observed throughout the  $C_{Dwave}$ - $Re$  curve as implied by the asymptotic behaviour of the  $Re_{crit}$  curve for the higher Mach number. All these examples of scale effect on wave drag are related to changes in the load distribution over the aerofoil: extra viscous effects generally result in an increase in the shock strength for a given  $C_L$ .

So, we can conclude

- (i) the results support the concept expressed by Fig 4.2,
- (ii) the scale effect on wave drag persists when a rear separation is present and this can be detected when the separation occurs ahead of about  $0.97c$ ,
- (iii) this extra scale effect on wave drag persists up to higher Reynolds numbers after the appearance of a shock-induced separation.

These can be regarded as general conclusions.

### 4.3.2 Conversion of aft transition to $Re_{eff}$ with forward transition

As noted already, the WG report merely made suggestions as to which simulation criterion should be chosen on which to base the conversion from an aft transition position at the test Reynolds number into an effective Reynolds number to associate with the flight transition position. Considering first the proposed zero-order criterion, the boundary momentum thickness at the trailing edge of the equivalent flat plate, this is very simple to use: all one needs is the single chart reproduced here as Fig 4.6(a). The AGARD Working Group found that this was remarkably successful in giving a good correlation particularly as regards shock position which is probably the most significant single feature in a transonic pressure distribution. This experience has been further confirmed by the calculations for section A. This is shown in Fig 4.6(b); using the zero-level criterion, one obtains very good agreement in the shock positions for  $Re = 6.05 \times 10^6$ ,  $x_{TR} = 0.40c$  and for  $Re = 30 \times 10^6$ ,  $x_{TR} = 0.05c$ . These calculations were made using the BVGK code and Fig 4.6(b) again shows the good agreement between these results and experiment at  $Re = 6.05 \times 10^6$ ; all the results for aerofoil A in the following discussion are obtained using this code.

While this apparent success of the zero-order criterion is encouraging, it was felt by the Working Group and by the present author that this criterion should only be used to obtain a rapid first idea of what effective Reynolds number was being simulated by a given transition position. In detail, the agreement in Fig 4.6(b) is not as good as it might appear at first sight: neither the shock strength nor the rear loading are correct

to the accuracy that is required. More seriously, one should not really be content with a simulation criterion that takes no notice of the wing section geometry or the development of the boundary layer over the real wing. One should use a criterion based on this boundary layer development. This is where, initially, everyone became uncertain. As noted in Ref 183, the transition position needed to produce a given effective Reynolds number varied dramatically according to which boundary layer parameter was chosen and whether one used the value at the trailing edge or at the shock. In one of the examples considered in Ref 183, the required transition position varied between  $0.15c$  and  $0.44c$  according to the criterion that was chosen. The same point is made by Fig 4.6(c) taken from Ref 188. Goldhammer and Steinle in commenting on Fig 4.6(c) note that the low Reynolds number aft trip simulation can match some but not all the parameters.

To make a logical choice of simulation criterion, one should go back to consider the basic nature of the scale effects. It was noted at the outset that there are two types of scale effect:

- (i) 'direct' scale effects arising from changes with Reynolds number in the boundary layer (and wake) development for a given pressure distribution, and
- (ii) 'indirect' effects associated with changes in the pressure distribution that arise from the changes with Reynolds number in the boundary layer development.

If we begin by considering the simplest case of subcritical, attached flow, the only sources of scale effect are the direct effect of the change of skin friction with Reynolds number and the indirect effect due to the change in pressure distribution associated with the change in boundary layer displacement thickness. For these conditions, it seems clear that the most appropriate simulation parameter should be the boundary layer displacement thickness at the wing trailing edge, leaving the change in skin friction to be allowed for by a subsequent correction. This was confirmed by the BVGK results for aerofoil A at  $C_L = 0.4$ ,  $M = 0.735$  shown in Fig 4.7(a): almost complete agreement is achieved. It seemed sensible to build on this and so, moving on to the design condition at  $C_L = 0.65$ , produces the comparisons shown in Fig 4.7(b). Only the supersonic part of the upper surface pressure distribution is plotted because there is complete agreement between the two pressure distributions over the rest of the upper surface and over all the lower surface. There are however differences in the supercritical development. Looking at the distributions for the aft transition, low  $Re$  cases, the sudden local increase in suction near the transition position results from the fact that in these calculations by the BVGK method, the assumption is made that the laminar and turbulent momentum thicknesses are the same at transition and, as a consequence, there is a sudden decrease in the displacement thickness of the turbulent layer relative to the thickness of the laminar layer ahead of transition, ie a sudden expansion in the flow. Ignoring this local effect in the computed results, the more significant differences are that near  $0.04c$ , the suctions are too low; near  $0.10c$ , they are too high and finally ahead of the shock, they are again too low and the shock is too far forward relative to the target pressure distribution at the higher effective  $Re$ . (This difference in shock position could have been forecast because taking the lower comparison, a transition position of  $0.33c$  was used for the low  $Re$  case whereas  $0.40$  is needed to give good agreement as shown earlier in Fig 4.7(b)). Ref 183 notes that all these differences can be traced by a connected-point analysis to the differences in effective shape of the aerofoil + boundary layer displacement thickness as shown in Fig 4.6(b). Ref 183

then argues that despite these differences in supercritical development, one should still use the boundary layer displacement thickness at the trailing edge as the simulation criterion. It is producing the right amount of rear loading and one can apply corrections for the errors in shock strength and shock position based on the results of CFD calculations for the two cases. Ref 183 notes that for the examples shown, these corrections contribute less than 0.0002 to the wave drag coefficient. If the test results are in scenario 4, these corrections should be applied to the measured results before they are extrapolated to  $Re_{crit}$ . This may appear somewhat cumbersome but it is better to retain this simulation parameter and stay close to a sound physical understanding of the flow rather than change to some other parameter which might give better superficial agreement with the pressure distributions at  $Re_{effective}$ ,  $x_{TRight}$  but achieving this agreement coincidentally and with less regard for the physics. One detailed point is worth making: the low  $Re$ , aft transition result will not always give a shock strength that is too low: it depends on the incidence and the shape of the aerofoil in the supercritical region. The calculations for aerofoil B which covered a wider range of  $C_L$  and Mach number gave examples in both directions.

It is of interest to discover how much of the scale effect to full-scale can be avoided by the use of aft-fixing in present-day tunnels. The calculations and particularly those for aerofoil B not shown here have provided some evidence on this point. While it may be dangerous to generalise from results for just two aerofoils, it appears that for these examples at least, if it is possible to test with transition at 0.35c, a test at  $Re = 2.5 \times 10^6$  has the same viscous flow standard as a test with forward transition as in flight at  $Re = 7.4 \times 10^6$ ; with 0.25c transition,  $Re = 5.5 \times 10^6$  is equivalent to  $Re_{EFF} = 9.0 \times 10^6$ . These precise values may not apply to other wings but they should be a reasonable guide. Further, the calculations have shown that although, for a given aerofoil, they do vary with the operating condition, the variation is probably not sufficient as to make the procedure tedious. For example, using the results of the calculations for aerofoil B, Fig 4.7(d) gives an idea of the possible variation of  $Re_{EFF}$  for a given test combination of  $Re$  and transition position. There is little variation while the flow is subcritical and attached but then,

- (a)  $Re_{EFF}$  increases when the flow becomes supercritical but is still attached,
- (b)  $Re_{EFF}$  decreases when either a shock-induced or rear separation occurs.

As a result, effects tend to compensate for each other and it is probably fair to use a value at the design cruise condition for the purposes of the methodology.

It is not immediately obvious that the boundary layer displacement thickness at the trailing edge is still an appropriate parameter when considering scale effect on the development of flow separation. Ref 183 drew attention to the fact that if one used  $H_{TE}$  as the simulation criterion, the transition position needed to convert to a certain  $Re_{EFF}$  was appreciably further aft. Up to a point, this is confirmed by Fig 4.8(a) which shows results for aerofoil B. If the conversion based on the displacement thickness was still holding, one should find the points lying on the curves on a picture such as Fig 4.8(a). This is not true when considering the shape factor at the trailing edge but it is noteworthy that the agreement between the points and the relevant curve improves when one moves to positions ahead of the trailing edge. Further, when one repeats the exercise for a higher lift coefficient beyond the onset of a rear separation,

the agreement is even better as shown in Fig 4.8(b). Remembering that it was suggested earlier that a rear separation is only significant when it spreads ahead of 0.97c, this gives some hope that one can retain  $\delta^*_{TE}$  as a simulation parameter in this context and this is confirmed by the results in Fig 4.8(c). This conclusion is perhaps not too surprising: on theoretical grounds, one might have expected that the forward spread of the separation would be a function of the rate of growth of the boundary layer displacement thickness over the rear surface.

Use of the  $\delta^*_{TE}$  criterion is however not possible for all stages in the correlation of a shock-induced separation. It would be a means of finding the transition position that would give the correct shock strength for a given  $C_L$  (using the corrections mentioned earlier when discussing the supercritical development) but we do not want to correlate in terms of shock strength; rather, we want to equate the separation bubble lengths. The standard method in use in the UK for predicting the bubble length is that due to Fulker and Ashill<sup>189</sup> and Fig 4.9 taken from this report shows that the variation of the bubble length,  $l_b$ , with  $Re$  is not monotonic. It is only when  $Re_{osh}$  is greater than about  $4 \times 10^3$  would there be any hope in being able to apply the  $\delta^*_{TE}$  simulation or indeed any other criterion of this nature. Unfortunately, it will be found that in many cases  $Re_{osh}$  will be less than this. This non-monotonic behaviour has already been mentioned when discussing the flow at high lift over slender wings. As can be seen from Fig 4.9, it is supported by a fair number of experimental data points and also it is consistent with predictions made by Green<sup>159</sup> in 1972. Green pointed out that while at higher Reynolds numbers, the velocity profiles of the boundary layers become 'fuller' and thus, more resistant to separation as Reynolds number increases. However, below a value of  $Re_{osh}$  of 2000-5000, the similarity rules no longer apply and the outer part of the boundary layer becomes 'fuller' as Reynolds number decreases. The consequences of this behaviour on the scale effect on the development of a shock-induced separation bubble are discussed later in §4.3.4.2.

Despite the last difficulty, the recent research has undoubtedly shown the value of  $\delta^*_{TE}$  as a simulation criterion and it can now be recommended in preference to other criteria suggested in Ref 2; the only caveat is that one still has to calculate bubble length as a prelude to predicting the scale effect on bubble length; in other words, in this context, calculations have, in general, to be introduced to cope with the full Reynolds-number range from model test to full-scale and not just from  $Re_{crit}$ ; a separate report is needed to explain the procedure in detail.

### 4.3.3 Examples of scale effect

#### 4.3.3.1 Wave drag

The variation of  $C_{Dwave}$  with Reynolds number with transition at 0.03c for three values of  $C_L$  as determined by the CFD calculations for aerofoil B is shown in Fig 4.10(a). In passing, it will be noted that results with further aft positions of transition when plotted at values of  $Re_{EFF}$  are in fairly good agreement with the  $x_{TR} = 0.03c$  results, particularly bearing in mind that the corrections for the slightly different supercritical flow development have not yet been applied. On a point of detail, the results plotted in Fig 4.10(a) were obtained for a 2D section but have been converted to 3D conditions on a wing of moderate sweepback but they should not be regarded as 3D results because there could well be other sections on a 3D wing that are less sensitive to scale effect.

Fig 4.10(a) has been included to illustrate that for a modern aerofoil section, wave drag can be very subject to scale effect. Some reports in the literature still convey a misleading impression that if one finds a large variation with Reynolds number in the total  $C_D$  -  $M$  characteristics, this must imply that the viscous drag or even that a flow separation is responsible. It is much more likely that it is the wave drag that is responsible: at low Reynolds number, the effect of the relatively thick boundary layer is to reduce the amount of rear loading and thus, to maintain a given  $C_L$ , more lift has to be carried forward thus, in general, increasing the shock strength and the wave drag.

The scale effect on wave drag is a function of the wing section design. As shown by Fig 4.10(a), it is large for modern sections but it would have been small for the sections used in the 1960s for aircraft such as the VC10, ie before the introduction of rear-loading as a design concept. This prompts the question as to whether Fig 4.10(a), representative of today, is likely to continue to apply in the future. Fig 4.10(b) which, at first sight, looks innocuous, does, in fact, carry a warning for the future. Fig 4.10(b) taken from Ref 183 presents the results of the CFD calculations for aerofoil A at its design condition which show that  $C_{D_{wave}}$  after decreasing with Reynolds number up to about  $Re = 20 \times 10^6$ , then shows a slight tendency to increase. Examination of the pressure distributions indicated that this is a genuine trend associated with the fact that with increase in Reynolds number, the shock is moving back on to the more curved, sloping part of the wing upper surface and hence is beginning to strengthen. In this particular case, the effect is slight but in the future, when there are likely to be attempts, particularly on wings for laminar flow applications, to design for even further aft shock positions, the trend is likely to be more pronounced. Hence, in the future, one should be wary of assuming that the scale effect on wave drag is necessarily favourable; it may be adverse. Arguably, one should have always been wary of making this assumption: one could have quoted unpleasant surprises such as that encountered in the prototype flight testing of a long duct nacelle for the DC-8 where the high Mach-number drag increments were much higher than expected on the basis of the wind-tunnel data. This was subsequently explained in terms of the shock wave in the channel between the wing lower surface and nacelle being stronger and further aft in flight than in the tunnel tests - as a result of the thinner boundary layers in flight on all the surfaces including that of the pylon spanning the channel.

Despite the appreciable scale effect on wave drag with modern transport wings, there is one published example<sup>190</sup> which shows that the extrapolation to full-scale can be handled as proposed in the AGARD methodology (note: the example has no connection with the wave drag results for aerofoils A and B). Fig 4.11 reproduced from Ref 190 presents a comparison of the measured drag in flight of the A310-300 with predictions based on wind tunnel test data extrapolated by two methods described as "direct" and "enhanced". The "direct" method includes no allowance for the scale effect on the wave drag-due-to-lift but the "enhanced" method includes such an allowance based on the difference between the wave drags calculated for the model test and flight Reynolds number and transition positions by an Euler inviscid wing + body code with viscous coupling. It will be seen that the "enhanced" method greatly improves the accuracy of the prediction, particularly for the Mach number 0.02 above the basic cruise value. Ref 194 notes that a similar good standard of correlation has been obtained for the A320 aircraft. This exercise represents just a beginning in a plan to introduce CFD estimates into the routine extrapolation procedure.

#### 4.3.3.2 Shock-induced separation

It has already been noted that the scale effect on shock-induced separation is not necessarily favourable. Fig 4.12 shows the end-result of calculations for aerofoil B to determine the growth of the shock-induced separation bubble with increasing  $C_L$  at  $Re = 2.5 \times 10^6$ ,  $Re = 5.5 \times 10^6$  and a typical full-scale Reynolds number. The calculations have allowed for the favourable scale effect on shock strength for a given  $C_L$  and then, for the scale effect on bubble length for a given shock strength as shown in Fig 4.9. In the early stages when the bubble length is small, the first effect is dominant and the scale effect on bubble length is favourable but later, at higher  $C_L$ , it is a much more confused picture. Ultimately, the bubble length at  $Re = 2.5 \times 10^6$  is smaller than at full-scale and this can be explained by the fact that at  $Re = 2.5 \times 10^6$ , the relevant value of  $Re_{0sh}$  is about  $1.7 \times 10^3$ , ie below the value corresponding to the maxima in the curves in Fig 4.9. At  $Re = 5.5 \times 10^6$ , however, the value of  $Re_{0sh}$  is about  $2.7 \times 10^3$  and the scale effect to full-scale is in the normal favourable direction and substantial.

The graphs in the Fulker-Ashill method<sup>189</sup> were derived from experimental data for aerofoils with a certain type of pressure distribution downstream of the shock and ahead of the trailing edge. In particular, it was reasonably safe to assume that the flow breakdown was associated with the rearward extension of a shock-induced separation. However, for many modern aerofoils, particularly at the lower Reynolds numbers, a rear separation may also be present. None of the available prediction methods allow for an interaction of the rear separation on the development of the shock-induced separation bubble but some data obtained more than 20 years ago in the TACT program shows that such an interaction really does exist. Tests were made on a 1/6 scale half-model of the GD F-111 TACT aircraft with an aft-cambered supercritical wing at  $26^\circ$  sweep in the 11 ft x 11 ft tunnel at NASA Ames. The model was extensively pressure-plotted and some typical pressure distributions for a station at about  $0.75 \times$  semi-span at  $M = 0.85$  and  $Re = 2.5 \times 10^6$  per ft are shown in Fig 4.13(a). The development of the shock-induced and rear separations at this Reynolds number at a station further inboard at about  $0.40 \times$  semi-span are shown in Fig 4.13(b) and the corresponding picture for  $Re = 7.0 \times 10^6$  per ft is given in Fig 4.13(c). No rear separation is present at  $Re = 7.0 \times 10^6$  and a comparison of Figs 4.13(b,c) shows that its presence at the lower Reynolds number serves to inhibit the rearward extension of the shock-induced separation. This may not be true in all cases and an interaction in the opposite direction, ie an adverse interaction from a shock-induced separation on the development of a rear separation, is always likely to be present. The effect of the s-i separation on the rear separation should be allowed for, to some extent at least, by modern CFD codes.

Vane-type vortex generators have often been used to postpone the effects of a shock-induced separation to a higher  $C_L$  or Mach number. Their presence adds to the difficulties of knowing how to fix transition in a model test to obtain a better simulation of the full-scale performance. If the generators are in the region where, in the absence of the generators, one would have allowed the boundary layer to remain laminar ahead of an aft-fix to obtain a higher  $Re_{EFF}$ , the addition of the generators would almost certainly induce transition ahead of the generators, thus partly nullifying the aft-fixing approach. If, on the other hand, the generators are located behind the aft-fix transition position, they may well increase the boundary layer thickness to an extent that reduces  $Re_{EFF}$  significantly below the value achieved with the clean wing. This could produce a

misleading comparison for the effectiveness of the generators. This is only one of several problems affecting model/full-scale comparisons of vortex generator effectiveness - as already noted in §2.1.1, the generators in the model tests should be scaled geometrically from full-scale without regard to the change with Reynolds number in the wing non-dimensional boundary layer thickness but this may lead to the need to correct the drag results and also, it has been shown<sup>319</sup> that increase of Reynolds number reduces the rate of decay of the vortices downstream and this could imply that full-scale, the generators retain their ability to control a separation over a greater chordwise distance.

#### 4.3.3.3 Buffet-onset

The report<sup>190</sup> by Fulker and Ashill contains a method for predicting buffet-onset when this is caused by the development of a shock-induced separation. It is based on the concept that when the bubble extended back to a point 'R' at the start of the relatively rapid pressure-rise close to the trailing edge, it will burst and not re-attach ahead of the trailing edge; the condition at which this happens is assumed to correspond to buffet-onset. If there is no clearly defined point 'R', one takes 'R' to be at the trailing edge and this brings us back to the classic Model 'A' introduced by Pearcey et al<sup>192</sup> in 1968.

Various authors have tried to define a criterion for 'significant flow separation' leading to buffet. In an early unpublished analysis of aerofoil data, Haines used a divergence of trailing-edge pressure of between -0.04 and -0.08 from the trend with lift or free-stream Mach number existing before divergence. It then became common practice in the UK to use a divergence of -0.05 while in Germany, an absolute value of  $C_{pTE}$  of 0.05 was used; in many cases, these two criteria are likely to give very similar results. Recent tests<sup>193</sup> at Göttingen in which the unsteady flow over a CAST 7/DAI aerofoil was explored in detail have suggested however that these criteria are very conservative and that buffet-onset may more nearly correspond to  $C_{pTE} = -0.05$ . If a shock-induced and rear separation are both present, the prediction of scale effect on buffet-onset is even more uncertain. Assuming perhaps incorrectly that experience from the calculations for aerofoil B is representative, it appears that  $C_p = 0.05$  and  $C_p = -0.05$  at say, 0.015c ahead of the trailing edge are reached respectively before and after the two separations have linked up. This suggests that a prudent approach would be to relate buffet-onset to this condition at which the two separations link up; in other words, there is a separation from the foot of the shock with no subsequent reattachment. There are at least three reasons why the predicted pressure distributions could be in error:

- (i) typically, the separations link at 0.2-0.3c ahead of the trailing edge and the rear separation at this stage cannot really be described as a local separation,
- (ii) the CFD calculation that has predicted the length of the rear separation has not allowed for the presence of the shock-induced separation bubble, and
- (iii) the separate calculation for the development of the bubble has not allowed for the presence of the rear separation.

However, for the record, some results taken from the calculations for aerofoil B are shown in Fig 4.14. If it is correct to adopt the criterion for buffet-onset suggested above, it follows from Fig 4.14, that the scale effect varies from  $\Delta C_L = 0.085$  if transition is fixed at 0.15c at  $Re = 2.5 \times 10^6$  to  $\Delta C_L = 0.03$  if it is fixed at 0.35c. The comparison is dominated by the very

strong favourable scale effect on the rear separation but this impression is accentuated by the fact that, as noted earlier, thanks to the trends at low Reynolds numbers, the scale effect on the shock-induced separation in this particular comparison is adverse. One more effect enters into this comparison: the more serious rear separation at low Re reduces the pressure recovery at the trailing edge and, as a result, the shock is further forward and so, for a given bubble length, the re-attachment point is also further forward. More research backed by flight evidence is needed on this type of complicated interaction before quantitative estimates of the scale effect can be made with confidence but it is thought that Fig 4.14 is a reasonable qualitative guide to what might happen - at a Mach number above design.

#### 4.4 Limitations on Ability to Apply Methodology

It is significant that all the experience described above (except for the extrapolation of the drag data in Ref 190) related to results in two-dimensional flow. This is obviously the easiest application but there is no intrinsic reason why the methodology could not be applied to the 3D wing-body combinations of high aspect ratio typical of present subsonic transports. For buffet-onset, an analysis in a quasi-2D manner for just the critical section where the separation first appears could well suffice, but for drag, the procedure would become more laborious with the need to consider a number of stations across the span and then, conduct a spanwise integration. This has not yet been attempted by the present author.

There is also the question as to whether the theoretical methods are capable of handling the 3D case. The evidence in Ref 194 is somewhat disturbing. This report contains a comparison of measured and predicted pressure distributions and boundary layer characteristics on a transport wing model at two conditions -  $M = 0.5$ ,  $\alpha = 6^\circ$ ,  $Re_\tau = 3.4 \times 10^6$  where the flow is subcritical and  $M = 0.825$ ,  $\alpha = 4^\circ$ ,  $Re_\tau = 4.5 \times 10^6$  where the flow is supercritical. The predicted pressure distributions show reasonably good agreement with experiment but the same cannot be said about the boundary layer displacement thicknesses. Even if one ignores the results for the higher Mach number where there is some flow separation, the relative lack of agreement is disturbing. The model test data were obtained in the NASA Ames 14 ft tunnel on a half-model of the transport wing shown in Fig 41.5(a). Some comparisons for the growth of boundary layer displacement thickness at the  $M = 0.5$  condition are presented in Figs 4.15(b,c). All the comparisons show better agreement on the outer wing than on the more highly loaded section at  $\eta = 0.45$ . The only theoretical prediction that approaches the measured value at the trailing edge at  $\eta = 0.45$  is the P D Smith integral method result in Fig 4.15(b) but even this result is fortuitous since the boundary layer development has been calculated for an inviscid pressure distribution with a steep adverse gradient approaching the trailing edge. The theoretical methods employed in these comparisons were:

- (a) in Fig 4.15(b), FLO-30 is an inviscid wing-body code<sup>195</sup>, and the viscous methods are the P D Smith 3D integral method<sup>196</sup> and the Cebeci-Smith 2D finite difference method<sup>197,198</sup>,
- (b) in Fig 4.15(c), three results were obtained by the Cebeci-Smith 3D method<sup>197</sup> with the starting conditions at the wing root taken alternatively from the results generated by the code or from the measured results at  $\eta = 0.3$ . The comparison between these two approaches

for the root starting conditions is included to show that uncertainty on this point is not the explanation for the disagreement between prediction and measurement near mid-semi-span.

On this evidence, it is questionable whether these methods meet the standards required for use in the methodology. This may be too harsh a judgement bearing in mind that displacement thickness is not needed in an absolute sense but merely as a means of equating two  $Re, x_{TR}$  combinations.

Lynch in Ref 199 points out that any viscous simulation technique is only as reliable as the CFD methods used to establish it. In his view, this limits their applicability to non-separated flow conditions. They do not succeed in situations where significant three-dimensional, ie spanwise, flow exists and Ref 199 includes some examples where the simulation techniques do not even succeed in 2D separated flow. These examples are reproduced in Figs 4.16(a,b,c). All these results were obtained in the 15 in x 60 in tunnel at IAR, Ottawa. Figs 4.16(a,b) present results from tests on an aft-loaded aerofoil with aileron in which the aileron effectiveness was measured at  $Re = 5, 15$  and  $25 \times 10^6$ . Transition occurred at the leading edge at  $Re = 25 \times 10^6$  but at the two lower Reynolds numbers, transition was fixed at positions that, it was believed, would give the same effective boundary layer over the aerofoil as at  $Re = 25 \times 10^6$ . This approach only succeeds at  $Re = 15 \times 10^6$  in the cruise condition; it fails at  $Re = 5 \times 10^6$  in the cruise and at both Reynolds numbers at buffet-onset. Lynch comments that in these 2D tests, the high  $Re$ -result is better than one would expect from the lower  $Re$  simulation attempts but in two sets of flight (3D) results, exactly the opposite was found: the aileron effectiveness in flight was poorer than one would have predicted from aft-transition tunnel tests. Fig 4.16(c) is concerned with the assessment of the base drag of an airfoil with trailing-edge thickness added as a wedge on the lower surface as on the MD-11. As in the previous example, the results in Fig 4.16(c) should have been independent of Reynolds number if the simulation technique had been successful but, in fact, the drag reduction due to the wedge decreased with increasing  $Re$ . Lynch and others therefore believe that one can only use the methodology when the flow is completely attached but the present author feels that this is too harsh a judgement.

It is possible that with further study and research, a viscous simulation technique will be found that will cope with examples such as those just described. The present author feels that a most important distinction can be drawn between these examples and the examples of successful application of the AGARD methodology as described earlier: in Fig 4.16 the aim was to find a transition position which, at low  $Re$ , would give exact simulation of the high  $Re$ -result whereas in the earlier examples, the aim was to simulate the viscous flow as closely as possible and to minimise the unpredictable features but not necessarily to strive for complete simulation of every feature. In other words, to be successful, one should recognise that extrapolation and correction of the low  $Re$ -results will still be necessary even after applying the simulation technique. This can be accepted as part of the methodology provided it is done on a sound physical basis. Referring to the last example in Fig 4.16(c), it is most unlikely that this can be addressed by a single simulation criterion; one should choose a criterion that will achieve some benefit in the most important respect and then allow for other effects by corrections - as was proposed in §4.3.2 for the different supercritical development over the forward upper surface having obtained the correct rear loading. Clearly, more research is needed to widen the range of applicability of techniques such as the AGARD methodology

but hopefully, the widening should be possible. The most significant improvements will come from advances in the ability to compute 3D flows with substantial areas of flow separation.

#### **4.5 Research not Directly Connected with Methodology**

##### **4.5.1 Unsteady flow in buffet**

Much has been written about scale effect on the buffet-onset boundary but less attention appears to have been paid to the scale effect on the unsteady flow in buffet itself. There is however one recent important and enlightening reference<sup>193</sup> on the subject. This report describes the results obtained in some tests in a Ludwig tube at DLR Göttingen on a 2D model of the CAST 7/DOI supercritical aerofoil section. The model was extensively instrumented for steady and unsteady pressure measurements and surface hot-film sensors. Also, the flow field was observed by a holographic, real-time interferometer. Appreciable fore-and-aft shock movements occur in the oscillatory flow in buffet and Fig 4.17(a) shows what happens in a typical cycle. This figure is interpreted in detail in Ref 193 and quoting from this description, "the increase in boundary layer thickness at the trailing edge is essentially caused by the increase in shock strength and the development of shock-induced separation reaching the trailing edge. There is, of course, a delay between the onset of separation at the foot of the shock and the time the separation bubble reaches the trailing edge. This can best be seen in the upper diagram where the shock strength is reduced during the latter stages of the forward movement, ie shock-induced separation disappears, while the boundary layer thickness still increases. Only after a certain time has elapsed will the reduced shock strength be felt at the trailing edge and the downstream movement of the shock will be initiated." This description contains the clue as to why the unsteady flow is subject to scale effect: we have already seen that the rate of growth of a shock-induced separation bubble varies with Reynolds number and this rate of growth is an essential factor in determining the frequency of the shock movements. Before considering the scale effect, Fig 4.17(b) shows how the frequency and amplitude of the oscillation varies with increase of incidence into buffet. In the incidence range prior to buffet-onset, the shock oscillates with a relatively high frequency and low amplitude but then as the separation becomes more severe, the average shock position moves more rapidly upstream, the frequency decreases and the amplitude increases until the full buffet state is reached. It should be noted that high frequency is accompanied by low amplitude and vice versa and this can be taken as a general conclusion. Stanewsky and Basler note that the amplitude of the oscillation is essentially determined by the average shock position and the change in shock location for a given disturbance,  $\Delta\alpha$ , at the trailing edge. Maximum amplitude corresponds to a condition where the flow alternates between attached and totally separated states.

Fig 4.17(c) shows the effects of Reynolds number on the reduced frequency and amplitude of the oscillation. The Reynolds number range has been extended up to  $Re = 30 \times 10^6$  by including data for two other aerofoils taken from Ref 200. The conclusions from Fig 4.17(c) are:

- (i) the reduced frequency decreases and amplitude increases with increase in Reynolds number throughout the range of the data. This is an important result because it indicates that the load variation on the aerofoil increases with  $Re$ ,

- (ii) the aerofoil shape has no noticeable effect on the reduced frequency at a given  $Re$  but has a major effect on the amplitude. The amplitude is low for the NACA 0012 aerofoil and this can be explained in terms of the shape of the pressure distribution upstream of the shock: with NACA 0012, the suction increase up to the shock whereas with the modern supercritical sections, the suction either reduce or are more nearly constant.

The reduction in frequency with  $Re$  can be related to the slower growth of the separation bubble with the thinner boundary layers at high Reynolds number; Fig 4.17(d) confirms that this trend in bubble growth does apply in this particular case.

One final point from Ref 193: Fig 4.17(e) shows that prior to buffet-onset, the scale effect on the shock oscillation frequency is in the opposite sense.  $M = 0.78$  is beyond the boundary but  $M = 0.74$  and  $0.76$  where the frequency increases with  $Re$  are before buffet. Ref 193 suggests that the reason is that, at the higher Reynolds number, there will be a higher average velocity in the boundary layer and this would lead to a higher convection speed of disturbances from the foot of the shock and hence, an increased frequency of the shock oscillation.

The material in Ref 193 has been described in some detail because scale effect on the unsteady flow in buffet has been a neglected area; Mabey, for example, in his review<sup>201</sup> of the papers at an AGARD S&M Panel Symposium in 1988 recommended that much greater attention should be given to establishing the magnitude of possible scale effects, both in experiments and calculations. The TACT programme was however a major programme in this area involving flight-tunnel comparisons for the F1-11. Results are presented in Ref 202. The report emphasises the difficulties in extracting evidence on scale effects from flight-tunnel comparisons because both Reynolds number and aircraft wing aeroelasticity contribute to the differences that are observed: indeed, they tend to act in opposition to each other. However, some evidence of scale effects on the fluctuating pressure data in the model tests was obtained by comparing results from tests on a steel wing at  $Re = 14 \times 10^6$  and on an aluminium wing at  $Re = 7 \times 10^6$  for which the wing shapes are closely similar. Flow separation was observed at  $0.06c$  at  $1^\circ$  lower incidence at the higher Reynolds number and this was consistent with the flight data which also suggested an adverse scale effect.

#### 4.5.2 Combat aircraft wings

Scale effect on the flow over the wings of combat aircraft at transonic speeds is discussed in detail in Ref 2 and as a general presentation of the subject, it is difficult to add to what was written in Ref 2. However, there are two recent reports which deserve a mention. First, Ref 190 includes some results from a flight-tunnel comparison of the pressure distributions over the wing of the EAP aircraft and second, Ref 203 presents some test results at two alternative relatively high test Reynolds numbers on a research model specially designed at NASA Ames to produce data for validation of CFD codes. Both these programmes provide new evidence in support of the discussion in Ref 2.

The flight tests<sup>190</sup> on the EAP aircraft were made to confirm the loads that had been predicted on the basis of model tests particularly on a 1/13 scale model in the ARA and DRA tunnels at Bedford. The pressure plotting coverage of the wing was extensive both in flight and on the model: 381 miniature ENDEVCO 8515 transducers on the aircraft and 604 pressure tapings on the model. To create the comparisons, the wind

tunnel data were interpolated to correspond to the flight trimmed conditions, ie matched foreplane and trailing edge flap angles.

Fig 4.18(a) compares the wing isobar patterns in flight and tunnel for a subsonic condition at  $\alpha = 12^\circ$ . It will be seen that there is good agreement between the two patterns: both show three part-span vortices. Ref 190 notes that as incidence is increased from this condition, the two inner vortices merge to form a 2-vortex system over the wing which ultimately becomes a single vortex from the wing apex. This type of development might have been forecast on the basis of the wing planform, leading-edge flap geometry and the experience of the tests on the F-106B discussed earlier in §3.3.5.3. Comparisons to illustrate the scale effect are presented in Figs 4.18(b-e). All these results relate to  $M = 0.80$ . Fig 4.18(b) compares pressure distributions as obtained in tests in the DRA tunnel at two alternative test Reynolds numbers,  $6$  and  $15 \times 10^6$  based on wing mean chord and then, Fig 4.18(c) gives a similar comparison between model test at  $Re = 6 \times 10^6$  and flight at  $Re = 6 \times 10^7$ . Both comparisons show that the suction near the leading edge increase with Reynolds number; it is thought that this indicates that the appearance of vortical flow is delayed by the increase in  $Re$  but the differences were only observed over a limited range of incidence: these results are for  $\alpha = 6.5^\circ$  but by  $\alpha = 12^\circ$ , the vortical flow is fully established and the changes with  $Re$  (not shown here) are then trivial. Since the main scale effects occur near the leading edge, Figs 4.18(d,e) have been included as they should indicate the most sensitive consequences. Fig 4.18(d) compares the integrated vertical shear load on the outboard droop section as measured in flight and as predicted from the model test data and Fig 4.18(e) presents a similar comparison for the wing root torque. In Fig 4.18(d), differences are evident above  $\alpha = 4^\circ$  but ultimately, at  $\alpha = 12^\circ$ , the results come into agreement. In Fig 4.18(e), the discrepancies increase with altitude (ie  $C_L$ ) but this is not true of the actual loads because of the reduction in dynamic pressure.

Looked at from the standpoint of the aircraft structural design engineer, these results are reassuring: he can rely on the design loads predicted from the model test data but from the standpoint of the aerodynamicist interested in scale effect, the results confirm the suggestions in Ref 2 that when the flow is dominated by part-span vortices originating near the leading edge (flow types B and C in chapter 3.3.2 in Ref 2), the appearance and development of this flow is likely to be delayed by increase in Reynolds number. This may not be an academic conclusion; it could have practical consequences for the aircraft stability and control characteristics, particularly the lateral characteristics.

Turning to the second report<sup>203</sup>, the NASA Ames research wing has, by comparison, a very simple geometry for the sake of facilitating the CFD calculations: a simple planform with an aspect ratio of 3.2 and a leading-edge sweepback of  $36.9^\circ$  as shown on the left in Fig 4.19 and a symmetrical NACA 64010 section. Model tests were made in the Ames High Reynolds Channel II at nominal Reynolds numbers of  $8$  and  $14 \times 10^6$ , based on the wing root chord. Repeatable scale effects were observed in the flow at the outermost three stations at  $\alpha = 8^\circ$  as shown in Figs 4.19(b,c). These conditions are in what was described in chapter 3.3.2 of Ref 2 as flow type D, viz a shock-induced separation behind a moderately swept shock outboard of the intersection of the three shocks in a 3-shock pattern. Ref 203 comments that the Reynolds-number effects are most noticeable at the stations at which the double-shock structure is most pronounced and where the two shocks coalesce. This is



as one might have expected from the discussion in Ref 2 but in detail, the results appear to cast doubt on whether the speculative discussion of this type of flow in Ref 2 is correct. However, it should be noted that these comparisons in Fig 4.19(b,c) are for a given incidence whereas the discussion in Ref 2 is based on comparisons for a given  $C_L$ . In Fig 4.19(b) in particular,  $C_L$  is clearly reduced by the increase in Reynolds number and if the incidence were increased to recover this lift, this could lead to a significant rearward movement of the shock on the outer wing, thus altering the appearance of the comparison. The results would certainly repay further analysis and study. (In passing, it may be worth noting that Fig 14 on page 187 in Ref 2 is not plotted correctly but the description in the text is correct).

### 4.5.3 Slender wings

The flight-tunnel comparisons<sup>161</sup> on the Fairey Delta 2 mentioned in §3.3.5.4 also included tests at  $M = 0.9$  and  $M = 1.17$  (flight) and  $M = 1.30$  (tunnel). At  $M = 0.9$ , the results at low incidence as at  $M = 0.5$ , suggested that the vortex origin was slightly further inboard in the tunnel than in flight but at low supersonic speeds, where the separation is shock-induced, the reattachment line position is apparently independent of Reynolds number.

As noted earlier in §3.3.5.1, the International Vortex Flow Experiment<sup>147</sup> included tests over the Mach-number range up to  $M = 4.0$  and also, the further tests at NLR in the later cooperative programme<sup>151</sup> which specifically investigated Reynolds number effects including tests at transonic Mach numbers such as  $M = 0.85$ ,  $0.90$ ,  $0.95$  and  $1.2$ . In principle, increasing the Mach number to the transonic range introduces two new features in the flow which could be subject to scale effect:

- (i) the flow under the primary vortex can now contain a shock wave at a constant percentage local semi-span just outboard of the suction peak; this shock being termed the cross-flow shock, and
- (ii) in the decelerating flow towards the rear of the wing near the centre-line, a shock at about constant  $x/c_R$ ; this shock being termed the rear or terminating shock.

The boundaries in the  $(M, \alpha)$  plane which mark the appearance of these features are shown in Fig 4.20(a).

Fig 4.20(b) shows the development with incidence of the spanwise pressure distributions at  $M = 0.85$ . This figure can be compared with Fig 3.68(b) which is a corresponding figure for  $M = 0.2$ . Once again at high incidence, the peak suction in the plateau region outboard of the primary vortex reveals the presence of the secondary vortex and this is more pronounced at the higher Reynolds number. This will lead to a stronger interaction with the primary vortex at the higher Reynolds number, an earlier formation of the cross-flow shock and a further inboard location for the secondary separation. The presence of the cross-flow shock has therefore had no radical influence on the scale effect which, in nature, is the same as at low Mach number; quantitatively, however, there is an impression that the interaction with the primary vortex is greater but more pressure plotting points are really needed to be sure of this.

The effect of the terminating shock is possibly of more interest. Fig 4.20(c) shows that at an incidence such as  $15^\circ$ , well below that for vortex bursting, this shock appears at about  $0.75 \times$  root

chord above  $M = 0.80$  and then moves back towards the trailing edge in an orderly fashion; it is not strong enough for there to be any likelihood of scale effect. The really interesting developments occur in an apparent interaction between this shock and the vortex bursting process. Fig 4.20(d) shows the chordwise pressure distribution in the plane of symmetry before and after vortex breakdown at  $M = 0.85$ . It will be seen that there is a sudden change from a single to a two-shock system. Ref 151 poses the question as to whether the rear shock provokes vortex bursting or whether vortex breakdown causes the branching to the second type of shock system. Elsenaar and Hoeijmakers advance a possible hypothesis in favour of the second interpretation but in the context of this Agardograph, the more relevant query is whether this complex interaction is likely to be subject to scale effect. At first sight, Fig 4.20(e) suggests that Reynolds number does have an influence: the sudden change associated with the vortex breakdown occurs between  $\alpha = 22^\circ$  and  $23^\circ$  at  $Re = 9 \times 10^6$  but not at  $Re = 4.5 \times 10^6$  but it is probably best to accept the tentative conclusion in Ref 151 that Reynolds number is not a primary variable; the flow development merely depends weakly on  $Re$ . However, one cannot be sure bearing in mind that the whole phenomenon is not completely understood.

As at low Mach number, therefore, scale effects can be found in the transonic flow over slender wings but it is not clear that they would be significant in practice.

Before leaving slender wings, it is of interest to refer to some results at supersonic speeds. The tests on the 5% thick slender wing with  $65^\circ$  leading-edge sweep and a rounded leading-edge in the International Vortex Flow Experiment<sup>147</sup> extended up to  $M = 4.0$ . At  $M = 1.72$ , Fig 4.21(a), there is no suction peak at the leading edge; a supersonic pressure plateau develops terminated by a shock at about 90% semi-span with local separation at the foot of this shock which develops into a vortical flow at incidences above  $3.8^\circ$ . At  $M = 2.18$ , Fig 4.21(b), the plateau is more pronounced with the shock situated at about 75% semi-span. Above  $\alpha = 6^\circ$  at  $M = 1.72$  or  $10^\circ$  at  $M = 2.18$ , the flow starts to separate at the leading edge itself. Changes in Reynolds number were not explored in this programme but one can refer to a separate programme<sup>204</sup> at NASA Langley in which Reynolds-averaged Navier-Stokes calculations were made for a  $65^\circ$  delta wing with various leading-edge geometries for a stream Mach number of 1.6 and three alternative Reynolds numbers, 1, 2 and  $5 \times 10^6$ . Spanwise pressure distributions for a wing with a symmetrical elliptic leading edge are shown in Fig 4.21(c); the Reynolds number did not affect the prediction of separated flow for this case but the increase in Reynolds number increases the well-defined peak suction below the vortex. This implies an increase in the vortex core's crossflow Mach number and Fig 4.21(c) also shows that the vortex core moves slightly outboard with increase in  $Re$ . Hence, the primary vortex becomes stronger and more compact with increase in Reynolds number. Introducing  $10^\circ$  camber results in the flow becoming attached at the leading edge but then, increasing the Reynolds number introduces a weak separation at the foot of the shock as shown in Fig 4.21(d). It should be noted that in these cases in supersonic flow, the crossflow shock is above the vortex in contrast to the crossflow shock below the vortex that was being discussed in the  $M = 0.85$  results.

## 4.6 Conclusions and Possible Future Trends

First, to summarise the main conclusions about the AGARD methodology:

- (i) the best simulation criterion to use for the conversion from  $(Re, x_{TR})_{test}$  to  $(Re_{EFF}, x_{TR})_{flight}$  is the boundary layer displacement thickness at the wing trailing edge. For cases where in the test at low Reynolds number, transition has only been fixed in an aft position on the upper surface, a second order correction has to be made as described in Ref 183,
- (ii) in subcritical flow, use of the boundary layer displacement thickness gives a perfect correlation but when the flow over the forward upper surface is supercritical, corrections have to be made for the different supercritical development. These can easily be obtained from CFD calculations and are unlikely to amount to more than 0.0002 in  $C_{D wave}$ ,
- (iii) the value of the effective Reynolds number which, with forward (ie flight) transition corresponds to an aft transition position in a low Re model test, does not vary greatly with Mach number and  $C_L$ . It is suggested that, for a transport aircraft, one should use the value derived for a design cruise condition,
- (iv) the above simulation criterion can be used in the extrapolation to full-scale of both wave drag and the rear separation characteristics. As regards shock-induced separation, however, it can only be used in the first stage of finding the shock strength for a given  $C_L$  but not in finding the length of the shock-induced separation bubble for a given shock pressure-rise. This reservation applies particularly when  $Re_{Qsh}$  in the model test is less than about  $2 \times 10^5$ ,
- (v) the most difficult problem is to predict the scale effect on buffet-onset when both a shock-induced and a rear separation are present. Lynch in Ref 199 notes that in one particular case, a buffet intensity of  $\pm 0.1$  g occurred when about 10% of the wing area was covered by separated flow,
- (vi) CFD has already been used successfully to extrapolate model test drag data to full-scale,
- (vii) all the above conclusions are encouraging but at present, there are some clear limitations on the applicability of the methodology; it is only easy to apply to results in two-dimensional flow and some US experience suggests that viscous simulation is only successful for cases where no flow separation is present,
- (viii) to be successful, one should recognise that full simulation at lower Reynolds numbers may never be possible; rather, the aim should be to test in a way that will minimise the difficult-to-predict aspects of the scale effect and then to accept that corrections to the measured data will still have to be applied for features that can be predicted.

Many writers have attempted to answer the question as to what is the Reynolds number above which there is little scale effect at transonic speeds or above which the scale effect is at least predictable. There is no unique answer to this question. In the 1950s and 1960s before the introduction of design concepts such as rear loading or the supercritical type of section, the scale effect between  $Re = 2.5 \times 10^6$  and full-scale was relatively small. Today, as we have seen, the scale effect in this range can be large, particularly as regards wave drag and buffet-onset and it is mostly favourable. Looking to the future, there are signs that the scale effect may be dramatic, difficult to predict to the

required accuracy and unfavourable: the comfortable feeling that the model test data are likely to be conservative will be lost. Let us quote some evidence in support of these statements.

First, the past: in Ref 205, Poisson-Quinton and Vauchieret presented the results of tests on the largest model (M5) in a family of calibration models in various large transonic tunnels in 7 different countries and drew the overall conclusion that scale effects were small provided that one tested at a Reynolds number of at least  $Re = 2 \times 10^6$ . Lift and stability characteristics from these tests are presented in Figs 4.22(a,b). These particular tests were made with natural transition but it is likely that in most conditions of interest, transition was well forward because the wing section was designed to produce a "peaky" pressure distribution. In general, however, an early conclusion from UK research was that one should always test at transonic speeds with fixed transition. Ref 206, a general review of the development of the subject, included examples of where, in the period up to 1966, it was possible to obtain good agreement between shock positions as measured in flight and in model tests with transition fixed in a forward position. Figs 4.23(a,b) show the two examples that have usually been quoted in support of this conclusion. Fig 4.23(a) is a comparison for a combat aircraft with a 10% thick,  $35^\circ$  swept wing and the Reynolds number for the model tests was  $1.75 \times 10^6$ ; Fig 4.23(b) gives the results for a very detailed, careful comparison<sup>207</sup> on the Super VC10 where the model test  $Re_z = 5.5 \times 10^6$ . However, advances in wing design then led to the need to introduce the aft-fixing technique in model tests: the sensitivity of shock position to transition position and by implication, Reynolds number is illustrated in Fig 4.23(c) which compares the shock positions with forward and aft transition at  $Re = 3.0 \times 10^6$  on a wing that was a forerunner of the A300B. This became standard practice and, for a time, new designs were validated in model tests with aft transition at Reynolds numbers of around  $4-6 \times 10^6$ . However, this advance has now proceeded to the point where, for example, the Boeing design philosophy<sup>188</sup> is to test half-models at a Reynolds number of about  $15 \times 10^6$  in an attempt to minimise the scale effect that has to be allowed for by CFD calculations.

The lesson from the past, therefore, is that one must not assume that well-established conclusions will continue to apply in the future. Lynch in Ref 199 gives a good example of the changes that may come from further advances in wing design. A series of calculations were made with the TLNS3D Navier-Stokes code<sup>209</sup> for both a contemporary wing configuration and an advanced concept. Calculations were made for conditions representing full-scale flight Reynolds numbers at nominal cruise Mach numbers. The results for the contemporary section in Fig 4.24(a) were in good agreement with evidence from tuft behaviour in flight. The development of the flow with increasing incidence in this case is a familiar picture: the shock-induced separation appears at the foot of the shock and extends progressively rearward and is ultimately joined by a rear separation. It was found that there was a linear correlation between the growth of the predicted separated-flow area and the intensity of the buffet in flight. However, on the future section, the results in Fig 4.24(b) indicate a completely different type of behaviour beyond separation-onset. Severe separation aft-of-the-shock and back to the trailing edge develops immediately and rapidly. These calculations were for the full-scale Reynolds number and although no results are shown in Ref 199 for model test Reynolds numbers, it is easy to visualise that then, the shock will be further forward and the separation would develop as for the contemporary section. In other words, a gradual development in the model tests would

be replaced by a rapid development, full-scale; this could lead to an adverse scale effect on boundaries that relate to some finite development of separated flow - and a more undesirable flow behaviour, full-scale. The author understands that examples of such an adverse scale effect have, in fact, already been observed in test data from cryogenic, high-Re tunnels.

A far-aft shock position is not the only reason why it is wrong to assume that favourable scale effect at transonic speeds will always be present. Experience suggests that little or no favourable and quite possibly adverse scale effect should be expected in any case where the separation contains a strongly three-dimensional element. This remark is relevant, for example, to flows in wing-body junctions or in three-dimensional situations such as an underwing nacelle installation. One experienced observer has indeed described the AGARD methodology as "naive"; if this is true, it must reflect the belief that most of the presently unpredictable examples of scale effect are either connected with separated flow or include a strong element of spanwise or interference flows.

A final point about the future is that none of the above discussion has addressed the complex problems of scale effect on wings designed to achieve long extents of laminar flow under full-scale conditions. A first attempt to develop an extrapolation procedure to cope with the scale effects on such a laminar-flow wing is described in Ref 210 and illustrated in Figs 4.25(a,b). In Fig 4.25(a), three different flow regimes are distinguished: region I is the laminar flow bucket with fully developed laminar flow up to a steep adverse pressure gradient on both the upper and lower surfaces; in region II, transition will occur near the leading edge on the upper surface and in region III, only the lower surface will be turbulent. In between these regions, there are transitional regions in which the transition point moves forward either gradually or discontinuously. The picture could be more complicated than this but even this picture implies that considerable skill will be needed to interpret the model test data and to devise an extrapolation procedure to allow for the scale effects indicated in Fig 4.25(b). The main features of this scale effect are:

- (a) in general, the range of the laminar-flow bucket will be smaller in flight than in the model test. Linear boundary layer stability calculations will have to be undertaken as part of the extrapolation procedure for model test data to determine this scale effect,
- (b) the increase in drag marking the upper bound of the bucket is likely to be more gradual at full-scale Reynolds numbers. This is because at low Reynolds number in particular, the direct effect of the forward movement of transition is compounded by a loss in rear loading which, for a given  $C_{L_0}$ , results in a steepening of the adverse pressure gradient over the forward part of the upper surface, thus accentuating the forward movement of transition and the possible increase in wave drag,
- (c) it is quite possible that transition on both surfaces in region I is provoked by a laminar separation. The separation itself will be independent of Reynolds number but the extent of the separation-bubble will vary as described in another context in §3. At the cruise condition, it is likely that this separation occurs as part of a laminar boundary layer - shock interaction and scaling laws for this situation are largely unknown,

- (d) in regions II and III, the issues are the same as for a turbulent wing but the Reynolds-number effects could well be larger,
- (e) in the upper transitional region, aft-fixing can be used in principle to simulate the flight transition positions or preferably, the flight boundary layer displacement thickness but this approach could place a premium on the ability to predict the transition positions in the transitional range in flight.

Clearly, this can only be regarded as the first instalment of a story that will need to be extended and revised in the future. Merely considering the likely scale effect in the design condition and how this can be reduced by a suitable test technique in the wind tunnel presents a challenge. It is unlikely that there will be any difficulty about obtaining the same extent of laminar flow in the tunnel as in flight but this still leaves one with the problem of either finding a means of reducing the boundary layer thickness in the tunnel or of trusting a CFD calculation for estimating the effects of a serious difference in thickness. The latter approach may not offer the necessary accuracy: Green in Ref 210A notes that if the ratio of Reynolds numbers in flight and tunnel is 10, the boundary layer displacement thickness at the trailing edge of a typical laminar aerofoil is 220% thicker in the tunnel than in flight whereas for a turbulent aerofoil, the corresponding figure is only about 60%. The likely effect of this is compounded by the fact that the pressure distribution on the rear upper surface of the laminar aerofoil will contain a particularly severe adverse gradient; the risk of a premature separation in the tunnel and a notable loss in rear loading is therefore great. This is a real problem; to say that the boundary layers in flight and tunnel are both thin compared with past experience is unlikely to be an acceptable response. Aft-fixing is no longer available as a means of reducing the boundary layer thickness and so, the most obvious suggestion is to use suction. Calculations suggest that this approach should be possible but at the present time, there is uncertainty as to how much suction would be required. To quote Green in Ref 201A, "it will require good engineering and good fluid dynamics to develop the technique and to win the confidence of the aircraft designer".

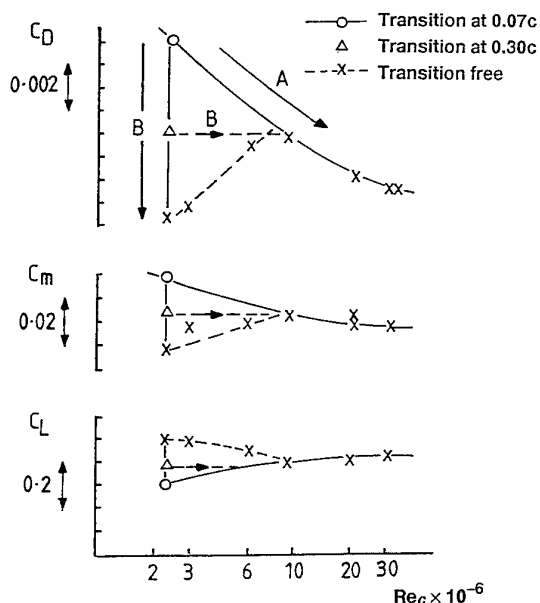
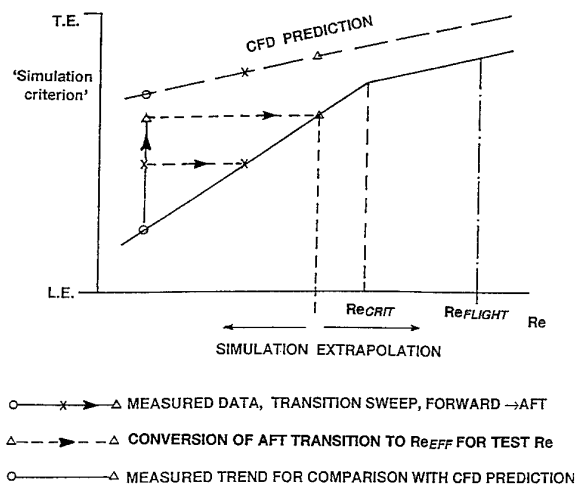


FIG 4.1 Example of Two Simulation Approaches  
(from ref 183)



EXTRAPOLATION TO  $Re_{FLIGHT}$  BASED ON

- (i) MEASURED TREND UP TO  $Re_{CRIT}$
- (ii) PARALLEL TO COMPUTED TREND FROM  $Re_{CRIT}$  TO  $Re_{FLIGHT}$

FIG 4.2 Basis of Methodology  
(from ref 183)

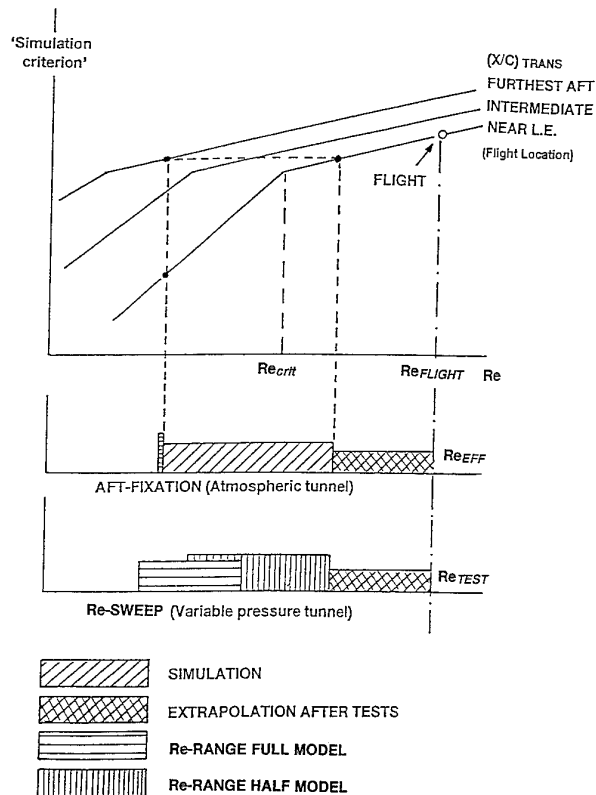


FIG 4.3 Simulation Scenario 3  
(Maximum  $Re_{EFF}$  (TR-SWEEP) or  
 $R_{TEST}$  (Re-SWEEP) >  $R_{CRIT}$ )  
(from ref 183)

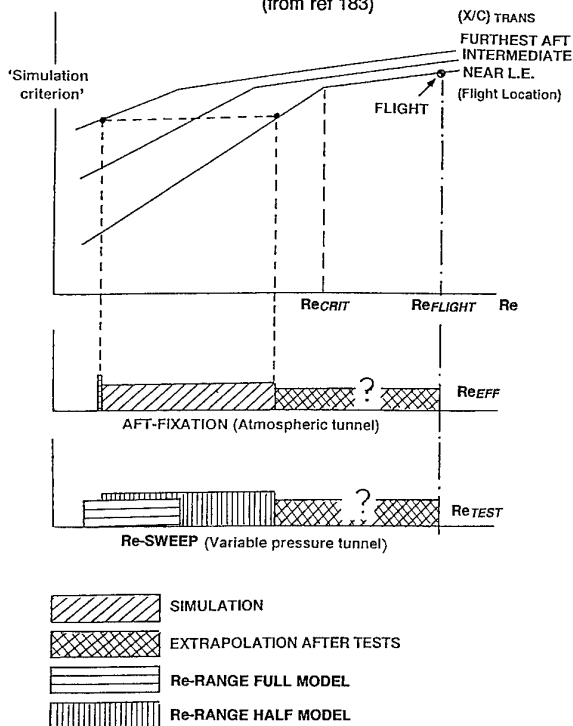
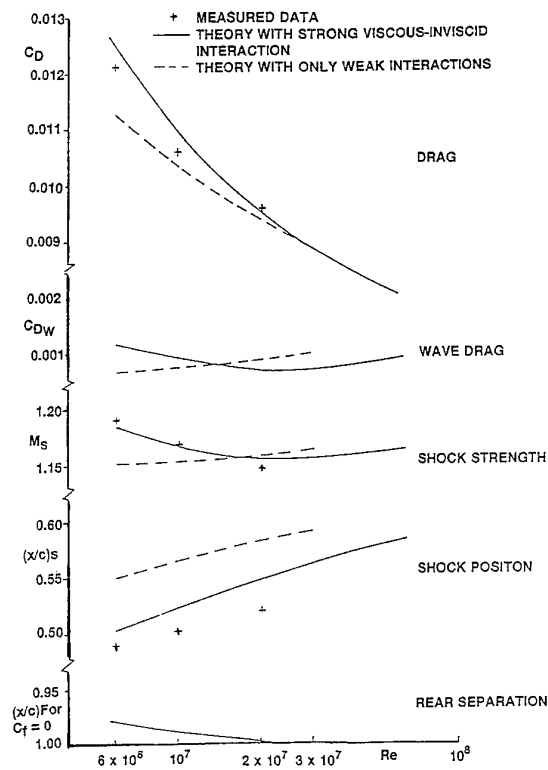
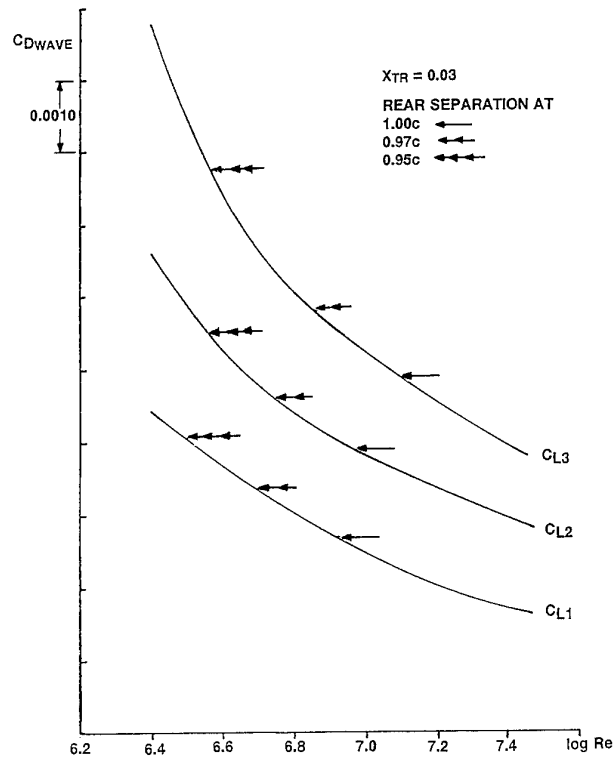


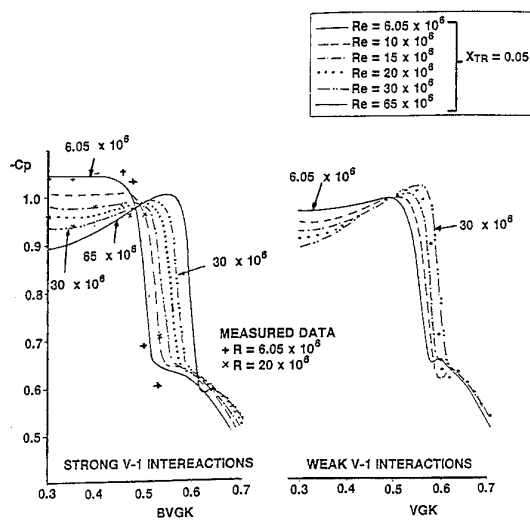
FIG 4.4 Simulation Scenario 4  
(Maximum  $Re_{EFF}$  (TR-SWEEP) or  
 $R_{TEST}$  (Re-SWEEP) <  $R_{CRIT}$ )  
(from ref 183)



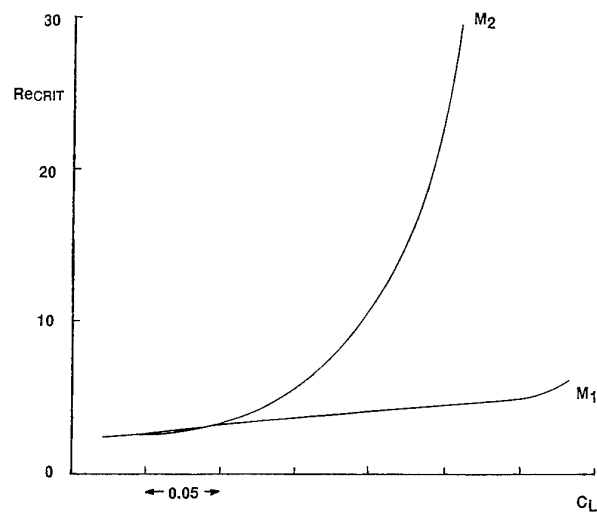
(a) Aerofoil A  
(from ref 183)



(c) Aerofoil B



(b) Aerofoil A  
(from ref 183)



(d) Aerofoil B

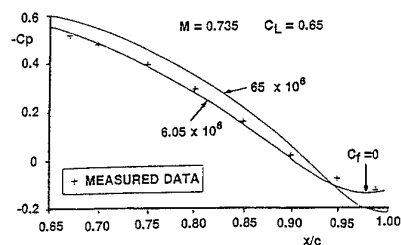


FIG 4.5 Effects of Rear Separation

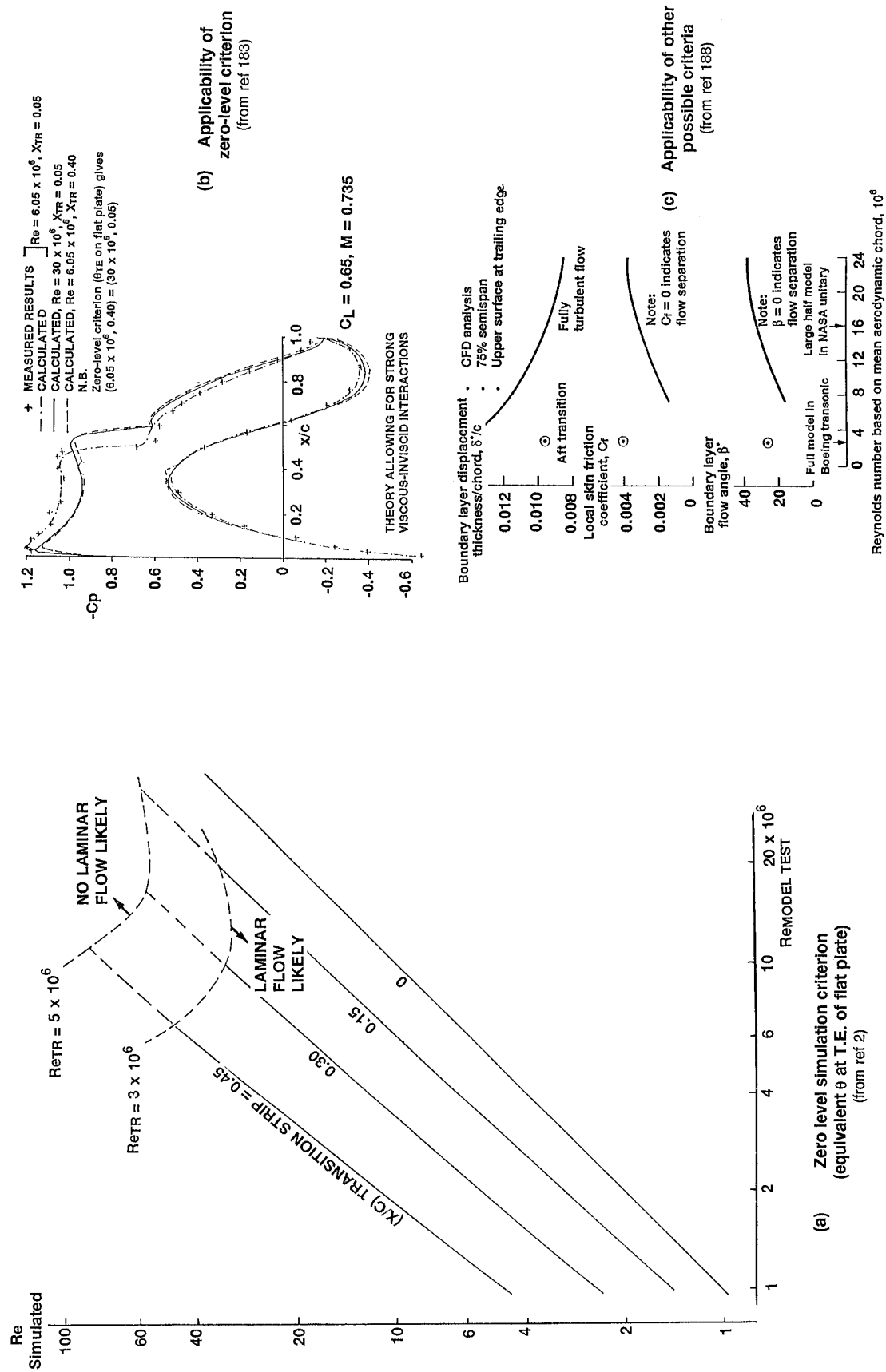
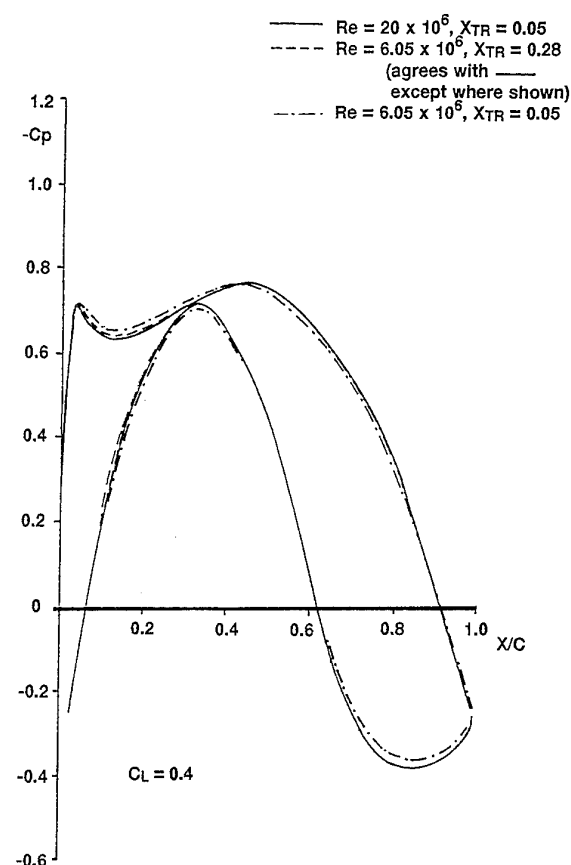
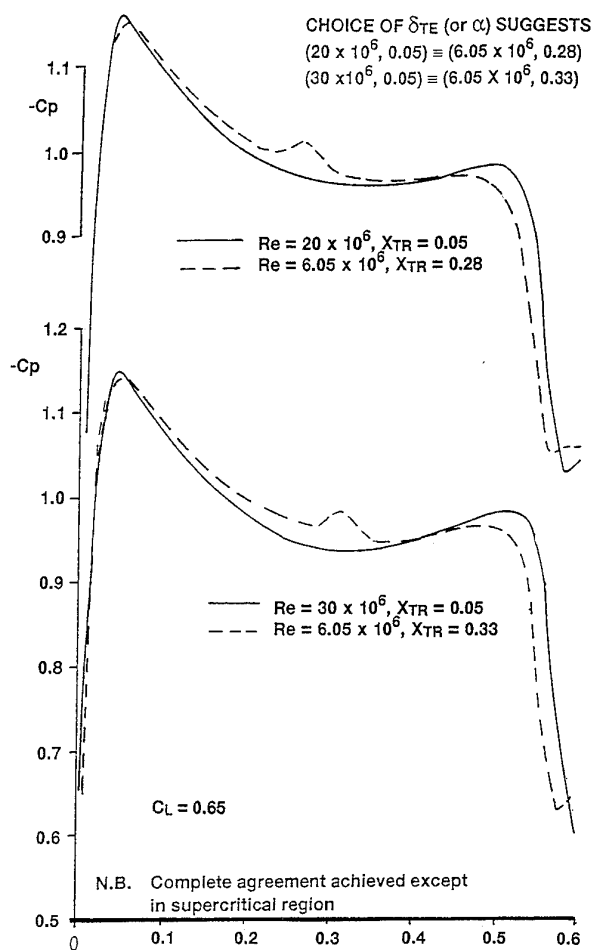


FIG 4.6 Effect of Zero Level and Other Simulation Criteria



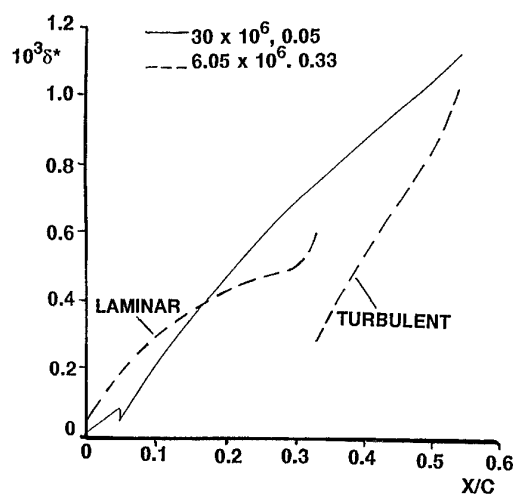
CHOICE OF  $\delta_{TE}^*$  (or  $\alpha$ ) AS SIMULATION CRITERION SUGGESTS  
 $(20 \times 10^6, 0.05) \equiv (6.05 \times 10^6, 0.28)$

(a) Aerofoil A  
(from ref 183)

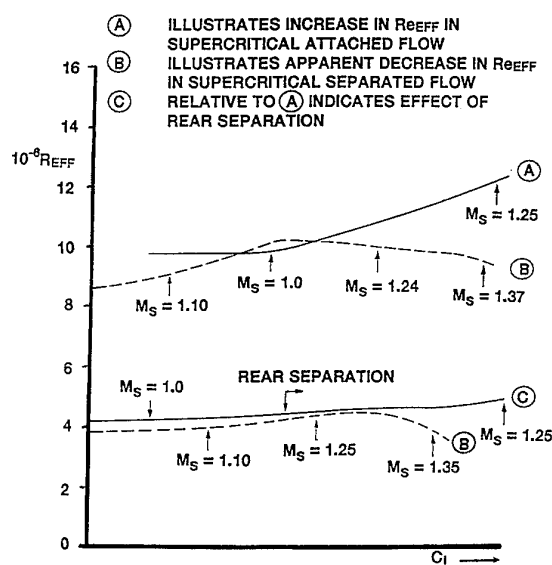


(b) Aerofoil A  
(from ref 183)

4 CURVES FOR DIFFERENT COMBINATIONS OF ( $Re_{TEST}, X_{TR}$ )  
 — CURVES FOR  $M_1$   $M_2 > M_1$   
 - - - CURVES FOR  $M_2$

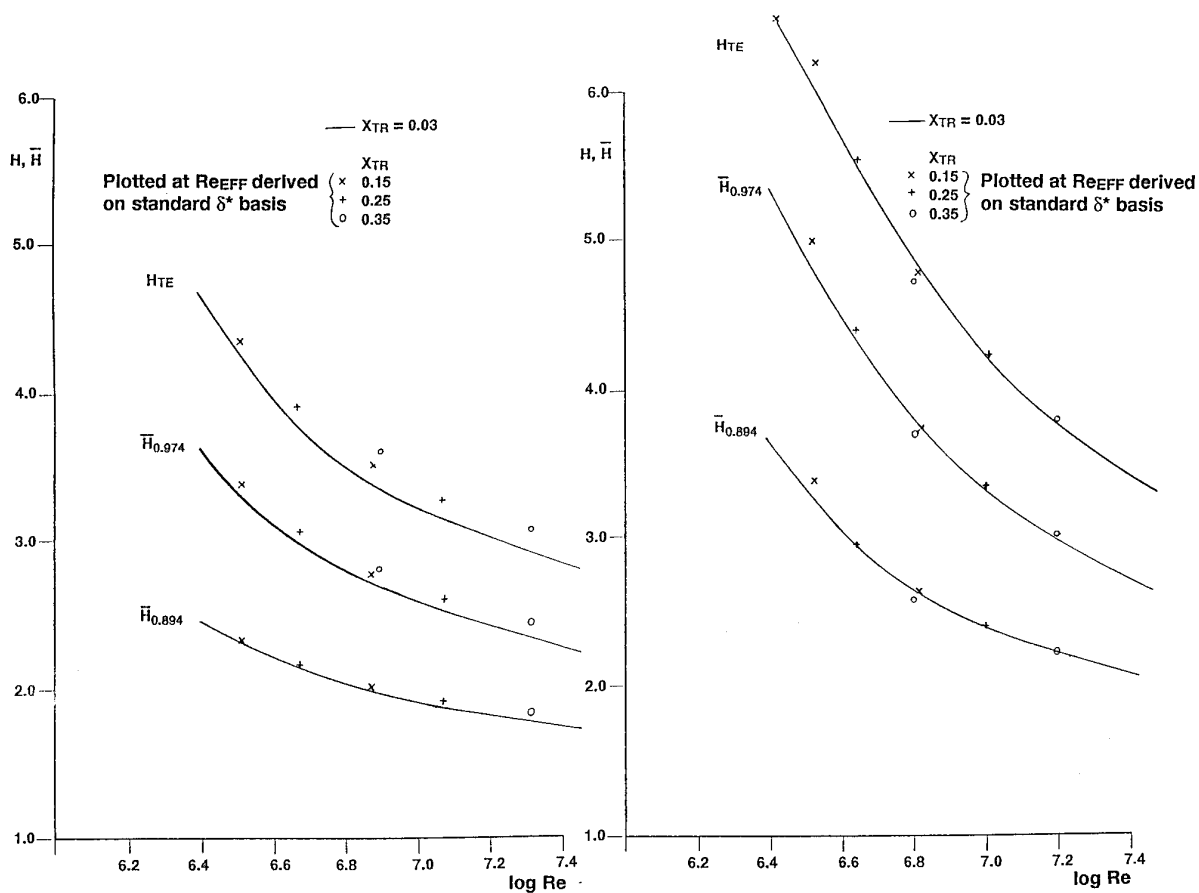


(c) Aerofoil A  
(from ref 183)



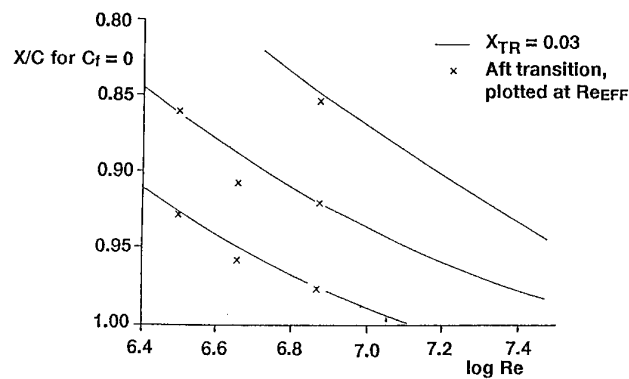
(d) Aerofoil B  
Variation of  $Re_{EFF}$  with flow condition

FIG 4.7 Applicability of  $\delta_{T.E.}^*$  as Simulation Criteria



(a) Scale effect on  $H$  near T.E.  
(no extensive separation)

(b) Scale effect on  $H$  near T.E.  
(after separation-onset)



(c) Scale effect on extent of rear separation

FIG 4.8 Analysis of Scale Effect on Rear Separation  
Aerofoil B



$l_B$  = LENGTH OF BUBBLE  
 $M$  = MACH NUMBER NORMAL TO ISOBARS  
 $\theta$  = BOUNDARY LAYER MOMENTUM THICKNESS  
 $'s'$  = SIGNIFIES IMMEDIATELY UPSTREAM OF SHOCK

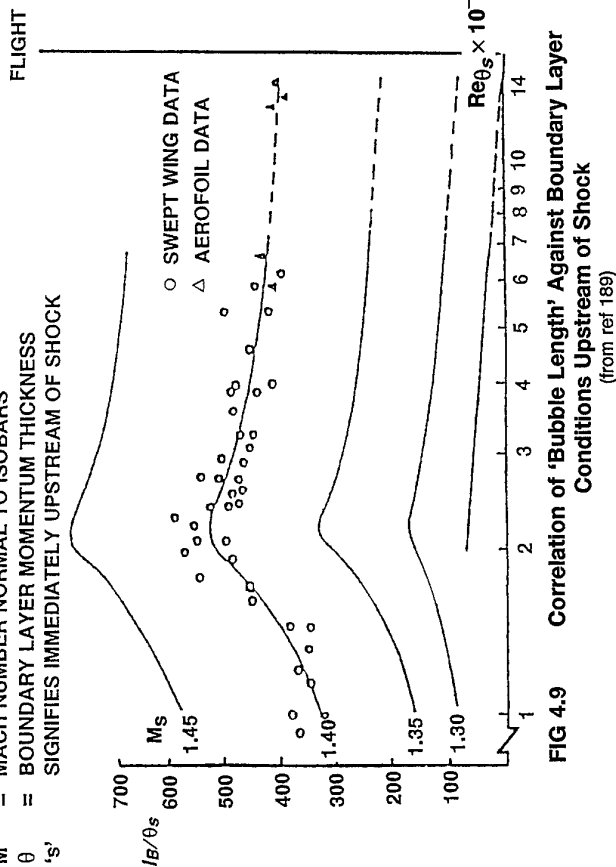


FIG 4.9 Correlation of 'Bubble Length' Against Boundary Layer Conditions Upstream of Shock (from ref 189)

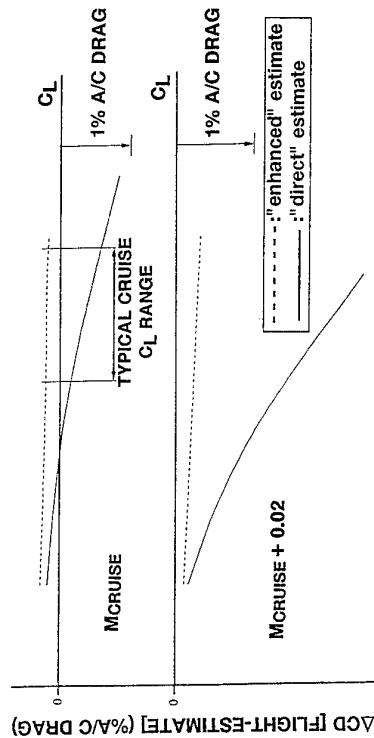


FIG 4.11 Effect of CFD Extrapolation in "Enhanced" Estimate on Flight-Tunnel Drag Comparison (from ref 190)

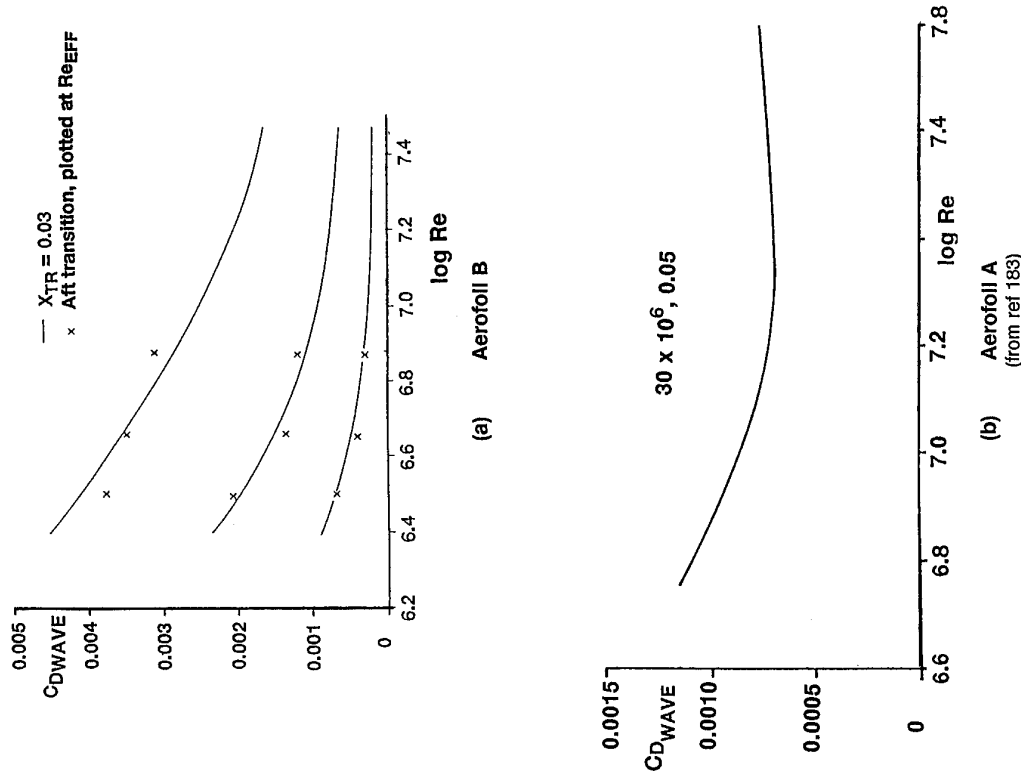


FIG 4.10 Scale Effect on Wave Drag

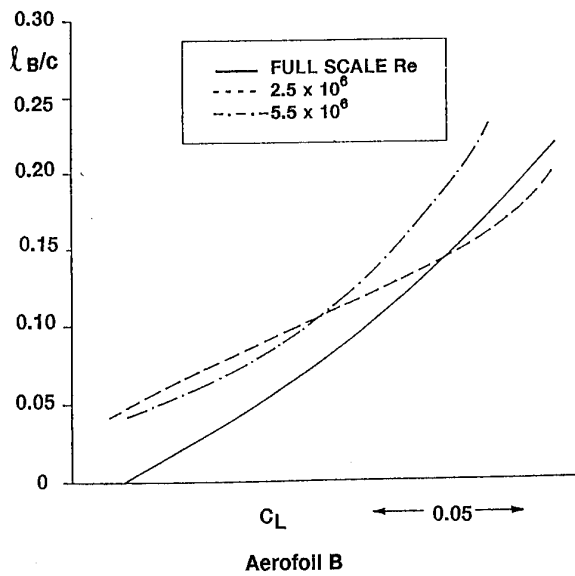
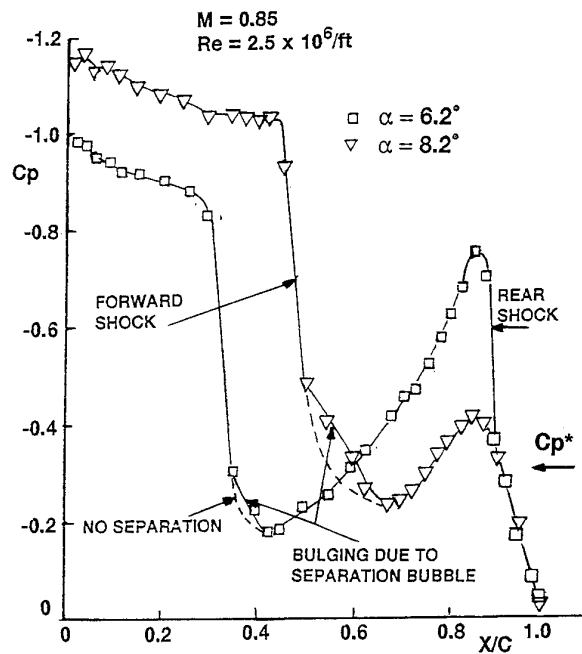
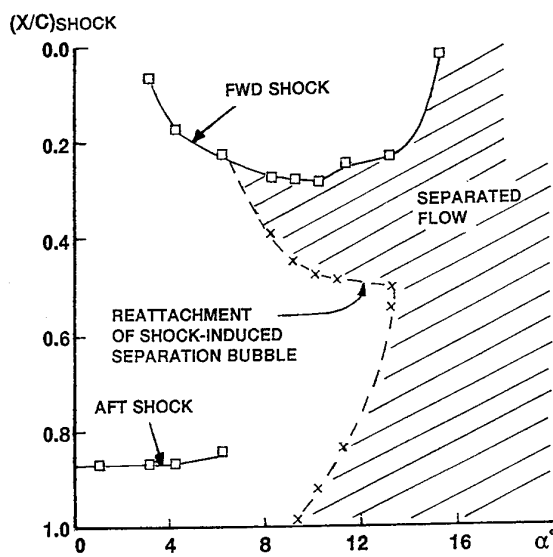
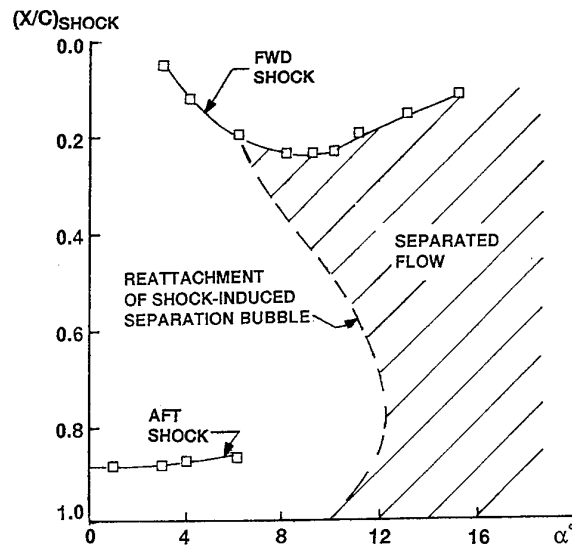


FIG 4.12 Scale Effect on Shock Induced-Separation

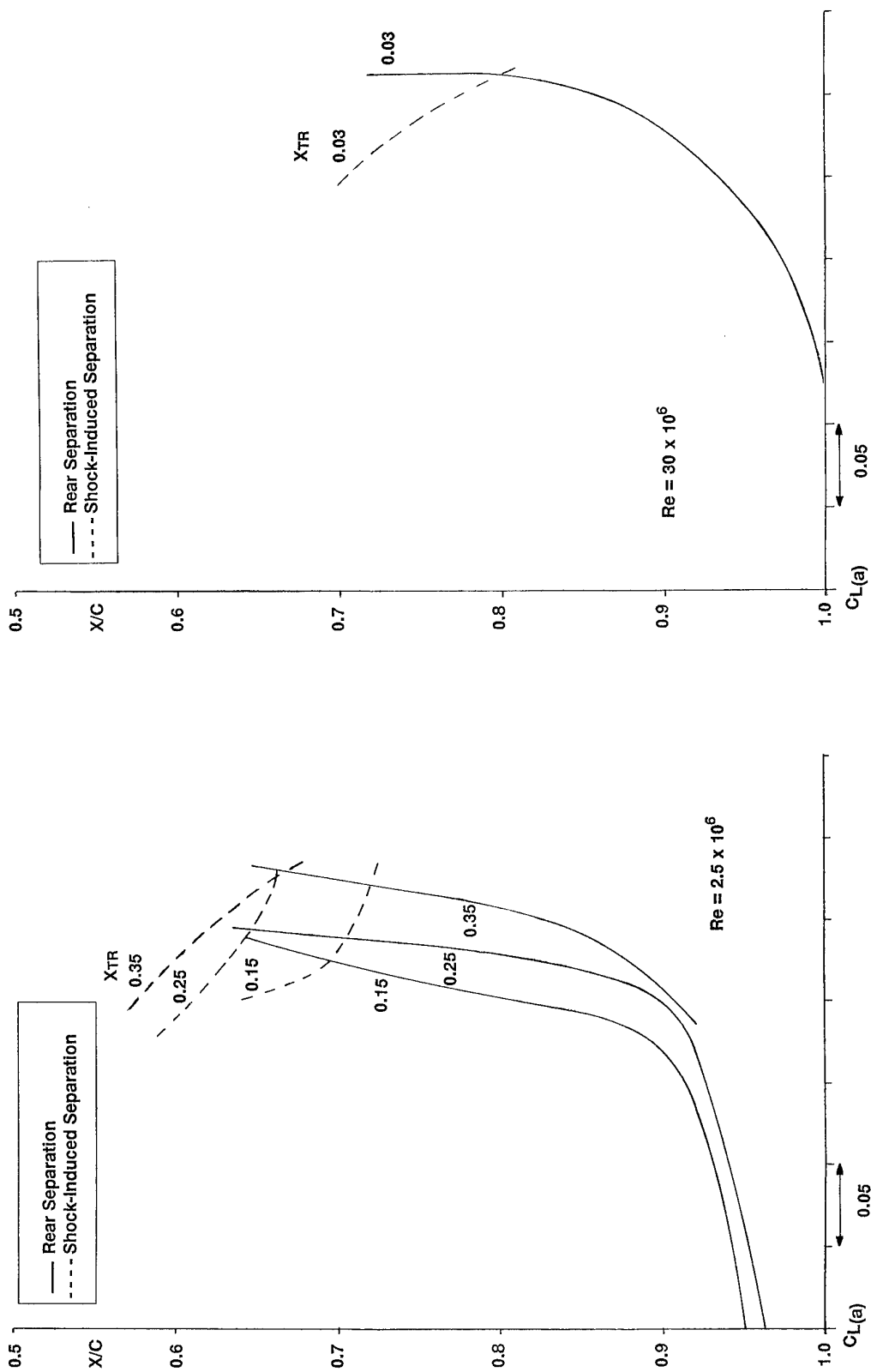


(a) Typical pressure distributions approaching separation-onset

(b)  $Re = 2.5 \times 10^6/ft$ (c)  $Re = 7.0 \times 10^6/ft$ 

(b,c) Scale effect demonstrating interaction of rear separation with S-I separation at low Re

FIG 4.13 Evidence on Scale Effect on Shock-Induced Separation from TACT Tests  
(from ref 190)



$C_{L(a)}$  is the same on both of these figures

Aerofoil B

FIG 4.14 Effects of  $Re$  on growth of Shock-Induced and Rear Separation

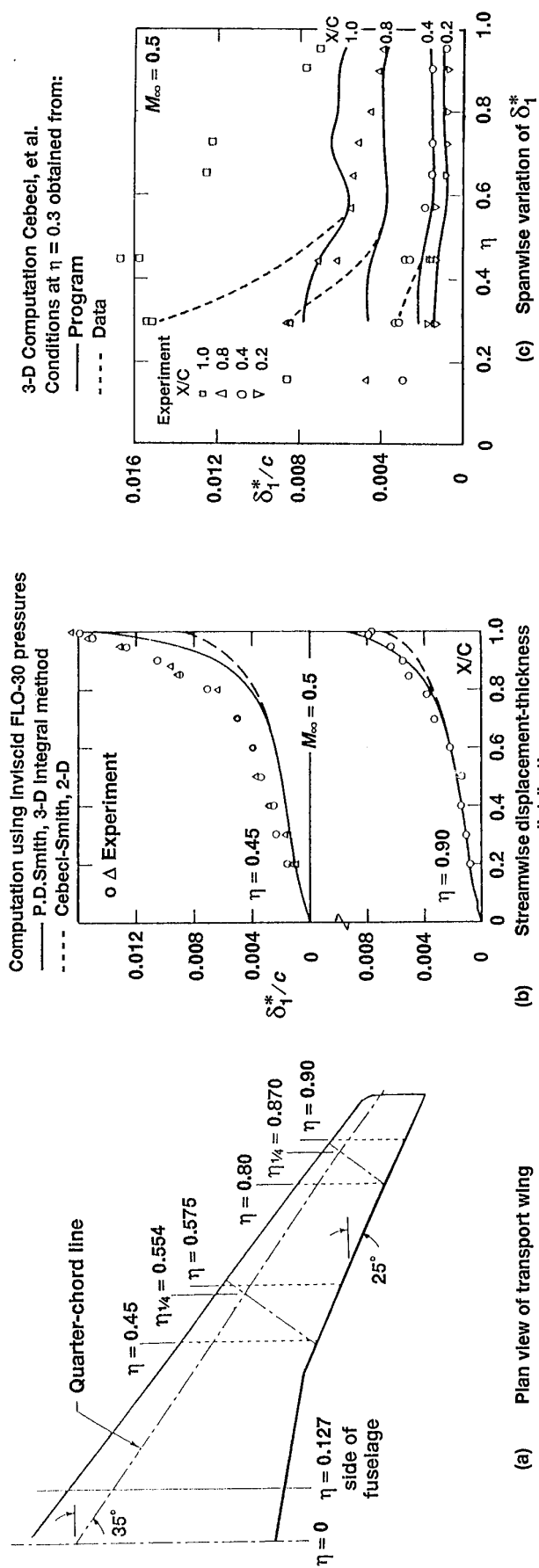


FIG 4.15 Comparison of Measured and Calculated Boundary Layer Development

(a) Plan view of transport wing

(b) Streamwise displacement-thickness distributions

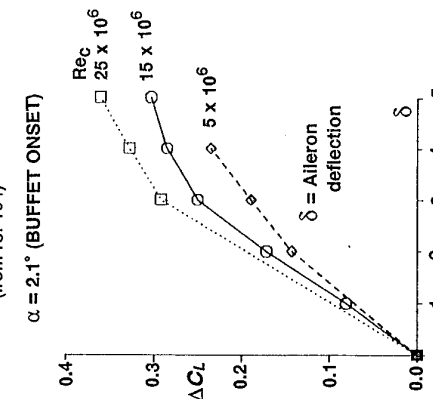
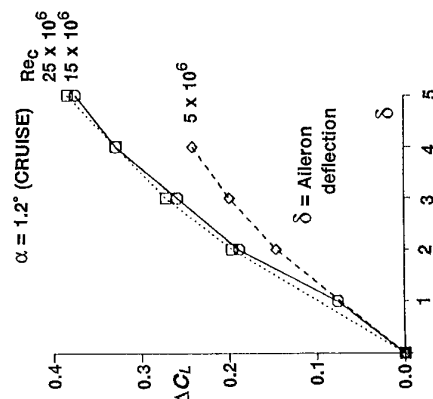
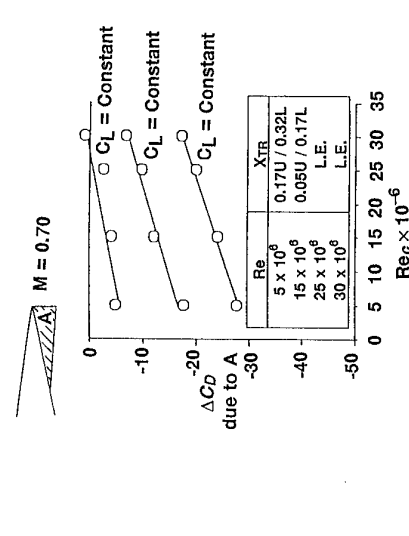
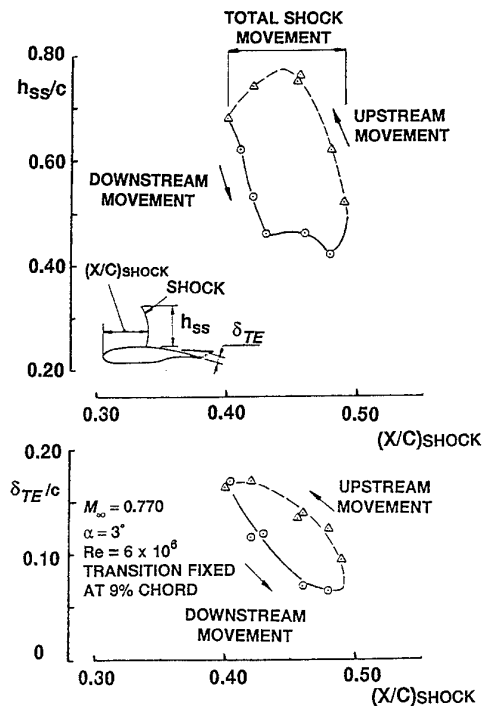
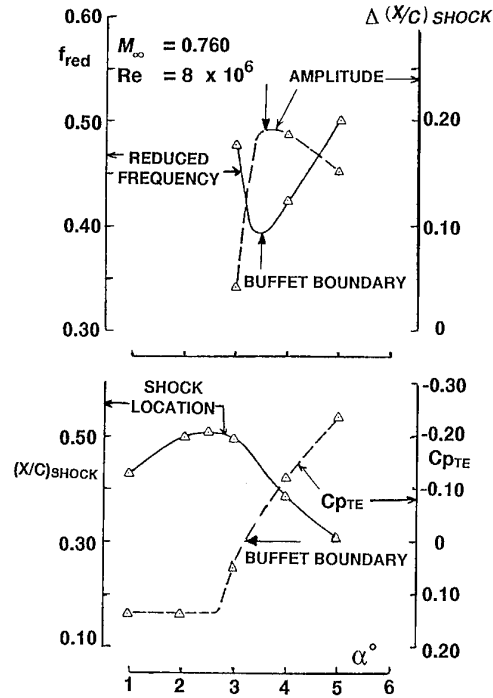
(c) Spanwise variation of  $\delta_1^*$ 

FIG 4.16 Inadequacy of Viscous Simulation Techniques (from ref 199)

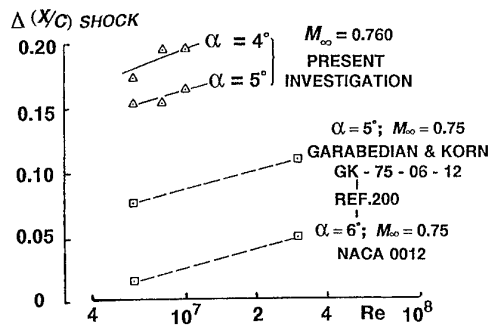




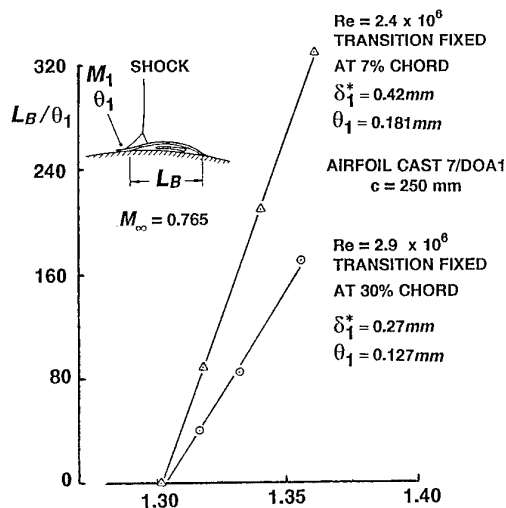
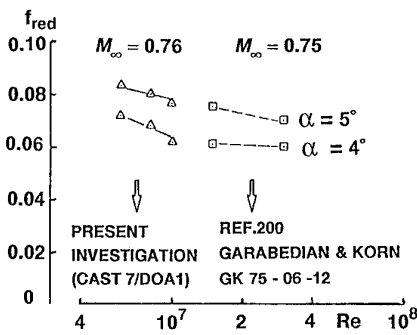
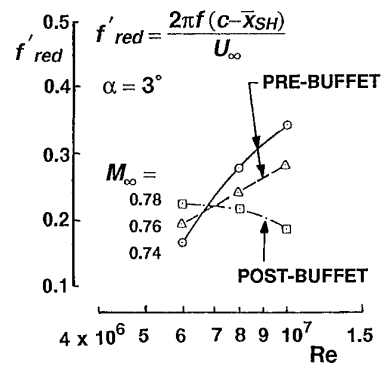
(a) Changes in typical oscillation cycle



(b) Changes with alpha in shock oscillation frequency and amplitude



(c) Effect of Re on shock oscillation, frequency and amplitude

(d) Effect of  $\delta_1^*$  on growth of S-I separation bubble

(e) Effect of Re on frequency for pre- and post-buffet onset

FIG 4.17 Study of Unsteady Flow in Buffet  
(from ref 193)

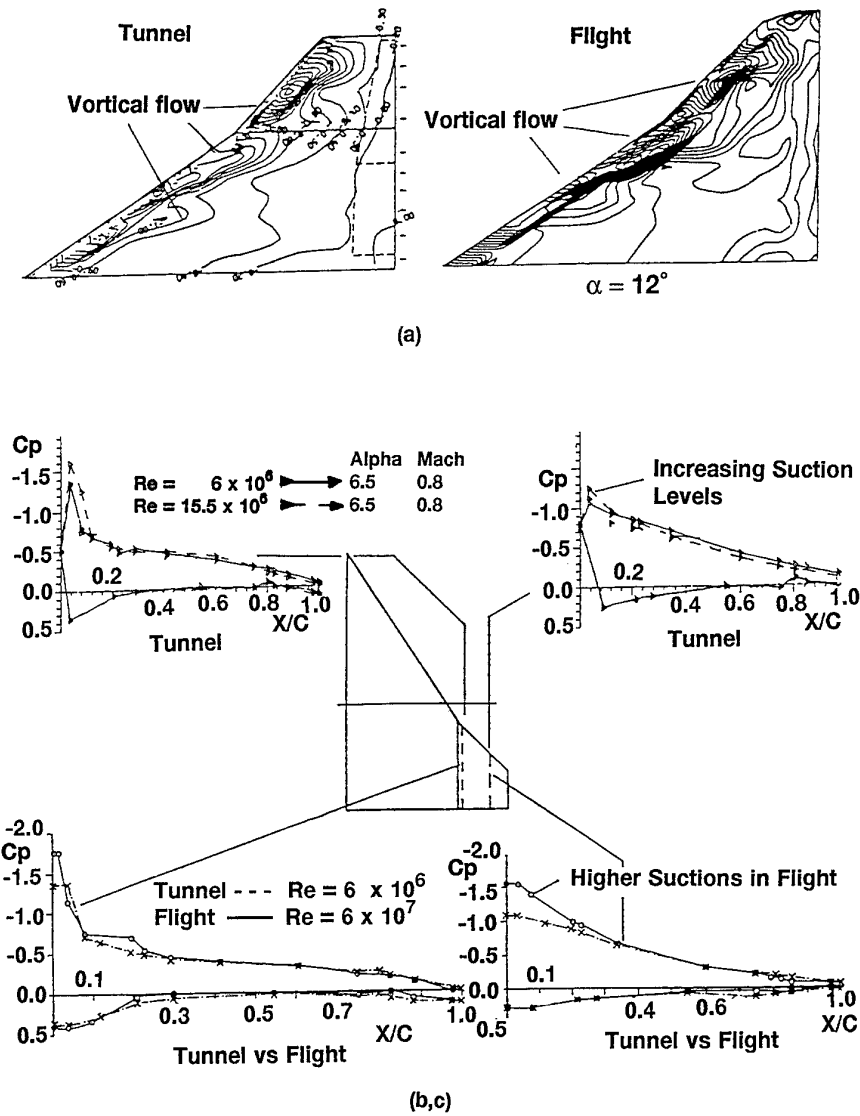
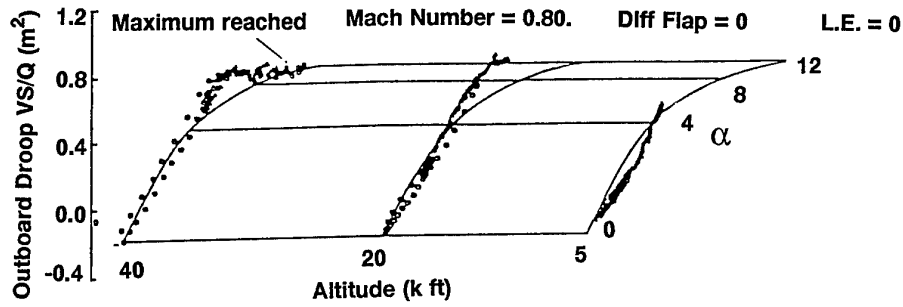
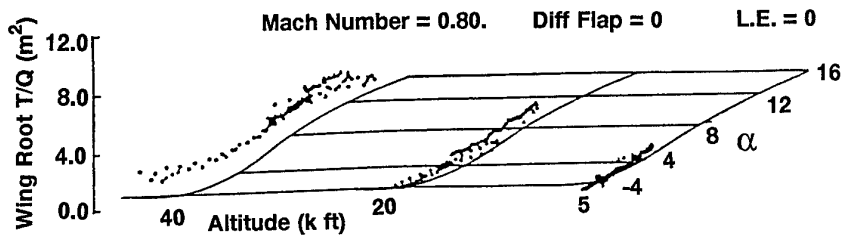


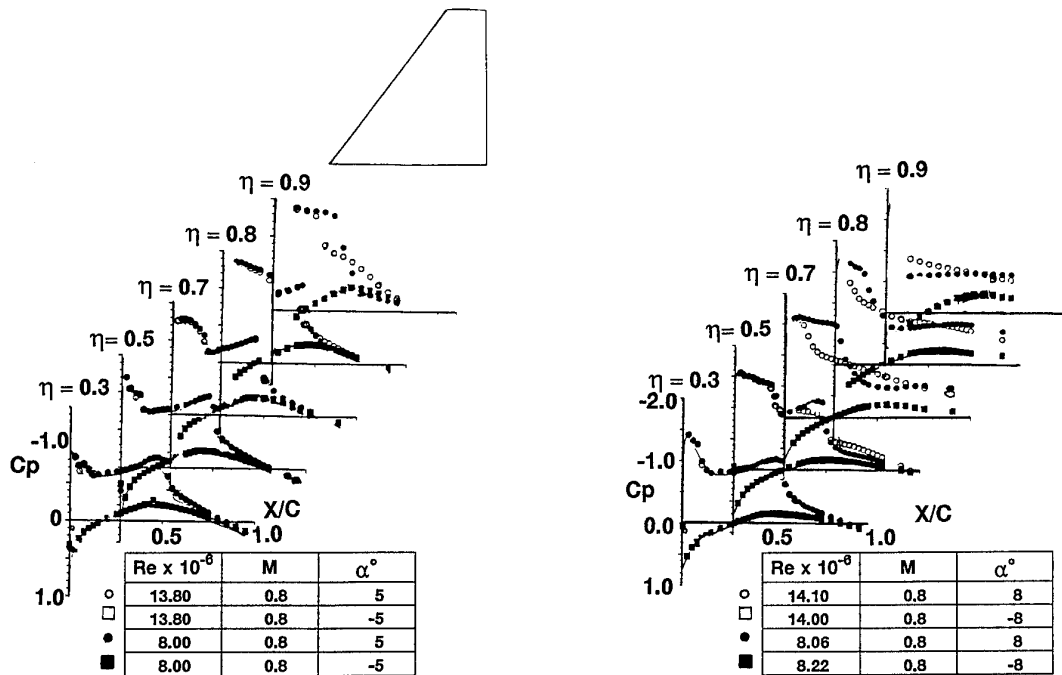
FIG 4.18 (a,b,c) Possible Scale Effects on Flow over EAP Wing  
(from ref 189)

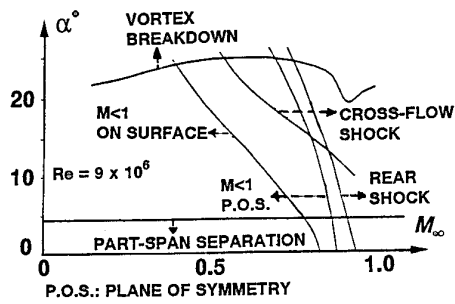


(d) Outboard Droop Vertical Shear

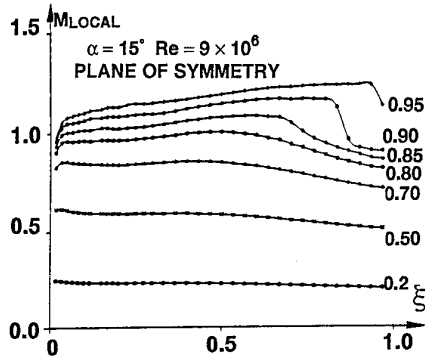


(e) Wing Root Torque

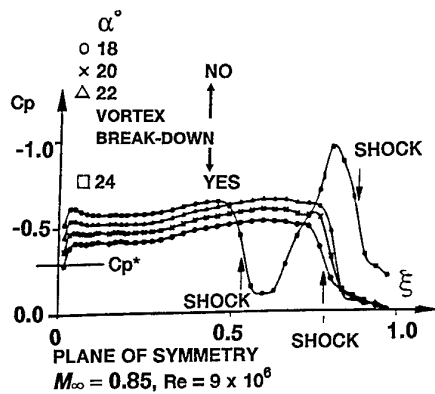
FIG 4.18 (d,e) Possible Scale Effects on Flow over EAP Wing  
(from ref 189)FIG 4.19 Effects of Re on Pressure Distributions  
over NASA Ames Research Wing  
(from ref 203)



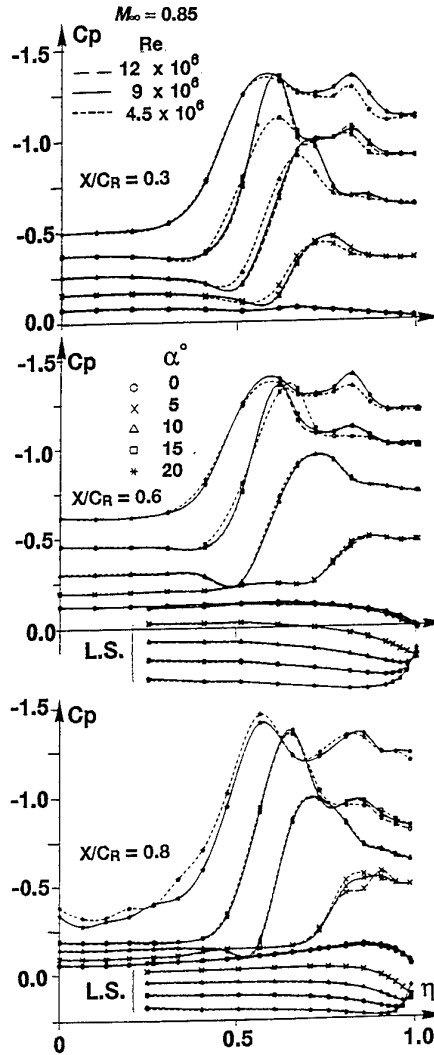
(a) Summary of flow features in  $M_\infty, \alpha$  plane



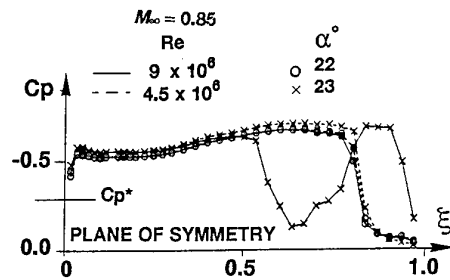
(c) Effect of  $M_\infty$  on chordwise local Mach number distribution at  $\alpha = 15^\circ$



(d) Chordwise pressure distribution at  $M_\infty = 0.85$  before and after vortex break-down



(b) Effect of  $Re$  on spanwise pressure distributions at  $M_\infty = 0.85$



(e) Effect of  $Re$  on vortex breakdown

FIG 4.20 Results for Sharp-Edged  $65^\circ$  Cropped Delta Wing at Transonic Speeds  
(from ref 151)



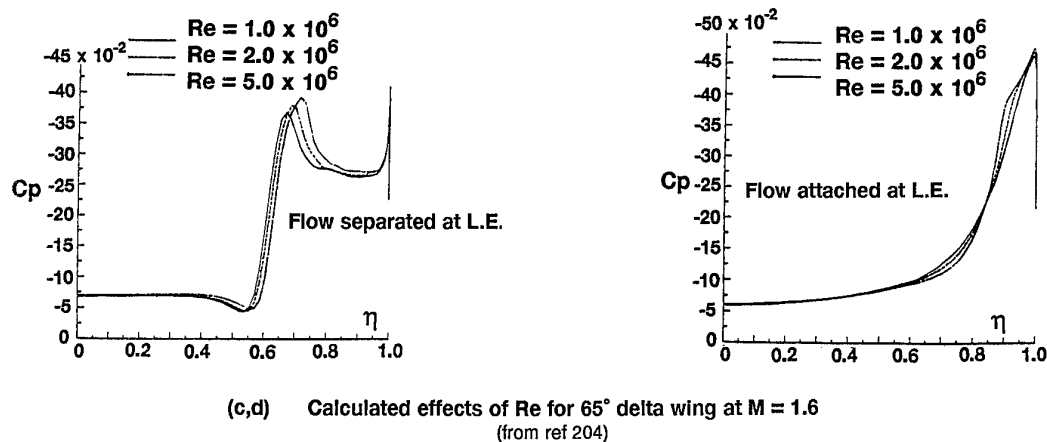
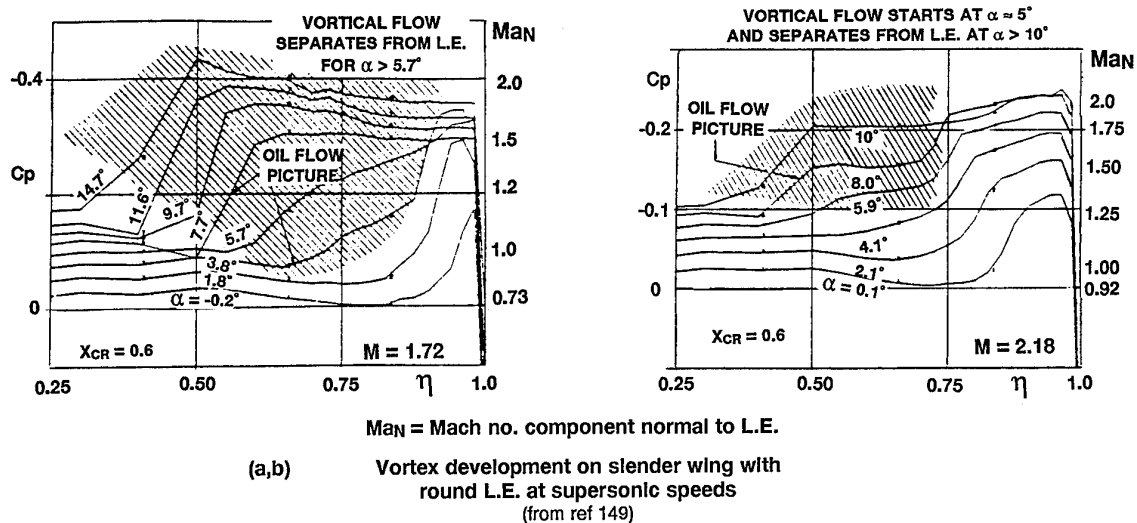
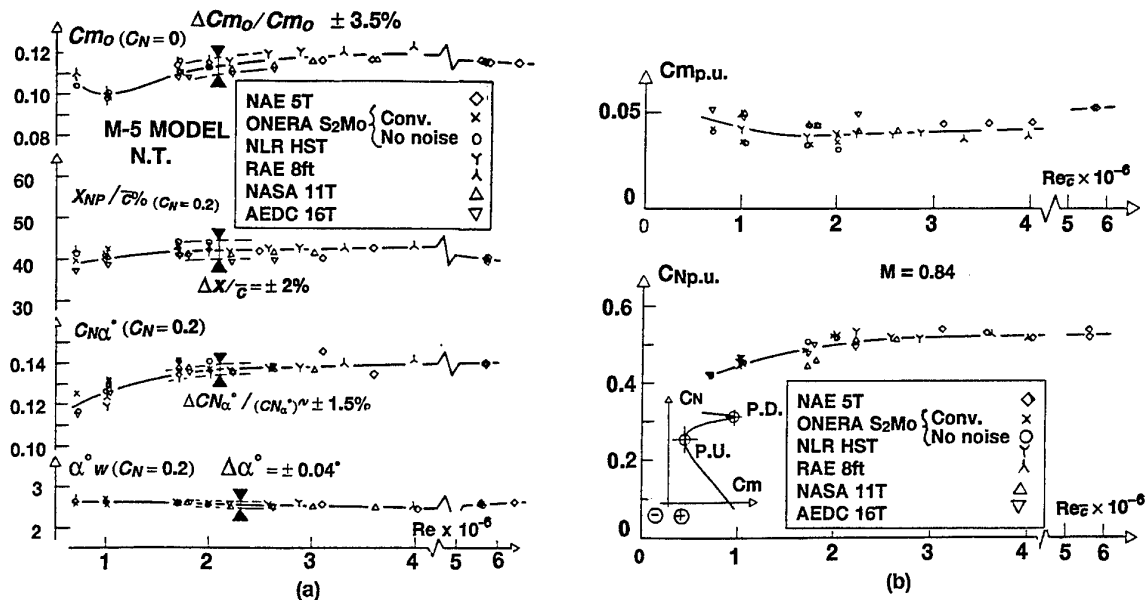


FIG 4.21 Scale Effect on Vortical Flow on Slender Wings

FIG 4.22 Effect of  $Re$  in Tests on ONERA Calibration Model M5 (from ref 205)

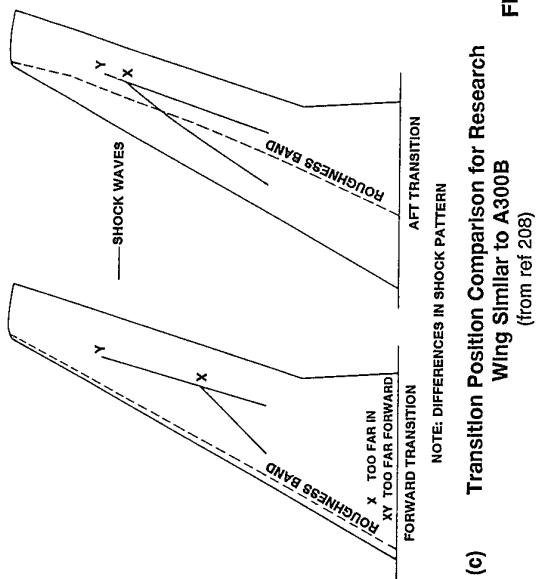
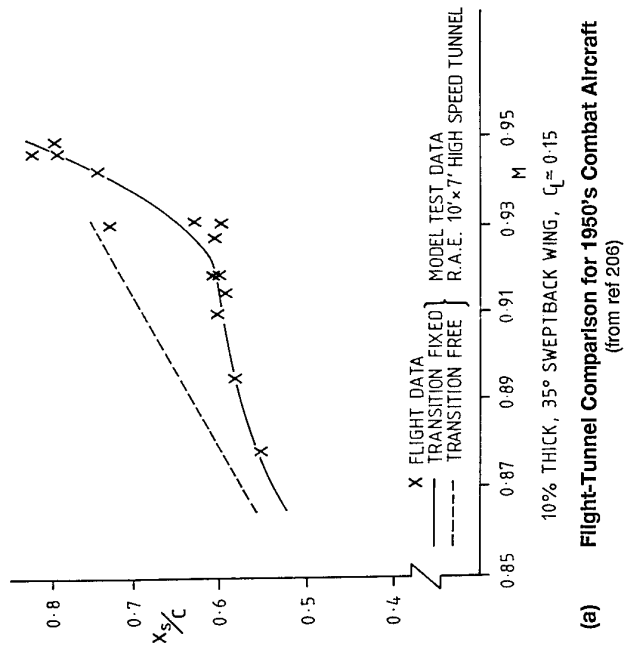
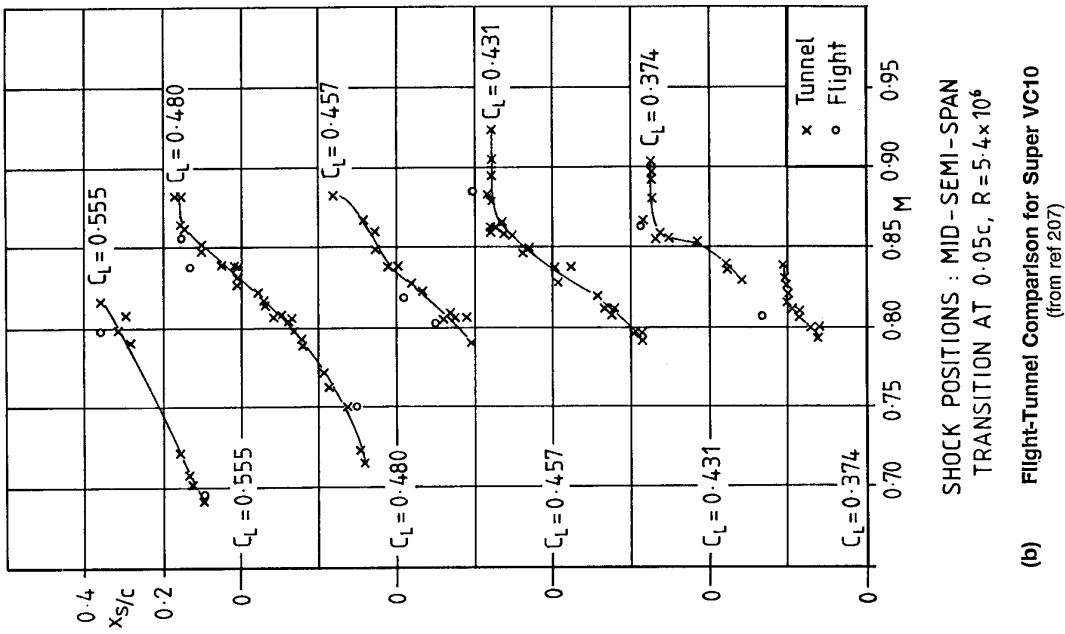
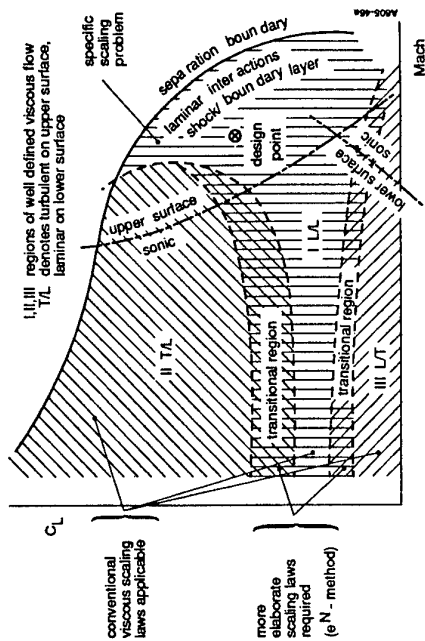
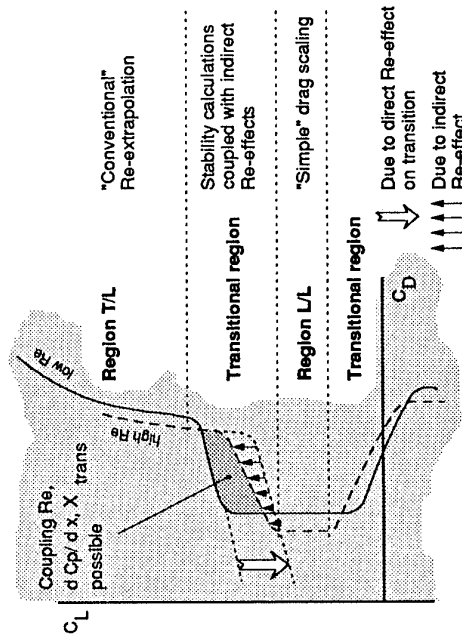


FIG 4.23 Effect of Re (or Boundary Layer Thickness) on Shock Position



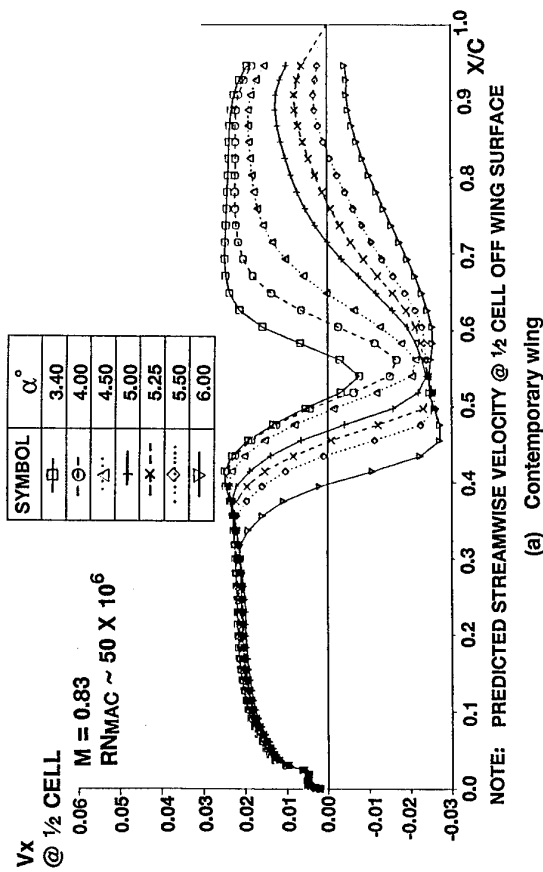


(a) Flow regimes for laminar flow configuration

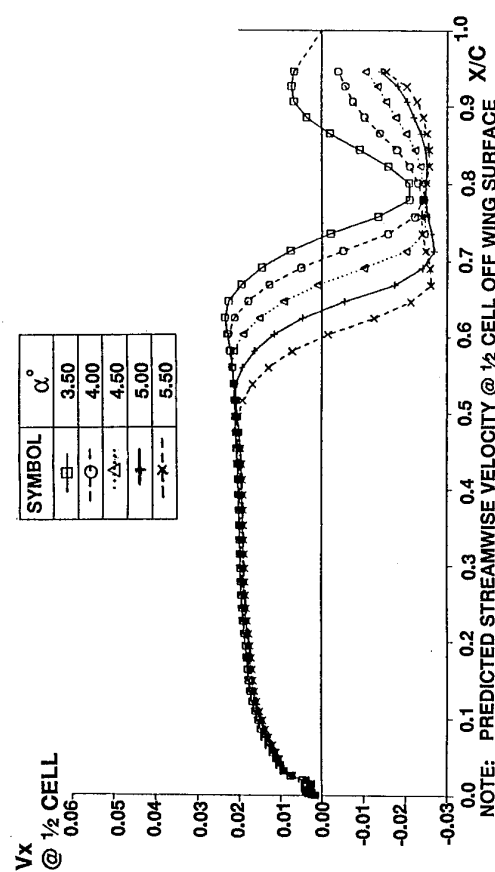


(b) Drag changes with Re

FIG 4.25 Basis of Possible Reynolds Number Extrapolation Methodology (Eisenaar ref 210)



(a) Contemporary wing



(b) Future advanced wing

FIG 4.24 Contrasted Flow Separation Development (from ref 199)

## 5 SCALE EFFECTS ON AIRCRAFT DRAG

This section is not a comprehensive guide to the prediction of scale effect on aircraft drag but rather, it is a brief review of some important aspects of the subject.

### 5.1 Prediction of Wave Drag and Viscous Drag

Considering first an aircraft in cruising flight, it has already been emphasised in §4.3.3.1 that, with modern wing sections, wave drag as well as viscous drag can vary appreciably with Reynolds number. The civil aircraft designer, in particular, needs to have an accurate method for predicting this variation. Most countries will have their own favourite method but one of the most recent and accurate methods is that produced by Lock. This is described in Refs 211, 212 and was extended and modified (see below) in a form suitable for user-application in Ref 213.

Regarding the scaling of the wave drag, the simple formulae given originally by Lock are as follows:

for a 2D section,

$$C_{D_w} = \frac{1}{c\kappa_w} F(M_\infty, M_{10}) \quad (5.1)$$

$$F(M_\infty, M_{10}) = 0.243 \frac{1 + 0.2M_\infty^3}{M_\infty} \cdot \frac{(M_{10} - 1)(2.0 - M_{10})^4}{M_{10}(1 + 0.2M_{10}^2)} \quad (5.2)$$

where  $\kappa_w$  = surface curvature at foot of shock  
 $M_\infty$  = free-stream Mach number  
 $M_{10}$  = local Mach number ahead of the shock and close to the surface

and for a swept 3D wing,

$$C_D = \int_{\eta_{body}}^1 \frac{c(\eta)}{\bar{c}} C_{D_w}(\eta) d\eta \quad (5.3)$$

where  $c(\eta)$  = local chord  
 $\eta$  =  $y/s$   
 $s$  = semi-span,  $\bar{c}$  = mean chord

$$\text{and } C_{D_w}(\eta) = \frac{\cos^4 \Lambda_s}{c\kappa_w} F(M_\infty \cos \Lambda_s, M_{10}^*) \quad (5.4)$$

where  $\Lambda_s$  = sweep of the shock front at  $\eta$   
 $M_{10}^*$  = Mach-number component normal to the shock at its foot

Relations (5.2) and (5.4) cannot be used if the shock wave is located on a flat surface since they would predict that  $C_{D_w} = 0$ . The more refined formulae in Ref 213 are designed to cope with this difficulty.

These equations produce a change in  $C_{D_w}$  with Re because both  $M_{10}$  and the position of the shock and hence,  $\kappa_w$  vary with Re. The above formulae are likely to be unreliable when the shock is in, or is located just downstream of, a region of rapid variation of surface curvature. More elaborate methods are available for estimating the wave drag based on an integration along the forward surface of the shock; these can be used in association with calculations of the flow field by either Euler or Navier-Stokes methods.

The viscous drag is obtained<sup>212</sup> by calculating the boundary layer momentum thickness at the wing trailing edge by an infinite tapered wing version of the lag-entrainment method. The skin-friction relation underlying this method when applied to a flat plate is in close agreement at high Reynolds numbers with the formula suggested by Winter and Gaudet<sup>214</sup> and at low Reynolds numbers with an unpublished analysis by Green of low Re data. Ref 212 shows that values of  $C_{D_{visc}}$  calculated by this method increase with  $C_L$ ; also, they decrease with Re by more than the variation of the basic skin friction. In other words, in terms of the simple data sheet approach of estimating the viscous drag, they imply that the commonly used form factors,  $\lambda$ , should really increase with  $C_L$  and decrease with Re. These changes are however often ignored in industry and indeed, consciously ignored. For example, Jobe in Ref 215 comments that "the drag-due-to-lift of the wind-tunnel model (without wing separations) is generally accepted as being representative of the full scale drag-due-to-lift". On the other hand, the standard data-sheet approach<sup>216</sup> in the UK to estimating the drag-due-to-lift does include a dependence on Re through the fact that it depends on the ratio of the lift-curve slope in viscous flow to the slope in inviscid flow.

One company with access to flight and tunnel data on a fair number of combat aircraft compared the data with a number of different simple rules for the variation of both drag at zero lift and drag-due-to-lift with Re as listed below.

#### Drag at zero lift

- (i) parallel to the skin-friction variation: this would imply  $\lambda$  increasing with Re,
- (ii) estimated profile drag proportional to skin friction: this implies constant  $\lambda$  on this part of the drag but excess drag due to interference, separation etc independent of Re,
- (iii) proportional to skin friction: in other words,  $\lambda$  independent of Re,
- (iv)  $\lambda$  decreasing with Re as would be forecast theoretically by methods such as those by Lock.

#### Drag-due-to-lift

- (a) independent of Re,
- (b) decreasing with Re as would be forecast theoretically.

The analysis of the data appeared to show conclusively that the best assumptions were (ii,a); only in one case was there a suggestion that the drag-due-to-lift decreased with Re.

The present author feels that these conclusions should be regarded with caution. It is noteworthy that most of the wind-tunnel data used in this latter survey were obtained in tests with natural transition. This could mean that at low and moderate  $C_L$ , with some laminar flow over the wings in the model tests, the drag-due-to-lift was probably lower than it would have been with transition further forward as in flight. This could account for why the drag-due-to-lift apparently did not decrease with Reynolds number between model test and flight. One could also argue that the drag due to roughness and excrescences present on the aircraft but not represented on the model could increase with  $C_L$  and so, tend to compensate for the favourable scale effect that should be present on the basic drag-due-to-lift.

It is important to recognise that even the choice of the relation for the variation of skin friction with  $Re$  is not an academic issue. 5 relations that have been in common use are compared in Fig 5.1. At first sight, all these predict a similar variation with  $Re$  but the Spalding-Chi relationship is sufficiently different at the low Reynolds numbers typical of many model tests to lead to significantly different conclusions from flight-tunnel comparisons. For example, in a very careful study<sup>217</sup> of the drag of the Trident<sup>214</sup>, it was finally concluded that the standard of agreement between the values of drag from the flight tests and those predicted from tunnel data was within  $\pm 3\%$  but if the Spalding-Chi relation for skin friction had been used in place of the Prandtl-Schlichting, these figures would have been 1% to -5%. The Winter-Gaudet relation mentioned earlier gives very similar results to the Prandtl-Schlichting relation.

The other important operating condition for drag estimation is the second segment climb from take-off. The semi-empirical method in use at Deutsche Airbus for predicting the drag in this condition is described in Ref 218. The main features of the scaling part of this method are

- (i) for the drag at zero lift, the drag for different surfaces is calculated for model and full-scale Reynolds numbers by an appropriate  $\lambda \times C_f$  estimated by the Prandtl-Schlichting relation. The Reynolds numbers used for the different components are based on the local chord for the wing (prior to a spanwise integration on a strip-theory approach), the outer cowl length for the nacelle, a mean chord for the pylon and the fuselage length for the fuselage. For the A310, the difference in this "shape drag" for model and aircraft amounts to 96 drag counts or 7% of the total aircraft drag for a typical take-off configuration,
- (ii) the estimated scale effect on the drag-due-to-lift is based on the assumption that the polar shapes are stretched from model to full scale in sympathy with the scale effect on  $C_{Lmax}$ . To be more precise, if the scale-sensitive part of the drag as measured in the model test is  $C_{DC}$  where  $C_{DC}$  is given by the equation

$$C_{DC} = C_{D(M)} - C_{D0(M)} - C_{L(M)} / \pi A \quad (5.4)$$

(Strictly, the second term should be the true vortex drag-due-to-lift rather than the ideal value). then, it is assumed that

$$C_{DC} = f(C_L / C_{Lmax}) \text{ is independent of } Re.$$

Haftmann et al in Ref 218 note that this part of the total correction can amount to about 2-3% of the total drag.

- (iii) for a flight-tunnel comparison, further corrections have to be applied for trimming effects, for the effect of the thrust contribution to pitching moments and for the drag contribution from the excrescences not represented on the model, this contribution being itself a function of Reynolds number.

Fig 5.2 demonstrates the success of the above scaling procedure in predicting wind tunnel results at  $Re = 3.1 \times 10^6$  on the basis of measured data at the lower Reynolds number of  $1.7 \times 10^6$ . Experience on a number of projects has indicated a scatter of the order of  $\pm 0.5\%$  on the polar-stretching part of the correction for a range of  $Re$  from  $2 \times 10^6$  to  $6 \times 10^6$ . Flight-tunnel comparisons obtained by this method are presented in Fig 5.3(a,b) and will be discussed later in §5.2.

The above method for estimating the scale effect on the drag in the second segment climb retains the traditional approach of dividing the drag into zero-lift and drag-due-to-lift components. Butler, as long ago as 1973 however, argued<sup>219</sup> that this should be abandoned in favour of predicting the drag at the appropriate  $C_L$  and this is, of course, what one does when using the more refined methods for the drag in the cruise condition.

## 5.2 Flight-Tunnel Comparisons

Flight-tunnel drag comparisons in the open literature are a scarce commodity. This is partly because of considerations of commercial security but it also reflects the fact that to be sufficiently accurate to merit publication, they require a great deal of effort and they are often abandoned in mid-stream out of frustration.

An important lesson from the comparison<sup>217</sup> for the Trident mentioned earlier was the importance of having a thrust calibration of the full-scale engine in an altitude test chamber rather than relying on an extrapolation from a sea-bed chamber. In that particular case, in the first phase of the exercise, only a calibration in a sea-level test chamber was available and one of the conclusions of the programme was that there was no change in  $C_D$  in flight above a value of  $Re$  based on aerodynamic mean chord of  $45.8 \times 10^6$ , thus implying an equivalent sand-grain roughness of about 0.00045 in., but when, subsequently, the accurate calibration in an altitude test chamber became available, it was found that  $C_D$  varied with  $Re$  in the manner predicted for an aerodynamically smooth surface throughout the range of the tests, ie up to  $Re = 54.4 \times 10^6$ .

Great precision in the data is therefore required. A general view of the issues that have to be considered in producing a reliable flight-tunnel comparison is given in Chapter IV in Ref 215. One has to allow not only for the drag of excrescences on the aircraft but not represented on the model but also for differences in the aeroelastics and for dynamic effects in flight. One aircraft company has found that these dynamic effects for a combat aircraft can contribute the equivalent of 50 drag counts to the apparent measured drag in flight in a manoeuvre condition.

Despite all the difficulties, there are some noteworthy flight-tunnel comparisons in the open literature. First, there are the comparisons<sup>220,221</sup> undertaken by Lockheed Georgia for the C-141A and the C-5A. Results for the C-141A at  $M = 0.70$  prior to the drag-rise with Mach number are presented in Figs 5.4(a-c). Fig 5.4(a) compares the derived profile drag polars, Fig 5.4(b) shows the scale effect on the minimum profile drag and Fig 5.4(c) compares the actual drag polars. Some words of explanation about these figures are needed here. The wind tunnel test data were first corrected for support interference, empty-tunnel buoyancy, nacelle internal drag, the known extent of laminar flow on the wing and for the induced (ie vortex drag-due-to-lift) drag. They were then converted to full-scale Reynolds number by correcting for the drag of the excrescences on the full-scale aircraft (but not on the model), the nacelle afterbody pressure drag and the estimated  $Re$ -effect on both minimum and lift-dependent profile drag. Method B uses the Karman-Schoenherr skin-friction relation and shape factors based on the supersonic velocity method; method C uses a theory in use at Lockheed in 1973 for deriving the viscous drag from the measured pressure distributions. The flight data had been corrected to obtain the drag for the equivalent rigid aircraft. Ref 220 makes these comments on the results in Fig 5.4:

- (i) the agreement between prediction and flight is within the quoted accuracy for the test data,
- (ii) the values of minimum profile drag predicted by method B are in very close agreement with the flight data both as regards level and variation with  $Re$ . The values predicted by method C are about 5 drag counts lower,
- (iii) this close agreement may be coincidental. The predicted values of profile drag have been obtained on the assumption that the excess drag, ie the amount by which the measured drag in the model tests exceeds the predicted drag for the model test Reynolds number, is independent of  $Re$ . If all this excess drag were assumed to vary with  $Re$  in the manner predicted for the profile drag, the predicted values for the flight  $Re$  would then be 10 drag counts lower, thus spoiling the excellent agreement, particularly for method C,
- (iv) the most likely explanation for the discrepancy in the drag-due-to-lift in Fig 5.4(c) is that the corrections for aircraft flexibility are incorrect.

It is likely that interference drag is a main reason for the excess drag mentioned above. If so, it is quite plausible to conclude in the light of current experience that the excess drag would not reduce with increasing Reynolds number; there have even been cases where interference drag is thought to increase with  $Re$ .

The results of the Lockheed Georgia comparison<sup>221</sup> for the C-5A, as presented in Fig 5.5, are very similar to those for the C-141A. Comparisons for a number of other aircraft are to be found in Refs 215 and 222 but several should be reconsidered either because the results with different transition fixes need to be analysed with the help of the AGARD methodology discussed in §4.1 or because the tunnel data have clearly not been fully corrected for wind-tunnel wall interference. As examples of scale effect, they are therefore misleading and so, they are not reproduced in this AGARDograph except for one interesting case from Ref 222. This concerns the NASA Langley comparison<sup>223</sup> for the XB-70. Results for  $M = 2.52$  and  $M = 1.18$  are presented in Figs 5.6(a,b). The model-extrapolated results for  $M = 2.52$  are within 5% of the flight results for the 1 g condition at about  $C_L = 0.1$  despite the fact that the prediction of elevon angle to trim was in error by about  $2^\circ$  and that the angle of attack was underpredicted. At  $M = 1.18$ , on the other hand, the model-extrapolated drag is low by about 10% and this disagreement is even greater at Mach numbers nearer  $M = 1.0$  thereby showing that tunnel wall interference is responsible. The important result from this XB-70, therefore, is the indication that the scale effect at supersonic speeds can be predicted reasonably.

Finally, we return to the paper<sup>218</sup> by Haftmann et al which is the best recent account of a flight-tunnel comparison. Figs 5.3(a,b) are taken from this paper; these figures show the variation of  $L/D$  with  $C_L$  for three take-off and one landing configurations on respectively the A310 and the A300-600. The marked area around the curves indicates a bandwidth of  $\pm 1\%$  LD around the mean; the tunnel data for the A310 in Fig 5.3(a) from tests in the DRA 5 metre (triangles) and DNW (circles) tunnels have been scaled by the method described briefly above in §5.1. In general, there is good agreement with the drag data back-figured from flight. It is only for configuration I (slat out/flap in) that the scaled tunnel values lie outside the shaded area. The agreement for the more limited data for the A300-600 in Fig 5.2(b) is not quite as good, the maximum discrepancy being about 2%  $L/D$  outside the band. The authors conclude that the

comparisons perhaps indicate that further measurements in different tunnels and with various models are needed to establish a well-proven technique.

The present author hopes that in the future, refinement of the methods may be possible. Bearing in mind the earlier discussion in §3.4 which showed that there were several quite distinct possible reasons for scale effect on  $C_{L_{max}}$ , it is possibly surprising that the stretching of the polars in sympathy works so successfully. It is encouraging that such a simple approach is helpful but one must accept that there must be cases where the changes in drag in the second segment climb would not have any direct connection with the effects on  $C_{L_{max}}$ .

### 5.3 Afterbody Drag

#### 5.3.1 Genuine or pseudo Re-effect?

Scale effect on afterbody drag became a very live topic in the 1970s because of the inconsistencies apparent in some of the results as illustrated in Fig 2.6. Some of the measurements showed what was thought to be an implausible increase of afterbody pressure drag with Reynolds number as shown in Fig 5.7. Aulehla and Besigk<sup>12</sup> were the first to draw attention to the fact that the results of tests on a partial model such as an afterbody could be sensitive to errors in the calibration of the flow in the empty tunnel. They analysed the results of tests on axisymmetric bodies in the tunnel at Göttingen. The pressure distributions from these tests at two Reynolds numbers are shown in Fig 5.8(a) and the changes with  $Re$  in Fig 5.8(b) and the build-up of pressure drag along the body in Fig 5.8(c). The genuine effects in these comparisons are the increases with  $Re$  in the expansions and recompressions over the forebody and afterbody; the spurious effect is the general reduction in suction level over the complete body. It will be seen that there is only a slight increase in the pressure drag coefficient for the complete body - from 0.0155 to 0.0178, but on the afterbody itself the increase is much greater - from 0.0008 to 0.0153. Most of this increase is related to the spurious change in pressure level, this change being judged as spurious because, as indicated in Fig 5.9, roughly the same change was observed in the pressure on the wind-tunnel wall. This circumstantial evidence led Aulehla and Besigk to question whether the calibration of the Göttingen and AEDC tunnels which had produced much of the implausible evidence on scale effect on afterbody pressure drag could be relied upon. The results suggested that the calibrations in use were giving the wrong values of free-stream static pressure. This was ultimately confirmed: in both the Göttingen and AEDC tunnels, it was found that the calibration actually varied with tunnel stagnation pressure whereas, earlier, it had been assumed without proof that it would be independent of pressure. Aulehla<sup>12</sup> suggested that such a variation was only to be expected for a tunnel with perforated walls with  $60^\circ$  inclined holes: the forward inclined perforations would act as flush inlets with a pressure recovery increasing as the wall boundary layer becomes thinner with increase in Reynolds number. In fact, it is likely that the calibration of any pressurised tunnel will change with  $Re$  because of the change in tunnel wall boundary layer thickness. Fig 5.10, which was also included earlier as Fig 2.7, shows the effect<sup>224</sup> of using the correct calibration for the AEDC tunnel. The original trend for the afterbody pressure drag to increase with Reynolds number has been virtually eliminated.

Pozniak in Ref 11 (an excellent review of the whole subject of afterbody drag information up to 1980) comments that failure to appreciate that the tunnel flow calibration could be a function of unit Reynolds number is not the only reason for the

apparent increases of afterbody pressure drag with  $Re$  in Fig 5.7. Some results at high subsonic speeds could be genuine (see later) while, in other cases, the apparent variation with Reynolds number is obtained by comparing data from tests on different models and for these, different support interference not allowed for in the reduction of the results may be responsible for the variation in afterbody drag rather than Reynolds number.

### 5.3.2 Evidence from research tests

Results from model and flight tests<sup>225,226</sup> at NASA Lewis on a modified F-106B with different afterbody boattail geometries on two aft-mounted underwing nacelles were published as long ago as 1973 but despite the fact that, as noted above, the conclusions from these tests may be influenced by support interference, the results can still be regarded as a clear, useful introduction to the subject of scale effect on afterbody drag. Results for two Mach numbers are presented in Fig 5.11 with some sketches of the principal effects of Reynolds number on the afterbody pressure distributions. To comment first on the sketches, the expansion around the shoulder at the start of the afterbody predicted to occur in inviscid flow is not generated at low Reynolds number when the boundary layer is relatively thick. Flow separation occurs soon after the shoulder but only a small amount of recompression is needed to cancel the effect of the limited expansion at the shoulder and so, there is little pressure drag. At higher Reynolds numbers in the second picture, the boundary layer is thinner, the expansion at the shoulder is greater and with separation still occurring fairly far forward on the afterbody, the drag is high - because of both the high suction just downstream of the shoulder and the separation further aft. At still higher Reynolds numbers in the last picture, the flow is mostly attached, the pressure distribution approaches that predicted for inviscid flow and the drag has decreased again because the recompression is now sufficient almost to compensate for the high suction. This interpretation of the flow is based on the descriptions in Refs 225, 226 but there are other examples in the literature where the effect of the thick boundary layer at low Reynolds number is sufficient to suppress the expansion at the shoulder, reduce the adverse gradient further aft and thereby, eliminate the separation, but the overall effect is the same: small drag at low  $Re$  and initially, an adverse scale effect with increasing  $Re$ .

Pozniak in Ref 11 notes however that Reynolds number may not be the only relevant variable in Fig 5.11. The data at low  $Re$  were obtained from tests on a 0.05 scale F-106 half model whereas the data at intermediate Reynolds numbers came from a test on a 0.22 scale complete model. It is therefore possible that the apparent  $Re$ -trends in this range came not from Reynolds number but from uncorrected differences in support interference. Despite this reservation, however, it seems clear that the general pattern shown in Fig 5.11 represents genuine scale effect. There are plenty of other data that can be quoted in support. For example,

- (i) in a programme<sup>227</sup> in the Langley 1/3 metre transonic cryogenic tunnel, the same boattails as those tested above on the nacelles on the F-106B were tested both in isolation and in the presence of a delta wing mounted on top of the nacelle at different fore-and-aft positions. The advantage in this programme was that it was possible to test over a very wide range of Reynolds number with no change of model support. Based on the distance from the nose to the start of the boattail, the Reynolds-number range was from  $3.5 \times 10^6$  to  $68 \times 10^6$  at  $M = 0.9$ , for example. Fig 5.12(a) presents a typical set of results from this programme. These results are with the wing

mounted in an aft-position but the presence of the wing merely affected the level of the pressures on the afterbody and did not alter the changes with  $Re$ . As in the tests on the F-106B, increasing Reynolds number increased the suction near the shoulder and also increased the pressure recovery approaching the base. These changes were self-compensating and, as a result, there was virtually no change in pressure drag with  $Re$  in any of the tests,

- (ii) in an entirely separate programme<sup>228</sup> in the UK, eight afterbodies were tested at  $M = 0.8$  with two boundary layer thicknesses - a thick, natural layer and a thinner layer produced by sucking through slots in a forward sting supporting the models. As in the above tests, decreasing the boundary layer thickness increased the suction near the start of the boattail and also, the pressure recovery towards the rear giving no significant change in pressure drag. In cases where the flow separated on the boattail, decreasing the boundary layer thickness moved the separation point downstream. Typical results are shown in Fig 5.12(b),
- (iii) an extensive programme to improve nozzle testing techniques at transonic speeds was undertaken under the auspices of the AGARD Propulsion and Energetics Panel<sup>229,230</sup>. The programme involved pressure measurements in different facilities on a range of axisymmetric nozzle-afterbody shapes. The range of shapes is shown in Fig 5.13. The flow over the  $10^\circ$  boattail was completely attached at subcritical speeds; on the  $15^\circ$  boattail, a shock-induced separation was present at some Mach numbers while the flow over the  $25^\circ$  boattail with rounded shoulders was separated at all Mach numbers. The effects of Reynolds number and boundary layer thickness were investigated at Mach numbers from  $M = 0.8$  to  $0.95$  and are reported in Ref 231. Some results are plotted in Fig 5.13 as a function of the ratio of the quoted or estimated boundary layer thickness at the start of the boattail divided by the body diameter. The changes in the boundary layer thickness were obtained in the AEDC and ARL tests by changing the tunnel stagnation pressure and at Rolls-Royce by blowing. A jet was present in the AEDC and RR tests but at ARL, the jet was simulated by a cylindrical sting. It is clear that differences in boundary layer thickness are not the only reason for differences in the level of afterbody pressure drag in the various facilities and an examination of these other factors formed the main subject of the AGARD programme. However, tests in a single facility should give a true indication of the effects of  $Re$  or boundary layer thickness. The range of thicknesses investigated in each of the facilities was of the order of model to full-scale  $Re$  and at ARL and RR, the absolute values extended to likely full-scale values. At  $M = 0.8$  for the  $10^\circ$  and  $15^\circ$  boattails, the changes in drag did not exceed 0.005 which was about the precision of the data but at  $M = 0.95$ , increasing the Reynolds number or decreasing the boundary layer thickness over a range that encompassed tunnel and full-scale values, resulted in an increase in afterbody pressure drag of about 0.02, ie 20 aircraft drag counts for the  $15^\circ$  and  $25^\circ$  boattails. The pressure distributions (not included in Fig 5.13) showed that the increase in drag with  $Re$  at  $M = 0.95$  was principally due to a reduced recompression at the rear in a flow that was apparently separated. At  $M = 0.9$ , however,

the drag changes were more related to the changes in pressure near the shoulder,

- (iv) further tests<sup>232</sup> to investigate the effects of boundary layer thickness were made in the 8 ft x 6 ft tunnel at NASA Lewis on sting-supported axisymmetric boattail afterbodies in which the boundary layer thickness was varied by changing the model length and by using a series of slotted rings. One sharp-shouldered and four round-shouldered afterbodies were tested, the geometry of one of these is shown in Fig 5.14(a). The main effect of decreasing boundary layer thickness, ie effectively increasing the Reynolds number, was to reduce the drag-rise Mach number - as in the previous test programme (iii). Similar results were obtained in tests in other facilities and also, as shown in Fig 5.14(b), the same trend was predicted theoretically. This analytic prediction was based on the viscous-inviscid interaction approach of Chow et al<sup>233</sup> which does not take account of any flow separation. The drag levels are different theoretically and experimentally but the trends are predicted successfully for both  $M = 0.6$  and  $M = 0.9$  - a commendable achievement for 1975,
- (v) the need to incorporate viscous effects into calculations of the flow over afterbodies was recognised in the 1970s and two examples of this activity are shown in Figs 5.15(a,b). Presz and Pitkin<sup>234,235</sup> developed an engineering approach for predicting aircraft afterbody performance which included the effects of flow separation and this was further refined<sup>236</sup> with an analytical model that included the effects of skin friction, axial pressure gradient and nozzle jet entrainment on the separated reverse flow region. Fig 5.15(a) presents comparisons between theoretical predictions by this method with the experimental data<sup>227</sup> from the tests in the NASA Langley cryogenic tunnel discussed under (i) above. The method succeeds in predicting a reduction in afterbody drag with  $Re$  but in magnitude, it is about twice that observed in the experiment. These results are for a subcritical Mach number ( $M = 0.6$ ) but Willmoth<sup>237</sup> coupled a conventional viscous method for an attached boundary layer and Presz's model for a flow separation to a full potential solution for an inviscid transonic flow. An example of results obtained by this method for a transonic Mach number of  $M = 0.96$  is presented in Fig 5.15(b): the viscous effects, as would be expected, reduce the suctions around the shoulder and the pressure recovery at the base. Calculations by this method could clearly have been made for a range of Reynolds number provided that the techniques used for predicting separation were acceptable.

### 5.3.3 Evidence from tests for specific aircraft

It will be appreciated from the discussion in §5.3.2 that it is difficult to isolate Reynolds number effects from other technique issues in this field of afterbody drag measurement. This is even more apparent when one moves on from tests on research axisymmetric afterbodies to tests on models of real aircraft. Large numbers of pressure tapings have to be used in order to obtain a reliable integrated pressure drag. Results for various aircraft are however to be found in the open literature including:

- (i) a flight-tunnel comparison<sup>238</sup> for the B-1 nacelle. The afterbody/nozzle was pressure plotted very comprehensively on both the aircraft in the No 2 structural test flight development programme and on a

0.06 scale model of the aircraft mounted inverted on a swept strut from the floor of the AEDC 16 ft transonic propulsion tunnel (Fig 5.16). The values of  $C_D$  obtained by integration of the measured pressures are compared in Fig 5.16 for the transonic range up to  $M = 1.5$  in flight and  $M = 1.2$  in the tunnel. Prior to drag-divergence, the drag values from flight and tunnel differ by no more than 6 aircraft drag count and one has obtained what might be termed reasonable agreement. At  $M = 1.2$ , however, the difference is about 15 drag counts. A study of pressures showed that at subsonic speeds, there were small differences similar to those that have been described in the research tests on simpler configurations. These were genuine Reynolds-number effects but, as before, tended to be self-compensating and so, had little or no effect on the integrated drag. At  $M = 1.2$ , however, the suctions over the top and sides of the rearward-facing surfaces of the nacelle afterbody are consistently higher in the model tests than in flight by about 0.05 or more. The authors of Ref 236 commented that these differences needed further analysis but suggested that they could be due to support system interference, inlet fairing effects and the general transonic flow simulation in the wind tunnel. It is significant that the authors do not mention Reynolds number in this context and indeed, the trend is in the opposite direction to that observed in a limited Resweep in the tunnel. In the intermediate Mach-number range close to  $M = 1.0$ , no data are presented, presumably because the model data were thought unreliable because of tunnel wall and/or support interference. If it had been possible to obtain reliable data, evidence discussed earlier suggests that one would have found that the drag-divergence Mach number was higher in the tunnel than in flight,

- (ii) an extensive programme<sup>239</sup> of tests, again including a flight-tunnel comparison, on the YF-17 twin nozzle fighter. Fig 5.17(a,b,c) presents the comparisons for the total axial force on the nozzle/afterbody and for the nozzle on its own. There is a fair amount of scatter in these results but the forces on the nozzle clearly vary with pressure ratio. The "scale effects" are small at subsonic speeds but substantial at  $M = 1.2$ . Again it is doubtful whether Reynolds number is responsible for these differences; the nozzle pressure ratios in flight, but not on the model, are higher than the design value and there are, of course, differences in jet temperature,
- (iii) tests<sup>240</sup> on the F-16 nozzle-afterbody again with emphasis on model scale effects. In this case, the comparison is between the results for a 0.11 and a 0.25 scale model with respectively 0.14 and 0.71% blockage in the AEDC 16 ft tunnel. The models were sting-supported and test results plotted against  $Re$  are presented in Fig 5.18(a). The Reynolds-number effects are not great: tending to be favourable at  $M = 0.6$ , adverse at  $M = 0.9$  near drag-divergence and at supersonic speeds but the differences between the two sizes of model are more substantial - presumably, a further example of "scale effects" due to different model support interference. Fig 5.18(b) shows that for the  $M = 1.2$  data presented in Fig 5.18(a), results for both models should be clear of wall interference but close to  $M = 1.0$ , at  $M = 1.05$ , neither model is clear of this problem.



### 5.3.4 Conclusions

Some of the early results on afterbody pressure drag are misleading because of a failure to recognise that the calibration of the flow in an empty transonic tunnel can be a function of stagnation pressure or unit Reynolds number.

Apparent scale effects at transonic speeds can often be related to tunnel wall interference or model support interference rather than Reynolds number.

For most afterbodies, increase of Reynolds number will increase the suction near the shoulder and, at subcritical speeds, the pressure recovery at the rear. At subcritical speeds and with afterbody geometries for which there is no flow separation, these changes tend to be self-compensating and the effects on afterbody drag are slight.

On boattails that are steep enough to provoke a flow separation, the changes in pressure drag with  $Re$  can be significant and in either direction. The thinner boundary layers at high  $Re$  can negotiate a steeper adverse pressure gradient without separating but, on the other hand, the adverse gradients will increase with  $Re$ . A common trend is for the pressure drag first to increase and then to decrease with  $Re$  between model and full-scale and it is wrong to assume without proof that the performance will be better in flight.

The general tendency is for the drag-divergence Mach number to decrease with Reynolds number - because of the higher suction around the shoulder at higher Reynolds numbers.

Throughout this discussion of scale effects on afterbody drag, the difficulties of extracting evidence on  $Re$ -effects from data comparisons that are heavily influenced by issues such as tunnel wall interference and model support interference have been emphasised repeatedly. These other issues were reviewed in detail by an AGARD Working Group that reported in 1986 in Ref 241. This report also includes an assessment of the CFD methods available up to the middle of 1984 with an evaluation of user-experience on a number of test cases. Reynolds-number effects are not however discussed in this major review.

Since 1984, there has been progress in the development of theoretical methods for calculating the flow over afterbodies. Ref 242 by Peace presents a method in which an Euler solution is modified to include a representation of the viscous effects on the afterbody surface and in the wake region predicted by an integral boundary-layer method used in inverse mode and hence, capable of handling a region of separated flow. Moderate agreement with experimental data is shown for examples involving both shock waves and separated flow. A later report<sup>243</sup> by the same author presents some results obtained by a Reynolds-averaged Navier-Stokes code which can be applied to axisymmetric body/nozzle configurations with sharp trailing edge or finite bases. Good agreement with experiment is shown for cases with attached flow but the results when separated flow is present are very dependent on the choice of turbulence model and further improvements in modelling are clearly required. No evidence on scale effects is included in these references but the methods presented could clearly be used to obtain such evidence.

If, in the future, it proves possible to rely on theoretical methods for prediction of where the flow will separate on an afterbody/nozzle configuration, the empirical method of Ref 244 with its concept of correlating the afterbody drag in terms of an

effective base area over which the flow is separated may be useful as a quick first-order approach to drag prediction.

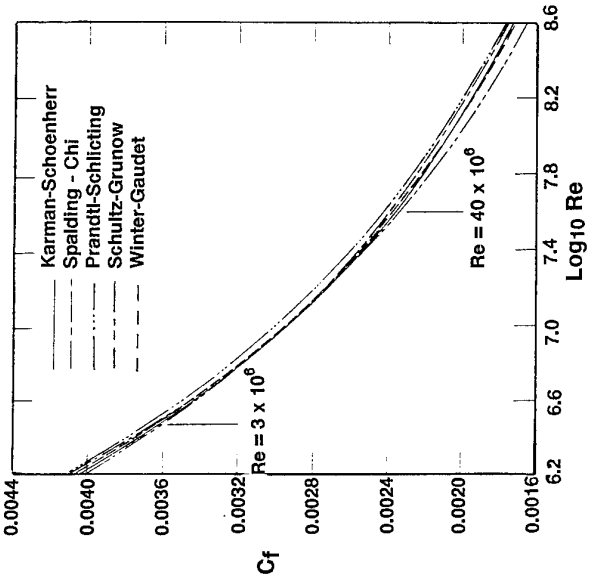
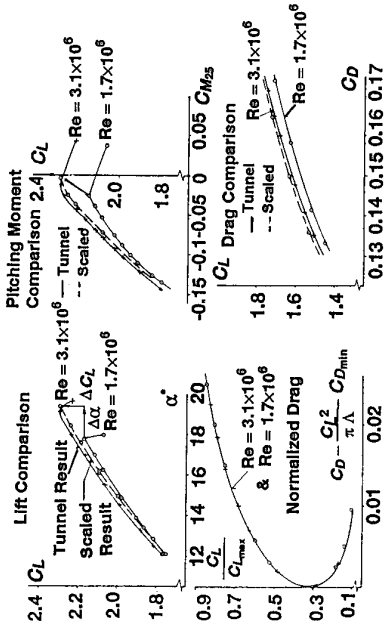


FIG 5.1 Comparison of Empirical Flat-plate Skin Friction Formulae for Incompressible Turbulent Flow (from ref 215)



Prediction of Results for  $Re = 3.1 \times 10^6$   
Based on Results for  $Re = 1.7 \times 10^6$

FIG 5.2 Example of Prediction Methodology

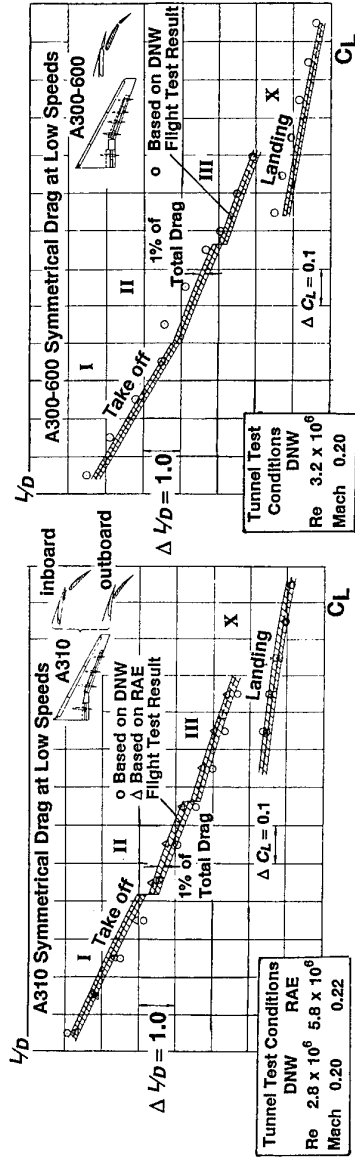
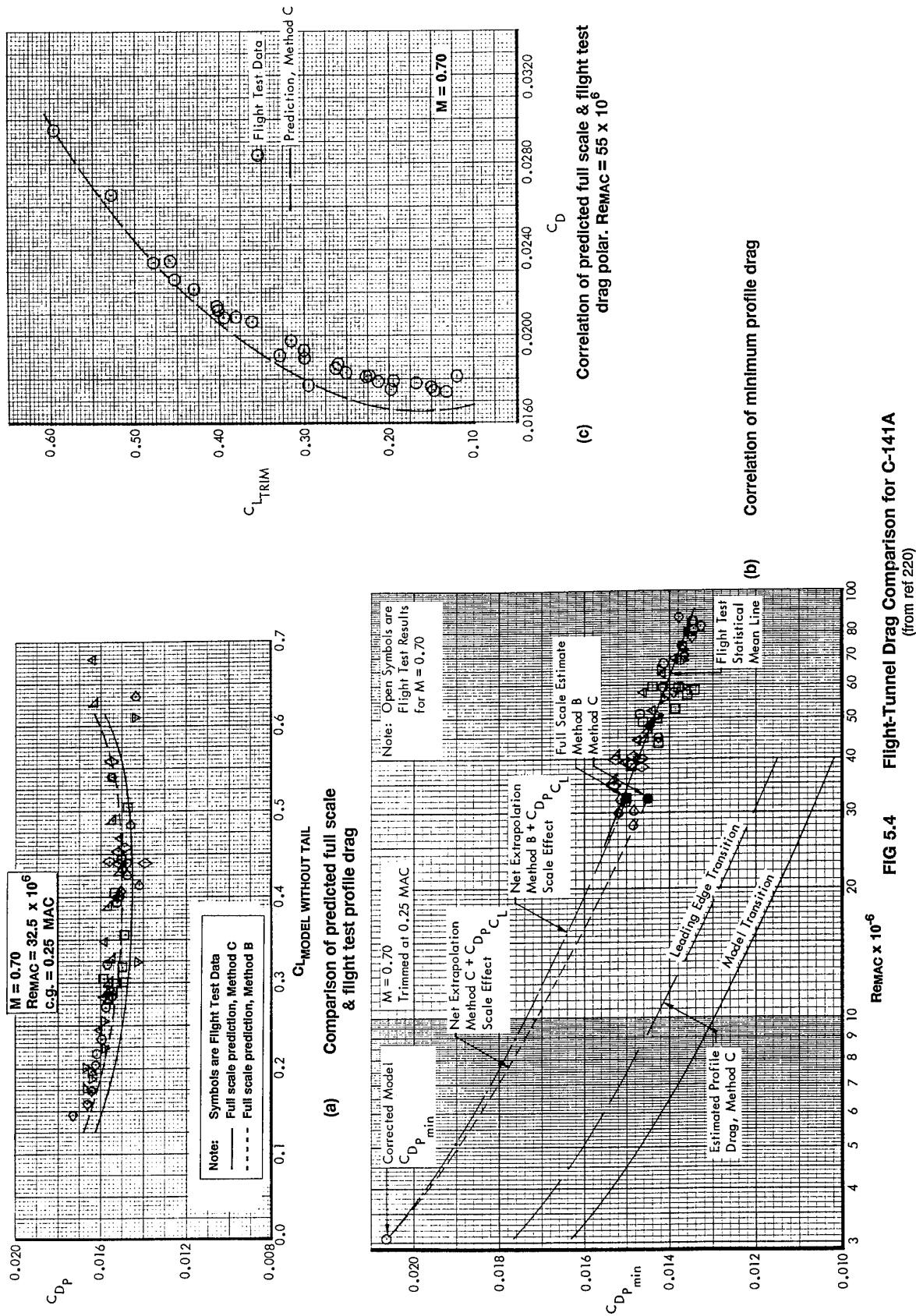


FIG 5.3 Flight-Tunnel Drag Comparison Using Methodology of Ref 218 (from ref 218)



**FIG 5.4 Flight-Tunnel Drag Comparison for C-141A**  
(from ref 220)

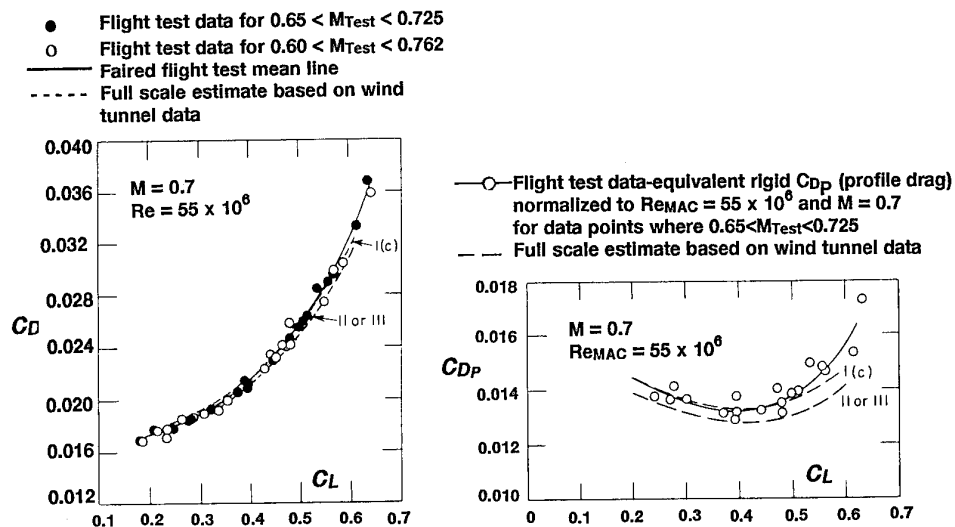


FIG 5.5 Flight-Tunnel Drag Comparison for the C-5A at  $M = 0.7$   
(from ref 221)

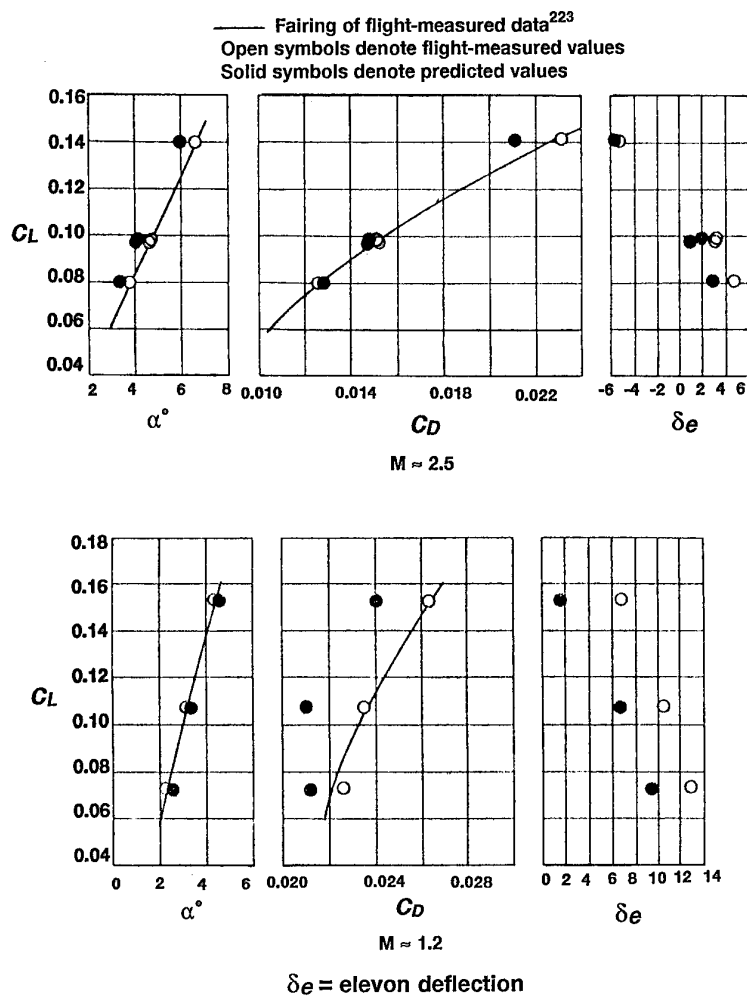


FIG 5.6 Flight-Tunnel Drag Comparison for the XB-70  
(from ref 222)

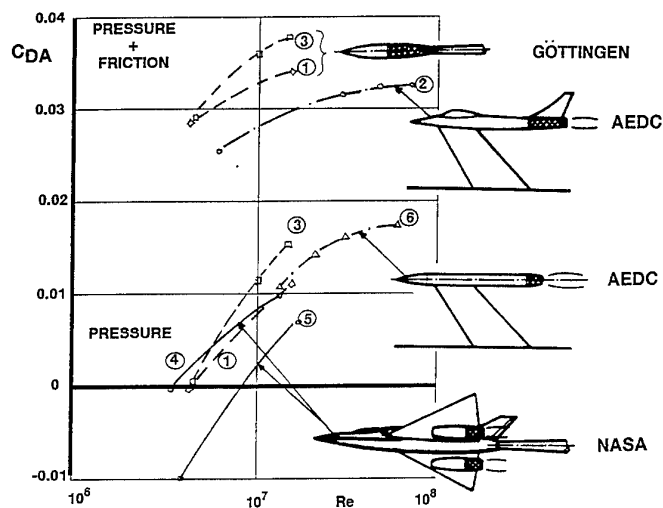


FIG 5.7 Apparent Re - effects on Afterbody Drag  
(from ref 11)

Curve No.	M	$\frac{P_j}{P}$		Ref.
①	0.8	-	AB1	1
③			AB3	2
②	0.9	3	twin jet fighter	3
④	0.6	?	J-85 nacelle on F-106 $\beta_T = 16^\circ$	18
⑤	0.9			
⑥	0.6	3	axisym. body, $\beta_C = 10^\circ$	

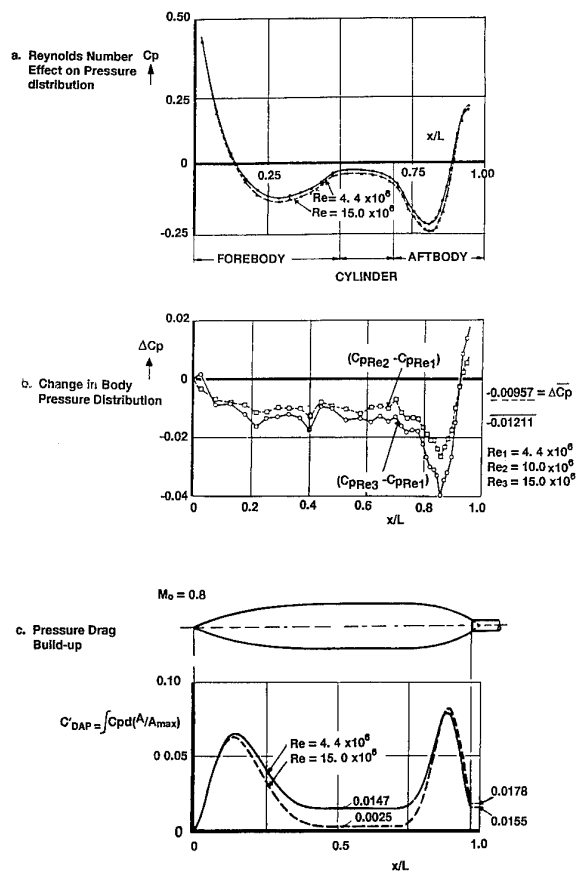


FIG 5.8 Effect of Re at  $M = 0.6$  on Pressures on Axisymmetric Model  
(from ref 12)

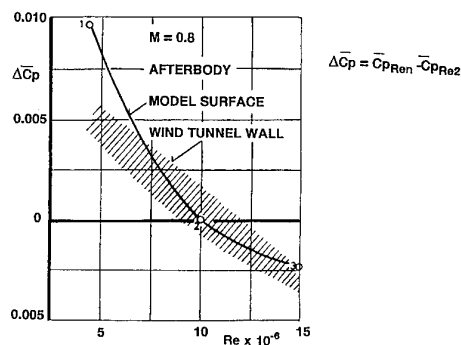


FIG 5.9 Comparison of Apparent Re - effects on Model and Tunnel Wall  
(from ref 12)

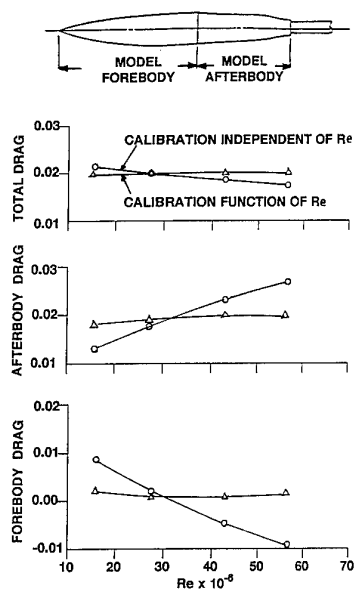
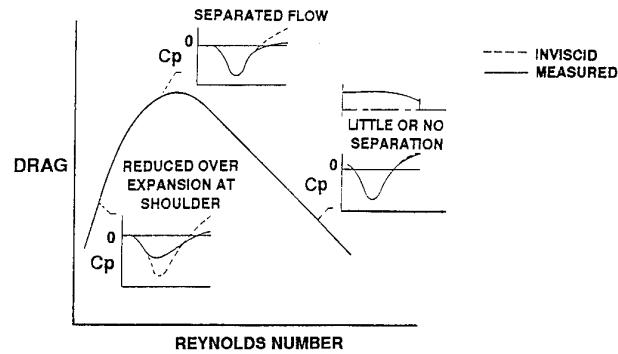
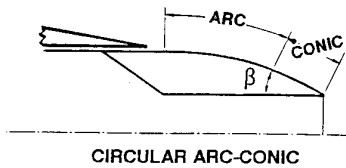


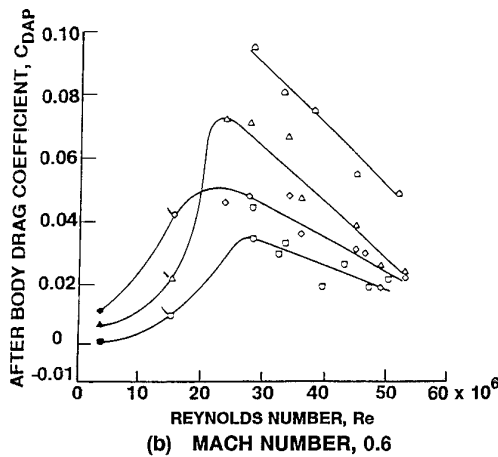
FIG 5.10 Effect of Re and Tunnel Calibration on Afterbody Pressure Drag  
(from refs 13, 224)

$R$  = Radius of boattail shoulder  
 $R_c$  = radius of circular arc of same projected area and terminal boattail angle.

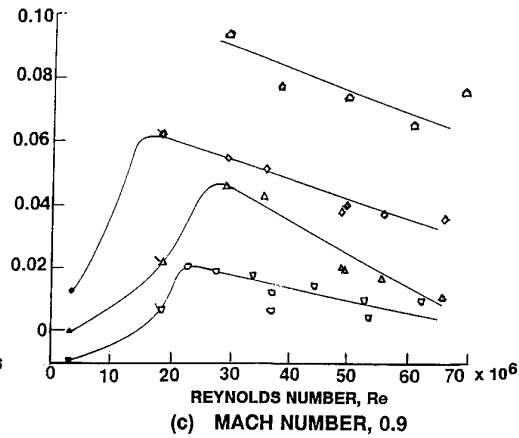
WIND TUNNEL TESTS		FLIGHT TESTS	NOZZLE	
5% scale solid plume simulator	22% scale half model turbojet simulator		100 R/R <sub>c</sub>	β
			25	24
▲	△	△	65	24
◆	◇	◇	25	24
■	□	□	25	16



(a) COMPARISON OF MEASURED AND INVISCID PRESSURE DISTRIBUTIONS



(b) MACH NUMBER, 0.6



(c) MACH NUMBER, 0.9

FIG 5.11 Effect of Re on Pressure Drag of Circular Arc Boattails  
 (Programme on modified F-106B)  
 (from refs 225, 226)

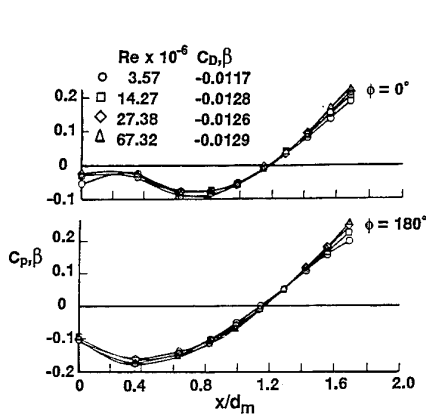


FIG 5.12(a) Effects of Re on Boattail Pressure Distributions  
 (Tests in NASA Langley 1/3m Cryogenic Tunnel)  
 (from ref 227)

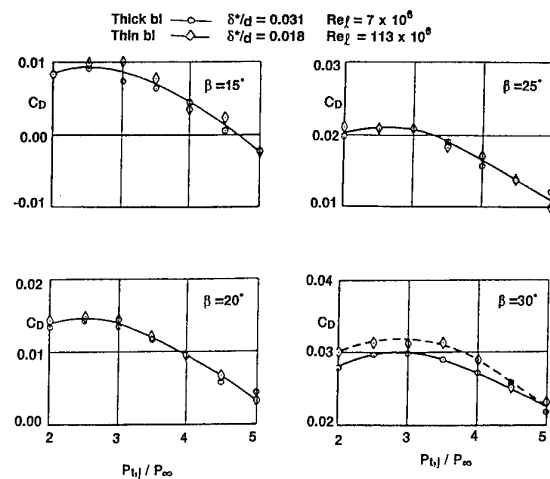


Fig 5.12(b) Effects of Boundary Layer Thickness on Boattail Pressure Distributions  
 (Tests at DRA Farnborough)  
 (from ref 228)

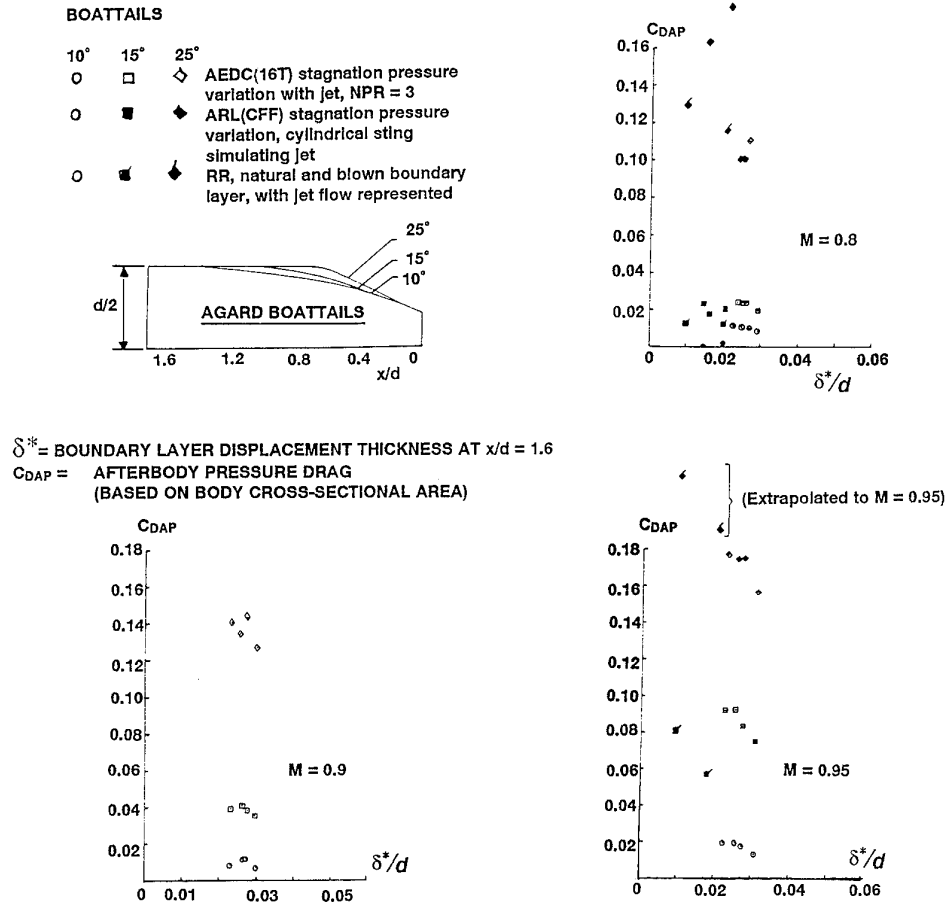


FIG 5.13 Effect of Boundary Layer Thickness on Pressure Drag of AGARD Boattails (from ref 231)

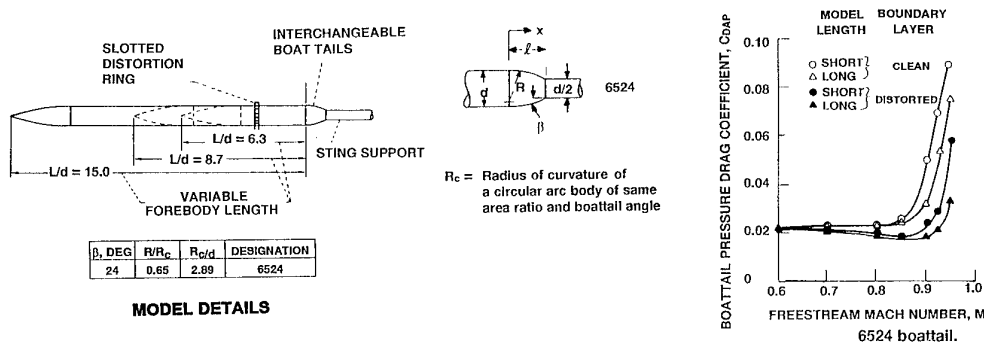
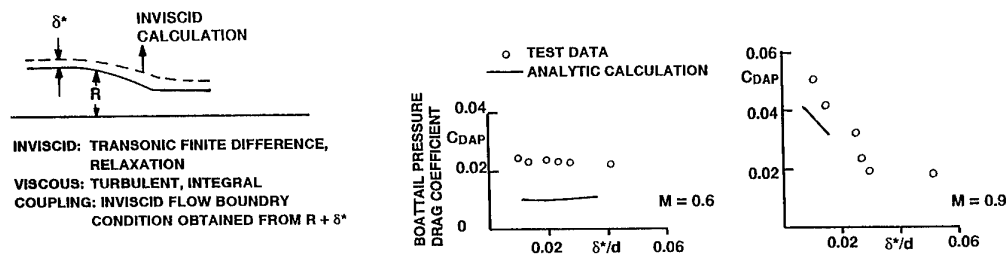
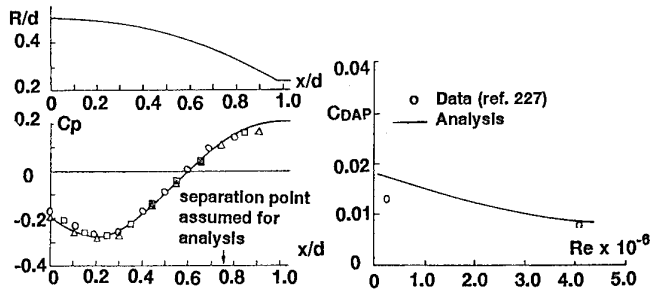


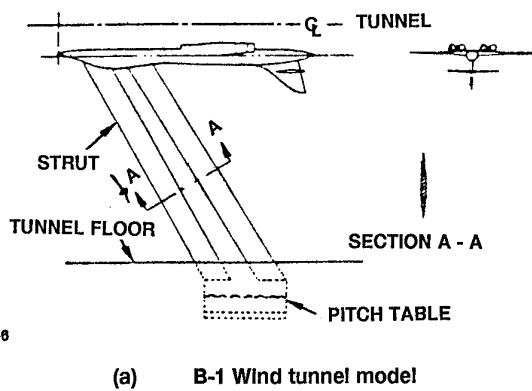
FIG 5.14(a) Effect of Boundary Layer Profile and Thickness on Pressure Drag (from ref 232)



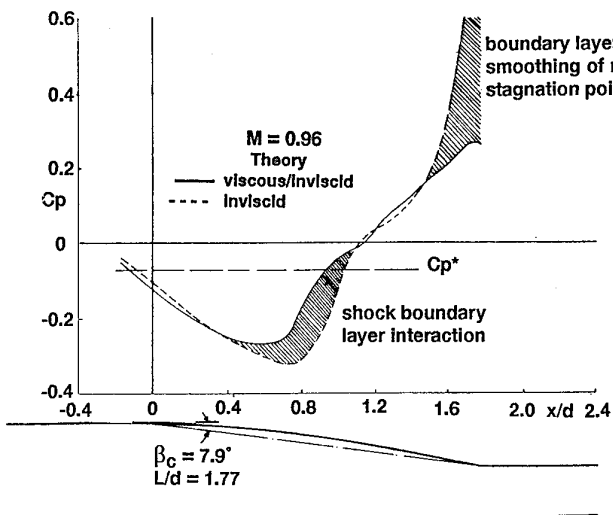
— Analysis  
 ○△□ Data (ref. 227)  
 $C_D \text{ exp.} = 0.009$   
 $C_D \text{ appl.} = 0.010$



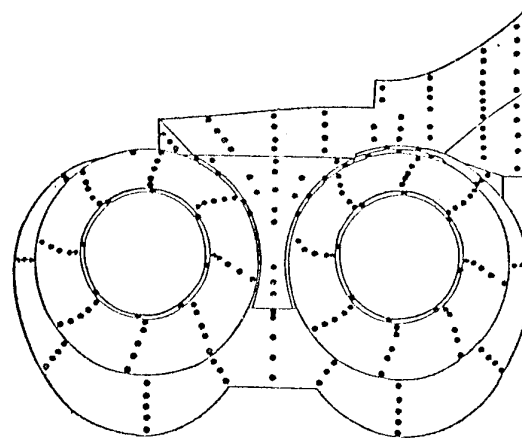
(a) Conical boattail at  $M = 0.6$   
 (from ref 236)



(b) Wind tunnel nozzle contours

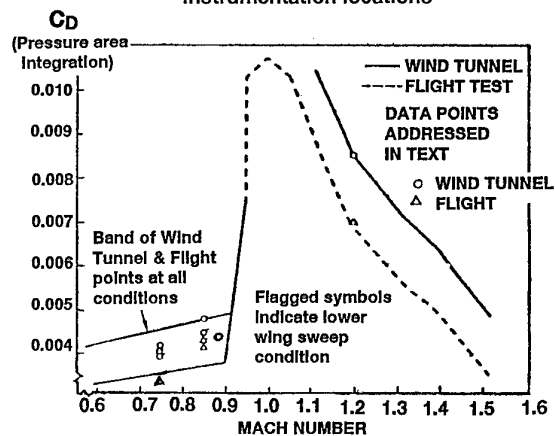


(b) Boattail at  $M = 0.96$   
 (from ref 237)



(c) Afterbody/Nozzle pressure instrumentation locations

FIG 5.15 Experiment - Theory Comparisons for Afterbody Pressures



(d) Wind tunnel/flight test  $C_D$  comparison

FIG 5.16 Flight - Tunnel Drag Comparisons for B-1 Afterbody Drag  
 (from ref 238)



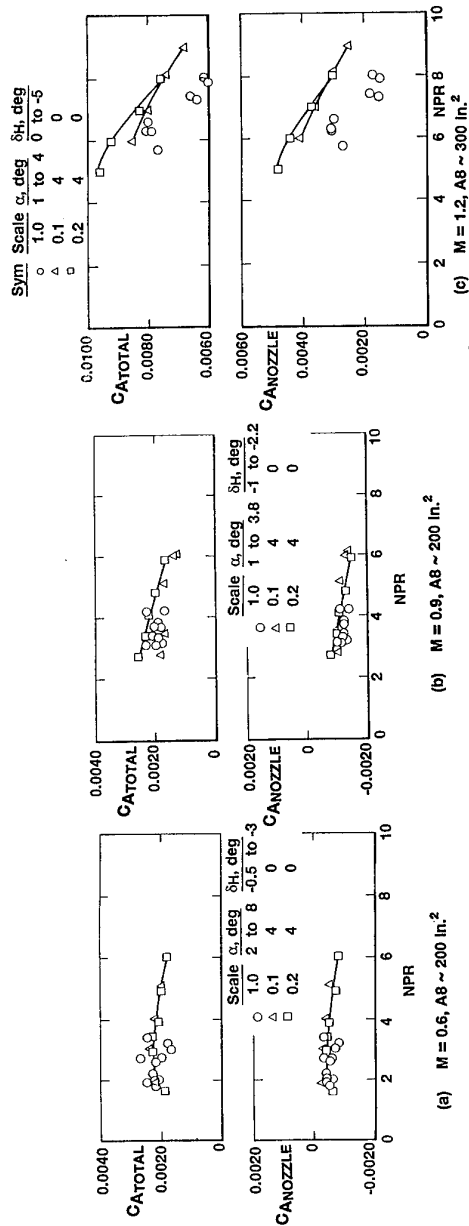


FIG 5.17 Flight - Tunnel Comparison of Total Afterbody - Nozzle and Nozzle Pressure Drags for YF-17 (from ref 239)

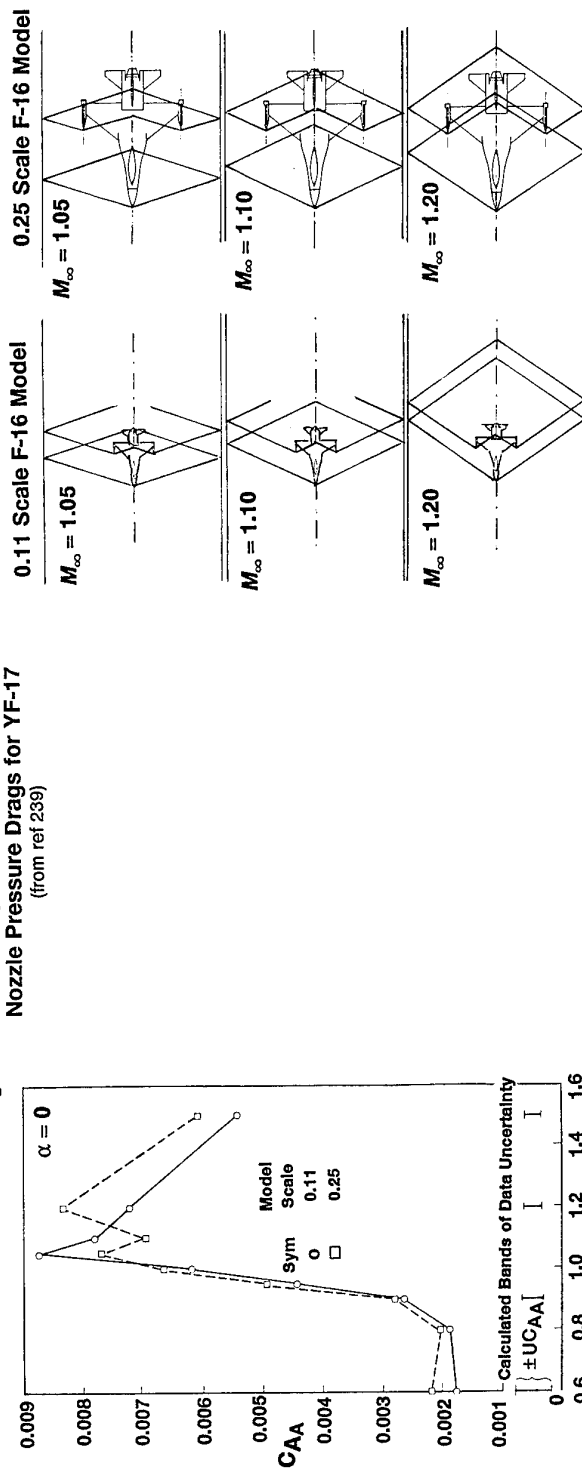


FIG 5.18(a) Effect of Model Scale and Re on Afterbody Drag for F-16A (from ref 240)

FIG 5.18(b) Sketches of Tunnel Wall Interference at Transonic Speeds for F-16A Models (from ref 240)

## 6 SCALE EFFECTS IN FLOW OVER BODIES

No review of scale effect would be complete without referring to the dramatic changes with Reynolds number that can occur in the flow over bodies at subsonic speeds. It has, of course, been known for more than eighty years that the drag coefficient of a sphere shows a rapid decrease as the Reynolds number based on sphere diameter increases beyond a critical value of about  $Re = 3 \times 10^6$  and that this is associated with a change from a laminar separation-bubble (with no reattachment) to a turbulent separation-bubble but the main thrust of research in more recent times has been to explain the large changes with Reynolds number that can occur in the flow over a body at high incidences above about  $30^\circ$ . Under these conditions, the two vortices shed from the nose of the body generally develop asymmetrically, thus creating<sup>245,246,247,248</sup> large side forces and yawing moments even on a circular body at zero yaw. The prediction and, if possible, alleviation of these effects is an important issue for the design of both weapons and combat aircraft that are required to achieve high standards of manoeuvrability. Research on scale effect in this field was reviewed by Polhamus in Ref 249 which included a large number of references. This review was published in 1984 and covers work up to about 1982. In this Agardograph, the emphasis is on research since that date bearing in mind that great strides have now been made in the understanding of these effects.

### 6.1 Transition and Types of Flow

The asymmetric flows are dominated by two vortices trailing back over the leeside of the body. The orientation and position of these vortices depends on the location of boundary layer separation and so, it was obvious from the outset that sudden changes in the characteristics could be expected when there was a change from a laminar to a turbulent separation. Various workers<sup>250,251</sup> in the field appreciated that the first step towards predicting the Reynolds-number effects was to consider where and how transition was likely to occur in the flow over a body at incidence. The best review of this subject is that provided by Poll in Ref 252. Poll noted that for aerodynamically smooth bodies without discontinuities in surface slope and immersed in a stream of low turbulence, transition is usually the result of an instability of the laminar boundary layer. As would be expected by the reader of §3.3.2 of this Agardograph, Poll identified 4 distinct mechanisms by which this instability could occur:

- (i) free shear-layer instability, ie transition in a laminar separation-bubble,
- (ii) contamination along the attachment-line,
- (iii) cross-flow instability, and
- (iv) streamwise-flow (Tollmien-Schlichting) instability.

Some aspects of the following discussion will be familiar to those who have read §§3.1.3 and 3.3.2 but, for convenience, all the main points of Poll's description are included in an abridged form below.

Figs 6.1(a-e) taken from Ref 252 illustrate the flow developments that can take place near the attachment line of a body at incidence. The two pictures in Fig 6.1(a) show the two possible consequences of a separation of the laminar boundary layer to form a free shear layer. In the upper picture, transition does not occur close to the body surface and so, a vortex flow

originates from the laminar separation line relatively close to the windward generator. In the lower sketch, transition does occur and the turbulent boundary layer re-attaches to the surface before separating a second time at a location further from the windward generator.

For a body at incidence, the flow has a velocity component along the windward generator as shown in Fig 6.1(b). For a tangent-ogive-cylinder (a typical body for many of the research tests) at incidence, there will be a peak suction on the attachment line just downstream of the ogive-cylinder junction followed by an adverse pressure gradient. To quote from Poll, "the effect of an adverse pressure gradient is to lower the stability limit of a laminar boundary layer and, therefore, at a sufficiently high Reynolds number, a localised source of turbulence will be established on the attachment line just aft of the nose-cylinder junction. As the turbulence is convected downstream it will spread laterally in the form of a wedge - as shown in Fig 6.1(c). Since the flow inside the wedge is turbulent from the attachment line there can be no separation bubble and a turbulent feeding sheet will leave the body from the line indicated in the figure". This quotation provides a description of the second mechanism for transition.

Fig 6.1(b) shows that away from the attachment line, the streamlines at the edge of the boundary layer are curved in planes drawn parallel to the surface and this leads to a cross-flow in the boundary layer as shown in Fig 6.1(d). When the flow is laminar, the cross-flow velocity profile exhibits an instability to small disturbances at a much lower Reynolds number than the streamwise profile and this leads to transition with typically a transition front with a 'saw-tooth' appearance as sketched in Fig 6.1(e) - this is the third mechanism for transition.

Finally, if none of the above mechanisms has induced transition, it will be induced by Tollmien-Schlichting instability of the streamwise boundary layer.

From the above qualitative description of the different mechanisms for transition, it can be readily appreciated that the flow over a body at incidence can lie in one of several regions in the  $Re-\alpha$  plane separated by boundaries denoting

- (a) the failure of a separated laminar boundary layer to re-attach, ie bubble bursting in the language of §3.1.3.1,
- (b) the occurrence of transition due to contamination of the flow along the attachment line, ie ALT in the language of §3.3.2.2,
- (c) the occurrence of transition due to cross-flow instability, as discussed in §3.3.2.1, and
- (d) the occurrence of streamwise instability if none of the other mechanisms for inducing transition has occurred at lower Reynolds numbers.

At Reynolds numbers below (a), the flow will be as in the upper sketch in Fig 6.1(a); between (a) and (b), it will be as in the lower sketch in Fig 6.1(a); above (b), it will be as on the aft part of the body in Fig 6.1(c) and finally, above (c), if (b) has not occurred, it will be as in Fig 6.1(e). In the event, it has been found both experimentally and from the prediction formulae detailed below, that in many cases, there are just two boundaries, the lower boundary being (a) above and the upper boundary being sometimes (b) and sometimes (c) according to

the relative values of  $Re$  at a given  $\alpha$  for transition by mechanisms (ii) and (iii).

Relations for predicting boundaries (a,b,c) for a circular cylinder at incidence are given in Ref 252:

(a) bubble bursting

The critical free-stream Reynolds number for bubble bursting on a cylinder at incidence is given by the relation:

$$Re_d = \frac{1.0 \times 10^6 \tan \alpha}{\cos \alpha [1 + 3.3 \tan^2 \alpha]} \quad (6.1)$$

where  $d$  = body diameter

Assumptions made in the derivation of this relation include

- (i) bubble bursting will occur when the pressure-rise coefficient between separation and re-attachment reaches the value of 0.30. In §3.1.3.1, it was concluded that this value lay between 0.27 and 0.36,
- (ii) the pressure distributions over the body were taken from the results published in Ref 253 and this, coupled with (i) led to a bubble length at bursting of  $0.14d$  and an assumption that transition would be occurring at half this length, ie  $l_t = 0.7d$ , downstream of separation,
- (iii)  $l_t/\theta_s = 4 \times 10^4$  as proposed by Horton in Ref 69,
- (iv) from the pressure distributions in (ii), the laminar boundary layer separates when the local velocity,  $U_s = 1.82U$ . For a body at zero incidence, it would follow that  $Re_{d \text{ crit}} = 3.1 \times 10^5$ , in reasonable agreement with experiment,
- (v) the "independence principle" applied to the maximum pressure-rise that the bubble can withstand.

The variation of  $Re_{d \text{ crit}}$  with  $\alpha$  as given by relation 6.1 is shown in Fig 6.2 and compared with experimental data from Refs 254, 255, 256, 257, these experimental values being defined as the value at which the cross-flow drag coefficient has fallen to 0.7. The critical Reynolds numbers have been normalised with respect to the value at  $50^\circ$  incidence. It will be seen that relation 6.1 produces good agreement with the trend of the experimental data; the predicted maximum is lower than the measured value by about 4%. Also shown in Fig 6.2 are two other relations proposed by Clark<sup>254</sup> and Reding and Ericsson<sup>250,251</sup>; these are not in such good agreement with the experimental data and Poll in Ref 252 argues that any agreement with Clark's relation would have been fortuitous and that the reasoning behind Reding and Ericsson's relation is physically unsound.

(b) contamination along the attachment line

The critical Reynolds number for attachment-line contamination is given by the relation:

$$Re_{d \text{ crit}} = 1.1 \times 10^6 \frac{\tan \alpha}{\cos \alpha} \quad (6.2)$$

This relation is based on the assumption that on an ogive-cylinder body, it is sensible to take  $Re = 540$  as the criterion for attachment-line contamination.

(c) cross-flow instability

The critical Reynolds number for cross-flow instability is given by the relation:

$$Re_{d \text{ crit}} = 1.45 \times 10^5 \left[ \frac{1 + 3.3 \tan^2 \alpha}{\sin \alpha} \right] \quad (6.3)$$

This relation is based on the assumption that  $\chi = 235$  is the appropriate criterion for cross-flow instability.

(d) streamwise instability

The experimental results in Ref 253 suggest that a suitable criterion for the suppression of a short laminar separation bubble by streamwise flow transition is

$$Re_{d \text{ crit}} = 4 \times 10^6$$

for  $30^\circ < \alpha \leq 90^\circ$ .

The most comprehensive set of tests on tangent-ogive-cylinder bodies over a wide range of Reynolds numbers from 0.2 to  $4 \times 10^6$  were those undertaken in the NASA Ames 16 ft pressurised tunnel and described by Lamont in Refs 246, 247. Lamont concluded that it was possible to draw two boundaries in the  $Re$ - $\alpha$  plane separating regions which he described as laminar flow at separation (L), transitional (T) and fully turbulent at separation (FT). This terminology has been retained in many other reports but in the light of the discussion above, it seems more appropriate to describe the regimes as laminar (L), bubble (B/T) and turbulent (T). By these terms, the inference is that the vortices are induced by a pure laminar separation in L, by a turbulent separation following re-attachment of a short laminar separation bubble in B/T and by a turbulent separation with no preceding bubble in T. The boundaries derived from the experiments and alternatively by the relations 6.1, 6.2, 6.3 and 6.4 are presented in Figs 6.3(a,b). Good agreement between experiment and prediction is shown and the comparison shows that there are two boundaries, the lower indicating when the bubble reattaches and hence when there is a turbulent separation downstream of re-attachment and the upper indicating, first, for incidences below  $26^\circ$ , contamination of the flow along the nose attachment-line and then for incidences between  $26^\circ$  and  $70^\circ$ , the occurrence of transition due to cross-flow instability and finally, from  $70^\circ$  to  $90^\circ$ , the occurrence of transition due to streamwise instability.

It will be seen in §§6.2 and 6.3 below that it would be highly desirable to manipulate the boundary layer in the model tests to eliminate the scale effects due to the changes in transition mechanism and thus, position as described above. Unlike the methodology for tests on wings in transonic flow, the aim here should be to manipulate the boundary layer so that the transition fronts and hence, the separation lines are in the same positions as at full-scale. The relations 6.1, 6.2, 6.3 and 6.4 now enable one, in principle, to achieve this objective but one also needs information on how the use of roughness is likely to

modify the boundaries in Fig 6.3(b). These effects can be substantial: for example, Poll in Ref 252, notes that uniformly distributed sand grain roughness with an effective particle diameter of  $0.003d$  will reduce the critical value of  $Re_d$  from  $3 \times 10^6$  to  $1 \times 10^6$  for a cylinder at  $90^\circ$  incidence where  $d$  is the diameter of the cylinder. Fig 6.3 shows the effect of this roughness on the boundaries for bubble re-attachment and nose attachment line contamination. Research in the use of roughness, ie "nose gritting", is discussed in Ref 258 and there is also some evidence in Ref 264.

## 6.2 Body Forces and Moments at High Incidence and Zero Yaw

It has been shown in §6.1 above that the flow separation on a body at high incidence can be of one of three types depending on the Reynolds number and incidence: laminar (L), laminar bubble followed by turbulent re-attachment and separation (B/T) and finally, turbulent with no preceding bubble (T). The normal force and side force and the distribution of these along the length of the body and hence, the pitching and yawing moments, have been shown to depend greatly on which of these separations is present.

The most comprehensive set of force and moment data is that reported by Lamont<sup>245,246,247,259</sup> from tests in the 12 ft pressurised tunnel at NASA Ames. Surface pressure distributions were obtained at  $10^\circ$  steps in roll angle over a range of angles of attack from  $20^\circ$  to  $90^\circ$  at eight Reynolds numbers from  $0.2 \times 10^6$  to  $4 \times 10^6$ , based on the diameter,  $D$ , of the cylinder for two tangent-ogive-cylinder models. The results to be presented here mostly relate to the model with a nose length of  $2D$  and a cylindrical afterbody of length  $5.5D$  where  $D$  = cylinder diameter. Ignoring for the moment the detailed variation of the side force and normal force with roll angle, Figs 6.4(a,b) present the variation of the maximum overall side force and of the integrated overall normal force with angle of attack at zero yaw for 4 of the test Reynolds numbers. Reference back to Fig 6.3(b) shows that the separation is of type L for  $Re = 0.2 \times 10^6$ , B/T for  $Re = 0.4$  and  $0.8 \times 10^6$  and T for  $Re = 4 \times 10^6$ . It is immediately obvious that both the side and normal forces are high when the separation is either L or T and low when it is B/T; indeed, at  $Re = 0.8 \times 10^6$ , in the range where the separation is of type B/T, the maximum side force is near zero at most angles-of-attack, implying no asymmetric flow development. The shaded areas on the normal force figure indicate the variation obtained with angle of roll; it will be seen that this is particularly large at  $Re = 4.0 \times 10^6$  and this was due to the fact that this Reynolds number is close to the upper boundary in Fig 6.3(b) and as the model was rolled, the results varied between values representative of conditions above and below this boundary. These two figures, Figs 6.4(a,b) are sufficient to demonstrate the difficulties in any quantitative prediction of the scale effects and the desirability of either testing at full-scale Reynolds numbers or of manipulating the model boundary layer as suggested at the end of §6.1.

Despite these last remarks, Poll in Ref 252 was able to provide a clear understanding of even the detailed trends in the normal force graph, Fig 6.4(b). He defined a viscous cross-flow drag coefficient,  $C_{dN}$  such that

$$C_{dN} = \frac{(\text{total normal force} - \text{inviscid normal force})}{\frac{1}{2}\rho U^{\frac{1}{2}} \times (\text{plan area}) \times \eta} \quad (6.5)$$

where  $\eta$  is a correction factor to account for the finite length of the cylinder.

Poll continues<sup>252</sup> "Consider, in the first instance, a situation in which the body is held at fixed incidence whilst the free-stream Reynolds number (speed) is gradually increased. Initially, the Reynolds number will be low and the boundary layer will be laminar at separation. Consequently, the cross-flow drag coefficient,  $C_{dN}$  will remain at about this level until the free shear-layer re-attachment boundary is reached. As this boundary is crossed  $C_{dN}$  will drop rapidly to a value of about 0.2-0.3. Moreover, since the re-attachment takes place on the cylindrical afterbody before it takes place on the nose, the decrease in cross-flow drag coefficient may be accompanied by a rapid forward movement of the centre of pressure. Further increases in the Reynolds number produce a rise in the cross-flow drag coefficient with the rate of increase being dependent on the value of incidence. If the incidence for the current example is greater than  $26^\circ$  (see Fig 6.3(b)),  $C_{dN}$  will rise continuously until either the cross-flow transition boundary or the streamwise-flow transition boundary is encountered. At this condition the boundary layer transition front has just reached the location of the leading edge of the short separation bubble and, from the two-dimensional cylinder data of Ref 253, the cross-flow drag coefficient is expected to be between 0.4 and 0.5. This progressive increase in the loading on the afterbody may cause the centre of pressure to move back as Reynolds number is increased. If the Reynolds number continues to rise, the next significant event is the onset of attachment-line contamination which causes the transition front to move, in a discontinuous jump, from a point just downstream of the minimum pressure location to the windward generator position - see Fig 6.1(c). With the transition front at this location, the cross-flow drag coefficient is that appropriate to very high Reynolds number flow, ie  $C_{dN}$  jumps to a value of about 0.7. Once again a corresponding shift in the centre of pressure location is to be expected. No further significant changes in the cross-flow drag coefficient are anticipated at higher Reynolds number. If the incidence is fixed at a value below  $26^\circ$  then the picture is altered slightly. In this case the upper boundary corresponds to the attachment-line contamination condition. Consequently, at low incidence, small changes in Reynolds number can produce large, and possibly discontinuous variations in the cross-flow drag coefficient. We note also that once the attachment-line contamination condition has been exceeded the flow over the windward face of the cylindrical afterbody will be fully turbulent and, therefore, the cross-flow transition boundary can never be encountered. This conclusion does not, however, apply to the tangent-ogive nose where the Reynolds numbers are smaller and attachment-line contamination may be avoided."

Schematically, the variations in  $C_{dN}$  as described above are shown in Fig 6.5(a) for a long cylinder and continuing to ignore the effects of the nose and finite body length, this leads to Fig 6.5(b) which shows the idealised dependence of the normal force coefficient on incidence at constant  $Re$ . The resemblance of these predictions in Fig 6.5(b) with Lamont's experimental data in Fig 6.4(b) is striking. This is true even on points of detail, eg the maximum present in both figures in the curve for  $Re = 4 \times 10^6$  near  $50^\circ$  which can now be interpreted as being due to the crossing of the boundary for attachment-line contamination. Similarly, the crossing of the curves for  $Re = 0.8 \times 10^6$  and  $0.4 \times 10^6$  is related to the crossing of the boundary for transition due to cross-flow instability (see Fig 6.3(b)).

Turning to the side force results in Fig 6.4(a), the maximum values for the laminar (L),  $Re = 0.2 \times 10^6$  and turbulent (T),  $Re = 4.0 \times 10^6$  separation cases occur near  $\alpha = 55^\circ$ . The values are similar, as are the distributions of local side force along the length of the ogive-cylinder but, as would be expected, the pressure distributions are completely different as can be seen from Fig 6.6(a). Laminar separation occurs near an azimuth angle,  $\theta$ , of  $80^\circ$ - $90^\circ$  whereas turbulent separation is further round the body at about  $100^\circ$ - $120^\circ$ . The pressure distribution for a B/T condition where there is a laminar separation followed by turbulent re-attachment and separation shown in Fig 6.6(b) highlights an important difference in the flow compared with the turbulent case in Fig 6.6(a): the asymmetry only exists upstream of the separation. This is just one indication of a fundamental difference in the mechanism causing the (smaller) asymmetry in the B/T region. Whereas in the L and T regions, the side-force is due to asymmetric vortex patterns extending into the wake of the body in a manner similar to that predicted by the impulsive flow analogy<sup>260</sup> first introduced by Allen and Perkins in 1951, the asymmetry in B/T arises because of small differences in the bubble re-attachment and subsequent separation positions on the two sides of the body. The asymmetric flow in L and T was very repeatable for a given body at a given  $Re$  but the flow in B/T was highly non-repeatable. The general feeling is that in B/T, the asymmetry is induced by minor imperfections and roughness on the model; no coherent vortex shedding is observed in this B/T regime. This distinction should not cause any surprise: it is similar to what had been observed earlier in the flow around a two-dimensional cylinder for which, at low  $Re$ , when there is a laminar separation, the vortex shedding in the wake has a clearly-defined periodicity but where, at somewhat higher  $Re$  when there is a bubble re-attachment and turbulent separation, the wake is random with no dominant periodicity.

The earliest experiments on the flow around bodies at high incidence showed that the direction of the vortex asymmetry and the resulting side forces could not be predicted ahead of the actual test: the sign appeared to depend on either small imperfections in the model surface or random disturbances in the wind tunnel flow. Initially, this led to the practice of plotting the variation of the absolute value of the side force without regard to the sign of the actual results. Polhamus<sup>249</sup> however drew attention to the fact that this practice meant that some trends with Reynolds number that could be significant were being hidden. For example, the true variation of the maximum side force at zero yaw,  $C_{Y_0}$ , from Lamont's tests<sup>247</sup> on a body with a 3.5D long ogive nose + 4D cylinder is shown in Fig 6.7(a) and it will be seen that there are two changes of sign in the variation with  $Re$ . Fig 6.7(a) also shows the variation of the local side force along the length of the body for three values of  $Re$ : the negative side force in the intermediate range of  $Re$  appears from a second peak in the loading on the rear of the body. Polhamus related this variation of  $C_{Y_0}$  with  $Re$  to changes in the vortex shedding frequency but Lamont later showed<sup>259</sup> that the variation could, more correctly, be explained in terms of the changes with  $Re$  in how and where transition occurred along the length of the tapered body nose and afterbody.

This analysis by Lamont is worth presenting in some detail. There are two fundamental points: first, when  $Re$  is based on the diameter of the cylinder, the critical  $Re$  boundaries discussed earlier in §6.1 change along the length of the tapered nose and second, the shape of the longitudinal distribution of the local side force over the aft part of the body is different in the B/T regime when, as noted earlier, there is no coherent vortex shedding. In support of the first point, the boundaries for two stations near the forward tip of the nose are compared in Fig

6.7(b) with those for the cylindrical afterbody; the lower full-line boundaries mark the change from L to B/T as explained earlier and the upper boundaries mark the change from B/T to T with transition induced in general by cross-flow instability (contamination along the attachment line is unlikely to occur on the nose). It follows that with bodies with long slender noses, it is possible for two or even three forms of separation to co-exist, eg L on the nose and B/T on the cylindrical afterbody or L near the nose tip followed by B/T further aft and then finally, T.

Let us now consider the longitudinal distributions of local side force presented in Fig 6.7(c) for the 3.5D nose/4.0D afterbody at  $40^\circ$  incidence:

- (a) At  $Re = 0.2 \times 10^6$ , the flow at all stations is in the L regime and the distribution is related to the asymmetric development of the vortices shed as a result of a laminar separation,
- (b) with increase in  $Re$ , the flow over the afterbody and aft part of the nose changes to B/T first on the side of the body developing the higher suction and then on the opposite side. The sign of the local side force remains the same and this can be explained by reference to the pressure distributions for a 2-D cylinder in Fig 6.7(d): high suctions ahead of the separation are maintained in B/T and so, the sign of the side force remains the same as in the L flow at lower  $Re$ . The second factor noted above, ie the change in shape of the side force distribution over the aft part of the body when there is no coherent vortex shedding now begins to influence the overall side force. At  $Re = 0.4 \times 10^6$ , the distribution loses its damped sinusoidal appearance and tends to flatten out at the rear to a near-constant value. The results in Fig 6.7(c) may not be too convincing in this respect but the effect is clearly visible in the results from Champigny<sup>255</sup> in Fig 6.7(e) for a longer body. Indeed, body length now becomes an important parameter in determining the overall side force: if the afterbody in Lamont's case had been shorter, the overall side force would have been smaller while if it had been longer, it would have been greater: hence, one should be cautious about accepting the earlier conclusion that the side force is small when the flow separation is in the B/T regime as a completely general conclusion irrespective of body length.
- (c) with further increase in  $Re$  to say,  $Re = 0.8 \times 10^6$ , one arrives at a situation where all the possible types of flow are present: a laminar separation (L) on the forward nose, a bubble separation + reattachment + turbulent separation (B/T) on the middle nose followed by a turbulent separation (T) on the rear nose. This may sound complicated but Figs 6.8(a-d) taken from Ref 261 should serve to clarify the details of the flow. These figures show the azimuthal pressure distributions at four fore-and-aft stations along the ogive-cylinder tested by Lamont annotated with the locations of the primary separations, re-attachments and secondary separations derived from either the pressure distributions from Lamont's tests or, when marked K, from flow visualisation tests by Keener<sup>262</sup> on the same ogival nose without the cylindrical afterbody. The presence of this afterbody did not appreciably affect the forces on the nose and so, it is valid to draw on both sets of data when analysing the flow. The roll orientation was chosen to give good agreement between the integrated

side force values in the two tests and the azimuthal angles in Lamont's tests were reversed to give the same direction for the asymmetry in the two tests. Hall's analysis demonstrates the value of undertaking both types of test and using both to remove uncertainties in the interpretation of the data. The results for  $x/D = 0.5$  indicate an L separation, those for  $x/D = 2.0$  a B/T separation and those for  $x/D = 3.5$  and  $6.0$ , a T separation. Taking the results for  $x/D = 2.0$  as an example to explain the notation, the laminar boundary separates at LS and forms a bubble; transition occurs in the bubble, the flow re-attaches and the turbulent boundary layer then separates at TS; the flow over the vortex comes down to the surface and re-attaches at R and then separates at SS (secondary separation). The suction peak at an azimuth angle of  $190^\circ$  is thought to be due to the dominant vortex having moved close to the surface. Fig 6.8(e) will give further help in the interpretation of the flow. The asymmetry in the fully turbulent (T) region is in the opposite direction to what it was in the L and B/T regions. This can be explained by reference to Fig 6.7(d): the change to T will occur first on the side which until then has been the high suction side but with T the suction ahead of the separation is lower than with B/T: hence, the reversal in sign of the side force. The overall side force, therefore, being composed of a positive side force on the forebody which is decreasing and a negative side force on the rear body which is increasing with Re is found to decrease with Re in this range. The overall value passes through zero between  $Re = 0.8 \times 10^6$  and  $Re = 1.2 \times 10^6$ ,

- (d) with further increase in Re, the change to fully turbulent flow (T) will occur progressively further forward until ultimately, it occurs so near the nose tip that the fully turbulent asymmetric flow will assume the nose tip-dictated direction as for the laminar flow at lower Re. This leads to a relatively sudden second reversal in the sign of  $C_y$ ; this change being sometimes accompanied by severe model buffeting. In the case tested by Lamont, this occurred when the fully turbulent separation has spread forward to about one radius from the nose tip. This second reversal can be seen in the values of  $C_{y0}$  for different azimuthal angles in Fig 6.8(f),
- (e) by implication, this second reversal of sign is still to appear at higher incidences at Reynolds numbers beyond the test range. In Ref 259 Lamont speculates that the full variation of  $C_{y0}$  with Re might be as plotted in Fig 6.8(f): a good picture to demonstrate the need to test, if possible, at full-scale Reynolds numbers. An increase from a low test Reynolds number towards the full-scale value but not all the way does not necessarily help! Prediction of the scale effect is clearly difficult but knowledge of the pressure distributions and use of the relations in §6.1 for predicting transition position coupled with detailed flow visualisation should serve to establish in which Re-range one is testing.

At several points in the above description of the changes of flow with Reynolds number, it was noted that in any test, the sign of the asymmetric side force was dependent on the effect of minor imperfections in the model near the nose or in the tunnel flow. Having established the asymmetric direction at the nose - the "nose-tip bias" - what then happens further aft and the changes with Reynolds number have been satisfactorily explained at least qualitatively. The direction of the nose-tip bias cannot, however, be forecast. On the other hand, Ref 261 does offer

some thoughts as to the Re-effects on the flow close to the nose. These are difficult to determine experimentally because significant changes are likely to take place immediately downstream of the nose tip. This is illustrated by comparing Figs 6.9(a,b): Fig 6.9(a) presents the variation of the measured local side forces with  $\alpha$  and Re at a station at  $x/D = 0.5$  (the first pressure-plotting station where the flow regime is either B/T or T) while Fig 6.9(b) is an attempt to show what might be happening at  $x = 0$ , this being constructed by forward extrapolation of the measured data. The initial boundary layer immediately downstream of the nose,  $x/D = 0$ , would, of course, be laminar and some of the trends in Fig 6.9(b) are in accord with theoretical calculations<sup>263</sup> which suggested that for impulsively started cylinders, perturbations would have more effect if they were applied at larger values of non-dimensional time. In the present context, this implies that an increase in angle-of-attack would strengthen the ability of a given non-uniformity to create asymmetry and also, one would expect an increase in Reynolds number to strengthen the tendency because a non-uniformity would become more significant as the thickness of the laminar boundary reduced with increase in Reynolds number. These trends are evident in Fig 6.9(b) although they are restricted by a decision in the light of the experimental data in Lamont's tests to impose a limit of  $C_y = 2.3$  in regions like the nose tip where the boundary layer is laminar. A practical consequence of the evidence in Fig 6.9(b) is that the incidence for the appearance of asymmetric flow would be expected to reduce somewhat with increase in Reynolds number.

Another important practical issue is whether the asymmetric flows are stable or not. This issue was addressed in some tests<sup>264</sup> by Champigny in the F1 tunnel at le Fauga. Tests were made on a model with a high standard of surface finish with average roughness smaller than  $1 \mu\text{m}$ . This is significant: data repeatability was much better than for models with a rough surface and there was no switching from side to side. Fig 6.10 presents the power spectral densities,  $\phi_{cy}$ , of the unsteady side force from tests at  $\alpha = 50^\circ$  for various Reynolds numbers spanning the different flow regimes - see Fig 6.3(b). The peaks at 15 Hz are due to the model motion and these would have been less pronounced if the model had been mounted more rigidly rather than on a balance.

Leaving aside the effects of model motion, the main features of the results in Fig 6.10 are as would be expected from the earlier discussion:

- (a) the highest values of the fluctuations are observed at  $Re = 0.44 \times 10^6$  in the upper part of the range where there is an L-type separation,
- (b) the fluctuations are relatively small in the range ( $Re = 0.54$  and  $0.9 \times 10^6$ ) for B/T-type flow where there is no coherent vortex shedding,
- (c) the fluctuations are most noticeable around the predicted frequencies for Karman vortex shedding - 45 Hz for the L case and 90 Hz for the T case.

All the results discussed above referred to bodies with circular cross-sections. Little evidence is available in the open literature from research tests on bodies with non-circular cross-sections but Keener et al in a test programme on forebodies<sup>265</sup> investigated the effects of changing from circular to elliptic cross-sections with the major axis alternatively vertical and horizontal. Care has to be exercised in setting up a realistic comparison between these results; Figs 6.11(a,b) in this

Agardograph are taken from the review by Polhamus<sup>249</sup> rather than the earlier paper<sup>248</sup> by Hunt which also compared the results on a different basis. Polhamus noted that the elliptic tangent-ogive forebody with the major axis vertical had the same planform area as the circular body with a fineness ratio of 5 and the body with the major axis horizontal had the same planform area as the circular body of fineness ratio of 3.5. This suggested the appropriate basis for illustrating the effects of cross-sectional shape: the comparisons are made for the same fineness ratio and with the side force coefficient based on the area of a circle of diameter equal to the width of the elliptic planform at the base. Also, the Reynolds numbers are based on the maximum body dimension (in plane of the major axis) at the base in all cases (see Fig 6.11).

Considering first the comparison in Fig 6.11(a) for the ellipse with the major axis vertical, it will be seen that

- (i) at subcritical  $Re$  (flow separation  $L$ ), the maximum side force coefficient was higher for the elliptic body, the increase being approximately in the ratio of the fuselage side areas,
- (ii) at supercritical  $Re$  (flow separation  $T$ ), the maximum side force (now of the opposite sign and located near the rear of the body as explained earlier) is considerably less in magnitude for the elliptic forebody than for the circular. Polhamus suggests that this is because the vortex strength is less for the more "streamlined" shape of the elliptic body.

It is, of course, possible that at higher Reynolds numbers beyond the range covered in Fig 6.11(a), there will be a second change of sign and so, it may be that this figure gives no clue as to the comparison at full-scale Reynolds numbers.

The comparison in Fig 6.11(b) for an elliptic body with its major axis horizontal is probably of more practical interest for aircraft applications. In this case, the maximum side force for the elliptic cross-section body is lower than for the circular body at both subcritical and supercritical Reynolds numbers and also, there is a much higher critical  $Re$  for the elliptic body. This last change is ascribed to the more severe adverse pressure gradient encountered by the cross-flow downstream of the attachment line with the elliptic shape in this case.

No direct evidence on the scale effect on the high incidence characteristics for bodies of other cross-sections, eg square, rectangular or triangular, can be presented but, following the analogy with the drag of 2D cylinders found for circular cylinders, it is clear that the change to such cross-sections is likely to have a major effect on the  $Re-\alpha$  boundaries discussed earlier in §6.1. Results showing the effects of cross-sectional shape on the variation of the drag of a 2D cylinder with  $Re$  are included in Ref 249; Figs 6.12(a-c) taken from this review show that the Reynolds number for the sudden decrease in drag, ie the change from a laminar to a turbulent separation, is highly dependent on the section shape and on details such as the corner radius of a basically square cylinder with rounded corners. These results are discussed in detail in Ref 249. One is left with the feeling that while the extensive research at high incidence on cylinders with circular cross-sections has been an excellent introduction to the changes in flow with Reynolds number that can occur, the precise values of  $Re$  at which these changes will occur on, for example, the possibly non-circular nose of a combat aircraft, could well be significantly different. Further research including flow visualisation tests on the effects

of cross-sectional shape is required to confirm (or otherwise) this point.

### 6.3 Forebody Flow on the F/A 18

The best example of an investigation into the scale effects on forebody flows at high angles of attack on an actual aircraft is undoubtedly the major effort led by NASA Ames in the High Angle-of-Attack Technology Programme (HATP) on the F/A 18 High Alpha Research Vehicle (HARV). This aircraft is designed to exploit vortex flows over the forebody and an inboard wing leading-edge extension (LEX) at high angles-of-attack in order to obtain enhanced manoeuvrability. The programme has embraced tests on the full-scale aircraft in flight and in the NASA Ames 80- by 120-Foot Wind Tunnel, tests on 6%, 7% and 16% scale models in a variety of different wind tunnels, water tunnel tests on small scale models, a great amount of flow visualisation and some pioneering Navier-Stokes calculations. The tests have covered a Reynolds number range from 8700 up to  $25 \times 10^6$ . The research has been reported in a large number of different papers in recent years, eg Refs 266, 269-282.

Ref 266 is an early review of the conflicting evidence on the F-18 which showed the need to understand the apparent scale effect on the directional and lateral stability characteristics of the aircraft at high angles-of-attack. The serious differences are illustrated in Figs 6.13(a-c). The flight data showed that both the directional and lateral characteristics at small angles of sideslip were non-linear at the high  $\alpha$ s ( $33^\circ$ - $35^\circ$ ) chosen for this comparison. It will be seen that only the tests on the 16% scale model in the NASA Langley 30 x 60 ft tunnel gave reasonable agreement with the flight data. In the other model tests, positive lateral stability was retained throughout the test incidence range. Partial model tests showed that the differences were associated with the vortex flow over the forebody and LEX of the aircraft (the geometry is shown in Figs 6.14(a,b)). This confirmed earlier experience<sup>267,268</sup> that forebody flows on slender configurations dominate the high-incidence aerodynamics. It appeared that a more severe flow breakdown occurred on the 0.16 scale model (and by implication, the full-scale aircraft) than on the smaller models. Ref 266 suggested that the likely cause of the discrepancies lay in subtle differences in the contours of the forebodies of the models and full-scale aircraft but later work has shown that, as would be expected from the discussion in §§6.1 and 6.2 above, changes in transition position and in the type of separation on the forebody are perhaps the main contributory factor. They are not, however, the only factor: there are cases, for example, where different results have been obtained on the same model at the same test Reynolds numbers in different tunnels. The results will be discussed in detail below because it makes a very interesting story of how the ideas from the research on a simple circular cylinder can carry across to the complex geometry of a forebody/LEX configuration with major consequences for the flow over the rest of the aircraft, creating problems not only in lateral and directional stability but also in buffeting on the twin vertical surfaces<sup>279</sup>.

#### 6.3.1 Surface flow patterns

The clearest introduction to the nature of the flow over the forebody and canopy is provided by Ref 269. This paper presents pressure distributions and flow patterns from oil flow visualisation tests on the 16% scale model in the Langley 14 x 22 ft wind tunnel. Fig 6.15(a,b) presents sketches of a typical flow pattern: a side view and one cross-section at a station whose position is defined in Fig 6.14(a,b). Readers will

recognise immediately that the flow over the forebody just ahead of and near the LEX is in the B/T regime discussed earlier. To quote from Ref 269, "the model shows a significant amount of laminar flow on the lower windward side prior to separation. The initial separation on the forebody was a laminar separation bubble. In the forward nose region, where the cross-section is circular (stations 1-3), the flow reattached briefly on the lee side of the laminar separation bubble (probably as turbulent flow) and then separated again. A separation line can be defined by a pooling of the oil mixture on the lee side of a demarcation or by a sudden change of direction of the flow lines across a demarcation. In the aft forebody region (stations 4 and 5) where the cross-section is rounded at the top and bottom but relatively flat on the sides, the flow appeared to reattach and form a region of attached turbulent flow terminated by a distinct separation as the body contour transitions to the highly curved upper surface. Moving aft on the forebody, the laminar separation bubble progressively migrated upward until it intersected the LEX apex. On the top (lee side) of the forebody, including the canopy, oil flows indicated reattachment of the separated vortex sheets and also showed a secondary separation forming near and aft of station 3. Introduction of sideslip skewed the previously described oil-flow patterns, with the windward separation lines having moved downward. The associated shifts in the laminar separation bubble caused the region of turbulent attached flow to shrink on the windward side and to expand on the leeward side." The flow patterns in these pictures are confused by the presence of a nose boom which is responsible for the shedding of an additional pair of vortices. It appeared that, as a result, the forebody primary vortices were displaced to a higher position above the fuselage. Tests on the 16% scale model were made with and without the nose boom; as shown in Fig 6.16(a,b), the boom modified the stability characteristics in detail but did not change their general character.

The quantitative development of the flow on the forebody and LEX of this 16% scale model is illustrated in Figs 6.17(a,b) for two incidences:  $36^\circ$  which is below the incidence for aircraft maximum lift and  $52^\circ$ , well beyond maximum lift. It should be noted that, in these figures (but not in those that appear later),  $\theta = 0^\circ$  corresponds to the top of the fuselage and so, the cross-flow is from  $\theta = 180^\circ$  to respectively,  $0^\circ$  and  $360^\circ$  on the two sides of the fuselage. The LEX pressures are plotted against the local span distance,  $y$ , measured from the LEX-fuselage junction normalised by the local distance,  $b'$ , from the LEX-fuselage junction to the LEX leading edge. Features identified in the flow visualisation tests are marked on the curves and, in general, can be interpreted successfully in terms of the pressure distributions. LSB denotes the initial laminar separation bubble, PS, the primary turbulent separation and SS, the secondary separation below the primary vortex. The forebody vortices strengthen with increasing incidence; the footprints under these vortices can be seen near, for example,  $\theta = 24^\circ$  and  $330^\circ$  at station 3 at  $52^\circ$ . At  $36^\circ$ , the highest suction occurs below the LEX vortices at station 6; further aft, the suction is not so pronounced because, as will be seen later, the vortices have probably burst, or at the very least, have lifted off the surface. At  $52^\circ$ , the LEX vortices burst ahead of station 6 and this accounts for the fact that the suction at station 6 has decreased, relative to those at  $36^\circ$ . The LEX vortices form a stable system, always originating from the LEX (sharp) LE-fuselage junction; as we will see, however, this is not true of the forebody vortices whose position is much more variable and dependent on the local shape of the fuselage and on the Reynolds number, transition position and possibly, other factors. The impression that the forebody vortices are relatively weak at the lower incidences such as  $36^\circ$  does not mean that they are

unimportant; quite apart from their direct effects, they influence the level of suction on the LEX.

Some asymmetries in the flow can be seen, notably at  $52^\circ$  incidence and these presumably contribute to the explanation for the non-zero sideforce at zero sideslip shown in Fig 6.16. It should be noted that the asymmetry in the suction on the LEX changes sign between  $36^\circ$  and  $52^\circ$  and that this is consistent with the change in sign of the side force at zero sideslip (Fig 6.16).

The flow visualisation tests showed that there were major differences between the forebody flows in this test on the 16% scale model in the NASA Langley tunnel and those observed in flight. This can be seen from the pictures reproduced from Ref 269 in Figs 6.18(a,b). The distinction is clearly between a largely B/T flow on the 16% scale model and, in general, a T flow in flight. This is only what might have been predicted from the difference in test Reynolds number: for  $50^\circ$  incidence,  $Re$  based on wing mean chord of  $0.96 \times 10^6$  for the model and  $6.6 \times 10^6$  for flight. It is probably more relevant to quote the values of  $Re_d$  based on the local forebody diameter,  $d$ , at a given station. For station 4, these are  $0.3 \times 10^6$  for the model and  $2.15 \times 10^6$  for flight; these are appropriate values for respectively, B/T and T flows as indicated in §6.1. However, the full picture is not as tidy as this.

Figs 6.19(a), 6.20(a) present comparisons for respectively, the forebody and the LEX between three sets of data: the pressures as measured in the flight tests<sup>270,271</sup>, as measured in tests in the David Taylor Research Center 7 x 10 ft tunnel on a 6% scale model<sup>272</sup> and finally, the results just discussed from the NASA 14 x 22 ft tunnel tests on the 16% scale model; the nose probe is not present for any of these results. The comparison in Fig 6.19(a) is not perfect in the sense that the incidence is  $50^\circ$  in the first two cases and  $52^\circ$  in the third case; however, this should not have a major effect on the comparison. It should also be noted that the scale chosen for  $C_p$  is not the same as in the earlier Fig 6.17; that the definition of  $\theta$  is different: in this and succeeding figures,  $\theta = 0$  is the bottom of the fuselage; that the LEX comparison in Fig 6.20(a) is for  $40^\circ$  incidence not  $50^\circ$  in order to show what happens before the LEX vortices have burst at station 6 and finally, that the Mach numbers for the three cases are different, which is significant for the LEX pressures in Fig 6.20(a) but not for the forebody pressures in Fig 6.19(a). Fig 6.19(b) compares results for the 6% scale model as obtained in respectively, the DTRC tunnel and the NASA Langley tunnel; the differences between these results are discussed in (iii) below. Fig 6.20(b) is included to give an idea of the effects of Mach number on the LEX pressures.

The analysis of the differences in all these results is tortuous and quite possibly, controversial. The interpretation given below reflects the opinion of the present author; in all its detail, it does not completely agree with the opinions expressed in Refs 266 and 272 and the present author not connected with the research is conscious that Ref 272 is a report that has been written jointly by a large number of authors who have been intimately associated with the research.

It seems likely - and plausible - that in all these tests, the type of flow separation on the forebody changes from an L separation close to the nose to a B/T type further aft and then finally to a pure T separation with no preceding laminar bubble. It is the present author's contention that the essential overriding reason for the differences between the different test results lies in where, fore-and-aft, these changes in type of separation take place. To comment in detail on these comparisons:



- (i) as already explained, the flow on the forebody of the 16% scale model in the Langley tunnel is a clear case of being mostly, a B/T separation development, although at station 1 (and stations 2 and 3 at lower incidences such as  $36^\circ$  - see Fig 6.17), only the laminar separation bubble is visible,
- (ii) the flight results are mostly an example of a T separation although even in this case, the pressure distributions<sup>271</sup> at the forward station 3 where  $Re_d$  is relatively low, still reveal the presence of a laminar separation bubble near  $\theta = 112^\circ$ , Fig 6.19(a). However, it is only a very short bubble compared with those observed in the model tests
  - (i). The suction peaks below the primary vortices, ie the vortex footprints, can be seen at, for example,  $\theta \approx 160^\circ$  and  $200^\circ$  at station 4; the peaks at  $90^\circ$  and  $270^\circ$  should be disregarded as they are due to a local separation behind two small ECM antenna covers and also, at station 5, the peaks at  $\theta \approx 48-60^\circ$  and at  $300-312^\circ$  should be ignored since these are due to local separations caused by some pitot-static probes. At station 4, the vortex footprints are less clear at  $\theta = 160^\circ$  than at  $200^\circ$  because there are some doors for the refuelling probes near  $\theta = 160^\circ$  and, as a result, the surface is not as smooth. The peak suctions below the primary vortices are appreciably less than for the B/T flow in (i); also, the vortex footprints are observed to be at a lower position on the fuselage implying, as would be expected, that the T separation in flight occurs sooner in the cross-flow than the final T separation in the B/T flow in the 16% scale model tests,
- (iii) the suction peaks in the vortex footprints in the tunnel tests on the 6% scale model in the DTRC tunnel in Fig 6.19(a) are generally lower by up to 0.2 than those observed in the flight tests (ii). If the results from the NASA Langley tunnel on the 6% scale model (see Fig 6.19(b)) had been selected for the comparison in Fig 6.19(a) rather than the results from DTRC, a stronger forebody vortex footprint would have been seen at station 3 but not at stations 4 or 5. These differences between the results for the 6% scale model in the two tunnels are believed to be due to a difference in transition position - this is a point on which all authors appear to agree. In the tests at DTRC, trips were applied both around the fuselage at 0.40 inches, model scale, aft of the nose and, more significantly, along the full length of the fuselage on the bottom generator. Also, at DTRC, the model was painted matt black. At NASA Langley, on the other hand, there were no trips and the model was painted glossy black. It is therefore likely that transition will occur further forward in the tests at DTRC than in those at Langley. Ref 272 notes that at station 3, there is no laminar separation in the DTRC tests and the primary vortex is induced by a pure turbulent separation; this contrasts with the results for the 16% scale model already discussed where the separation was still of the B/T type even further aft at station 4. The DTRC tests on the 6% model are therefore an example of a T separation produced artificially at relatively low Reynolds number while the NASA Langley results for this model, on the other hand, may well be an example of an L separation, ie a laminar separation that fails to reattach and which therefore induces a vortex far forward as observed at station 3 but which then lifts off the surface,
- (iv) the contrast between the forebody flows is reinforced by the further comparison in Fig 6.21(a); this comparison is for  $40^\circ$  rather than  $50^\circ$  incidence. To reiterate: the flow over the 16% scale model certainly at stations 4 and 5 is in the B/T regime and that over the 6% scale model is in the T regime. In addition to the reasons given earlier, it is possible that the premature transition on the 6% scale model may be partly due to the pressure plotting holes whose effect would be more pronounced on the smaller model. As noted earlier, the difference in test Mach number is not the explanation: the differences in Fig 6.21(a) are much greater than the effects (not shown here but see Ref 272) of increasing Mach number from 0.2 to 0.8,
- (v) so, we have a sequence with progressively decreasing level of peak suctions under the primary vortices just ahead of and opposite the LEX (stations 4 and 5): decreasing from the 16% scale model at NASA Langley to the flight results and then to the 6% scale model at DTRC and finally to the 6% model at NASA Langley. Returning to the opening Figs 6.13(a,b,c) of this paragraph, we have also now established a link between the nature of the forebody flow and the stability characteristics at high incidence: the non-linear stability characteristics at low incidence tend to correlate with the tests producing the stronger primary vortex footprints. It is not simply a question of the flow over the forebody itself: there are the consequential effects on the flow over the LEX. All authors accept that an interaction exists and it is confirmed by Figs 6.20(a), 6.21(b), even allowing for the Mach-number difference whose effect can be estimated with the aid of Fig 6.20(b): high suctions on the forebody imply high suctions on the LEX but it should be remembered that some of the difference in Fig 6.21(b) is due to the difference in test Mach number.

The above discussion has linked the differences in stability at high angle-of-attack to the difference flow regimes on the forebody and their effects on the LEX vortices. It appears that the crucial issues are the location and strength of the forebody and LEX vortices. Various early reports, eg Ref 266, attempted to link the differences in stability to the breakdown of the LEX vortices but the comparisons in Ref 276 show that there is very little scale effect on the forward movement of the position of this breakdown with increasing incidence. This is illustrated in Fig 6.22: there is a slight tendency for the vortex breakdown to be further aft at a given incidence in the tests at low Reynolds number (less than  $10^6$ ) but the agreement between the values from the flow visualisation tests in flight and on the 6% scale model in the DTRC tunnel at  $Re_c = 1.75 \times 10^6$  is remarkable. Fig 6.22 shows good agreement between flight and water tunnel ( $Re_c = 8.3 \times 10^5$ ) in the location, aft of LEX vortex breakdown where the forebody and LEX vortices are found to interact in the flow visualisation pictures. In this interaction, the core of the forebody vortex is pulled under the core of the LEX vortex.

The full-scale aircraft was also tested in the 80 x 120 ft tunnel at NASA Ames. Some results from these tests are presented in Ref 277. The pressures on the forebody are in good agreement with those measured in flight. There are differences in the suction levels on the LEX but, in this case, this is primarily due to the difference in test Mach number (0.15 in the tunnel and 0.26 in flight).

Any attempt to summarise the above evidence on the scale effects on the forebody flows and their consequences is liable to fail on the grounds that a lot of supporting detail should strictly be included. However, making such an attempt, we can conclude

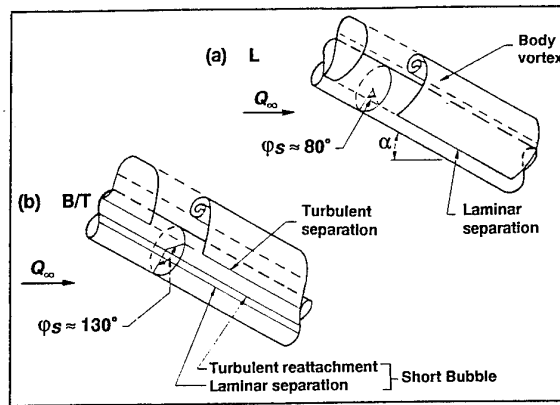
- (i) the scale effects can be substantial and significant for the lateral and directional stability characteristics of the aircraft at high angles-of-attack,
- (ii) there may be more hope in obtaining agreement between tunnel and flight if one aims to fix transition far forward as in the DTRC tests on the 6% scale model. Transition fixing should include trips along the entire length of the fuselage on the bottom generator and a ring around the nose,
- (iii) the most serious discrepancies with flight occur when one allows a B/T separation to develop in the model tests. Unless one knows how to implement (ii) successfully, it follows that there may be an intermediate range of Reynolds number where the scale effects relative to flight are more serious than at lower Reynolds numbers,
- (iv) the changes with Reynolds number appear to be qualitatively in line with the conclusions from experiments on simple circular cylinders but one is left with a distinct impression that quantitatively, the Re-boundaries are different, being higher for the F/A 18 forebody. This is perhaps not too surprising bearing in mind the evidence in Fig 6.12 for simple changes in forebody shape.

Turning to other aspects of the research on the F/A 18, Ref 277 also includes a comparison between the non-dimensional tail buffet frequency as measured in these full-scale tests in the 80 x 120 ft tunnel and results from tests on 11, 12 and 16% scale models<sup>279,280</sup>. This comparison is presented in Fig 6.23; very good agreement is shown between the full-scale data and the 12% and 16%-scale data; the 11% scale data are thought to be affected by tunnel wall interference. These experimental data were derived from pressures measured at the 45% chord, 60% span of the vertical tail while the CFD data point was based on integrated forces and so, is not directly comparable. Buffeting on the vertical tail surfaces has been one of the main issues and a separate 6% scale model has been tested<sup>278</sup> in the NAE 5 ft x 5 ft tunnel to investigate the unsteady pressures on the fins. The same transition fixing technique was practised as at DTRC and it is interesting to note that the overall results from the two sets of tests were in good agreement. Also, the fore-and-aft location of the position for the bursting of the LEX vortex was the same as in low Re water tunnel tests. The main aim of these tests was to show the beneficial effects on the unsteady flow over the vertical tails due to the addition of a fence mounted on the upper surface of the LEX. The addition of the fence introduced a second vortex on the LEX and the interference between these two vortices rotating in the same direction weakened the primary vortex and gave large reductions in the unsteady pressures on the vertical fin.

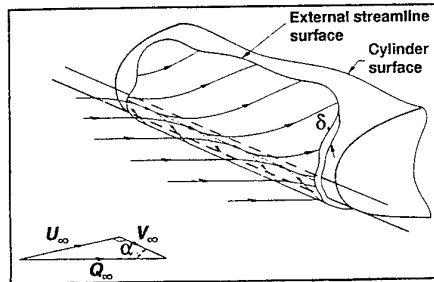
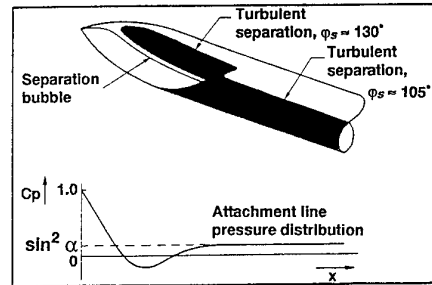
Many studies have been made on unconventional lateral control techniques to restore lateral control at high angles-of-attack when a conventional rudder will have lost its effectiveness. One of the most promising concepts has been to use tangential slot blowing on the forebody. Experiments on this theme began in small scale tests in a water tunnel but results for the full-scale aircraft in the NASA Ames 80 x 120 ft tunnel are presented in

Ref 281. Fig 6.24(a) is a schematic sketch of the blowing slot; the best results were obtained with a 16 in long slot positioned 11 or 19 ins aft of the radome apex. In the tests, the active blowing slot was located at  $\theta = 270^\circ$  and typical results are shown in Fig 6.24(b): it will be seen that at high incidence, the blowing produces far more lateral control than that obtained from the maximum rudder deflection. The tests included two indications that the effects of the pneumatic control were unlikely to be subject to scale effect: first, in Fig 6.24(c), results are presented for a range of tunnel speeds from 68 to 168 ft/sec and only small changes result from this appreciable change of Reynolds number and second, tests were made with and without serrated tape trips which were applied to the radome at  $45^\circ$  and  $315^\circ$  in an effort to fix transition and simulate flow at higher Reynolds numbers but these produced no significant change in the yawing moments due to blowing.

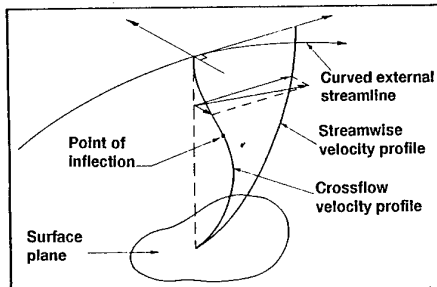
In passing, one further figure, Fig 6.24(d), is included to show how the blowing achieves its effect. At station 3, in the no-blowing case, the primary vortices are visible at  $\theta = 165^\circ$  and  $195^\circ$  but, in the blowing case, these are absent and instead, the pressure is reduced on the blowing-side of the radome. Similar changes are evident at stations 4 and 5 with the highest suction now below the primary vortex on the blowing-side; hence, blowing from the left-side of the radome produces a nose-left yawing moment. Ref 282 shows that NASA Ames have used a thin-layer Navier-Stokes flow solver to calculate the flow around the complete aircraft including the effects of sideslip and slot blowing and there is general agreement with experiment in the effects of blowing on vortex bursting.



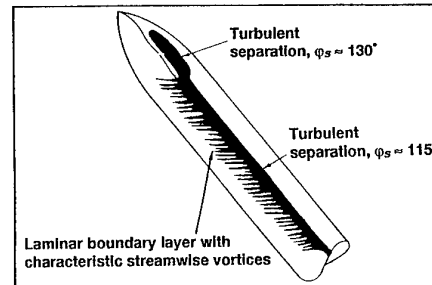
(a) Two types of separation involving laminar bubble

(b) Flow near the windward generator ( $\phi = 0$ ) on an inclined cylinder

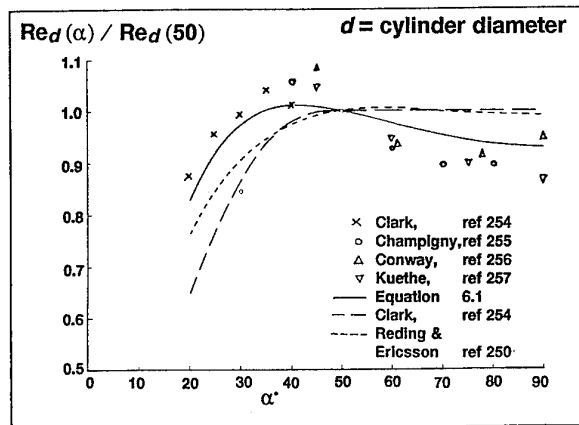
(c) Flow with attachment-line contamination



(d) Typical velocity distribution for a 3-D boundary layer flow



(e) Flow with cross-flow instability

FIG 6.1 Types of Flow Transition and Separation in Inclined Cylinder  
(from ref 252)FIG 6.2 Variation of  $Re_d$  with  $\alpha$  for Bursting of Laminar Separation Bubble on Long Inclined Cylinder  
(from ref 252)

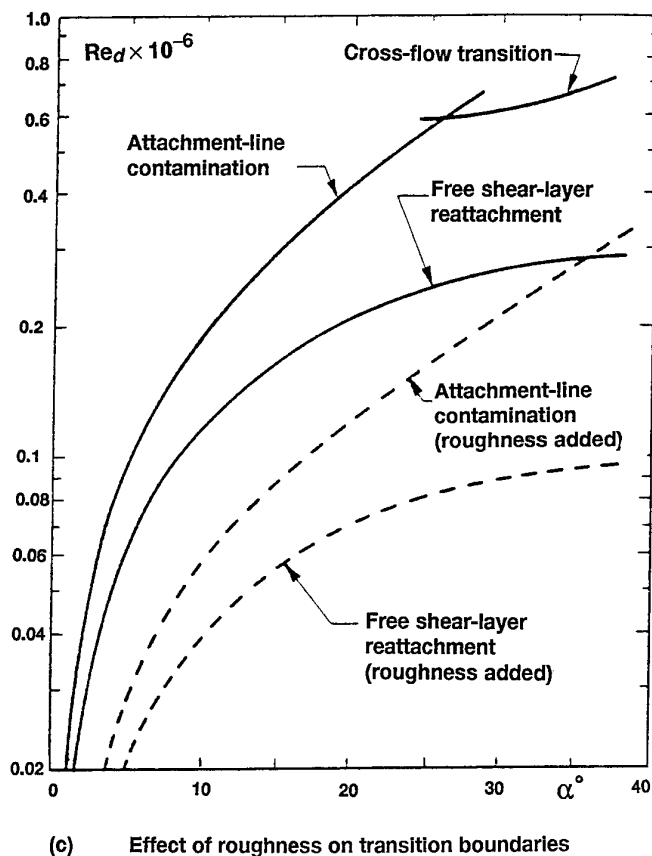
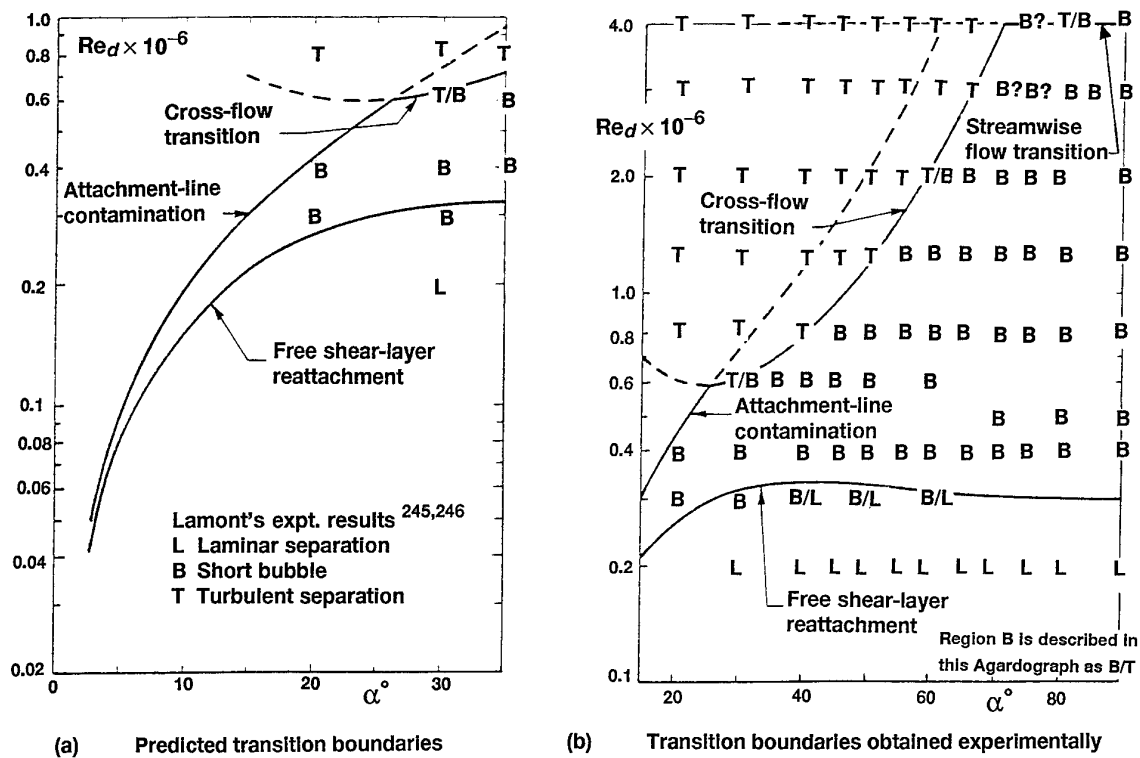


FIG 6.3 Comparison of Predicted and Measured Transition Boundaries  
(from ref 252)

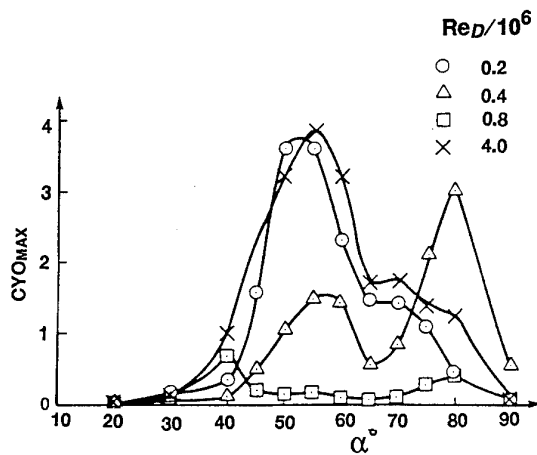


FIG 6.4(a) Variation of Maximum Overall Side Force with  $\alpha$   
(from ref 245)

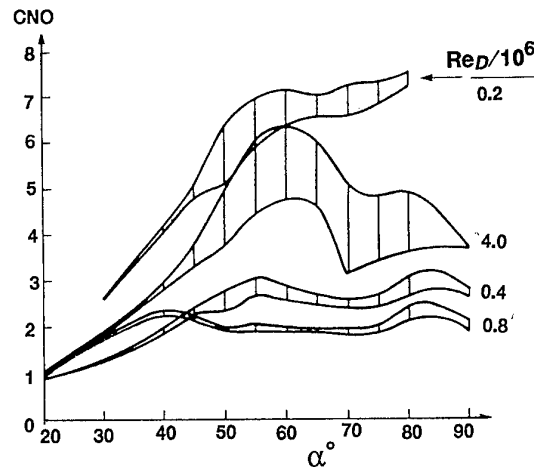
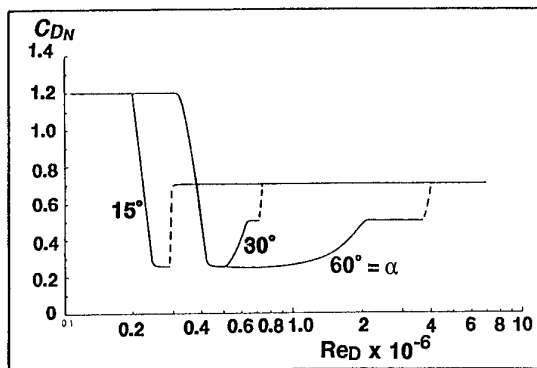
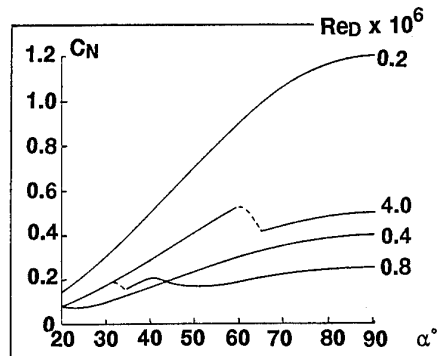


FIG 6.4(b) Variation of Normal Force with  $\alpha$   
(from ref 245)

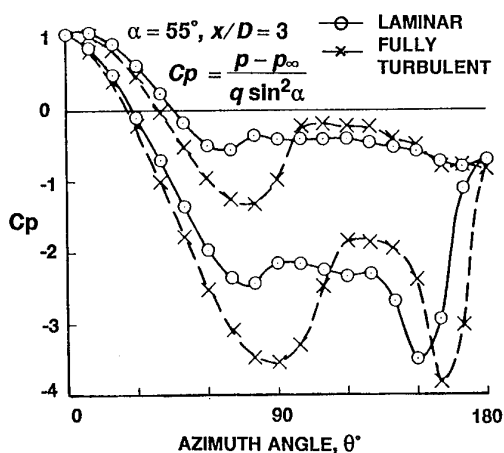


$$C_{DN} = \frac{(\text{total normal force} - \text{inviscid normal force})}{\frac{1}{2} \rho U_{\infty}^2 \times (\text{plan area}) \times \eta}$$

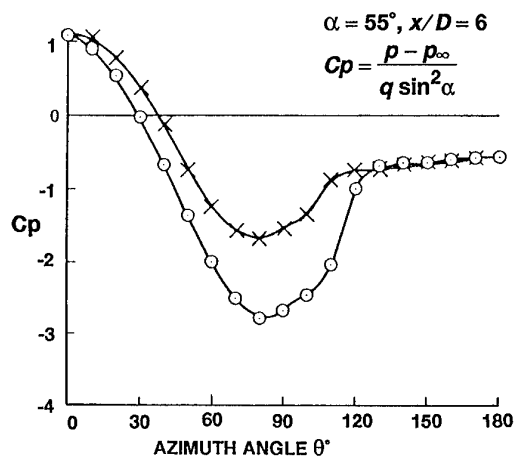
FIG 6.5(a) Predicted Variation of Cross-Flow Drag  
(from ref 252)



Predicted Variation of Normal Force with Incidence  
FIG 6.5(b) Idealised Predictions for Long Cylinder in a Flow with Constant Free-stream Reynolds Number  
(from ref 252)

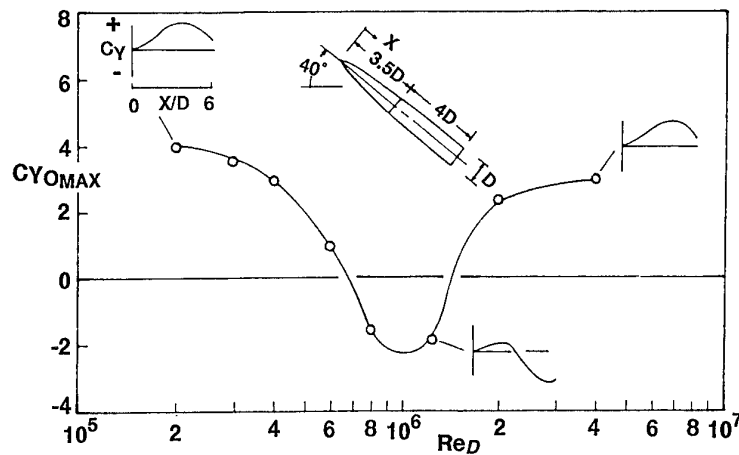


(a) L and T Flow

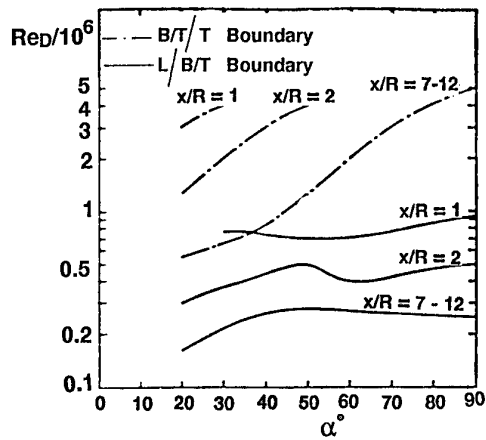


(b) B/T Flow

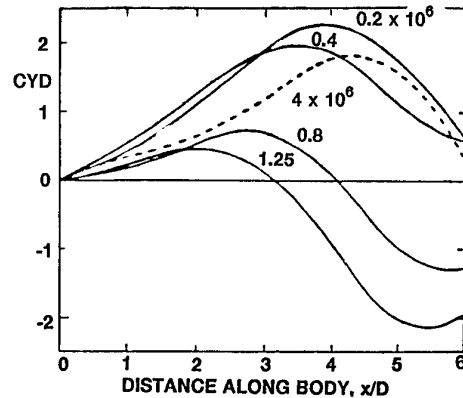
Two curves in each case: P.D.'s on two sides of cylinder  
FIG 6.6 Typical Asymmetric Pressure Distributions  
(from ref 245)



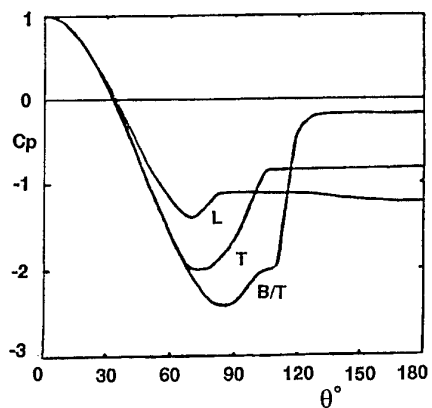
(a) Variation of local and integrated maximum out-of-plane force coefficient for an ogive-cylinder



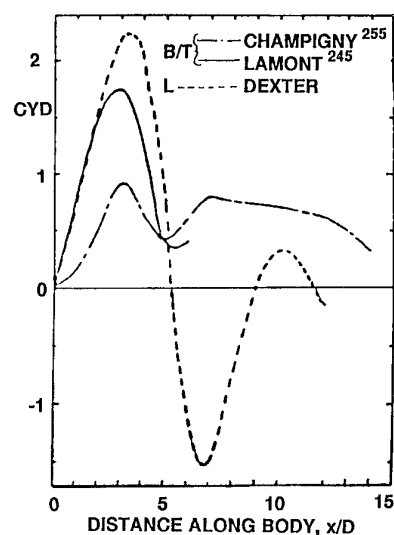
(b) Critical Re boundaries on ogive nose



(c) Side force distributions at  $\alpha = 40^\circ$



(d) 2-D cylinder pressure distributions



(e) Side force distributions on long models

FIG 6.7 Figures to Assist in the Interpretation of Re-effects on flow over Ogive-Cylinder at high  $\alpha$  (see § 6.2)  
(from refs 247, 259)

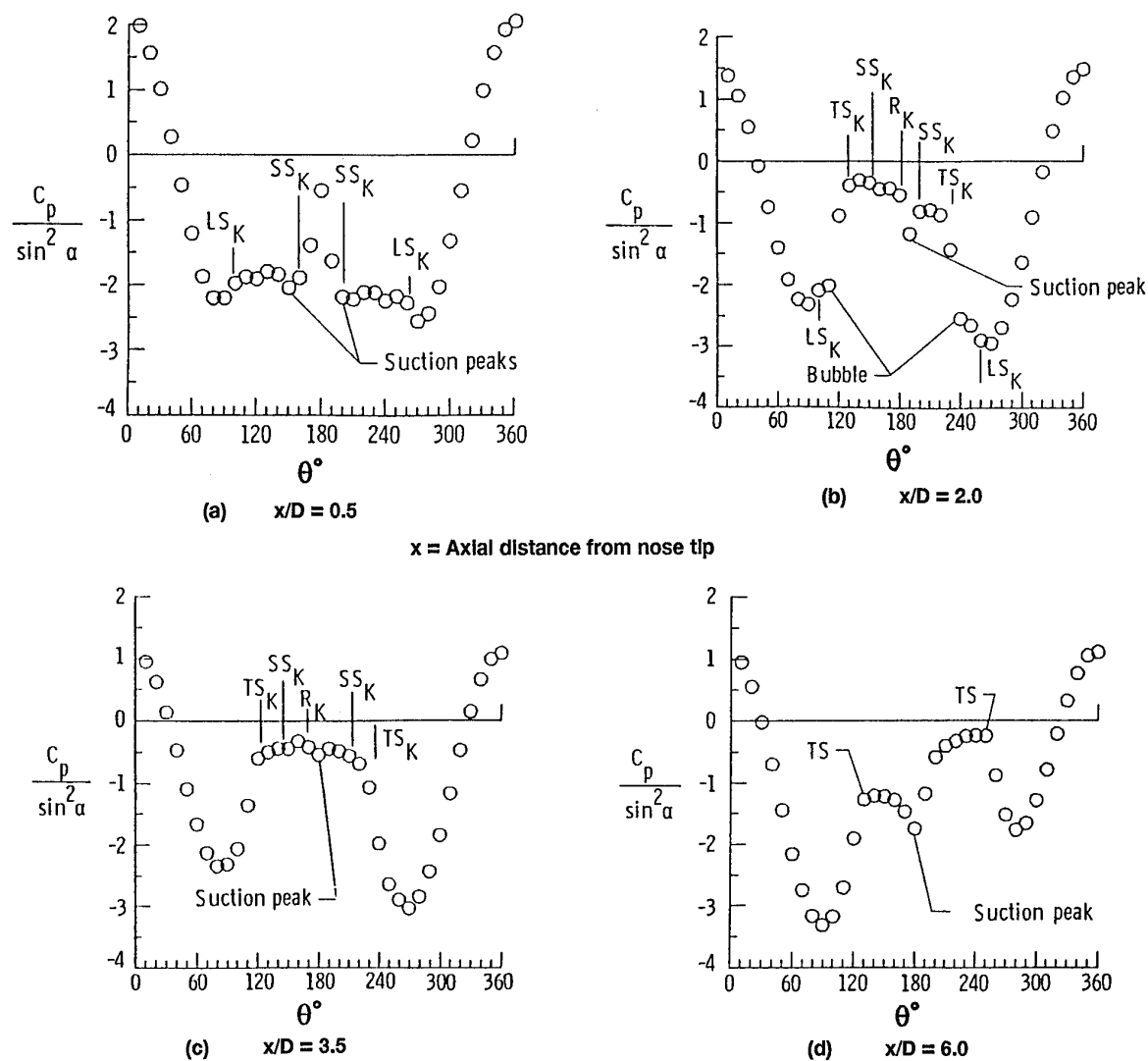


FIG 6.8 (a,b,c,d) Pressures on Inclined 3.5D Ogive - Circular Cylinder  
(from ref 261)

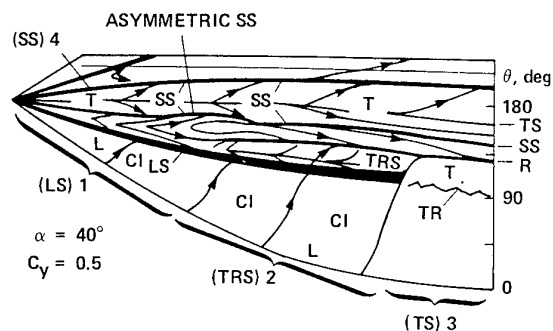


FIG 6.8 (e) Typical Vortex Flow on Inclined Cylinder Nose  
(from ref 262)

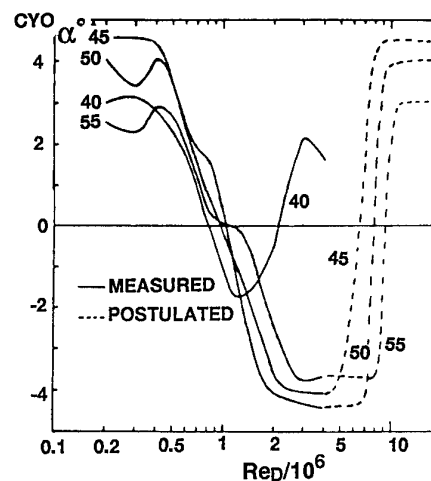
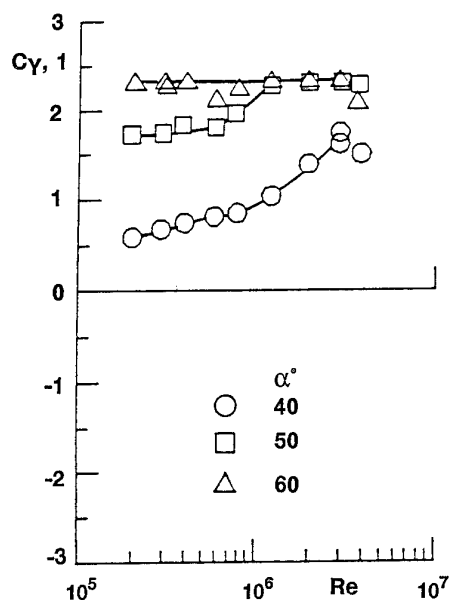
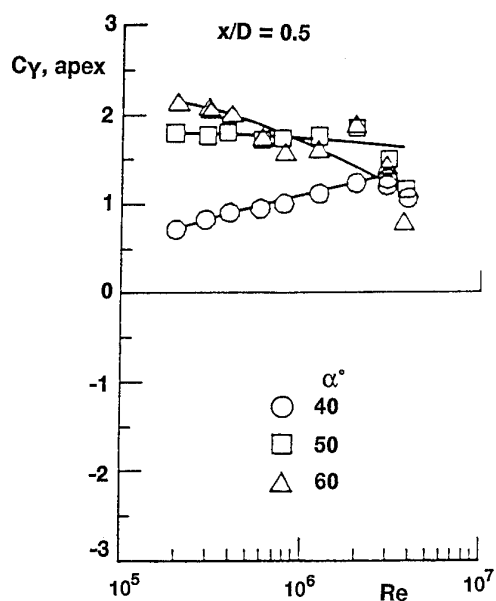


FIG 6.8 (f) Possible Variation of Side Force on Inclined Cylinder at High Re  
(from ref 259)



(a) Sectional side force coefficient at first pressure-plotting station



(b) Extrapolated sectional side force coefficient at apex

FIG 6.9 Effect of  $Re$  on Pressures Near Nose of Ogive-Cylinder at High Incidence (from ref 261)

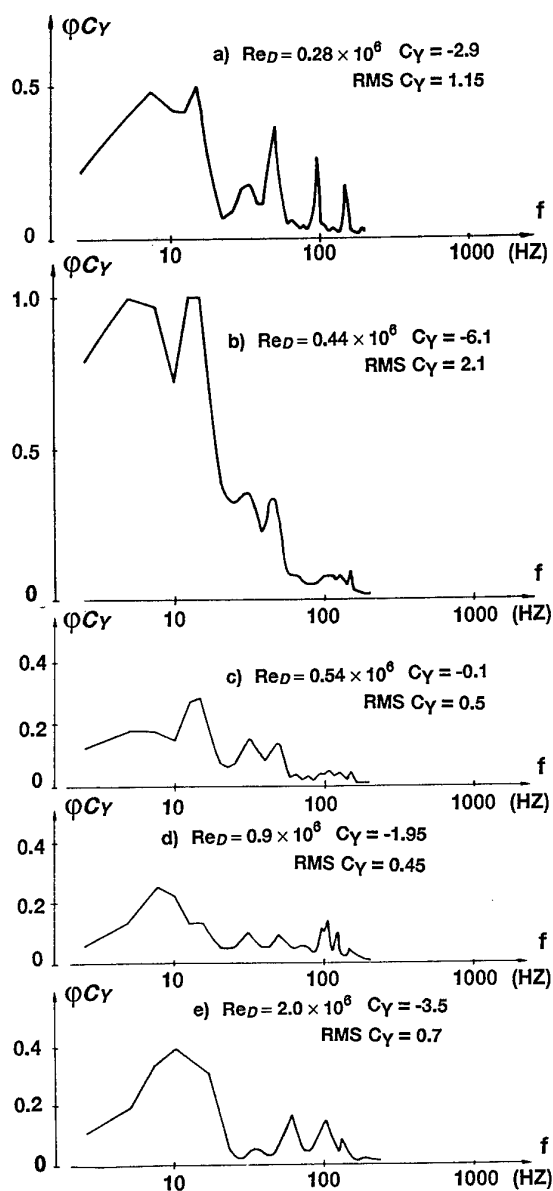


FIG 6.10 Effect of  $Re$  on Power Spectral Density of Unsteady Side Force Coefficient (Tests on Ogive-Cylinder in F1 Tunnel) (from ref 264)



$C_Y$  Based on area of circle of diameter  
equal to the ellipse plan form width at cylinder base

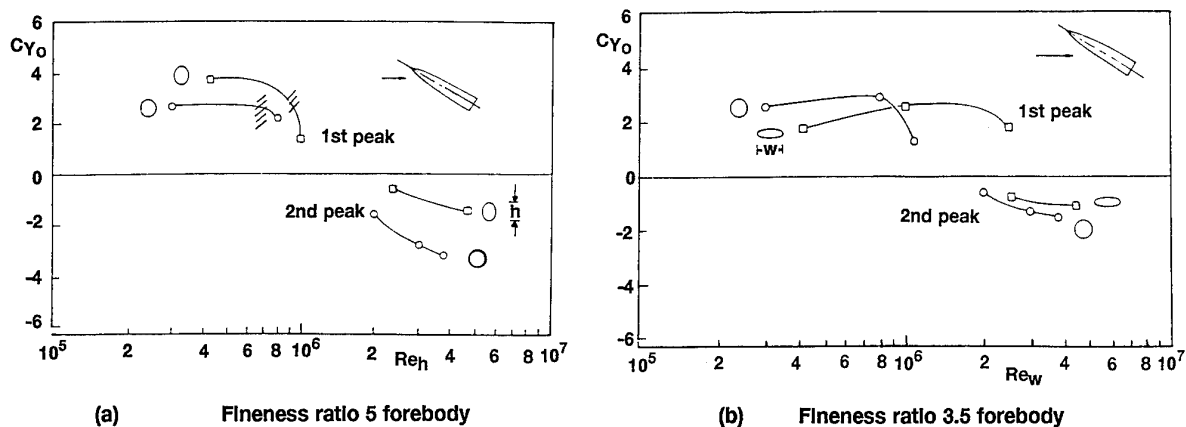


FIG 6.11 Effect of Cross Section on Maximum Side Force at Zero Yaw  
(from ref 265)

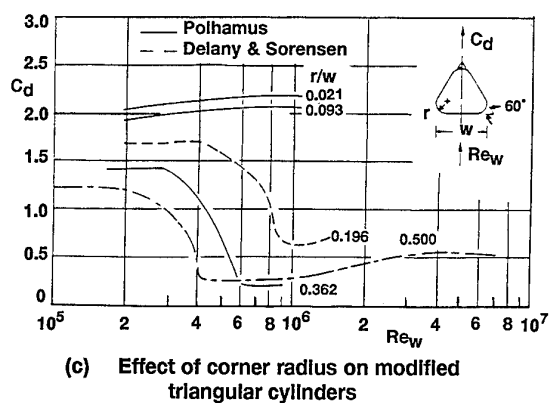
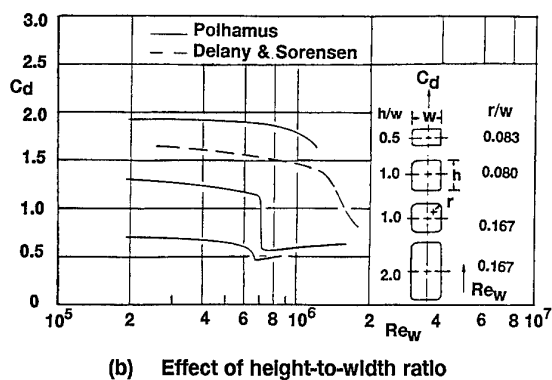
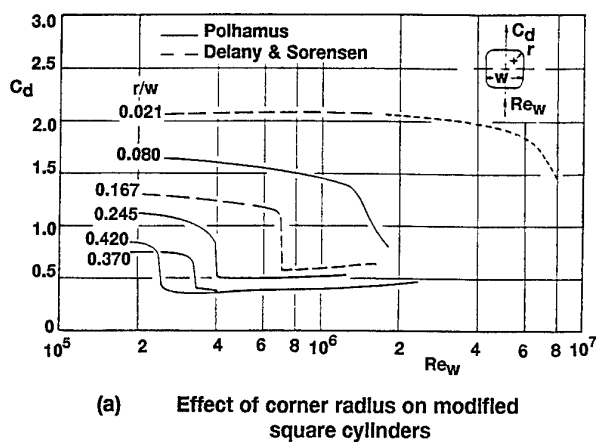


FIG 6.12 Influence of Cross-Sectional Shape on  
Re-effects on 2D Cylinder Drag Coefficient,  $C_d$   
(from ref 249)

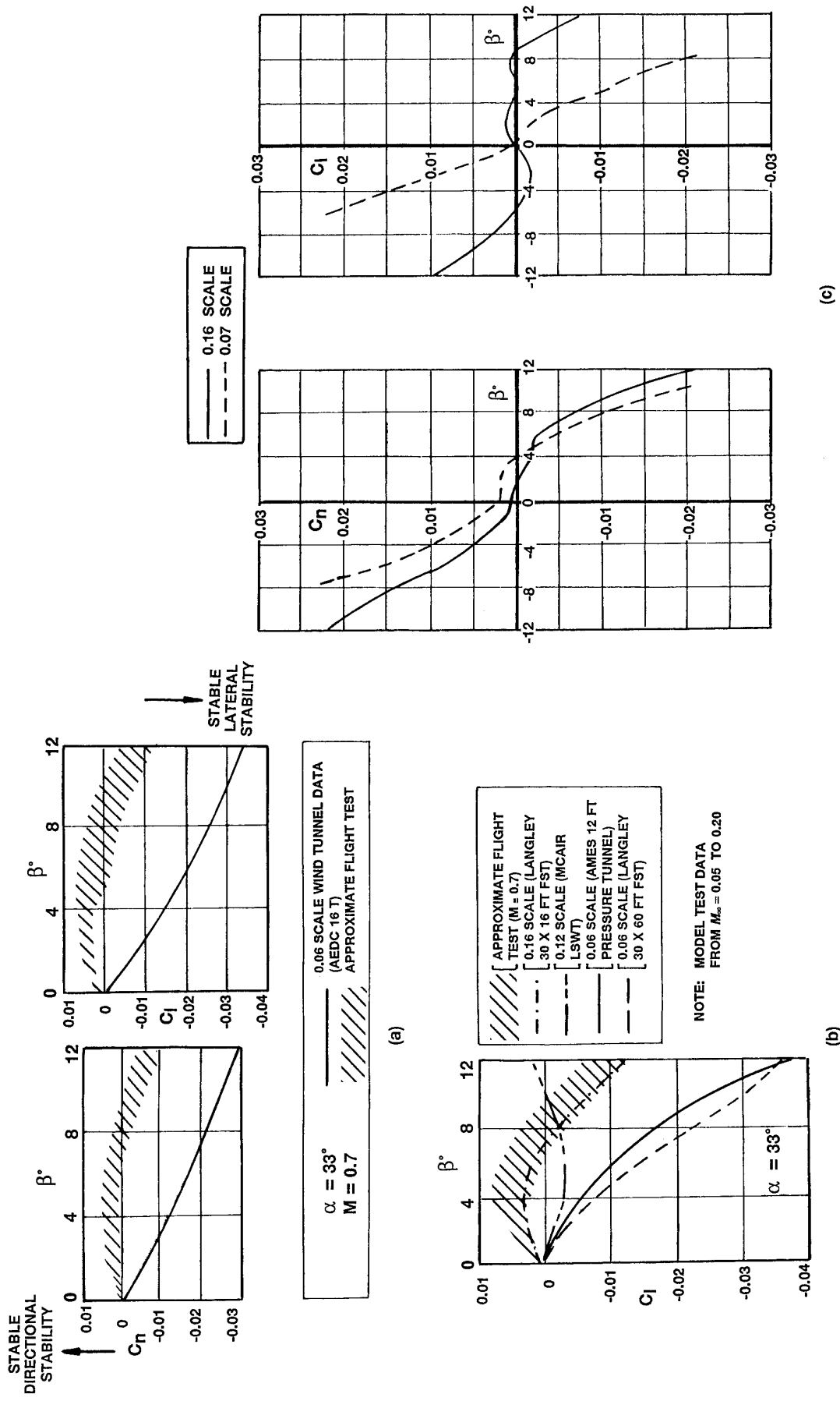
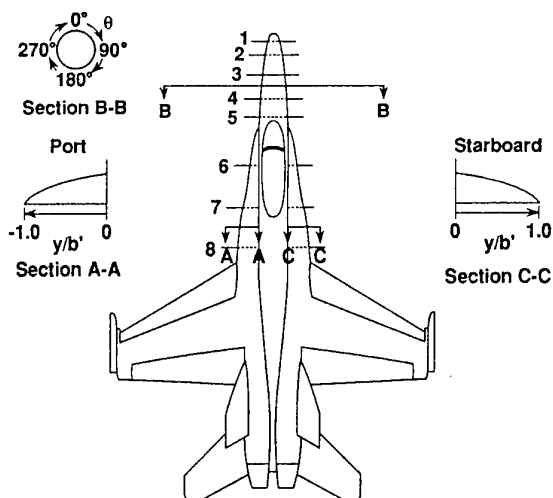
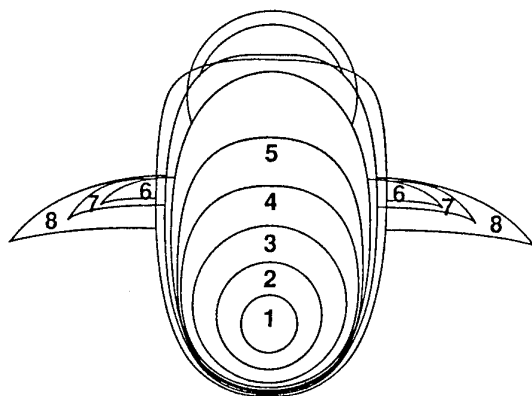


FIG 6.13 Lateral - Directional Stability Data Comparisons  
From Early Review of F-18 Test Data  
(from ref 266)

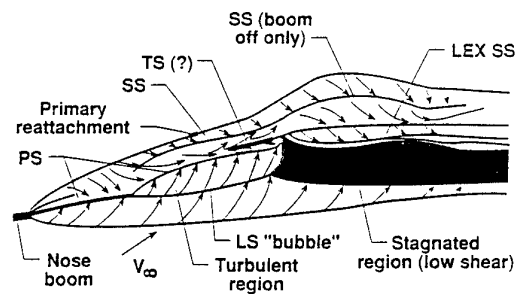


(a) Pressure port station locations and orientation

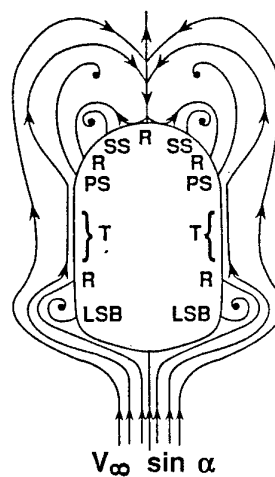


(b) Station cross-sectional shapes

FIG 6.14 F-18 HARV Geometry  
16% Scale Model  
(from ref. 269)

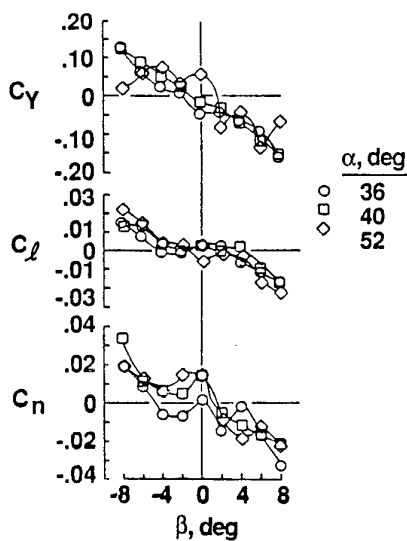


(a) Side view

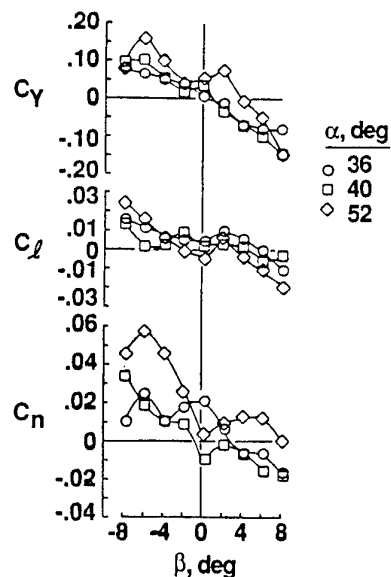


(b) Cross-section at station 4

FIG 6.15 Typical Flow Pattern on  
16% Scale Model  
(from ref. 269)

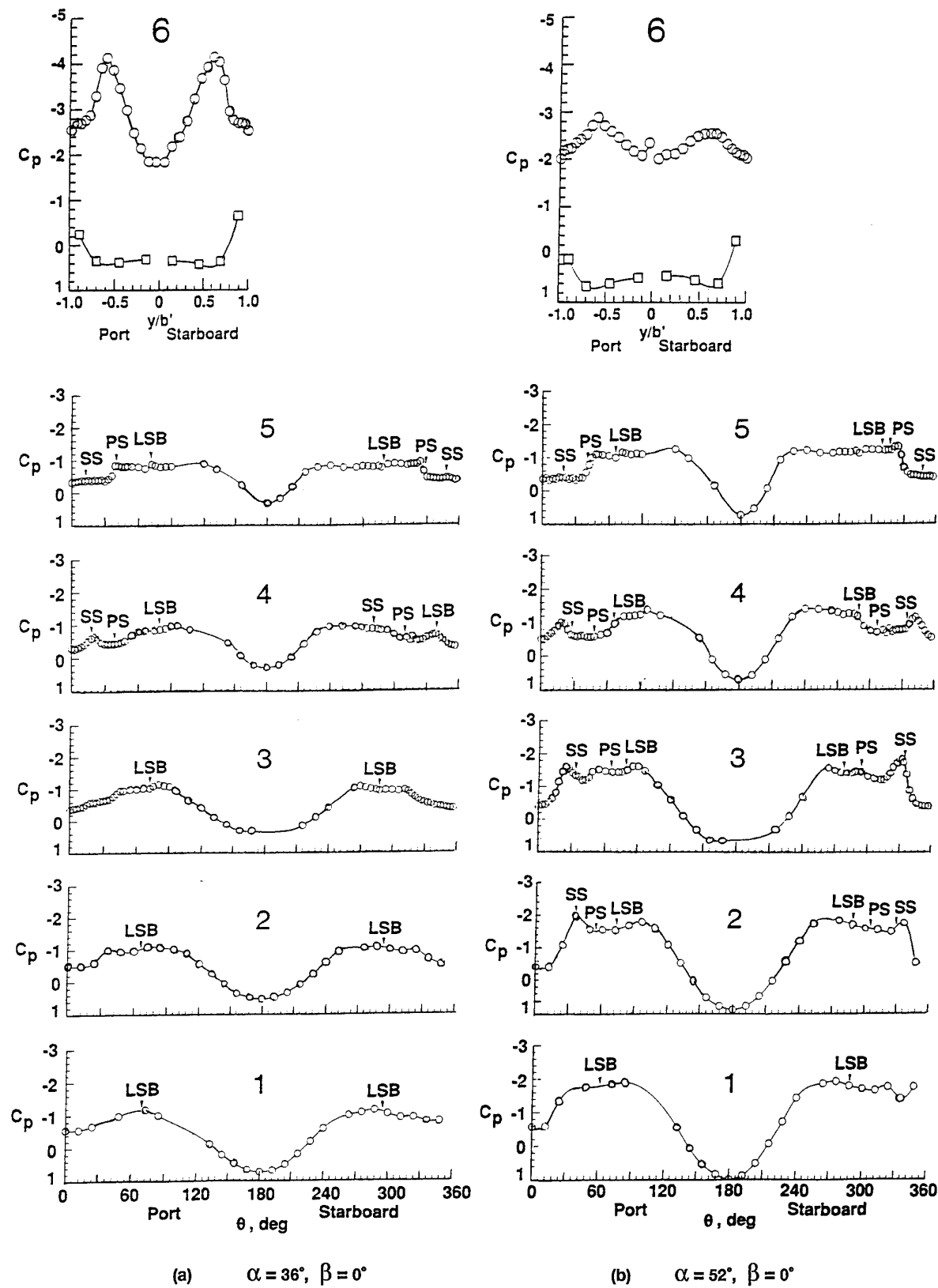


(a) Nose boom off



(b) Nose boom on

Fig 6.16 Lateral - Directional Stability Characteristics  
16% Scale Model  
(from ref 269)



Nose Boom Off

FIG 6.17 Forebody & LEX Pressure Distributions on 16% Scale Model  
(from ref. 269)

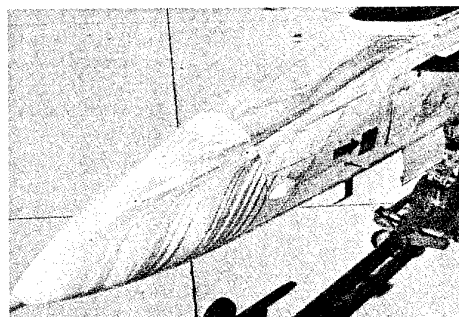
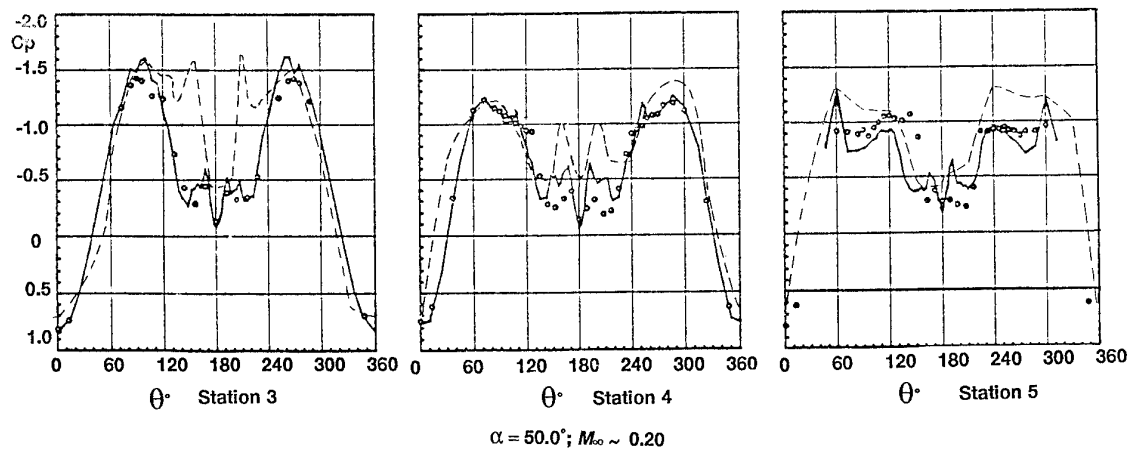
(a) Flight Test,  $\alpha = 34^\circ$ (b) 16% Model Test,  $\alpha = 36^\circ$ 

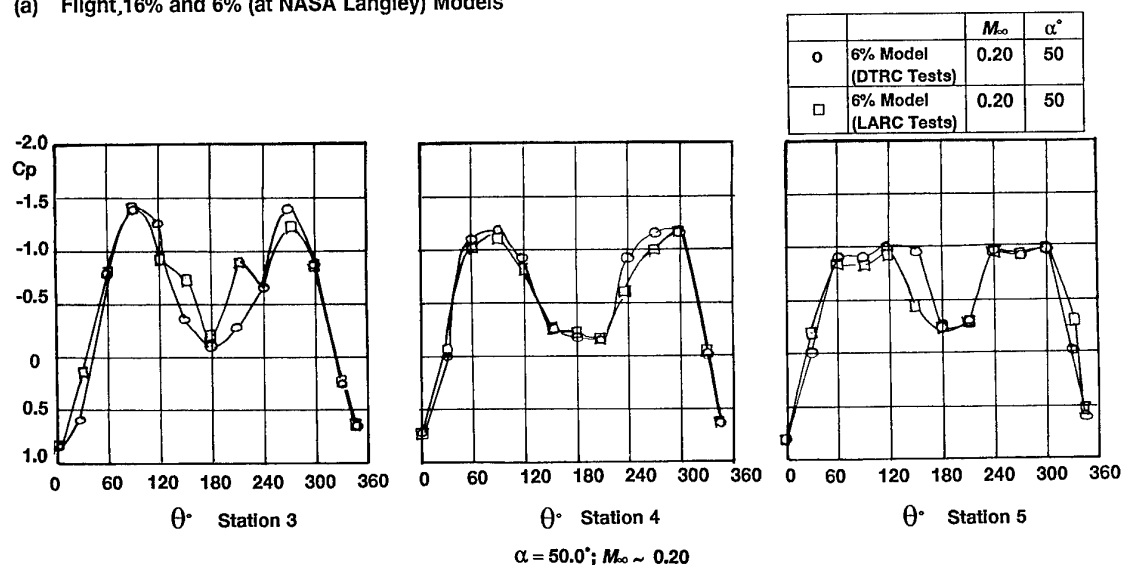
FIG 6.18 Forebody Flow Visualization  
(from ref 269)

Values of $Re_d \times 10^6$				$M_\infty$	$\alpha^\circ$	$\beta^\circ$	$Re_{\bar{c}} \times 10^6$
	Station 3	Station 4	Station 5				
6% Model	0.25	0.31	0.39				
Flight	1.72	2.15	2.70				

		$M_\infty$	$\alpha^\circ$	$\beta^\circ$	$Re_{\bar{c}} \times 10^6$
o	6% Model (DTRC Tests)	0.20	50	0	0.96
—	Flight	0.23	50	0	6.6
- - -	16% Model (NASA Langley Tests)	—	52	0	—



(a) Flight, 16% and 6% (at NASA Langley) Models



(b) 6% Model at DTRC and NASA Langley

FIG 6.19 (a,b) Comparison of Forebody Pressure Distributions  
(from refs 269, 270, 272)

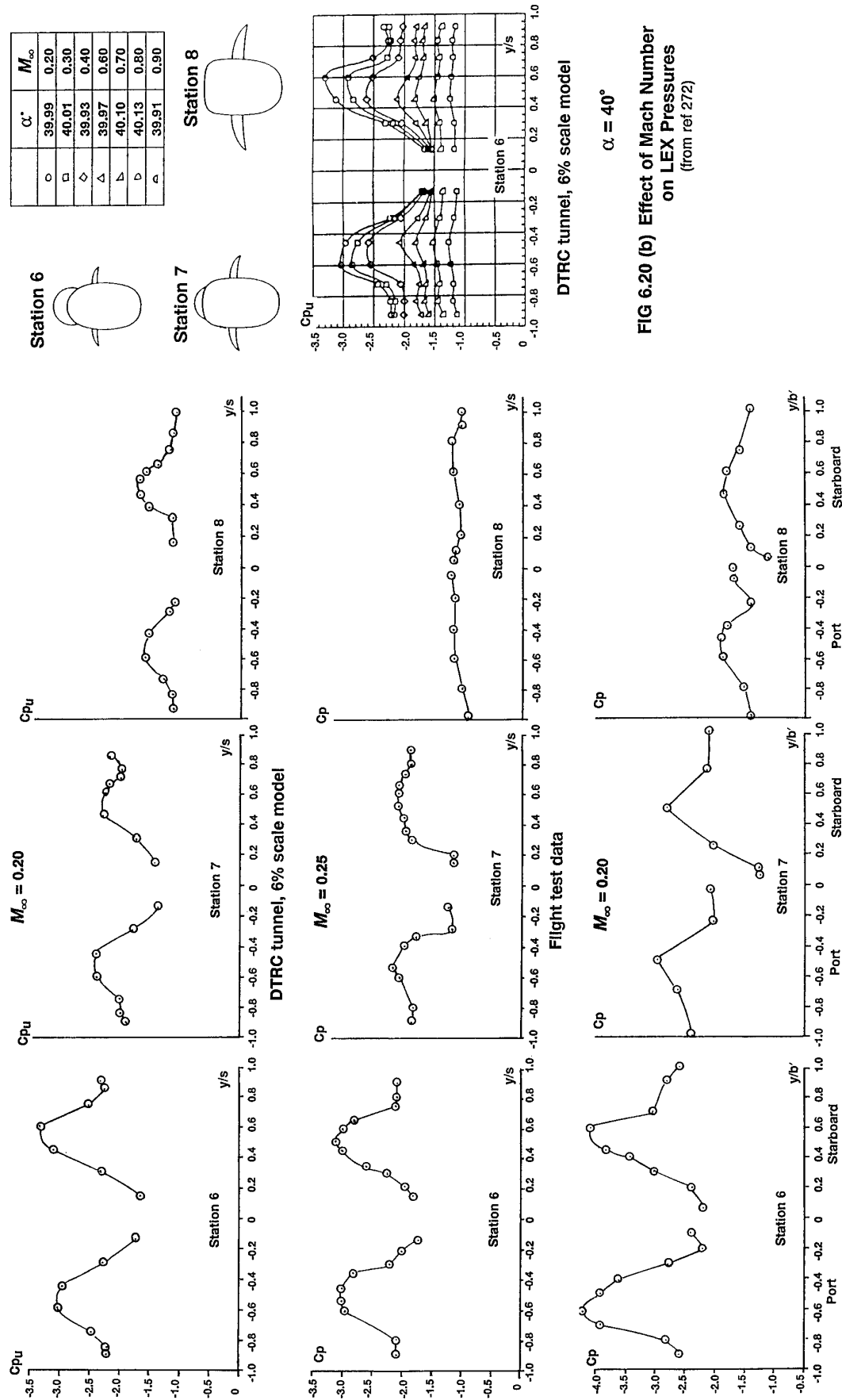
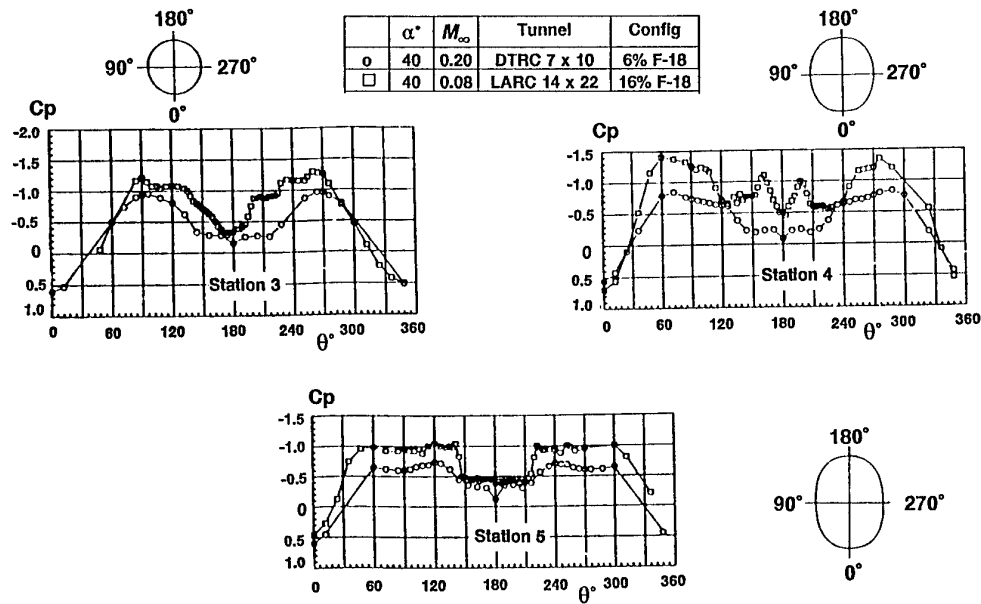


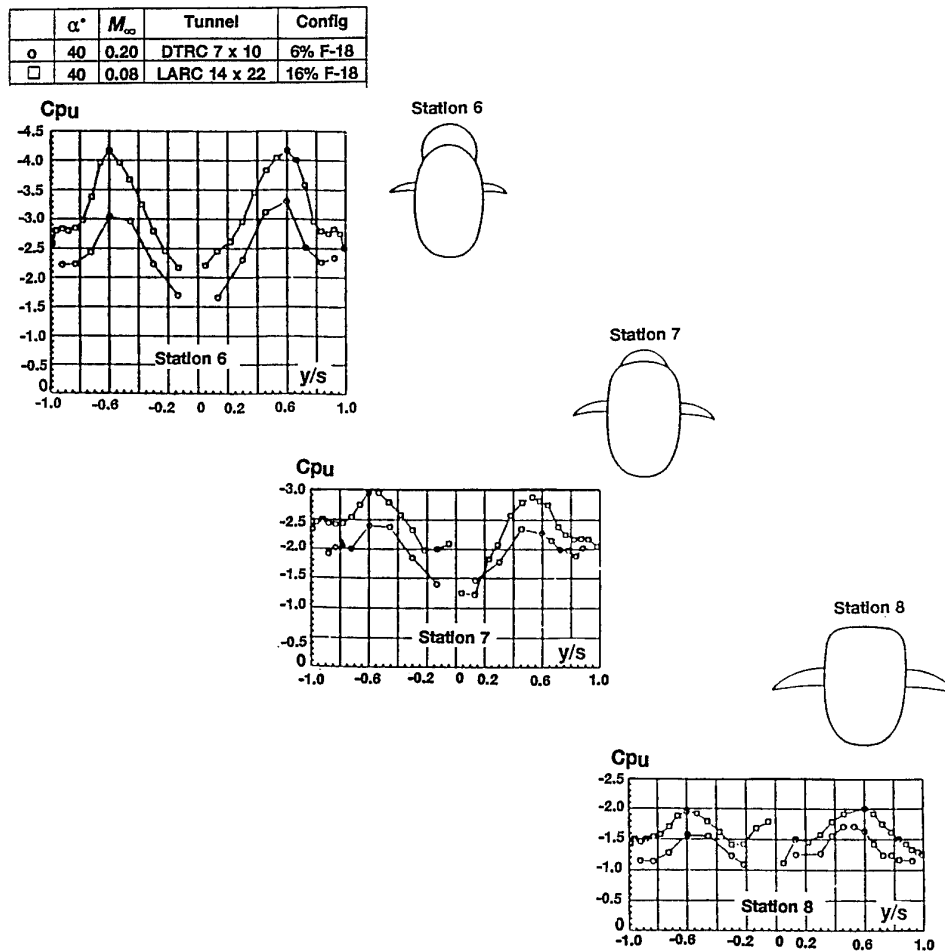
FIG 6.20 (a) Comparison of Pressures on LEX from different tests  
(from refs 270, 271, 272)

NASA Langley 14 x 22 ft tunnel, 16% scale model

$\alpha = 40^\circ$



(a) Forebody



(b) LEX

FIG 6.21 (a,b) Further Comparison of Pressure Data  
on 6% & 16% Scale Models  
(from ref. 272)

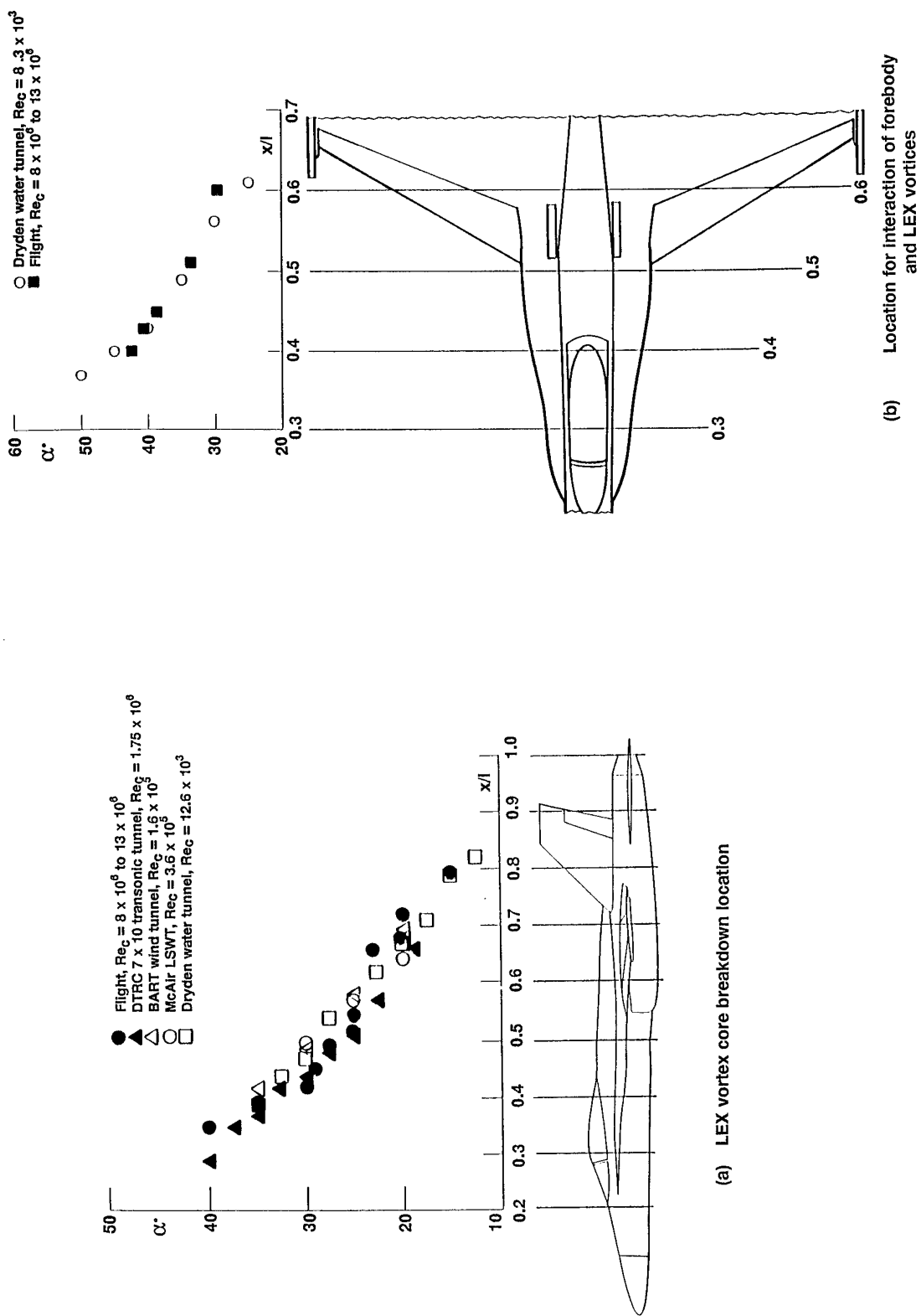


FIG 6.22 (a,b) Effect of Incidence on Vortex Flow Phenomena, F-18,

$$\beta = 0^\circ$$

(from ref 276)



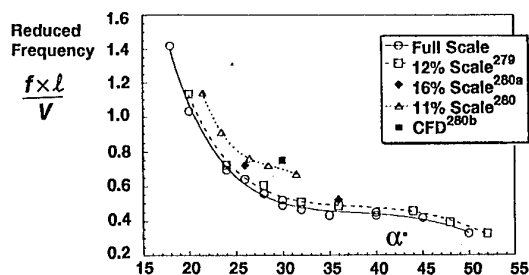
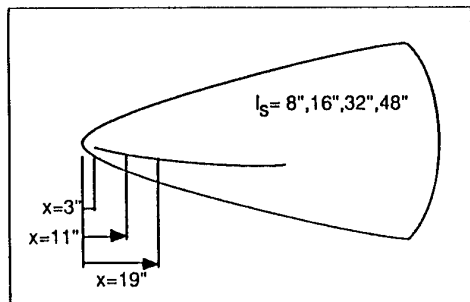
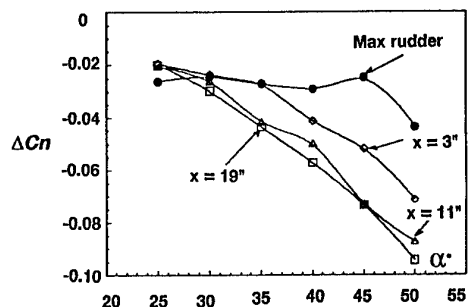


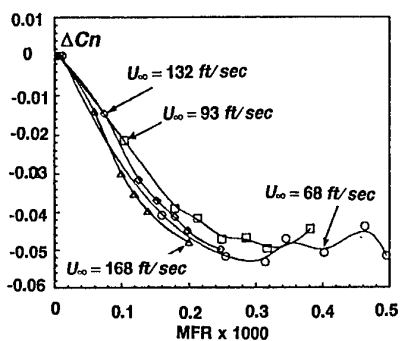
FIG 6.23 Effect of Model Scale on Variation of Buffet Frequency with Alpha  
(from ref 277)



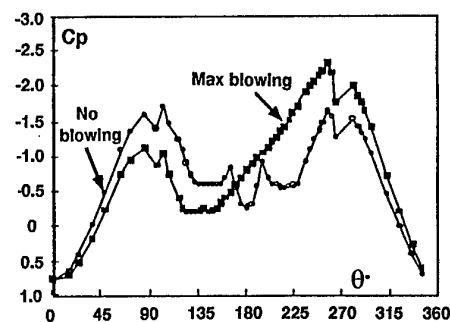
(a) Slot positions



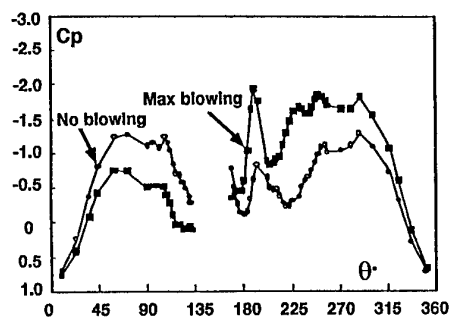
(b) Slot blowing vs rudder for directional control. MFR =  $0.26 \times 10^{-3}$



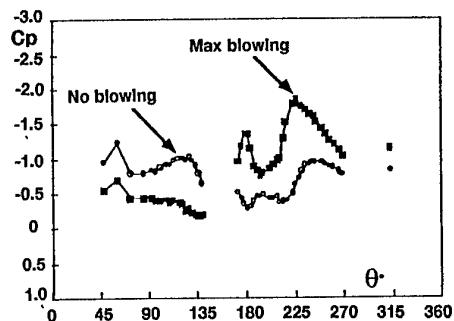
(c) Effect of blowing rate  
 $\alpha = 40^\circ$ ,  $\beta = 0^\circ$



(d) Station 3



Station 4



Station 5

(d) Effect of blowing on vortex flow,  $\alpha = 50^\circ$ ,  $\beta = 0^\circ$

FIG 6.24 Effect of Forebody Flow Control: F/A - 18  
(from ref. 281)

## 7 SCALE EFFECTS IN OTHER IMPORTANT AREAS

### 7.1 Internal Store Carriage

It was noted in §2.1.1 that tunnel tests on external stores provided many examples of where scale effects could be present because of an inability to reproduce at a small scale, all the detailed features of the full-scale geometry. If differences in store loads or release trajectories are observed in test comparisons, the natural first step is to question the model geometric fidelity or the test technique. It is only on rare occasions that Reynolds number has been thought to be responsible. In recent years, attention has shifted to the problems posed by internal carriage of the stores. Internal carriage has obvious advantages in terms of improved aircraft performance and the present emphasis on stealth technology but it introduces its own problems which cannot be dismissed as a simple extrapolation of experience with external store carriage. When the cavity doors are opened in flight, the store can be subjected to severe pressure oscillations and the stores on release have to pass through the shear layer lying across the entry to the cavity. Methods are needed to predict both the steady and unsteady flow. This challenge is currently being met in three ways: first, by developing new experimental techniques<sup>283</sup>; second, by devising<sup>284,285</sup> an engineering model prediction method based on fundamental fluid dynamic principles and mixing-zone theory which does not need advanced computer hardware and finally, by developing<sup>286,287</sup> Navier-Stokes codes that can be used to provide analytical predictions. This has been a relatively new field of activity and an obvious matter for concern has been whether the results from these prediction methods are likely to be subject to scale effect. There are several reasons why scale effects may exist: the unsteady pressure spectrum depends on the actual size of the cavity and hence it changes between model and full-scale; the shear layer across the cavity will depend on the thickness of the boundary layer on the aircraft surface ahead of the cavity and more generally, Reynolds number effects can be expected in the complex cavity flows which are likely to be dominated by viscous effects. The emphasis to date has been on developing the prediction methods; further experience in their use is needed before drawing definitive conclusions about possible scale effects but useful indications can already be found in the published literature and these are summarised below.

It has been established<sup>288,289</sup> that one can distinguish between three types of cavity flow depending on the geometry of the cavity:

- (i) "closed" or shallow cavities with, typically,  $L/D > 13$  where  $L$  = cavity length and  $D$  = cavity depth. Here, the flow expands into the cavity and attaches to the floor before separating ahead of the downstream wall of the cavity. High pressures are observed on the downstream wall,
- (ii) "transitional",  $9 < L/D < 13$  cavities, where the flow may or may not expand into the cavity depending on the Mach number, and
- (iii) "open" or deep cavities,  $L/D < 9$ , where the flow does not expand into the cavity but develops into an undulating shear layer which, at the rear, moves in and out of the cavity during a pressure cycle.

Figs 7.1(a,b) present sketches, taken from Ref 285, of the flow in the closed and open cavities. The flow in the closed cavity is relatively benign but with the open, deep cavity, large

pressure fluctuations are observed at the rear of the cavity. As the shear layer enters the cavity in its time-dependent movement, a pressure pulse reflects from the downstream wall as an acoustic wave and when this arrives at the upstream wall, vortices are shed at a frequency that has been predictable by an equation derived by Rossiter<sup>290</sup> 30 years ago. Now, Dix and Bauer<sup>284,285</sup> have provided, for the first time, a simple method for a prediction of the full pressure spectrum in both amplitude and frequency. Figs 7.2(a,b) show two comparisons of prediction and experiment for a cavity with  $L/D = 4.5$  at  $M = 0.6$  and  $M = 0.95$ . The experimental data were recorded by a Kulite pressure transducer installed on the centre of the downstream wall at a vertical position 18% of the cavity depth below the cavity opening. At higher Mach numbers, the agreement between prediction and experiment is not as good for reasons explained in Refs 284, 285. The peaks in the spectra occur as noted by Rossiter at the predicted edgetone frequencies.

The edgetone frequencies depend on several variables including the ratio of the mean velocity of the vortices springing from the leading edge of the cavity divided by the free stream velocity. The effects of the approaching boundary layer are taken into account by assuming that the vortices move at the velocity on the dividing streamline, defined as being the streamline above which all mass flow comes from the approaching flow and boundary layer. This ratio depends on a turbulent mixing position parameter and a semi-empirical relation is used to represent the effect of the boundary layer on this parameter. Dix and Bauer admit that this relation is not rigorous and could be improved if experience shows this to be necessary. To show the influence of the thickness of the initial boundary layer at the upstream edge of the cavity on the final results, one comparison is included in Refs 284, 285 of the predicted variation of the Overall Sound Pressure Level (OASPL) against Mach number, calculated by assuming either zero boundary layer thickness or alternatively, the boundary layer thickness measured in the tests. This comparison is shown in Fig 7.3; it is sufficient to indicate that the pressure spectrum does depend significantly on the boundary layer thickness but it is intriguing that, at transonic speeds where the predictions were thought for other reasons to be at their most reliable, the experimental values agree better with the predictions based on the mistaken assumption that  $\delta = 0$ . Strictly, the boundary layer thickness was only measured at  $M = 2.5, 3.5$  and  $5$  and this could be part of the explanation but probably, the comparison points to the need for further refinement of the prediction method.

NASA Langley<sup>291</sup> have measured the acoustic field of one particular cavity model over a very wide range of Reynolds number in their 0.3-metre cryogenic tunnel. The cavity depth was varied to obtain  $L/D$  values of 4.4, 6.7, 12.67 and 20 and so, all types of flow have been investigated. The Reynolds number was varied from  $3.75 \times 10^6$  to  $93.75 \times 10^6$  based on cavity length and tests were made with two angles of yaw,  $0^\circ$  and  $15^\circ$ . Results are presented in Ref 291 for three Mach numbers,  $M = 0.6, 0.8$  and  $0.9$  and all show that Reynolds number has no significant effect on the acoustic spectrum at zero yaw; the results for  $M = 0.9$  are reproduced here as Fig 7.4(a-d). In passing, it will be noted that this sequence of pictures provides a clear illustration of the change from a spectrum with high peaks at discrete tones for a deep cavity to a much lower signature with no tones for a shallow cavity (the peaks evident for  $L/D = 20$  coincide with the fan blade passing frequency and are therefore irrelevant). An important point must, however, be made about these results: the thickness of the boundary layer ahead of the cavity was held approximately constant as the Reynolds number was changed. This would not

be true in practice if one was comparing results at low Reynolds number on a model and at high Reynolds number on a full-scale aircraft. NASA Langley in their tests were trying to isolate the effects of Re and the approach boundary layer thickness but, on the assumption that this thickness does have an effect (as suggested by the comparison discussed above), one should not conclude that there are no Reynolds number effects in going from model to full-scale. Even the results as presented in Ref 291 indicate that Reynolds number has an effect on the effect of yaw on the cavity acoustics. This is illustrated in Fig 7.5; it will be seen that the reduction with yaw in the second mode pressure peak is greater in the high Reynolds number case.

Further experimental evidence on the effects of Reynolds number for a cavity with  $L/D = 4.5$  is presented in Fig 7.6(a,b). This test covered a much smaller range of Reynolds number and as plotted in Fig 7.6(a) appears to show a Re-effect. However, in this case, the variation of Reynolds number was obtained by changing the tunnel total pressure and so when, appropriately, the SPL values are normalised by the tunnel dynamic pressure, as in Fig 7.6(b), it is found that this almost removes the apparent Re-effect, thus bringing the results into line with the evidence in Fig 7.4.

As explained, however, at the outset, the absence of Re-effects, even if true, does not necessarily mean that there are no scale effects. A systematic study of the effects of cavity scale was made<sup>292</sup> at WADC and Fig 7.7 taken from this work shows that, as the scale is reduced, ie the model becomes smaller relative to full-scale, the trend is for the acoustic pressure level divided by the dynamic pressure to decrease - by up to 0.1. Two of the points at  $\lambda = 0.5$  come from an entirely independent investigation at a different establishment and the good agreement is reassuring but, as will be seen, these points are not in a sensitive area of the graph.

So, to sum up, the evidence at present is fairly sparse but it appears that Re as such has little effect but there are at least two indications that the pressure oscillations in a deep cavity may be subject to an adverse scale effect in going from model to full-scale - partly as a result of the reduction in approach boundary layer thickness. Now that prediction methods have been developed, they should be used to establish whether there are significant scale effects in practice - a familiar plea in this Agardograph!

## 7.2 Intakes

The aerodynamic design of an air intake and the external cowl for the nacelle is inevitably a compromise between different requirements. Reliance has to be placed on model tests and the answer to the question as to whether the data are likely to be subject to significant scale effect when applied to the full-scale installation depends on which features of the results one is considering. The important issues are:

- (i) the internal pressure recovery both at subsonic speeds and for military combat aircraft, at supersonic speeds at low incidence,
- (ii) the flow distortion standard in the intake duct,
- (iii) the design of the lower lip to avoid an internal separation at high mass-flow and high angle-of-attack when maximum thrust is required, and
- (iv) the design of the upper lip and cowl to avoid a separation on the external surface at reduced mass-flow

conditions in the required operational envelope both at low incidence and more particularly at high angle-of-attack in the second segment climb with one engine inoperational on a transport aircraft.

As regards (i), (ii) and (iii), there are many potential sources of flow separation in a typical intake, all of which could lead to a loss in overall pressure recovery, appreciable pressure distortion and, in principle, significant scale effect. These are illustrated in Figs 7.8(a-f) taken from Ref 293. Some are inherent in the geometric and aerodynamic design, eg intake shock and boundary layer interaction on an adjacent aircraft surface or on an intake compression surface leading to separation behind a terminal shock (Fig 7.8(a)); separation in a duct as a result of too high a rate of diffusion and/or the presence of sharp bends (Fig 7.8(b)); the absence of auxiliary intakes combined with thin intake lips giving separation at take-off and static conditions (Fig 7.8(c)). Also, there is the possibility of internal separation from a sharp lower lip induced by either high angle-of-attack or yaw (Fig 7.8(d)) and finally, there may be problems due to a mismatch of the intake and engine airflows in subcritical (Fig 7.8(e)) or supercritical operation (Fig 7.8(f)). The aim of a good design is to avoid such problems in the operational flight envelope and this could be why evidence on Reynolds-number effects is relatively sparse. The generally accepted rule-of-thumb that is frequently quoted is that to avoid serious scale effects, the test Reynolds number based on intake maximum diameter should be at least  $1 \times 10^6$ . It is important to note that this rule was originally devised to relate to the testing of intakes with external compression surfaces at supersonic speeds and to use it more generally is taking it out of context. Nevertheless, it appears to be a reasonable guide in respect of (i), (ii) and (iii) above but emphatically not in respect of (iv) where, as we will see below, much higher Reynolds numbers are needed to avoid serious scale effects.

Ref 297 includes one example of a comparison designed to show the Re-effects on internal pressure recovery and the steady and unsteady distortion represented respectively by the parameters,  $DC_{50}$  and  $DC_{601X}$  defined in Ref 297. In this example, intake models of a common design (RAE Model 742L, cowl 2: a simple subsonic-type intake with a circular cross-section and a blunt lip and a NACA-1 external profile with a highlight diameter ratio of 0.85 and a length/diameter ratio of 1.00) were tested in the S2MA (1.75 m x 1.75 m) tunnel at ONERA (Modane) and the 1 m x 1 m tunnel at DLR (Göttingen). The differences between the results at  $Re = 1.25 \times 10^6$  and  $Re = 1.9 \times 10^6$  (and two higher Reynolds numbers not shown) are trivial but the values at  $Re = 0.39 \times 10^6$  show that going below the "rule-of-thumb" value of  $1 \times 10^6$  introduces larger adverse effects.

Turning to (iv) where the Reynolds-number effects can be substantial, this problem has been investigated<sup>294,295</sup> by the General Electric Company in a series of tests on relatively large intake models in the F1 tunnel at the le Fauga establishment of ONERA. It was found that flow separation on the outer cowl could easily be detected by observing when the peak suction collapsed on the upper surface as incidence was increased. Fig 7.10(a) shows the increase with Reynolds number in the angle-of-attack for separation-onset at various Mach numbers. The Reynolds number in this case is based on the intake highlight diameter. It will be seen that the results from the tests on two model scales, 15% and 35%, overlap and lie on the same curves. Re-effects persist up to about  $Re = 10^7$ . If only the results for the smaller model had been available, the limiting angles-of-attack without separation would have been thought to

be about 2-3° lower than the values obtained with the larger model. An error of this magnitude can be serious; the second example shown in Fig 7.10(b) indicates the improvement from the small to the large model makes all the difference as to whether the design meets the minimum operational requirement.

Clearly, the results in Fig 7.10(a) relate to the particular nacelle shape tested; it was an axisymmetric nacelle with a highlight diameter ratio of 0.855, a highlight/throat diameter ratio of 1.124 and an external length/diameter ratio of 0.435. The surface pressure distributions were analysed in order to generalise the results and to obtain a prediction method that could be applied to any axisymmetric nacelle. Fig 7.11(a) compares the measured pressure distributions with predictions<sup>296</sup> by inviscid theory; good agreement is obtained except near the peak suction. Fig 7.11(b) shows the variation of the peak local Mach number with angle-of-attack at two Reynolds numbers, again compared with inviscid theory; at separation, the measured value exceeds the prediction by 0.05 and 0.11 at the two Reynolds numbers; these discrepancies are presumably due to the effect of the boundary layer displacement thickness which is not allowed for in the calculations. Ref 295 argues that in view of the relatively high Reynolds numbers of the tests and the bluff nose of the inlet lips, the flow separation is not due to the bursting of a laminar separation bubble but to a turbulent separation as postulated by van den Berg in Ref 62. This suggested that it should be possible to establish a correlation between separation-onset and the adverse gradient in Mach number downstream of the peak suction and this is confirmed by the plot in Fig 7.11(c). This was further simplified, Fig 7.11(d), by plotting the ratio of the velocity at a station just downstream of the highlight divided by the free-stream velocity. It will be seen that the effects of both  $Re$  and  $M$  are virtually eliminated in this way. Finally, an attempt was made to predict the turbulent boundary layer separation using the methods of Refs 296, 297 and this gave the results shown in Fig 7.11(e). This approach fails to predict the scale effect but this is again due to the fact that the effects of the boundary layer displacement thickness have been ignored; good agreement was achieved if the calculations used the measured pressure distributions. The implication is therefore that if the calculations had allowed for weak viscous-inviscid interactions, the scale effects would probably have been predicted successfully. Such a method would reduce the need to test every intake design at large scale.

### 7.3 Propellers

There are not many tunnels where it is possible to test a full-scale propeller with a diameter of between 10 ft and 15 ft and even when it is possible, such tests can be expensive. There has therefore always been a demand to test model propellers and this leads to the obvious question as to what is the smallest propeller that one can test and still obtain results that will give a reliable guide to the performance of the full-scale propeller. This is not an academic question; it has been known for about 50 years that data for small-scale propellers can be misleading, particularly as regards their static and take-off thrust. For example, in the 1940s, the RAF 6 section gained a somewhat undeserved reputation for giving a much better  $C_{L,max}$  than the Clark Y section on the basis of the results of tests on model propellers mounted ahead of a model Mercury nacelle at the NPL. When, later, the corresponding full-scale propellers were tested on a Mercury nacelle in the 24 ft tunnel at RAE Farnborough, it was found that the advantage in favour of the RAF 6 section was only about half as great as that shown in the model tests<sup>298</sup>. The model and full-scale Reynolds numbers based on the blade chord at 0.7 radius in these tests were typically  $0.55 \times 10^6$  and  $1.73 \times 10^6$  respectively. The comparative results are shown in

Fig 7.12(a,b); the lift and drag data have been back-figured from the propeller thrust and power results by a single-radius version of the standard strip theory.

Moving on to more recent times, the two most familiar references on scale effects on propellers are those by Bass<sup>299,37</sup>; Figs 7.13 and 7.14 present examples from these two papers. Fig 7.13(a) shows results obtained from tests on a model propeller in a pressurised tunnel covering a Reynolds-number range from about  $0.45 \times 10^6$  to about  $1.4 \times 10^6$  based on the blade chord at 0.7 x radius. Tests were run at different Reynolds numbers while maintaining the same blade angle, Mach number and rpm at a given power coefficient,  $C_p$ ; the Reynolds number varied slightly with  $C_p$  since, at constant rotational speed and blade angle, a change in  $C_p$  implies a change in forward speed. It will be seen that an increase in  $Re$  up to about  $1 \times 10^6$  gives an increase in thrust but there is little further change beyond  $Re = 1 \times 10^6$ .

Further results on two other model propellers are plotted in Figs 7.13(b,c). Both figures show a somewhat random and unpredictable variation in efficiency with  $Re$  below  $0.5 \times 10^6$  followed by a gentle increase up to near  $Re = 1.0 \times 10^6$ . In Ref 299, Bass suggests that the erratic variation for the NACA-16 propeller at low Reynolds number could be due to changes in the flow near the blade root bearing in mind that with the modern ARA-D propeller, a more regular behaviour was obtained when transition was fixed on the inboard sections. It may be significant that the efficiency of the ARA-D propeller is maintained down to a lower value of  $Re$  than with the NACA-16 propeller before it collapses abruptly: the ARA-D blades would tend to stall at the trailing edge in contrast to the NACA-16 blades which would exhibit a leading-edge stall. There are however matters of detail; the practical conclusion is that it is safer to test at or above  $Re = 1.0 \times 10^6$  or at least,  $0.5 \times 10^6$ .

As already discussed in §2.2.2.4, it is not as easy as it might appear to draw reliable conclusions about Reynolds-number effects from a comparison of results of tests on two sizes of the same propeller design. To obtain the same operating conditions, viz, a given advance ratio ( $J$ ) and tip Mach number, the smaller propeller has to be run at a higher rotational speed and this appears to introduce a pseudo-Reynolds number effect which is assumed to depend on  $\Omega^2 R$ . Fig 7.14(a) provides some evidence that a rotational-speed effect does exist: the figure compares the calculated and measured reductions in efficiency as  $\Omega^2 R$  is increased at a given  $J$ ; the calculated trends include the predicted effects of increasing tip Mach number but, particularly at the higher values of  $J$ , this is not enough for the results to match the measured variation in efficiency and so, some other effect must be involved. Fig 7.14(b) offers further evidence suggesting a possible  $\Omega^2 R$  effect. When one attempts to cover a cruise  $J$  condition in a low speed tunnel, one has to run the tunnel as fast as possible and reduce the propeller rpm to suit. The curves of power coefficient or efficiency against  $J$  at a given blade angle are therefore built up in segments in this way but one generally finds that where the segments obtained at a given tunnel speed overlap, they do not line up perfectly, as illustrated in Fig 7.14(b). These discrepancies cannot be ascribed to either Mach number or Reynolds number because the Mach number is too low and the Reynolds number is too high and so, one is left with an explanation based on an  $\Omega^2 R$  effect.

No experimentally confirmed explanation for this particular apparent  $\Omega^2 R$  effect has yet been put forward. Bass notes<sup>37</sup> that calculations have shown that it cannot be due to blade live

twist. He suggests that "a plausible hypothesis is that it arises from a centrifugally driven radial migration of the boundary layer, together with any separated flow at the spinner root junction; the consequently increased angular momentum appears as an increased pressure on the pressure face of the blade. Since  $J$  is a measure of the blade pitch, it is reasonable to anticipate that at higher values of  $J$ , the component of the increase in pressure in the plane of the torque is greater than at lower values" and this is what is observed. Accepting that the  $\Omega^2 R$  effect is genuine means that differences between test results for model<sup>301</sup> and full-scale<sup>302</sup> propellers have to be ascribed to an amalgam of  $Re$  and  $\Omega^2 R$  effects. Bass derived two correction charts for these effects and these are presented in Figs 7.14(c,d). Fig 7.14(d) should not be used if  $Re$ , based on the chord at 0.7 radius is less than  $0.5 \times 10^6$ . More evidence is required before Fig 7.14(c) can be safely extrapolated to lower values of  $\Omega^2 R$  and  $J$ . Ref 37 notes that the corrections in Figs 7.14(c,d) were based on an analysis of the results for one particular propeller but test data for other model propellers have been corrected successfully using these charts and experience has shown that the agreement between the measured full-scale and corrected 1/5th scale model efficiencies is generally within  $\pm 1.0\%$ .

The results in Figs 7.13 and 7.14 came from UK sources. Figs 7.15(a,b) present further evidence on  $Re$ -effects drawn from US data<sup>303</sup>. Once again, the graphs suggest that major  $Re$ -effects do not exist above  $Re = 1.0 \times 10^6$ , based on the blade chord at 0.7 radius. The important (in the present context) comparison in Fig 7.15(b) is between the curve for the 13.2 ft diameter propeller and the dashed curve for the 5 ft diameter propeller having been adjusted for tunnel wall interference; this demonstrates agreement within 1% between results at  $Re = 2$  and  $5 \times 10^6$ .

The use of a Reynolds number based on the blade chord at 0.7 radius is a convenient artifice and appears to have been generally accepted in the propeller industry. However, it could be misleading; almost certainly, the scale effect when it exists is related primarily to the flow near the blade root where the Reynolds number will be lower and, in the past at least, the aerodynamic cleanliness of the propeller not so good. The standards of the blade root design have steadily improved over recent years and so, some caution should be exercised as to whether Figs 7.14(c,d) necessarily apply to all modern propellers. It is not suggested that one should hesitate about the basic recommendation about testing at above  $Re = 0.5 \times 10^6$  or preferably  $1.0 \times 10^6$ ; the hesitation is more about whether the effects of  $Re$  and more particularly,  $\Omega^2 R$  on modern propellers with clean, faired root designs are as large as suggested by Figs 7.14(c,d).

The concept that the centrifugal effects on the boundary layer have a significant effect on propeller performance is long-established. In the 1940s, this was recognised as the reason why the values of  $C_{l,max}$  back-figured (eg Fig 7.12) from propeller overall results were higher than in 2D data banks. The concept was confirmed in a classic paper<sup>300</sup> by Himmelskamp published in 1950. Recently, there has been further confirmation from the results of pressure-plotting tests<sup>304</sup> on a model propeller at Southampton University. Fig 7.16(a), taken from Ref 304, presents comparisons of the pressure distributions at two Reynolds numbers for sections at 0.25 and 0.8 radius on this propeller. These blades were designed such that the aeroelastic distortion was negligible and so, these comparisons can be accepted as a genuine indication of the  $Re$  and  $\Omega^2 R$  effects. These pressure distributions were obtained under static running conditions; at 0.8 radius, the effects of  $Re$  are trivial but at 0.25 radius, it is a much more interesting story. There are two main conclusions:

- (i) at the higher test Reynolds number, the section is producing  $C_{l,max} = 1.91$  compared with a  $C_{l,max}$  of 1.18 in the 2D data bank for this section, thus confirming that one can obtain far more  $C_{l,max}$  near the root of a propeller blade than in 2D flow,
- (ii) at the lower Reynolds number, the suction on the upper surface have collapsed, suggesting that the reduction of thrust and efficiency at very low  $Re$  can be due to a laminar separation on the upper surface.

It is tempting to say that the high loading near the root at the higher Reynolds number is associated with the centrifugal effects on the boundary layer but before accepting this conclusion, one should consider Fig 7.16(b). This figure shows the results<sup>305</sup> of a full Reynolds-averaged Navier-Stokes calculation compared with a lifting-surface calculation for the rotor blade on the V-22 Osprey. It will be noted that the Navier-Stokes code predicts extra loading on the inboard sections and so it seems likely that the same code would have predicted the high load measured on the propeller section at 0.25 radius in Fig 7.16(a). Narramore in Ref 305 refers to the fact that similar increases in inboard loading have been observed experimentally by other investigators<sup>306,307,308</sup> and that this has been "attributed to spanwise flow velocities that effectively thin the boundary layer separation region on the blade surface in the inboard region". Narramore continues "however, the Navier-Stokes results that were produced during this study indicate that the three-dimensionality of the flow allows the flow to remain attached to very high angles of attack. No outward radial flow velocities were observed in the inboard region of the blade over the collective range that corresponds to the test results". In other words, high loading near the root is confirmed but this is ascribed to 3D effects rather than to spanwise drift in the boundary layer. Further research is clearly needed and this is, in fact, in progress at the University of Toronto where a new finite-difference code is being developed to solve the generalised, three-dimensional, laminar boundary layer equations in the frame of reference of a rotating propeller blade. The numerical scheme being used in this code is based on earlier three-dimensional schemes developed at NASA Ames<sup>310</sup> and VKI<sup>311</sup>. The ultimate aim is to apply the fully developed code to compute the flow over a rotating propeller blade with allowance for centrifugal Coriolis effects.

There may be some confusion in the mind of the reader at this point. There seems to be clear experimental and theoretical evidence for saying that  $C_{l,max}$  is higher on a rotating propeller than in 2D flow but this discussion started from the need to explain a reduction in propeller efficiency with increasing rotational speed. The distinction lies in what happens in separated or, on the other hand, attached flow: in separated flow, the centrifugal effects are generally thought to be favourable; in attached flow, Fig 7.14(c) suggests that the centrifugal effects are adverse.

The open literature contains relatively few examples of comparisons between results on model and full-scale propellers. To some extent, this could be due to considerations of commercial security but it should be recognised that to obtain a meaningful comparison is far from a trivial task. The scale effect at the end of the exercise may be comparable with the absolute accuracy of the results on either of the propellers and, in this case, one cannot take refuge in saying that differences will be more accurate than the absolute numbers. For example, the two propellers could well have been mounted in a different manner and the different terms in the bookkeeping determined

in a different fashion; hence, comparing the efficiencies for the two sizes of propeller does not necessarily mean that errors in either result cancel out. The bookkeeping can be quite complicated: for example, if one is measuring the shaft thrust by a shaft balance mounted inside the spinner, one has to subtract the measured values with and without blades, to obtain an apparent thrust and then integrate pressures over the non-metric part of the nacelle to obtain a genuine net thrust; one also has to allow for the effect of the rotating propeller on the pressure force on the spinner back-plate and this can be a large correction. Therefore, not only the shaft thrust with propeller operating but various correction terms have to be measured with great precision to obtain a final absolute accuracy that is better than the scale effect one is trying to determine. Another important issue is whether in testing at a given nominal blade angle, the live twist under load is the same for the model and full-scale propeller and it is only recently that reliable methods have been introduced for measuring this twist. These are some of the technical difficulties that frustrate attempts to derive the scale effect. However, one comparison is shown in Fig 7.17 from an extensive test programme undertaken some years ago in the ARA transonic tunnel on model propellers of respectively, 15 and 36 in diameter giving test Reynolds numbers based on the chord at  $0.7 \times$  radius of about  $0.4$  and  $1.0 \times 10^6$  respectively. This graph suggests that near the maximum efficiency condition, the scale effect is small and favourable as would be expected from the test Reynolds numbers. It may be more significant to note that in more recent tests in the ARA tunnel on the 36 in diameter pressure-plotted model propeller mentioned in Ref 311, very good agreement has been achieved in design cruise conditions between the measured pressure distributions and predictions by an Euler code with no allowance for viscous effects on the blades suggesting that, in these conditions, the viscous effects and hence, the scale effects (apart from changes in skin friction) would be trivial above  $Re = 1.0 \times 10^6$ .

The need to achieve a Reynolds number of at least  $0.5 \times 10^6$  at  $0.7$  radius on the propeller (and at least  $2.0 \times 10^6$  on the wing chord) led Fokkers to test a 1/5 scale powered model of the F27 aircraft in the  $8 \times 6 \text{ m}^2$  DNW tunnel. The main aim of these tests was to investigate the stability and control characteristics. The results were compared with those obtained at lower Reynolds numbers in the NLR  $3 \times 2 \text{ m}^2$  Low Speed Tunnel. Some significant Re-effects were observed, notably in the lateral and directional stability and control characteristics, as illustrated in Figs 7.18(a,b) for the roll stability and rudder hinge moment. The trend for the stability in roll to decrease with propeller thrust, flaps down, particularly at the higher angles of yaw as observed at  $Re_c = 1.4 \times 10^6$ ,  $Re_{0.7R} = 0.4 \times 10^6$  but not at  $Re_c = 0.33 \times 10^6$ ,  $Re_{0.7R} = 0.1 \times 10^6$  is in line with expectations from flight behaviour but it is not immediately obvious whether the scale effect is primarily due to the change in test Reynolds number on the propeller or on the aircraft.

So, the overall conclusion is to test if possible at a Reynolds number (at  $0.7$  radius) of at least  $0.5 \times 10^6$  and preferably  $1.0 \times 10^6$ . If this is not possible, one should study flow patterns from flow visualisation tests and if there is evidence of a laminar separation, repeat the tests with transition fixed on the inboard part of the blade.

#### 7.4 Ice Accretion

As the final subject in this Agardograph, let us consider how Reynolds number can modify the effects of ice accretion on  $C_{L,max}$ . Initial ice accretion on the leading edge of aerofoils, wings and tailplanes resembles distributed roughness with a height nominally equal to the thickness of the ice buildup. The

effects of distributed roughness on  $C_{L,max}$  have been discussed in an earlier Agardograph<sup>314</sup>, AG 264, published in 1981. It was found possible to correlate the results from 4 references<sup>315,316,317,318</sup> by means of three curves of  $\Delta C_{L,max}/C_{L,max}$  plotted against  $\Delta D/D$  where  $\Delta C_{L,max}$  is the loss in  $C_{L,max}$  due to the roughness and  $\Delta D$  is the drag penalty due to the addition of the same roughness to both sides of a flat plate at the same Reynolds number. The 3 curves were derived for (i) a wing + trailing edge flap, (ii) a clean wing and (iii) a wing + flap + leading-edge slat. All 3 curves reached about  $\Delta C_{L,max}/C_{L,max} = 0.32$  as an asymptote at high  $\Delta D/D$  but the increase in  $\Delta C_{L,max}$  at low  $\Delta D/D$  varied greatly between the curves, being greatest for (i) and least for (iii). A trend in this direction could have been forecast since it is the roughness near the leading edge that has most effect on  $C_{L,max}$  and (i)→(ii)→(iii) implies a progressive decrease in the local velocities near the leading edge. All the evidence came from model tests in UK tunnels at Reynolds numbers in the range  $2.5 - 6 \times 10^6$ . Hopefully, it was suggested that it would be possible to allow for scale effects through the fact that  $\Delta D$  would vary with Reynolds number.

The emphasis in the above UK research was on determining the effects of hoar frost deposits but more recently, there has been serious concern in the effects of ice accretion. For some years, the common practice in the US was to estimate the loss in maximum lift by means of the empirical correlations devised<sup>320</sup> by Brumby and shown in Fig 7.19(a). These correlations suggest that the reduction in maximum lift for ice accretion around the leading edge will be less than 5% if the non-dimensional thickness,  $k/c$ , of the ice buildup is less than  $6 \times 10^{-5}$  when the leading-edge devices are retracted or  $4 \times 10^{-4}$  when they are deployed. However, some tests<sup>105</sup> in the NASA Langley LTPT on a single element aerofoil in 1985 indicated that the use of the Brumby correlation could seriously underestimate the effects of a typical ice accretion. This can be seen from the comparison in Fig 7.20(b) which also shows the results of some theoretical calculations by Cebeci using the turbulence model suggested by Cebeci and Chang<sup>321</sup> for flow over rough surfaces. Both the measured and predicted results indicated that the reductions in maximum lift for relatively small buildups of ice merely around the leading edge were well above the relevant Brumby prediction and were, in fact, close to those for the Brumby curve for the effects of ice applied over the complete surface. For  $k/c = 4 \times 10^{-5}$  roughness around the leading edge, for example, the reduction in maximum lift amounts to about 15% rather than 5%.

In view of these results, a comprehensive investigation into the effects of roughness simulating ice accretion was included in the cooperative Douglas/NASA Langley programme on 2D aerofoils discussed in §3.2.2.1. Tests were made on an aft-loaded aerofoil with a leading-edge slat and 2-segment slotted flap with the high-lift devices both retracted and deployed. In addition, Douglas tested a large three-dimensional tailplane model in the F1 tunnel at le Fauga. All these tests were made at Reynolds numbers of at least  $5 \times 10^6$  unlike the earlier tests which had formed the basis of the Brumby correlations. Fig 7.19(c) shows that the results of these tests confirmed that the Brumby correlations seriously underestimated the penalties of small and moderate roughness around the leading edge. Lynch<sup>313</sup> notes that on the new figures, there could be a 40% loss in maximum lift for an ice buildup of 0.03 in, a thickness that might be thought of as the smallest that could be reliably removed by a typical deicing system.

In the context of the present Agardograph, the leading question is why there was such a striking apparent Reynolds-number

effect on the US results. The answer lies not so much in the maximum lift characteristics of the wings with roughened leading edges as in the scale effects already discussed for the wings with smooth leading edges. Fig 7.19(d) shows that, for the single-element aerofoil tested at NASA Langley for Douglas, a laminar separation is present at high lift on the upper surface at  $Re = 2.5 \times 10^6$  but not at  $Re = 5 \times 10^6$ . The results at  $Re = 2.5 \times 10^6$  are therefore typical of those for a leading-edge stall and as noted in §3.1.4,  $C_{L,max}$  would be expected to increase with  $Re$  in such a case. This is, in fact, what was observed for the smooth aerofoil:  $C_{L,max}$  increased from 1.48 at  $Re = 2.5 \times 10^6$  to 1.68 at  $Re = 5 \times 10^6$ . The addition of even a small amount of roughness around the leading edge suppressed the laminar separation bubble and the leading-edge stall;  $C_{L,max}$  was then independent of Reynolds number (at a value of 1.36). The reduction in  $C_{L,max}$  therefore increased with  $Re$  and is shown in Fig 7.19(e). It is interesting to note that the data from the earlier UK work are broadly consistent with the new high  $Re$ -values from the most recent US tests and it is significant that in the derivation of the UK correlations as in Ref 318, results for the smooth wings at low Reynolds number when  $C_{L,max}$  was increasing with  $Re$  were ignored; if they had been used, much lower values of  $\Delta C_{L,max}$  would have been obtained.

The new tests confirmed that the penalties in maximum lift were much smaller when a slat was extended. Fig 7.19(f) presents the results for the 4-element configuration, all devices extended at a test Reynolds number of  $9 \times 10^6$ ; little scale effect was observed in this case in the range  $5 \times 10^6$  to  $16 \times 10^6$ . A 0.03 in buildup of ice on the slat would give a 10% loss in maximum lift as compared with 40% for the slat retracted case - for a 200-seater transport aircraft.

The important conclusion, therefore, is that the scale effect on the loss in  $C_{L,max}$  due to ice accretion is essentially a mirror image of the scale effect on the smooth wing  $C_{L,max}$ . It is therefore mandatory that tests on simulated ice accretion should be made at Reynolds numbers above the range when the stall on the clean wing is of either the thin-wing or leading-edge type, ie for many wings, the tests should be made at Reynolds numbers above  $Re = 5 \times 10^6$ .

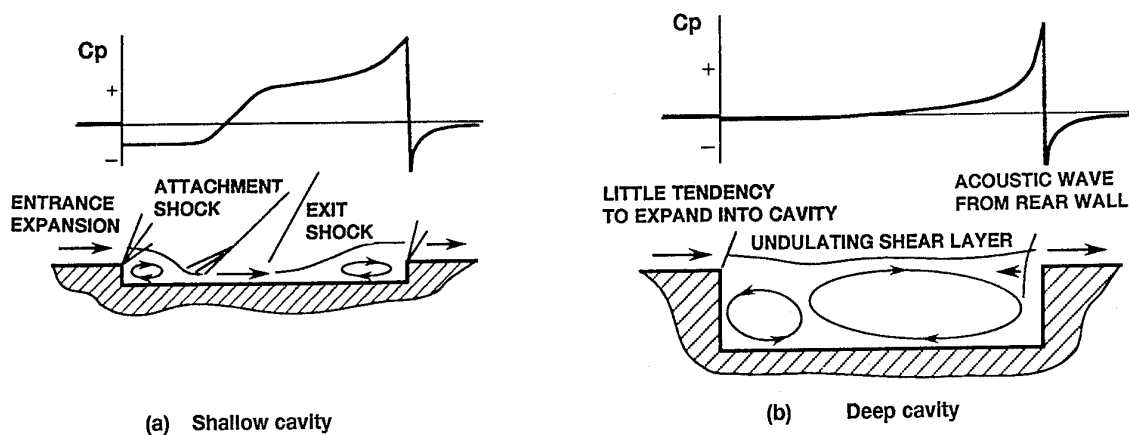


FIG 7.1(a,b) Representative Cavity Flow Fields  
(from ref 285)

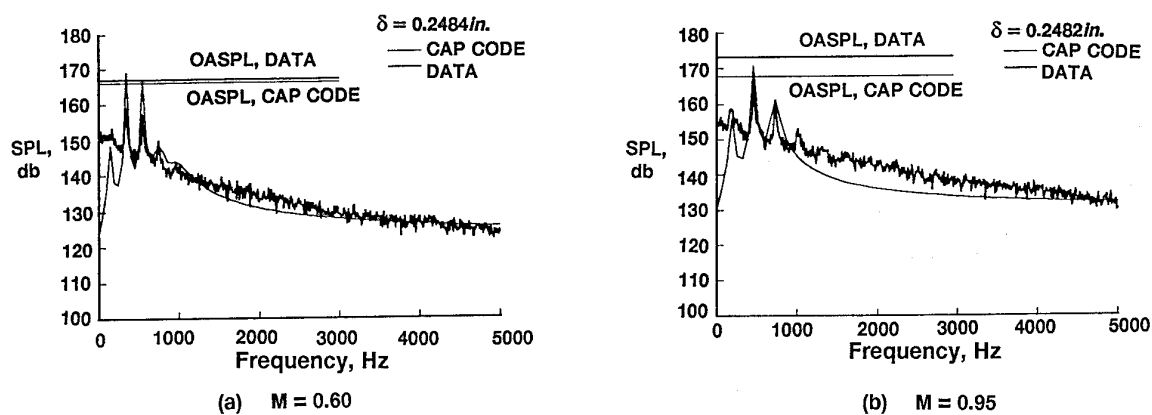


FIG 7.2 (a,b) Comparison of Data with Spectra  
Predicted using Non-Optimized Damping,  $L/D = 4.5$   
(from ref 285)

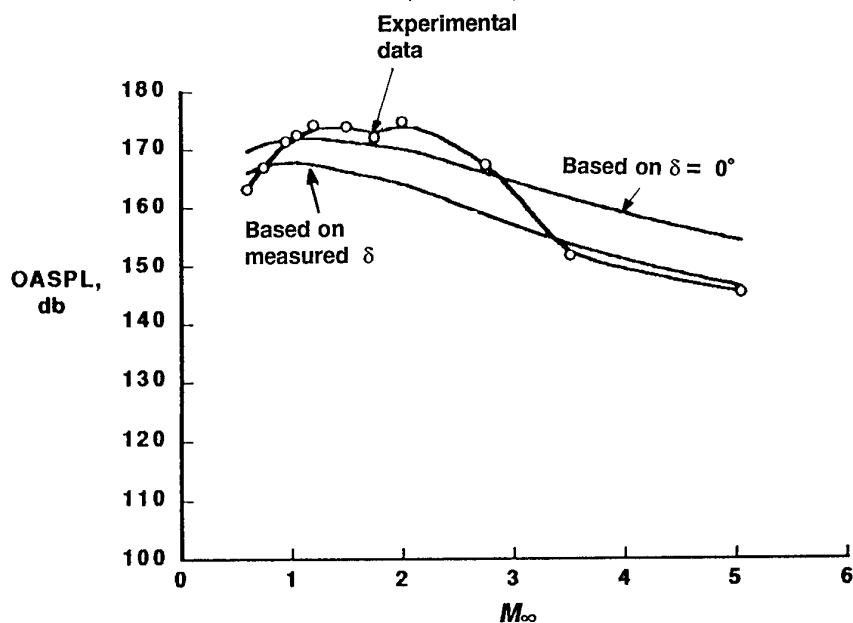
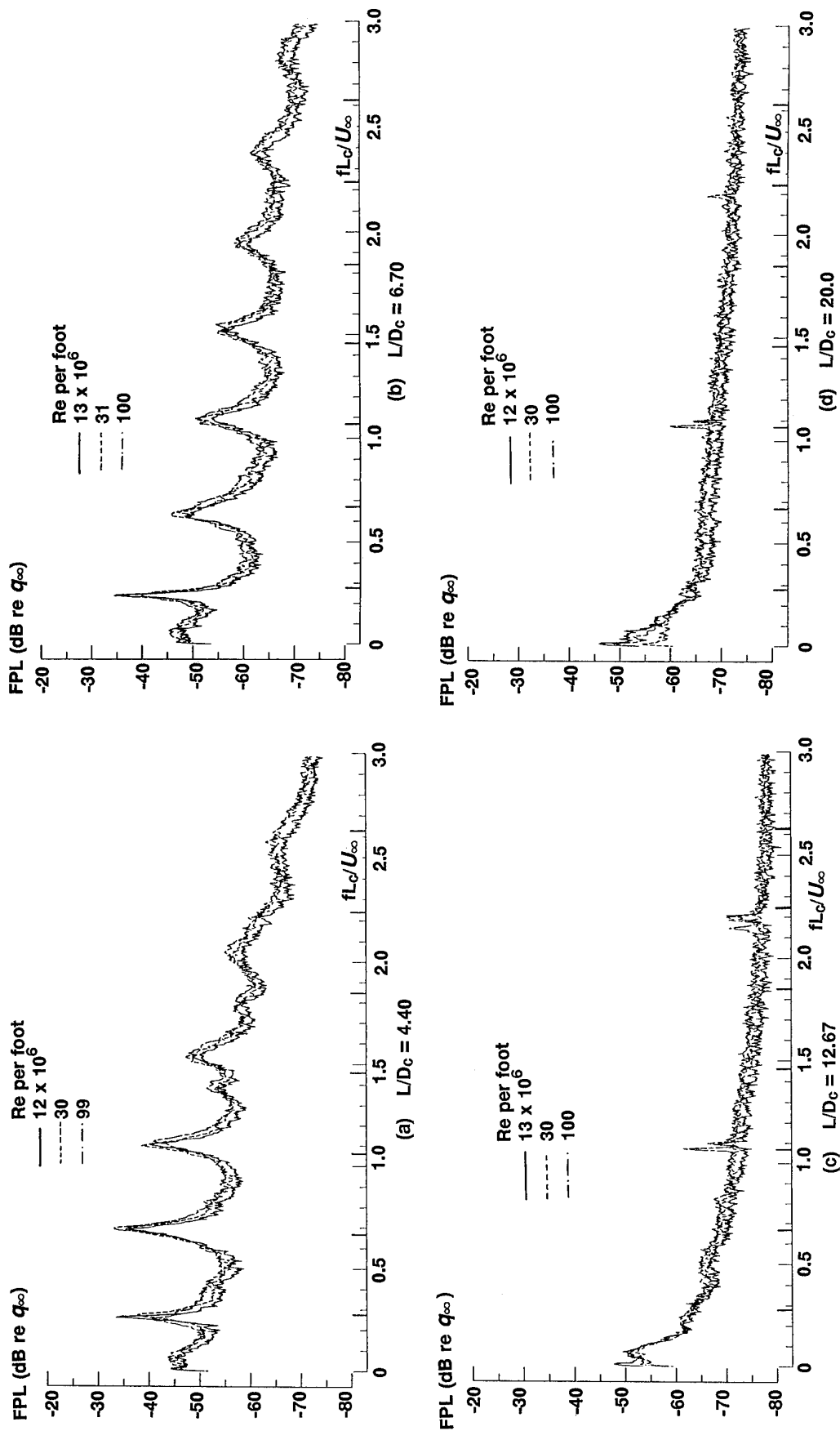


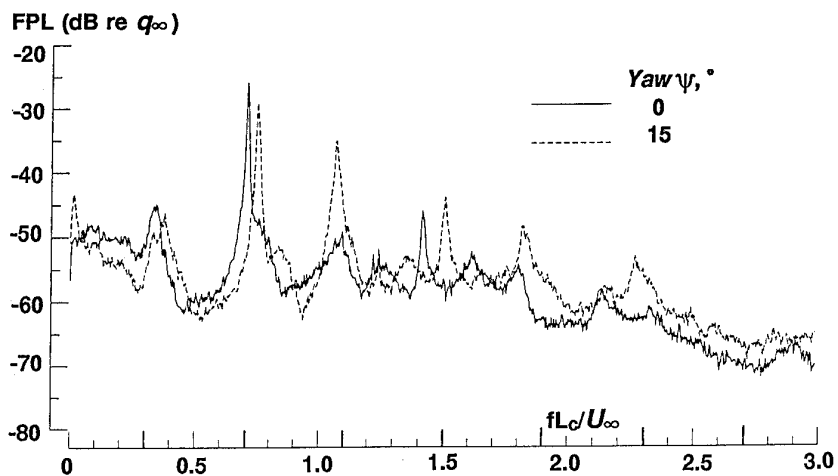
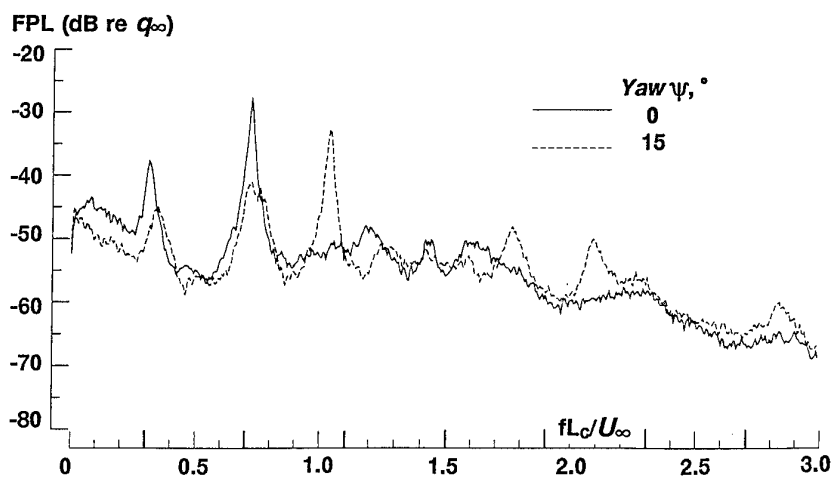
FIG 7.3 Predicted Effect of Approach Boundary Layer  
Thickness  $\delta$  on OASPL  
(from ref 285)





$M = 0.90$ ; Cavity Length  $L_c = 11.25''$ ; Cavity width  $W_c = 2.50''$ ; Zero yaw;  
 Bold ticks on abscissa scale: Edge tone frequencies by modified Rossiter equation  
 (see ref 291)

FIG 7.4 Effect of Re on Cavity Fluctuating Pressures  
 (from ref 291)

(a)  $Re = 6 \times 10^6$  per foot(b)  $Re = 100 \times 10^6$  per foot

$M = 0.80$ ; Cavity Length  $L_c = 11.25$ ";  
 Cavity width  $W_c = 2.50$ ";

$L_c / D_c = 4.40$
--------------------

FIG 7.5 Effect of Yaw on Cavity Fluctuating Pressures  
 (from ref 291)

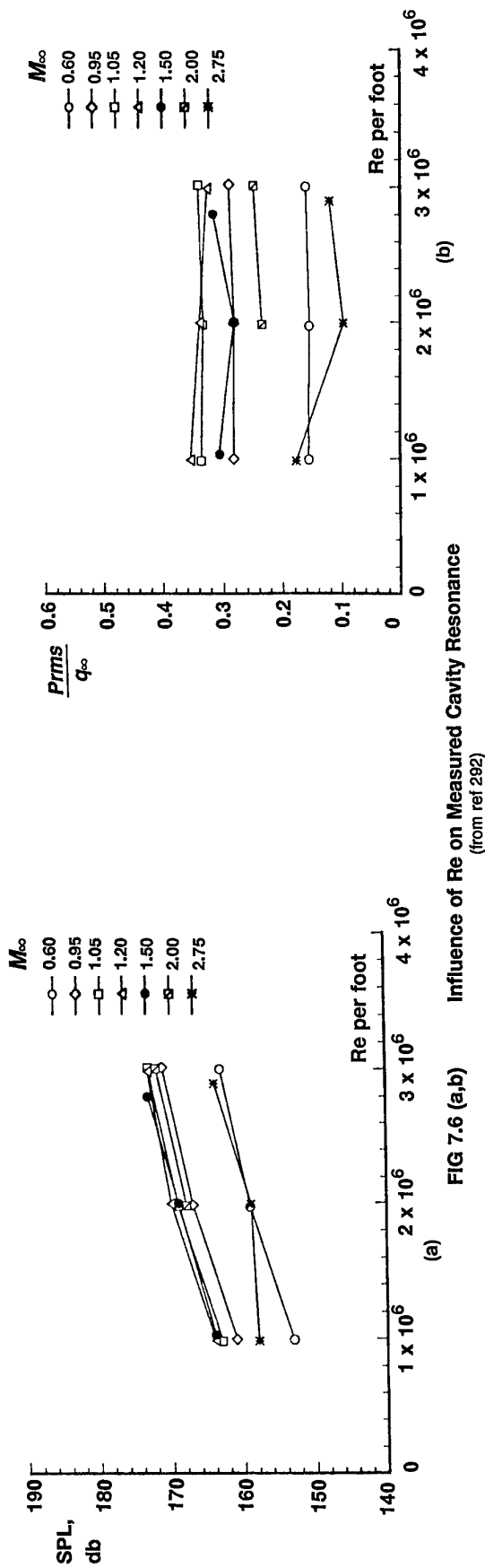


FIG 7.6 (a,b) Influence of Re on Measured Cavity Resonance  
(from ref 292)

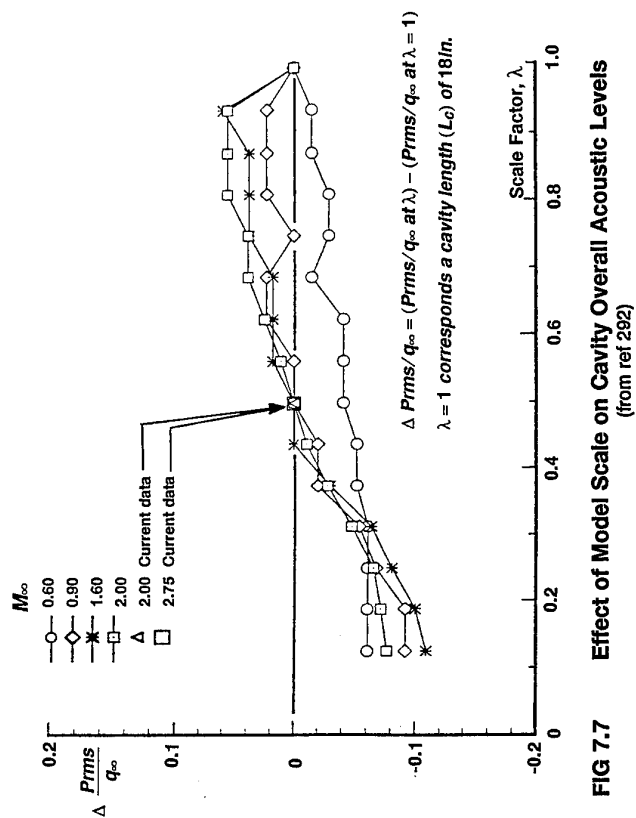


FIG 7.7 Effect of Model Scale on Cavity Overall Acoustic Levels  
(from ref 292)

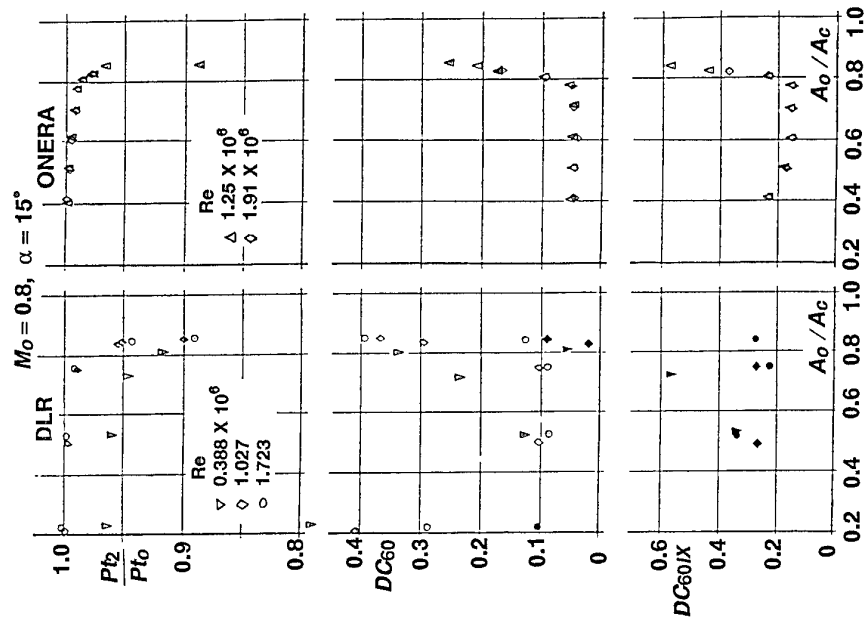


FIG 7.9 Effect of Re on Internal Flow Characteristics of Model 742L, Cowl 2;  $\alpha = 15^\circ$ ,  $M = 0.8$  (from ref 293)

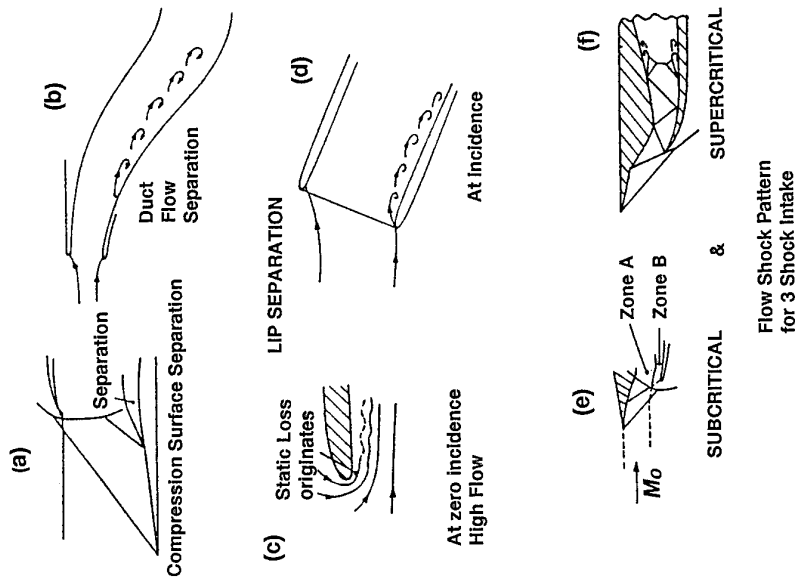


FIG 7.8 Sources of Internal Flow Separation (from ref 293)

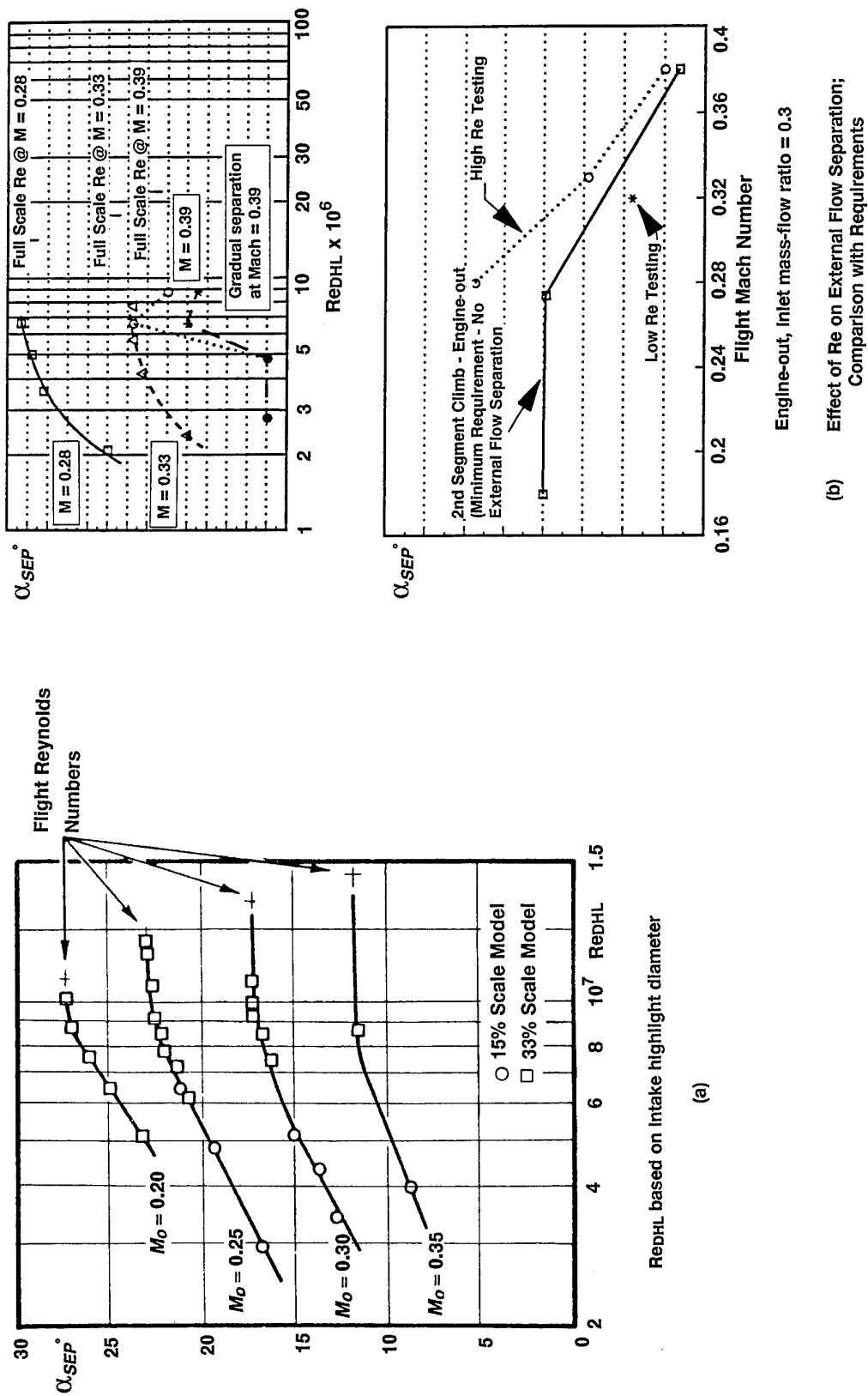
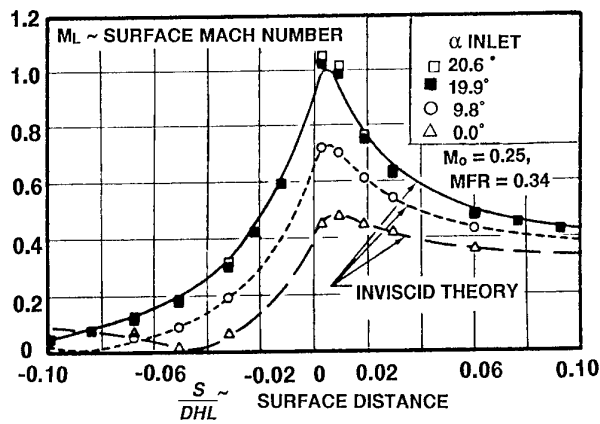
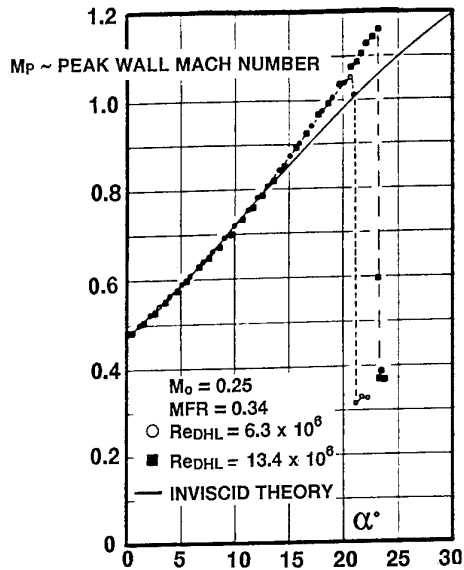


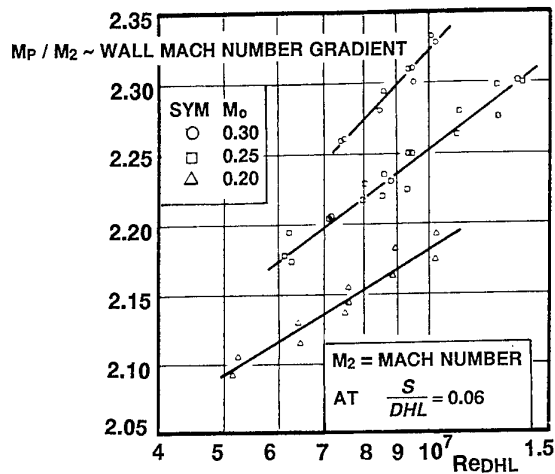
FIG 7.10 Effect of Re on Incidence for External Flow Separation  
(from ref 295)



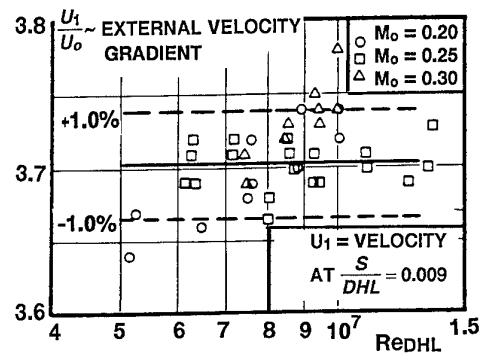
(a) Inviscid theory vs experiment:  
External surface pressures



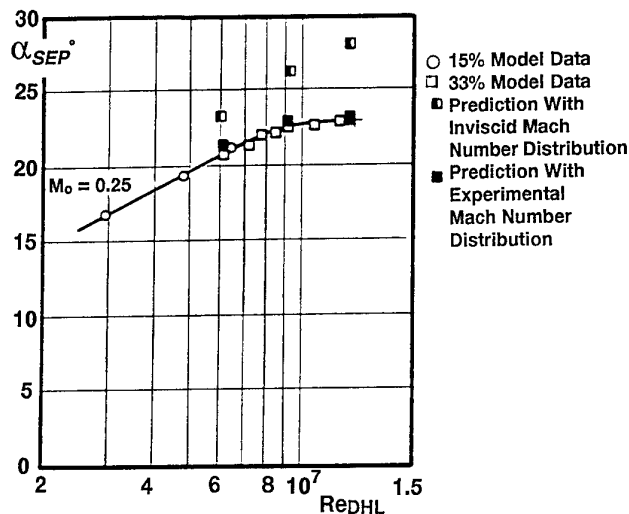
(b) Inviscid theory / experiment:  
External peak suction



(c) Mach number gradient at  
conditions for external flow separation



(d) Velocity gradient at conditions  
for external flow separation



(e) Prediction / measurement:  $\alpha_{SEP}^\circ$

FIG 7.11 Analysis of Results on External Nacelle Surface  
(from ref 295)

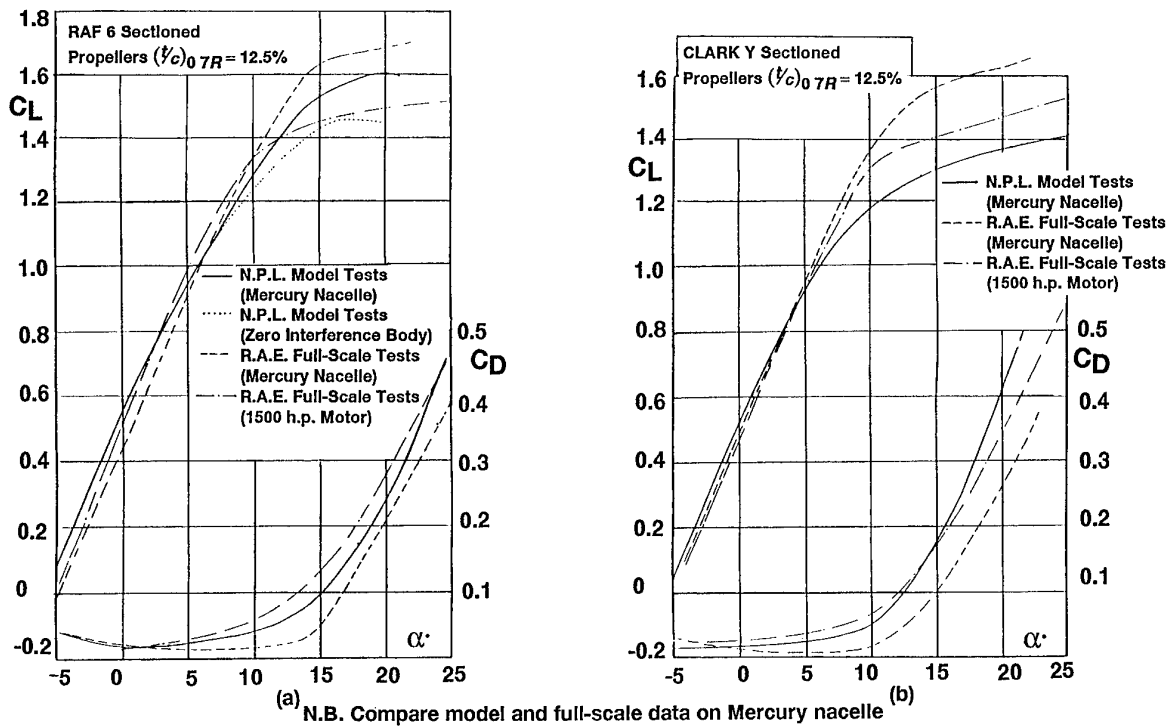


FIG 7.12 (a,b) Scale Effect on Early RAF 6 and Clark Y Propellers  
(from ref 297)

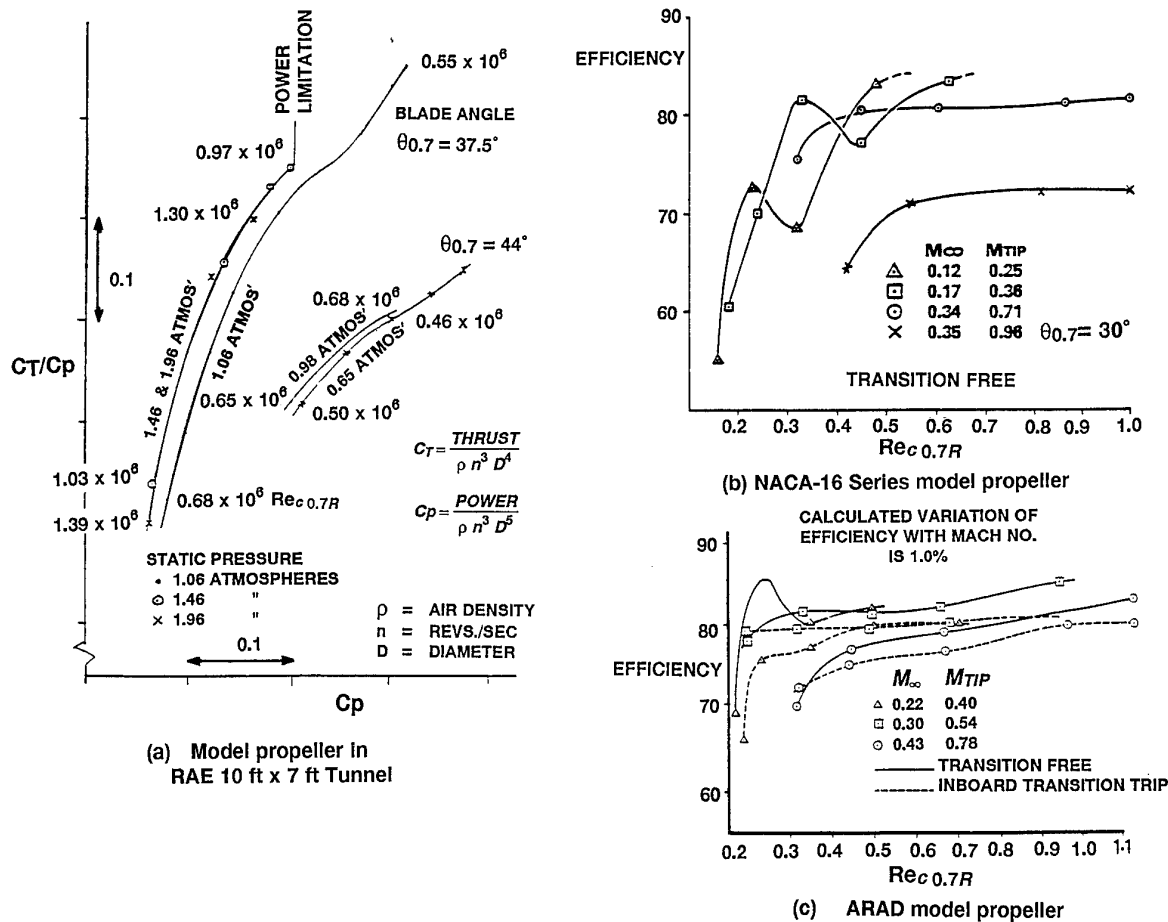
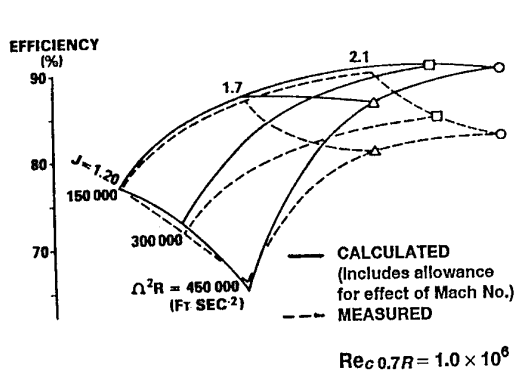
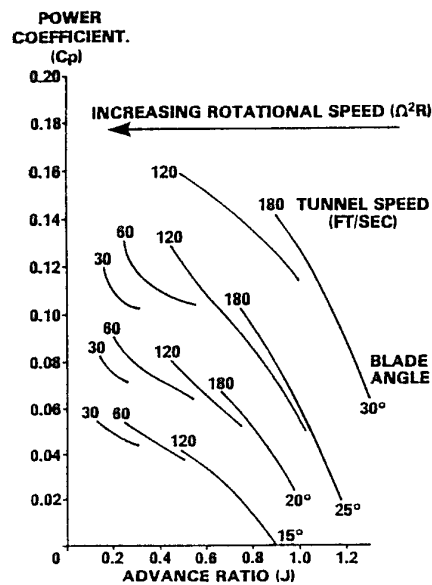
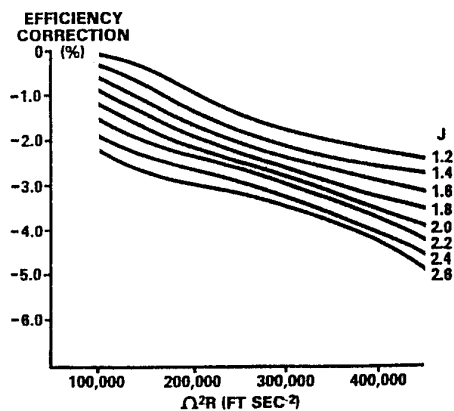
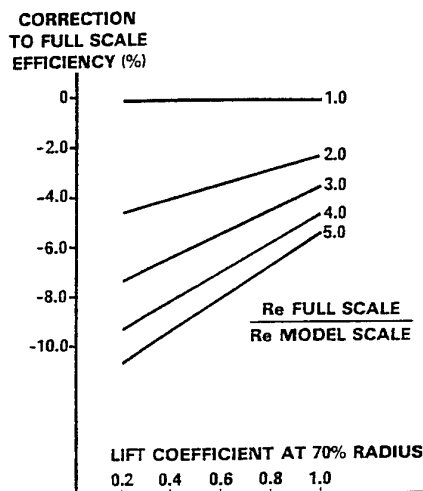
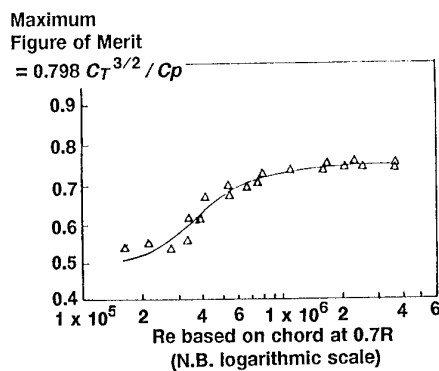
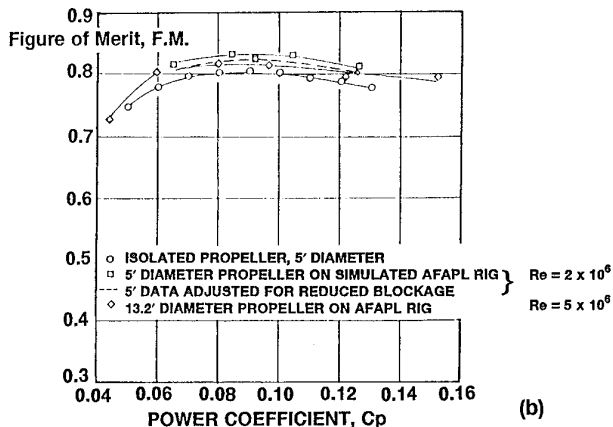


FIG 7.13 Effect of  $Re$  on Measured Propeller Efficiency  
(from refs 298, 299)

(a) Variation of  $\eta$  with  $\Omega^2 R$  at constant  $Re$ (b) Results suggesting presence of  $\Omega^2 R$  effect(c) Derived correction for effect of  $\Omega^2 R$ (d) Derived correction for effect of  $Re$  not to be used when  $Re < 0.5 \times 10^6$ FIG 7.14 Effect of  $Re$  and  $\Omega^2 R$  on Propeller Efficiency  
(from ref 299)

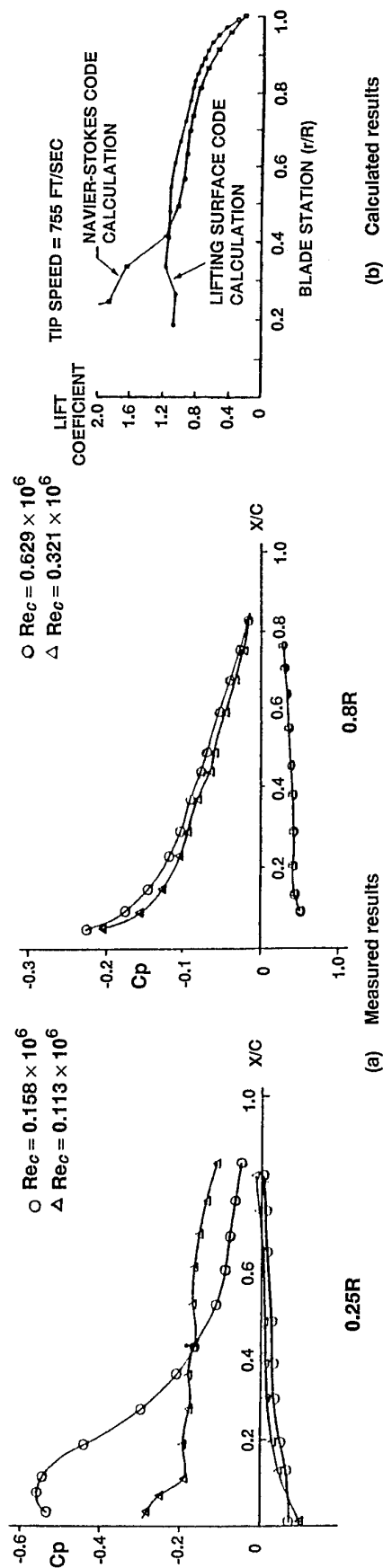
(a)



(b)

FIG 7.15 (a,b) Effect of  $Re$  on Propeller Performance ( U.S. Data )  
(from ref 303)





N.B. (a, b) Do not refer to the same propeller

FIG 7.16(a,b) Effects of Re (or  $\Omega^2 R^2$ ) on Blade Pressures and Loading  
(from refs 304, 305)

THRUST OBTAINED FROM SHAFT BALANCE

APPARENT THRUST = { (SHAFT THRUST) WITH BLADES - (SHAFT THRUST) NO BLADES }

Note: Nett efficiencies cannot be compared because  
no measurements of nacelle drag with smaller  
propeller

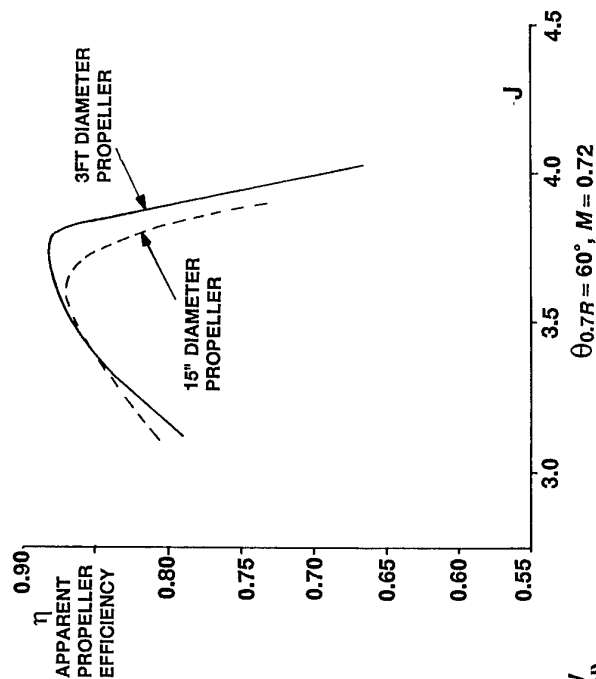
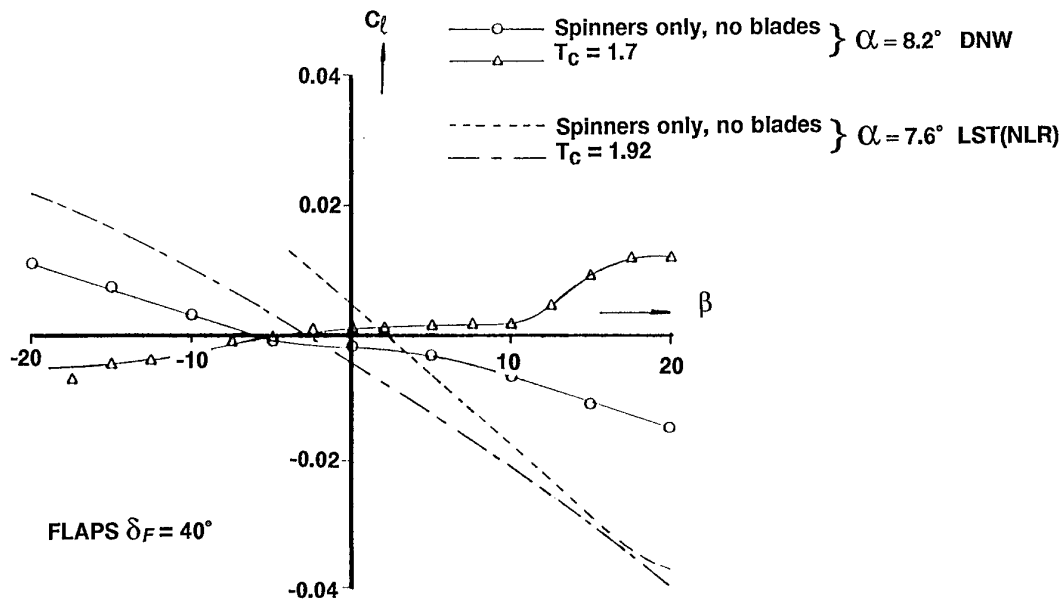
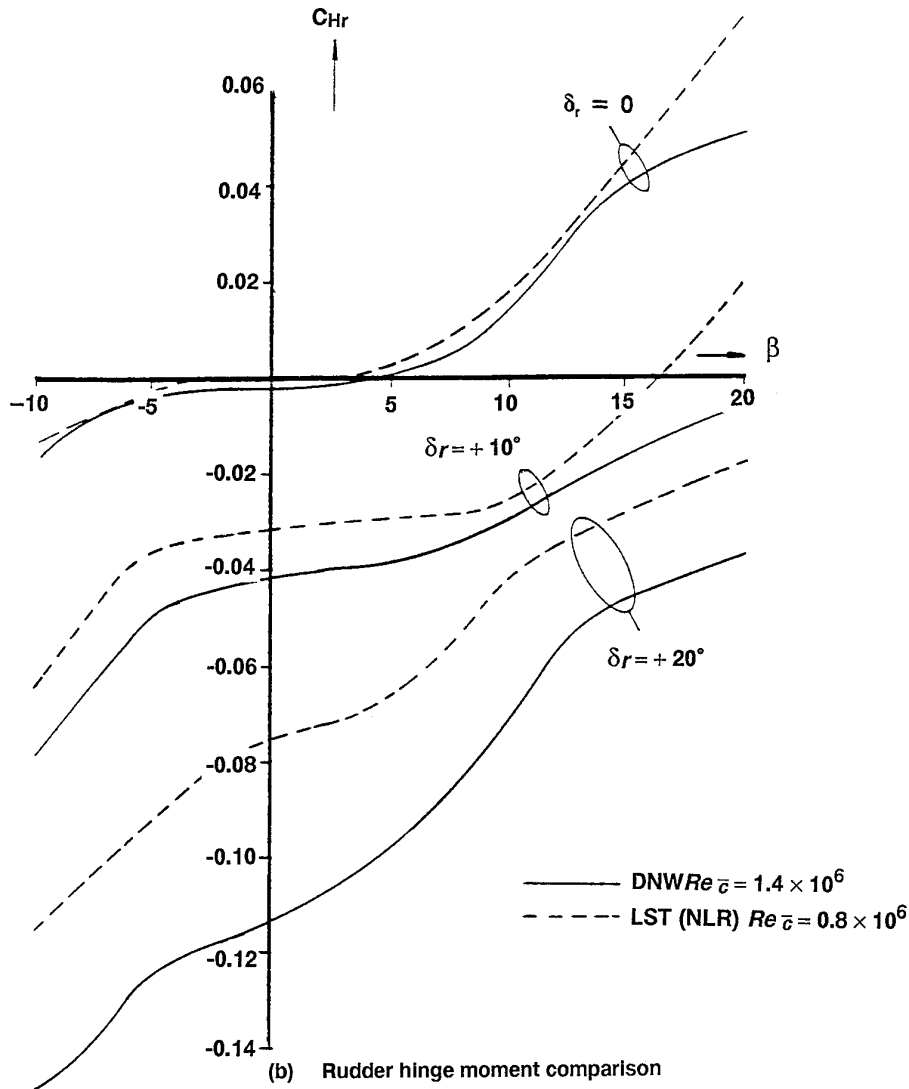


FIG 7.17 Scale Effect on Propeller Efficiency  
(from tests in ARA Transonic Tunnel)

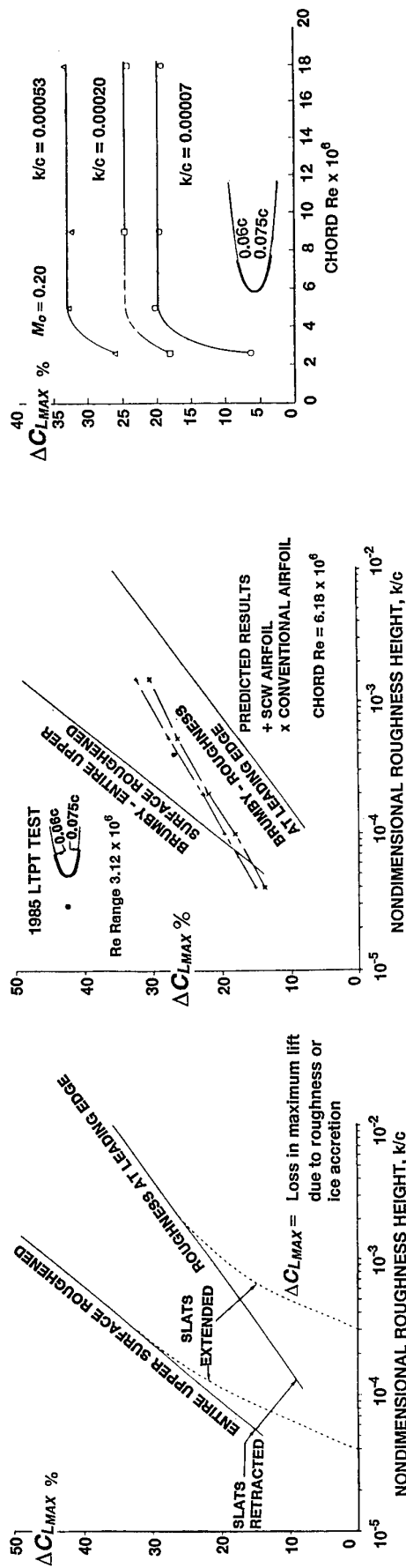


(a) Rolling moment comparison

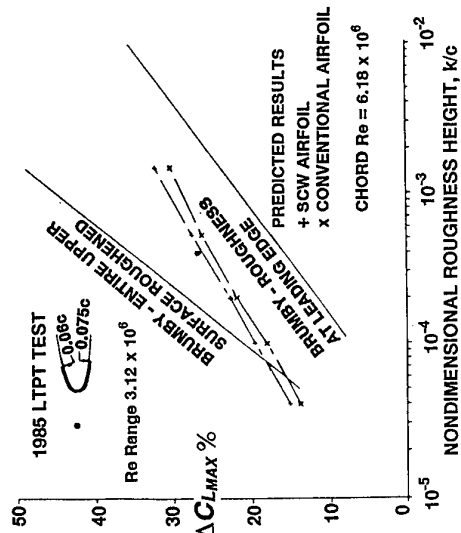


(b) Rudder hinge moment comparison

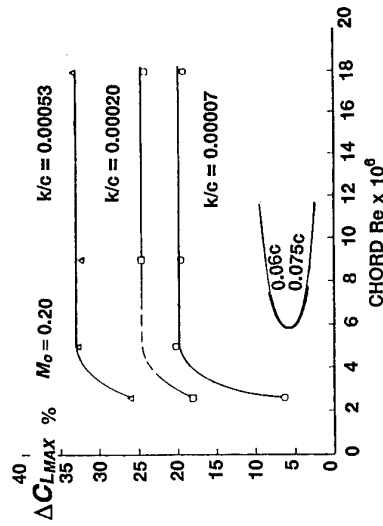
FIG 7.18 Effect of  $Re$  on F27 Model Test Data



(a) Brumby correlation for roughness effects

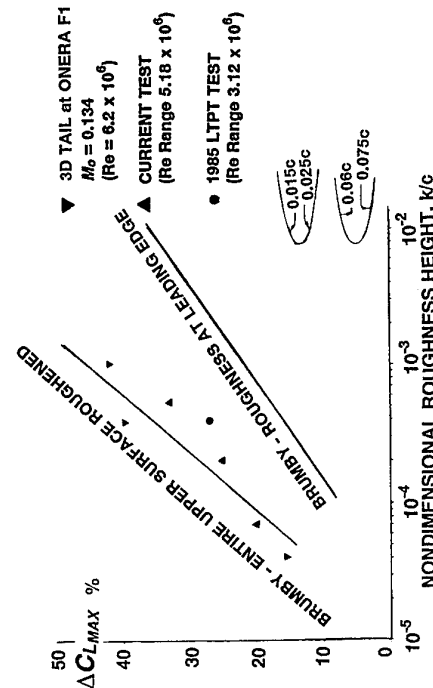
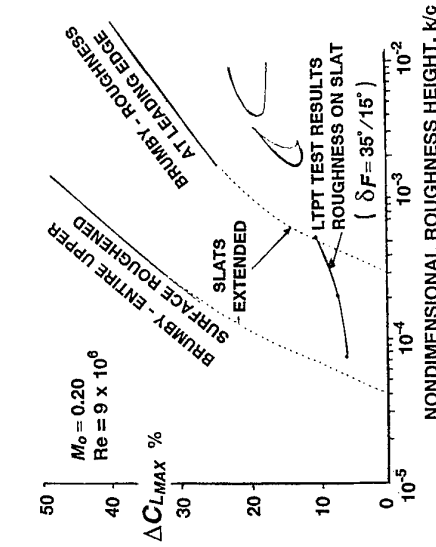


(b) Initial challenges to interpretation of Brumby roughness correlation



(c) 2D and 3D Test data for effect of roughness on maximum lift of single element configurations

(e) Re-effect on maximum lift loss due to L.E. roughness on single element aerofoil

(d) Indicated laminar separation bubble on clean single-element aerofoil at chord  $Re = 2.5 \times 10^6$ 

(e) Re-effect on maximum lift loss due to L.E. roughness on single element aerofoil

(f) Effect of roughness on L.E. slat

FIG 7.19 Effect of Simulated Ice Accretion on Aerofoil Lift Characteristics (from ref 315)

## 8 CONCLUSIONS AND RECOMMENDATIONS

Detailed conclusions about scale effect have been included in most of the preceding chapters. The reader is therefore referred to

- (i) §3.1.4.3 for conclusions on scale effect on high lift characteristics at low speed for 2-dimensional single-element aerofoils,
- (ii) §3.2.4 for conclusions on scale effect on high lift characteristics at low speed for multiple-element aerofoils,
- (iii) §3.3.2.3 for conclusions on sources of scale effect on high lift characteristics at low speed for three-dimensional wings,
- (iv) §3.3.5.4 for conclusions on scale effect on high lift characteristics at low speed for slender wings,
- (v) §3.4.2.1 for a summary of conclusions on the variation of  $C_{L,max}$  with Reynolds number in model tests of various specific complete aircraft,
- (vi) §3.4.2 for the important conclusion that in general, a model test Reynolds number of  $Re = 7 \times 10^6$  is not sufficient to prevent serious scale effect being present in tunnel-flight comparisons of the stalling characteristics at low speed for modern transport aircraft,
- (vii) §3.4.5 for general conclusions on scale effect as shown in flight-tunnel comparisons at high lift, low speed on various specific aircraft types,
- (viii) §4.6 for conclusions on the merits and limitations of the AGARD methodology for testing and extrapolating the results of tests at transonic speeds to predict the performance at full-scale Reynolds numbers,
- (ix) §4.6 for comments on what Reynolds number is sufficient for model tests at transonic speeds (see also the discussion below),
- (x) §4.6 for comments on future testing requirements for laminar flow designs (see also discussion below),
- (xi) §5.3.4 for conclusions on scale effect on afterbody drag,
- (xii) §6.3 for conclusions on scale effect on the forebody flow on the F/A 18 aircraft at high angle-of-attack,
- (xiii) §7.3 for the main conclusions on scale effect on propellers.

The question that is most frequently asked in general discussion on scale effect is what is the Reynolds number beyond which one can extrapolate to full-scale with certainty and confidence. There is no unique answer to this question. One is tempted to say in reply that the only general statement that can be made is that almost every advance in aerodynamic design standards in the past 40 years has led to an apparent need to increase the model test Reynolds number and that this trend is likely to continue in the future<sup>178,316,317</sup>.

For example, when considering high lift at low speeds, it was believed at one time that a test Reynolds number of around  $6-7 \times 10^6$  would be acceptable but the results discussed in this

Agardograph have shown that this view is no longer tenable. While it is true that  $6-7 \times 10^6$  is sufficient to avoid the strong favourable scale effect that often exists in the Reynolds-number range in which there is either a thin-aerofoil (long bubble) or leading-edge (short bubble bursting or turbulent re-separation following re-attachment) stall, experience has shown that further significant scale effect can still be present at higher Reynolds numbers. Comparisons of the  $C_{L,max}$  values for 9 different aircraft types indicate that the values of  $C_{L,max}$  in flight and in model tests at about  $Re = 7 \times 10^6$  can differ by up to  $\pm 0.2$ . The implications for payload at a given approach speed are substantial.

Similarly, when considering drag or buffet onset in cruising flight at transonic speeds, advances in wing design have meant that for reliable prediction of full-scale performance, the model test Reynolds number has had to be increased first from  $2 \times 10^6$  to  $5 \times 10^6$  and then to  $15 \times 10^6$  and there are now indications that with future advances, the normal past experience of favourable scale effects below these values will be replaced by the risk of strongly adverse effects above these model test values unless they are raised further.

The suggestion that there may be adverse scale effects in any situation may come as somewhat of a surprise to the newcomer to the subject and it may be helpful to list the reasons why decreases in  $C_{L,max}$  between model and full-scale can occur. Results discussed in this Agardograph have shown that there can be at least 5 such reasons:

- (i) a forward movement of transition with Reynolds number and, as a result, a reversal of the normal trend for the boundary layer thickness near the trailing edge to decrease with  $Re$ ,
- (ii) trend (i) reinforced by transition being induced by contamination along the leading-edge attachment line (ALT), possibly followed by relaminarisation,
- (iii) a failure to relaminarise beyond a certain Reynolds number,
- (iv) a choice of a highly tuned slat/flap design at the model test Reynolds number and a failure to realise that it needs retuning for operation at the full-scale Reynolds number,
- (v) a change with Reynolds number in the origin of the stall on a three-dimensional configuration because the flow separations in different problem areas, eg in the wing-fuselage junction and near the nacelles or the wing tip are affected to a different degree by scale effect thus leading to a change in the development of the stall, eg the disappearance of one area of local separation may allow another to expand and become more detrimental.

The possible reversal of established trends in the scale effects at transonic speeds is a consequence of the frequent design aim of extending the supercritical region further aft and therefore running the risk that at high Reynolds numbers (but not necessarily at low Reynolds numbers), the shock wave moves on to an aft-facing surface and the separation when it occurs develops more abruptly than at lower Reynolds numbers.

It follows from the above that apart from the NTF and, in some cases the ETW, existing tunnels do not provide a high enough Reynolds number to be sure that the prediction of scale effect is a simple matter of estimating a slow-moving monotonic

trend. Obviously, the first recommendation must be to exploit the NTF and ETW for further study of Reynolds-number effects. In particular, tests in these tunnels should not be limited to obtaining results at a single Reynolds number; more will be learnt by covering a range of Reynolds numbers. It has not been possible to include any results from the NTF in this Agardograph but in Ref 316 there are some intriguing sentences: "One test programme in the NTF provides the aerodynamicist with all the incentive needed to resolve these issues. The information gathered on Reynolds number effects on a wide range of flow situations is truly fantastic to behold".

Leaving aside the NTF and the ETW, the design aerodynamicist has to predict the scale effect on the basis of model tests at the best possible but probably still inadequate Reynolds number. It may be helpful at this point to lay down a recommended procedure in principle for this prediction. In general, one should be wary of uncritical use of "rules of thumb" such as applying the same correction from model to full-scale as on the previous "similar aircraft design". Such practices should certainly be treated with reserve unless one is absolutely sure that the nature of the flow over the two aircraft in the model tests is similar. The maxim "know your flow" should be at the heart of any good prediction procedure. To help in this respect, one should

- (i) test over a range of Reynolds numbers and include small steps in  $Re$  in order to uncover sudden changes in the values of  $C_{L,max}$  such as those shown in Figs 3.55(a) and 3.59,
- (ii) test more than the one favoured configuration; one should explore at the model test Reynolds number, the effects of small changes in the configuration similar to those that might result effectively from the likely changes in viscous effects with Reynolds number,
- (iii) if tests are being made with fixed transition, investigate sensitivity to the precise method adopted for fixing transition,
- (iv) ensure that any supporting CFD calculations should be made for both the model and full-scale Reynolds numbers: a most important point that has been mentioned many times in this document,
- (v) ahead of the tests when possible and certainly during the analysis of the results, identify either with the aid of flow visualisation or calculation where the flow over the model in the tunnel tests lies in various sequences, eg

- (a) thin aerofoil stall - LE stall - TE stall

Fig 3.3 and equations 3.1-3.5 should help in this respect,

- (b) regimes A-B-C in the flow over multi-element aerofoils where

in A, the flow over the flap(s) is attached as a result of favourable interference from a thick wake and downwash from forward elements,

in B, the flow over the flap(s) is separated at incidences below the stall but attached at the stall,

in C, the flow over the flap(s) is separated both below and at the stall.

It should be possible to recognise in which regime the model test is situated by reference to the shape of the lift-incidence curve (see Fig 3.26) and from a study of the pressure distributions. If the results are in A, an increase in Reynolds number should initially bring a gradual increase in  $C_{L,max}$  and then, little further change provided the configuration is forecast to remain in A. Otherwise, if it transfers to B, increasing Reynolds number will bring a reduction in  $C_L$  at a given incidence and possibly an increase in  $C_{L,max}$  prior to a reduction in  $C_{L,max}$ . If B applies in the model test, increase of Reynolds number can bring a sudden reduction in  $C_{L,max}$  by as much as 0.3.

- (c) Attachment line flow laminar - Attachment line flow contaminated (ALT)

ALT is predicted to occur when  $\bar{Re} = [\sin\phi/a]^{1/2}$  is greater than a figure lying between 245 and 700 according to the wing spanwise loading and presence or otherwise of disturbances in the vicinity, where  $\phi$  = LE sweepback and  $a$  = velocity gradient normal to the attachment line. Typically, on a subsonic transport at high lift, this implies that ALT occurs at a chord Reynolds number of about  $7 \times 10^6$  at high lift and so, it may occur within the model test range of some but not all wings in the best (as regards  $Re$  capability) of existing tunnels,

- (d) ALT followed by re-laminarisation - no re-laminarisation

Relaminarisation may occur when  $K > 3 \times 10^{-6}$  and will certainly occur when  $K > 5 \times 10^{-6}$  where  $K$  is given by equation 3.6. Relaminarisation has been observed on part of the leading edge of two civil transports in flight. It is however likely that on many aircraft at high lift, both (c) and (d) will occur between the model test and flight Reynolds numbers,

- and (e) for a slender wing,  $Re_p < 12000$ ,  $12000 < Re_p < 20000$ ,  $Re_p > 20000$  where  $Re_p$  is the Reynolds number based on leading-edge radius.

These ranges correspond respectively to a vortex flow analogous to a long bubble, turbulent separation after reattachment of a laminar bubble and turbulent separation with no laminar separation-bubble.

Similarly, for the flow over a forebody, one should determine where the model tests are relative to the boundaries between the L,B/T and T flow regimes as plotted in Figs 6.3(a,b) for a circular cylinder and appropriately modified in the future for other cross-sections.

In tests in transonic flow, one should determine when the tests with different transition positions form a sequence in scenario 3 or 4 as defined in the AGARD methodology, ie determine whether with the furthest aft transition position, the effective  $Re_{test}$  is above or below  $Re_{crit}$ , marking the lowest Reynolds number where CFD can currently be used for the extrapolation to full-scale.

The prediction of the full-scale results from the model test data is dependent on where the tests lie in these sequences. However, for a subsonic transport aircraft, the scale effect on the stalling data at low speeds is likely to depend ultimately on some detailed local geometrical feature of the design in problem areas such as the wing-fuselage junction, near the nacelles or near the wing tip. These configuration-related scale effects can easily amount to 0.2 or more in  $C_{l,max}$  and can therefore swamp predictions based on what might happen with an idealised configuration. It is this feature of the results that makes it so difficult to extrapolate from past experience even when, in retrospect, one has understood the reasons for the scale effect on a previous aircraft in the family. Even a pipe protruding from the leading edge can have a significant effect!

Before turning to specific recommendations for research, one final point should be made about desirable test Reynolds numbers. The hope must always be that in the model tests, the nature of the flow is similar to that over the full-scale aircraft. In other words, referring back to the various sequences listed above, ideally model and full-scale should both lie above the same boundary, eg if the stall on the full-scale aircraft is triggered by a trailing-edge separation near the nacelle, the same should be true in the model test. This does not mean that one should always strive for the highest possible model test Reynolds number. Approaching but not reaching the desired target carries its dangers. Various examples can be quoted in support of this important conclusion, eg:

- (i) the flow changes on a three-dimensional wing will not occur at the same Reynolds number, based on the wing mean chord, at all stations across the span - because of the wing taper and spanwise loading. To test at a Reynolds number where the change in question has already occurred at a lower Reynolds number on the inner wing sections but has not yet occurred near the tip can lead to very misleading results: this is probably the main reason why pitching moment scale effects can appear to be so mysterious - see §3.4.2.3,
- (ii) in transonic flow, increasing the Reynolds number merely to a value where it is no longer possible to practise aft-transition fixing may be counter-productive as the effective Reynolds numbers could then be lower than at lower test Reynolds numbers,
- (iii) with forebody flows, results obtained when the flow separations are of the B/T type (laminar separation followed by reattachment and then by turbulent separation) may be highly unrepresentative of full-scale on the assumption that the full-scale separation is a pure turbulent separation (T); results at lower Reynolds numbers could be a better guide.

It will be realised that although great progress has been made in the understanding and prediction of scale effects, uncertainties remain and further research is required. One of the difficulties has always been that the scene has been confused by the pseudo-Reynolds number effects discussed in §2. In particular, the effects of Reynolds number, wall interference and support interference are often interlocked in the comparisons and so, advances in the techniques for predicting wall and support interference<sup>324</sup> are important in the context of understanding scale effects.

Finally, to list a set of recommendations for further research:

- 1 Programmes such as that described by Yip et al in Ref 138 should be strongly supported. In this programme, tests are being made in flight (on a Boeing 737-100) in which measurements of surface pressures, surface boundary layer characteristics, wake and off-body flows and structural deformations are being made by a range of advanced techniques and the results are being compared with model test data. This programme is an ambitious exercise being planned on a 5-year basis. Hopefully, the programme will be extended to include tests on advanced high-lift concepts.
- 2 Similar programmes (but with limited focussed objectives) should be undertaken for cases which have exhibited large or unexpected scale effect.
- 3 New CFD codes including allowance for viscous effects should be applied at both model test and full-scale Reynolds numbers in order to improve understanding of likely scale effects. For example, CFD calculations for a test case in which a multiple aerofoil configuration at high lift migrated from region A to B and/or C with increase in Reynolds number would be particularly valuable.
- 4 Research aimed at improving the prediction of transition and the ability to determine transition experimentally in routine testing should be encouraged. In particular, efforts should be made to reduce the present uncertainties as to the values of Re for ALT for tapered, swept wings with different spanwise loadings and fitted with high-lift devices, nacelles and other features present on practical aircraft.
- 5 To improve accuracy of predictions of scale effect at high lift and low speeds, undertake research
  - (a) to further improve the modelling in CFD codes of confluent wakes and boundary layers and also, the development of wakes in regions of adverse pressure gradient in the hope that it will be possible to place less reliance on uncertain empirical factors,
  - (b) to explain examples where there is significant adverse scale effect at high Reynolds number, eg to confirm or otherwise the speculative thoughts in the discussion on slender wings in §3.3.5.2,
  - (c) in the light of results from 4, to design and test wing leading-edge shapes aimed at achieving laminar attachment-line flow at full-scale Reynolds numbers,
  - (d) to understand why, apparently, there is little scale effect on separation in wing-fuselage junctions or separations with a strong degree of spanwise flow.
- 6 To improve accuracy of predictions of scale effect at transonic speeds, undertake research
  - (a) to explore the interaction between a shock-induced and a rear separation and to devise a method for predicting the scale effect when both separations are present in the model tests,

- (b) to demonstrate the likely adverse scale effects on advanced wing sections with extensive supercritical flow,
  - (c) to develop the use of boundary layer control, eg, by suction, as a means of increasing the effective Reynolds number of a model test and so, to avoid the limitations on aft-fixing,
  - (d) to develop scaling laws for laminar/ transitional shock/boundary layer interactions and more generally, to develop a methodology for testing "laminar-flow" designs.
- 7 To improve the ability to obtain a realistic representation of the full-scale flow over aircraft forebodies, undertake research to show how the  $Re-\alpha$  boundaries between different types of flow are affected by forebody cross-sectional shape and also, explore the interaction between two vortex systems lying close together laterally.
  - 8 Undertake further research to clarify the effects of scale on the unsteady flow in deep cavities.
  - 9 Undertake research to confirm and if so, explain the effects of rotational speed as distinct from Mach number on propeller performance.

The above list of about 20 recommendations for research is doubtless not fully comprehensive; the present author takes responsibility for any personal bias. The conclusions in other chapters as listed at the start of chapter 8 may suggest other recommendations to the reader.

## **9 ACKNOWLEDGEMENTS**

The author would like to acknowledge the great help he has received from many experts in many countries while preparing this Agardograph. In particular, he would like to thank his editor, Professor A D Young, for his invaluable comments. He takes full responsibility however for the views expressed and, in particular, for the conclusions and recommendations in chapter 8.

## References

- 1 Elsenaar, A, Binion, T W Jr, Stanewsky, E, "Reynolds Number Effects in Transonic Flow", AGARDograph AG-303, December 1988.
- 2 Laster, M L (ed), "Boundary Layer Simulation and Control in Wind Tunnels", AGARD AR 228, April 1988.
- 3 Jones, B M, Journal RAe Society, Vol 38, 1934, pp 753-770.
- 4 Mabey, D G, "Physical Phenomena Associated with Unsteady Transonic Flows. Unsteady Transonic Aerodynamics", Progress in Astronautics & Aeronautics, Vol 120, 1989.  
and "A Review of Scale Effects in Unsteady Aerodynamics", ICAS 90-341, 1990.
- 5 Aulehla, F, "Calibration-Related Pseudo-Reynolds Number Trends in Transonic Wind Tunnels", Journal of Aircraft, Vol 29, July-August 1992, pp 545-552.
- 6 Elsenaar, A, "On Reynolds Number Effects and Simulation", AGARD CP 429, 1987, Paper no 20.
- 7 Fiddes, S P, Kirby, D A, Woodward, D S, Peckham, D H, "Investigations into the Effects of Scale and Compressibility on Lift and Drag in the RAE 5m Pressurised Low-Speed Wind Tunnel", Journal RAe Society, March 1985, pp 93-108.
- 8 Pearcey, H H, "Shock-Induced Separation and its Prevention by Design and Boundary-Layer Control", in Boundary Layer and Flow Control, its Principles and Application, Volume 2, ed G V Lachman, Pergamon Press, Oxford, 1961.
- 9 Sorrells, R B, Towne, M C, Anderson, C F, Tolbert, R H, "Effects of Inlet Spillage on Store Carriage Loads and Launch Trajectories", AEDC-TMR-84-P23, January 1985.
- 10 "Wall Interference in Wind Tunnels", Fluid Dynamics Panel Specialists Meeting, AGARD CP 335, London, May 1982.
- 11 Pozniak, O M, "A Review of the Effect of Reynolds Number on Afterbody Drag", ARA Report 56, May 1980.
- 12 Aulehla, F, Besigk, G, "Fore- and Afterbody Flow Field Interaction with Consideration of Reynolds Number Effects", AGARD CP 150 and AGARD-AG-208, September 1974 and October 1975.
- 13 Kennedy, T L, "An Evaluation of Wind Tunnel Test Techniques for Aircraft Nozzle Afterbody Testing at Transonic Mach Numbers", AEDC-TR-80-8 (AD-A091775), November 1980.
- 14 Aulehla, F, "Drag Measurements in Transonic Wind Tunnels", AGARD Specialists Meeting in Paris on Aircraft Performance Prediction Methods, October 1977, Paper 7.
- 15 Garner, H C, Rogers, E W E, Acum, W E A, Maskell, E C, "Subsonic Wind Tunnel Corrections", AGARDograph 109, 1966.
- 16 Goethert, B H, "Transonic Wind Tunnel Testing", AGARDograph 49, Pergamon Press, Oxford, 1981.
- 17 Chan, Y Y, "Wall Boundary-Layer Effects in Transonic Wind Tunnels", AGARD CP-335, September 1982.
- 18 Jacocks, J L, "Aerodynamic Characteristics of Perforated Walls for Transonic Tunnels", AEDC-TR-77-61 (AD-A040904), 1977.
- 19 Sickles, W, Erickson, J, "Wall Interference Correction for Three-Dimensional Transonic Flows", AIAA 90-1408, June 1990.
- 20 Binion, T W, Private Communication.
- 21 Stanewsky, E, et al, "High Reynolds Number Tests on the CAST 10-2/DOA 2 Transonic Aerofoil at Ambient and Cryogenic Temperature Conditions", AGARD CP 348, 1983, Paper 10.
- 22 Elsenaar, A, Stanewsky, E, A Report of the GARTEur Action Group on "Two-Dimensional Transonic Testing Methods", AGARD CP 335, 1982, Paper 5.
- 23 Barnwell, R W, "Similarity Rule for Sidewall Boundary-Layer Effect in Two-Dimensional Wind Tunnels", AIAA Journal, September 1980.
- 24 Sewell, W G, "The Effects of Sidewall Boundary Layers in Two-Dimensional Subsonic and Transonic Wind Tunnels", AIAA-81-1297, 1981.
- 25 Bateman, T E B, Private Communication.
- 26 Jones, D J, Chan, Y Y, Nishimura, Y, "A Numerical and Experimental Evaluation of the Boundary Layer Effects on Aerofoils Tested in Wind Tunnel Facilities", RAeS Conference "Wind Tunnels and Wind Tunnel Test Techniques, Paper no 43, September 1992.
- 27 Paschal, K, Goodman, W, McGhee, R, Walker, B, "Evaluation of Tunnel Sidewall Boundary-Layer Control Systems for High-Lift Airfoil Testing", AIAA 91-3243, September 1991.
- 28 Dougherty, N S Jr, Steinle, F W Jr, "Transition Reynolds Number Comparison in Several Major Transonic Tunnels", AIAA 74-627, 1974.
- 29 Murthy, S V, "Effects of Compressibility and Free Stream Turbulence on Boundary Layer Transition in High Subsonic and Transonic Flows", AIAA 86-0764, 1986.
- 30 Sinclair, D W, "A Comparison of Transition Reynolds Number Measured in a Wind Tunnel and in Flight", ASME FED, Vol 114, 1991.
- 31 Green, J E, "On the Influence of Free Stream Turbulence on a Turbulent Boundary Layer, as it Relates to Wind Tunnel Testing at Subsonic Speeds", AGARD-R-602, 1973, Paper 4.
- 32 Buckner, J K, Webb, J B, "Selected Results from the YF-16 Wind-Tunnel Test Program", AIAA 74-619, 1974.
- 33 Vaucheret, X, Bazin, M, Armand, C, "Comparaison d'Essais Transsoniques Bi- et Tridimensionnels Effectués dans Diverses Grandes Souffleries", AGARD CP 187, 1975, Paper 1.
- 34 Sinclair, D W, "Calculated Viscous Effects on Aerofoils at Transonic Speeds", AIAA 88-2027, 1988.
- 35 Elsenaar, A, "Experiences with Transition Fixing in the High Speed Regime at NLR", Grenzschicht Steuerung durch Transitionfixierung, DFVLR Mitteilung 84-17, 1984.
- 36 Private Communication from ONERA.
- 37 Bass, R M, "Small Scale Wind Tunnel Testing of Model Propellers", AIAA-86-0392, January 1986.
- 38 Stanewsky, E, "Interaction between the Outer Inviscid Flow and the Boundary-Layer on Transonic Airfoils", Z Flugwiss, Weltraumforsch 7, Heft 4, 1983, pp 242-252.
- 39 Green, J E, Weeks, D J, Pugh, P G, "Heat Transfer as a Source of Spurious Scale Effects in Subsonic and Transonic Wind Tunnels", AGARD LaWs Paper No 135, 1972.
- 40 Mignosi, A, Arnal, D, Prudhomme, S, "Problems Connected with Laminar Flows in a Cryogenic Wind Tunnel", DFVLR-Bericht 92-06, March 1992, Paper 92-01-015.
- 41 Dougherty, N S, Fisher, D F, "Boundary-Layer Transition on a 10° Cone: Wind Tunnel/Flight Data Correlation", AIAA 80-0154, January 1980.



- 42 Mabey, D G, "A Summary of the Effects of Heat Transfer on Aerodynamics and Possible Implications for Wind Tunnel Tests", AIAA 91-0401, January 1991.
- 43 Reaser, J S, Hallissy, J B, Campbell, R L, "Design and True Reynolds Number 2-D Testing of an Advanced Technology Aerofoil", AIAA-83-1792, July 1983.
- 44 de Bruin, A C, "The Effect of a Single Cylindrical Roughness Element on Boundary Layer Transition in a Favourable Pressure Gradient", IUTAM Symposium, Toulouse, 1989.
- 45 Nikuradse, J, "Strömungsgesetze in Röhren. Forschungschafft 361, 1961.
- 46 Bobbitt, P J, "The Pros and Cons of Code Validation", AIAA 88-2535, 1988.
- 47 Somers, D M, Stack, J P, Harvey, W D, "Influence of Surface Static-Pressure Orifices on Boundary-Layer Transition", NASA TM-84492, July 1982.
- 48 Plentovich, E B, "The Application to Aerofoils of a Technique for Reducing Orifice-Induced Pressure Error at High Reynolds Numbers", NASA TP-2537, January 1986.
- 49 Gloss, B B, "Some Aerodynamic Considerations Related to Surface Definition", NASA CP-2122, Part II, November 1979.
- 50 Radezsky, R H, Reibert, M S, Saric, W S, "Effect of Micron-sized Roughness on Transition in Swept-Wing Flows", AIAA-93-0076.
- 51 Beach, H I Jr, Bushnell, D M, "Aeronautical Facility Requirements into the 2000s", AIAA-90-1375, 1990.
- 52 Johnson, J L, Grafton, S B, Yip, L Y, "Exploratory Investigation of Vortex Bursting on the High Angle-of-Attack Lateral-Directional Stability Characteristics of Highly-Swept Wings", Presented at AIAA 11th Aerodynamic Testing Conference, Colorado Springs, March 1980.
- 53 Earnshaw, P B, Green, A R, Hardy, B C, Jelly, A R, "A Study of the Use of Half-Models in High-Lift Wind-Tunnel Testing", AGARD-CP-515, September 1993, Paper 20.
- 54 DNW Annual Report, 1990.
- 55 Abbott, I H, Von Doenhoff, A E, Stivers, L S, "Summary of Aerofoil Data", NACA Report 824, 1945
- 56 Loftin, L K, Bursnall, W J, "The Effects of Variations in Reynolds Number between  $3.0 \times 10^6$  and  $25 \times 10^6$  upon the Aerodynamic Characteristics of a Number of NACA 6-Series Airfoil Sections", NACA Report 964, 1950
- 57 Jacobs, E N, Sherman, A, "Airfoil Section Characteristics as Affected by Variations of the Reynolds Number", NACA Report 586, 1937
- 58 McCullough, G B, Gault, D E, "Examples of Three Representative Types of Airfoil-Section Stall at Low Speed", NACA TN 2502, September 1951
- 59 Gault, D E, "A Correlation of Low-Speed, Airfoil-Section Stalling Characteristics with Reynolds Number and Airfoil Geometry", NACA TN 3963, January 1957
- 60 Evans, W T, Mort, K W, "Analysis of Computed Flow Parameters for a Set of Sudden Stalls in Low-Speed Two-Dimensional Flow", NACA TN D-85, August 1959
- 61 van den Berg, B, "Reynolds Number and Mach Number Effects on the Maximum Lift and the Stalling Characteristics of Wings at Low Speeds", NLR TR 69025 U, March 1969
- 62 van den Berg, B, "Role of Laminar Separation Bubbles in Airfoil Leading-Edge Stalls", AIAA 81-4104, May 1981
- 63 Woodward, D S, Hardy, B C, Ashill, P R, "Some Types of Scale Effect in Low-Speed, High-Lift Flows", ICAS-88-4.9.3, September 1988
- 64 McGhee, R J, Bingham, C J, "Low-Speed Aerodynamic Characteristics of a 17% Thick Supercritical Airfoil Section, Including a Comparison between Wind-Tunnel and Flight Data", NASA TM X 2571, July 1972
- 65 van den Berg, B, Private Communication
- 66 Valarezo, W O, Dominik, C J, McGhee, R J, Goodman, W L, Paschal, K B, "Multi-Element Airfoil Optimisation for Maximum Lift at High Reynolds Numbers", AIAA-91-3332, September 1991
- 67 Gaster, M, "The Structure and Behaviour of Laminar Separation Bubbles", AGARD CP 4, 1966, pp 819-854
- 67A Young, A D, Horton, H P, "Some Results of Investigations of Separation Bubbles", AGARD CP4, 1966, pp 279-812
- 68 Wallis, R A, "Boundary Layer Transition at the Leading Edge of Thin Wings and its Effect on General Nose Separation", Advances in Aeronautical Sciences, Pergamon Press, Vol 3, 1962, pp 161-184
- 69 Horton, H P, "A Semi-Empirical Theory for the Growth and Bursting of Laminar Separation Bubbles", ARC Report 29185, June 1967
- 70 Arnal, D, Juillen, J C, "Résultats Expérimentaux Relatifs à l'Influence des Processus de Transition sur la Structure Initiale d'une Couche Limite Turbulente", AGARD CP 271, 1979, Paper 22
- 71 van Ingen, J L, "On the Calculation of Laminar Separation Bubbles in Two-Dimensional Incompressible Flow", AGARD CP 168, May 1975, Paper No 11
- 72 Crabtree, L F, "Effects of Leading Edge Separation on Thin Wings in Two-Dimensional Incompressible Flow", Journal Aeronautical Sciences, Vol 24, pp 597-604
- 73 Stratford, B S, "Flow in the Laminar Boundary Layer near Separation", ARC R&M 3002, 1957
- 74 Owen, P R, Klanfer, L, "On the Laminar Boundary Layer Separation from the Leading Edge of a Thin Aerofoil", ARC CP 220, 1955
- 75 Kao, H C, "Some Aspects of Airfoil Stall in Low-Speed Flow", J Aircraft, Vol 11, No 3 March 1974,
- 76 Roshko, A, Lau, J C, "Some Observations on Transition and Reattachment of a Free Shear Layer in Incompressible Flow", Proceedings of the 1965 Heat Transfer and Fluid Mechanics Institute Stanford University, 1965, pp 157-167
- 77 Wallis, B A, "Experiments with Air Jets to Control the Nose Stall on a 3 ft Chord NACA 64A006 Aerofoil", Dept of Supply, ARL Australia Aero Note 139, September 1954
- 78 Moore, T W F, "A Note on the Causes of Thin Airfoil Stall", Journal R Ae Society, Vol 63, December 1959, pp 724-730
- 79 Townend, A A, "Equilibrium Layers and Wall Turbulence", Journal of Fluid Mechanics, Vol 11, August 1961, pp 97-119
- 80 McGregor, I, "Regions of Localised Boundary Layer Separation and their Role in the Nose-Stalling of Aerofoils", PhD Thesis, QMC London, 1954
- 81 Green, J E, Weeks, D J, Brooman, J W F, "Prediction of Turbulent Boundary Layers and Wakes in Compressible Flow by a Lag-Entrainment Method", ARC R&M 3791, 1973
- 82 Smith, A M O, "Aerodynamics of High-Lift Systems", AGARD CP 102, 1972
- 83 Head, M R, "Entrainment in the Turbulent Boundary Layer", ARC R&M 3152, 1958
- 84 Cebeci, T, Smith, A M O, "Analysis of Turbulent Boundary Layers", Academic Press, New York, 1974

- 85 Hahn, M, "Evaluation of Separation Criteria and their Application of Separated Flow Analysis", AFFDL-TR-72-145, 1973
- 86 Simpson, R L, Chew, Y T, Shivaprasad, B G, "The Structure of a Separating Turbulent Boundary Layer", Parts 1,2,3, Journal Fluid Mechanics, Vol 113, December 1981
- 87 Oskam, B, "A Calculation Method for the Viscous Flow around Multi-Component Airfoils", NLR TR 79097 U, September 1980
- 88 Racisz, S F, "Investigation of NACA 65(112)A111 Airfoil with 0.35-Chord Slotted Flap at Reynolds Numbers up to 25 Million", NACA TN 1463, 1947
- 89 McRae, D M, "The Aerodynamic Development of the Wing of the A300B2, Journal of the R Ae Society, July 1973
- 90 Valarezo, W O, Dominik, C J, McGhee, R J, "Reynolds and Mach Number Effects on Multielement Airfoils", Paper presented at 5th Symposium on Numerical and Physical Aspects of Aerodynamic Flows, California State University, Long Beach, January 1992
- 91 McCroskey, W J, Carr, L W, McAllister, K W, "Dynaic Stall Experiments on Oscillating Airfoils", AIAA Journal, Vol 14, No 1, January 1976, pp 56-63
- 92 McCroskey, W J, Phillipe, J J, "Unsteady Viscous Flow on Oscillating Airfoils", AIAA Journal, Vol 13, January 1975, pp 71-79
- 93 Ridder, S O, "Experimental Studies of the Leading-Edge Suction Force, including the Maximum Attainable Suction Force versus Reynolds Number and the Induced Distributions on Various Wing Planforms and Air Intakes", 9th ICAS Congress, Haifa, Israel, August 1974, Paper 74-47
- 94 Foster, D N, Ashill, P R, Williams, B R, "The Nature, Development and Effect of the Viscous Flow round an Aerofoil with High Lift Devices", RAE TR 72227, 1972
- 95 Smith, A M O, "High-Lift Aerodynamics", 37th Wright Brothers Lecture, AIAA 74-939, 1974
- 96 Woodward, D S, Lean, D E, "Where is High Lift Today? - A Review of Past UK Research Programmes", AGARD-CP-515, September 1993, Paper No 1
- 97 Finch, B S P, Wedderspoon, J R, "Investigation into the Performance of a 40° Single-Slotted Flap on a Quasi Two-Dimensional Endplate Model", BAe Weybridge Aero/FM/Report 046, 1978
- 98 van den Berg, B, "Boundary Layer Measurements on a Two-Dimensional Wing with Flap and a Comparison with Calculations", AGARD CP 271, January 1980, Paper No 18
- 99 King, D A, Williams, B R, "Developments in Computational Methods for High-Lift Aerodynamics", Journal RAeSoc, Vol 92, August/ September 1988, pp 265-287
- 100 Vogelaar, H L J, "Description and Validation of the Two-Dimensional Test Setup for Multiple Aerofoils in the Pressurised Wind Tunnel HST", NLR TR 83031 U, March 1983
- 101 Obert, E, "Forty Years of High-Lift R&D - An Aircraft Manufacturer's Experience", AGARD-CP-515, September 1993, Paper No 27
- 102 Meredith, P T, "Viscous Phenomena Affecting High-Lift Systems and Suggestions for Future CFD Development", AGARD-CP-515, September 1993, Paper No 19
- 103 Kusunose, K, Wigton, L, Meredith, P T, "A Rapidly Converging Viscous/Inviscid Coupling Code for Multi-Element Airfoil Configurations", AIAA-91-0177, 1991
- 104 Giles, M, Drela, M, Thompkins, W T Jr, "Newton Solution of Direct and Inverse Transonic Euler Equations", AIAA-85-1530, 1985
- 105 Valarezo, W O, "High Lift Testing at High Reynolds Numbers", AIAA-29-3986, July 1992
- 106 Valarezo, W O, Dominik, C J, McGhee, R J, "High Reynolds Number Configuration Development of a High-Lift Aerofoil", AGARD-CP-515, September 1992, Paper No 10
- 107 Lin, J C, Robinson, S K, McGhee, R J, Valarezo, W O, "Separation Control on High Reynolds Number Multi-Element Airfoils", AIAA 92-2636, June 1992
- 108 Morgan, H L Jr, Ferris, J C, McGhee, R J, "A Study of High-Lift Airfoils at High Reynolds Numbers in the Langley Low-Turbulence Pressure Tunnel", NASA TM 89125, July 1987
- 109 Eggleston, B, Poole, R J D, "High Lift Systems for Transport Aircraft with Advanced Aerofoils", AGARD-CP-515, September 1993, Paper No 32
- 110 van den Berg, B, "An Experimental Investigation on an Airfoil with a Slat into the Effect of the Separation Bubble in the Slat Cove", NLR Memorandum AI-85-001 U, February 1985
- 111 Thibert, J J, "The GARTEur High Lift Research Programme", AGARD-CP-515, September 1993, Paper No 16
- 112 Garner, P L, Meredith, P T, Stoner, R C, "Areas of Future CFD Development as Illustrated by Transport Aircraft Applications", AIAA-91-1527-CP, 1991
- 113 Rogers, S E, Wiltberber, N L, Kwak, D, "Efficient Simulation of Incompressible Viscous Flow over Multi-Element Airfoils", AGARD-CP-515, September 1992, Paper No 7
- 114 Schuster, D M, Birkelbaw, L D, "Numerical Computations of Viscous Flowfields about Multicomponent Aerofoils", AIAA 85-0167, January 1985
- 115 Barth, T J, "Numerical Aspects of Computing Viscous High Reynolds Flows on Unstructured Meshes", AIAA 91-0721, January 1991
- 116 Mavriplis, D, "Turbulent Flow Calculations Using Unstructured and Adaptive Meshes", ICASE Report 90-61, September 1990
- 117 Lynch, F T, Private Communication
- 118 Baldwin, B, Barth, T, "A One-Equation Turbulence Transport Model for High Reynolds Number Wall-Bounded Flows", NASA TM 102847, August 1990
- 119 Baldwin, B, Lomax, H, "Thin Layer Approximation and Algebraic Model for Separated Turbulent Flows", AIAA 78-257, January 1978
- 120 Adair, D, Horne, W C, "Turbulent Separated Flow Over and Downstream of a Two-Element Airfoil", Experiments in Fluids, 7, 1989, pp 531-541
- 121 Omar, E, Zierten, T, Sapiro, E, Mahal, A, "Supercritical Airfoil with Various High-Lift Systems", NACA CR-2215, September 1973
- 122 Valarezo, W O, Chin, V D, "Maximum Lift Prediction for Multielement Wings", AIAA-92-0401, January 1982
- 123 Hall, M G, Treadgold, D A, "Transition on Swept Wings", RAE Technical Memorandum Aero 1465, 1972
- 124 Granville, P S, "The Calculation of the Viscous Drag of Bodies of Revolution", David Taylor Model Basin Report 849, 1953

- 125 Arnal, D, Habiballah, M, Delcourt, V, "Synthèse sur les Méthodes de Calcul de Transition", Rapport Technique No 11/5018, 1980  
Also "Laminar Instability Theory and Transition Criteria in Two and Three Dimensional Flows", La Recherche Aérospatiale no 1984- , 1984
- 126 Launder, B E, Jones, W P, "On the Prediction of Laminarisation", ARC CP 1036, 1969
- 127 Anscombe, A, Illingworth, L N, "Wind Tunnel Observations of Boundary Layer Transition on a Wing at Various Angles of Sweepback", R&M 2968, 1952
- 128 Stuart, J T, "The Instability of Three-Dimensional Boundary Layers", Section 6, Chapter 9 (Hydrodynamic Stability) in 'Laminar Boundary Layers', ed L Rosenhead, Oxford University Press, 1963, pp 549-555
- 129 Michel, R, Arnal, D, Coustols, E, "Stability Calculations and Transition Criteria in Two- and Three-Dimensional Boundary Layers", 2nd Symposium IUTAM on Laminar-Turbulent Transition, Springer Verlag, 1984
- 130 Michel, R, Arnal, D, Coustols, E, Juillen, J C, "Experimental and Theoretical Studies of Boundary Layer Transition on a Swept Infinite Wing", 2nd Symposium IUTAM on Laminar-Turbulent Transition, Springer Verlag, 1984
- 131 Arnal, D, Juillen, J C, Casalis, G, "The Effects of Wall Suction on Laminar-Turbulent Transition in Three-Dimensional Flow", Symposium on Boundary Layer Stability and Transition to Turbulence, Portland, Oregon, June 1991
- 132 Poll, D I A, "Transition in the Infinite Swept Attachment Line Boundary Layer", The Aeronautical Quarterly, Vol XXX, Part 4, November 1979, pp 607-629
- 133 Poll, D I A, "Some Aspects of the Flow near a Swept Attachment Line with Particular Reference to Boundary Layer Transition", C of A Report 7805, August 1978
- 134 Paisley, D J, Poll, D I A, "Further Studies of Flow over Swept Back Wings", Cranfield CIT Contractors Report NFP 4, 1983
- 135 Gaster, M, "On the Flow along Swept Leading Edges", the Aeronautical Quarterly, Vol XVIII, May 1967, pp 165-184
- 136 Hardy, B C, "Experimental Investigation of Attachment-Line Transition in Low-Speed, High-Lift Wind-Tunnel Testing", AGARD CP 438, 1988, Paper 2
- 137 Brune, G W, McMasters, J H, "Computational Aerodynamics Applied to High-Lift Systems", Applied Computational Aerodynamics, ed P A Henne, Progress in Astronautics and Aeronautics, 1990, Vol 125
- 138 Yip, L P, Vijgen, P M H W, Hardin, J D, van Dam, C P, "In-Flight Pressure Distributions and Skin-Friction Measurements on a Subsonic Transport High-Lift Wing Section", AGARD-CP-515, September 1993, Paper 21
- 139 Haines, A B, "Some Evidence Concerning Scale Effect on Low Speed Stalling Characteristics", ARA Aero Memo 52, October 1964
- 140 Furlong, G C, McHugh, J C, "A Summary and Analysis of the Low-Speed Longitudinal Characteristics of Swept Wings at High Reynolds Numbers", NACA Report 1339, 1957
- 141 Haines, A B, Rhodes, C W, "Tests in the Royal Aircraft Establishment 10 ft x 7 ft High Speed Tunnel on 50° Sweptback Wings", ARC R&M 3043, 1957
- 142 Haines, A B, "Aerodynamic Interference - a General Overview", AGARD Report 712, 1983
- 143 Moir, I R M, "An Experimental Investigation of the Optimum Slat Setting on a Combat Aircraft Model", AGARD-CP-515, September 1993, Paper 17
- 144 Hardy, B C, "An Experimental Investigation of Attachment-Line Transition on the Slat of a Combat Aircraft Model", AGARD-CP-515, September 1993, Paper 18
- 145 Gregory, N, Love, E M, "Laminar Flow on a Swept Leading Edge", NPL Aero Memo 26, 1965
- 146 Poll, D I A, "On the Generation and Subsequent Development of Spiral Vortex Flow over a Swept-Back Wing", AGARD-CP-342, 1983, Paper 6
- 147 Elsenaar, A, Eriksson, G, (eds), Proceedings of the Symposium on the "International Vortex Flow Experiment on Euler Code Validation", Stockholm, October 1-3 1986, published by FFA
- 148 de Bruin, A C, Hoeijmakers, H W M, "Transition and Separation on a 65 deg Swept Delta Wing at 20 deg Angle of Attack", NLR MP 86075, 1986 (also included in Ref 146)
- 149 Elsenaar, A, Hjelmberg, L, Butefisch, K, Bannink, W J, "The International Vortex Flow Experiment", AGARD-CP-437, 1988
- 150 Elsenaar, A, Butefisch, K A, "Experimental Study on Vortex and Shock Wave Development on a 65° Delta Wing", Proceedings of Symposium Transsonicum III, IUTAM, 1988
- 151 Elsenaar, A, Hoeijmakers, H W M, "An Experimental Study of the Flow over a Sharp-Edged Delta Wing at Subsonic and Transonic Speeds", AGARD-CP-494, 1990
- 152 Ashill, P R, Fulker, J L, Simmons, N J, Betts, C J, "Flow Features of Highly-Swept Wings at Subsonic and Supersonic Speeds", ICAS-90-3.9.1, September 1990
- 153 Ashill, P R, Betts, C J, "A Study of the Flow around a Leading Edge of a Highly Swept Wing in a Low Speed Tunnel", ASME Symposium on Transitional and Turbulent Compressible Flows in the 1993 ASME Fluid Engineering Conference, Washington DC, June 21-24 1993
- 154 Lamar, J E, Johnson, T D Jr, "Sensitivity of F-106E Leading-Edge-Vortex Images to Flight and Vapor-Screen Parameters" NASA TP 2818, June 1988
- 155 Lamar, J E, "Vapor-Screen Technique Applied to a Delta-Wing Aircraft", Proceedings of the 5th International Symposium on Flow Visualisation, Prague, Czechoslovakia, August 21-25, 1989
- 156 Sutton, E P, "Some Observations of the Flow over a Delta-Winged Model with 55 deg leading-edge Sweep, at Mach Numbers between 0.4 and 1.8", ARC R&M 3190, 1960
- 157 Erickson, G E, "Water-Tunnel Studies of Leading-Edge Vortices", Journal of Aircraft, Vol 19, No 6, 1982, pp 442-448
- 158 FDP Panel, "Symposium on Aerodynamics of Vortical Type Flows in Three Dimensions - Round Table Discussion", AGARD-CP-342, April 1983
- 159 Green, J E, "A Discussion of Viscous-Inviscid Interactions at Transonic Speeds", RAE Technical Report 72050, 1972
- 160 Fulker, J L, Ashill, P R, "A Study of the Factors Influencing Shock-Induced Separation on Swept Wings", RAE Technical Report 83088, 1983
- 161 Dee, F W, Nicholas, O P, "Flight Determination of Wing Flow Patterns and Buffet Boundaries for the Fairey Delta 2 Aircraft at Mach Numbers between 0.4 and 1.3, and Comparison with Wind Tunnel Results", ARC R&M 3482, 1967

- 162 O'Hara, F, Scott-Wilson, J B, "An Investigation of the Flow over a Half-Wing Model with 60.5° Leading Edge Sweepback, at a High Subsonic and Supersonic Speeds", ARC CP 471, 1955
- 163 Sutton, E P, Evans, G P, McGuinness, M D, Svehla, K M, "Influence of Wall Vibrations on a Flow with Boundary-Layer Separation at a Convex Edge", Proceedings IUTAM Symposium on Unsteady Turbulent Shear Flows, Toulouse, France, 1981
- 164 Sutton, E P, "Experiments on a Flow with Swept Separation and Reattachment of a Boundary Layer", Proceedings IUTAM Symposium on Three-Dimensional Turbulent Boundary Layers, Berlin, March 1982
- 165 Poll, D I A, "On the Generation of Subsequent Development of Spiral Vortex Flow over a Swept-Back Wing" AGARD-CP-342, 1983, Paper 6
- 166 Jordan, R, Private Communication, ARA Ltd.
- 167 Lamar, J E, Campbell, J F, "Recent Studies at NASA-Langley of Vortical Flows Interacting with Neighbouring Surfaces", AGARD-CP-342, 1983, Paper 10
- 168 Beasley, J A, "Calculation of the Laminar Boundary Layer and the Prediction of Transition on a Sheared Wing", ARC R&M 3787, 1973
- 169 Narasimha, R, "Transition-Zone Models for 2-Dimensional Boundary Layers: a Review", Sadhana, Vol 14, Part 2, November 1989, pp 93-120
- 170 Emmons, H W, "The Laminar-Turbulent Transition in a Boundary Layer - Part I", J Aerospace Sciences, Vol 18, No 7, July 1951, pp 490-498
- 171 Schubauer, G B, Kelbanoff, P S, "Contributions on the Mechanics of Boundary Layer Transition", Proceedings of a Symposium on 'Boundary Layer Effects in Aerodynamics', NPL, March 1955, Paper 4
- 172 Narasimha, R, "On the Distribution of Intermittency in the Transition Region of a Boundary Layer", J Aerospace Sciences, Vol 24, No 9, September 1957, pp 711-712
- 173 Gaudet, L, Betts, C J, Ashill, P R, "Experimental Investigation of Boundary-Layer Transition on a Natural Laminar Flow Aerofoil", DFVLR-Bericht 92-06, March 1992, Paper 92-01-018
- 174 Elsenaar, A, "The Wind Tunnel as a Tool for Laminar Flow Research", Proceedings 17th Congress of ICAS, Stockholm, September 1990, Paper 90-6.1.1
- 175 Henderson, M L, "Two-Dimensional Separated Wake Modelling and its Use to Predict Maximum Section Lift Coefficient", AIAA-78-156, January 1978
- 176 McIntosh, W, Wimpres, J E, "Prediction and Analysis of the Low Speed Stall Characteristics of the Boeing 747", AGARD LS 74, March 1975
- 177 Saiz, M, Quemard, C, "Essais dans la Soufflerie F1 de l'ONERA Comparaison Vol-Soufflerie", AGARD CP-348, February 1984, Paper 22
- 178 Mack, M D, McMasters, J H, "High Reynolds Number Testing in Support of Transport Airplane Development", AIAA 92-3982
- 179 McMasters, J H, Roberts, W H, Payne, F M, Sanford, M C, Durham, M, "Recent Air-Freon Tests of a Transport Airplane in High-Lift Configurations", AIAA 88-2034, May 1988
- 180 Schaufele, R D, Ebeling, A W, "Aerodynamic Design of the DC-9 Wing and High-Lift System", SAE 670846, October 1967
- 181 Flaig, A, Hilbig, R, "High-Lift Design for Large Civil Aircraft", AGARD-CP-515, September 1993, Paper 31
- 182 Wedderspoon, J R, "The High Lift Development of the A320 Aircraft", ICAS-86-2.3.2, August 1986
- 183 Haines, A B, "Experience in the Use of a Viscous Simulation Methodology for Tests in Transonic Tunnels", AIAA 90-1414, June 1990
- 184 Elsenaar, A, "Experience with Transition Fixing in the High Speed Regime at NLR", Grenzschicht Steuerung durch Transitionfixierung, DFVR Mitteilung 84-17, October 1984
- 185 Ashill, P R, Weeks, D J, Fulker, J L, "Wind Tunnel Experiments on Aerofoil Models for the Assessment of Computational Flow Methods", AGARD CP-437, 1988, Paper 4
- 186 Collyer, M R, Lock, R C, "Prediction of Viscous Effects in Steady Transonic Flow past an Aerofoil", Aero Qu, 30, 3, 1979, pp 485-505
- 187 Ashill, P R, Wood, R F, Weeks, D J, "An Improved, Semi-Inverse Version of the Viscous Garabedian and Korn Method (VGK)", RAE TR 87002, January 1987
- 188 Goldhammer, M I, Steinle, F W Jr, "Design and Validation of Advanced Transonic Wings Using CFD and Very High Reynolds Number Wind Tunnel Testing", ICAS-90-2.6.2, September 1990
- 189 Fulker, J L, Ashill, P R, "A Study of the Factors Influencing Shock-Induced Separation on Swept Wings", RAE TR 83088, December 1983
- 190 Pallister, K C, Parker, J, Probert, B, "Comparison of Recent Results from Different Wind Tunnel Facilities along with Comparisons of Measured Flight Results and Wind Tunnel Based Predictions", AIAA-92-3985, July 1992
- 191 Stanewsky, E, "Interaction Between the Outer Inviscid Flow and the Boundary Layer on Transonic Aerofoils", Dissertation TU-Berlin (D83), 1981 (also Z Flugwiss Weltraumforsch 7 (1983), Heft 4, pp 242-252)
- 192 Pearcey, H H, Osborne, J, Haines, A B, "The Interaction Between Local Effects at the Shock and Rear Separation - a Source of Significant Scale Effects in Wind-Tunnel Tests on Aerofoils and Wings", AGARD CP-35, 1968, Paper 11
- 193 Stanewsky, E, Basler, D, "Experimental Evidence of Buffet Onset and Penetration on a Supercritical Airfoil at Transonic Speeds", AGARD CP-483, 1988, Paper 4
- 194 Spaid, F W, "Comparisons among Measured and Computed Boundary-Layer Properties on a Transport Wing", AIAA-87-2555, 1987
- 195 Caughey, D A, Jameson, A, "Recent Progress in Finite Volume Calculations for Wing-Fuselage Combinations", AIAA-79-1513, July 1979
- 196 Smith, P D, "An Integral Prediction Method for Three-Dimensional Compressible Turbulent Boundary Layers", R&M 3739, 1974
- 197 Cebeci, T, Kaups, K, Ramsey, J A, "A General Method for Calculating Three-Dimensional Compressible Laminar and Turbulent Boundary Layers on Arbitrary Wings", NASA CR-2777, 1977
- 198 Cebeci, T, Kaups, K, Ramsey, J A, Schimke, S M, "A Two-Point Finite-Difference Boundary-Layer Method for Incompressible and Axisymmetric Laminar and Turbulent Flows Including Infinite Swept Wings", DAC Report MDC J7986, 1978
- 199 Lynch, F T, "Experimental Necessities for Subsonic Transport Configuration Development", AIAA-92-0158, January 1992
- 200 Hirose, N, Miwa, H, "Computational and Experimental Research on Buffet Phenomena of Transonic Airfoils", IUTAM Symposium Transsonicum III, Springer-Verlag, Berlin Heidelberg, 1989, pp 489-499

- 201 Mabey, D G, "Review of Aircraft Dynamic Loads due to Flow Separation", AGARD CP-494, July 1991, Paper 12
- 202 Coe, C F, Cunningham, A M, "Prediction of F-111 TACT Aircraft Buffet Response and Correlation of Fluctuating Pressures Measured on Aluminium and Steel Models and the Aircraft", NACA CR 4069, May 1987
- 203 Olsen, M E, Seegmiller, H L, "Low Aspect Ratio Wing Code Validation Experiment", AIAA-92-0402, January 1992
- 204 McMillan, S N, Pittman, J L, Thomas, J L, "A Computational Study of Incipient Leading-Edge Separation on a 65° Delta Wing at  $M = 1.60$ ", AIAA-90-3029-CP, August 1990
- 205 Poisson-Quinton, Ph, Vaucheret, X, "Prediction of Aerodynamic Characteristics of an Aircraft from a Correlation of Results on a Calibration Model Tested in Various Large Transonic Tunnels", AGARD-CP-242, 1977, Paper 15
- 206 Haines, A B, "27th Lanchester Memorial Lecture - Scale Effect in Transonic Flow", J RAeS, Vol 91, No 907, 1987, pp 291-313
- 207 Browne, C G, Bateman, T E B, Pavitt, M, Haines, A B, "A Comparison of Wing Pressure Distributions Measured in Flight and on a Wind Tunnel Model of the Super VC10", R&M 3707, 1972
- 208 Hutton, P G, "An Investigation of Transition Fixing Technique for a 10.5% Thick, 28° Sweptback Wing at High Subsonic Speeds and  $R = 3 \times 10^6$ ", ARC CP 1215, 1972
- 209 Vatsa, V N, Wedan, B W, "Development of an Efficient Multigrid Code for 3-D Navier-Stokes Equations", AIAA-89-1791, June 1989
- 210 Elsenaar, A, "The Wind Tunnel as a Tool for Laminar Flow Research", ICAS-90-6.1.1, September 1990
- 210A Green, J E, "The Second Goldstein Lecture: Modern Developments in Fluid Dynamics - an Addendum", Journal RAeS, Vol 96, No 953, March 1992, pp 69-86.
- 211 Lock, R C, "The Prediction of the Drag of Aerofoils and Wings at High Subsonic Speeds", Journal RAe Society, June/July 1986
- 212 Lock, R C, "Prediction of the Drag of Wings at Subsonic Speeds by Viscous/Inviscid Interaction Techniques", AGARD R-723, 1985
- 213 "A Method of Determining the Wave Drag and its Spanwise Distribution on a Finite Wing in Transonic Flow", ESDU TM 87003, 1987
- 214 Winter, K G, Gaudet, L, "Turbulent Boundary Layer Studies at High Reynolds Numbers at Mach Numbers between 0.2 and 2.8", RAE TR 70251, 1970
- 215 Covert, G, (ed), "Thrust and Drag: its Prediction and Verification", Progress in Astronautics and Aeronautics, Vol 98, 1985
- 216 "Subcritical Lift-Dependent Drag of Wings", ESDU Data Sheets 66031, 66032, March 1967
- 217 Hutton, P G, Unpublished ARA Report
- 218 Haftmann, B, Debbeler, F-J, Gielen, H, "Takeoff Drag Prediction for Airbus A300-600 and A310 Compared with Flight Test Results", AIAA Journal of Aircraft, Vol 25, No 12, pp 1088-1096, December 1988
- 219 Butler, S F J, "Technical Evaluation Report on Fluid Dynamics Panel Specialists' Meeting on Aerodynamic Drag", AGARD-AR-58, 1973
- 220 MacWilkinson, D G, Blackerby, W T, Paterson, J H, "Correlation of Full-Scale Drag Predictions with Flight Measurements on the C-141A Aircraft - Phase II, Wind Tunnel Test Analysis and Prediction Techniques - Volume 1", NASA CR-LG73R0058, June 1973
- 221 Paterson, J H, MacWilkinson, D G, Blackerby, W T, "A Survey of Drag Prediction Techniques Applicable to Subsonic and Transonic Aircraft Design", AGARD-CP-124, 1973
- 222 Saltzman, E J, Ayers, T G, "A Review of Flight-to-Wind Tunnel Drag Correlation", AIAA-81-2475, 1981
- 223 Arnaiz, H H, Peterson, J B Jr, Daugherty, J C, "Wind-Tunnel/Flight Correlation Study of Aerodynamic Characteristics of a Large Flexible Supersonic Cruise Airplane (XB-70-1). III - A Comparison between Characteristics Predicted from Wind-Tunnel Measurements and those Measured in Flight", NASA TP-1516, 1980
- 224 Spratley, A B, Thompson, E R, Kennedy, T L, "Reynolds Number and Nozzle Afterbody Configuration Effects on Model Forebody and Afterbody Drag", AIAA-77-103, January 1977
- 225 Chamberlin, R, Blaha, B J, "Flight and Wind Tunnel Investigation of the Effects of Reynolds Number on Installed Boattail Drag at Subsonic Speeds", AIAA-73-139, January 1978
- 226 Wilcox, F A, Chamberlin, R, "Reynolds Number Effects on Boattail Drag of Exhaust Nozzles from Wind Tunnel and Flight Tests", AGARD-CP-150, Paper 21, NASA TM X-71548, March/September 1974
- 227 Reubush, D E, "The Effect of Reynolds Number on the Boattail Drag of Two Wing-Body Combinations", AIAA/SAE 11th Propulsion Conference, Anaheim, September 1975
- 228 Reid, J, Kurn, A G, "The Effect of Boundary Layer Thickness on Afterbody Drag", RAE Report 79083, 1979
- 229 Ferri, A, (ed), "Improved Nozzle Testing Techniques in Transonic Flow", AGARD-AG-208, October 1975
- 230 Postlewaite, J E, Slaeman, U, "Exhaust System Interaction Programme - Final Technical Report", AFATL-TR-73-59, AD-769086, 1973
- 231 Zonars, D, Laughrey, J A, Bowers, D L, "Effect of Varying Reynolds Number and Boundary Displacement Thickness on the External Flow over Nozzle Boattails", AGARD-AG-208, Paper I-F, October 1975
- 232 Blaha, B J, Chamberlin, R, Baber, L J, "Boundary Layer Thickness Effect on Boattail Drag", AIAA 76-676, NASA TM-X-73443, July 1976
- 233 Chow, W L, Bober, L H, Anderson, B H, "Numerical Calculation of Transonic Boattail Flow", NASA TN D-7984, 1975
- 234 Presz, W M, Pitkin, E T, "Flow Separation over Axisymmetric Afterbody Models", J Aircraft, Vol 11, pp 677-682, November 1974
- 235 Presz, W M, Pitkin, E T, "An Analytical Model of Axisymmetric Afterbody Flow Separation", AIAA-75-65, January 1975
- 236 Presz, W M, King, R W, Buteau, J D, Putnam, L E, "An Improved Analytical Model of the Separated Region of Nozzle Boattails", AIAA-78-995, 1978
- 237 Wilmoth, R G, "Analytical Study of Viscous Effects on Transonic Flow over Boattail Nozzles", AIAA-77-223, January 1977
- 238 Richey, G K, Bowers, D L, "Wind Tunnel/Flight Test Correlation Program on the B-1 Nacelle Afterbody/Nozzle at Transonic Conditions", AIAA-78-989, July 1978
- 239 Lucas, E J, "Evaluation of Wind Tunnel Nozzle Afterbody Test Techniques Utilising a Modern Twin Engine Fighter Geometry at Mach Numbers from 0.6 to 1.2", AEDC-TR-79-2098, October 1980

- 240 Price, E A, Jr, "An Investigation of F-16 Nozzle-Afterbody Forces at Transonic Mach Numbers with Emphasis on Model Scale Effects", AEDC-TR-80-57, AFWAL-TR-81-2110, September 1981
- 241 "Report of the Working Group on Aerodynamics of Aircraft Afterbodies", AGARD-AR-226, June 1986
- 242 Peace, A J, "A Method for Calculating Axisymmetric Afterbody flows", *Journal of Propulsion and Power*, Volume 3, No 4, pp 357-364, July-August 1987
- 243 Peace, A J, "Turbulent Flow Predictions for Afterbody/Nozzle Geometries Including Base Effects", *Journal of Propulsion and Power*, Vol 7, No 4, pp 396-403, May-June 1991
- 244 Pozniak, O M, Haines, A B, "Afterbody Drag Measurement at Transonic Speeds on a Series of Twin and Single Afterbodies Terminating at the Jet Exit", *ARA Report 29*, ARC 34280, February 1973
- 245 Lamont, P J, "Pressure Measurements on an Ogive-Cylinder at High Angles of Attack with Laminar, Transitional and Turbulent Separation", *AIAA-80-1556*, 1980
- 246 Lamont, P J, "Pressures Around an Inclined Ogive-Cylinder with Laminar, Transitional or Turbulent Separation", *AIAA Journal*, 20, 11, pp 1492-1499, November 1982
- 247 Lamont, P J, "The Complex Asymmetric Flow over a Nose and Cylindrical Afterbody at High Angles of Attack", *AIAA-82-0053*, 1982
- 248 Hunt, B L, "Asymmetric Vortex Forces and Wakes on Slender Bodies", *AIAA-82-1336*, 1982
- 249 Polhamus, F C, "A Review of Some Reynolds Number Effects Related to Bodies at High Angles of Attack", *NASA CR 3809*, 1984
- 250 Reding, J P, Ericsson, L E, "Maximum Side Forces and Associated Yawing Moments on Slender Bodies", *Journal of Spacecraft and Rockets*, 17, 6, pp 515-521, 1980
- 251 Ericsson, L E, Reding, J P, "Aerodynamic Effects of Asymmetric Vortex Shedding from Slender Bodies", *AIAA-85-1797*, 1985
- 252 Poll, D I A, "On the Effects of Boundary-Layer Transition on a Cylindrical Afterbody at Incidence in Low-Speed Flow", *Journal RAe Society*, pp 315-327, October 1985
- 253 James, W D, Paris, S W, "Study of Viscous Crossflow Effects on Circular Cylinders at High Reynolds Numbers", *AIAA Journal*, 18, 9, pp 1062-1072, September 1980
- 254 Clark, W H, "Body Vortex Formation on Missiles in Incompressible Flows", *AIAA-77-1154*, August 1977
- 255 Champigny, P, "Reynolds Number Effect on the Aerodynamic Characteristics of an Ogive-Cylinder at High Angles of Attack", *AIAA-84-2176*, June 1984
- 256 Conway, J T, "An Effect of Boundary Layer Transition on Axisymmetric Bodies at Incidence", *MSc Dissertation*, Cranfield Institute of Technology, September 1982
- 257 Kueth, A M, "Some Aspects of Boundary-Layer Transition and Flow Separation on Cylinders in Yaw", *Proceedings of the 1st Mid-Western Conference on Fluid Dynamics*, Ann Arbor, Michigan, USA, 1950
- 258 Banks, D W, Fisher, D F, Erickson, G E, Jordan, F L, Hall, R M, Sewell, W G, "Comparison of Wind Tunnel and Flight Forebody Flow Fields on the NASA F-18 High-Alpha Research Vehicle", *NASA High-Angle-of-Attack Technology Conference*, *NASA CP-3139*, Part 1, Vol 1, pp 243-264, May 1992
- 259 Lamont, P J, "The Effect of Reynolds Number on Normal and Side Forces on Ogive-Cylinders at High Incidence", *AIAA-85-1799*, 1985
- 260 Allen, H J, Perkins, E W, "Characteristics of Flow over Inclined Bodies of Revolution", *NACA RM-A50L07*, March 1951
- 261 Hall, R M, "Influence of Reynolds Number on Forebody Side Forces for 3.5-Diameter Tangent-Ogives", *AIAA-87-2274*, 1987
- 262 Keener, E R, "Flow-Separation Patterns on Symmetric Forebodies", *NASA TM 86016*, January 1986
- 263 Sarpkaya, T, Schoaff, R L, "Inviscid Model of Two-Dimensional Vortex Shedding by a Circular Cylinder", *AIAA Journal*, Vol 17, No 11, pp 1193-2000, November 1979
- 264 Champigny, P G, "Stability of Side Forces on Bodies at High Angles of Attack", *AIAA-86-1776-CP*, June 1986
- 265 Keener, E R, Chapman, G T, Cohen, L, Talaghani, J, "Side Forces on Forebodies at High Angles of Attack and Mach Numbers from 0.1 to 0.7. Two Tangent Ogives, Paraboloid and Cone", *NASA TM X-3438*, February 1977
- 266 Erickson, G E, "Water Tunnel Flow Visualisation and Wind Tunnel Data Analysis of the F/A-18", *NASA CR-165859*, May 1982
- 267 Grafton, S B, Chambers, J R, Coe, P L, Jr, "Wind-Tunnel Free-Flight Investigation of a Model of a Spin Resistant Fighter Configuration", *NASA TN D-7716*, June 1974
- 268 Carr, P C, Gilbert, W P, "Effects of Fuselage Forebody Geometry on Low-Speed Lateral-Directional Characteristics of a Twin-Tail Fighter Model at High Angles of Attack", *NASA TP 1592*, December 1979
- 269 Banks, D W, "Wind-Tunnel Investigation of the Forebody Aerodynamics of a Vortex-Lift Fighter Configuration at High Angles of Attack", *SAE Technical Paper Series 881419*, October 1988
- 270 Fisher, D F, Richwine, D M, Banks, D W, "Surface Flow Visualisation of Separated Flows on the Forebody of an F-18 Aircraft and Wind-Tunnel Model", *NASA TM-100436*, June 1988
- 271 Fisher, D F, Banks, D W, Richwine, D M, "F-18 High Alpha Research Vehicle Surface Pressures: Initial In-Flight Results and Correlation with Flow Visualisation and Wind-Tunnel Data", *NASA TM-101724*, 1990
- 272 Erickson, G E, Hall, R M, Banks, D W, Del Frate, J H, Schreiner, J A, Hanley, R J, Pulley, C T, "Experimental Investigation of the F/A-18 Vortex Flow at Subsonic Through Transonic Speeds", *AIAA-89-2222*, July-August 1989
- 273 Ghaffari, G F, Luckring, J M, Thomas, J M, Bates, B L, "Navier-Stokes Solutions about the F/A-18 Forebody-LEX Configuration", *AIAA-89-0338*, January 1989
- 274 Schiff, L B, Cummings, R M, Sorenson, R L, Rizk, Y M, "Numerical Simulation of High-Incidence Flow over the F-18 Fuselage Forebody", *AIAA-89-0339*, January 1989
- 275 Del Frate, J H, Fisher, D F, Zuniga, F A, "In-Flight Flow Visualisation with Pressure Measurements at Low Speeds on the NASA F-18 High Alpha Research Vehicle", *NASA TM 101726*, October 1990
- 276 Del Frate, J H, Zuniga, F A, "In-Flight Analysis on the NASA F-18 High Alpha Research Vehicle with Comparisons to Ground Facility Data", *AIAA-90-0231*, January 1990
- 277 Meyn, L A, Lanser, W R, James, K D, "Full-Scale High Angle-of-Attack Tests of an F/A-18", *AIAA-92-2676*, June 1992

- 278 Lee, B, Brown, D, "Wind Tunnel Studies of F/A-18 Tail Buffet", AIAA-90-1432, June 1990
- 279 Zimmerman, N H, Ferman, M A, "Prediction of Tail Buffet Loads for Design Application", NADC-88043-60, July 1987
- 280 Martin, C A, Glaister, M K, MacLaren, L D, Meyn, L A, Ross, J, "F/A-18 1/9th Scale Model Tail Buffet Measurements", Flight Mechanics Report 188, ARL Melbourne, June 1990
- 280A Shah, G H, Grafton, S B, Guynn, M D, Brandon, J B, Dansberry, B E, "Effect of Vortex Flow Characteristics on Tail Buffet and High-Angle-of-Attack Aerodynamics of a Twin-Tail Fighter Configuration", High-Angle-of-Attack Technology Conference, October 1990
- 280B Rizk, Y M, Gee, K, "Numerical Prediction of the Unsteady Flowfield around the F-18 Aircraft at Large Incidence", AIAA-91-0020, 29th Aerospace Sciences Meeting, January 1989
- 281 Lanser, W R, Meyn, L A, "Forebody Flow Control on a Full-Scale F/A-18 Aircraft", AIAA-92-2674, June 1992
- 282 Gee, K, Rizk, Y M, Murman, S M, Lanser, W R, Meyn, L A, Schiff, L B, "Analysis of a Pneumatic Forebody Control Concept About a Full Aircraft Geometry", AIAA-92-2678, June 1992
- 283 Dix, R E, "On Simulation Techniques for the Separation of Stores from Internal Installations", SAE Technical Paper Series 871799, October 1977
- 284 Bauer, R C, Dix, R E, "Engineering Model of Unsteady Flow in a Cavity", AEDC-TR-91-17, December 1991
- 285 Dix, R E, Bauer, R C, "Engineering Model Predictions of Aeroacoustic Amplitudes in a Weapons Cavity", AIAA-93-0858, January 1993
- 286 Suhs, N E, "Computations of Three-Dimensional Cavity Flow at Subsonic and Supersonic Mach Numbers", AIAA-87-1208, June 1987
- 287 Suhs, N E, "Transonic Flow Calculations for a Cavity with and without a Store", AEDC-TR-92-4, September 1992
- 288 Wilcox, F J Jr, "Experimental Measurements of Internal Store Separation Characteristics at Supersonic Speeds", Store Carriage, Integration and Release, RAe Society, pp 5.1-5.16, 1990
- 289 Stallings, R L Jr, Wilcox, F J Jr, "Experimental Cavity Pressure Distributions at Supersonic Speeds", NASA TP-2683, 1987
- 290 Rossiter, J E, "Wind-Tunnel Experiment on the Flow over Rectangular Cavities at Subsonic and Transonic Speeds", R&M 3438, October 1964
- 291 Tracy, M B, Plentovich, E B, Chu, J, "Measurements of Fluctuating Pressure in a Rectangular Cavity in Transonic Flow at High Reynolds Number", NASA TM-4363, June 1992
- 292 Shaw, L, Banaszak, D, "Weapons Internal Carriage/Separation - "WICS", Aeroacoustic Research", AFWAL-TM-86-243-FIBG, March 1987
- 293 AGARD FDP WG13, "Air Intakes for High Speed Vehicles", AGARD-AR-270, September 1991
- 294 Youngmans, J L, Hoelmer, W, Stockman, N O, "Low Speed Effects of Reynolds Number and Lip Geometry on High Bypass Ratio Inlet Performance", AIAA-28-0059, January 1982
- 295 Hoelmer, W, Youngmans, J L, Raynal, J C, "Effect of Reynolds Number of Upper Cowl Flow Separation", ICAS Paper No 1.10.1, September 1984
- 296 Stockman, N O, Farrel, C A Jr, "Improved Computer Programs for Calculating Potential Flow in Propulsion System Inlets", NASA TM-73728, 1977
- 297 Harris, J E, Blanchard, D K, "Computer Program for Solving Laminar, Transitional or Turbulent Compressible Boundary-Layer Equations for Two-Dimensional and Axi-Symmetric Flow", NASA TM-83207, 1982
- 298 Haines, A B, "A Comparison of Aerofoil Data for use in Single Radius Propeller Calculations", R&M 2188, January 1947
- 299 Bass, R M, "Techniques of Model Propeller Testing", SAE Technical Paper Series 830750, April 1983
- 300 Himmelskamp, H, "Profiluntersuchungen an ein Umlaufenden Propeller Mitteilung aus dem Max-Planck Institut für Strömforschung", Göttingen, 1950
- 301 Trebble, W J G, "Investigation of the Aerodynamic Performance and Noise Characteristics of a 1/5th Scale Model of the Dowty Rotol R212 Propeller", RAE TM Aero 1983, November 1983
- 302 Trebble, W J G, "Investigations of the Aerodynamic Performance of a Dowty Rotol Propeller at Full-Scale in the 24 ft Tunnel", RAE TM 2012, August 1984
- 303 Private communication.
- 304 Hurst, D W, Methven, P N, Owen, D T, "Wind Tunnel Testing of Small Scale Pressure Tapped Model Propellers", RAe Society Conference on Low Speed Aerodynamics, October 1986
- 305 Narramore, J C, "Use of Navier-Stokes Code to Predict Flow Phenomena near Stall as Measured on a 0.658-Scale V-22 Tiltrotor Blade", AIAA-89-1814, June 1989, NLR TR 90341 L
- 306 Harris, F D, "Preliminary Study of Radial Flow Effects on Rotor Blades", Journal of the American Helicopter Society, Vol 11, No 3, 1966
- 307 Milborrow, D J, "Changes in Aerofoil Characteristics due to Radial Flow on Rotating Blades", British Wind Energy Association, 7th Annual Workshop, Oxford, March 1985
- 308 Schlichting, H, "Boundary-Layer Theory", 7th Edition, McGraw-Hill Book Company, New York, pp 694-696, 1979
- 309 Steger, J, Van Dalsem, W R, "Navier-Stokes and Viscous-Inviscid Interactions", NASA CP 3020, Vol 1, Part 2, 1988
- 310 Johnston, L J, "A Calculation Method for Compressible Three-Dimensional Flows", VKI Tech Note 167, 1988
- 311 Forsey, C R, Maina, M, Scrase, N, "Development and Evaluation of an Euler Code for Propeller Flow Field Prediction and Thrust/Drag Accounting", Paper no 29, RAe Society 1993 European Forum 'Recent Developments and Applications in Aeronautical CFD', September 1993
- 312 Borst, H V, "Aerodynamic Design and Analysis of Two Propellers for Mini-Remotely Piloted Air Vehicles, Vol 1 - Open Propellers", USA AMRDL-TR-77-45A, January 1978
- 313 Lynch, F T, Valarezo, W O, McGhee, R J, "The Adverse Aerodynamic Impact of Very Small Leading-Edge Ice (Roughness) Buildups on Wings and Tails", AGARD-DP-496, Paper No 12, 1992
- 314 Young, A D, Paterson, J H, "Aircraft Excrescence Drag", AGARD-AG-264, July 1981
- 315 Jones, R C, Williams, D H, "The Effects of Surface Roughness on Characteristics of Aerofoils NACA 0012 and RAF 34", R&M 1708, 1936
- 316 Ljungstrom, B L G, "Wind Tunnel Investigation of Simulated Hoar Frost on a Two-Dimensional Wing Section with and without High Lift Devices", FFA Report AU-902, 1972

- 317 Gregory, N, O'Reilly, C L, "Low Speed Aerodynamic Characteristics of NACA 0012 Aerofoil Section including the Effects of Upper Surface Roughness Simulating Hoar Frost", R&M 3726, 1973
- 318 Weeks, D J, "Tests on the Effects of Simulated Frost Deposits on Take-Off Performance of a Model of Transport Aircraft (Hawker-Siddeley Trident 3B)", RAE TR 71178, 1971
- 319 Wendt, B J, Greber, J, Hingst, W R, "The Structure and Development of Streamwise Vortex Arrays Embedded in a Turbulent Boundary Layer", NASA Tech Memo 105211, 1991
- 320 Brumby, R E, "The Effect of Wing Ice Contamination on Essential Flight Characteristics", SAE Aircraft Ground De-Icing Conference, September 1988
- 321 Cebeci, T, Chang, K C, "Calculation of Incompressible Rough-Wall Boundary-Layer Flows", AIAA Journal, Vol 16, No 7, pp 730-735, July 1978
- 322 Lynch, F T, "Experimental Necessities for Subsonic Transport Configuration Development", AIAA-92-0158, January 1992
- 323 Lynch, F T, Klinge, M D, "Some Practical Aspects of Viscous Drag Reduction Concepts", SAE Technical Paper No 912129, September 1991
- 324 Lynch, F T, Crites, R C, Spaid, F W, "The Crucial Role of Wall Interference, Support Interference and Flow Field Measurements in the Development of Advanced Aircraft Configurations", AGARD FDP Symposium, Brussels, Paper No 1, October 1993
- 325 Woodward, D S, "An Investigation of the Parameters Controlling the Behaviour of Laminar Separation Bubbles", ARC 29, 446, FM 3888, 1967  
also  
Woodward, D S, "The 2D Characteristics of a 12% Thick RAE 100 Aerofoil Section", R&M 3648, 1971



REPORT DOCUMENTATION PAGE											
1. Recipient's Reference	2. Originator's Reference AGARD-AG-323	3. Further Reference ISBN 92-835-0754-1	4. Security Classification of Document UNCLASSIFIED/ UNLIMITED								
5. Originator	Advisory Group for Aerospace Research and Development North Atlantic Treaty Organization 7 rue Ancelle, 92200 Neuilly sur Seine, France										
6. Title	SCALE EFFECTS ON AIRCRAFT AND WEAPON AERODYNAMICS										
7. Presented on											
8. Author(s)/Editor(s) A.B. Haines Edited by A.D. Young		9. Date July 1994									
10. Author(s)/Editor's Address See Flyleaf		11. Pages 246									
12. Distribution Statement		There are no restrictions on the distribution of this document. Information about the availability of this and other AGARD unclassified publications is given on the back cover.									
13. Keywords/Descriptors											
<table border="0"> <tr> <td>Aerodynamics</td> <td>High lift at low speeds</td> </tr> <tr> <td>Scale effects</td> <td>Transonic flow</td> </tr> <tr> <td>Reynolds number effects</td> <td>Wind tunnels</td> </tr> <tr> <td>Aircraft drag</td> <td></td> </tr> </table>				Aerodynamics	High lift at low speeds	Scale effects	Transonic flow	Reynolds number effects	Wind tunnels	Aircraft drag	
Aerodynamics	High lift at low speeds										
Scale effects	Transonic flow										
Reynolds number effects	Wind tunnels										
Aircraft drag											
14. Abstract											
<p>The present state of knowledge on scale effects at high lift and low speeds, at transonic speeds, and on aircraft drag are presented. In addition, scale effects in various important specific scale-sensitive areas such as forebody vortex flows, the flow in and near open cavities, the flow into an air intake, the flow over propellers, and on ice accretion simulation testing are discussed. The emphasis is on scale effects that have been observed in flight-tunnel comparisons for specific aircraft.</p> <p>It is concluded that much has been learned about scale effects; however, precise prediction can still be difficult. Twenty recommendations for further research are mentioned.</p> <p>This AGARDograph has been produced at the request of the Fluid Dynamics Panel of AGARD.</p>											

<p>AGARDograph 323 Advisory Group for Aerospace Research and Development, NATO SCALE EFFECTS ON AIRCRAFT AND WEAPON AERODYNAMICS By A.B. Haines; Edited by A.D. Young Published July 1994 246 pages</p> <p>The present state of knowledge on scale effects at high lift and low speeds, at transonic speeds, and on aircraft drag are presented. In addition, scale effects in various important specific scale-sensitive areas such as forebody vortex flows, the flow in and near open cavities, the flow into an air intake, the flow over propellers, and on ice accretion simulation testing are discussed. The emphasis is</p> <p>P.T.O.</p>	<p>AGARD-AG-323</p> <p>Aerodynamics Scale effects Reynolds number effects Aircraft drag High lift at low speeds Transonic flow Wind tunnels</p>	<p>AGARDograph 323 Advisory Group for Aerospace Research and Development, NATO SCALE EFFECTS ON AIRCRAFT AND WEAPON AERODYNAMICS By A.B. Haines; Edited by A.D. Young Published July 1994 246 pages</p> <p>The present state of knowledge on scale effects at high lift and low speeds, at transonic speeds, and on aircraft drag are presented. In addition, scale effects in various important specific scale-sensitive areas such as forebody vortex flows, the flow in and near open cavities, the flow into an air intake, the flow over propellers, and on ice accretion simulation testing are discussed. The emphasis is</p> <p>P.T.O.</p>	<p>AGARD-AG-323</p> <p>Aerodynamics Scale effects Reynolds number effects Aircraft drag High lift at low speeds Transonic flow Wind tunnels</p>
<p>AGARDograph 323 Advisory Group for Aerospace Research and Development, NATO SCALE EFFECTS ON AIRCRAFT AND WEAPON AERODYNAMICS By A.B. Haines; Edited by A.D. Young Published July 1994 246 pages</p> <p>The present state of knowledge on scale effects at high lift and low speeds, at transonic speeds, and on aircraft drag are presented. In addition, scale effects in various important specific scale-sensitive areas such as forebody vortex flows, the flow in and near open cavities, the flow into an air intake, the flow over propellers, and on ice accretion simulation testing are discussed. The emphasis is</p> <p>P.T.O.</p>	<p>AGARD-AG-323</p> <p>Aerodynamics Scale effects Reynolds number effects Aircraft drag High lift at low speeds Transonic flow Wind tunnels</p>	<p>AGARDograph 323 Advisory Group for Aerospace Research and Development, NATO SCALE EFFECTS ON AIRCRAFT AND WEAPON AERODYNAMICS By A.B. Haines; Edited by A.D. Young Published July 1994 246 pages</p> <p>The present state of knowledge on scale effects at high lift and low speeds, at transonic speeds, and on aircraft drag are presented. In addition, scale effects in various important specific scale-sensitive areas such as forebody vortex flows, the flow in and near open cavities, the flow into an air intake, the flow over propellers, and on ice accretion simulation testing are discussed. The emphasis is</p> <p>P.T.O.</p>	<p>AGARD-AG-323</p> <p>Aerodynamics Scale effects Reynolds number effects Aircraft drag High lift at low speeds Transonic flow Wind tunnels</p>

<p>on scale effects that have been observed in flight-tunnel comparisons for specific aircraft.</p> <p>It is concluded that much has been learned about scale effects; however, precise prediction can still be difficult. Twenty recommendations for further research are mentioned.</p> <p>This AGARDograph has been produced at the request of the Fluid Dynamics Panel of AGARD.</p> <p>ISBN 92-835-0754-1</p>	<p>on scale effects that have been observed in flight-tunnel comparisons for specific aircraft.</p> <p>It is concluded that much has been learned about scale effects; however, precise prediction can still be difficult. Twenty recommendations for further research are mentioned.</p> <p>This AGARDograph has<sup>a</sup> been produced at the request of the Fluid Dynamics Panel of AGARD.</p> <p>ISBN 92-835-0754-1</p>
<p>on scale effects that have been observed in flight-tunnel comparisons for specific aircraft.</p> <p>It is concluded that much has been learned about scale effects; however, precise prediction can still be difficult. Twenty recommendations for further research are mentioned.</p> <p>This AGARDograph has been produced at the request of the Fluid Dynamics Panel of AGARD.</p> <p>ISBN 92-835-0754-1</p>	<p>on scale effects that have been observed in flight-tunnel comparisons for specific aircraft.</p> <p>It is concluded that much has been learned about scale effects; however, precise prediction can still be difficult. Twenty recommendations for further research are mentioned.</p> <p>This AGARDograph has been produced at the request of the Fluid Dynamics Panel of AGARD.</p> <p>ISBN 92-835-0754-1</p>

AGARD

NATO OTAN

7 RUE ANCELLE · 92200 NEUILLY-SUR-SEINE

FRANCE

Télécopie (1)47.38.57.99 · Téléc 610 176

DIFFUSION DES PUBLICATIONS

AGARD NON CLASSIFIEES

Aucun stock de publications n'a existé à AGARD. A partir de 1993, AGARD détiendra un stock limité des publications associées aux cycles de conférences et cours spéciaux ainsi que les AGARDographies et les rapports des groupes de travail, organisés et publiés à partir de 1993 inclus. Les demandes de renseignements doivent être adressées à AGARD par lettre ou par fax à l'adresse indiquée ci-dessus. *Veuillez ne pas téléphoner.* La diffusion initiale de toutes les publications de l'AGARD est effectuée auprès des pays membres de l'OTAN par l'intermédiaire des centres de distribution nationaux indiqués ci-dessous. Des exemplaires supplémentaires peuvent parfois être obtenus auprès de ces centres (à l'exception des Etats-Unis). Si vous souhaitez recevoir toutes les publications de l'AGARD, ou simplement celles qui concernent certains Panels, vous pouvez demander à être inclut sur la liste d'envoi de l'un de ces centres. Les publications de l'AGARD sont en vente auprès des agences indiquées ci-dessous, sous forme de photocopie ou de microfiche.

# CENTRES DE DIFFUSION NATIONAUX

## ALLEMAGNE

Fachinformationszentrum,  
Karlsruhe  
D-7514 Eggenstein-Leopoldshafen 2

## BELGIQUE

Coordonnateur AGARD-VSL  
Etat-Major de la Force Aérienne  
Quartier Reine Elisabeth  
Rue d'Evere, 1140 Bruxelles

## CANADA

Directeur du Service des Renseignements Scientifiques  
Ministère de la Défense Nationale  
Ottawa, Ontario K1A 0K2

## DANEMARK

Danish Defence Research Establishment  
Ryvangs Allé 1  
P.O. Box 2715  
DK-2100 Copenhagen Ø

## ESPAGNE

INTA (AGARD Publications)  
Pintor Rosales 34  
28008 Madrid

## ETATS-UNIS

NASA Headquarters  
Attention: CF 37, Distribution Center  
300 E Street, S.W.  
Washington, D.C. 20546

## FRANCE

O.N.E.R.A. (Direction)  
29, Avenue de la Division Leclerc  
92322 Châtillon Cedex

## GRECE

Hellenic Air Force  
Air War College  
Scientific and Technical Library  
Dekelia Air Force Base  
Dekelia, Athens TGA 1010

## ISLANDE

Director of Aviation  
c/o Flugrad  
Reykjavik

## ITALIE

Aeronautica Militare  
Ufficio del Delegato Nazionale all'AGARD  
Aeroporto Pratica di Mare  
00040 Pomezia (Roma)

## LUXEMBOURG

Voir Belgique

## NORVEGE

Norwegian Defence Research Establishment  
Attn: Biblioteket  
P.O. Box 25  
N-2007 Kjeller

## PAYS-BAS

Netherlands Delegation to AGARD  
National Aerospace Laboratory NLR  
P.O. Box 90502  
1006 BM Amsterdam

## PORTUGAL

Força Aérea Portuguesa  
Centro de Documentação e Informação  
Alfragide  
2700 Amadora

## ROYAUME UNI

Defence Research Information Centre  
Kentigern House  
65 Brown Street  
Glasgow G2 8EX

## TURQUIE

Milli Savunma Başkanlığı (MSB)  
ARGE Daire Başkanlığı (ARGE)  
Ankara

**Le centre de distribution national des Etats-Unis ne détient PAS de stocks des publications de l'AGARD.**

D'éventuelles demandes de photocopies doivent être formulées directement auprès du NASA Center for Aerospace Information (CASI) à l'adresse suivante:

# AGENCES DE VENTE

NASA Center for  
Aerospace Information (CASI)  
800 Elkridge Landing Road  
Linthicum Heights, MD 21090-2934  
United States

ESA/Information Retrieval Service  
European Space Agency  
10, rue Mario Nikis  
75015 Paris  
France

The British Library  
Document Supply Division  
Boston Spa, Wetherby  
West Yorkshire LS23 7BQ  
Royaume Uni

Les demandes de microfiches ou de photocopies de documents AGARD (y compris les demandes faites auprès du CASI) doivent comporter la dénomination AGARD, ainsi que le numéro de série d'AGARD (par exemple AGARD-AG-315). Des informations analogues, telles que le titre et la date de publication sont souhaitables. Veuillez noter qu'il y a lieu de spécifier AGARD-R-nnn et AGARD-AR-nnn lors de la commande des rapports AGARD et des rapports consultatifs AGARD respectivement. Des références bibliographiques complètes ainsi que des résumés des publications AGARD figurent dans les journaux suivants:

Scientific and Technical Aerospace Reports (STAR)  
publié par la NASA Scientific and Technical  
Information Program  
NASA Headquarters (JTT)  
Washington D.C. 20546  
Etats-Unis

Government Reports Announcements and Index (GRA&I)  
publié par le National Technical Information Service  
Springfield  
Virginia 22161  
Etats-Unis

(accessible également en mode interactif dans la base de données bibliographiques en ligne du NTIS, et sur CD-ROM)



Imprimé par Specialised Printing Services Limited  
40 Chigwell Lane, Loughton, Essex IG10 3TZ

AGARD

NATO OTAN

7 RUE ANCELLE · 92200 NEUILLY-SUR-SEINE

FRANCE

Telefax (1)47.38.57.99 · Telex 610 176

# DISTRIBUTION OF UNCLASSIFIED AGARD PUBLICATIONS

AGARD holds limited quantities of the publications that accompanied Lecture Series and Special Courses held in 1993 or later, and of AGARDographs and Working Group reports published from 1993 onward. For details, write or send a telefax to the address given above. *Please do not telephone.*

AGARD does not hold stocks of publications that accompanied earlier Lecture Series or Courses or of any other publications. Initial distribution of all AGARD publications is made to NATO nations through the National Distribution Centres listed below. Further copies are sometimes available from these centres (except in the United States). If you have a need to receive all AGARD publications, or just those relating to one or more specific AGARD Panels, they may be willing to include you (or your organisation) on their distribution list. AGARD publications may be purchased from the Sales Agencies listed below, in photocopy or microfiche form.

## NATIONAL DISTRIBUTION CENTRES

### BELGIUM

Coordonnateur AGARD — VSL  
Etat-Major de la Force Aérienne  
Quartier Reine Elisabeth  
Rue d'Evere, 1140 Bruxelles

### CANADA

Director Scientific Information Services  
Dept of National Defence  
Ottawa, Ontario K1A 0K2

### DENMARK

Danish Defence Research Establishment  
Ryvangs Allé 1  
P.O. Box 2715  
DK-2100 Copenhagen Ø

### FRANCE

O.N.E.R.A. (Direction)  
29 Avenue de la Division Leclerc  
92322 Châtillon Cedex

### GERMANY

Fachinformationszentrum  
Karlsruhe  
D-7514 Eggenstein-Leopoldshafen 2

### GREECE

Hellenic Air Force  
Air War College  
Scientific and Technical Library  
Dekelia Air Force Base  
Dekelia, Athens TGA 1010

### ICELAND

Director of Aviation  
c/o Flugrad  
Reykjavik

### ITALY

Aeronautica Militare  
Ufficio del Delegato Nazionale all'AGARD  
Aeroporto Pratica di Mare  
00040 Pomezia (Roma)

### LUXEMBOURG

*See Belgium*

### NETHERLANDS

Netherlands Delegation to AGARD  
National Aerospace Laboratory, NLR  
P.O. Box 90502  
1006 BM Amsterdam

### NORWAY

Norwegian Defence Research Establishment  
Attn: Biblioteket  
P.O. Box 25  
N-2007 Kjeller

### PORTUGAL

Força Aérea Portuguesa  
Centro de Documentação e Informação  
Alfragide  
2700 Amadora

### SPAIN

INTA (AGARD Publications)  
Pintor Rosales 34  
28008 Madrid

### TURKEY

Milli Savunma Başkanlığı (MSB)  
ARGE Daire Başkanlığı (ARGE)  
Ankara

### UNITED KINGDOM

Defence Research Information Centre  
Kentigern House  
65 Brown Street  
Glasgow G2 8EX

### UNITED STATES

NASA Headquarters  
Attention: CF 37, Distribution Center  
300 E Street, S.W.  
Washington, D.C. 20546

**The United States National Distribution Centre does NOT hold stocks of AGARD publications.**

Applications for copies should be made direct to the NASA Center for Aerospace Information (CASI) at the address below.

## SALES AGENCIES

### NASA Center for

Aerospace Information (CASI)  
800 Elkridge Landing Road  
Linthicum Heights, MD 21090-2934  
United States

### ESA/Information Retrieval Service

European Space Agency  
10, rue Mario Nikis  
75015 Paris  
France

### The British Library

Document Supply Centre  
Boston Spa, Wetherby  
West Yorkshire LS23 7BQ  
United Kingdom

Requests for microfiches or photocopies of AGARD documents (including requests to CASI) should include the word 'AGARD' and the AGARD serial number (for example AGARD-AG-315). Collateral information such as title and publication date is desirable. Note that AGARD Reports and Advisory Reports should be specified as AGARD-R-*nnn* and AGARD-AR-*nnn*, respectively. Full bibliographical references and abstracts of AGARD publications are given in the following journals:

Scientific and Technical Aerospace Reports (STAR)  
published by NASA Scientific and Technical  
Information Program  
NASA Headquarters (JTT)  
Washington D.C. 20546  
United States

Government Reports Announcements and Index (GRA&I)  
published by the National Technical Information Service  
Springfield  
Virginia 22161  
United States  
(also available online in the NTIS Bibliographic  
Database or on CD-ROM)



Printed by Specialised Printing Services Limited  
40 Chigwell Lane, Loughton, Essex IG10 3TZ